Unveiling the superfluid and solid behaviour in dipolar supersolids

– DISSERTATION –

by

Elena Poli, MSc.

submitted to the Faculty of Mathematics, Computer Science,
and Physics of the University of Innsbruck

in partial fulfillment of the requirements
for the degree of Doctor of Philosophy (PhD)

advisor:

Univ.-Prof. Dr. Francesca Ferlaino,
Institute for Experimental Physics, University of Innsbruck

Innsbruck, September 2025

Abstract

Ultracold atomic gases offer a highly controllable platform for studying fundamental properties of quantum matter. Since the first realization of Bose-Einstein condensation, the field has progressed rapidly, enabling increasingly sophisticated experiments aimed at deepening our understanding of quantum matter under controllable conditions. Among the atomic species brought to quantum degeneracy, highly magnetic atoms such as chromium, erbium, and dysprosium have opened new directions for research. Their large magnetic dipole moments introduce long-range and anisotropic dipolar interactions, which, in competition with short-range contact interactions, give rise to a rich landscape of many-body phenomena. A particularly exciting development is the possibility to access supersolid phase of matter, which uniquely combine superfluid and crystalline properties–two properties typically considered mutually exclusive.

This thesis presents a theoretical study of two-dimensional dipolar supersolids, with a focus on the characterization of their solid and superfluid properties. Using extensive numerical simulations, we identify the key control parameters that enabled the first experimental observation of the transition from one-dimensional to two-dimensional supersolidity. We further study the formation dynamics of the supersolid states and characterize the excitation spectrum to determine the nature of the gapless modes, each associated with a spontaneously broken symmetry. Within a hydrodynamic framework, we extract sound velocities and elastic parameters, including the shear modulus, which serves as signature of solid behaviour.

The superfluid nature is explored via studies of the system's rotational dynamics. We first focus on collective angular oscillations, known as the scissor mode, and assess whether the frequency of this mode provides information about the superfluid fraction. We then explore a different regime by implementing full rotations through magnetic field stirring. This protocol enables the nucleation of quantized vortices, topological defects manifesting as phase singularities. These are one of the most distinctive manifestation of superfluid nature. These studies led to the first experimental observations of vortices in rotating dipolar supersolids.

Finally, the results of this thesis are extended to propose a novel application of dipolar supersolids as quantum analogues of the inner crust of neutron stars. We develop a model to simulate glitches, sudden spin-up events usually observed in pulsars, via vortex unpinning mechanisms. We show how dipolar supersolids provide a unique opportunity to study both vortex and crystal dynamics during such events, which remain inaccessible through direct astrophysical observation. This work marks the first concrete application of supersolids to large scale systems, like neutron stars, and an important step towards quantum simulations of stellar objects from Earth.

Zusammenfassung

Ultrakalte atomare Gase bieten eine äußerst kontrollierbare Plattform zur Untersuchung grundlegender Eigenschaften quantenmechanischer Materie. Seit der ersten Realisierung der Bose-Einstein-Kondensation hat sich das Forschungsfeld rasant entwickelt und ermöglicht zunehmend anspruchsvollere Experimente, die darauf abzielen, unser Verständnis quantenmechanischer Materie unter kontrollierbaren Bedingungen zu vertiefen. Unter den atomaren Spezies, die in den Zustand quantenmechanischer Entartung gebracht wurden, haben hochmagnetische Atome wie Chrom, Erbium und Dysprosium neue Forschungsrichtungen eröffnet. Ihre großen magnetischen Dipolmomente führen zu langreichweitigen und anisotropen Dipol-Dipol-Wechselwirkungen, die im Zusammenspiel mit kurzreichweitigen Kontaktwechselwirkungen eine Vielzahl komplexer Vielteilchenphänomene hervorrufen. Eine besonders spannende Entwicklung ist der Zugang zu einer supersoliden Phase der Materie, die auf einzigartige Weise superfluide und kristalline Eigenschaften vereint–zwei Merkmale, die üblicherweise als unvereinbar gelten.

Diese Arbeit präsentiert eine theoretische Untersuchung zweidimensionaler dipolarer Supersolide mit dem Schwerpunkt auf der Charakterisierung ihrer festen und superfluiden Eigenschaften. Mithilfe umfangreicher numerischer Simulationen identifizieren wir die entscheidenden Kontrollparameter, die die erste experimentelle Beobachtung des Übergangs von eindimensionaler zu zweidimensionaler Supersolidität ermöglichten. Wir untersuchen darüber hinaus die Formationsdynamik der supersoliden Zustände und charakterisieren das Anregungsspektrum, um die Natur der masselosen Moden zu bestimmen, die jeweils mit einer spontan gebrochenen Symmetrie assoziiert sind. Innerhalb eines hydrodynamischen Modells extrahieren wir Schallgeschwindigkeiten und elastische Parameter, einschließlich des Schermoduls, der als Kennzeichen des festen Verhaltens dient.

Die superfluide Natur wird durch Untersuchungen der Rotationsdynamik des Systems erforscht. Zunächst konzentrieren wir uns auf kollektive Winkeloszillationen, bekannt als "Scissor Mode", und analysieren, ob die Frequenz dieser Mode Informationen über den Superfluidanteil liefert. Anschließend untersuchen wir ein anderes Regime, indem wir vollständige Rotationen durch Rühren mit Magnetfeldern implementieren. Dieses Protokoll ermöglicht die Nukleation quantisierter Wirbel–topologischer Defekte, die sich als Phasensingularitäten manifestieren und eine der deutlichsten Erscheinungsformen der Superfluidität darstellen. Diese Studien führten zur ersten experimentellen Beobachtung von Wirbeln in rotierenden dipolaren Supersoliden.

Abschließend werden die Ergebnisse dieser Arbeit genutzt, um eine neuartige Anwendung dipolarer Supersolide als Quantenanaloga der inneren Kruste von Neutronensternen vorzuschlagen. Wir entwickeln ein Modell zur Simulation sogenannter "Glitches" –plötzlicher Spin-up-Ereignisse, wie sie typischerweise bei Pulsaren beobachtet werden– über Mechanismen des Wirbel-Entpinnens. Wir zeigen, wie dipolare Supersolide eine

einzigartige Möglichkeit bieten, sowohl Wirbel- als auch Kristalldynamik während solcher Ereignisse zu untersuchen, die einer direkten astrophysikalischen Beobachtung bislang unzugänglich sind. Diese Arbeit stellt die erste konkrete Anwendung von Supersoliden auf großskalige Systeme wie Neutronensterne dar und einen wichtigen Schritt hin zu quantenmechanischen Simulationen stellaren Objekte von der Erde aus.

Contents

List of Acronyms

ADI-TSSP Alternate direction implicit-time splitting pseudospectral

AR Aspect ratio

BdG Bogoliubov–de Gennes

BEC Bose–Einstein condensate

BECs Bose–Einstein condensates

DDI Dipole-dipole interaction

GP Gross-Pitaevskii

GPE Gross-Pitaevskii equation

eGPE Extended Gross-Pitaevskii equation

LHY Lee-Huang Yang

MF Mean-field

NCRI Non-classical rotational inertia

NCTI Non-classical translational inertia

SeGPE Stochastic extended Gross-Pitaevskii equation

TOF Time-of-flight

Introduction

In our everyday life, we instinctively categorize the objects around us based on their characteristics. We often consider properties like colour, size, and shape, as well as textures—whether something is rough or smooth, shiny or dull, hard or soft, flexible or rigid. We also classify objects by their fundamental nature, for example distinguishing between solids and fluids. These qualities help us make sense of the world and organize our perceptions.

However, when we enter the quantum realm, objects follow different rules. The clear distinctions we use to classify things in the classical world often no longer apply. Instead, quantum objects can exhibit a blend of properties that seem contradictory from a classical perspective. New states of matter originate, like fluids that can flow without viscosity commonly known as *superfluids*. But, most importantly, quantum systems can simultaneously display behaviours typical of different natures, challenging our conventional understanding of how matter behaves.

<p align="center">"Can a solid be superfluid?"</p>

This is the paradoxical question that Leggett proposed to the community in 1970. The story of this query is anything but linear. Over the last 50 years, this problem has been investigated, seemingly solved, denied, reversed into "*Can a superfluid be solid?*" and eventually resolved thanks to scientific and technological advances in the platform of ultracold quantum gases. The heritage of this question forms the core of this doctoral thesis: the study of paradoxical quantum objects with a dual solid-superfluid nature, namely a *supersolid*.

Motivation and historical background

Ultracold gases have proven to be ideal platforms to study quantum phenomena [1]. Indeed, cooling a system to extremely low temperatures enables access to the quantum realm, where particles no longer follow well-defined trajectories. Instead, they lose their individuality and exhibit wave-like properties, which can overlap and interact. This overlap brings quantum mechanics to the forefront, enhancing effects like superposition, interference, and entanglement [2]. What makes ultracold atomic gases particularly valuable is their high degree of control and tunability. Parameters like temperature, interaction strength, and dimensionality can be precisely controlled, creating an ideal setting for probing fundamental phenomena.

Once particles are in the quantum regime, they obey different statistics. Fermions, characterized by half-integer spins such as protons, neutrons and electrons, obey Fermi-Dirac statistics and are constrained by Pauli's exclusion principle. The focus of this
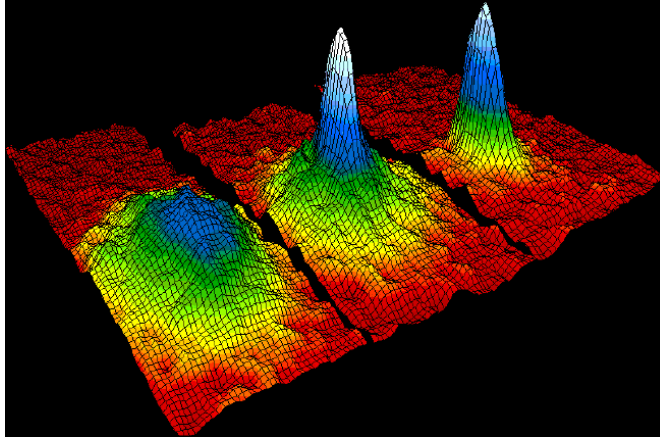
Figure 1.: First experimental realization of a Bose-Einstein condensate. This 3D plots show the evolution of atomic density as the cloud is progressively cooled toward the absolute zero (from left to right). The appearance of a sharp central peak signals the onset of Bose-Einstein condensation.

thesis will be on bosons, that are particles which follow Bose-Einstein statistics which allows multiple particles to occupy the same quantum state.

When bosonic particles occupy all the same quantum state at the lowest energy, i. e. the *ground state*, they become indistinguishable and collectively behave as a single coherent quantum entity described by a giant wave function. This phase of matter is called Bose-Einstein condensate (BEC). Initially predicted in 1925 by Einstein [3], building on a paper by Bose about the statistical behaviour of light quanta published the year before [4], it took many years to access experimental observe Bose-Einstein condensation. The first important step was done in 1938 by London [5], who connected the phenomenon of Bose-Einstein condensation to the recently observed inviscid liquid helium [6, 7]. The absence of viscosity on a quantum fluid was called *superfluidity*, a property that will be deeply investigated in this thesis. Since then, numerous studies have been conducted to better understand the relationship between condensation and superfluidity and most of them were tested experimentally on superfluid helium. Landau developed the first comprehensive theory of superfluidity based on the spectrum of elementary excitations [8] and a decade after Penrose and Onsager consolidated the concept that the existence of dissipationless motion is really linked to BEC [9].

Liquid helium provided an excellent platform to test the first theoretical predictions on Bose-Einstein condensation and superfluidity. However, the strong particle interactions in these systems introduce complexities far beyond Einstein's ideal-gas paradigm. Decades later, advancements in atomic physics, particularly techniques like laser cooling and magneto-optical trapping [10], enabled experimental studies on dilute atomic gases of neutral atoms. Remarkably, alkali atoms emerged as ideal candidates for laser-based cooling methods due to their optical transitions aligning with available laser frequencies and their advantageous internal energy-level structures, which enable efficient cooling to ultralow temperatures. Once trapped, their temperature can be further reduced using evaporative cooling techniques [11]. This groundbreaking approach led to the first observation of Bose-Einstein condensation in 1995. Nobel laureates Cornell and Wieman achieved this milestone in Boulder with ^{87}Rb atoms [12], while Ketterle ac-

complished it with ^{23}Na atoms at MIT [13]; see Fig.1. In the same years, the first evidence of the occurrence of Bose–Einstein condensation in vapours of ^{7}Li was also reported [14,15]. Nowadays, Bose–Einstein condensation has been achieved in a variety of atomic species [16–28].

Among the species that have undergone Bose-Einstein condensation, highly magnetic atoms with a permanent large magnetic moment such as chromium, erbium, dysprosium, and more recently thulium and europium, have given rise to richer physics due to the long-range and anisotropic dipolar interaction. Indeed, the competition between the short-range contact interaction and the long-range contact interaction opens the possibility to access to the *supersolid phase of matter*, where a crystalline structure coexist with superfluid properties [29].

Thesis overview

At the start of my work in the Theory Group in Francesca Ferlaino's team, dipolar supersolids made of gases of strongly magnetic elements had just been realized in ^{162}Dy BECs by Giovanni Modugno's group in Pisa [30], Tilman Pfau's group in Stuttgart [31] and in ^{166}Er and ^{164}Dy BECs by my group in Innsbruck [32]. The observed supersolid state manifested as a one-dimensional crystalline structure composed of a few crystal sites. This discovery prompted a plethora of fundamental questions: How scalable is this system? What is the optimal geometry to reveal the coexisting superfluid and solid nature? What is the most unambiguous evidence of these properties? Finally, is there any potential practical application for such a system?

It is exactly with these open questions that I started my PhD in the Theory Group of Univ. Prof. Dr. Francesca Ferlaino. In collaboration with the experimental team of the *Er-Dy* laboratory, we extended supersolidity to two-dimensional crystalline structures. During my PhD, I contributed to the theoretical characterization of two-dimensional dipolar supersolids, with a particular focus on the study of the excitation spectrum and the rotational dynamics. These studies reveal the paradoxical nature of this state, highlighting the simultaneous solid and superfluid behaviour, and the possible application as analogue of neutron stars interior dynamics. This work resulted in a total of 10 publications, among which 8 constitute the core of this thesis.

The thesis is divided into different chapters, structured as follows.

Chapter 1 provides an introduction into the theory of dipolar quantum gases, from the point of view offered by numerical simulations. This chapter starts with a short summary of the modelling techniques for the contact and dipolar interactions. We present a full description of the Gross-Pitaevskii equation and the different numerical techniques to solve it in various scenarios. We then introduce the Bogoliubov-de Gennes formalism for the study of the excitation spectrum. This knowledge set the basis for the study of the ground state phase diagram of a dipolar BEC, where supersolidity emerges.

Chapter 2 introduces dipolar supersolids. After a brief overview of the historical background and their fundamental properties, we focus on the structural transition from one-dimensional to two-dimensional supersolids. We characterize the main properties of these systems, as the control parameter to maintain supersolidity across different

geometries and the best dynamical protocol to form these systems. These theoretical insights are complemented by the achievement of the first experimental observation of 2D supersolids.

Chapter 3 explores the solid properties of 2D supersolids. Through the numerical study of the excitation spectrum and the elastic parameters, we extract information about the speeds of sound of a 2D supersolid. One of the elastic parameters is the shear modulus, which is unique to systems with solid nature. We present these results for both soft-core and dipolar supersolids, using the former as a simplified model to validate the theoretical framework.

Chapter 4 investigates the superfluid properties of 2D dipolar supersolids. We first study the rotational behaviour of the system undergoing small oscillations around the trap axis and then the vortex nucleation through a continuous magnetic field stirring. The theoretical analysis are enriched by the first experimental observation of vortices in 2D supersolids.

Chapter 5 introduces an application of rotating 2D dipolar supersolids, which is the possibility to simulate glitches events, in analogy of neutron star's glitches. Exploiting the structural analogy between the inner crust of neutron stars and supersolids, we develop a model to simulate the sudden spin-up events caused by vortex unpinning in neutron stars.

Finally, the **Conclusions** summarize the main findings of this thesis and offer a brief outlook on potential future research directions. Additionally, **Appendix A** provides an in-depth discussion of the concept of the superfluid fraction, while **Appendix B** includes supplementary publications not part of the thesis's core content but to which the author made significant contributions.

List of publications

The following list contains the 8 publications forming the main core of this thesis. While not presented in chronological order, they correspond to the thematic progression of the chapters.

- **Two-dimensional supersolidity in a dipolar quantum gas.**
  M. A. Norcia*, C. Politi*, L. Klaus, **E. Poli**, M. Sohmen, M. J. Mark, R. Bisset, L. Santos, and F. Ferlaino.
  Nature, **596**, 357–361 (2021)
  These authors contributed equally to this work.

- **Maintaining supersolidity in one and two dimensions.**
  E. Poli, T. Bland, C. Politi, L. Klaus, M. A. Norcia, F. Ferlaino, R. N. Bisset, and L. Santos.
  Phys. Rev. A **104**, 063307 (2021)

- **Two-Dimensional Supersolid Formation in Dipolar Condensates.**
  T. Bland, **E. Poli**, C. Politi, L. Klaus, M. A. Norcia, F. Ferlaino, L. Santos, and R. N. Bisset.
  Phys. Rev. Lett. **128**, 195302 (2022)

- **Excitations of a two-dimensional supersolid**
  E. Poli, D. Baillie, F. Ferlaino and P. B. Blakie.

Phys. Rev. A, **110**, 053301 (2024)

- **Can Angular Oscillations Probe Superfluidity in Dipolar Supersolids?**
  M. A. Norcia, **E. Poli**, C. Politi, L. Klaus, T. Bland, M. J. Mark, L. Santos, R. N. Bisset, and F. Ferlaino.
  Phys. Rev. Lett. **129**, 040403 (2022)

- **Observation of vortices and vortex stripes in a dipolar condensate**
  L. Klaus*, T. Bland*, **E. Poli**, C. Politi, G. Lamporesi, E. Casotti, R. N. Bisset, M. J. Mark, and F. Ferlaino.
  Nature Physics, **18**, 1453–14580 (2022)
  These authors contributed equally to this work.

- **Observation of vortices in a dipolar supersolid**
  E. Casotti*, **E. Poli***, L. Klaus, A. Litvinov, C. Ulm, C. Politi, M. J. Mark, T. Bland and F. Ferlaino.
  Nature, **635**, 327–331 (2024)
  These authors contributed equally to this work.

- **Glitches in Rotating Supersolids**
  E. Poli, T. Bland, S. J. M. White, M. J. Mark, F. Ferlaino, S. Trabucco, and M. Mannarelli.
  Phys. Rev. Lett., **131**, 223401 (2023)

Additional publications

In addition to the main publications, I also contributed to other two projects within the course of the PhD. These publications are presented in the Appendix B and listed below:

- **Alternating-domain supersolids in binary dipolar condensates.**
  T. Bland, **E. Poli**, L. A. Peña Ardila, L. Santos, F. Ferlaino, and R. N. Bisset.
  Phys. Rev. A **106**, 053322 (2022)

- **Synchronization in rotating supersolids.**
  E. Poli*, A. Litvinov*, E. Casotti, C. Ulm, L. Klaus, M. J. Mark, G. Lamporesi, T. Bland and F. Ferlaino.
  arXiv:2412.11976 (2024)
  These authors contributed equally to this work.

1

Simulating dipolar quantum gases

Research on Bose-Einstein condensation holds significant importance in physics, providing a highly controllable quantum environment in laboratory experiments. This chapter introduces the fundamental properties of dipolar BECs and the necessary theoretical framework to understand the emergence of the supersolid phase. We first explore the key properties of BECs with dipolar interactions and introduce the theoretical tools used to describe them. The well-established Gross-Pitaevskii framework serves as the foundation for numerical simulations of dipolar quantum gases. To capture the physics in the strongly dipolar regime, like the supersolid phase, we incorporate a beyond-mean-field description that account for quantum fluctuations. We provide a detailed discussion on the numerical methods employed to solve the Gross-Pitaevskii equation in various scenarios. Additionally, we introduce the Bogoliubov-de Gennes formalism for computing the excitation spectrum, illustrating characteristic spectra for dipolar BECs in different geometries. Finally, by combining all these ingredients, we present the ground state phase diagram of a dipolar gas focusing on the emergence of the supersolid phase.

> **N.B.** Throughout the chapter, numerical details on the simulations presented in this thesis are provided in separate grey-shaded boxes.

1.1. Modelling interactions

Bose-Einstein condensates are extremely dilute systems, with densities several orders of magnitude lower than those of conventional matter. For instance, liquid water has a number density of approximately $n \sim 10^{22}$ atoms/cm^3, whereas a BEC typically has $n \sim 10^{13} - 10^{15}$ atoms/cm^3. This extreme diluteness has consequences in the description of the interaction between particles. In this regime, the range of the interatomic forces, R, is much smaller than the average inter-particle distance, $d \sim 1/n^{1/3}$, such that $R \ll d$ [33]. As a result, interactions involving three or more particles can be effectively neglected. The key idea is that the probability of three particles simultaneously coming close enough to interact is dramatically lower than that for two particles. In denser systems, like the aforementioned liquid water, this is no longer true. Three-body and, more generally, many-body interactions become significant and complicate

Figure 1.1.: Periodic table with highlighted the contact-interacting atoms (teal) and dipolar atoms (orange) that have been Bose-condensed [12–28].

the theoretical description [34].

The nature of two-body interactions in ultracold gases depends on the electronic properties of the atomic species, see Fig.,1.1. Atomic species highlighted in teal interact predominantly through a short-range contact interaction. In contrast, atomic species highlighted in orange possess a large magnetic moment and exhibit both short-range contact interactions and long-range anisotropic dipolar interactions. In the following, we present the details on the modelling of these two type of interactions. Understanding their interplay is crucial for exploring novel quantum phases.

1.1.1. Contact interaction

One contribution of the two-body interaction between neutral particles in a BEC is described by an isotropic, short-range van der Waals potential $V_{\mathrm{vdW}} \propto 1/r^6$, which decreases rapidly with distance. This interaction originates from instantaneous fluctuations in the charge distribution of the atoms, leading to interacting transient dipole moments; for more details, see Ref. [35]. In general, a collision event is described by the travelling wave functions of the two atoms, obtained from the solution of the Schrödinger equation [36]. In the low-energy regime, the typical momentum of the interacting particle satisfies $k \ll 2\pi/R$. In this regime, scattering theory reveals that the detailed form of the interaction potential is not critical, provided that the interaction correctly accounts for the behaviour of particles before and after collisions [37]. The low-energy properties of an isotropic interatomic potential decaying as $1/r^n$ with $n > 3$ can be fully approximated, at the level of the Born approximation, by a pseudo-potential of the form

$$U(\mathbf{r} - \mathbf{r}') = g\delta(\mathbf{r} - \mathbf{r}') = \frac{4\pi\hbar^2 a_s}{m}\delta(\mathbf{r} - \mathbf{r}')\,. \tag{1}$$

where m is the atomic mass, δ is a Dirac delta function and $\mathbf{r}$, $\mathbf{r}'$ are the position of the two interacting atoms. This result is rigorously derived from quantum scattering
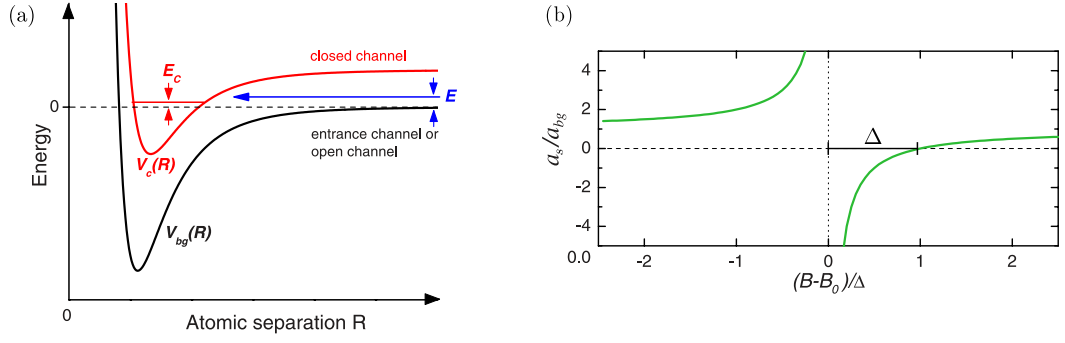
Figure 1.2.: Illustration of a basic model of a Feshbach resonance. (a) Illustration of the two-channel model: $V_{bg}(R)$ represents the open channel, $V_c(R)$ is the closed channel with a molecular bound state E_c. Resonant coupling is realized by tuning $E_c \to 0$ through a magnetic field. (b) Effect of the magnetic field B on a_s, normalized to the background scattering length a_{bg}. Adapted from Ref. [38].

theory [37]. The quantity a_s is the scattering length, which is related to the phase shift acquired by the wave function of the scattered particle. It can be interpreted as a measure of how much the potential influences particle scattering[1]. The sign of a_s determines whether the interaction is repulsive ($a_s > 0$) or attractive ($a_s < 0$).

The sign and the magnitude of a_s can be tuned experimentally by means of the so-called Feshbach resonances [38]. In brief, when we consider a two body scattering process, we can define open channels and close channels. An open channel represents a scattering state where two particles can separate after the interaction. A closed channel supports bound states where the particles interact strongly and form a quasi-stable composite system. The relative energy of these channels can be altered by an external magnetic field B. A Feshbach resonance occurs when the energy of the closed channel bound state becomes comparable to the energy of the scattering states in the open channel. This process is schematically illustrated in Fig. 1.2(a). The corresponding behaviour of the scattering length is shown in (b) and it is modelled according the expression

$$a_s = a_{bg} \left(1 - \frac{\Delta}{B - B_0} \right). \tag{2}$$

Here, a_{bg} is the background scattering length (i.e. the off-resonant value of a_s), Δ is the width of the resonance and B_0 is the magnetic field at resonance and a_s diverges at resonance. The tunability of the contact interaction strength confers extraordinary degree of control on ultracold gas systems.

1.1.2. Dipolar interaction

When particles possess a magnetic or electric dipole moment, the interaction potential is modified [39,40]. In addition to the short-range pseudo-potential described in Eq. (1), it is necessary to consider the dipole-dipole interaction term proportional to $\sim 1/r^3$. This dependence comes directly from the $1/r^3$ scaling of the field created by a single dipole.

---

[1]When considering a_s, the subscript s recalls the orbital nomenclature for orbital angular momentum $l = 0$. In fact, in the low-energy regime, the scattered wave function is a spherical wave proportional to the spherical harmonic $Y_{l=0,m=0}$, regardless how complicated the actual potential is [36].

In fact, the interaction energy between two dipoles with magnetic moment $\boldsymbol{\mu}_1$ and $\boldsymbol{\mu}_2$ is

$$V_{\mathrm{dd}} = -\boldsymbol{\mu}_2 \cdot \mathbf{B_1} \tag{3}$$

where $\mathbf{B}_1 = \nabla \times \mathbf{A}_1$ is the magnetic field created by $\boldsymbol{\mu}_1$ in the location of $\boldsymbol{\mu}_2$ [41]. The vector potential $\mathbf{A}_1$ far from the dipole itself is

$$\mathbf{A}_1 = \frac{\mu_0}{4\pi} \frac{\boldsymbol{\mu_1} \times \mathbf{r}}{r^3} \tag{4}$$

Notice that $|\mathbf{A}_1|$ decreases as $1/r^2$, and when calculating the curl one gets $|\mathbf{B}_1| \sim 1/r^3$. The analogous result can be obtained from the far-field approximation of a generic electric dipole [41].

The general form of the dipole-dipole interaction (DDI) potential between two dipoles with arbitrary orientation is expressed as

$$V_{\mathrm{dd}}(\mathbf{r}) = \frac{C_{\mathrm{dd}}}{4\pi} \left(\frac{(\hat{\mathbf{e}}_1 \cdot \hat{\mathbf{e}}_2)\, r^2 - 3\, (\hat{\mathbf{e}}_1 \cdot \mathbf{r})\, (\hat{\mathbf{e}}_2 \cdot \mathbf{r})}{r^5} \right) , \tag{5}$$

where $\mathbf{r}$ is the vector pointing from one interacting particle to the other, while $\hat{\mathbf{e}_1}$ and $\hat{\mathbf{e}_2}$ are the unit vectors denoting the orientation of the two dipoles; see Fig. 1.3(a). The pre-factor C_{dd} depends on the type of the dipole involved:

- For magnetic dipoles, $C_{dd} = \mu_0 \mu^2$, where μ_0 is the vacuum permeability and μ the magnetic dipole moment.
- For electric dipoles, $C_{dd} = d^2/\epsilon_0$ where d is the electric dipole moment and ϵ_0 the permittivity of free space.

An external magnetic or electric field polarizes the orientation of the dipoles, so

$$\hat{\mathbf{e}}_1 = \hat{\mathbf{e}}_2 = (\sin\theta\cos\varphi, \sin\theta\sin\varphi, \cos\theta) \tag{6}$$

where θ and φ are the polar and azimuthal angle of the field, respectively. When the polarization direction is the $z-$axis, Eq. (5) simplifies to

$$V_{\mathrm{dd}}(\mathbf{r}) = \frac{3\hbar^2 a_{dd}}{m} \left(\frac{1 - 3\cos^2\theta}{r^3} \right) , \tag{7}$$

where θ now is defined as the angle between the vector $\mathbf{r}$ and the polarization direction of the dipoles; see Fig. 1.3(b). Notice that the prefactor has been rewritten in terms the dipolar length $a_{dd} = \mu_0 \mu_m^2 m / 12\pi\hbar^2$. To compare the characteristic lengths of the two interactions, it is customary to define the parameter

$$\varepsilon_{dd} = \frac{a_{dd}}{a_s} \tag{8}$$

so that $\varepsilon_{dd} < 1$ means contact dominated regime, whereas $\varepsilon_{dd} > 1$ means dipolar dominated regime.

Mathematically, an interaction potential is considered long-range when it scales as $1/r^n$ (with $n > 0$), provided that the system's dimensionality D satisfies $D \geq n$. In the case a three-dimensional system with dipolar interaction ($n = 3$, $D = 3$), this
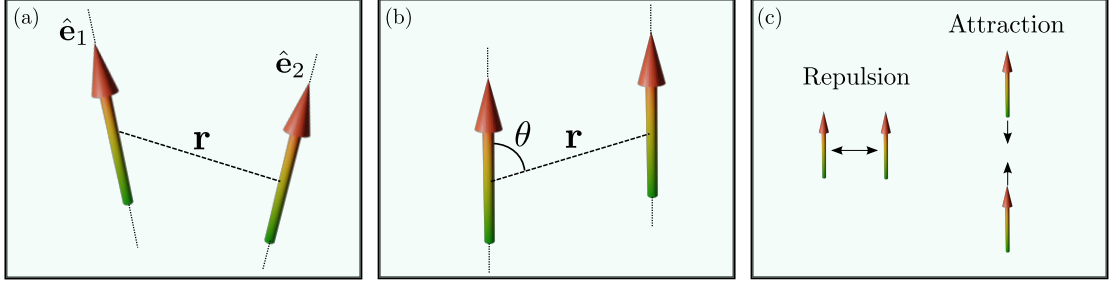
Figure 1.3.: Schematic illustration of interaction between dipoles. (a) Generic case of two interacting dipoles without any external magnetic field that gives a polarization direction to the them, described by Eq. (5). (b) Polarized dipoles, interacting through Eq. (7). (c) Schematic representation of the repulsive and attractive configuration between two dipoles.

condition is satisfied[2]. Furthermore, dipolar interaction is also anisotropic due to its dependence on the angle θ. Similar to classical magnets, two dipoles repel if they sit side-by-side ($\theta = \pi/2 \to V_{dd} > 0$), they will attract if they arrange in the head-to-tail configuration ($\theta = 0 \to V_{dd} < 0$); see Fig. 1.3(c). As a consequence of that, two dipoles in will always have the tendency to arrange head-to-tail, leading to crucial effects on the stability of the dipolar gas. Interestingly, the dipolar interaction is zero when $\theta = \arccos(1/\sqrt{3}) \simeq 54.7°$.

The anisotropy and long-range character of the dipolar interaction is reflected also in momentum space. The Fourier transform of the dipolar interaction in Eq. (7) $\tilde{V}_{dd}(\mathbf{k})$ is analytical

$$\tilde{V}_{dd}(\mathbf{k}) = \frac{C_{dd}}{3}\left(3\cos^2 \alpha_k - 1\right), \tag{9}$$

with α_k being the angle between the vector $\mathbf{k}$ and the polarization direction of the dipoles [44]. This form of the DDI in momentum space will be particularly useful for the numerical study of dipolar BECs, see Sec. 1.2. Furthermore, the momentum dependence of the interaction in Fourier space is one of the key ingredients for exploring the supersolid phase of matter, see Sec. 1.6 and Chapter 2.

In the following, we briefly discuss the case of electric dipolar systems before exclusively focusing on magnetic dipolar systems for the rest of this thesis.

Electric dipoles

Atoms and molecules in their rotational ground states lack permanent electric dipole moments due to rotational symmetry. However, in some systems the application of an external electric field E can perturb the energy levels, resulting in an induced electric dipole moment [42].

Rydberg atoms provide an example. These states, with degenerate levels of opposite parity, can acquire electric dipole moments even in the presence of weak electric fields.

---

[2]The reason comes from a thermodynamic point of view. Short-range interactions lead to an energy that is thermodynamically extensive, i.e. when the integral $\int_0^\infty U(r)d^D r$. This happens only if $U(r) \sim 1/r^n$ with $n > D$. Long-range interactions are defined for the complementary case, when the interaction energy is not extensive, thus $n \geq D$ [42]. However, although not mathematically defined as long-range, in the context of many-body physics the dipolar interaction might lead to qualitatively new behaviours also at lower dimensions $D < 3$ [43].

Atomic species	Magnetic moment μ
Rb	$1\,\mu_{\mathrm{B}}$
Tm	$4\,\mu_{\mathrm{B}}$
Cr	$6\,\mu_{\mathrm{B}}$
Er	$7\,\mu_{\mathrm{B}}$
Eu	$7\,\mu_{\mathrm{B}}$
Dy	$10\,\mu_{\mathrm{B}}$

Table 1.1.: Magnetic moments in units of Bohr magneton μ_B for different atomic species. Values are taken from Refs. [25–28, 62].

The magnitude of the induced dipole moment scales as n^2, where n is the principal quantum number of the Rydberg state [45]. By associating a Rydberg atom with a ground state atom one can form a Rydberg molecule, which exhibit permanent dipole moments [46]. These systems have become a hub of experimental and theoretical research, enabling advances in understanding strongly correlated dipolar gases, lattice spin models, and applications in quantum computing [47–53].

Another promising direction involves heteronuclear molecules, which exhibit strong dipole moments that arises when two rotational states are mixed by an external electric field [54]. However, cooling and trapping these systems is challenging, due to molecular losses during collisions [55]. These losses can be mitigated with techniques like collisional shielding, which prevents molecule-molecule complexes by engineering their dipolar interactions. A significant milestone has been reached in 2020, with the observation of the first quantum degenerate Fermi gas of KRb polar molecules [56, 57]. In 2024, the developement of more advanced collisional shielding techniques, including static fields and rotating microwave fields, led to the creation the first long-lived Bose–Einstein condensate with NaCs polar molecules [58]. At the moment, ultracold molecules constitute a fast-expanding and promising field, especially for exploring novel states of matter and quantum simulation [55].

Magnetic dipoles

In contrast to electric dipoles, elementary particles can have permanent magnetic dipoles even at zero external magnetic field due to many unpaired valence electrons. The key quantity for this effect is the atomic magnetic moment $\mu = -m_J g_J \mu_{\mathrm{B}}$, defined as a function of the magnetic quantum number m_J, the Landé g-factor g_J and the Bohr magneton μ_{B}. Due to their hydrogen-like electronic configuration, alkali atoms possess a magnetic moment of the order of $\mu \sim \mu_{\mathrm{B}}$. In principle, it is possible to study dipolar physics but the energy scale associated with the dipolar interaction is quite small [59–61]. However, *dipolar atoms* such as Chromium (Cr), Erbium (Er), and Dysprosium (Dy) possess significantly larger magnetic moments—about an order of magnitude higher than non-dipolar species. Table 1.1 highlights the magnetic moments of atoms that have currently achieved quantum degeneracy. From Eq. (7) it is clear that the magnetic dipole-dipole interaction scales with the square of the magnetic moment. Therefore, for dipolar atoms this interaction is enhanced by a factor of approximately $\sim$10 to $\sim$100 compared to alkali atoms.

> **In this thesis**, we focus on BECs made of Dysprosium atoms, which is the most strongly dipolar natural atomic species in the periodic table. This choice is motivated by the collaboration with the experimental team of the *Er-Dy* laboratory, one of the experimental divisions within Univ. Prof. Dr. Francesca Ferlaino's research group in Innsbruck.

1.2. The Gross-Pitaevskii equation

Experiments with ultracold gases usually involve weakly interacting Bose-Einstein condensates, where interatomic correlations are small. As discussed in Sec. 1.1.1, the interparticle interaction strength, given by the scattering length a_s, can be tuned via Feshbach resonances. A gas is typically considered weakly interacting when

$$a_s \ll d. \tag{10}$$

This condition is not always fulfilled: a gas may remain dilute yet lie outside the weakly interacting regime. An extreme example is the unitary Fermi gas [33]. However, this topic lies beyond the scope of this thesis.

Working in the weakly interacting regime simplifies the theoretical framework and enables the effective application of mean-field (MF) theories. In this section, we derive the Gross-Pitaevskii equation (GPE), which governs the dynamics of the macroscopic wave function of a Bose-Einstein condensate [33].

In the second quantization formalism, particles in a BEC are described by the many-body field operator

$$\hat{\Psi}(\mathbf{r}) = \sum_i \phi_i(\mathbf{r})\hat{a}_i \tag{11}$$

with $\hat{a}_i$ ($\hat{a}_i^\dagger$) being the annihilation (creation) operators of a bosonic particle in the state ϕ_i. According to the bosonic statistics, these single particles operators satisfy the following commutation relations

$$[\hat{a}_i, \hat{a}_j^\dagger] = \delta_{ij} \,, [\hat{a}_i, \hat{a}_j] = [\hat{a}_i^\dagger, \hat{a}_j^\dagger] = 0 \tag{12}$$

meaning that particles in the condensate are indistinguishable.

The Hamiltonian of a Bose gas with two-body interactions in terms of the fields operator $\hat{\Psi}(\mathbf{r})$ reads

$$\hat{H} = \int d\mathbf{r}\, \hat{\Psi}^\dagger(\mathbf{r}) \left[-\frac{\hbar^2\nabla^2}{2m} + V_{\text{ext}}(\mathbf{r}) \right] \hat{\Psi}(\mathbf{r}) + \frac{1}{2}\int d\mathbf{r} \int d\mathbf{r}'\, \hat{\Psi}^\dagger(\mathbf{r})\hat{\Psi}^\dagger(\mathbf{r}')V(\mathbf{r}-\mathbf{r}')\hat{\Psi}(\mathbf{r}')\hat{\Psi}(\mathbf{r}), \tag{13}$$

where the first term describes the kinetic energy, $V_{\text{ext}}(\mathbf{r})$ is an external confining potential and $V(\mathbf{r} - \mathbf{r}')$ is the two-body interaction potential between two bosons. The integrals are performed over all space. The time evolution of the field operator $\hat{\Psi}(\mathbf{r})$ is

then obtained through the Heisenberg relation

$$
i\hbar \frac{\hat{\Psi}(\mathbf{r}, t)}{\partial t} = \left[\hat{\Psi}(\mathbf{r}), \hat{H} \right] =
$$
$$
= \int d\mathbf{r} \left[-\frac{\hbar^2 \nabla^2}{2m} + V_{\text{ext}}(\mathbf{r}) \right] \hat{\Psi}(\mathbf{r}) + \int d\mathbf{r}' \, \hat{\Psi}^\dagger(\mathbf{r}') V(\mathbf{r} - \mathbf{r}') \hat{\Psi}(\mathbf{r}') \hat{\Psi}(\mathbf{r}) \, . \tag{14}
$$

The assumption that, in a BEC, the majority of particles occupy the same quantum state, while the contribution of particles outside the condensate is negligible, simplifies the problem. This simplification is known as *Bogoliubov approximation*. The first step involves replacing the condensate operators with a classical field[3]. For simplicity, we associate the single-particle state at $i = 0$, represented by $\phi_0(\mathbf{r})$, with the state to which all particles in the condensate belong. The condensate field operator $\hat{\Psi}(\mathbf{r})$ reduces to

$$
\hat{\Psi}(\mathbf{r}) = \phi_0(\mathbf{r}) \hat{a}_0 + \sum_{i \neq 0} \phi_i(\mathbf{r}) \hat{a}_i = \tag{15}
$$

$$
= \sqrt{N_0} \phi_0(\mathbf{r}) + \sum_{i \neq 0} \phi_i(\mathbf{r}) \hat{a}_i = \tag{16}
$$

$$
= \psi(\mathbf{r}) + \delta\hat{\psi}(\mathbf{r}) \, , \tag{17}
$$

where the Bogoliubov approximation is applied between Eq. (15) and Eq. (16). The final expression Eq. (17) reports the result in a simplified form.

In this decomposition:
- $\psi(\mathbf{r})$ is the classical mean-field condensate wave-function;
- $\delta\hat{\psi}(\mathbf{r})$ is the fluctuation operator including quantum and thermal fluctuations around the condensate.

Here, we assume the system is at zero temperature, so the thermal component vanishes entirely. Additionally, given the weakly interacting nature of the condensate, quantum depletion at zero temperature is expected to be negligible. Therefore, it is reasonable to neglect the non-condensed atoms and approximate the field operator as a classical quantity

$$
\hat{\Psi}(\mathbf{r}) = \psi(\mathbf{r}) \, . \tag{18}
$$

The fluctuation operator $\delta\hat{\psi}(\mathbf{r})$ will be revisited in later sections to account for beyond-mean field corrections and the excitations above the condensate.

By replacing the time dependent field operator $\hat{\Psi}(\mathbf{r}, t)$ with the corresponding condensate wave function $\psi(\mathbf{r}, t)$ in Eq. (14), we obtain the so-called *Gross-Pitaevskii equation* (GPE)

$$
i\hbar \frac{\partial \psi(\mathbf{r}, t)}{\partial t} = \left[-\frac{\hbar^2 \nabla^2}{2m} + V_{\text{ext}}(\mathbf{r}) + \int d\mathbf{r}' V(\mathbf{r} - \mathbf{r}') \left| \psi(\mathbf{r}', t) \right|^2 \right] \psi(\mathbf{r}, t) \, . \tag{19}
$$

The GPE is a non-linear differential equation that governs the dynamics of the condensate wave function $\psi(\mathbf{r}, t)$. In the following subsections, we provide a detailed explanation of each term in the equation and its significance in the context of dipolar gases. Additionally, we outline the numerical methods used to solve the equation.

---

[3]This approximation can be interpreted as ignoring the non-commutativity of $[\hat{a}_0, \hat{a}_0^\dagger] = \delta_{ij}$. This is a good approximation when $N_0 = \langle \hat{a}_0^\dagger \hat{a}_0 \rangle \gg 1$, i.e. when the condition of macroscopic occupation of the ground state is satisfied.

Condensate wave function $\psi(\mathbf{r}, t)$

This quantity represents the macroscopic wave function that describes the state of the many-body system. In general, it is a complex quantity characterized by a modulus and a phase

$$\psi(\mathbf{r}, t) = |\psi(\mathbf{r}, t)|e^{i\theta(\mathbf{r}, t)} . \tag{20}$$

The modulus is related to the density n of the condensate, $|\psi(\mathbf{r}, t)| = \sqrt{n(\mathbf{r}, t)}$, such that the wave function is normalized to the total atom number

$$\int d\mathbf{r} |\psi(\mathbf{r}, t)|^2 = \int d\mathbf{r}\, n(\mathbf{r}, t) = N . \tag{21}$$

The phase $\theta(\mathbf{r}, t)$ is related to the global coherence of the condensate and the velocity field $\mathbf{v}(\mathbf{r}, t)$ during the time evolution of the system, i.e.

$$\mathbf{v}(\mathbf{r}, t) = \frac{\hbar}{m}\nabla\theta(\mathbf{r}, t) . \tag{22}$$

Therefore, a stationary solution of the GPE in the laboratory frame has a uniform phase.

The GPE is non-linear, so an exact analytical solution for $\psi(\mathbf{r}, t)$ is rare and it is possible only under very specific conditions–for example, in homogeneous infinite systems or in trapped systems within the Thomas-Fermi approximation (see Sec. 1.3.1). Therefore, we rely on numerical methods to calculate its values at discrete points on a mesh in either real or momentum space. From now on, it will be implicitly assumed that $\psi(\mathbf{r})$ is evaluated on a regular Cartesian mesh in real space. Additionally, it is often advantageous to consider the Fourier transform, $\tilde{\psi}(\mathbf{k})$, which is discretized on the corresponding reciprocal mesh in momentum space.

> **In this thesis**, the grids used to discretize the wavefunction and solve the GPE for finite systems typically consist of either ($256 \times 256 \times 64$) or ($256 \times 256 \times 128$) mesh points in the *x-y-z* directions (Chapters 2, 4, 5). For studies involving the time expansion of a finite system in the absence of an external trap, the grid size is usually increased to ($768 \times 768 \times 1024$) mesh points (Chapters 2, 4). In contrast, when dealing with infinite systems (Chapter 3), the wave function is computed for a single unit cell. This requires a significantly smaller mesh, usually with ($21 \times 21 \times 21$) points.

Kinetic energy $-\frac{\hbar^2 \nabla^2}{2m}$

The first contribution to the GPE operator is the kinetic energy. It is computationally convenient to calculate the Laplace operator ∇^2 acting on the condensate wave function in the momentum space. The Fourier transform of $\nabla^2 \psi(\mathbf{r})$ is simply $-k^2\tilde{\psi}(\mathbf{k})$, where the tilde means the Fourier transform. The numerical procedure to calculate this term is:

- Calculate the Fourier transform of the wave function $\tilde{\psi}(\mathbf{k}) = \int d\mathbf{r}\psi(\mathbf{r})e^{i\mathbf{k}\cdot\mathbf{r}}$. This calculation is performed numerically with high efficiency using the standard Fast
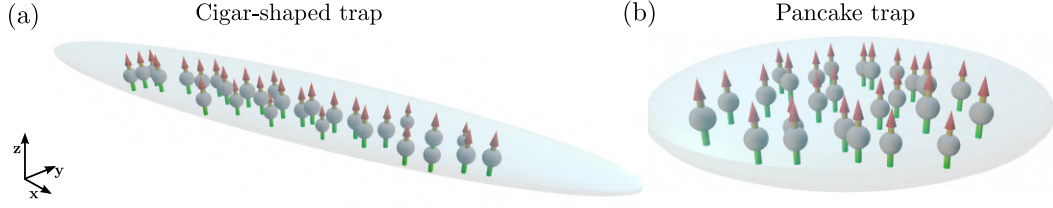
Figure 1.4.: Cigar and pancake shaped trap geometries for a dipolar gas, with tight confinement along the polarization direction of the dipoles ($z-$axis).

Fourier Transform[4] (FFT) algorithm, implemented via the FFTW library [63].

- Calculate the kinetic term in the momentum space $-k^2\tilde{\psi}(\mathbf{k})$.
- Calculate the inverse Fourier transform and obtain the kinetic energy term in position space.

External trapping potential $V_{\text{ext}}(\mathbf{r})$

The majority of the results presented in this thesis assumes an three-dimensional external harmonic potential of the form

$$V_{\text{ext}}(\mathbf{r}) = \frac{1}{2}m\left(\omega_x^2 x^2 + \omega_y^2 y^2 + \omega_z^2 z^2\right) , \tag{23}$$

where $\omega_i = 2\pi f_i$ is the harmonic frequency along the spatial direction $i = x, y, z$.

According to the geometry of the trap, the dipolar interaction can be dominantly attractive or repulsive. For simplicity, let us fix the dipoles polarization along the $z-$axis. When the trap confinement along z is weak compared to the confinement in the $x - y$ plane, the system favours the atoms disposing in the head-to-tail configuration. In this case, the dipolar interaction is on average attractive. On the contrary, for tight confinement along z, atoms dispose themselves mostly side-by-side and the dipolar interaction is dominantly repulsive. The stability of the system across these different geometries has been studied with a variational method [65].

As will be discussed later in the following sections, for the study of the supersolid state of matter we consider two relevant trap geometries; see Fig. 1.4. The cigar-shaped geometry is obtained with an elongated trap ($f_x < f_y, f_z$), while the pancake geometry is obtained with a flattened trap ($f_x, f_y < f_z$). In both configurations, the repulsive nature of the dipolar interaction is dominant.

---

[4]This algorithm has had a transformative impact on numerous computational methods and remains the most widely employed technique for calculating Fourier transforms across all programming languages. Actually, it was Gauss who first proposed this technique to calculate the coefficients in a trigonometric expansion of an asteroid's orbit. This happened about 160 years before Cooley and Tukey's paper [63], but he never published the paper in his lifetime [64].

> **In this thesis**, most of the results are obtained using a pancake trap (Chapters 2, 4, 5). The absence of confining potential in one or more directions enables the study of an infinite system (Chapter 3). Additionally, a common experimental approach involves preparing a finite system in equilibrium and then removing the trapping potential, allowing it to expand. This technique is frequently used to investigate the phase coherence of the wave function (Chapters 2, 4).

Two-body interaction potential $V(\mathbf{r} - \mathbf{r}')$

Given a system with atoms polarized along the same direction, the two-body interaction term includes the short-range pseudo-potential and the dipolar term discussed in Secs. 1.1.1 and 1.1.2, so:

$$V(\mathbf{r} - \mathbf{r}') = g\delta(\mathbf{r} - \mathbf{r}') + V_{\mathrm{dd}}(\mathbf{r} - \mathbf{r}')\,. \tag{24}$$

In the GPE, this quantity appears inside a non-local integral. The presence of a δ function for the contact interaction partially simplifies the expression

$$\int d\mathbf{r}' V(\mathbf{r} - \mathbf{r}')|\psi(\mathbf{r}',t)|^2 = g|\psi(\mathbf{r},t)|^2 + \int d\mathbf{r}' V_{\mathrm{dd}}(\mathbf{r} - \mathbf{r}')|\psi(\mathbf{r}',t)|^2\,, \tag{25}$$

but evaluating the non-local integral for the dipolar interaction makes the GPE solution computationally expensive. However, similar to the kinetic term, in the momentum space the convolution integral becomes a simple multiplication

$$\int d\mathbf{r}' V_{\mathrm{dd}}(\mathbf{r} - \mathbf{r}')|\psi(\mathbf{r}',t)|^2 = \tilde{V}_{\mathrm{dd}}(\mathbf{k})\tilde{n}(\mathbf{k})\,. \tag{26}$$

Luckily, as discussed in Sec. 1.1.2, the Fourier transform of the dipolar interaction $\tilde{V}_{\mathrm{dd}}(\mathbf{k})$ is analytical [44].

The numerical procedure to calculate this contribution is analogue to the kinetic term, but with extra complications due to the long-range character of the interaction. In fact, when working in the Fourier space we are implicitly imposing boundary condition, that for a fully trapped systems are clearly unphysical and may introduce fake interactions between the contiguous alias copies of the original simulation cell. To prevent this problem, it is customary to use a truncated dipolar interaction. The most common truncation is a spherical cut-off, so that the dipolar interaction reduces to

$$V_{\mathrm{dd}}^{R_c}(\mathbf{r}) = \begin{cases} \frac{C_{\mathrm{dd}}}{4\pi}\frac{1 - 3\cos^2\theta}{r^3}, & r < R_c \\ 0, & \text{otherwise} \end{cases} \tag{27}$$

in position space and

$$\tilde{V}_{\mathrm{dd}}^{R_c}(\mathbf{k}) = \frac{C_{\mathrm{dd}}}{3}\left[1 + 3\frac{\cos(R_c k)}{R_c^2 k^2} - 3\frac{\sin(R_c k)}{R_c^3 k^3}\right]\left(3\cos^2\alpha_k - 1\right) \tag{28}$$

in momentum space [44]. It is important to choose a cut-off radius R_c larger than the system size, so that all the atoms within the system interact with each other even when they are far apart. Another possibility is a cylindrical truncation

$$
V_{\mathrm{dd}}^{R_c, Z_c}(\mathbf{r}) = \begin{cases} \frac{C_{\mathrm{dd}}}{4\pi} \frac{1 - 3\cos^2\theta}{r^3}, & \sqrt{x^2 + y^2} < R_c \text{ and } |z| < Z_c \\ 0, & \text{otherwise} \ . \end{cases}
\tag{29}
$$

In momentum space it becomes a quasi-analytical expression

$$
\begin{aligned}
\tilde{V}_{\mathrm{dd}}^{R_c, Z_c}(\mathbf{k}) =\ & \frac{C_{\mathrm{dd}}}{3}(3\cos^2\alpha_k - 1) \\
& + C_{\mathrm{dd}} e^{-Z_c k_r} \left[\sin^2\alpha_k \cos\left(Z_c k_z\right) - \sin\alpha_k \cos\alpha_k \sin\left(Z_c k_z\right) \right] \\
& - C_{\mathrm{dd}} \int_{r_c}^{\infty} r\mathrm{d}r \int_0^{Z_c} \mathrm{d}z \cos(k_z z) \frac{r^2 - 2z^2}{(r^2 + z^2)^{5/2}} J_0(k_r r),
\end{aligned}
\tag{30}
$$

where $k_r = \sqrt{k_x^2 + k_y^2}$ and J_0 is the zeroth-order Bessel function. The remaining integral term in Eq. (30) can easily be obtained by using numerical integration at the beginning of the simulation.

> **In this thesis**, the majority of the results are obtained by applying a spherical cut-off to the dipolar interaction. The cut-off radius is chosen based on the specific case, but a typical and reliable choice is $R_c = L$, with the size of the simulation cell covering $[-L, L]$ in the three directions [66]. The value of L is generally set to be at least twice the average radial size of the system. For most of the simulations results shown in this thesis we used $L = 20\,\mu\mathrm{m}$.

Final expression

Summarizing, the *dipolar Gross-Pitaevskii equation* reads

$$
i\hbar \frac{\partial \psi(\mathbf{r}, t)}{\partial t} = \mathcal{L}_{\mathrm{GP}} \psi(\mathbf{r}, t),
\tag{31}
$$

where $\mathcal{L}_{\mathrm{GP}}$ is the Gross-Pitaevskii (GP) operator

$$
\mathcal{L}_{\mathrm{GP}} = \left[-\frac{\hbar^2 \nabla^2}{2m} + V_{\mathrm{ext}}(\mathbf{r}) + g|\psi(\mathbf{r}, t)|^2 + \int d\mathbf{r}' V_{\mathrm{dd}}\left(\mathbf{r} - \mathbf{r}'\right) \left|\psi\left(\mathbf{r}', t\right)\right|^2 \right].
\tag{32}
$$

Rotating frame

We anticipate that it is useful to study the system under the effect of the trap rotation about the $z-$axis. In this case, it's necessary to include a Coriolis-like term in the Gross-Pitaevskii operator to solve the GPE in the rotating frame:

$$
\mathcal{L}_{\mathrm{GP}} \rightarrow \mathcal{L}_{\mathrm{GP}} - \Omega \hat{L}_z,
\tag{33}
$$

where $\hat{L}_z = x\hat{p}_y - y\hat{p}_x$ is the angular momentum operator about the $z-$axis and Ω the constant trap rotation frequency [33]. This is obtained by changing the viewpoint from the laboratory frame to the rotating frame through a coordinate change in the GP operator, see Table 1.2.

Viewpoint	GPE
Laboratory frame	$i\hbar\dfrac{\partial\psi(\mathbf{r},t)}{\partial t} = \bigg[-\dfrac{\hbar^2\nabla^2}{2m} + V_{\text{ext}}(\mathbf{r},t) + g|\psi(\mathbf{r},t)|^2 +$ $\int d\mathbf{r}' V_{\text{dd}}\left(\mathbf{r}-\mathbf{r}'\right)\left|\psi\left(\mathbf{r}',t\right)\right|^2 \bigg]\psi(\mathbf{r},t)\,,$ with $V_{\text{ext}}(\mathbf{r},t) = V_{\text{ext}}(R(t)\mathbf{r})$ and $R(t) = \begin{bmatrix} \cos\Omega t & -\sin\Omega t & 0 \\ \sin\Omega t & \cos\Omega t & 0 \\ 0 & 0 & 1 \end{bmatrix}$
Rotating frame	$i\hbar\dfrac{\partial\psi(\mathbf{r},t)}{\partial t} = \bigg[-\dfrac{\hbar^2\nabla^2}{2m} + V_{\text{ext}}(\mathbf{r}) + g|\psi(\mathbf{r},t)|^2 +$ $\int d\mathbf{r}' V_{\text{dd}}\left(\mathbf{r}-\mathbf{r}'\right)\left|\psi\left(\mathbf{r}',t\right)\right|^2 - \Omega\hat{L}_z \bigg]\psi(\mathbf{r},t)$

Table 1.2.: Two equivalent points of view to treat the problem of a dipolar BEC in a rotating trap about the $z-$axis with angular frequency Ω. In the laboratory frame, the confining potential is time dependent and rotating through the rotation matrix $R(t)$ about the $z-$axis. After changing the reference frame to the co-rotating position coordinates $\mathbf{r} \to R^{-1}(t)\mathbf{r}$, the GP operator acquires an extra term $-\Omega\hat{L}_z$. It is possible to switch from one viewpoint to the other also by applying a unitary transformation to the wave function $\hat{U} = e^{i\Omega\hat{L}_z t/\hbar}$ [67].

1.3. Solving the Gross-Pitaevskii equation

Except for some specific cases, the Gross-Pitaevskii Equation (GPE) does not have an analytical solution. However, numerical methods provide a powerful tool for studying both the ground state properties and the dynamics of ultracold dipolar systems. To describe the different scenarios captured by the GPE, it is useful to re-write Eq. (31) with an additional complex pre-factor:

$$i\hbar\frac{\partial\psi(\mathbf{r},t)}{\partial t} = (\alpha - i\gamma)\mathcal{L}_{\text{GP}}\psi(\mathbf{r},t)\,. \tag{34}$$

By switching on and off the real and/or the imaginary part of this complex number, we can solve the GPE for different purposes. We first analyse the time-independent solution and explore a specific scenario where analytical solutions are possible. Afterwards, we provide a detailed description of the numerical tools and algorithms used to solve the time-dependent GPE.

1.3.1. Time-independent solution

The lowest-energy configuration of the condensate can be found by looking for solutions of the GPE of the form $\psi(\mathbf{r},t) = e^{-i\mu t/\hbar}\psi(\mathbf{r})$. This ansatz describes a stationary solution to the GPE, because the spatial and temporal parts are separated so that the density

distribution $n = |\psi(\mathbf{r}, t)|^2 = |\psi(\mathbf{r})|^2$ is time-independent. When using this ansatz, the GPE reduces to

$$\mu\psi(\mathbf{r}) = \mathcal{L}_{\mathrm{GP}}\psi(\mathbf{r}) \,. \tag{35}$$

The quantity μ can be interpreted as the chemical potential, which is the energy required to add or remove a particle from the system. Basically, having μ as eigenvalue associated to the stationary state means fixing the total number of particles of the system.

The time-independent solution of the GPE can be obtained from the minimization of the energy functional $E[\psi] = \langle\psi| \hat{H} |\psi\rangle$, with $\hat{H}$ defined in Eq. (13). The energy functional reads

$$
\begin{aligned}
E[\psi] = & \int d\mathbf{r}\psi^*(\mathbf{r}) \left(-\frac{\hbar^2}{2m}\nabla^2 + V_{\mathrm{ext}}(\mathbf{r}) \right) \psi(\mathbf{r}) \\
& + \frac{g}{2} \int d\mathbf{r}|\psi(\mathbf{r})|^4 + \frac{1}{2} \int d\mathbf{r}d\mathbf{r}'|\psi(\mathbf{r})|^2 V_{\mathrm{dd}}(\mathbf{r} - \mathbf{r}') \left|\psi(\mathbf{r}')\right|^2 \,.
\end{aligned}
\tag{36}
$$

For a conserved big number of particles N, we can minimize $E[\psi]$ imposing the stationarity condition and the normalization constraint, i.e.

$$\delta(E[\psi] - \mu N) = 0 \,. \tag{37}$$

This yields exactly to Eq. (35) [33].

In this thesis, the ground state solutions of the GPE in absence of rotation are found by minimizing the energy functional. This approach is used in different contexts to study both finite and infinite systems:

- To generate supersolid states for comparison with in-situ experimental results (Chapters 2 and 4);

- To produce the initial states on top of which elementary excitations are calculated (Chapters 2 and 3);

- To create the initial states used to study dynamical properties (Chapters 2, 4, 5);

- To calculate ground state solutions and extract elastic parameters for an infinite supersolid system (Chapter 3);

Ground state calculations for trapped systems are performed using a conjugate gradient algorithm [68, 69], as this method is significantly fast.

The convergence criterion is set on Eq. (35)

$$\|\mathcal{L}_{\mathrm{GP}}\psi - \mu\psi\| < \gamma_0\mu\|\psi\|\,, \tag{38}$$

where γ_0 is an arbitrary small tolerance parameter. Typically, setting $\gamma_0 = 10^{-9}$ is sufficient to achieve a well converged ground state wave functions. For certain cases, such as studies of the excitation spectrum (see Section 1.6 and Chapter 2), more stringent tolerances of $\gamma_0 = 10^{-10}$ to 10^{-11} have been used to ensure highly converged ground states.

For the infinite systems treated in Chapter 3, the ground state is determined by minimizing the energy functional using the backward Euler method [70], with a convergence criterion of $\gamma_0 = 3 \times 10^{-9}$.

Thomas-Fermi limit

An analytic solution of the time-independent dipolar GPE can be obtained in the limit of negligible kinetic energy contribution, called Thomas-Fermi limit [71,72]. This simple case can be used as a toy-model to understand the effect of dipolar interaction on the density distribution. For simplicity, let us consider a system with dipoles oriented along the z-axis and confined in a radially symmetric harmonic trap ($\omega_x = \omega_y = \omega_\perp$). In the Thomas-Fermi limit, the GPE in Eq. (35) for the ground state configuration reduces to

$$V_{\mathrm{trap}}(\mathbf{r}) + g|\psi(\mathbf{r})|^2 + \int d\mathbf{r}' V_{dd}(\mathbf{r} - \mathbf{r}')\,|\psi(\mathbf{r}')|^2 = \mu\,, \tag{39}$$

that admits solutions of the form

$$|\psi(\mathbf{r})|^2 = n(\boldsymbol{r}) = n_0\left(1 - \frac{r_\perp^2}{R_\perp^2} - \frac{z^2}{Z^2}\right)\,. \tag{40}$$

Here, $R_\perp$ and Z are the Thomas-Fermi radii in radial and axial direction. The pre-factor n_0 is instead the peak density, that is related to the total number of atoms through the expression $N = \frac{8\pi}{15}n_0 R_\perp^2 Z$. Remarkably, this solution is similar to the inverted parabola wave function in the pure contact interacting BEC [33]. However, the aspect ratio of the trapped gas does not coincide with the aspect ratio of the harmonic trap

$$\frac{R_\perp}{Z} < \frac{\omega_z}{\omega_\perp}\,. \tag{41}$$

This means that the dipolar gas is always stretched in the direction of the dipoles polarization. For further details on the analytical expressions for $R_\perp$ and Z we direct the reader to Ref [72]. The analysis of the shape of the density profile of a trapped dipolar condensate reveals a very important property called *magnetostriction*, as the global tendency for a dipolar system to align along the magnetic field direction. The intuitive picture behind this phenomenon is that the dipoles prefer to align in the head-to-tail configuration, because of the energetically favourable attractive nature of the

dipolar interaction.

> **In this thesis**, the phenomenon of magnetostriction will be revisited in Chapter 4 as a tool to impart rotation to the system through magnetic field rotations.

1.3.2. Imaginary time evolution

The ground state results obtained from energy minimization can also be achieved using a numerical technique known as *imaginary time evolution* [73]. This method relies on the decomposition of the condensate wave function into a superposition of eigenstates:

$$\psi(\mathbf{r}, t) = \sum_n \phi_n(\mathbf{r}) e^{\frac{-i E_n t}{\hbar}} \,, \tag{42}$$

where $\phi_n(\mathbf{r})$ is an eigenstate of $\psi(\mathbf{r}, t)$ with energy E_n. The eigenstates are ordered such that $E_n < E_{n+1}$, with the state at index $n = 0$ corresponding to the ground state. The numerical trick involves substituting $t \to -it$, effectively converting the time into an imaginary quantity. Under this transformation, the wave function becomes

$$\psi(\mathbf{r}, -it) = \sum_n \phi_n(\mathbf{r}) e^{-\frac{E_n t}{\hbar}} \,. \tag{43}$$

By factoring out the exponential term associated with the ground state energy, we can rewrite Eq. (43) as

$$\psi(\mathbf{r}, -it) = e^{-\frac{E_0 t}{\hbar}} \left[\phi_0(\mathbf{r}) + \sum_{n \neq 0} \phi_n(\mathbf{r}) e^{-\frac{(E_n - E_0) t}{\hbar}} \right] \,. \tag{44}$$

As t increases, the higher-energy terms in the sum decay exponentially due to their negative exponents $(E_{n \neq 0} - E_0 > 0)$. Therefore, the wave function converges to the ground state over time

$$\lim_{t \to +\infty} \psi(\mathbf{r}, -it) = e^{-\frac{E_0 t}{\hbar}} \phi_0(\mathbf{r}) = \psi_0(\mathbf{r}) \,. \tag{45}$$

Notice that the pre-factor $e^{-\frac{E_0 t}{\hbar}}$ also evolves with time. Therefore, the wave function must be renormalized at each time step during the imaginary time evolution to ensure proper normalization. In practice, imaginary time evolution is implemented by solving Eq. (34) with $\alpha = 0$ and $\gamma = 1$. This technique provides a very robust way to obtain the ground state wave function of the system.

> **In this thesis**, imaginary time evolution has been employed to study ground state solutions in the rotating frame (Chapters 4 and 5). In general, the convergence to the ground state wave function is slower than energy functional minimization. However, it is much more robust in presence of many metastable states with energies similar to the ground states. This is the case for rotating systems with many quantized vortices studied in Chapters 4 and 5. The numerical evolution is performed using a split-step method that incorporates rotations, known as the alternate direction implicit-time splitting pseudospectral (ADI-TSSP) method [74].

1.3.3. Real time evolution

The Gross-Pitaevskii operator can, in general, be time-dependent. This time dependence may arise either from intrinsic dynamics or from the application of a time-dependent protocol to the ground state. Indeed, one of the most common methods for probing the properties of a system involves applying an external perturbation and observing the resulting dynamics. This can be done by performing a *real time evolution* of the GPE, by setting $\alpha = 1$ and $\gamma = 0$ in Eq. (34).

> **In this thesis**, real time evolution of the GPE will be implemented to study the dynamical properties of a dipolar system during:
>
> - a ramp of the scattering length, to access the supersolid state of matter (Chapter 2);
>
> - the time-of-flight expansion to study the phase coherence of the system (Chapters 2 and 4);
>
> - the change of trapping frequencies to excite angular collective modes (Chapter 4);
>
> - a rotation of the dipoles polarization direction to dynamically induce vortex nucleation in supersolids (Chapter 4);
>
> The algorithm employed to solve the GPE in real time is the same as the imaginary time evolution, namely the ADI-TSSP method [74].

Time-of-flight expansion

A particularly intriguing real time simulation that will be exploit in this thesis, is the *time-of-flight* expansion. This protocol examines the evolution of the condensate wave function after a sudden removal of the trapping potential. Interestingly, while the expansion occurs in position space, it gives access to the momentum distribution of the system. Interacting BECs may initially undergo a non-ballistic expansion, with interatomic collisions causing an initial redistribution of momentum. However, as time progresses, the expansion transitions to a ballistic regime, where the density distribution reflects the system's momentum distribution. This phenomenon draws an analogy to Fraunhofer diffraction model in optics, where the far-field distribution corresponds to the Fourier transform of the initial complex field. Such measurements are widely used to probe the phase coherence of the system, since the first experimental observation of a BEC [12, 13], and will be used in the next chapters to experimentally detect the structure and the coherence properties of a dipolar supersolid state.

1.3.4. Complex time evolution

Real time simulations usually capture a wide range of perturbative phenomena in dipolar systems across different phases of matter. However, they sometimes fail reproducing the experimental timescales. This discrepancy is particularly evident in dynamical pro-

cesses that rely on instabilities, such as vortex nucleation. In such cases, experimental imperfections and finite-temperature effects introduce dissipation, which often acts as a seed for dynamical instabilities. As a result, these phenomena can occur on shorter timescales than those predicted by zero-temperature GPE simulations.

A simple numerical approach to mimic these effects is to employ a *complex time evolution* of the GPE. This method can be interpreted as a hybrid of real time and imaginary time evolution: at each time step, the system undergoes real time evolution in response to external perturbations while simultaneously relaxing slightly toward the stationary state under those conditions through an imaginary time component. This phenomenological dissipative equation was first proposed by Pitaevskii in the context of superfluid helium [75], and it was reintroduced into the cold-atom community 40 years later, especially in the context of vortex nucleation [76–78].

In practice, complex time evolution is implemented by solving Eq. (34) for $\alpha = 1$ and $\gamma \neq 0$. The value of the dissipation parameter γ must be carefully adjusted depending on the specific case.

> **In this thesis**, complex time evolution of the GPE will be used to investigate the the vortex dynamics during the glitch mechanism of a rotating dipolar supersolid (Chapter 5). The algorithm employed is the same as that used for both imaginary time and real time evolution, namely the ADI-TSSP method [74]. The values of γ usually range from 10^{-3} to 10^{-1}.

There exist more advanced techniques to account for dissipation as well as quantum and thermal effects [79]. Among these, the finite-temperature Stochastic eGPE (SeGPE) will be employed in Chapter 2 to simulate an experimental protocol, allowing for a comparison with the results obtained using the zero-temperature GPE. However, since the majority of the results in this thesis are derived using the zero-temperature GPE, these advanced methods will not be discussed in detail. For further information, we refer the reader to Refs. [79, 80].

1.4. Quantum and thermal noise

In GPE simulations, breaking the symmetry of the initial state is often useful, particularly when computing the ground state wave function—if its symmetry differs from the initial density distribution—or when performing real time simulations under perturbations. To address this problem, quantum and thermal fluctuations can be introduced into the initial state using the truncated-Wigner prescription [79]. Given the single-particle basis states ϕ_n and the complex Gaussian random variables α_n satisfying

$$\langle |\alpha_n|^2 \rangle = \left(e^{\epsilon_n/k_B T} - 1 \right)^{-1} + \frac{1}{2} \,, \tag{46}$$

the initial state at time $t = 0$ is initialized as

$$\psi(\mathbf{r}, t = 0) = \psi(\mathbf{r}) + \sum_n \alpha_n \phi_n(\mathbf{r}) \,. \tag{47}$$

Here, $\psi(\mathbf{r})$ represents either an initial guess or the ground state wave function, depending on whether the simulation is time-independent or time-dependent. The summation is

restricted to modes with energy $\epsilon_n \leq 2k_B T$, where T is the temperature.

1.5. Beyond mean-field correction

The GPE in Eq. (31) is widely used in the literature as it accurately describes the physics of dipolar BECs. However, within the mean-field framework, the dipolar interaction is predicted to drive the system into collapse when it dominates, as it favours an attractive head-to-tail configuration. This theoretical prediction was contradicted by experiment conducted by Pfau's group in 2016 [81]. In analogy to classical ferrofluids, the team observed that a dipolar condensate exhibited a Rosensweig instability following a sudden quench of the scattering length, forming high-density peaks of ^{162}Dy atoms called *droplets*. Surprisingly, these droplets remained stable for approximately 300 ms, suggesting that a crucial stabilizing mechanism was missing from the mean-field theory. The authors speculated that quantum fluctuations could play a stabilizing role, in analogy to the stabilization mechanism studied for quantum droplets in bosonic mixtures [82]. By incorporating dipolar quantum fluctuations into the GPE [83], theoretical models successfully reproduced the formation and stability of these droplets [65]. Similar results have been obtained using path-integral Monte Carlo simulations, albeit for small atom numbers [84].

Quantum fluctuations introduce an energy shift and result into a modified form of the Gross-Pitaevskii operator. Extending the Hamiltonian in Eq. (13) beyond the mean-field description requires not only the condensate particle operators $\hat{a}_0$, $\hat{a}_0^\dagger$ but also quadratic terms with particle operators at $\mathbf{p} \neq 0$, i.e. $\hat{a}_\mathbf{p}$, $\hat{a}_\mathbf{p}^\dagger$. This approach leads to the first beyond mean-field correction of the ground state energy of a BEC. The first calculation was done by Lee, Huang and Yang (LHY) in 1957 [85,86], then more recently adapted to the dipolar case [83,87]. Quantum fluctuations of interacting particles result in a small portion of particles occupying non-zero momentum states, even at zero temperature [83, 88]. This phenomenon is known as *quantum depletion* of the condensate population [33, 89–91].

For a three dimensional homogeneous dipolar BEC, the LHY beyond mean-field correction to the energy per unit volume is given by

$$\frac{\Delta E}{V} = \frac{1}{2}gn^2 \frac{128}{15\sqrt{\pi}}\sqrt{na^3}\mathcal{Q}_5\left(\varepsilon_{\mathrm{dd}}\right) , \qquad (48)$$

where the monotonic auxiliary function $\mathcal{Q}_5\left(\varepsilon_{\mathrm{dd}}\right)$ is defined as

$$\mathcal{Q}_5\left(\varepsilon_{\mathrm{dd}}\right) = \int_0^1 du \left(1 - \varepsilon_{\mathrm{dd}} + 3u^2\varepsilon_{\mathrm{dd}}\right)^{5/2} . \qquad (49)$$

Here, $n = |\psi|^2$ is the constant density of the system, so the energy shift due to quantum fluctuations scales as $\propto n^{5/2}$. Often, in literature this function is simplified to $\mathcal{Q}_5\left(\varepsilon_{\mathrm{dd}}\right) \sim 1 + \frac{3}{2}\varepsilon_{\mathrm{dd}}^2$ [65].

The extension of this approach to non-homogeneous systems is achieved through the local density approximation. Under this framework, the energy functional in Eq. (36)

turns into

$$E[\psi] = \int d\mathbf{r}\psi^*(\mathbf{r}) \left(-\frac{\hbar^2}{2m}\nabla^2 + V_{ext}(\mathbf{r}) \right) \psi(\mathbf{r}) +$$
$$+ \frac{g}{2}\int d\mathbf{r}|\psi(\mathbf{r})|^4 + \frac{1}{2}\int d\mathbf{r}d\mathbf{r}'|\psi(\mathbf{r})|^2 V_{dd}(\mathbf{r}-\mathbf{r}')\left|\psi(\mathbf{r}')\right|^2 + \qquad (50)$$
$$+ \frac{2}{5}\gamma(\varepsilon_{\mathrm{dd}})\int d\mathbf{r}|\psi(\mathbf{r})|^5 \ ,$$

where the coefficient $\gamma(\varepsilon_{\mathrm{dd}})$ is

$$\gamma\left(\varepsilon_{dd}\right) = \frac{32}{3\sqrt{\pi}}ga^{\frac{3}{2}}\mathcal{Q}_5\left(\varepsilon_{\mathrm{dd}}\right) \ . \qquad (51)$$

Similarly, the GPE turns into the *extended Gross-Pitaevskii equation* (eGPE), where the operator $\mathcal{L}_{\mathrm{GP}}$ is modified as

$$\mathcal{L}_{\mathrm{GP}} = \left[-\frac{\hbar^2\nabla^2}{2m} + V_{\mathrm{trap}}(\mathbf{r}) + g|\psi(\mathbf{r},t)|^2 + \int d\mathbf{r}'V_{dd}\left(\mathbf{r}-\mathbf{r}'\right)\left|\psi\left(\mathbf{r}',t\right)\right|^2 + \gamma(\varepsilon_{\mathrm{dd}})|\psi|^3 \right] \ .$$
$$(52)$$

The beyond-mean-field correction introduces an isotropic repulsive term that scales as $\propto n^{3/2} = |\psi|^3$, increasing rapidly with density. At typical condensate densities of $\sim 10^{20}$ atoms/m^3, this correction is negligible [65]. However, in strongly interacting dipolar systems, where mean-field theory predicts collapse, this correction becomes not only significant but is the primary mechanism responsible for stabilizing the system.

> **In this thesis**, results from numerical simulations are *always* obtained using the *extended* version of the Gross-Pitaevskii equation and the energy functional. Crucially, this beyond-mean field correction is responsible for the stability of the dipolar supersolid state analysed in the next chapters.

1.6. Excitation spectrum and Bogoliubov-de Gennes equations

The excitation spectrum of a BEC gives information about the energy needed to create a perturbation around the equilibrium configuration. A simple picture of the meaning of the excitation spectrum is given by Fig. 1.5. A container full of water plays the role of a BEC. At equilibrium, water is at rest. But, in principle, one can create a wave perturbation on top of it with a specific wavelength $2\pi/|\mathbf{k}|$, where $\mathbf{k}$ is the momentum of the wave. The excitation spectrum collects the information about how much energy ω one should give to the system to excite that precise wave with that wavelength and momentum. The shape of the spectrum highly depends on the nature of the system under consideration, since the collective waves are shaped by the interactions between atoms. In some cases $\omega(\mathbf{k})$ is a continuous function, in other cases it is discrete. In general, low-energy excitations are like long, gentle ripples (called *sound waves* or *phonons*). High-energy excitations are more like short, steep waves resembling the free motion of individual atoms (*single-particle*-like excitations). In this section, we show how Bose-Einstein condensates with dipolar interaction enrich this general picture.
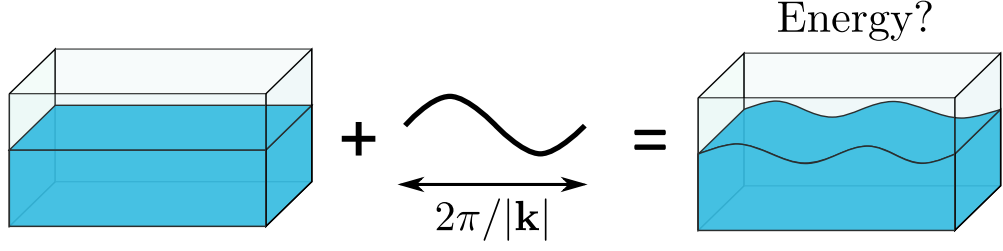
Energy?

$$+ \quad 2\pi/|\mathbf{k}| \quad =$$

Figure 1.5.: Illustration giving a simple interpretation of the excitation spectrum.

The excitation spectrum of dipolar BECs is a crucial component for understanding the emergence of the supersolid phase of matter.

In order to calculate the excitation spectrum of a BEC, we use the Bogoliubov-de Gennes approach. Originally derived by Bogoliubov in 1947 [92], this formalism was later extended to superconductivity by de Gennes [93]. The key idea is to describe small fluctuations of the system around the ground state solution $\psi(\mathbf{r})$ obtained from Eq. (31). This is equivalent to perturb the wave function in the following way:

$$\psi(\mathbf{r}, t)' = e^{-i\mu t/\hbar} \left\{ \psi(\mathbf{r}) + \eta \left[u_n(\mathbf{r}) e^{-i\omega_n t} + v_n^*(\mathbf{r}) e^{i\omega_n t} \right] \right\} \tag{53}$$

Here, $u_n(\mathbf{r})$ and $v_n(\mathbf{r})$ are the Bogoliubov amplitudes associated to the n-th excitation mode with energy ω_n. The coefficient η is a small number. The Bogoliubov amplitudes are normalized to preserve bosonic commutation relations [94], so that the integral over the volume

$$\int d\mathbf{r} \left[|u_n(\mathbf{r})|^2 - |v_n(\mathbf{r})|^2 \right] = 1 \,. \tag{54}$$

By substituting the perturbed wave function into Eq. (31), we can linearize GPE around the ground state solution, keeping only the linear terms in η. This linearization problem can be rewritten in form of the Bogoliubov-de Gennes (BdG) equations, that consist of two coupled differential equations here reported in the matrix form

$$\begin{pmatrix} \mathcal{L}_{\mathrm{GP}}[\psi] + \hat{X} & -\hat{X} \\ \hat{X} & -\mathcal{L}_{\mathrm{GP}}[\psi] - \hat{X} \end{pmatrix} \begin{pmatrix} u_n \\ v_n \end{pmatrix} = \hbar \omega_n \begin{pmatrix} u_n \\ v_n \end{pmatrix} \,. \tag{55}$$

The operator $\hat{X}$ acts on a generic function $f(\mathbf{r})$ so that

$$\hat{X} f(\mathbf{r}) = g |\psi(\mathbf{r})|^2 f(\mathbf{r}) + \psi(\mathbf{r}) \int d\mathbf{r}' V_{dd} \left(\mathbf{r} - \mathbf{r}' \right) \psi \left(\mathbf{r}' \right) f \left(\mathbf{r}' \right) \,. \tag{56}$$

Quantum fluctuations can be easily incorporated by adding the LHY term computed for the ground state wave function to the operators $\mathcal{L}_{\mathrm{GP}}$ and $\hat{X}$:

$$\mathcal{L}_{\mathrm{GP}} \to \mathcal{L}_{\mathrm{GP}} + \gamma \left(\varepsilon_{dd} \right) |\psi|^3 \tag{57}$$

$$\hat{X} \to \hat{X} + \frac{3}{2} \gamma \left(\varepsilon_{dd} \right) |\psi|^3 \,. \tag{58}$$

Solving the BdG equations provides the excitation modes $u_n(\mathbf{r})$ and $v_n(\mathbf{r})$, along with their corresponding energies ω_n. The derivation presented above assumes a real ground

state wave function; however, a modified version of the BdG equations can also be applied in rotating or translating reference frames [95, 96].

> **In this thesis**, BdG equations are solved using the Matlab routine `eigs`, which is a matrix-free iterative implementation of the Arnoldi algorithm [97]. Being matrix-free means that the BdG operator does not need be constructed in a matrix form which would be prohibitively memory intensive, but instead is defined as a function by its action [68]. For finite two-dimensional supersolid systems (Chapter 2), high resolution grids are necessary for the convergence of the BdG modes. Usually, tests for convergence have been successful using 3D meshes with *at least* $(300 \times 300 \times 64)$ points. Also increasing the size of Krylov subspace ('`SubspaceDimension`' input parameter for `eigs`) has been found to be crucial for the convergence of the eigenvalue problem.

1.6.1. Spectrum of a dipolar BEC

Homogeneous case

The solution of the BdG equations for an homogeneous dipolar BEC is analytical and given by

$$\omega(\mathbf{k}) = \sqrt{\frac{\hbar^2 k^2}{2m} \left[\frac{\hbar^2 k^2}{2m} + 2n_0 \tilde{U}(\mathbf{k}) \right]}, \tag{59}$$

where n_0 represents the uniform density of the system and $\tilde{U}(\mathbf{k})$ is the Fourier transform of the total inter-particle interaction potential in Eq. (24). Using Eq. (9) for the dipolar interaction and considering that the Fourier transform of the δ-function in the contact interacting term is a constant, the dispersion relation becomes

$$\omega(\mathbf{k}) = \sqrt{\frac{\hbar^2 k^2}{2m} \left\{ \frac{\hbar^2 k^2}{2m} + 2n_0 \left[g + g_{\mathrm{dd}} \left(3\cos^2 \theta_k - 1 \right) \right] \right\}}. \tag{60}$$

In the low-momentum limit $(k \to 0)$, this dispersion relation is linear because the quadratic terms are negligible:

$$\omega(\mathbf{k} \to 0) \sim \hbar k \sqrt{\frac{n_0}{m} \left[g + g_{\mathrm{dd}} \left(3\cos^2 \theta_k - 1 \right) \right]} \sim \hbar k v_s, \tag{61}$$

where the excitations correspond to long-wavelength *phonons* excitations propagating at the speed of sound v_s. In the opposite limit, large k excitations asymptotically approaches the quadratic free particle behaviour

$$\omega(\mathbf{k} \to \infty) \sim \frac{\hbar^2 k^2}{2m}. \tag{62}$$

Importantly, the presence of a gapless branch in the dispersion relation $(\lim_{\mathbf{k} \to 0} \omega(\mathbf{k}) = 0)$ is related to the spontaneously broken continuous gauge symmetry of the BEC[5].
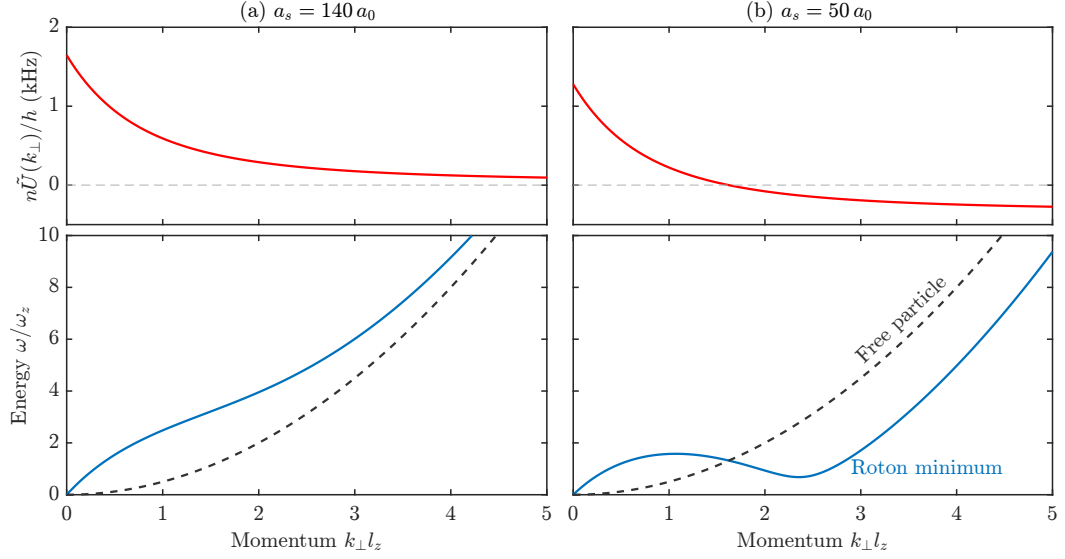
Figure 1.6.: Excitation spectrum of an infinite planar dipolar BEC for a (a) large scattering length and for a (b) small scattering length. The upper panels show the momentum dependence of the total interaction in momentum space. The lower panels show the excitation spectrum (blue solid line) with the the free-particle quadratic behaviour (dark gray dashed line) expected at large momenta. Results are obtained from a quasi-2D model in Ref. [98], using the parameters $n = 10^{20}\,\mathrm{m}^3$, $\omega_z/2\pi = 100\,\mathrm{Hz}$.

Infinite trapped dipolar BEC

The introduction of a trapping potential significantly alters the excitation spectrum. To gain insights, it's useful to consider a planar infinite system with dipoles polarized along the axis of the confinement ($z-$axis). We assume an harmonic confinement ω_z, with characteristic length $l_z = \sqrt{\hbar/m\omega_z}$. This geometry was first explored by Santos, Shlyapnikov and Lewestein in 2003 to present the novel features of the dipolar spectrum [99]. Similar features, however, also emerge in an infinitely elongated system [100]. Here, for consistency with the rest of the thesis, we consider the flattened geometry.

Under the quasi-2D approximation–where the wave function in the $z-$direction is assumed to have a Gaussian profile–this system admits a simple analytical spectrum [98]. For a condensate with areal density n_{2D}, the Bogoliubov spectrum for *in-plane modes* takes a form similar to Eq. (59):

$$\omega(\mathbf{k}_\perp) = \sqrt{\frac{\hbar^2 k_\perp^2}{2m}\left[\frac{\hbar^2 k_\perp^2}{2m} + 2n\tilde{U}(k_\perp)\right]}. \tag{63}$$

Here, $\mathbf{k}_\perp$ represent the momentum in the direction perpendicular to the confinement and the 3D density is $n = n_{2D}/\sqrt{2\pi}l_z$. The Fourier transform of the effective 2D interaction potential is expressed as

$$\tilde{U}(k_\perp) = g\left[1 + \epsilon_{dd}F_\perp\left(\frac{k_\perp l_z}{\sqrt{2}}\right)\right]. \tag{64}$$

---

[5]This is also called $U(1)$ symmetry, due to the BEC choosing one value of the phase $\theta \in [0, 2\pi]$.

where the auxiliary function $F_\perp$ is defined as

$$F_\perp(x) = 2 - 3\sqrt{\pi}x e^{x^2}\text{erfc}(x) \tag{65}$$

and $\text{erfc}(x)$ denoting the complementary error function.

Figure 1.6 illustrates the excitation spectrum for two values of the scattering length. The interplay between the transverse confinement and the anisotropic dipolar interaction yields to a momentum-dependent total interaction, as shown in the upper panels. For large values of a_s, $\tilde{U}(k_\perp)$ decreases but remains positive (left). However, for smaller values of a_s, $\tilde{U}(\mathbf{k})$ changes sign (right). The negative contribution of the effective interaction in momentum space leads to the emergence of a minimum at finite momentum k_{rot}, known as *roton* minimum. Additionally, at intermediate momentum, the spectrum exhibits a local maximum, referred to as the *maxon*. This characteristic roton-maxon structure is also observed in liquid helium [101], but in dipolar Bose-Einstein condensates (BECs), the energy gap of the roton minimum is fully tunable via a_s. As a consequence, it is possible to drive the system into a regime where there is no energy cost to modulate the density at the roton wavelength $\sim 2\pi/k_{rot}$. This simple pictures hints toward the interpretation of the roton as a precursor of crystallization [102].

Finite trapped dipolar BEC

In the previous section we showed how the dispersion relation $\omega(k_\perp)$ is a continuous function of $k_\perp$, when the system has no confinement in the plane perpendicular to the polarization direction. This means that every excitation mode is a plane wave with an associated momentum $k_\perp$ and the excited system develops a characteristic density modulation with wavelength $2\pi/k_\perp$.

When the system is fully trapped in the three directions the momentum k is no longer a good quantum number. This prevents the association of a Bogoliubov mode with a single momentum or, equivalently, a single wavelength. To analyse the excitation spectrum in this scenario, the dynamic structure factor becomes a particularly valuable tool, offering a clear representation of the spectrum. The dynamic structure factor is defined as [33]

$$S(\mathbf{k},\omega) = \sum_n \left| \int d\mathbf{r}[u_n^* + v_n^*]e^{i\mathbf{k}\cdot\mathbf{r}}\psi(\mathbf{r}) \right|^2 \delta(\omega - \omega_n) \tag{66}$$

and it gives information about the density response of the system when it is perturbed at specific momentum $\mathbf{k}$ and energy ω.

In Fig. 1.7 we show four exemplar excitation spectra for three-dimensional dipolar BECs in the dipolar dominated regime ($\epsilon_{dd} \sim 1.4$) confined in a pancake trap. The spectrum is computed along the k_x direction. However, due to the system's cylindrical symmetry, the results apply equivalently to any radial direction. The light regions mark the position of the excitation modes, revealing the characteristic roton minimum around $k\,l_z \sim 1$, similarly to Fig. 1.6. The confining potential leads to a discrete excitation spectrum and causes a broadening of each mode along $\mathbf{k}$ for a given energy. Additionally, finite-size effects may even yield multiple peaks in at the same k. To improve visualization, the modes in Fig.1.7 are also artificially broadened in energy, mimicking the spectral resolution observed in experimental Bragg scattering measurements [103, 104].
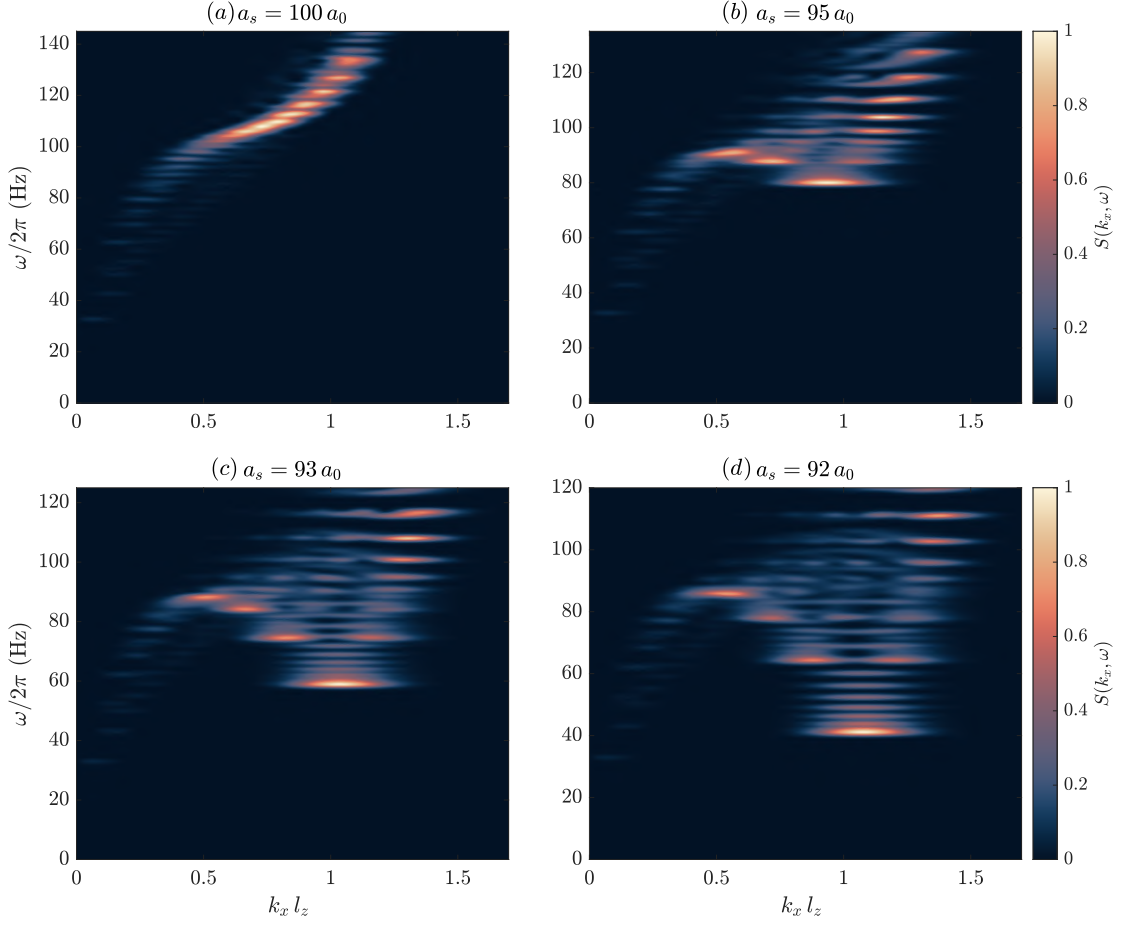
Figure 1.7.: Excitation spectrum of a two-dimensional dipolar BEC with ^{164}Dy atoms for three values of the scattering length in the dipolar dominated regime. The dynamic structure factor is normalized to its maximum value. For each scattering length the first 64 lowest energy modes are shown. Parameters: trap frequencies $\omega = 2\pi \times (33, 33, 167)\,\text{Hz}$, atom number N $= 210000$, dipoles polarized along z-axis.

It is useful to consider the moments of the dynamic structure factor $m_p(\mathbf{k})$, defined as the integrals

$$m_p(\mathbf{k}) = \hbar^{p+1} \int \omega^p S(\mathbf{k}, \omega) d\omega\,. \tag{67}$$

The $p = 0$ moment is the static structure factor, $S(\mathbf{k}) = \int d\omega S(\mathbf{k}, \omega)$ which reflects the symmetries of the state and of the highest response modes. Instead, the $p = 1$ moment is particularly useful from the numerical point of view. In fact, reaching the convergence of the BdG modes can be problematic. One way to ensure the convergence is to compare the energy of some modes with the expected theoretical value, but this is not always possible. However, another possibility is to calculate the $p = 1$ moment of $S(\mathbf{k}, \omega)$ and check the validity of the $f-$sum rule [33]

$$\int \omega S(\mathbf{k}, \omega) \, d\omega = \frac{\hbar^2 k^2}{2m}\,. \tag{68}$$

This rule is generally applicable regardless of the interaction potential and sets the range

of k within which modes are well converged.

> **In this thesis**, excitation spectra for dipolar gases in the supersolid phase are presented for both fully trapped system (Chapter 2) and 2D planar infinite systems (Chapter 3). All the spectra are plotted for a k range for which the $f-$sum rule is satisfied and the convergence of the modes has been benchmarked with theoretical predictions (when possible).

1.6.2. Exemplar collective modes

The excitation spectrum and dynamic structure factor are constructed using the Bogoliubov modes u_n and v_n, which also provide insights into the perturbation profiles. Figure 1.8 illustrates the shapes of several exemplar modes obtained from solving the BdG equations for a fully trapped dipolar BEC in a cylindrical trap (upper panel). The corresponding excitation spectrum is depicted in Fig. 1.7(c).

The density perturbation is visualized by plotting

$$\Delta\psi = (u_n + v_n^*)|\psi| \tag{69}$$

normalized to its maximum value. Regions in red indicate an increase in density due to the excitation, while regions in blue signify areas where the density decreases. Effectively, one can visualize the effect of the mode picturing the density of the system moving from blue to red regions. The modes could be classified according to the symmetry properties: axially symmetric along y-axis, axially symmetric along x-axis, possessing both axial symmetries, or antisymmetric about the center. Because the ground state is confined in a cylindrically symmetric trap ($\omega_x = \omega_y = \omega_r$), axially symmetric modes with respect to the to x-axis and y-axis are degenerate.

The lowest-energy mode with $y-$axial symmetry is the *dipole mode*, which describes the axial oscillation of the entire system around the center of mass. Its frequency always matches the trap frequency in that direction (in this case, $\omega = \omega_r = 33\,\text{Hz}$). The frequency of this mode is often used as a benchmark to assess the convergence of the BdG modes. The first mode symmetric along x and y is the *quadrupole mode*. It represents deformations of the system where one axis stretches while the perpendicular axis contracts, preserving the overall volume. For dipolar systems, the frequency of this mode depends on many parameters and it is possible to predict the value analytically in the Thomas-Fermi limit [105]. However, regardless the regime, it is typically close to the theoretical prediction for contact-interacting BECs $\omega = \sqrt{2}\,\omega_r$ (in this case, $\omega = 43.11\,\text{Hz} \sim 1.3\,\omega_r$) [33]. Other surface modes with increasing angular nodal lines emerge in all the symmetry manifolds at progressively higher frequencies.

Interestingly, in addition to surface modes, many localized modes also appear at low energies and are crucial in dipolar gases [106–108]. These modes form the roton minimum in the excitation spectrum shown in Fig. 1.7(c), so they will be referred to as *roton modes*. The corresponding dynamic structure factor is very enhanced, making them the most favorable modes to be populated in response to external perturbations. They exhibit different symmetries and angular nodal lines but, in contrast to surface modes, they are highly localized at the system's center. By adjusting the scattering
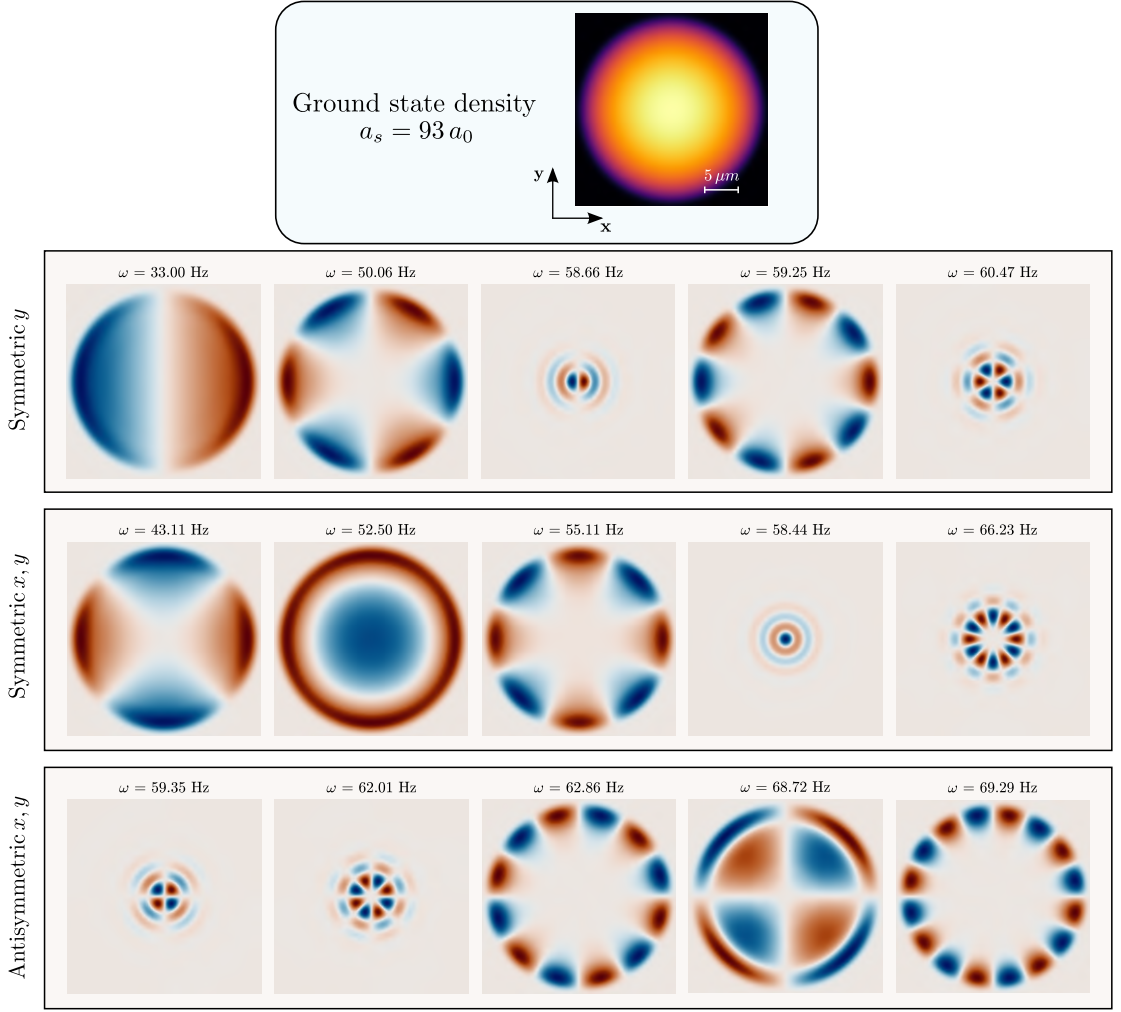
Figure 1.8.: Exemplar excitation modes calculated from BdG equations. Upper panel shows the ground state density of the unperturbed state, lower panels show the density perturbation defined in Eq. (69). For each symmetry manifold, the five lowest energy modes are visualized through the positive (red) and negative (blue) density variation. Degenerate modes appearing in more than a symmetry manifold have ben removed and showed only once. Parameters: trap frequencies $\omega = 2\pi \times (33, 33, 167)\,\mathrm{Hz}$, atom number N = 210000, $a_s = 93\,a_0$, dipoles polarized along z-axis.

length, the energy of these modes decreases, eventually leading to the complete softening of the roton minimum at zero-energy.

The instability of roton modes is the driving mechanism behind the emergence of the *supersolid* phase of matter, which will be explored in the next section[6].

---

[6]A this point, the reader may wonder whether these modes called *rotons* are related to rotations, as the name suggests. The short answer is: they are not. The name "roton" has been assigned by Landau and Feynman after arguing that a roton minimum in the excitation spectrum was related to local vorticity, with the roton being the "*ghost of a vanishing vortex ring*" [109]. The name remained unchanged since then, even though further studies showed the absence of connection with local vorticity and, instead, the relation with crystallization instability. As Nozières said, the roton can be interpreted more as a "*ghost of a Bragg spot*" [102].
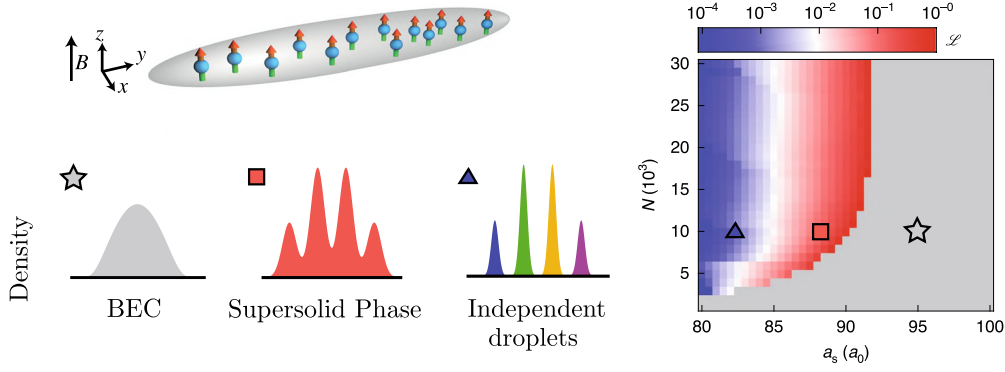
Figure 1.9.: Ground state phase diagram of a dipolar gas composed of ^{164}Dy atoms, as a function of atom number and scattering length. The system is confined in a cigar-shaped trap with frequencies $\omega/2\pi = (229, 37, 135)$ Hz. Three regimes are identified: unmodulated BEC, supersolid, and independent droplets. The order parameter $\mathcal{L}$ quantifies the density links between the peaks. The color of the density highlights the difference between a supersolid phase, where droplets share global phase coherence, and independent droplets, where each droplet exhibits a random phase (indicated by distinct colors). Subplots are adapted from Refs. [32,110].

1.7. Ground state phase diagram of a dipolar gas

The ground state phase diagram of a dipolar Bose-Einstein condensate encompasses distinct phases, each characterized by unique properties and behaviours. The origin of the new phases relates to the ability to control the shape of the excitation spectrum, particularly by adjusting the energy gap at the roton minimum. Notably, when the roton energy gap is reduced to zero, the system can spontaneously modulate its density without incurring any energy cost. The wavelength of this density modulation is related to the roton momentum.

Figure 1.9 presents the ground state phase diagram for a quantum degenerate dipolar gas, calculated by solving the eGPE. The system, confined in a cigar-shaped trap, reflects the geometry used in the first experimental observations of this diagram [30–32]. The theory predicts three distinct phases, which can be explored by varying the atom number and the scattering length a_s:

- **Unmodulated BEC phase**: it is the ordinary BEC state, described by a macroscopic wave function characterized by a global phase coherence. Because of that, the system has superfluid properties.

- **Supersolid phase**: the BEC state spontaneously develops a density modulation, while maintaining the global phase coherence. The global phase coherence arises from non-negligible density links connecting adjacent peaks. The periodic structure confers solid properties, while keeping simultaneously superfluid nature. Usually, these density peaks are called *droplets*.

- **Independent droplet regime**: this is a modulated state that can be reached in the strongly dipolar regime. The droplets that are fully disconnected, so that the tunnelling of particles between droplets is suppressed. The system has crystalline properties due to the periodic density modulation but no global phase coherence. Each droplet maintains its phase coherence and superfluid character only within itself.

The order parameter used to identify the modulated phases is $\mathcal{L} = 1 - C$, where

$$C = \frac{n_{\max} - n_{\min}}{n_{\max} + n_{\min}} \tag{70}$$

is the density contrast that measures the strength of the link between the peaks. Here, $n_{\max}$ and $n_{\min}$ are the density maximum and minimum in the central region of the density distribution.

As will be clear in the next chapter, understanding that a dipolar BEC could support a ground state density modulation, corresponding to the long-sought supersolid phase, marked a significant breakthrough [111]. While mean-field theory predicts collapse, quantum fluctuations stabilize these intriguing phases. The next chapter will provide a detailed historical overview of this development and elaborate on the key properties of the supersolid state in comparison to the other phases.

2

Supersolidity in Dipolar Quantum Gases: from 1D to 2D supersolids

The intuitive image of a superfluid as a system capable of sustaining perfect, frictionless flow inherently seems incompatible with the with the concept of localization as emerging in crystalline structures of solid bodies. Yet, in the quantum realm, the coexistence of these seemingly opposing properties becomes possible. This phenomenon finds realization in the supersolid phase of matter. The ground state phase diagram of a dipolar BEC features a supersolid phase, providing a versatile platform where to test this coexistence of seemingly competing natures.

In this chapter, we first provide a brief historical overview of the supersolid phase. We then discuss the early hints and the first experimental observations of supersolid phases in dipolar gases confined within elongated traps. Following this, we examine the essential ingredients required to induce the structural transition from one-dimensional to two-dimensional supersolids, addressing both theoretical insights and experimental advancements. The final sections highlight the publications to which the author of this thesis has contributed.

2.1. Historical overview

Supersolidity arises in systems that spontaneously break two fundamental symmetries: the continuous translational symmetry, leading to the formation of a discrete periodic spatial structure, and the gauge symmetry, which establishes the global phase coherence characteristic of superfluid systems, such as Bose-Einstein condensates. Tracing the historical development of this phenomenon reveals the key concepts that continue to underpin our understanding of supersolid systems today.

The concept of combining BECs with solid-like properties was first introduced by Penrose and Onsager in 1956 [9]. In their work, however, they concluded that achieving BEC within a solid at absolute zero temperature was not possible, as the localization of atoms at fixed lattice sites was deemed incompatible with off-diagonal long-range order. A few years later, Andreev and Lifshitz revisited this idea, proposing a novel theory in which BEC could emerge through defects within a crystal lattice [112]. Chester reached the same conclusion the following year [113]. These defects, such as delocalized
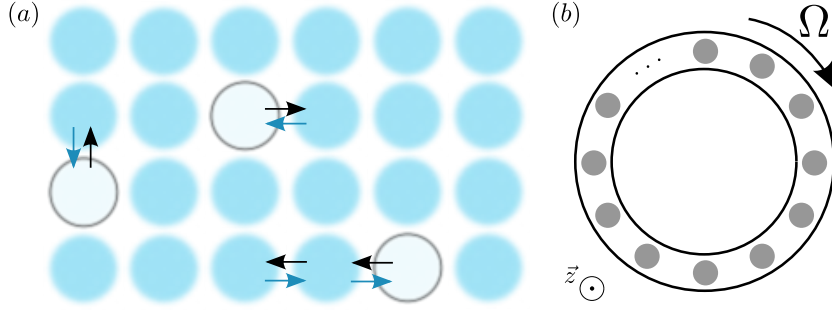
Figure 2.1.: Original models for supersolidity. (a) Defect supersolid according to Ref. [112]: lattice containing vacancies (gray circles) that can easily move in different directions throughout the whole system. The mobility of the vacancies (black arrows) translates into the mobility of the particles (blue arrows). (b) Particles confined in a rotating annulus according to Ref. [117].

impurities or vacancies, could obey bosonic statistics and condense while remaining embedded in the crystal. The motion of these impurities could then be translated into an effective motion of particles within the lattice, enabling the system to simultaneously exhibit both solid and superfluid properties; see Fig.,2.1(a). However, the first attempts to observe a superfluid flow in a sample of solid ^{4}He under a pressure gradient yielded no positive results in the observation of any superfluid flow[1] [115, 116].

In 1970, Leggett introduced a key concept for the study of supersolid [117]. He proposed that the defining hallmark of a supersolid state would be a sudden deviation in the moment of inertia from its classical value, which is calculated based on the mass distribution. This phenomenon, known as *non-classical rotational inertia* (NCRI), results in a diminished response of the system to external rotational forces. The deviation arises from the superfluid component of the system, which does not participate in the rotation due to its frictionless nature–a hallmark of superfluidity. Leggett modelled this behaviour by considering individual particles, which obey bosonic statistics, arranged periodically in a cylindrical annulus; see Fig.2.1(b).

Considering a small rotation at frequency Ω about the z-axis, Leggett defines the fraction of non-classical rotational inertia as

$$f_{\mathrm{NCRI}} = 1 - \frac{I}{I_{rig}} = 1 - \lim_{\omega \to 0} \frac{\langle \hat{L} \rangle}{I_{rig}\, \omega}\,, \tag{1}$$

where the supersolid moment of inertia $I = \langle \hat{L} \rangle/\omega$ is reduced with respect to the classical one $I_{rig} = \int d\mathbf{r}\, n(\mathbf{r}) r^2$ because of the partial superfluid nature of the system [118]. Here, $\langle \hat{L} \rangle$ is the expectation value of the angular momentum calculated for the wave function in equilibrium in the rotating frame.

In the annulus geometry, the fraction of non-classical rotational inertia f_{NCRI} is a measure of the superfluid fraction $f_s = \rho_s/\rho$, which quantifies the fraction of the mass that does not respond to perturbations due to the superfluid nature (in this case, rotations). Here, ρ denotes the total average density and ρ_s is the superfluid density. Importantly, ρ_s does not necessarily correspond to a physical fraction of particles that

---

[1]Systems made of solid ^{4}He were the most promising candidate to observe this effect because of the large zero-point motion, which causes its atoms to remain mobile even at absolute zero, potentially creating vacancies [112, 114].

can be individually identified and localized in space. Rather, it quantifies the system's reduced response to external perturbations. In other words, ρ_s is not a count of particles that are part of a superfluid state, but it reflects an effective mass density that measures the system's reduced response due to the superfluid nature. In general, calculating f_s is challenging and it requires a careful theoretical analysis that depends a lot on the geometry of the system, see Appendix A.

Leggett estimates an upper bound for the superfluid fraction of the system at zero-temperature as

$$f_s \leq \frac{1}{n_0} \left[\frac{1}{2\pi} \int_0^{2\pi} \frac{\mathrm{d}\theta}{\frac{1}{L} \int_0^L \mathrm{d}r\, n(r,\theta)} \right]^{-1} , \tag{2}$$

where $r \in [0, L]$ is the the radial coordinate, $\theta \in [0, 2\pi]$ is the angular coordinate and n_0 denotes the average density over the entire spatial domain of the system. Notice that when the system is angularly uniform, $f_s = 1$. Conversely, any angular density variation along the annulus, which signals the breaking of the translational symmetry, automatically reduces the upper bound, implying a diminished superfluid response $f_s < 1$.

Following these ideas, the famous experiment by Kim and Chan in the early 2000 claimed evidences of NCRI behaviour in a ^{4}He experiment with a torsional pendulum, thus stating the observation of a supersolid behaviour [119, 120]. This work sparked an intense debate among researchers. The interpretation of the results was soon called into question, when Day and Beamish observed a temperature-dependent increase in the shear modulus of solid helium, suggesting that the apparent NCRI signal could instead be attributed to changes in the material's elastic properties [121]. In light of these findings and further investigations, Kim and Chan's results have been disproven a decade after [122]. At the time of this thesis, no clear evidence of supersolidity in ^{4}He has been observed[2].

The turning point for the experimental evidence of supersolidity was a change of perspective: rather than beginning with a system exhibiting solid properties and searching for the ingredients to induce superfluidity, one could instead start with a superfluid system and introduce elements that give rise to solid-like behaviour. Following the same approach of Gross in 1957 [126], one could start from a superfluid BEC and add some conditions for which the condensate wave function could spontaneously develop a periodic density modulation, thereby acquiring a solid-like behaviour. In 1994 Pomeau and Rica demonstrated that such behaviour is achievable when the inter-particle interaction becomes momentum-dependent in Fourier space, leading to a tunable roton gap in the excitation spectrum [127]. A very simple model meeting this criterion is a many-body bosonic system with a soft-core interaction [128–130]. Despite being an excellent toy model from the theoretical point of view (indeed, it will be used in Chapter 3), the experimental implementation of such a system is very challenging and no experimental results have been obtained so far in this type of platform.

A momentum-dependent inter-particle interaction can be obtained in other ways. In the last decades, supersolid properties have been probed across various experimental

---

[2]Actually, recent studies have highlighted some new connections between helium and supersolidity. In 2021 it was demonstrated that a thin film of ^{4}He on a graphite substrate can form a spatially modulated superfluid [123]. Additionally, indirect measurements have recently suggested the existence of a non-uniform pair density wave in a superfluid composed of bosonic pairs of ^{3}He particles [124, 125].

platforms, particularly in the context of ultracold atoms and photonics platforms. Here, the high tunability and precise control of the parameters enable detailed exploration of the different regimes. It is important to stress that the understanding of the physics behind the experimental results with ^{4}He has been fundamental for the research on supersolidity in other platforms. Below, we review some of the most famous alternative experimental platforms before focusing exclusively on the dipolar case for the rest of this thesis.

Cavity mediated supersolids

In ultracold systems, cavity-mediated long-range interactions can be engineered using external cavities. These interactions are controlled by a pump laser, with the interaction strength adjustable via the laser's power and detuning. Similar to the dipolar case discussed in Sec. 1.6.1, momentum-dependent interactions can result in the softening of a roton-type mode, ultimately leading to a supersolid phase [131–134]. The supersolid state that emerges is stiff. This means that in the excitation spectrum there are no low-momentum phonons modes associated to a change of the modulation wavelength. However, the modes associated to a change in modulation amplitude or phase were experimentally probed [135]. The realization of non-stiff supersolid is based on multimode cavity QED [136], which was also recently realized experimentally [137].

Spin-orbit coupled supersolids

Bose-Einstein condensates with spin-orbit coupling are composed of particles whose internal spin states are linked to their momentum through optical coupling [138]. Due to the modified interactions between the two dressed atomic spin states, these systems have been shown to host a supersolid state with a stripe density modulation [139, 140]. In a very recent study by the Tarruell group, the investigation of the excitation spectrum revealed that this stripe phase has a compressible crystal structure [141].

Exciton-polariton supersolids

A very recent work showed that a supersolid phase can be reached also in the context of a driven-dissipative non-equilibrium exciton-polariton condensates [142]. Here, the strongly coupled hybrid light-matter excitations in a photonic crystal waveguide, called exciton-polaritons [143], could occupy all the same coherent quantum state and simultaneously show a density modulation due to the inter-polariton interaction. Also here, the wave vector of the density modulation depends on interaction parameters.

2.2. Dipolar supersolids

All the systems discussed above rely on some form of engineered momentum-dependent interactions to induce supersolidity. In contrast, dipolar systems naturally possess such interactions due to their intrinsic long-range and anisotropic character, making the emergence of supersolid behaviour significantly more robust. As presented in Chapter 1, the excitation spectrum of a dipolar gas develops a roton minimum. This feature,
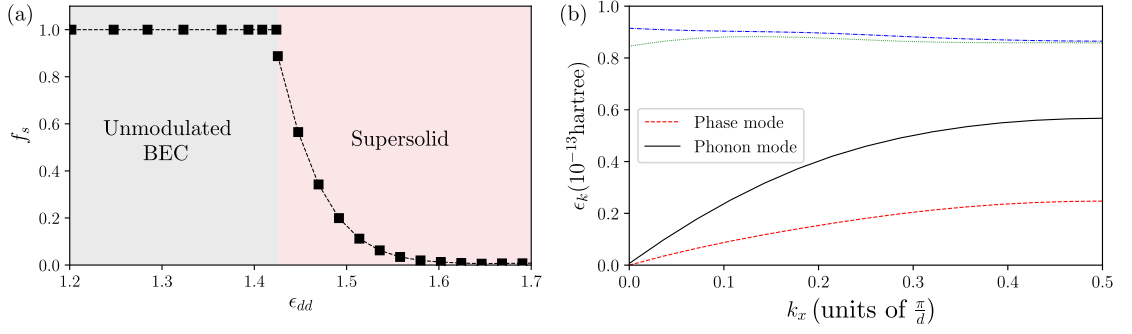
Figure 2.2.: Theoretical investigation of an infinite 1D supersolid: (a) superfluid fraction f_s calculated from the non-classical translational inertia (see Appendix A) and (b) excitation spectrum along the density modulation direction up to the first Brillouin zone. Adapted from Ref. [111].

as suggested by Nozières, can be seen as a soft mode precursor of a crystallization instability [102].

It is instructive to compare the features of the roton spectrum in helium with the one in dipolar gases. For helium the roton minimum originates from the strong correlations and the wavelength is on the order of the inter-particle spacing. Consequently, when the roton softens [144], it leads to conventional crystallization with approximately one atom per lattice site. Instead, in dipolar gases the system is very dilute and the roton comes from the mean-field competing interactions. Additionally, the roton wavelength is much larger than the inter-particle distance, so the crystallization involves thousands of atoms for each lattice site.

The observation of the roton modes population in a system of magnetic atoms provided the first hint that dipolar gases could be a good platform to observe supersolid properties [107]. The population of roton modes was dynamically seeded in a cigar-shaped dipolar BEC by quickly quenching the scattering length to a lower value, effectively softening the roton energy gap of the spectrum, and quench it up to the original value. Then, by letting the system expand, the interference pattern reflected the system's momentum distribution. The results showed that the system populates roton modes at finite momenta, whose dependence on the geometry of the system and interaction parameters was successfully tested. Notably, the population of these modes eventually saturated, suggesting that additional mechanisms may become significant after the initial exponential growth.

Inspired by these results, a theoretical work by Roccuzzo and Ancilotto showed that when the roton gap softens the system on an infinitely elongated geometry does not collapse but it spontaneously develop a periodic density modulation made of clusters of particles connected by a superfluid background [111]. These clusters are dipolar droplets stabilized by quantum fluctuations containing thousands of atoms. The supersolid nature was theoretically detected through different analysis:

- The system exhibits a finite f_s, calculated through the non-classical translational inertia; see Fig. 2.2(a). Notice that an infinite supersolid made of a single chain of droplets is equivalent to Leggett's ring geometry

- The excitation spectrum has two gapless branches, each one for a spontaneously

broken continuous symmetry. There is a density branch including phonon crystal excitations, due to the broken translational symmetry. The phase branch is associated to phase excitations and it results from the broken gauge symmetry, similar to an unmodulated BEC. See Fig. 2.2(b).

The stabilization mechanism of dipolar systems via quantum fluctuations was first hinted at in an earlier experiment by the group of Tilman Pfau, which observed the emergence of a crystalline structure upon reducing the contact interaction in a dipolar Bose gas [81]. This finding was later reinforced by other experiments using Dy and Er atoms, which demonstrated the formation of stable dipolar droplet states [145, 146] and the subsequent theoretical works [65, 147, 148].

Finally, as a consequence of all the experimental efforts and theoretical support, in 2019 three research groups independently observed a dipolar supersolid. This happened in Pfau's group in Stuttgart [31], in Modugno's group in Pisa [30] and in our Ferlaino's group in Innsbruck [32]. Two distinct techniques have been employed to reach the supersolid state, see Fig. 2.3(a). The group in Stuttgart and Pisa initially produced an unmodulated BEC of ^{162}Dy atoms and then gradually ramped the scattering length across the BEC-to-supersolid transition [30, 31]. The team in Innsbruck, instead, used two different methods. They achieved a supersolid state with ^{166}Er atoms by using a similar ramp of the scattering length and also realized a supersolid with ^{164}Dy atoms by directly evaporating from a thermal cloud [32]. In the second case, the sample was cooled down while keeping the scattering length fixed at its target value [149]. While the supersolid states produced from the scattering length ramp had a lifetime of ≈ 20 ms, the supersolid state from evaporative cooling was long-lived with a lifetime > 100 ms.

The periodic density distribution of the supersolid state is observed by imaging in-situ the system confined in the trap, see Fig. 2.3(b). Instead, the global phase coherence shared between the droplets is detected by time-of-flight expansions, see Fig. 2.3(c). The resulting interference pattern is reminiscent of the in-trap density distribution. Importantly, to claim the global phase coherence the matter-wave interference pattern *must* be repeatable over different experimental shots. If it is not, each time every droplet is having a random phase and the system is in the independent droplet regime, see Sec. 1.7.

2.3. From 1D to 2D supersolids

The first experimental observations of dipolar supersolids have been obtained by using an cigar-shaped trap, where few droplets were forming a single row along the axial direction. This triggered many theoretical and experimental works on the study of the excitation modes and dynamics of a supersolid in that geometry [103, 110, 151–155]. In these studies, the system is always three-dimensional, but since the periodic density modulation is acquired in one direction, this state is called a *1D supersolid*. Then, the question was whether this system could be scaled to larger sizes and geometries. The first intuitive step, is to extend supersolidity to a second dimension and search for what is commonly called a *2D supersolid*.

Most of the theoretical works at that time studied 2D supersolid properties in infinite systems [29, 156–158], and the only experimentally realized 2D dipolar droplet states lacked global phase coherence [81]. It was not clear what were the key ingredients to
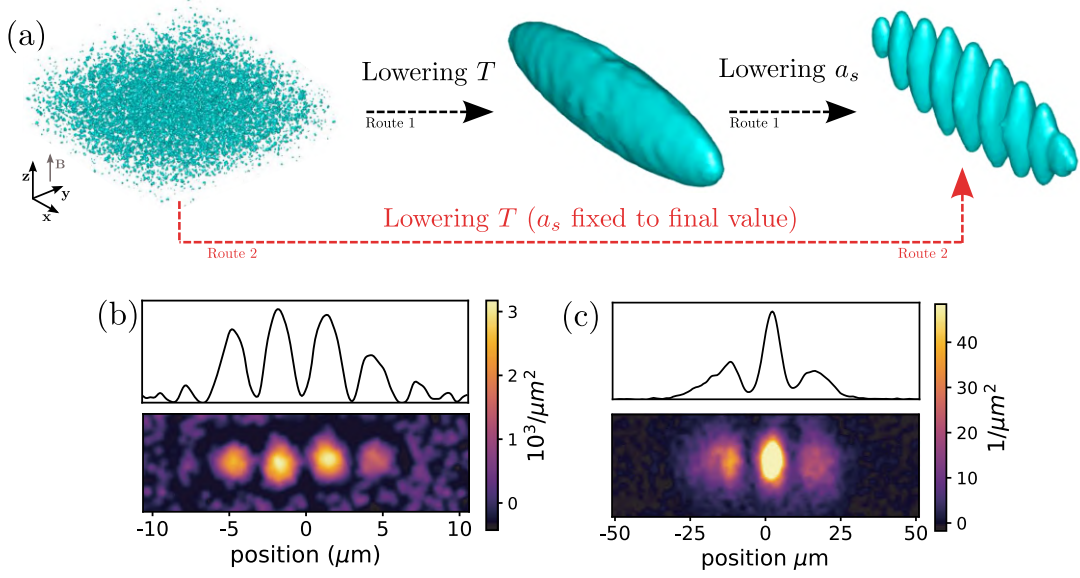
Figure 2.3.: Supersolid formation and experimental observation. (a) Routes to enter the supersolid phase. Route 1 first creates a stable BEC and then tunes the a_s, crossing the roton instability. Route 2 starts with a thermal could at fixed a_s and directly evaporates in the supersolid regime, without crossing the BEC-to-supersolid phase transition. Images are obtained by plotting density isosurfaces, adapted from Ref. [150]. (b) In-situ density distribution of a four-droplets supersolid made of ^{164}Dy and (c) interference pattern after 35 ms time of flight expansion. The lower plots show the in plane distribution, the upper plot is the integrated version along the vertical axis. Figures adapted from Ref. [149].

experimentally observe the structural phase transition from 1D to 2D supersolids. And it was an open question whether the role of the experimental procedure could affect the stability of the supersolid. We addressed these questions and the results are contained in the three publications reported in the next sections [150, 159, 160], whose content is briefly summarized below.

Experimental observation of 2D supersolids

Through a theory-experiment collaboration with the *Er-Dy* laboratory in Innsbruck, we experimentally observe 2D supersolids for the first time. Inspired by the structural phase transition occurring in ion crystals from linear chains to zig-zag patterns [161], we observe a similar behaviour of the droplets when increasing the radial aspect ratio of the trap. Importantly, achieving this regime required an increase in atom number, that was obtained experimentally by improving the cooling sequence; see the left part of Fig. 2.4. The experimental findings are strongly supported by theoretical comparisons, including ground state eGPE simulations and a simplified variational model. Finally, we study the interference pattern of the 2D supersolid to detect the global phase coherence.
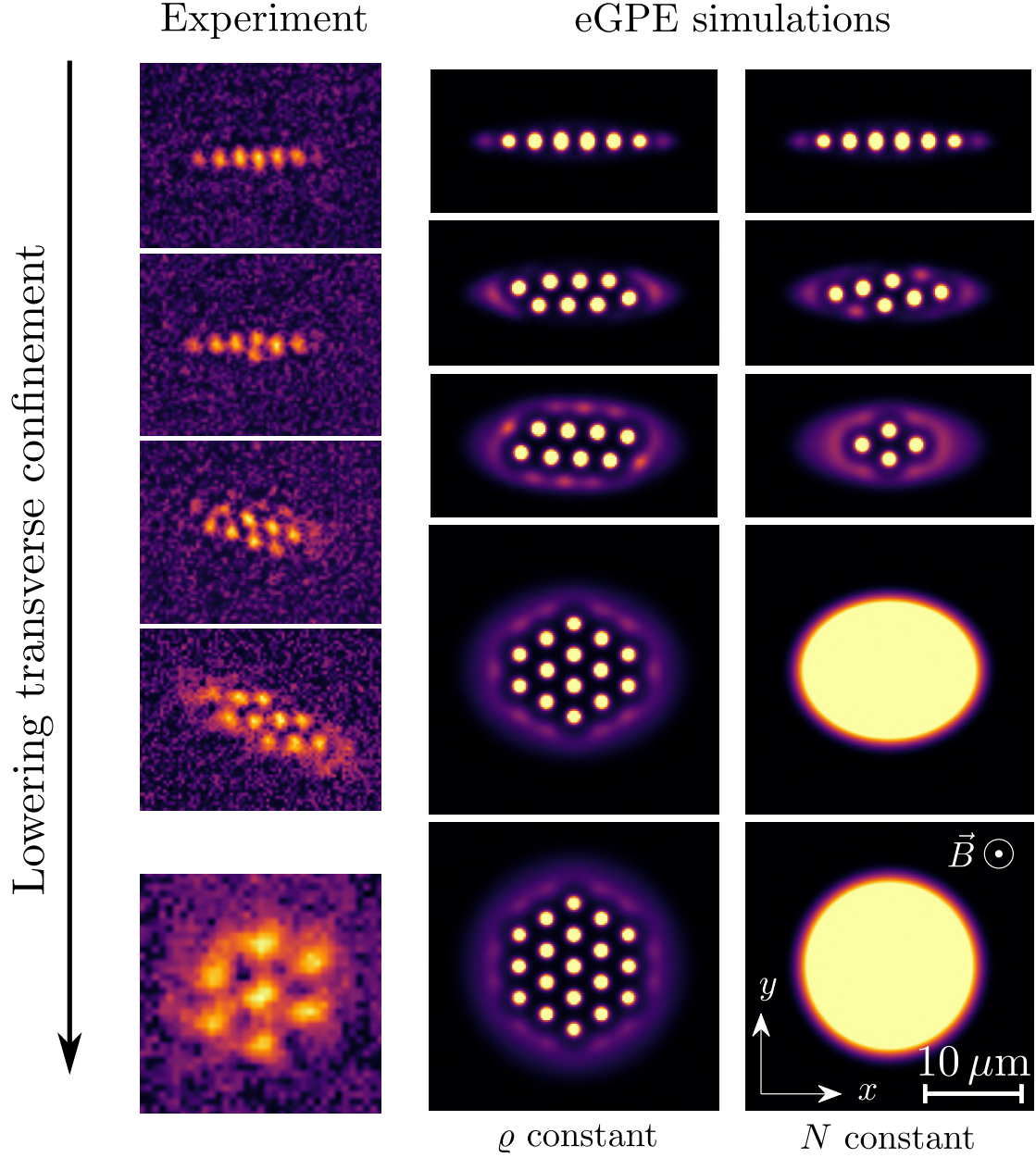
Figure 2.4.: 1D-to-2D structural supersolid transition in the experiment and in the theory. On the left, experimental in-situ images of the 1D-to-2D supersolid transition, up to a circular supersolid. The atom number in the experiment varies from 2.5×10^4 to 6.5×10^4. On the right, eGPE ground states simulations crossing a similar structural transition. The first column shows states with constant ϱ, so supersolidity is maintained. The second column shows states at constant $N = 6.3 \times 10^4$, where supersolidity is lost. Figures adapted from Ref. [150,159,160].

Control parameter, phase diagram and collective modes

To cross the 1D-to-2D transition, we theoretically demonstrate that the control parameter is the average 2D density ϱ, defined as

$$\varrho = N\, f_x\, f_y\,. \tag{3}$$

Here, N is the atom number and f_x, f_y are the in-plane frequencies (with dipoles polarized along z). This parameter provides an intuitive way to explore the transition: by fixing f_x and reducing f_y, an higher N is required to maintain the supersolid character. If instead N is kept constant, supersolidity is lost across the transition; see the right part of Fig. 2.4. We extend the phase diagram in Ref. [159] keeping constant the average 2D density and compare the results obtained from the eGPE with those from a variational model. The variational approach was developed to efficiently explore the energy landscape of a 2D supersolid, which hosts a multitude of nearly degenerate states differing slightly in energy and droplet arrangement. In addition, we numerically investigate the emergence of high-density exotic phases as the control parameter ρ increases, and present some exemplar collective modes from the excitation spectrum.

2D supersolid formation

We theoretically investigate the formation of 2D supersolids by comparing two dynamical approaches: the interaction quench and the evaporative cooling. The first approach involves preparing a BEC and then perform an ramp of a_s into the supersolid regime. The second approach keeps the interaction strength constant, while evaporating directly into the supersolid regime. While the first approach is simulated with the zero-temperature eGPE described in Chapter 1, the second protocol includes the description of atoms in the condensate as well as in a thermal cloud. We developed a finite-temperature stochastic eGPE (SeGPE) theory to model the full evaporation into the supersolid and mimic the interaction between the condensate atoms and the thermal cloud [79]. We quantify the quality of the resulting supersolid by analysing two ingredients:

- The density excitation through the overlap parameter

$$C^d = \frac{\int d\mathbf{r}\, n(\mathbf{r}-\mathbf{r_0},\phi_0,t)n_{GS}}{\int d\mathbf{r}\, n_{GS}^2}\,, \tag{4}$$

  that measures the overlap between the current system's density and the target ground state density n_{GS}. The optimization parameters r_0, ϕ_0 are translations and rotations that maximize C^d.

- The phase excitations through the parameter

$$C^p = 1 - \frac{2}{\pi}\frac{\int dxdy\, n(x,y)|\theta(x,y)-\beta|}{\int dxdy\, n(x,y)} \tag{5}$$

  measuring the phase coherence of the 2D supersolid in the $x-y$ plane. Here, $\theta(x,y)$ is the phase of the wave function in the $z=0$ plane and β is an optimization parameter that maximizes C^p. This integrals are all performed in the minimal coherent region that encompasses the droplets in the $x-y$ plane.

We find that evaporative cooling is a more robust method, that minimize possible excitations that could disrupt the system's global phase coherence. Using this method, we experimentally realize the first 2D supersolid in a circular trap; see Fig. 2.4.

Finally, a special remark on the results presented in the next sections: the experimental achievement of 2D supersolids and the theoretical characterization of these systems unlocked very important possibilities. In fact, they are an excellent platform to study and disentangle the effects of the coexisting solid and superfluid natures. Having a 2D system allows the study of transverse modes due to non-zero shear modulus, a property unique to solids (Chapter 3). A 2D supersolid is also an excellent platform to study rotations, whose behaviour is deeply affected by the superfluid nature (Chapter 4).

2.4. Publication: Two-dimensional supersolidity in dipolar quantum gases

M. A. Norcia[1,4], C. Politi[1,2,4], L. Klaus[1,2], **E. Poli**[2], M. Sohmen[1,2], M. J. Mark[1,2],
R. N. Bisset[2], L. Santos[3] and F. Ferlaino[1,2]

[1] *Institut für Quantenoptik und Quanteninformation, Österreichische Akademie der Wissenschaften, 6020 Innsbruck, Austria*
[2] *Institut für Experimentalphysik, Universität Innsbruck, 6020 Innsbruck, Austria*
[3] *Institut für Theoretische Physik, Leibniz, Universität Hannover, Hanover, Germany*
[4] *These two authors contributed equally.*

† The author of the present thesis performed the numerical eGPE simulations together with R. N. B. and L. S. and contributed in writing the manuscript.

‡ Here, the arXiv version is attached.

Two-dimensional supersolidity in a dipolar quantum gas

Matthew A. Norcia,[1, *] Claudia Politi,[1, 2, *] Lauritz Klaus,[1, 2] Elena Poli,[2] Maximilian
Sohmen,[1, 2] Manfred J. Mark,[1, 2] Russell Bisset,[2] Luis Santos,[3] and Francesca Ferlaino[1, 2, †]

[1]*Institut für Quantenoptik und Quanteninformation,
Österreichische Akademie der Wissenschaften, Innsbruck, Austria*

[2]*Institut für Experimentalphysik, Universität Innsbruck, Austria*

[3]*Institut für Theoretische Physik, Leibniz Universität Hannover, Germany*

(Dated: February 11, 2021)

Supersolidity — a quantum-mechanical phenomenon characterized by the presence of both superfluidity and crystalline order — was initially envisioned in the context of bulk solid helium, as a possible answer to the question of whether a solid could have superfluid properties [1–5]. While supersolidity has not been observed in solid helium (despite much effort)[6], ultracold atomic gases have provided a fundamentally new approach, recently enabling the observation and study of supersolids with dipolar atoms [7–16]. However, unlike the proposed phenomena in helium, these gaseous systems have so far only shown supersolidity along a single direction. By crossing a structural phase transition similar to those occurring in ionic chains [17–20], quantum wires [21, 22], and theoretically in chains of individual dipolar particles [23, 24], we demonstrate the extension of supersolid properties into two dimensions, providing an important step closer to the bulk situation envisioned in helium. This opens the possibility of studying rich excitation properties [25–28], including vortex formation [29–31], as well as ground-state phases with varied geometrical structure [7, 32] in a highly flexible and controllable system.

Ultracold atoms have recently offered a fundamentally new direction for the creation of supersolids — rather than looking for superfluid properties in a solid system like ⁴He, ultracold atoms allow one to induce a crystalline structure in a gaseous superfluid, a system which provides far greater opportunity for control and observation. This new perspective has enabled supersolid properties to be observed in systems with spin-orbit coupling [33] or long-range cavity-mediated interactions [34], though in these cases the crystalline structure is externally imposed, yielding an incompressible state. In contrast, dipolar quantum gases of highly magnetic atoms can spontaneously form crystalline structure due to intrinsic interactions [11–13], allowing for a supersolid with both crystalline and superfluid excitations [14–16]. In these demonstrations, supersolid properties have only been observed along a single dimension, as a linear chain of phase-coherent "droplets", i.e. regions of high density connected by low-density bridges of condensed atoms, confined within an elongated optical trap.

The extension of supersolidity into two dimensions is a key step towards creating an ultracold gas supersolid that is closer to the states envisioned in solid helium. Compared to previous studies of incoherent two-dimensional dipolar droplet crystals [8, 35], we work with both a substantially higher atom number N and relatively strong repulsive contact interactions between atoms. This leads to the formation of large numbers of loosely bound droplets, enabling us to establish phase coherence in two dimensions. In our system, the repulsive dipolar interactions between droplets facilitate a structural transition from a linear to a two-dimensional array, analogous to the Coulomb-interaction-mediated structural phase transitions observed with ions [17–20]. Unlike ions however, our droplets are compressible and result from the spontaneous formation of a density wave, allowing for dynamical variation in both droplet number and size. Further, the exchange of particles between droplets enables the spontaneous synchronization of the internal phase of each droplet across the system, and the associated superfluid excitations [14–16].

Dipolar quantum gases exhibit a rich set of ground- and excited-state phenomena due to the competition between many energetic contributions. These include mean-field interactions of both contact and dipolar nature, quantum fluctuations, and external confinement, parameterized by potentially anisotropic trapping frequencies $f_{x,y,z}$. Such systems can be described with great accuracy by using an extended Gross–Pitaevskii equation (eGPE) [36–39]. Even a fine variation of the
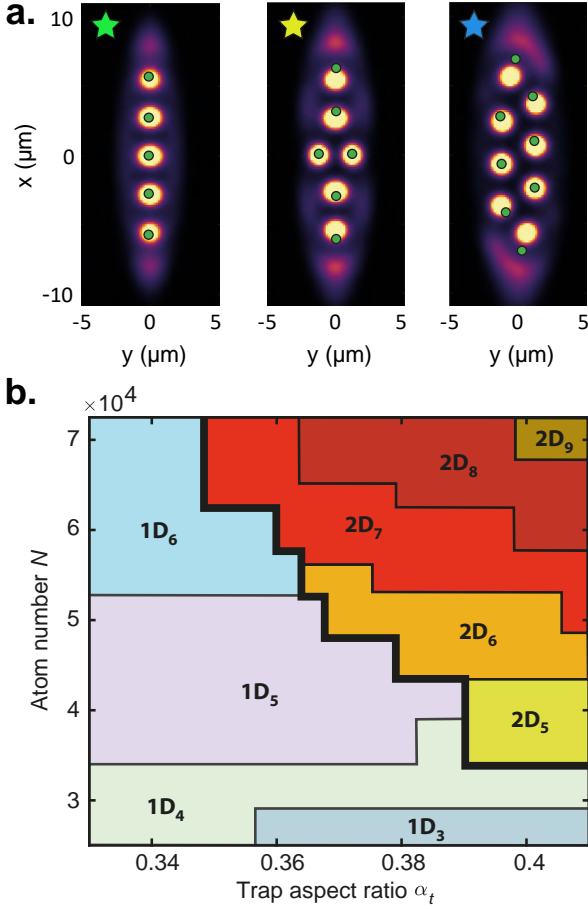
FIG. 1. **Calculated phases of dipolar droplet array. a.** In-trap ground-state density profiles calculated using eGPE for atom numbers $N \in [3.3, 4.4, 5.8] \times 10^4$ in the droplets and trap aspect ratios $\alpha_t = f_x/f_y \in [0.33, 0.35, 0.39]$ (left to right). The scattering length $a = 88\,a_0$, where a_0 is the Bohr radius. Green dots depict the droplet positions obtained from the variational model, assuming the same N and droplet number N_D as the eGPE. Stars connect to experimentally observed density profiles in Fig. 2b. **b.** Phase diagram, obtained from our variational model, as a function of N and α_t for $f_x = 33\,\mathrm{Hz}$, $f_z = 167\,\mathrm{Hz}$. Linear (two-dimensional) phases with N_D droplets are labelled as $1D_{N_D}$ $(2D_{N_D})$.

strength of these energetic contributions can lead to dramatic qualitative changes in the state of the system, for example enabling a transition from a uniform condensate to a supersolid, or in our present case, from a linear supersolid to a two-dimensional one.

Fig. 1a shows ground-state density profiles calculated across this transition using the eGPE at zero temperature. These profiles feature arrays of high-density droplets, immersed in a low-density coherent "halo" that establishes phase-coherence across the system. As the trap becomes more round, the initially linear chain of droplets acquires greater transverse structure, eventually forming a zig-zag state consisting of two offset linear arrays.

Although the eGPE has remarkable predictive power, full simulations in three dimensions are numerically intensive, making a global survey of the array properties as a function of our experimental parameters difficult. To overcome this limitation, we employ a variational ansatz that captures the key behavior of the system, and allows us to disentangle the competing energetic contributions. In this approach, we describe an array of N_D droplets by the wavefunction $\psi(\mathbf{r}) = \sum_{j=1}^{N_D} \psi_j(\mathbf{r})$, where the j–th droplet is assumed to be of the form: $\psi_j(\mathbf{r}) \propto \sqrt{N_j} \exp\left(-\frac{1}{2}\left(\frac{|\boldsymbol{\rho} - \boldsymbol{\rho}_j|}{\sigma_{\rho,j}}\right)^{r_{\rho,j}}\right) \exp\left(-\frac{1}{2}\left(\frac{|z - z_j|}{\sigma_{z,j}}\right)^{r_{z,j}}\right)$, interpolating between a Gaussian and a flat-top profile characteristic of quantum droplets [40]. For a given total number of atoms N and droplet number N_D, energy minimization provides the atom number N_j in each droplet, as well as their widths $\sigma_{\rho(z),j}$, exponents $r_{\rho(z),j}$, and positions $\boldsymbol{\rho}_j = (x_j, y_j)$. Repeating this energy minimization as a function of N_D gives the optimal number of droplets. This model provides a good qualitative description of the overall phase diagram (Fig. 1b), revealing that the interplay between intra-droplet physics and inter-droplet interaction results in a rich landscape of structural transitions as a function of the atom number and the trap aspect ratio $\alpha_t = f_x/f_y$.

Several trends are immediately visible from the phase diagram. Larger N and higher α_t generally produce states with larger numbers of droplets. Further, as with ions, a large number of droplets favors a 2D configuration, while tighter transverse confinement (small α_t) favors 1D [17–20]. A transition from 1D to 2D is thus expected when moving towards larger N or to higher α_t. In stark contrast to the case of ions, the number of droplets typically increases across the 1D to 2D transition, implying a first-order nature, while only narrow regions in the phase diagram may allow for a 1D-to-2D transition at constant droplet number.

The variational results are in excellent agreement with our eGPE numerics, in terms of predicting the qualitative structure of droplet array patterns, as shown in Fig. 1a. Slight discrepancies exist between the two theories regarding the predicted droplet positions and the location of the 1D-to-2D transition. This is likely because of the presence of the halo in the eGPE simulation (and presumably in the experiment), visible in Fig. 1a, which is not accounted for in the variational model. This halo appears to accumulate at the ends of the trap, pushing the droplets toward the trap center and likely increasing the effective trap aspect ratio experienced by the droplets.

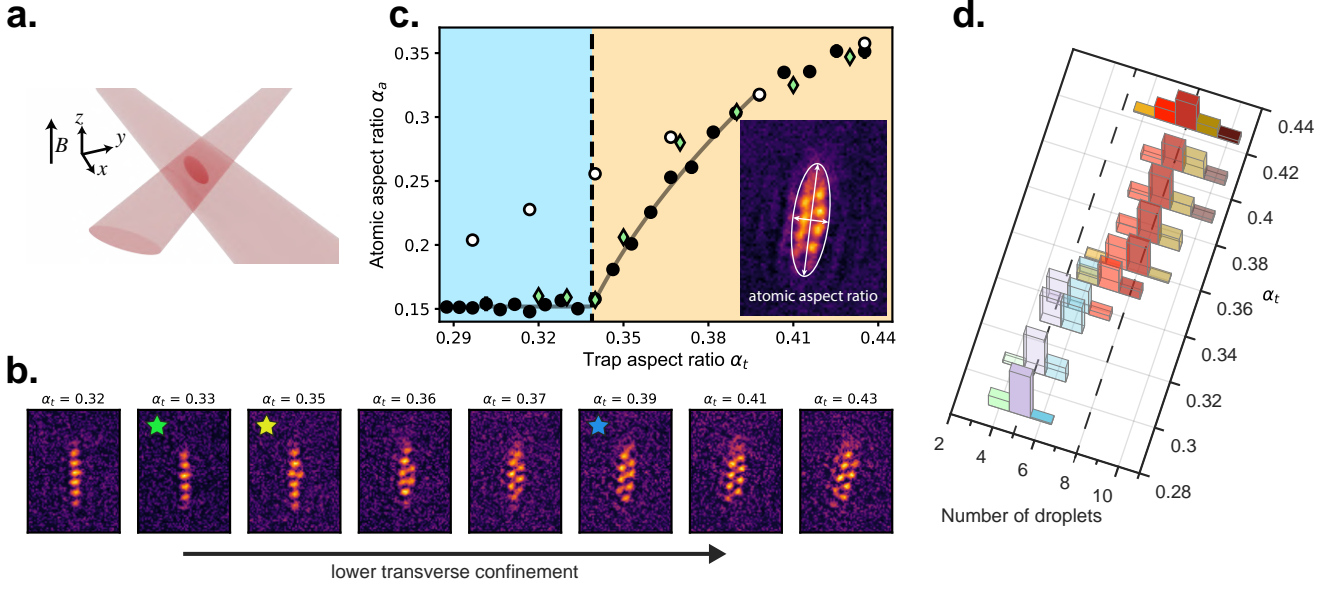To explore the 1D to 2D transition experimentally, we

FIG. 2. **Linear to zig-zag transition in an anisotropic trap. a.** We confine and condense dipolar ^{164}Dy atoms within an anisotropic optical dipole trap (ODT) formed by the intersection of two laser beams. By tuning the aspect ratio of the trap in the x-y plane (α_t), perpendicular to an applied magnetic field B, we induce a transition between linear and zig-zag configurations of droplets. **b.** Single-trial images of the in-trap density profile of atoms at different α_t, showing structural transition from linear to zig-zag states, as well as an increase in droplet number for higher α_t. Stars indicate values α_t and N corresponding to the eGPE calculations of Fig. 1a. **c.** Atomic aspect ratio α_a versus trap aspect ratio α_t. α_a is the ratio of minor to major axes of a two-dimensional Gaussian fit to the imaged in-trap density profile (inset). For the supersolid droplet array (black markers) we see an abrupt change in α_a at the critical trap aspect ratio α_t^*, extracted from the fit (gray line, see methods). The shape of the transition agrees well with eGPE prediction (green diamonds, see methods). For an unmodulated condensate (white markers), no abrupt change is evident. **d.** Distribution of droplet number versus α_t, showing a distinct increase in droplet number at the transition of linear to zig-zag configurations.

use a condensate of highly magnetic ^{164}Dy atoms confined within an anisotropic optical dipole trap with independently tunable trap frequencies $f_{x,y,z}$. The trap, shown in Fig. 2a, is shaped like a surf-board with the tight axis along gravity and along a uniform magnetic field that orients the atomic dipoles and allows tuning of the contact interaction strength. Typically, we perform evaporation directly into our state of interest at our desired final interaction strength, as demonstrated in Refs. [13, 41]. A combination of in-trap and time-of-flight (TOF) imaging provides us with complementary probes of the density profile of our atomic states, and the phase coherence across the system.

We begin by studying the transition from one to two dimensions by changing the strength of transverse confinement provided by the trap. Our optical setup allows us to tune f_y from roughly 75 to 120 Hz, while leaving f_x, f_z nearly constant at 33(2), 167(1) Hz, and thus to vary the trap aspect ratio α_t in the plane perpendicular to the applied magnetic field and our imaging axis.

For small α_t, the atoms are tightly squeezed transversely, and form a linear-chain supersolid (as seen in in-trap images of Fig. 2b). As we increase α_t above a critical value $\alpha_t^* = 0.34(2)$, we observe a structural phase transition to a two-dimensional (2D) state with two side-by-side droplets in the center of the chain. By further increasing α_t, the 2D structure extends to two offset lines of droplets in a zig-zag configuration. The observed patterns match well with the ground-state predictions from the eGPE calculations when we globally fix the scattering length to $88a_0$.

We obtain higher atom numbers in the more oblate traps (higher α_t), giving $N = 6.5(5) \times 10^4$ at $\alpha_t = 0.44$ and $N = 2.5(4) \times 10^4$ at $\alpha_t = 0.28$. This further facilitates the crossing of the 1D to 2D transition, by favoring states with larger numbers of droplets in the broader traps. In the zig-zag regime, two-dimensional modulation is clearly visible for durations beyond one second. Further, the droplet configuration patterns are fairly repeatable, with clear structure visible in averaged images
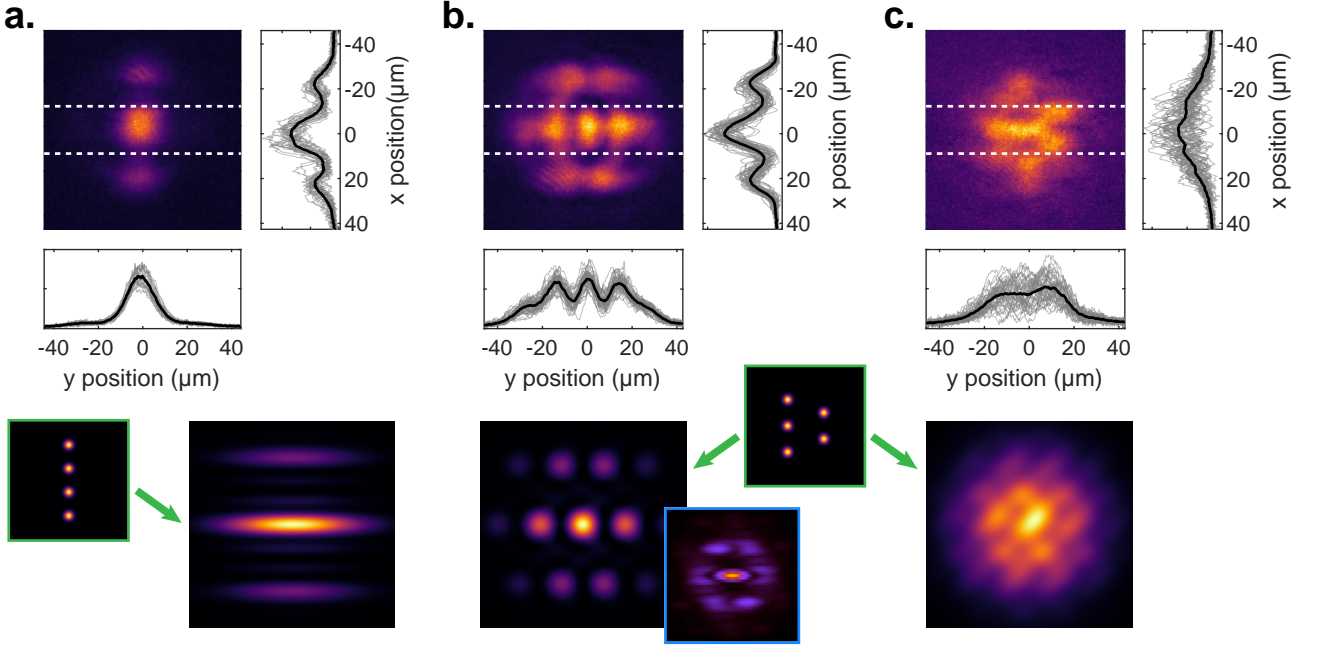
FIG. 3. **Coherence in linear and zig-zag states.** Upper panels show averaged images of experimental TOF interference patterns, along with projections along horizontal and vertical directions of average (solid black lines) and individual images (gray lines). The vertical projection is calculated between the dashed lines. Lower panels show interference patterns calculated for the pictured in-trap droplet configurations (green outlines). **a.** Linear chain of phase-coherent droplets, showing uniaxial modulation persisting in averaged image (26 trials). **b.** Zig-zag configuration of phase-coherent droplets, showing modulation along two directions that persists in averaged image (51 trials), and hexagonal structure. The spacing of rows in the simulation was adjusted to approximate the observed aspect ratio of TOF image. The image outlined in blue shows the average momentum distribution calculated from a series of 20 variational calculations converging to slightly different droplet configurations, showing the tendency of such fluctuations to broaden features in the interference pattern while maintaining the underlying structure. **c.** Zig-zag configuration of phase-incoherent droplets. Modulation remains in single images, as evidenced by the spread of gray traces in projection, but washes out in average (43 trials).

as shown in the inset of Fig. 2c, which is an average of 23 trials taken over roughly two hours.

The transition from 1D to 2D is immediately visible when plotting the atomic aspect ratio α_a versus α_t, as shown in Fig. 2c. We find that α_a undergoes a rapid change at α_t^*, as the single linear chain develops two-dimensional structure. For comparison, we plot α_a measured for an unmodulated BEC, formed at a different magnetic field, which does not feature the sharp kink present for the supersolid state.

In Fig. 2d, we show the number of droplets present for different α_t. In the 1D regime, we typically see between five and six droplets. This number abruptly jumps up by approximately one droplet for 2D states near the transition point, and then increases up to an average value of eight droplets as α_t is further increased. The change in droplet number indicates that the transition that we observe is not of simple structural nature, but is also

accompanied by a reconfiguration of atoms within the droplets, as expected from theory (see Fig. 1).

The measurements of in-trap density presented above inform us about the structural nature of the transition, but not about phase coherence, which is the key distinguishing feature between an incoherent droplet crystal and a supersolid. Previous observations of 2D droplet arrays [35] were performed in traps where the ground state is a single droplet [8], and the observed droplet crystal was likely a metastable state lacking inter-droplet phase coherence. In contrast, we expect from our theoretical calculations that the 2D array is the ground state of our surfboard-shaped trap (for $\alpha_t > \alpha_t^*$), facilitating the formation of a phase-coherent, and therefore supersolid state for our experimental parameters.

We experimentally demonstrate the supersolid nature of our 2D modulated state using a matter-wave interference measurement, as previously used in linear supersolid

chains [11–13], (Fig. 3a). In this measurement, an array of uniformly spaced droplets creates an interference pattern with spatial period proportional to the inverse of the in-trap droplet spacing. The relative internal phase of the droplets determines both the contrast and spatial phase of the interference pattern [42]. When averaging over many interference patterns, obtained on separate runs of the experiment, clear periodic modulation persists for phase-coherent droplets, but averages out if the relative droplet phases vary between experimental trials. Thus, the presence of periodic modulation in an average TOF image provides a clear signature of supersolidity in our system, as it indicates both periodic density modulation and phase coherence.

Figure 3a shows an example of such an averaged interference pattern for a linear chain. Uniaxial modulation is clearly present along the direction of the chain, indicating a high degree of phase coherence. For comparison, we also show the expected interference pattern calculated for a linear array of four droplets from free-expansion calculations, showing similar structure.

For conditions where in-trap imaging shows a 2D zig-zag structure, the averaged interference pattern exhibits clear hexagonal symmetry (Fig. 3b). This is consistent with our expectation, and is indicative of the triangular structure of the underlying state. To confirm that the observed modulation is not present without phase coherence, we repeat the measurement of Fig. 3b at a magnetic field corresponding to independent droplets, and also compute averaged interference pattern for a zig-zag state with the phases of the individual droplets randomized between simulated trials (Fig. 3c). In both cases, the averaged image does not show clear periodic modulation.

By exploiting the transition between linear and zig-zag states, we have accessed a regime where the supersolid properties of periodic density modulation and phase coherence exist along two separate dimensions. Future work will focus on further understanding the spectrum of collective excitations in the full two-dimensional system [26–28, 43], where both the crystalline structure and the exchange of particles between droplets will play an important role. Further investigations may elucidate in more detail the nature of the phase transitions and expected configurations in a wider range of trap aspect ratios, as well as the role that defects play in the 2D system, either as phase-slips in the zig-zag patterns [44, 45], or as vortices trapped between droplets of the array [29–31].

We thank the Innsbruck Erbium team and Blair Blakie for discussions. We acknowledge R. M. W. van Bijnen for developing the code for our eGPE ground-state simulations.

Author Contributions: M.A.N, C.P., L.K., M.S., M.J.M and F.F. contributed experimental work. E.P and R.B. performed eGPE calculations. L.S. contributed variational model. All authors contributed to interpretation of results and preparation of manuscript.

––––––––––

* M. A. N. and C. P. contributed equally to this work.

† Correspondence should be addressed to Francesca.Ferlaino@uibk.ac.at

[1] E. P. Gross, Unified theory of interacting bosons, Phys. Rev. **106**, 161 (1957).

[2] E. P. Gross, Classical theory of boson wave fields, Annals of Physics **4**, 57 (1958).

[3] A. F. Andreev and I. M. Lifshitz, Quantum theory of defects in crystals, Sov. Phys. JETP **29**, 1107 (1969).

[4] G. V. Chester, Speculations on Bose–Einstein condensation and quantum crystals, Phys. Rev. A **2**, 256 (1970).

[5] A. J. Leggett, Can a solid be "Superfluid"?, Phys. Rev. Lett. **25**, 1543 (1970).

[6] M. H.-W. Chan, R. Hallock, and L. Reatto, Overview on solid 4 he and the issue of supersolidity, Journal of Low Temperature Physics **172**, 317 (2013).

[7] Z.-K. Lu, Y. Li, D. S. Petrov, and G. V. Shlyapnikov, Stable dilute supersolid of two-dimensional dipolar bosons, Phys. Rev. Lett. **115**, 075303 (2015).

[8] D. Baillie and P. B. Blakie, Droplet crystal ground states of a dipolar bose gas, Phys. Rev. Lett. **121**, 195301

(2018).

[9] S. M. Roccuzzo and F. Ancilotto, Supersolid behavior of a dipolar bose-einstein condensate confined in a tube, Phys. Rev. A **99**, 041601 (2019).

[10] M. Boninsegni and N. V. Prokof'ev, Colloquium: Supersolids: What and where are they?, Rev. Mod. Phys. **84**, 759 (2012).

[11] L. Tanzi, E. Lucioni, F. Famà, J. Catani, A. Fioretti, C. Gabbanini, R. N. Bisset, L. Santos, and G. Modugno, Observation of a dipolar quantum gas with metastable supersolid properties, Phys. Rev. Lett. **122**, 130405 (2019).

[12] F. Böttcher, J.-N. Schmidt, M. Wenzel, J. Hertkorn, M. Guo, T. Langen, and T. Pfau, Transient supersolid properties in an array of dipolar quantum droplets, Phys. Rev. X **9**, 011051 (2019).

[13] L. Chomaz, D. Petter, P. Ilzhöfer, G. Natale, A. Trautmann, C. Politi, G. Durastante, R. M. W. van Bijnen, A. Patscheider, M. Sohmen, M. J. Mark, and F. Ferlaino, Long-lived and transient supersolid behaviors in dipolar quantum gases, Phys. Rev. X **9**, 021012 (2019).

[14] M. Guo, F. Böttcher, J. Hertkorn, J.-N. Schmidt, M. Wenzel, H. P. Büchler, T. Langen, and T. Pfau, The low-energy goldstone mode in a trapped dipolar supersolid, Nature **574**, 386 (2019).

[15] G. Natale, R. M. W. van Bijnen, A. Patscheider, D. Petter, M. J. Mark, L. Chomaz, and F. Ferlaino, Excitation spectrum of a trapped dipolar supersolid and its experimental evidence, Phys. Rev. Lett. **123**, 050402 (2019).

[16] L. Tanzi, S. Roccuzzo, E. Lucioni, F. Famà, A. Fioretti, C. Gabbanini, G. Modugno, A. Recati, and S. Stringari, Supersolid symmetry breaking from compressional oscillations in a dipolar quantum gas, Nature **574**, 382 (2019).

[17] G. Birkl, S. Kassner, and H. Walther, Multiple-shell structures of laser-cooled 24 mg+ ions in a quadrupole storage ring, Nature **357**, 310 (1992).

[18] M. G. Raizen, J. M. Gilligan, J. C. Bergquist, W. M. Itano, and D. J. Wineland, Ionic crystals in a linear paul trap, Phys. Rev. A **45**, 6493 (1992).

[19] S. Fishman, G. De Chiara, T. Calarco, and G. Morigi, Structural phase transitions in low-dimensional ion crystals, Phys. Rev. B **77**, 064111 (2008).

[20] E. Shimshoni, G. Morigi, and S. Fishman, Quantum zigzag transition in ion chains, Phys. Rev. Lett. **106**, 010401 (2011).

[21] W. K. Hew, K. J. Thomas, M. Pepper, I. Farrer, D. Anderson, G. A. C. Jones, and D. A. Ritchie, Incipient formation of an electron lattice in a weakly confined quantum wire, Phys. Rev. Lett. **102**, 056804 (2009).

[22] A. C. Mehta, C. J. Umrigar, J. S. Meyer, and H. U. Baranger, Zigzag phase transition in quantum wires, Phys. Rev. Lett. **110**, 246802 (2013).

[23] G. E. Astrakharchik, G. Morigi, G. De Chiara, and J. Boronat, Ground state of low-dimensional dipolar gases: Linear and zigzag chains, Phys. Rev. A **78**, 063622 (2008).

[24] J. Ruhman, E. G. Dalla Torre, S. D. Huber, and E. Altman, Nonlocal order in elongated dipolar gases, Phys. Rev. B **85**, 125121 (2012).

[25] L. Santos, G. V. Shlyapnikov, and M. Lewenstein, Roton-maxon spectrum and stability of trapped dipolar bose-einstein condensates, Phys. Rev. Lett. **90**, 250403 (2003).

[26] S. Ronen, D. C. E. Bortolotti, and J. L. Bohn, Radial and angular rotons in trapped dipolar gases, Phys. Rev. Lett. **98**, 030406 (2007).

[27] R. M. Wilson, S. Ronen, J. L. Bohn, and H. Pu, Manifestations of the roton mode in dipolar bose-einstein condensates, Phys. Rev. Lett. **100**, 245302 (2008).

[28] R. N. Bisset, D. Baillie, and P. B. Blakie, Roton excitations in a trapped dipolar bose-einstein condensate, Phys. Rev. A **88**, 043606 (2013).

[29] A. Gallemí, S. M. Roccuzzo, S. Stringari, and A. Recati, Quantized vortices in dipolar supersolid bose-einstein-condensed gases, Phys. Rev. A **102**, 023322 (2020).

[30] S. M. Roccuzzo, A. Gallemí, A. Recati, and S. Stringari, Rotating a supersolid dipolar gas, Phys. Rev. Lett. **124**, 045702 (2020).

[31] F. Ancilotto, M. Barranco, M. Pi, and L. Reatto, Vortex properties in the extended supersolid phase of dipolar bose-einstein condensates, arXiv preprint arXiv:2012.15157 (2020).

[32] Y.-C. Zhang, F. Maucher, and T. Pohl, Supersolidity around a critical point in dipolar bose-einstein condensates, Phys. Rev. Lett. **123**, 015301 (2019).

[33] J.-R. Li, J. Lee, W. Huang, S. Burchesky, B. Shteynas, F. Ç. Top, A. O. Jamison, and W. Ketterle, A stripe

phase with supersolid properties in spin–orbit-coupled Bose-–Einstein condensates, Nature **543**, 91 (2017).

[34] J. Léonard, A. Morales, P. Zupancic, T. Esslinger, and T. Donner, Supersolid formation in a quantum gas breaking a continuous translational symmetry, Nature **543**, 87 (2017).

[35] H. Kadau, M. Schmitt, M. Wenzel, C. Wink, T. Maier, I. Ferrier-Barbut, and T. Pfau, Observing the rosensweig instability of a quantum ferrofluid, Nature **530**, 194 (2016).

[36] I. Ferrier-Barbut, H. Kadau, M. Schmitt, M. Wenzel, and T. Pfau, Observation of quantum droplets in a strongly dipolar bose gas, Phys. Rev. Lett. **116**, 215301 (2016).

[37] L. Chomaz, S. Baier, D. Petter, M. J. Mark, F. Wächtler, L. Santos, and F. Ferlaino, Quantum-fluctuation-driven crossover from a dilute bose-einstein condensate to a macrodroplet in a dipolar quantum fluid, Phys. Rev. X **6**, 041039 (2016).

[38] F. Wächtler and L. Santos, Quantum filaments in dipolar bose-einstein condensates, Phys. Rev. A **93**, 061603 (2016).

[39] R. N. Bisset, R. M. Wilson, D. Baillie, and P. B. Blakie, Ground-state phase diagram of a dipolar condensate with quantum fluctuations, Phys. Rev. A **94**, 033619 (2016).

[40] L. Lavoine and T. Bourdel, 1d to 3d beyond-mean-field dimensional crossover in mixture quantum droplets (2020), arXiv:2011.12394 [cond-mat.quant-gas].

[41] M. Sohmen, C. Politi, L. Klaus, L. Chomaz, M. J. Mark, M. A. Norcia, and F. Ferlaino, Birth, life, and death of a dipolar supersolid, arXiv preprint arXiv:2101.06975 (2021).

[42] Z. Hadzibabic, S. Stock, B. Battelier, V. Bretin, and J. Dalibard, Interference of an array of independent Bose–Einstein condensates, Phys. Rev. Lett. **93**, 180403 (2004).

[43] J.-N. Schmidt, J. Hertkorn, M. Guo, F. Böttcher, M. Schmidt, K. S. Ng, S. D. Graham, T. Langen, M. Zwierlein, and T. Pfau, Roton excitations in an oblate dipolar quantum gas, arXiv preprint arXiv:2102.01461 (2021).

[44] K. Pyka, J. Keller, H. Partner, R. Nigmatullin, T. Burgermeister, D. Meier, K. Kuhlmann, A. Retzker, M. B. Plenio, W. Zurek, *et al.*, Topological defect formation and spontaneous symmetry breaking in ion coulomb crystals, Nature communications **4**, 1 (2013).

[45] S. Ulm, J. Roßnagel, G. Jacob, C. Degünther, S. Dawkins, U. Poschinger, R. Nigmatullin, A. Retzker, M. Plenio, F. Schmidt-Kaler, *et al.*, Observation of the kibble–zurek scaling law for defect formation in ion crystals, Nature communications **4**, 1 (2013).

[46] A. Trautmann, P. Ilzhöfer, G. Durastante, C. Politi, M. Sohmen, M. J. Mark, and F. Ferlaino, Dipolar quantum mixtures of erbium and dysprosium atoms, Phys. Rev. Lett. **121**, 213601 (2018).

Methods

Experimental apparatus and protocols: Our experimental apparatus has been described in detail in Ref. [46]. Here, we evaporatively prepare up to $N = 6.5(5) \times 10^4$ condensed ^{164}Dy atoms in a crossed optical dipole trap formed at the intersection of two beams derived from the same 1064 nm laser, although detuned in frequency to avoid interference. One beam (the static ODT) has an approximately 60 μm waist. The second (the scanning ODT) has an 18 μm waist, whose position can be rapidly scanned horizontally at 250 kHz to create a variably anisotropic time-averaged potential. By tuning the power in each beam, and the scanning range of the scanning ODT, we gain independent control of the trap frequencies in all three directions. The two trapping beams propagate in a plane perpendicular to gravity, and cross at a 45° angle, which leads to the rotation of the zig-zag state at high α_t visible in Fig. 2b.

We apply a uniform magnetic field oriented along gravity and perpendicular to the intersecting dipole traps, with which we can tune the strength of contact interactions between atoms. This allows us to create unmodulated Bose-Einstein condensates, supersolid states, or states consisting of independent droplets at fields of $B = 23.2$ G, 17.92 G, and 17.78 G, respectively.

Details of our imaging setup are provided in Ref. [41]. In-trap and TOF images are performed along the vertical direction (along B and gravity), using standard phase-contrast and absorption techniques, respectively. The resolution of our in-trap images is approximately one micron. We use a 36 ms TOF duration for imaging interference patterns.

Atom number: We extract the condensed atom number N from absorption imaging performed along a horizontal direction in a separate set of experimental trials under otherwise identical experimental conditions. This allows for a larger field of view, and better fitting of thermal atoms. N is determined by subtracting the fitted thermal component from the total absorption signal.

For comparison between experiment and theory, and between the variational and eGPE theory methods, we associate N with the number of atoms in the droplets, and not in the diffuse halo that surrounds the droplets. From simulation of TOF expansion, we find that the halo is repelled at early expansion times, and is likely indistinguishable from the thermal cloud in our TOF measurements. While it is possible that some of the halo is counted in N, we neglect this possibility and assume that N includes only atoms within droplets.

Scattering length: The positions of phase boundaries between different droplet configurations are quite sensitive to the scattering length a, which is not known with high precision in our range of magnetic fields. For all theory, we use a value of $a = 88\,a_0$, where a_0 is the Bohr radius, as this value provides good agreement between experiment and theory for the 1D-to-2D transition point.

Extracting critical aspect ratio: The critical aspect ratio α_t^* is extracted from fit to the function $\alpha_a = \alpha_0$ for $\alpha_t < \alpha_t^*$, $\alpha_a = \sqrt{\alpha_0^2 + b(\alpha_t - \alpha_t^*)^2}$ for $\alpha_t > \alpha_t^*$, where α_t^*, α_0, and b are fit parameters. The error bars reported in Fig. 2c represent the standard error on the mean, and are smaller than the markers on most points.

Interference patterns: The predicted interference patterns of Fig. 3 are calculated by assuming free expansion of Gaussian droplets. In reality, the droplets are probably not Gaussian, and interactions during TOF expansion may modify the interference pattern. However, the droplet shape primarily effects the envelope of the interference pattern, which is not our primary interest here, and from eGPE simulations, we expect the effects of interactions to be minor, provided that the droplets become unbound in a time short compared to the TOF, which we verify by both looking at shorter TOFs and comparing the fringe spacing observed in TOF with that expected from the in-trap droplet spacing. The positions and size of the droplets are tuned to provide illustrative interference patterns.

Droplet number: We extract the droplet number from our in-trap images using a peak-finding algorithm applied to smoothed images. The algorithm finds the local maxima above a threshold, which is chosen to be 40% of the overall peak value. Each in-trap density distribution is classified as linear array or 2D zig-zag based on the atomic aspect ratio. Finally, the counts with a given droplet number are normalized by the total number of trials to get the probability shown in Fig. 2d. Fluctuations in the number of atoms in a given trial can push droplets above or below the threshold value, contributing to the spread in extracted droplet number for a given α_t.

2.5. Publication: Maintaining supersolidity in one and two dimensions

E. Poli[1], T. Bland[2], C. Politi[1,2], L. Klaus[1,2], M. A. Norcia[2], F. Ferlaino[1,2], R. N. Bisset[1], and L. Santos[3]

[1] *Institut für Experimentalphysik, Universität Innsbruck, 6020 Innsbruck, Austria*
[2] *Institut für Quantenoptik und Quanteninformation, Österreichische Akademie der Wissenschaften, 6020 Innsbruck, Austria*
[3] *Institut für Theoretische Physik, Leibniz, Universität Hannover, Hanover, Germany*

----

† The author of the present thesis performed the numerical simulations together with T. B., R. N. B., L. S. and contributed in writing the manuscript.

Maintaining supersolidity in one and two dimensions

E. Poli [1], T. Bland [2,*], C. Politi [2,1] L. Klaus [2,1] M. A. Norcia [2], F. Ferlaino [2,1] R. N. Bisset,[1] and L. Santos [3]

[1]*Institut für Experimentalphysik, Universität Innsbruck, 6020 Innsbruck, Austria*
[2]*Institut für Quantenoptik und Quanteninformation, Österreichische Akademie der Wissenschaften, 6020 Innsbruck, Austria*
[3]*Institut für Theoretische Physik, Leibniz Universität Hannover, 30167 Hannover, Germany*

We theoretically investigate supersolidity in three-dimensional dipolar Bose-Einstein condensates. We focus on the role of trap geometry in determining the dimensionality of the resulting droplet arrays, which range from one-dimensional to zigzag, through to two-dimensional supersolids in circular traps. Supersolidity is well established in one-dimensional arrays, and may be just as favorable in two-dimensional arrays provided that one appropriately scales the atom number to the trap volume. We develop a tractable variational model—which we benchmark against full numerical simulations—and use it to study droplet crystals and their excitations. We also outline how exotic ring and stripe states may be created with experimentally feasible parameters. Our work paves the way for future studies of two-dimensional dipolar supersolids in realistic settings.

I. INTRODUCTION

A supersolid concurrently exhibits both superfluidity and crystalline order [1–6]. Although predicted over half a century ago, supersolidity was only recently realized in experiments: a feat made possible by the flexibility and high degree of control afforded by quantum gas systems. While supersolid properties were observed in experiments with cavity-mediated interactions [7] and spin-orbit coupling [8,9], those platforms produce rigid lattices that are impervious to the usual excitations expected of crystals. In contrast, supersolids with deformable crystals have now been realized in dipolar Bose-Einstein condensates [10–12], in which genuine crystal and superfluid excitations have been observed [13–15].

Dipolar Bose-Einstein condensates (BECs) can be obtained from highly magnetic atoms such as chromium [16], dysprosium [17], and erbium [18]. It was already predicted in 2003 that dipolar BECs could undergo a roton instability [19]—where the unstable excitations occur at finite momenta—as observed in cigar-shaped Er BECs [13,20] and, more recently, in a pancake-shaped Dy BEC [21]. However, it was also expected from theory that the ensuing periodic density modulations would undergo a runaway collapse, and the regions of high local density would invoke three-body losses that rapidly destroy the underlying BEC. Indeed, a similar process was observed with the implosion of entire chromium BECs, driven by the attractive head-to-tail dipolar interactions [22]. From the perspective of supersolidity, the missing ingredient was a mechanism to stabilize against such implosions, and the answer came from the experimental discovery of dipolar droplets in Dy [23,24] and Er [25] BECs. Intriguingly, the stabilization mechanism is well described by including the leading-order effects of quantum fluctuations, resulting in a theory now known as the extended Gross-Pitaevskii equation (eGPE) [25–28]. These beyond-mean-field effects are especially important for the highly magnetic Er and Dy atoms. With this knowledge in hand, the first dipolar supersolids were created by crossing the roton instability from the BEC regime to the droplet array regime [10–12], or directly by evaporative cooling into the supersolid phase [12]. The supersolid ground-state region exists close to this phase transition, where the droplets overlap enough for the superfluid to globally conduct throughout the crystal.

While almost all dipolar supersolids have been experimentally realized as one-dimensional (1D) droplet arrays (see, for example, Refs. [10–15]), two recent experiments have created two-dimensional (2D) supersolids [29,30], thus opening an exciting frontier. An early theoretical study in 2D predicted a rich phase diagram determined by competing metastable crystal configurations [31]. More recent works in 2D have predicted supersolid edge phases [32], intriguing manifestations of quantum vortices and persistent currents [33–36], honeycomb supersolids [37], as well as ring and stripe phases [38,39].

Associated with this rich physics, dipolar supersolids have a large number of control parameters and their effects on the ground-state phase diagram interplay in a complicated way. Furthermore, the supersolid regime typically lies only within a small range of parameters, located between the ordinary unmodulated BEC and a crystal of isolated droplets. It is therefore paramount to develop strategies for maintaining supersolidity while exploring phase space. From a theoretical perspective, it is also necessary to develop tractable and accurate descriptions to supplement the computationally intensive eGPE.

In this work, we study supersolidity in three-dimensional (3D) dipolar BECs. We systematically explore 1D and 2D droplet arrays, identifying the crucial role that the *average 2D density* plays to maintain supersolidity for various trap geometries and atom numbers. We implement an eGPE formalism—and develop a tractable variational model—to examine the phase diagram from linear supersolids in elongated traps to 2D supersolids in circular traps, passing through

---
*Corresponding author: thomas.bland@uibk.ac.at

zigzag and multirow elliptical phases along the way. We find that 2D supersolids may be just as favorable as their 1D counterparts, provided that one fixes the average 2D density. Through increasing the average 2D density, we show how to observe the exotic ring and stripe phases [38,39] with realistic experimental parameters. Finally, we extend our variational model to study 2D crystal excitations and benchmark this against full numerical calculations.

The paper is structured as follows. In Sec. II, we outline our system and the eGPE, while Sec. III introduces the concept of the average 2D density and uses it to theoretically build a 1D-2D supersolid phase diagram. We also introduce our droplet crystal variational model. Section IV examines increasing the average 2D density to access the exotic ring and stripe phases. In Sec. V, we present some exemplary 2D crystal excitations, before concluding with Sec. VI.

II. FORMALISM

We consider 3D dipolar BECs under harmonic confinement and we use the eGPE, given by [25–28]

$$
i\hbar \frac{\partial \Psi(\mathbf{x}, t)}{\partial t} = \left[-\frac{\hbar^2 \nabla^2}{2m} + \frac{1}{2}m(\omega_x^2 x^2 + \omega_y^2 y^2 + \omega_z^2 z^2) \right.
$$
$$
+ \int d^3\mathbf{x}' \, U(\mathbf{x} - \mathbf{x}')|\Psi(\mathbf{x}', t)|^2
$$
$$
\left. + \gamma_{\mathrm{QF}}|\Psi(\mathbf{x}, t)|^3 \right] \Psi(\mathbf{x}, t), \tag{1}
$$

where m is the mass and $\omega_i = 2\pi f_i$ are the harmonic trap frequencies. The wave function Ψ is normalized to the total atom number $N = \int d^3\mathbf{x}|\Psi|^2$. For dilute gases, two-body interactions are well described by the pseudopotential,

$$
U(\mathbf{r}) = \frac{4\pi\hbar^2 a_{\mathrm{s}}}{m}\delta(\mathbf{r}) + \frac{3\hbar^2 a_{\mathrm{dd}}}{m}\frac{1 - 3\cos^2\theta}{r^3}, \tag{2}
$$

with the first term describing the short-range interactions governed by the s-wave scattering length a_s. The second term represents the anisotropic and long-range dipole-dipole interactions, characterized by dipole length $a_{\mathrm{dd}} = \mu_0\mu_m^2 m/12\pi\hbar^2$, with magnetic moment μ_m and vacuum permeability μ_0. We take the dipoles to be polarized along z, and θ is the angle between the polarization axis and the vector pointing from one of the interacting particles to the other. We always consider ^{164}Dy, such that $a_{\mathrm{dd}} = 130.8a_0$, where a_0 is the Bohr radius. The final term in (1) is the dipolar Lee-Huang-Yang correction arising from quantum fluctuations [40], having the coefficient

$$
\gamma_{\mathrm{QF}} = \frac{128\hbar^2}{3m}\sqrt{\pi a_s^5}\,\mathrm{Re}\{\mathcal{Q}_5(\varepsilon_{\mathrm{dd}})\}, \tag{3}
$$

where $\mathcal{Q}_5(\varepsilon_{\mathrm{dd}}) = \int_0^1 du\,(1 - \varepsilon_{\mathrm{dd}} + 3u^2\varepsilon_{\mathrm{dd}})^{5/2}$ is the auxiliary function, and the relative dipole strength is given by $\varepsilon_{\mathrm{dd}} = a_{\mathrm{dd}}/a_s$. Note that $\mathcal{Q}_5$ can be calculated analytically (Appendix A), but this is just a monotonically increasing function that is of the order of unity for the regimes that we consider here. Ground-state and metastable solutions of Eq. (1) are calculated by minimizing the energy functional corresponding to the eGPE using a conjugate-gradients technique [41].

III. TWO-DIMENSIONAL SUPERSOLIDITY

A. Average 2D density

In dipolar gases, the strong interplay between the confinement geometry and the long-range and anisotropic dipole-dipole interactions means that the ground-state phase diagram is complex and the relevant parameter space to consider is huge. This may conceal the identification of the most important control parameters. For example, it was demonstrated in Refs. [10–12,31,39,42] that varying a_s and f_z dramatically affects the supersolid ground state, with supersolidity easily being lost. In what follows, we identify an important control parameter for moving between or within the various supersolid regimes, as well as maintaining supersolidity while progressing from 1D to 2D droplet arrays.

Dipolar supersolids require tight confinement along the direction of dipole polarization, and the precise choice of f_z determines the narrow range of a_s over which supersolidity occurs. For this reason, we take both f_z and a_s to be fixed in the following argument. We propose that the *average 2D density* acts as an important control parameter. This can be thought of as an *average* over the droplet and interdroplet regions, and only the *2D density* is considered because f_z is fixed. A simple yet powerful estimate for how the average 2D density scales is furnished by the Thomas-Fermi approximation, where kinetic energy is neglected, and the x and y radii of a BEC scale $\sim 1/f_x$ and $\sim 1/f_y$, respectively, giving a BEC area scaling $\sim 1/f_x f_y$. The key point is then to realize that the average 2D density scales approximately with the parameter $\varrho = N f_x f_y$. In the next section, we explore the consequences of varying ϱ versus keeping it fixed.

B. From 1D to 2D

In order to illustrate the utility of the average 2D density—characterized by ϱ—the first two columns of Fig. 1 explore the 1D-2D transition for two different phase-space trajectories: first by allowing ϱ to vary and second by fixing ϱ. For both, we consider fixed interactions while moving from a cigar-shaped trap (top row) to a pancake-shaped trap (bottom row). The key difference between the trajectories is that column 1 has a fixed atom number—and hence ϱ decreases as the trap loosens—while column 2 instead fixes ϱ, with N increasing to compensate for the widening of the trap. Crucially, the reduction of ϱ in the first column leads to a loss of the supersolid phase, replaced by an unmodulated BEC, while fixing ϱ allows us to loosen the trap while remaining in the supersolid regime, eventually resulting in a large, 19-droplet supersolid for the circular trap [Fig. 1(j)]. We have theoretically verified in other work that this large 2D supersolid state is robust against thermal fluctuations [30].

C. Droplet variational theory

Although direct simulations of the eGPE have a remarkable predictive power, they are numerically intensive and hinder a thorough overview. We develop a variational model that permits a much simpler determination of the available droplet phases, while presenting an excellent qualitative, and largely quantitative, agreement with our eGPE calculations.
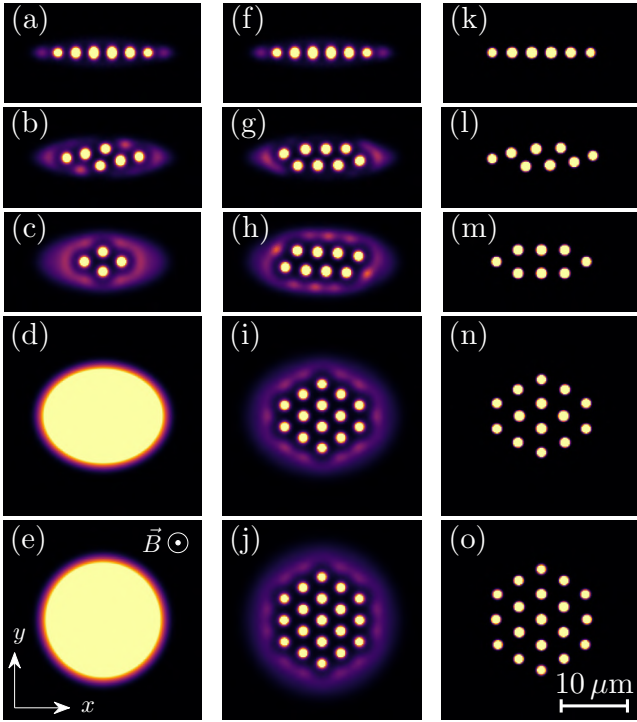
FIG. 1. Opening up the trap from 1D to 2D for ^{164}Dy atoms with $a_s = 88a_0$ and $a_{dd} = 130.8a_0$. In each panel, we fix $(f_x, f_z) = (33, 167)$ Hz and decrease $f_y \in \{110, 84.6, 60, 40, 33\}$ Hz, from top to bottom, showing the integrated column density. Column 1: eGPE result with constant $N = 6.3 \times 10^4$. Column 2: eGPE with constant average 2D density, increasing N to fix $\varrho = N f_x f_y$ with $N \in \{6.3, 8.19, 11.55, 17.325, 21\} \times 10^4$. Column 3: same as column 2, but the variational model. The atom number in the variational model is chosen to match the droplet atom number of the eGPE (see text). We always take the dipoles to be polarized by magnetic field $\vec{B}$ along z.

Inspired by recent work with nondipolar droplets [43], we assume the following *Ansatz* for a dipolar droplet:

$$\Psi(\mathbf{x}) = \sqrt{\mathcal{N}} \phi(\rho) \psi(z), \tag{4}$$

with $\mathcal{N}$ the number of particles and $\rho = \sqrt{x^2 + y^2}$. We again consider dipoles polarized along the z axis, and the droplets are cylindrically symmetric, which we have confirmed as a good approximation by comparing with full eGPE calculations. The radial and axial functions take the form, respectively,

$$\phi(\rho) = \sqrt{\frac{r_\rho}{2\pi \Gamma(2/r_\rho) \sigma_\rho^2}} e^{-\frac{1}{2}\left(\frac{\rho}{\sigma_\rho}\right)^{r_\rho}},$$

$$\psi(z) = \sqrt{\frac{r_z}{2\Gamma(1/r_z)\sigma_z}} e^{-\frac{1}{2}\left(\frac{|z|}{\sigma_z}\right)^{r_z}}, \tag{5}$$

with $\Gamma(x)$ being the Gamma function. The widths $\sigma_{\rho,z}$ and the exponents $r_{\rho,z}$ are variational parameters. Note that this function permits the interpolation between a Gaussian ($r = 2$) and a flat-top ($r \gg 1$) profile in a natural way. Furthermore, this *Ansatz* allows for a simple evaluation of the various ener-

gies in the system using well-known properties of the Gamma function.

Our general strategy is to first numerically minimize the single-droplet problem for a range of possible parameters to build interpolation functions for the variational widths $\sigma_{\rho,z}(\mathcal{N})$ and exponents $r_{\rho,z}(\mathcal{N})$. These functions are then used to solve the many-droplet problem.

For a single droplet, *Ansätze* (4) and (5) can be used to minimize the eGPE energy functional,

$$E_{sd}(\mathcal{N}) = E_{kin} + E_{trap} + E_{sr} + E_{dd} + E_{qf}, \tag{6}$$

where these quantities are the kinetic, trap, short-range interaction, dipole-dipole interaction, and quantum fluctuation contributions, respectively. The evaluation of these terms is detailed in Appendix A.

Now consider a droplet array with N_D droplets, with N_j atoms in the jth droplet. Within the variational model, the energy of the droplet array is then given by

$$E = \sum_{j=1}^{N_D} \left[E_{sd}(N_j) + \frac{m}{2}\left(\omega_x^2 x_j^2 + \omega_y^2 y_j^2\right) N_j \right] + \sum_{j=1}^{N_D} \sum_{j'>j} E_{jj'}, \tag{7}$$

where $E_{jj'}$ is the interdroplet interaction, detailed in Appendix B. By solving the single- then multidroplet problems separately, we effectively reduce the number of variational parameters from $7N_D - 1$ to $3N_D - 1$ ($\{\sigma_{\rho,z}^j, r_{\rho,z}^j, N_j, x_j, y_j\} \rightarrow \{N_j, x_j, y_j\}$), where the -1 arises from fixing the total atom number, $N = \sum_j N_j$.

It is worth noting that important early work employed a purely Gaussian variational model (i.e., $r_\rho = r_z = 2$) to explore crystal and supersolid configurations [31]. Our model goes a step further by allowing for the possibility of droplets with flat-top density profiles, which partially acts to shield interdroplet repulsion in the supersolid regime where the droplets are tightly packed together.

Example solutions of our variational *Ansatz* are shown in Fig. 1 (column 3), displaying excellent agreement with the corresponding eGPE results (column 2). It should be noted that for the eGPE solutions, a sizable number of atoms exist outside the droplets in an outer ring, which we term the "halo." To make direct comparisons between the variational and eGPE methods, we estimate the total number of atoms in the droplets alone from the eGPE and use this to set the total atom number for the corresponding variational calculation. For reference, the variational to eGPE atom number ratio varies from $N_{var} = 0.84 N_{eGPE}$ for the linear chain [Figs. 1(f) and 1(k)] to $N_{var} = 0.58 N_{eGPE}$ for the circular crystal [Figs. 1(j) and 1(o)]. Small deviations in the droplet positions occur between the models due to repulsion between the droplets and the halo in the eGPE, whereas the halo is absent in the variational model. In general, the halo leads to a slight compression of the crystal. Additionally, because the halo density is nonuniform around the perimeter of the droplet array (in some cases forming nearly-droplet-like regions of higher density), its presence can also qualitatively modify the structure and the symmetry of the droplet array in certain situations [cf. Figs. 1(h) and 1(m)].
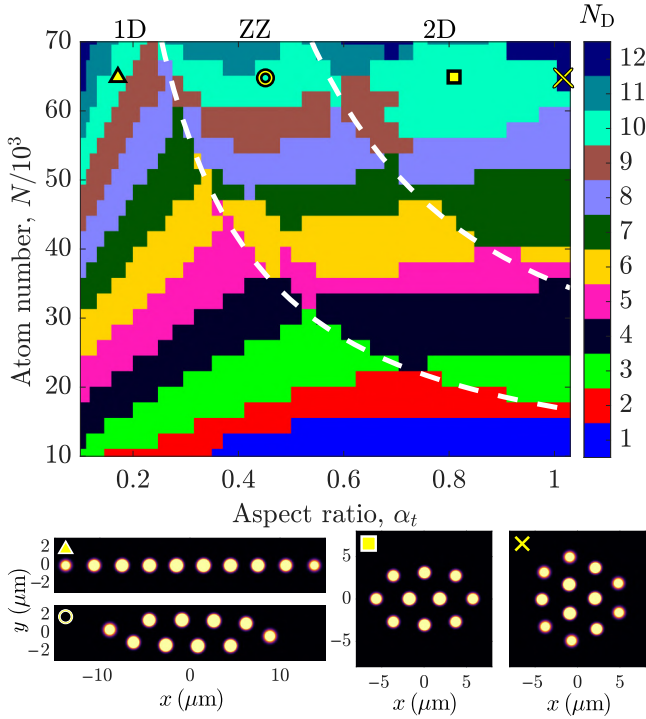
FIG. 2. Crystal phase diagram for ^{164}Dy atoms from 1D (left) to circular trap regime (right) using *Ansätze* (4) and (5). Color indicates ground-state droplet number vs total atom number N and aspect ratio $\alpha_t = f_x/f_y$. A constant average 2D density (controlled by fixing $\varrho = N f_x f_y$) is used throughout, which means the trap tightens from $\sqrt{f_x f_y} = 43$ Hz (top) to $\sqrt{f_x f_y} = 114$ Hz (bottom). White lines separate the 1D, zigzag (ZZ), and 2D regions. Example configurations for fixed $N = 5.4 \times 10^4$ are shown below. Parameters $f_z = 167$ Hz and $a_s = 88a_0$ remain constant.

D. Crystal phase diagram

Here, with the variational model, we seek to explore the full phase diagram of droplet crystal configurations while maintaining a fixed average 2D density, which we control by keeping ϱ constant. Figure 2 shows the droplet configurations of the ground state as a function of the trap aspect ratio $\alpha_t = f_x/f_y$ and atom number. Since ϱ is held fixed throughout, the bottom of the phase diagram corresponds to $N = 10^4$ and $\sqrt{f_x f_y} = 114$ Hz, while the top reaches $N = 7 \times 10^4$ and $\sqrt{f_x f_y} = 43$ Hz. Traversing right on the phase diagram equates to increasing f_x and decreasing f_y, hence moving to more circular configurations.

Several trends are apparent from this phase diagram. Larger N corresponds to ground states with a larger number of droplets. If the configuration is linear (left in Fig. 2), then the droplet number increases incrementally one droplet at a time; however, for large $\alpha_t \sim 1$ (right in Fig. 2), there are occasional jumps of two or more droplets—within the resolution of our phase diagram—corresponding to preferential triangular configurations of the lattice in 2D. For example, we find that for $\alpha_t = 1$, the ground state jumps from $N_D = 8$ to the $N_D = 12$ state shown in Fig. 2 ($\times$), with only a very narrow range of N corresponding to a 10-droplet configuration in between.

Following the solutions from bottom left to top right in Fig. 2, there are two distinct jumps in the average transversal spread ($\Delta y = 1/N_D \sum_j^{N_D} |y_j - \bar{y}|$, for the y position of the jth droplet y_j, and mean y position $\bar{y}$), marked as white dashed lines in Fig. 2. These signify the transition from linear [Fig. 2 ($\triangle$)] to zigzag [Fig. 2 ($\bigcirc$)] configurations, and then 2D solutions with three [Fig. 2 ($\square$)] or more [Fig. 2 ($\times$)] rows of droplets. The first three of these highlighted solutions contain the same number of droplets for a fixed atom number, until $\alpha_t \approx 1$, where the ground-state configuration consists of 12 droplets. Intriguingly, these jumps in Δy are also usually associated with a change in the ground-state droplet number. It is interesting to note that in the 1D regime, the regions of constant N_D slope downwards to the left. This can be understood by considering a horizontal trajectory, for which both N and ϱ are constant. As we move left along this trajectory, increasing f_y can no longer force the droplets closer together—since the array is already 1D—while the decreasing f_x provides more space for longer droplet arrays, with larger N_D.

IV. INCREASING AVERAGE 2D DENSITY

Previous theoretical works have found exotic two-dimensional supersolid states with either large atom numbers ($\sim 10^6$) or tight trapping (~ 1 kHz) [37–39]. Notably, honeycomb ground states have been predicted [37] with crystal arrays of *holes* rather than droplets. Such states are appealing due to their predicted strong superfluid conductance across the crystal, without relying on low-density connections between droplets. Also predicted are intriguing stripe and ring states [38], as well as labyrinthine instabilities [39] familiar in classical ferrofluids [44].

Using the eGPE, we investigate the feasibility of creating these exotic supersolids by increasing the average 2D density through tightening the radial trap frequencies, without relying on pushing the parameters to unrealistically large values. Figures 3(a)–3(f) show how the solution changes by increasing $f_x = f_y \in \{30, 50, 80, 90, 100, 150\}$ Hz, respectively, while holding fixed $N = 1.4 \times 10^5$, and hence ϱ increases. This trajectory through phase space takes us from an unmodulated BEC [Fig. 3(a)] to a hexagonal supersolid [Fig. 3(b)], a stripe supersolid [Fig. 3(d)], through to a ring state [Fig. 3(e)], and, finally, a macrodroplet [Fig. 3(f)]. Interestingly, while the peak density of the BEC phase is about 1.5×10^{20} m^{-3}, for all droplet and supersolid phases it is roughly constant at $\sim 1.5 \times 10^{21}$ m^{-3}, suggesting that the atom losses from inelastic three-body collisions—and hence also the lifetimes—of these exotic states may be comparable to that for the current generation of supersolid experiments.

V. EXCITATIONS OF A 2D SUPERSOLID

Following the recent experimental observation of a seven-droplet hexagon supersolid [30], we further investigate the excitations of this state in a circular trap using the eGPE [see Fig. 4(a1)] and variational model [see Fig. 4(b1)].

We find excitations in the Bogoliubov–de Gennes (BdG) framework, which consists of a linearization of the eGPE around the stationary solution ψ_0 with perturbations of the form $\delta\psi = u e^{-i\epsilon t/\hbar} + v^* e^{i\epsilon t/\hbar}$ [45]. To visualize the
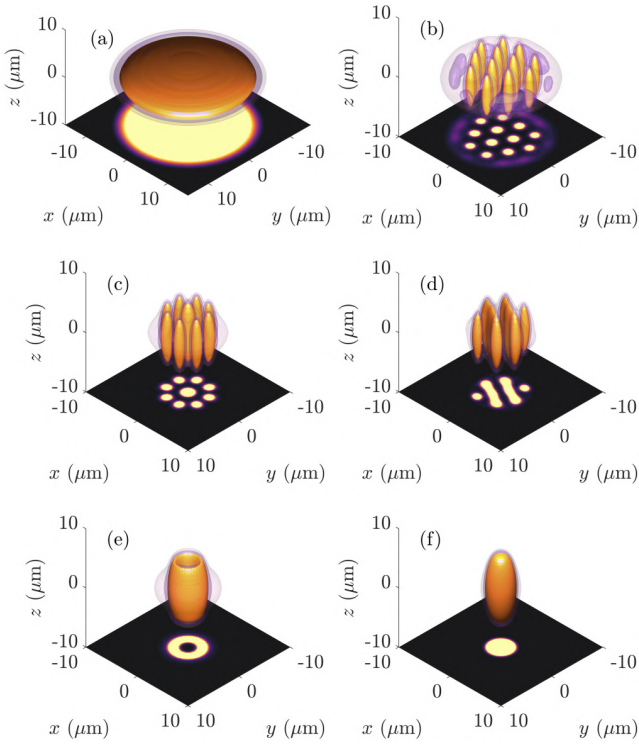
FIG. 3. Increasing the average 2D density. The radial trap frequency is increased from (a)–(f), respectively, as $f_x = f_y \in \{30, 50, 80, 90, 100, 150\}$ Hz, while $N = 1.4 \times 10^5$ is held fixed. Density isosurfaces are shown at the 5%, 0.1%, and 0.01% of the maximum density level. Shadow shows the 2D integrated density. Other parameters: $f_z = 167$ Hz and $a_s = 88\,a_0$.
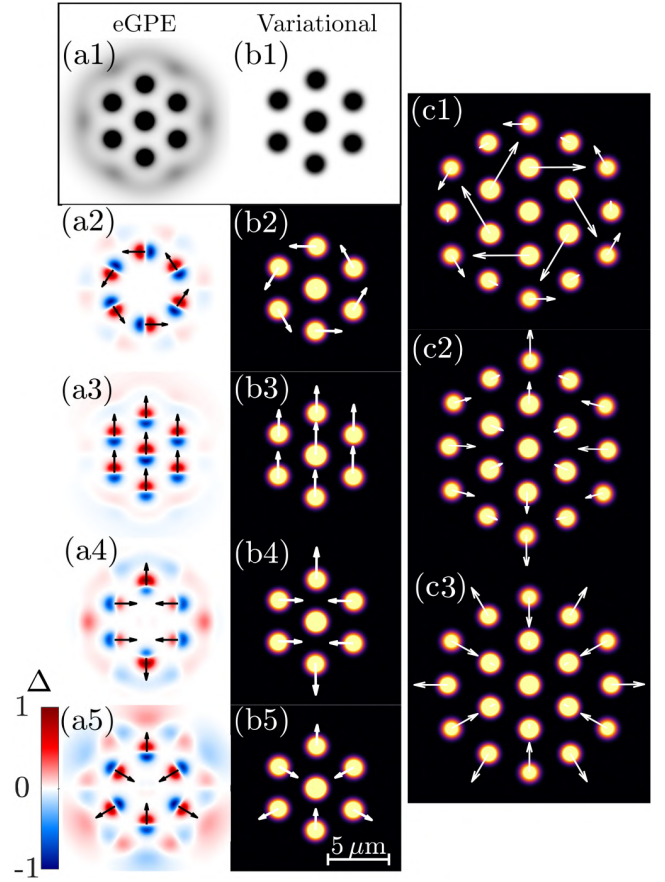

FIG. 4. Crystal excitations. (a1),(b1) Seven-droplet crystal state and corresponding excitations from the (a2)–(a5) eGPE-BdG calculations and (b2)–(b5) variational model. Arrows indicate relative droplet motion (see main text). Parameters: $a_s = 90 a_0$, $f_{x,y,z} = (52.83, 52.83, 167)$ Hz, $N = 9.5 \times 10^4$. (c) Exemplary excitations for the 19-droplet state from the variational model shown in Fig. 1(o).

excitations, we plot the density perturbation $\Delta \psi = (u + v^*)|\psi_0|$ for several exemplary excitations in Figs. 4(a2)–4(a5) (arbitrary normalization). The arrows represent the droplet displacement vectors (with arbitrary global scaling), calculated from the shift in density peaks caused by adding a small amount of excitation to the ground-state wave function. These results are compared with the corresponding excitations calculated with the variational model [Figs. 4(b2)–4(b5)], with droplet displacement vectors obtained through linearizing perturbations to the droplet positions (see Appendix C). Since these modes exist in the variational model—which does not account for superfluid flow between droplets—we can classify them as predominantly crystalline in nature.

Due to rotational symmetry, there is a zero-energy rotational mode [Figs. 4(a2) and 4(b2)], which is unique to circular trap supersolids. As expected, there are two degenerate Kohn modes at the radial trap frequency, one of which is shown in Figs. 4(a3) and 4(b3). Also plotted are quadrupole excitations [Figs. 4(a4) and 4(b4)], as well as an example surface crystal mode [Figs. 4(a5) and 4(b5)], which is a unique feature of 2D supersolids highlighting the rich tapestry of excitations. In the last two examples, the mode energy obtained in the BdG framework and the variational models differs. The energies are $E/h = 54$ Hz [Fig. 4(a4)] and $E/h = 72$ Hz [Fig. 4(a5)] from the BdG calculations and $E/h = 65$ Hz [Fig. 4(b4)] and $E/h = 69$ Hz [Fig. 4(b5)] from the variational

model. These deviations point to a measurable role played by the superfluid connection between the droplets, and the effect of the surrounding halo, which are not accounted for by the variational model. Such comparisons between models provide an excellent platform to distinguish contributions from the crystal and the superfluid surrounding and connecting the droplets.

The computational cost of obtaining modes from BdG linearization is high, requiring the diagonalization of large dense matrices consisting of the total number of position space grid points squared; in our case, $\sim 10^6 \times 10^6$. We achieve this using an eigensolver based on the implicitly restarted Arnoldi method. We also find that the linearization is slower when there is no appreciable superfluid connection between the droplets, making excitations in the isolated droplet regime difficult to obtain. However, in this regime, the variational model agrees well with the BdG calculations, and the former only requires the diagonalization of a $2N_D \times 2N_D$ matrix [i.e., the total number of (x_j, y_j) pairs]. This allows us to explore excitations of larger crystals.

In Figs. 4(c1)–4(c3), we show excitations of the 19-droplet crystal [Fig. 1(o)] using the variational model, a state that

would require months of computational time to obtain excitations within the eGPE-BdG framework. This configuration consists of two concentric hexagons with a single droplet in the middle, where the inner hexagon consists of six droplets and the outer hexagon has 12. In Fig. 4(c1), we highlight an interesting mode in which the two outer hexagons counterrotate. We also find a quadrupole mode [Fig. 4(c2)] and, in Fig. 4(c3), we show an analog of the surface crystal mode that we saw for the seven-droplet hexagon [Figs. 4(a5) and 4(b5)].

VI. CONCLUSIONS

We have investigated the scope and feasibility of 2D supersolidity in harmonically trapped dipolar Bose gases, identifying the crucial role of the average 2D density in maintaining both the crystal structure and global superfluidity while varying the dimensionality and size of the droplet array. By developing a variational multidroplet model, we explored the phase diagram of crystal configurations for a wide range of atom numbers and aspect ratios for a fixed 2D density, identifying the transition from one- to two-dimensional droplet arrays.

We theoretically explored how increasing the average 2D density may provide a route for creating exotic stripe and ring supersolids under experimentally realistic conditions. We also extended our variational model to explore crystal excitations, verified by direct comparison to the BdG analysis. This method allows for the investigation of crystal modes in large 2D supersolids, where exact diagonalization of the eGPE is demanding.

Future work will further explore the potential of the variational model. Implementing a system of Hamilton equations would allow for dynamics of the droplet arrays, and further open up the study of excitations in two-dimensional supersolid crystals. While we have revealed how to vary an important triplet of coupled parameters, i.e., N, and the two trapping frequencies perpendicular to the direction of dipole polarization, f_x and f_y, enabling the exploration of supersolids of various shapes and sizes, future studies will seek an easy determination for how best to vary other control parameters, such as the coupling between the interaction strengths and the remaining trap frequency, f_z.

ACKNOWLEDGMENTS

APPENDIX A: SINGLE-DROPLET VARIATIONAL MODEL

Here we detail the individual contributions to the single-droplet energy functional for $\mathcal{N}$ atoms,

$$E_{sd}(\mathcal{N}) = E_{kin} + E_{trap} + E_{sr} + E_{dd} + E_{qf}. \quad (A1)$$

These terms are given by

$$E_{kin} = -\frac{\hbar^2}{2m} \int d^3\mathbf{x} \ \Psi^* \nabla^2 \Psi,$$

$$E_{trap} = \frac{m}{2} \int d^3\mathbf{x} \ \Psi^* \sum_i \omega_i^2 x_i^2 \Psi,$$

$$E_{sr} = \frac{1}{2} \int d^3\mathbf{x} \ \Psi^* g |\Psi|^2 \Psi, \quad (A2)$$

$$E_{dd} = \frac{g \epsilon_{dd}}{2} \int \frac{d^3\mathbf{k}}{(2\pi)^3} \left(\frac{3k_z^2}{k^2} - 1 \right) |\tilde{n}(\mathbf{k})|^2,$$

$$E_{qf} = \frac{2}{5} \gamma_{QF} \int d^3\mathbf{x} \ |\Psi|^5,$$

corresponding to the kinetic, trap, short-range interaction, dipole-dipole interaction, and quantum fluctuation contributions, respectively. Here, the short-range interaction coefficient is $g = 4\pi \hbar^2 a_s/m$, and the quantum fluctuation coefficient is $\gamma_{QF} = \frac{32}{3} g \sqrt{\frac{a_s^3}{\pi}} \mathcal{Q}_5(\varepsilon_{dd})$, where $\mathcal{Q}_5(\varepsilon_{dd}) = \text{Re}[\int_0^1 du \, (1 - \varepsilon_{dd} + 3u^2 \varepsilon_{dd})^{5/2}]$, and the density in Fourier space is $\tilde{n}(\mathbf{k}) = \int d^3\mathbf{x} \ e^{-i\mathbf{k}\cdot\mathbf{x}} |\Psi(\mathbf{x})|^2$. The integral $\mathcal{Q}_5(\varepsilon_{dd})$ can be evaluated as

$$\mathcal{Q}_5(\varepsilon_{dd}) = \text{Re} \frac{(3\varepsilon_{dd})^{5/2}}{48} \left[(8 + 26\epsilon + 33\epsilon^2)\sqrt{1+\epsilon} \right.$$
$$\left. + 15\epsilon^3 \ln \left(\frac{1 + \sqrt{1+\epsilon}}{\sqrt{\epsilon}} \right) \right], \quad (A3)$$

where $\epsilon = (1 - \varepsilon_{dd})/(3\varepsilon_{dd})$. Note that when using this definition, care should be taken for the special cases $\mathcal{Q}_5(0) = 1$ and $\mathcal{Q}_5(1) = 3\sqrt{3}/2$.

These integrals are evaluated upon substitution of the *Ansatz* $\Psi(\mathbf{x}) = \sqrt{\mathcal{N}}\phi(\rho)\psi(z)$ [43] [see main text, Eq. (4)], with $\mathcal{N}$ the number of particles in the droplet. The radial and axial functions, normalized to one, are assumed to be of the form

$$\phi(\rho) = \sqrt{\frac{r_\rho}{2\pi \Gamma(2/r_\rho)\sigma_\rho^2}} e^{-\frac{1}{2}\left(\frac{\rho}{\sigma_\rho}\right)^{r_\rho}},$$
$$\psi(z) = \sqrt{\frac{r_z}{2\Gamma(1/r_z)\sigma_z}} e^{-\frac{1}{2}\left(\frac{|z|}{\sigma_z}\right)^{r_z}}, \quad (A4)$$

with $\Gamma(x)$ the Gamma function. The widths $\sigma_{\rho,z}$ and the exponents $r_{\rho,z}$ are variational parameters. Substituting the *Ansätze*

given by Eqs. (A4) into the energy contributions given by Eqs. (A2) gives the following results. The kinetic energy of the droplet is of the form

$$\frac{E_{\text{kin}}}{\mathcal{N}} = \frac{\hbar^2}{2m\sigma_\rho^2} \frac{r_\rho^2}{4\Gamma(2/r_\rho)} + \frac{\hbar^2}{2m\sigma_z^2} \frac{r_z f_K(r_z)}{2\Gamma(1/r_z)}, \qquad \text{(A5)}$$

with $f_K(r_z) = (r_z - 1)\Gamma(1 - 1/r_z) - \frac{r_z}{2}\Gamma(2 - 1/r_z)$. The trap energy is

$$\frac{E_{\text{trap}}}{\mathcal{N}} = \frac{m}{2}(\omega_x^2 + \omega_y^2)\left[\frac{\sigma_\rho^2 \Gamma(4/r_\rho)}{2\Gamma(2/r_\rho)}\right] + \frac{m}{2}\omega_z^2\left[\frac{\sigma_z^2 \Gamma(3/r_z)}{\Gamma(1/r_z)}\right]. \qquad \text{(A6)}$$

Short-range interactions lead to an energy contribution,

$$\frac{E_{\text{sr}}}{\mathcal{N}} = \frac{g\mathcal{N}}{8\pi \sigma_\rho^2 \sigma_z} \frac{r_\rho r_z}{2^{2/r_\rho + 1/r_z}\Gamma(2/r_\rho)\Gamma(1/r_z)}, \qquad \text{(A7)}$$

whereas quantum fluctuations result in the Lee-Huang-Yang correction:

$$\frac{E_{\text{qf}}}{\mathcal{N}} = \frac{64\mathcal{Q}_5(\varepsilon_{\text{dd}})}{15\sqrt{\pi}}\left(\frac{2}{5}\right)^{\frac{2}{r_\rho} + \frac{1}{r_z}} g n_0 \sqrt{n_0 a^3}, \qquad \text{(A8)}$$

where $n_0 = \frac{\mathcal{N}r_\rho r_z}{4\pi\Gamma(2/r_\rho)\Gamma(1/r_z)\sigma_\rho^2\sigma_z}$ is the central density.

The dipolar energy is best evaluated in momentum space. The *Ansatz* density in Fourier space can be decomposed as $\tilde{n}(\mathbf{k}) = \tilde{n}_\rho(k_\rho)\tilde{n}_z(k_z)$, with

$$\tilde{n}_\rho(k_\rho) = \frac{r_\rho}{\Gamma(2/r_\rho)}\int_0^\infty d\rho\, \rho e^{-\rho^{r_\rho}} J_0(k_\rho\sigma_\rho\rho),$$
$$\tilde{n}_z(k_z) = \frac{r_z}{\Gamma(1/r_z)}\int_0^\infty dz\, e^{-z^{r_z}}\cos(k_z\sigma_z z), \qquad \text{(A9)}$$

where J_0 is the first Bessel function of the first kind.

Interestingly, these functions can be very closely approximated by Gaussians: $\tilde{n}_\rho(k_\rho) \simeq e^{-\alpha_\rho(r_\rho)(k_\rho\sigma_\rho)^2}$ and $\tilde{n}_z(k_z) \simeq e^{-\alpha_z(r_z)(k_z\sigma_z)^2}$, where $\alpha_\rho(\rho)$ and $\alpha_z(z)$ are functions found through numerical fitting to Eqs. (A9) prior to variational minimization. The dipole-dipole interaction can then be easily expressed as

$$\frac{E_{\text{dd}}}{\mathcal{N}} = \frac{g\varepsilon_{\text{dd}}\mathcal{N}f(\ell_\rho/\ell_z)}{2(2\pi)^{3/2}\ell_\rho^2\ell_z}, \qquad \text{(A10)}$$

where $\ell_{\rho,z}^2 = 4\alpha_{\rho,z}(r_{\rho,z})\sigma_{\rho,z}^2$, and

$$f(\kappa) = \frac{1}{\kappa^2 - 1}\left[2\kappa^2 + 1 - 3\kappa^2\frac{\arctan(\sqrt{\kappa^2 - 1})}{\sqrt{\kappa^2 - 1}}\right]. \qquad \text{(A11)}$$

Our approach is to first minimize the single-droplet energy (A1) for a suitable range of atom numbers. Thus, in preparation for solving the multidroplet problem, we generate interpolating functions $E_{\text{sd}}(\mathcal{N})$, $\sigma_{\rho,z}(\mathcal{N})$, and $r_{\rho,z}(\mathcal{N})$, furnishing a library of single-droplet solutions for a given trap and interaction parameters.

Employing this two-step method reduces the number of variational parameters from seven per droplet to three ($\{\sigma_{\rho,z}^j, r_{\rho,z}^j, N_j, x_j, y_j\} \rightarrow \{N_j, x_j, y_j\}$). Note that the final populations of the droplets are constrained by the total atom number $N = \sum_j N_j$. The effect of interdroplet repulsion is not accounted for in calculating the shape of the droplets. We

replace $f_{x,y} \rightarrow 110$ Hz to simulate the effect of interdroplet interactions on a given droplet's shape; then, to get the energy, we use the $f_{x,y}$ of the actual trap.

For all minimization procedures related to variational calculations, we use the sequential quadratic programming algorithm implemented in the MATLAB function *fmincon*.

APPENDIX B: INTERDROPLET INTERACTION ENERGY

Let us consider two droplets with N_1 and N_2 atoms, respectively, which are sufficiently separated, such that we can neglect any overlapping. The center of mass of the droplets is placed at $\mathbf{r}_{j=1,2} = (x_j, y_j, 0)$, i.e., we permit displacements on the xy plane, but assume that $z_j = 0$. As for the single-droplet dipolar energy, the interdroplet dipole-dipole interaction is best calculated in momentum space,

$$E_{12} = g\epsilon_{\text{dd}}N_1 N_2 \int \frac{d^3\mathbf{k}}{(2\pi)^3}\left[3\frac{k_z^2}{k^2} - 1\right]\tilde{n}_1^*(\mathbf{k})\tilde{n}_2(\mathbf{k}), \qquad \text{(B1)}$$

where we can approximate the Fourier transform of the density profile of the droplets as

$$\tilde{n}_j(\mathbf{k}) \simeq e^{-k_\rho^2\ell_\rho(N_j)^2/4}e^{-k_z^2\ell_z(N_j)^2/4}e^{ik_\rho(x_j\cos\phi + y_j\sin\phi)}. \qquad \text{(B2)}$$

The phase ϕ is accumulated due to the central position of the droplets being different from the origin and plays no role in the energy calculation. We can then evaluate the interaction energy E_{12} as a function of the distance $r_{12} = \sqrt{(x_1 - x_2)^2 + (y_1 - y_2)^2}$ between the droplets:

$$E_{12}(r_{12}) = \frac{g\varepsilon_{\text{dd}}N_1 N_2}{\bar{\ell}_\rho^2 \bar{\ell}_z}\frac{\sqrt{2}}{\pi^2}$$
$$\times \int_0^1 du \frac{(\Lambda^2 + 2)u^2 - \Lambda^2}{(1 - \Lambda^2)u^2 + \Lambda^2}G\left[\frac{2r_{12}^2(1 - u^2)}{\bar{\ell}_\rho^2}\right], \qquad \text{(B3)}$$

where $2\bar{\ell}_{\rho,z}^2 = \ell_{\rho,z}(N_1)^2 + \ell_{\rho,z}(N_2)^2$, $\Lambda = \bar{\ell}_z/\bar{\ell}_\rho$, and

$$G(x) = \frac{\sqrt{\pi}}{4}e^{-x/8}\left\{I_0\left(\frac{x}{8}\right) + \frac{x}{4}\left[I_1\left(\frac{x}{8}\right) - I_0\left(\frac{x}{8}\right)\right]\right\}, \qquad \text{(B4)}$$

with $I_n(x)$ the modified Bessel function. The interaction energy (B3) is attractive at short distances, a spurious effect up to the radial size of a droplet. In order to prevent the droplets from "piling up" â in this inner region, we instead approximate the interdroplet potential as

$$E_{jj'}(r_{jj'}) \simeq \frac{V_0(N_j, N_{j'})N_j N_{j'}}{[r_{jj'} + r_0(N_j, N_{j'})]^3}, \qquad \text{(B5)}$$

for any two droplets j and j', where V_0 and r_0 are determined by fitting to Eq. (B3). This term is the last contribution to Eq. (7) and is utilized in the phase diagram given in Fig. 2. By considering a range of particle number pairs between droplets, we determine the interpolating functions $V_0(\mathcal{N}, \mathcal{N}')$ and $r_0(\mathcal{N}, \mathcal{N}')$ prior to solving the full many-droplet problem. Note that the shift r_0, which results from the z extension of the droplet, is relevant because typical interdroplet distances are comparable to the z size of the droplets.

APPENDIX C: EXCITATIONS OF THE VARIATIONAL MODEL

Expanding around the equilibrium positions $\mathbf{R}_j = (x_j, y_j)$, $\mathbf{r}_j = \mathbf{R}_j + \boldsymbol{\epsilon}_j$, the energy of the array becomes, up to second order in the displacement $\boldsymbol{\epsilon}_j = (\epsilon_{x;j}, \epsilon_{y;j})$, of the form $E = E_0 + E^{(2)}$ (the first-order contribution cancels because we move from an energy minimum), with E_0 the ground-state energy, and

$$E^{(2)} = \sum_{j=1}^{N_D} \boldsymbol{\epsilon}_j^T \cdot \left[\hat{A}_j \cdot \boldsymbol{\epsilon}_j - \sum_{j' \neq j} \hat{B}_{jj'} \cdot \boldsymbol{\epsilon}_{j'} \right], \quad (C1)$$

where

$$\hat{B}_{jj'} = V_0(N_j, N_{j'}) \sqrt{N_j N_{j'}} \begin{pmatrix} \beta_{jj'} + \gamma_{jj'} X_{jj'}^2 & \gamma_{jj'} X_{jj'} Y_{jj'} \\ \gamma_{jj'} X_{jj'} Y_{jj'} & \beta_{jj'} + \gamma_{jj'} Y_{jj'}^2 \end{pmatrix}, \quad (C2)$$

$$\hat{A}_j = \frac{m N_j}{2} \begin{pmatrix} \omega_x^2 & 0 \\ 0 & \omega_y^2 \end{pmatrix} + \sum_{j' \neq j} \hat{B}_{jj'}, \quad (C3)$$

with

$$\beta_{jj'} = \frac{-3}{2 R_{jj'} (R_{jj'} + r_{0,jj'})^4}, \quad (C4)$$

$$\gamma_{jj'} = \frac{3}{2 R_{jj'}^3 (R_{jj'} + r_{0,jj'})^4} + \frac{6}{R_{jj'}^2 (R_{jj'} + r_{0,jj'})^5}, \quad (C5)$$

and the separation matrices $X_{jj'} = x_j - x_{j'}$, $Y_{jj'} = y_j - y_{j'}$, and $R_{jj'} = |\mathbf{r}_j - \mathbf{r}_{j'}|$.

We can write $E^{(2)} = \vec{\Phi}^T \cdot \hat{M} \cdot \vec{\Phi}$, with $\vec{\Phi} = (\epsilon_{x,1}, \epsilon_{y,1}, \ldots \epsilon_{x,N_D} \epsilon_{y,N_D})$. Now, we can diagonalize $\hat{M}$ to obtain the eigenvalues λ_ν, which provide the excitation frequencies of the droplet array, $\Omega_\nu = \sqrt{2\lambda_\nu}$. Note that this is an expansion around the equilibrium positions only, and not a perturbation of the individual droplet shape or atom number, so other shape excitations, such as droplet breathing modes, will not be captured by this method. Some example excitations are shown in Figs. 4(b2)–4(b5) and 4(c1)–4(c3), where the arrow indicates the vector between $\mathbf{R}_j$ and $\mathbf{r}_j$ for each droplet j.

[1] E. P. Gross, Unified theory of interacting bosons, Phys. Rev. **106**, 161 (1957).

[2] A. F. Andreev and I. M. Lifshitz, Quantum theory of defects in crystals, Zh. Eksp. Teor. Fiz. **56**, 2057 (1969) [Sov. Phys. JETP **29**, 1107 (1969)].

[3] D. Thouless, The flow of a dense superfluid, Ann. Phys. **52**, 403 (1969).

[4] G. Chester, Speculations on Bose-Einstein condensation and quantum crystals, Phys. Rev. A **2**, 256 (1970).

[5] A. J. Leggett, Can a Solid Be" Superfluid"?, Phys. Rev. Lett. **25**, 1543 (1970).

[6] M. Boninsegni and N. V. Prokofêv, Colloquium: Supersolids: What and where are they?, Rev. Mod. Phys. **84**, 759 (2012).

[7] J. Léonard, A. Morales, P. Zupancic, T. Esslinger, and T. Donner, Supersolid formation in a quantum gas breaking a continuous translational symmetry, Nature (London) **543**, 87 (2017).

[8] J.-R. Li, J. Lee, W. Huang, S. Burchesky, B. Shteynas, F. Ç. Top, A. O. Jamison, and W. Ketterle, A stripe phase with supersolid properties in spin–orbit-coupled Bose-Einstein condensates, Nature (London) **543**, 91 (2017).

[9] T. M. Bersano, J. Hou, S. Mossman, V. Gokhroo, X.-W. Luo, K. Sun, C. Zhang, and P. Engels, Experimental realization of a long-lived striped Bose-Einstein condensate induced by momentum-space hopping, Phys. Rev. A **99**, 051602(R) (2019).

[10] L. Tanzi, E. Lucioni, F. Famà, J. Catani, A. Fioretti, C. Gabbanini, R. N. Bisset, L. Santos, and G. Modugno, Observation of a Dipolar Quantum Gas with Metastable Supersolid Properties, Phys. Rev. Lett. **122**, 130405 (2019).

[11] F. Böttcher, J.-N. Schmidt, M. Wenzel, J. Hertkorn, M. Guo, T. Langen, and T. Pfau, Transient Supersolid Properties in an Array of Dipolar Quantum Droplets, Phys. Rev. X **9**, 011051 (2019).

[12] L. Chomaz, D. Petter, P. Ilzhöfer, G. Natale, A. Trautmann, C. Politi, G. Durastante, R. M. W. van Bijnen, A. Patscheider, M.

Sohmen, M. J. Mark, and F. Ferlaino, Long-Lived And Transient Supersolid Behaviors in Dipolar Quantum Gases, Phys. Rev. X **9**, 021012 (2019).

[13] G. Natale, R. M. W. van Bijnen, A. Patscheider, D. Petter, M. J. Mark, L. Chomaz, and F. Ferlaino, Excitation Spectrum of a Trapped Dipolar Supersolid and Its Experimental Evidence, Phys. Rev. Lett. **123**, 050402 (2019).

[14] L. Tanzi, S. Roccuzzo, E. Lucioni, F. Famà, A. Fioretti, C. Gabbanini, G. Modugno, A. Recati, and S. Stringari, Supersolid symmetry breaking from compressional oscillations in a dipolar quantum gas, Nature (London) **574**, 382 (2019).

[15] M. Guo, F. Böttcher, J. Hertkorn, J.-N. Schmidt, M. Wenzel, H. P. Büchler, T. Langen, and T. Pfau, The low-energy goldstone mode in a trapped dipolar supersolid, Nature (London) **574**, 386 (2019).

[16] A. Griesmaier, J. Werner, S. Hensler, J. Stuhler, and T. Pfau, Bose-Einstein Condensation of Chromium, Phys. Rev. Lett. **94**, 160401 (2005).

[17] M. Lu, N. Q. Burdick, S. H. Youn, and B. L. Lev, Strongly Dipolar Bose-Einstein Condensate of Dysprosium, Phys. Rev. Lett. **107**, 190401 (2011).

[18] K. Aikawa, A. Frisch, M. Mark, S. Baier, A. Rietzler, R. Grimm, and F. Ferlaino, Bose-Einstein Condensation of Erbium, Phys. Rev. Lett. **108**, 210401 (2012).

[19] L. Santos, G. V. Shlyapnikov, and M. Lewenstein, Roton-Maxon Spectrum and Stability of Trapped Dipolar Bose-Einstein Condensates, Phys. Rev. Lett. **90**, 250403 (2003).

[20] L. Chomaz, R. M. W. van Bijnen, D. Petter, G. Faraoni, S. Baier, J. H. Becher, M. J. Mark, F. Wächtler, L. Santos, and F. Ferlaino, Observation of roton mode population in a dipolar quantum gas, Nat. Phys. **14**, 442 (2018).

[21] J.-N. Schmidt, J. Hertkorn, M. Guo, F. Böttcher, M. Schmidt, K. S. H. Ng, S. D. Graham, T. Langen, M. Zwierlein, and T. Pfau, Roton Excitations in an Oblate Dipolar Quantum Gas, Phys. Rev. Lett. **126**, 193002 (2021).

[22] T. Lahaye, J. Metz, B. Fröhlich, T. Koch, M. Meister, A. Griesmaier, T. Pfau, H. Saito, Y. Kawaguchi, and M. Ueda, d-Wave Collapse and Explosion of a Dipolar Bose-Einstein Condensate, Phys. Rev. Lett. **101**, 080401 (2008).

[23] H. Kadau, M. Schmitt, M. Wenzel, C. Wink, T. Maier, I. Ferrier-Barbut, and T. Pfau, Observing the Rosensweig instability of a quantum ferrofluid, Nature (London) **530**, 194 (2016).

[24] M. Schmitt, M. Wenzel, F. Böttcher, I. Ferrier-Barbut, and T. Pfau, Self-bound droplets of a dilute magnetic quantum liquid, Nature (London) **539**, 259 (2016).

[25] L. Chomaz, S. Baier, D. Petter, M. J. Mark, F. Wächtler, L. Santos, and F. Ferlaino, Quantum-Fluctuation-Driven Crossover from a Dilute Bose-Einstein Condensate to a Macrodroplet in a Dipolar Quantum Fluid, Phys. Rev. X **6**, 041039 (2016).

[26] I. Ferrier-Barbut, H. Kadau, M. Schmitt, M. Wenzel, and T. Pfau, Observation of Quantum Droplets in a Strongly Dipolar Bose Gas, Phys. Rev. Lett. **116**, 215301 (2016).

[27] F. Wächtler and L. Santos, Quantum filaments in dipolar Bose-Einstein condensates, Phys. Rev. A **93**, 061603(R) (2016).

[28] R. N. Bisset, R. M. Wilson, D. Baillie, and P. B. Blakie, Ground-state phase diagram of a dipolar condensate with quantum fluctuations, Phys. Rev. A **94**, 033619 (2016).

[29] M. A. Norcia, C. Politi, L. Klaus, E. Poli, M. Sohmen, M. J. Mark, R. N. Bisset, L. Santos, and F. Ferlaino, Two-dimensional supersolidity in a dipolar quantum gas, Nature (London) **596**, 357 (2021).

[30] T. Bland, E. Poli, C. Politi, L. Klaus, M. Norcia, F. Ferlaino, L. Santos, and R. Bisset, Two-dimensional supersolidity in a circular trap, arXiv:2107.06680.

[31] D. Baillie and P. B. Blakie, Droplet Crystal Ground States of a Dipolar Bose Gas, Phys. Rev. Lett. **121**, 195301 (2018).

[32] S. Roccuzzo, S. Stringari, and A. Recati, Supersolid edge and bulk phases of a dipolar quantum gas in a box, arXiv:2104.01068.

[33] A. Gallemí, S. M. Roccuzzo, S. Stringari, and A. Recati, Quantized vortices in dipolar supersolid Bose-Einstein-condensed gases, Phys. Rev. A **102**, 023322 (2020).

[34] S. M. Roccuzzo, A. Gallemí, A. Recati, and S. Stringari, Rotating a Supersolid Dipolar Gas, Phys. Rev. Lett. **124**, 045702 (2020).

[35] M. N. Tengstrand, D. Boholm, R. Sachdeva, J. Bengtsson, and S. M. Reimann, Persistent currents in toroidal dipolar supersolids, Phys. Rev. A **103**, 013313 (2021).

[36] F. Ancilotto, M. Barranco, M. Pi, and L. Reatto, Vortex properties in the extended supersolid phase of dipolar Bose-Einstein condensates, Phys. Rev. A **103**, 033314 (2021).

[37] Y.-C. Zhang, F. Maucher, and T. Pohl, Supersolidity Around a Critical Point in Dipolar Bose-Einstein Condensates, Phys. Rev. Lett. **123**, 015301 (2019).

[38] Y.-C. Zhang, T. Pohl, and F. Maucher, Phases of supersolids in confined dipolar Bose-Einstein condensates, Phys. Rev. A **104**, 013310 (2021).

[39] J. Hertkorn, J.-N. Schmidt, M. Guo, F. Böttcher, K. S. H. Ng, S. D. Graham, P. Uerlings, T. Langen, M. Zwierlein, and T. Pfau, Pattern formation in quantum ferrofluids: From supersolids to superglasses, Phys. Rev. Research **3**, 033125 (2021).

[40] A. R. P. Lima and A. Pelster, Quantum fluctuations in dipolar Bose gases, Phys. Rev. A **84**, 041604(R) (2011).

[41] S. Ronen, D. C. E. Bortolotti, and J. L. Bohn, Bogoliubov modes of a dipolar condensate in a cylindrical trap, Phys. Rev. A **74**, 013623 (2006).

[42] S. M. Roccuzzo and F. Ancilotto, Supersolid behavior of a dipolar Bose-Einstein condensate confined in a tube, Phys. Rev. A **99**, 041601(R) (2019).

[43] L. Lavoine and T. Bourdel, Beyond-mean-field crossover from one dimension to three dimensions in quantum droplets of binary mixtures, Phys. Rev. A **103**, 033312 (2021).

[44] A. J. Dickstein, S. Erramilli, R. E. Goldstein, D. P. Jackson, and S. A. Langer, Labyrinthine pattern formation in magnetic fluids, Science **261**, 1012 (1993).

[45] L. Pitaevskii and S. Stringari, *Bose-Einstein Condensation and Superfluidity* (Oxford University Press, Oxford, 2016).

2.6. Publication: Two-dimensional supersolid formation in dipolar condensates

T. Bland[1], **E. Poli**[2], C. Politi[1,2], L. Klaus[1,2], M. A. Norcia[1], F. Ferlaino[1,2],
L. Santos[3] and R. N. Bisset[2]

[1] *Institut für Quantenoptik und Quanteninformation, Österreichische Akademie der Wissenschaften, 6020 Innsbruck, Austria*
[2] *Institut für Experimentalphysik, Universität Innsbruck, 6020 Innsbruck, Austria*
[3] *Institut für Theoretische Physik, Leibniz, Universität Hannover, Hanover, Germany*

---

† The author of the present thesis performed the numerical eGPE simulations, the BdG simulations and contributed in writing the manuscript.

Two-Dimensional Supersolid Formation in Dipolar Condensates

T. Bland[1], E. Poli[2], C. Politi[1,2], L. Klaus[1,2] M. A. Norcia[1], F. Ferlaino[1,2] L. Santos[3], and R. N. Bisset[2,*]

[1]*Institut für Quantenoptik und Quanteninformation, Österreichische Akademie der Wissenschaften, Innsbruck 6020, Austria*
[2]*Institut für Experimentalphysik, Universität Innsbruck, Innsbruck 6020, Austria*
[3]*Institut für Theoretische Physik, Leibniz Universität Hannover, Hannover 30167, Germany*

Dipolar condensates have recently been coaxed to form the long-sought supersolid phase. While one-dimensional supersolids may be prepared by triggering a roton instability, we find that such a procedure in two dimensions (2D) leads to a loss of both global phase coherence and crystalline order. Unlike in 1D, the 2D roton modes have little in common with the supersolid configuration. We develop a finite-temperature stochastic Gross-Pitaevskii theory that includes beyond-mean-field effects to explore the formation process in 2D and find that evaporative cooling directly into the supersolid phase—hence bypassing the first-order roton instability—can produce a robust supersolid in a circular trap. Importantly, the resulting supersolid is stable at the final nonzero temperature. We then experimentally produce a 2D supersolid in a near-circular trap through such an evaporative procedure. Our work provides insight into the process of supersolid formation in 2D and defines a realistic path to the formation of large two-dimensional supersolid arrays.

The supersolid phase was predicted to simultaneously exhibit crystalline order and superfluidity [1–6]. While it remains elusive in helium, recent developments in ultracold quantum gases have finally made supersolidity a reality, providing an excellent platform for the control and observation of these states. Important early advances were made in systems with spin-orbit coupling [7,8] and cavity-mediated interactions [9], where supersolid properties were observed in rigid crystal configurations. Bose-Einstein condensates (BECs) with dipole-dipole interactions have now been observed in a supersolid state with deformable crystals [10–13], with their lattices genuinely arising from the atom-atom interactions [14–16].

In the first dipolar supersolid experiments, translational symmetry was broken only along one axis, giving rise to a one-dimensional (1D) density wave, commonly referred to as a 1D droplet array [10–12]. A more recent experiment has created the first states with two-dimensional (2D) supersolidity in elongated traps of variable aspect ratio [13]. This opens the door to study vortices and persistent currents [17–20], as well as exotic ground state phases predicted for large atom numbers [21–24].

It is still an open question whether 2D arrays provide as favorable conditions for supersolidity as 1D arrays do. In 1D, following an interaction quench from an unmodulated to modulated BEC, the density pattern induced by a roton instability [14,25–28] can smoothly connect with the final supersolid array [10–12]. This transition, hence, has a weakly first-order character or is even continuous [29,30], and such quenches through the transition cause only small excitations of the resulting supersolid [10–12]. While it has

been predicted that a similar procedure may lead to coherence between three droplets in a triangular configuration [31], earlier work with nondipolar superfluids suggests that such symmetry-breaking quenches may be unfavorable for supersolid formation in 2D and 3D [32,33].

An alternative method exists to experimentally produce dipolar supersolids. Instead of quenching the interactions to trigger a roton instability, it is possible to cool a thermal sample directly into the supersolid state using evaporative cooling techniques [12,34]. Crucially, this is the only known method for producing 2D supersolids to date [13]. While a dynamic interaction quench may be described by the extended Gross-Pitaevskii equation (eGPE) [35–38], we are not aware of any available theory to model the required evaporation process. From a theoretical perspective, much remains unknown about evaporative supersolid formation. Is it a general feature that the droplets form before global phase coherence develops, as reported in Ref. [34]? Under what conditions do defects persist? Such answers will be paramount in the quest for ever-larger 2D supersolids, as well as for the observation of vortices embedded within them.

In this Letter, we explore the formation of large 2D supersolids in circular-shaped traps. We develop a finite-temperature Stochastic eGPE (SeGPE) theory to model the entire evaporative cooling process. Importantly, our theory includes the beyond-mean-field quantum fluctuations responsible for stabilizing the individual droplets.

We compare the evaporative cooling formation dynamics with those resulting from an interaction quench, finding striking differences between the two protocols. Following
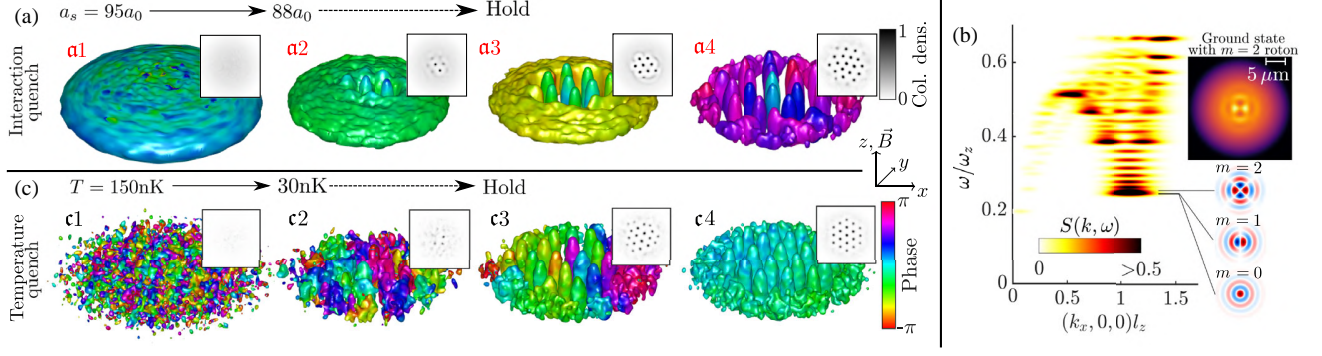
FIG. 1. (a) Crystal preparation from interaction quench, evolved with the eGPE, for $N \approx 2.1 \times 10^5$ Dy atoms [quench (i)]. Isosurfaces are at 5% max density, with color indicating phase. Insets: z column densities normalized to max value from the entire simulation. (b) Dynamic structure factor for an unmodulated BEC ($a_s = 92a_0$) in energy-momentum space, normalized to peak value. The lowest-energy roton modes are indicated, and the ground state with an $m = 2$ roton mode added is shown, revealing the localized nature of the rotons. Parameters are otherwise the same as in (a). (c) Crystal preparation from temperature quench (evaporative cooling) evolved with the SeGPE [quench (ii)]. The temperature decreases as the chemical potential and condensate number rise, with scattering length fixed at $a_s = 88a_0$. For all subplots $f_{x,y,z} = (33, 33, 167)$ Hz, and $l_z = \sqrt{\hbar/m\omega_z}$.

an interaction quench, the 2D crystal grows nonlinearly with the droplets developing sequentially, producing configurations that are unrelated to any roton mode combination of the original unmodulated BEC. The resulting crystal is substantially excited and lacks global phase coherence. Alternatively, by directly cooling into the supersolid regime, our SeGPE theory predicts the formation of large 2D supersolids in circular traps, with global phase coherence that remains robust at finite temperature. To benchmark our theory—as well as to test the direct cooling protocol for pancake-shaped trapping geometries—we perform experiments and observe a 7-droplet hexagonal supersolid in a near-circular trap.

Formalism.—We are interested in ultracold, dipolar Bose gases harmonically confined in 3D with trapping frequencies $\omega_{x,y,z} = 2\pi f_{x,y,z}$. Two-body contact interactions and the long-ranged, anisotropic dipole-dipole interactions are well described by a pseudopotential, $U(\mathbf{r}) = (4\pi\hbar^2 a_s/m)\delta(\mathbf{r}) + (3\hbar^2 a_{dd}/m)[(1 - 3\cos^2\theta)/r^3]$, with a_s being the s-wave scattering length and $a_{dd} = \mu_0\mu_m^2 m/12\pi\hbar^2$ the dipole length, with magnetic moment μ_m, and θ is the angle between the polarization axis (z axis) and the vector joining two particles. The ratio $\epsilon_{dd} = a_{dd}/a_s$ (for $a_s > 0$) is convenient to keep in mind, since for $\epsilon_{dd} \leq 1$ the ground state will be an unmodulated BEC, whereas for the dipole-dominated regime $\epsilon_{dd} > 1$ the unmodulated BEC may become unstable [39]. Here, we always consider ^{164}Dy, with $a_{dd} = 131a_0$. The eGPE has been described elsewhere [35–38], and its details have been deferred to Supplemental Material [40].

We phenomenologically introduce a finite-temperature simple growth SeGPE theory [55]. This describes the "classical" field, $\Psi(\mathbf{r}, t)$, of all highly populated modes up to an energy cutoff. The dynamics are governed by [56]

$$i\hbar\frac{\partial\Psi}{\partial t} = \hat{\mathcal{P}}\{(1 - i\gamma)(\mathcal{L}[\Psi] - \mu)\Psi + \eta\}. \quad (1)$$

Here, $\mathcal{L}$ is the eGPE operator defined in Ref. [40], and γ describes the coupling of the classical field modes to the high-lying modes. We find that $\gamma = 7.5 \times 10^{-3}$ gives good agreement to the condensate number growth rate of a recent experiment under comparable conditions [34] (see also Ref. [40]). The dynamical noise term η, subject to noise correlations given by $\langle\eta^*(\mathbf{r}, t)\eta(\mathbf{r}', t')\rangle = 2\hbar\gamma k_B T\delta(t - t')\delta(\mathbf{r} - \mathbf{r}')$, means that each simulation run is unique. Finally, $\hat{\mathcal{P}}$ is a projector which constrains the dynamics of the system up to energy cutoff $\epsilon_{cut}(\mu) = 2\mu$—consistent with previous treatments [57,58]—where we use the final μ after evaporative cooling.

Supersolid formation simulations.—With these two theories in hand, we perform two kinds of dynamic quench simulations in a pancake-shaped trap, where in both cases the ground state for the final parameters would be a 19-droplet supersolid:

(i) An interaction quench from an unmodulated BEC to the supersolid regime using the eGPE [Fig. 1(a)]. Noise is first added to the BEC ground state [59], and this is evolved for a 20 ms equilibration time before the interaction strength is linearly ramped over the next 30 ms from $a_s = 95a_0$ to $a_s = 88a_0$—crossing the roton phase transition to the supersolid regime—and then held constant again for the remainder of the simulation.

(ii) A temperature quench from a thermal cloud to the supersolid phase using the SeGPE [Fig. 1(c)]. Each simulation begins with a 200 ms equilibration time at fixed high temperature $T = 150$ nK to generate a thermal cloud. To simulate the evaporative cooling process, the chemical potential and temperature are then linearly ramped over 100 ms, from $(\mu, T) = (-12.64\hbar\omega_z, 150$ nK$)$ to

(12.64$\hbar\omega_z$, 30 nK), mimicking the growing condensate number observed in experiments [60,61], while the scattering length is always held fixed at $a_s = 88a_0$.

Focusing first on the interaction quench, the density isosurfaces in Fig. 1(a) represent snapshots at various times for a single simulation run, revealing intriguing formation dynamics. Initial droplets are seeded through unstable roton modes, but staggered droplet formation reveals a process of *nonlinear crystal growth*, as highlighted by the column densities shown as insets in Fig. 1(a). In Fig. 1(a2), two central droplets have already attained their final peak density, while a secondary ring of droplets is only just beginning to form. Then, in Fig. 1(a3), eight droplets have fully matured, and the process continues radially outward until a 19-droplet crystal is approximately attained. Similar droplet formation dynamics have been predicted in optical media [62].

The colors on the density isosurfaces in Fig. 1(a) represent the wave function phase. The color scale is recentered in each subplot, and an ideal phase coherent solution would have a uniform color everywhere. Importantly, the crystal growth process disrupts the global phase coherence, as evidenced by the various colors in Fig. 1(a4), leaving an excited crystal in which some outer droplets dissolve and reemerge from the halo. Note that the situation does not qualitatively change for reduced initial noise or gentler interaction ramps, suggesting that the strong excitations result from a first-order character of the roton instability in 2D.

We explain the interaction quench dynamics by calculating the elementary excitations of the unmodulated BEC close to the roton instability, i.e., for $a_s = 92a_0$. These results are displayed in Fig. 1(b) as the dynamic structure factor $S(\mathbf{k}, \omega)$, which predicts the system response to perturbations of momentum $\hbar\mathbf{k}$ and energy $\hbar\omega$ [28,63–65] (also see Ref. [40]). A roton minimum can be seen at $k_x l_z \approx 1.1$, and we plot the lowest roton modes corresponding to $m = 0, 1, 2$, with m being the angular quantum number in the z direction [66]. On the top right is the density obtained by adding an $m = 2$ roton mode to the BEC wave function, revealing how rotons are confined to high-density regions [67,68]. This reveals a qualitative difference between the 1D and 2D situations, since, from a simple geometric standpoint, in 2D the high-density region inherently encompasses a smaller proportion of the total atom number. Thus, the roton-induced droplet number is only a small fraction of the final droplet number, meaning the droplets appear sequentially for 2D.

Another qualitative difference between 1D and 2D is a kind of frustration. First, note that our target supersolid ground state for the final quench parameters is a 19-droplet crystal, with a central droplet [see the inset of Fig. 2(b)]. Only an $m = 0$ roton mode [see Fig. 1(b)] could directly trigger the formation of a central droplet, but then only concentric rings could form further out. Thus, unlike for
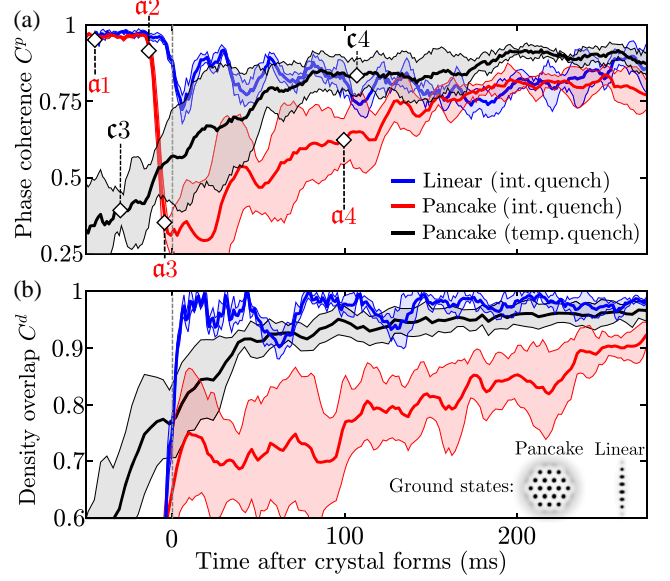

FIG. 2. Supersolid quality. (a) Global phase coherence C^p over time for interaction quenches [quench (i)] into linear chain (blue) and pancake crystal (red) and temperature quenches [quench (ii)] into the pancake crystal (black). Diamonds link to example frames in Figs. 1(a) and 1(c). Each curve is averaged over 3–5 runs with an error band marking one standard deviation. Time $t = 0$ corresponds to when the crystals first fully mature. (b) Density overlap C^d between the time-dependent and ground state densities. Parameters are the same as Fig. 1, but for linear chain $f_{x,y,z} = (33, 110, 167)$ Hz and $N = 82 \times 10^3$.

1D, no single roton mode can smoothly connect the unmodulated BEC to the 2D supersolid ground state.

Next, we analyze the finite-temperature quench results. Figure 1(c) shows snapshots of the condensate growth, demonstrating that both the crystal structure and the global phase coherence—evidenced by the uniform color in Fig. 1(c4)—develop soon after the quench. Note that timescales will be quantified shortly. It is also an important result in itself that we predict such a large 2D supersolid to be stable against thermal fluctuations (recall that $T_{\text{final}} = 30$ nK). As they form, each droplet individually has a uniform phase that may be different from that of its neighbors, sometimes creating vortex pairs between droplets of different phase. In this scenario, the droplets do not form as a result of a roton instability, and the partial phase coherence continues to improve after the crystal has formed, consistent with earlier observations [34]. Occasionally, long-lived isolated vortices remain near the center of the supersolid. Simulation videos are provided in Supplemental Material [40].

Supersolid quality.—We seek to quantify the resulting supersolid quality for both quench protocols. We start by analyzing the phase excitations, taking the phase coherence C^p with a similar measure presented in Ref. [10]. A value of $C^p = 1(0)$ implies global phase

coherence (incoherence) [69]. In Fig. 2(a), we plot this quantity for interaction quenches into the pancake supersolid regime (red) and linear supersolid regime (blue) and temperature quenches into the pancake supersolid (black). The time $t = 0$ indicates when the droplet number has approximately stabilized and the crystal has first matured [70]. For the linear chain, the system remains coherent (high $C^p \approx 0.8$), indicating a stable supersolid. However, quenching into the pancake geometry is qualitatively different, with strong incoherence ($C^p \approx 0.3$) soon after crystal formation, recovering a high value at around 150 ms after the crystal forms. During evaporative cooling, the global phase coherence is predicted by the high value of $C^p \approx 0.8$ around 50 ms after the crystal forms, with qualitatively similar values to the interaction quench simulations for the linear supersolid case.

We quantify the quality of the supersolid crystal by measuring the density overlap C^d between the ground state target solution and the time-dependent wave function [71]. We find the maximal value of C^d after applying translations and rotations to the state, noting that perfect overlap would give $C^d = 1$. In Fig. 2(b), this quantity is presented for the two geometries, with the ground state solutions shown as insets. For the linear chain, once the droplets have formed, the density overlap rapidly attains $C^d > 0.9$ and remains there, consistent with the interaction quenched state being close to the ground state supersolid. However, the pancake case shows weak overlap after the droplets are formed, which only recovers slowly—after around 300 ms—to values comparable with the linear chain. Primarily, this is due to the sensitivity of droplet positions of C^d and indicates that there are many excited supersolid modes present after the droplets form [40]. Direct evaporative cooling for the pancake case, however, shows that after the droplets have formed they rapidly settle into the expected crystal pattern ($C^d \approx 0.95$).

Finally, it is important to note that for the pancake interaction quench, while the phase coherence is restored by around $t = 150$ ms after the droplets are formed, the crystal remains highly excited until around 300 ms. On these timescales, three-body losses become significant, and it is unlikely that a large supersolid would be observed. In contrast, direct evaporative cooling may lead to a robust supersolid within around 50 ms of the crystal first appearing, a timescale that we find to be weakly dependent on the value of γ [40].

Experimental observation.—While experiments have evaporatively cooled directly into the supersolid phase for linear and elongated 2D configurations [12,13,34], this could prove an optimal method in circular traps for avoiding the excitations associated with crossing the roton instability. We confirm this by producing a 7-droplet hexagon supersolid in a near-circular trap, as shown in Fig. 3. The experimental apparatus and procedure is similar to that described previously [13], but new modifications in
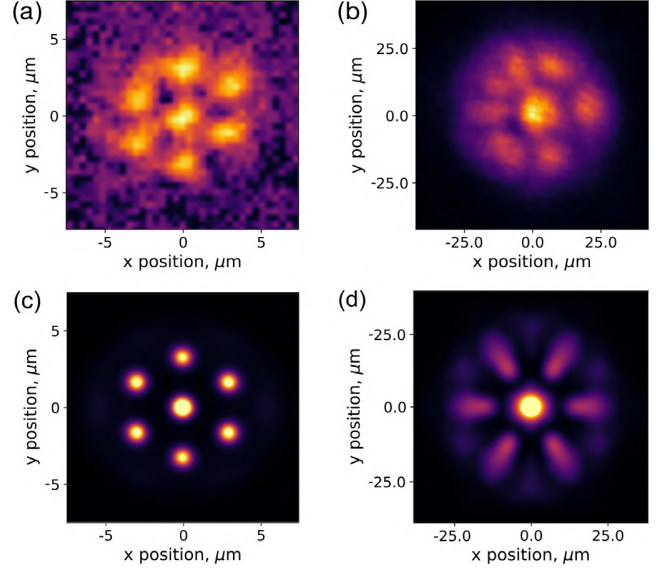

FIG. 3. Experimental realization of a 7-droplet hexagon state. (a) Exemplary *in situ* image of the density profile. (b) Image after 36 ms time-of-flight (TOF) expansion, averaged over 68 trials of the experiment. Hexagonal modulation structure is clearly present in the averaged image. Note the rotation of the hexagon between *in situ* and TOF images. (c),(d) Corresponding simulations for the same trap, and with $a_s = 90a_0$ and $\approx 4.4 \times 10^4$ atoms within the droplets.

the optical dipole trap setup have enabled us to tune between anisotropic and round traps. The current optical trap consists of three 1064 nm wavelength trapping beams, each propagating in the plane perpendicular to gravity. Two of the beams, which cross perpendicularly, have approximately 60 μm waists and define the horizontal trapping frequencies. The third, crossing at a roughly 45° angle from the others, has a waist of approximately 18 μm and is rapidly scanned to create a time-averaged light sheet that defines the vertical confinement.

In a harmonic trap with frequencies $f_{x,y,z} = [47(1), 43(1), 133(5)]$ Hz, we observe in trap a 7-droplet state consisting of a hexagon with a central droplet, with a condensate atom number of $N \sim 4 \times 10^4$ [Fig. 3(a)]. To confirm that this state is phase coherent, we release the atoms from the trap and image the interference pattern after 36 ms time of flight [Fig. 3(b)]. The presence of clear modulation in the interference pattern averaged over 68 runs of the experiment indicates a well-defined and reproducible relative phase between the droplets and is consistent with our expectations for a phase-coherent state undergoing expansion [Fig. 3(d)], obtained through 3D dynamic simulations starting from the eGPE ground state [Fig. 3(c)]. Even rounder traps are possible, but the slight anisotropy orients the state, helping to observe the reproducible interference pattern.

Summary.—We have theoretically explored the formation of large 2D supersolids using both an interaction

quench from an unmodulated BEC and a temperature quench from a thermal cloud. For the latter, we developed a finite-temperature stochastic Gross-Pitaevskii theory that can simulate evaporative cooling directly into the supersolid regime. Our simulations predict that a temperature quench provides a robust path for creating 2D supersolids in circular traps, and we confirm this experimentally by using this method to create a reproducible hexagonal 7-droplet supersolid.

In contrast, the interaction quench results in highly excited crystals that lack global phase coherence in the period following their formation. Interestingly, droplets appear sequentially rather than simultaneously, with the final crystal structure being unrelated to the roton modes that seeded the instability. This is in contrast to the situation for 1D arrays, where an interaction quench through a roton instability can smoothly connect an unmodulated BEC to the supersolid ground state.

Our finite-temperature theory is broadly applicable for future studies on topics such as formation dynamics, supersolid vortices, improved quench protocols to produce large 2D supersolids, and thermal resilience, as well as dipolar droplets in general.

―――――――――

*Corresponding author.
russell.bisset@uibk.ac.at

[1] E. P. Gross, Unified theory of interacting bosons, Phys. Rev. **106**, 161 (1957).

[2] A. Andreev and I. Lifshitz, Quantum theory of defects in crystals, Zh. Eksp. Teor. Fiz. **56**, 2057 (1969) [JETP **29**, 1107 (1969)].

[3] D. Thouless, The flow of a dense superfluid, Ann. Phys. (N.Y.) **52**, 403 (1969).

[4] G. Chester, Speculations on Bose-Einstein condensation and quantum crystals, Phys. Rev. A **2**, 256 (1970).

[5] A. J. Leggett, Can a Solid Be "Superfluid"?, Phys. Rev. Lett. **25**, 1543 (1970).

[6] M. Boninsegni and N. V. Prokof'ev, Colloquium: Supersolids: What and where are they?, Rev. Mod. Phys. **84**, 759 (2012).

[7] J.-R. Li, J. Lee, W. Huang, S. Burchesky, B. Shteynas, F. Ç. Top, A. O. Jamison, and W. Ketterle, A stripe phase with supersolid properties in spin–orbit-coupled Bose–Einstein condensates, Nature (London) **543**, 91 (2017).

[8] T. M. Bersano, J. Hou, S. Mossman, V. Gokhroo, X.-W. Luo, K. Sun, C. Zhang, and P. Engels, Experimental realization of a long-lived striped Bose-Einstein condensate induced by momentum-space hopping, Phys. Rev. A **99**, 051602(R) (2019).

[9] J. Léonard, A. Morales, P. Zupancic, T. Esslinger, and T. Donner, Supersolid formation in a quantum gas breaking a continuous translational symmetry, Nature (London) **543**, 87 (2017).

[10] L. Tanzi, E. Lucioni, F. Famà, J. Catani, A. Fioretti, C. Gabbanini, R. N. Bisset, L. Santos, and G. Modugno, Observation of a Dipolar Quantum Gas with Metastable Supersolid Properties, Phys. Rev. Lett. **122**, 130405 (2019).

[11] F. Böttcher, J.-N. Schmidt, M. Wenzel, J. Hertkorn, M. Guo, T. Langen, and T. Pfau, Transient Supersolid Properties in an Array of Dipolar Quantum Droplets, Phys. Rev. X **9**, 011051 (2019).

[12] L. Chomaz, D. Petter, P. Ilzhöfer, G. Natale, A. Trautmann, C. Politi, G. Durastante, R. M. W. van Bijnen, A. Patscheider, M. Sohmen, M. J. Mark, and F. Ferlaino, Long-Lived and Transient Supersolid Behaviors in Dipolar Quantum Gases, Phys. Rev. X **9**, 021012 (2019).

[13] M. A. Norcia, C. Politi, L. Klaus, E. Poli, M. Sohmen, M. J. Mark, R. N. Bisset, L. Santos, and F. Ferlaino, Two-dimensional supersolidity in a dipolar quantum gas, Nature (London) **596**, 357 (2021).

[14] G. Natale, R. M. W. van Bijnen, A. Patscheider, D. Petter, M. J. Mark, L. Chomaz, and F. Ferlaino, Excitation Spectrum of a Trapped Dipolar Supersolid and Its Experimental Evidence, Phys. Rev. Lett. **123**, 050402 (2019).

[15] L. Tanzi, S. Roccuzzo, E. Lucioni, F. Famà, A. Fioretti, C. Gabbanini, G. Modugno, A. Recati, and S. Stringari, Supersolid symmetry breaking from compressional oscillations in a dipolar quantum gas, Nature (London) **574**, 382 (2019).

[16] M. Guo, F. Böttcher, J. Hertkorn, J.-N. Schmidt, M. Wenzel, H. P. Büchler, T. Langen, and T. Pfau, The low-energy goldstone mode in a trapped dipolar supersolid, Nature (London) **574**, 386 (2019).

[17] A. Gallemí, S. M. Roccuzzo, S. Stringari, and A. Recati, Quantized vortices in dipolar supersolid Bose-Einstein-condensed gases, Phys. Rev. A **102**, 023322 (2020).

[18] S. M. Roccuzzo, A. Gallemí, A. Recati, and S. Stringari, Rotating a Supersolid Dipolar Gas, Phys. Rev. Lett. **124**, 045702 (2020).

[19] M. N. Tengstrand, D. Boholm, R. Sachdeva, J. Bengtsson, and S. M. Reimann, Persistent currents in toroidal dipolar supersolids, Phys. Rev. A **103**, 013313 (2021).

[20] F. Ancilotto, M. Barranco, M. Pi, and L. Reatto, Vortex properties in the extended supersolid phase of dipolar Bose-Einstein condensates, Phys. Rev. A **103**, 033314 (2021).

[21] D. Baillie and P. B. Blakie, Droplet Crystal Ground States of a Dipolar Bose Gas, Phys. Rev. Lett. **121**, 195301 (2018).

[22] Y.-C. Zhang, F. Maucher, and T. Pohl, Supersolidity Around a Critical Point in Dipolar Bose-Einstein Condensates, Phys. Rev. Lett. **123**, 015301 (2019).

[23] Y.-C. Zhang, T. Pohl, and F. Maucher, Phases of supersolids in confined dipolar Bose-Einstein condensates, Phys. Rev. A **104**, 013310 (2021).

[24] J. Hertkorn, J.-N. Schmidt, M. Guo, F. Böttcher, K. S. H. Ng, S. D. Graham, P. Uerlings, T. Langen, M. Zwierlein, and T. Pfau, Pattern formation in quantum ferrofluids: From supersolids to superglasses, Phys. Rev. Research **3**, 033125 (2021).

[25] L. Santos, G. V. Shlyapnikov, and M. Lewenstein, Roton-Maxon Spectrum and Stability of Trapped Dipolar Bose-Einstein Condensates, Phys. Rev. Lett. **90**, 250403 (2003).

[26] S. Giovanazzi and D. H. J. O'Dell, Instabilities and the roton spectrum of a quasi-1d Bose-Einstein condensed gas with dipole-dipole interactions, Eur. Phys. J. D **31**, 439 (2004).

[27] D. Petter, G. Natale, R. M. W. van Bijnen, A. Patscheider, M. J. Mark, L. Chomaz, and F. Ferlaino, Probing the Roton Excitation Spectrum of a Stable Dipolar Bose Gas, Phys. Rev. Lett. **122**, 183401 (2019).

[28] L. Chomaz, R. M. W. van Bijnen, D. Petter, G. Faraoni, S. Baier, J. H. Becher, M. J. Mark, F. Wächtler, L. Santos, and F. Ferlaino, Observation of roton mode population in a dipolar quantum gas, Nat. Phys. **14**, 442 (2018).

[29] P. B. Blakie, D. Baillie, L. Chomaz, and F. Ferlaino, Supersolidity in an elongated dipolar condensate, Phys. Rev. Research **2**, 043318 (2020).

[30] G. Biagioni, N. Antolini, A. Alaa, M. Modugno, A. Fioretti, C. Gabbanini, L. Tanzi, and G. Modugno, Dimensional Crossover in the Superfluid-Supersolid Quantum Phase Transition, Phys. Rev. X **12**, 021019 (2016).

[31] J. Hertkorn, J.-N. Schmidt, M. Guo, F. Böttcher, K. S. H. Ng, S. D. Graham, P. Uerlings, H. P. Büchler, T. Langen, M. Zwierlein, and T. Pfau, Supersolidity in Two-Dimensional Trapped Dipolar Droplet Arrays, Phys. Rev. Lett. **127**, 155301 (2021).

[32] T. Macrì, F. Maucher, F. Cinti, and T. Pohl, Elementary excitations of ultracold soft-core bosons across the superfluid-supersolid phase transition, Phys. Rev. A **87**, 061602 (R) (2013).

[33] N. Henkel, R. Nath, and T. Pohl, Three-Dimensional Roton Excitations and Supersolid Formation in Rydberg-Excited Bose-Einstein Condensates, Phys. Rev. Lett. **104**, 195302 (2010).

[34] M. Sohmen, C. Politi, L. Klaus, L. Chomaz, M. J. Mark, M. A. Norcia, and F. Ferlaino, Birth, Life, and Death of a Dipolar Supersolid, Phys. Rev. Lett. **126**, 233401 (2021).

[35] F. Wächtler and L. Santos, Quantum filaments in dipolar Bose-Einstein condensates, Phys. Rev. A **93**, 061603(R) (2016).

[36] R. N. Bisset, R. M. Wilson, D. Baillie, and P. B. Blakie, Ground-state phase diagram of a dipolar condensate with quantum fluctuations, Phys. Rev. A **94**, 033619 (2016).

[37] I. Ferrier-Barbut, H. Kadau, M. Schmitt, M. Wenzel, and T. Pfau, Observation of Quantum Droplets in a Strongly Dipolar Bose Gas, Phys. Rev. Lett. **116**, 215301 (2016).

[38] L. Chomaz, S. Baier, D. Petter, M. J. Mark, F. Wächtler, L. Santos, and F. Ferlaino, Quantum-Fluctuation-Driven Crossover from a Dilute Bose-Einstein Condensate to a Macrodroplet in a Dipolar Quantum Fluid, Phys. Rev. X **6**, 041039 (2016).

[39] T. Lahaye, C. Menotti, L. Santos, M. Lewenstein, and T. Pfau, The physics of dipolar bosonic quantum gases, Rep. Prog. Phys. **72**, 126401 (2009).

[40] See Supplemental Material http://link.aps.org/supplemental/10.1103/PhysRevLett.128.195302 for a detailed analysis of our finite-temperature theory parameters and discussion of the excitations of a two-dimensional supersolid, which includes additional Refs. [41–54].

[41] S. Ronen, D. C. E. Bortolotti, and J. L. Bohn, Bogoliubov modes of a dipolar condensate in a cylindrical trap, Phys. Rev. A **74**, 013623 (2006).

[42] A. R. P. Lima and A. Pelster, Quantum fluctuations in dipolar bose gases, Phys. Rev. A **84**, 041604(R) (2011).

[43] S. P. Cockburn and N. P. Proukakis, *Ab initio* methods for finite-temperature two-dimensional bose gases, Phys. Rev. A **86**, 033610 (2012).

[44] S. Eckel, A. Kumar, T. Jacobson, I. B. Spielman, and G. K. Campbell, A Rapidly Expanding Bose-Einstein Condensate: An Expanding Universe in the Lab, Phys. Rev. X **8**, 021021 (2018).

[45] M. Ota, F. Larcher, F. Dalfovo, L. Pitaevskii, N. P. Proukakis, and S. Stringari, Collisionless Sound in a Uniform Two-Dimensional Bose Gas, Phys. Rev. Lett. **121**, 145302 (2018).

[46] T. Bland, Q. Marolleau, P. Comaron, B. Malomed, and N. Proukakis, Persistent current formation in double-ring geometries, J. Phys. B **53**, 115301 (2020).

[47] S. De, D. L. Campbell, R. M. Price, A. Putra, B. M. Anderson, and I. B. Spielman, Quenched binary Bose-Einstein condensates: Spin-domain formation and coarsening, Phys. Rev. A **89**, 033631 (2014).

[48] C. W. Gardiner and M. J. Davis, The stochastic Gross-Pitaevskii equation:II, J. Phys. B **36**, 4731 (2003).

[49] S. J. Rooney, P. B. Blakie, and A. S. Bradley, Stochastic projected Gross-Pitaevskii equation, Phys. Rev. A **86**, 053634 (2012).

[50] R. Kubo, The fluctuation-dissipation theorem, Rep. Prog. Phys. **29**, 255 (1966).

[51] E. B. Linscott and P. B. Blakie, Thermally activated local collapse of a flattened dipolar condensate, Phys. Rev. A **90**, 053605 (2014).

[52] D. Petter, A. Patscheider, G. Natale, M. J. Mark, M. A. Baranov, R. van Bijnen, S. M. Roccuzzo, A. Recati, B. Blakie, D. Baillie, L. Chomaz, and F. Ferlaino, Bragg scattering of an ultracold dipolar gas across the phase transition from Bose-Einstein condensate to supersolid in the free-particle regime, Phys. Rev. A **104**, L011302 (2021).

[53] E. Poli, T. Bland, C. Politi, L. Klaus, M. A. Norcia, F. Ferlaino, R. N. Bisset, and L. Santos, Maintaining

supersolidity in one and two dimensions, Phys. Rev. A **104,** 063307 (2021).

[54] J. Goldstone, Field theories with superconductor solutions, Nuovo Cimento (1955–1965) **19,** 154 (1961).

[55] This method has been applied previously in a quasi-two-dimensional setting without quantum fluctuations [51].

[56] P. Blakie, A. Bradley, M. Davis, R. Ballagh, and C. Gardiner, Dynamics and statistical mechanics of ultra-cold Bose gases using c-field techniques, Adv. Phys. **57,** 363 (2008).

[57] S. J. Rooney, T. W. Neely, B. P. Anderson, and A. S. Bradley, Persistent-current formation in a high-temperature Bose-Einstein condensate: An experimental test for classical-field theory, Phys. Rev. A **88,** 063620 (2013).

[58] R. G. McDonald, P. S. Barnett, F. Atayee, and A. S. Bradley, Dynamics of hot Bose-Einstein condensates: Stochastic ehrenfest relations for number and energy damping, SciPost Phys. **8,** 029 (2020).

[59] Our initial state is $\psi(\mathbf{r}, 0) = \psi_0(\mathbf{r}) + \sum_n' \alpha_n \phi_n(\mathbf{r})$, where ϕ_n are the single-particle states, α_n is a complex Gaussian random variable with $\langle |\alpha_n|^2 \rangle = (e^{\epsilon_n/k_B T} - 1)^{-1} + \frac{1}{2}$, and the sum is restricted to modes with $\epsilon_n \leq 2k_B T$, with $T = 30$ nK.

[60] C. N. Weiler, T. W. Neely, D. R. Scherer, A. S. Bradley, M. J. Davis, and B. P. Anderson, Spontaneous vortices in the formation of Bose-Einstein condensates, Nature (London) **455,** 948 (2008).

[61] I.-K. Liu, S. Donadello, G. Lamporesi, G. Ferrari, S.-C. Gou, F. Dalfovo, and N. Proukakis, Dynamical equilibration across a quenched phase transition in a trapped quantum gas, Commun. Phys. **1,** 1 (2018).

[62] F. Maucher, T. Pohl, S. Skupin, and W. Krolikowski, Self-Organization of Light in Optical Media with Competing Nonlinearities, Phys. Rev. Lett. **116,** 163902 (2016).

[63] F. Zambelli, L. Pitaevskii, D. M. Stamper-Kurn, and S. Stringari, Dynamic structure factor and momentum distribution of a trapped bose gas, Phys. Rev. A **61,** 063608 (2000).

[64] P. B. Blakie, R. J. Ballagh, and C. W. Gardiner, Theory of coherent bragg spectroscopy of a trapped Bose-Einstein condensate, Phys. Rev. A **65,** 033602 (2002).

[65] P. B. Blakie, D. Baillie, and R. N. Bisset, Roton spectroscopy in a harmonically trapped dipolar Bose-Einstein condensate, Phys. Rev. A **86,** 021604(R) (2012).

[66] S. Ronen, D. C. E. Bortolotti, and J. L. Bohn, Radial and Angular Rotons in Trapped Dipolar Gases, Phys. Rev. Lett. **98,** 030406 (2007).

[67] M. Jona-Lasinio, K. Łakomy, and L. Santos, Roton confinement in trapped dipolar Bose-Einstein condensates, Phys. Rev. A **88,** 013619 (2013).

[68] R. N. Bisset, D. Baillie, and P. B. Blakie, Roton excitations in a trapped dipolar Bose-Einstein condensate, Phys. Rev. A **88,** 043606 (2013).

[69] We measure phase coherence as $C^p = 1 - (2/\pi) \int_C dx dy |\psi(x,y)|^2 |\theta(x,y) - \beta| / \int_C dx dy |\psi(x,y)|^2$, where $\theta(x,y)$ is the phase of $\psi(x,y)$ in the $z = 0$ plane and β is a fitting parameter to maximize C^p at each time. The integration region C encompasses the droplets.

[70] Relative to the crystal maturation time, each quench ramp ended at 5, -13, and -90 ms for the linear interaction quench, pancake interaction quench, and pancake temperature quench, respectively. Note that evaporative cooling continues after the $\{\mu, T\}$ quench ends, taking approximately a further 100 ms until the classical field modes have equilibrated with the high-energy modes [40].

[71] The density overlap is given by $C^d = \int d^3 \mathbf{x} n(\mathbf{x} - \mathbf{x}_0, \phi_0, t) n_{\mathrm{GS}} / \int d^3 \mathbf{x} n_{\mathrm{GS}}^2$, with the ground state density and time-dependent density, respectively, normalized as $\int d^3 \mathbf{x} n_{\mathrm{GS}} = \int d^3 \mathbf{x} n(\mathbf{x} - \mathbf{x}_0, \phi_0, t) = 1$. The optimization parameters $\mathbf{x}_0$ and ϕ_0 are translations and a rotation, respectively, applied to the wave function to maximize C^d.

Supplemental material: Two-dimensional supersolid formation in dipolar condensates

T. Bland,[1] E. Poli,[2] C. Politi,[1,2] L. Klaus,[1,2] M. A. Norcia,[1] F. Ferlaino,[1,2] L. Santos,[3] and R. N. Bisset[2]

[1] Institut für Quantenoptik und Quanteninformation,
Österreichische Akademie der Wissenschaften, Innsbruck, Austria
[2] Institut für Experimentalphysik, Universität Innsbruck, Austria
[3] Institut für Theoretische Physik, Leibniz Universität Hannover, Germany
(Dated: April 13, 2022)

FORMALISM

We utilize dynamic and ground state calculations of the extended Gross-Pitaevskii equation (eGPE), given by $i\hbar\psi_t = \mathcal{L}[\psi]\psi$, where the eGPE operator is [1–4]

$$\mathcal{L}[\psi] = -\frac{\hbar^2\nabla^2}{2m} + \frac{1}{2}m\left(\omega_x^2 x^2 + \omega_y^2 y^2 + \omega_z^2 z^2\right) \quad \text{(S1)}$$
$$+ \int d^3\mathbf{x}' \, U(\mathbf{x} - \mathbf{x}')|\psi(\mathbf{x}', t)|^2 + \gamma_{\text{QF}}|\psi(\mathbf{x}, t)|^3 \, ,$$

m is the mass and $\omega_{x,y,z} = 2\pi f_{x,y,z}$ are the external trapping frequencies. Two-body contact interactions and the long-ranged, anisotropic dipole-dipole interactions are described by the pseudo-potential

$$U(\mathbf{r}) = \frac{4\pi\hbar^2 a_s}{m}\delta(\mathbf{r}) + \frac{3\hbar^2 a_{dd}}{m}\frac{1 - 3\cos^2\theta}{r^3} \, , \quad \text{(S2)}$$

respectively, with θ being the angle between the polarization axis (z axis) and the vector joining two particles. This is characterized by s-wave scattering length a_s and dipole length $a_{dd} = \mu_0\mu_m^2 m/12\pi\hbar^2$, with magnetic moment μ_m. To find the ground state we employ a conjugate-gradients technique minimizing the corresponding energy functional [5]. The last term appearing in Eq. (S1) represents quantum fluctuations in the form of a dipolar Lee-Huang-Yang correction [6], $\gamma_{\text{QF}} = \frac{128\hbar^2}{3m}\sqrt{\pi a_s^5}\,\text{Re}\{\mathcal{Q}_5(\varepsilon_{dd})\}$, where $\mathcal{Q}_5(\varepsilon_{dd}) = \int_0^1 du\,(1 - \varepsilon_{dd} + 3u^2\varepsilon_{dd})^{5/2}$ is the auxiliary function, which can be solved analytically, and $\varepsilon_{dd} = a_{dd}/a_s$.

Primarily, we use the eGPE to simulate the formation dynamics of a supersolid through an interaction quench of the scattering length, constructing an initial state by adding non-interacting noise to an unmodulated BEC ground state (far from the roton instability). Thus, our initial state is $\psi(\mathbf{r}, 0) = \psi_0(\mathbf{r}) + \sum_n' \alpha_n\phi_n(\mathbf{r})$, where ϕ_n are the single-particle states, α_n is a complex Gaussian random variable with $\langle|\alpha_n|^2\rangle = (e^{\epsilon_n/k_B T} - 1)^{-1} + \frac{1}{2}$ with temperature T and the sum is restricted to modes with $\epsilon_n \leq 2k_B T$. On average, this adds about 1000 atoms when $T = 30$nK.

CHOICE OF γ FOR STOCHASTIC EXTENDED GPE THEORY (EQ. 1 OF MAIN TEXT)

Stochastic Gross-Pitaevskii equations have been benchmarked against numerous Bose gas experiments in various geometries [7–13], including Bose-Bose mixtures [14]. These comparisons to experimental data include direct modeling of the evaporative cooling process [7, 8]. In these works, γ is approximated by fitting the condensate atom number growth rate to experimental observations. However, there is also an approximate analytic solution appropriate for near-equilibrium solutions that depends on the chemical potential, energy cut-off, temperature, and interaction strength [15]. One comparison found γ extracted from condensate growth data is an order of magnitude larger than the analytic approximation [8]. The choice of γ does not affect the equilibrium properties of the system [16] (due to the fluctuation-dissipation theorem [17, 18]), however it affects many observables during equilibration.

To the best of our knowledge there does not exist any analytic prediction for γ for the dipolar system [18]. We approximate γ based on direct experiment-theory comparisons with the condensate growth rate in Ref. [19]. For that case we have the relevant experimental data available. There, the supersolid formation was studied in detail for a dysprosium supersolid in a cigar-shaped geometry, and a value of $\gamma = 0.0075$ was found to give quantitatively similar growth behavior as observed experimentally. Here, for a qualitatively similar regime [20] we initially assume the same value.

In Fig. S1 we investigate the γ dependency on the evaporative cooling protocol presented in the main text, namely a ^{164}Dy gas in a pancake trap with $(f_x, f_y, f_z) = (33, 33, 167)$Hz and $a_s = 88a_0$. Further details are given in the main text. We consider both half and double the initial value, i.e. $\gamma = (0.00375, 0.0075, 0.015)$. Interestingly, several observables are sensitive to the choice of γ. This includes: atom number versus time, onset time of global phase coherence versus onset time of crystal structure, and the number of free vortices trapped within the crystal. For our simulations we calculate the phase coherence C^p and density overlap C^d. Despite the c-field atom number increasing faster with larger γ, the growth of phase coherence does not appear as clearly dependent on γ. This is possibly due to the number of vortices gen-
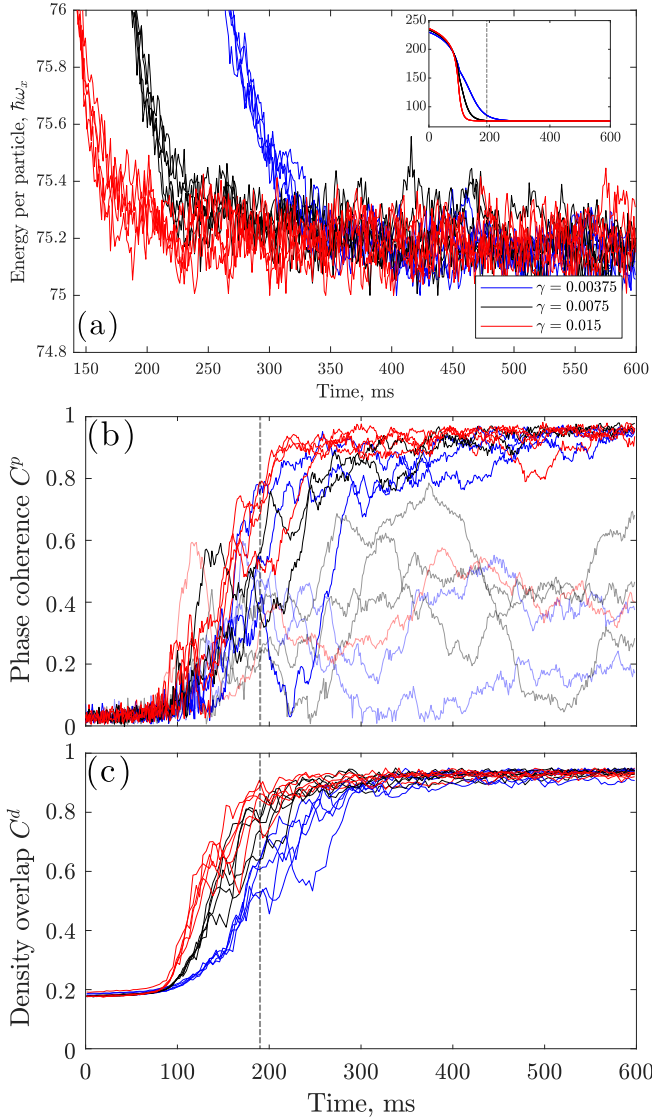
FIG. S1. Effect of varying γ. Five simulations are shown with the same color for each γ. (a) Energy per particle versus time. The average final value is independent of γ, as expected. Inset shows the same data over a longer time range, where $t = 0$ corresponds to the beginning of the 100ms temperature quench. (b) Phase coherence for all data. Curves with a lower opacity correspond to simulations with isolated vortices. (c) Density overlap with the ground state 19 droplet supersolid. In all plots the dashed vertical line indicates $t = 0$ in Fig. 2 of the main text.

erated through the quench, which have been shown to appear more readily with increasing γ, although there is also evidence they are damped quicker too [7]. Curves for simulations with a long-lived single vortex are shown with a lower opacity in Fig. S1(b), as this greatly influences C^p, and these simulations are not included in the averages shown in the main paper. It is also worth noting that we do not see free vortices after the interaction

quenches. Even in the presence of a free vortex the final state can still be considered as a coherent supersolid, with $C^d \sim 1$, however $C^p < 1$. Future improvements to this measure could involve finding the vortex centre and multiplying the phase by the opposite circulation. This is not easy however due to the nonlinear azimuthal phase profile of a vortex in a supersolid [21, 22].

The effect of varying γ is most obvious in the overlap between the simulation density and ground state density, C^d [Fig. S1(c)]. Larger γ forces the c-field atom number, and hence density, to rapidly increase, forcing the fast production of droplets. We believe that comparing a spectrum of observables such as these will provide important benchmarks to fine tune the simulations, and that this will also provide an important test in the future for the development of analytic theories that can predict γ. As supersolid production in 2D becomes more routine, direct comparison between the condensate atom number and droplet number growth rates in particular will become crucial in determining the appropriate choice of γ.

It is worth noting that even if the supersolid formation time was a few 100ms longer than the data presented here, the whole process would still be faster than evaporatively cooling into the BEC state, quenching the interactions and then waiting for the phase coherence to reappear. In this latter scenario, significant three-body losses play a negative role. Previous works in 1D have maximized phase coherence by increasing the final a_s, and hence increasing the superfluid connection between droplets [23], and decreasing the droplet peak density. However, the droplet number is strongly dependent on a_s, and we find that such a strategy significantly decreases the number of droplets.

THE ROLE OF ENERGY DURING SUPERSOLID FORMATION

It is instructive to investigate the role of energy during the formation of 2D droplet arrays, via both interaction quenches and the temperature quenches. In Fig. S2 (a), we show the energy versus time for the five interaction quench simulations considered in Fig. 1(a) of the main text. We have also marked the energy of the ground state before the interaction quench ($E_{\mathrm{GS}}^{\mathrm{BEC}}$), and the energy of the ground state following the interaction quench ($E_{\mathrm{GS}}^{\mathrm{SS}}$), with the superscript indicating that the ground state is initially in the BEC phase, then later in the supersolid phase. An estimate for the energy added by crossing the phase transition can be evaluated as $[E(t_{\mathrm{final}}) - E_{\mathrm{GS}}^{\mathrm{SS}}] - [E(t_{\mathrm{initial}}) - E_{\mathrm{GS}}^{\mathrm{BEC}}] \approx 0.35\hbar\omega_x$. Note that $E(t_{\mathrm{initial}}) - E_{\mathrm{GS}}^{\mathrm{BEC}}$ does not equal zero due to the random noise added to the initial state.

It is interesting at this point to compare the final energies of the eGPE simulations in Fig. S2 (a) with the final energies of the c-field simulations following the evapo-
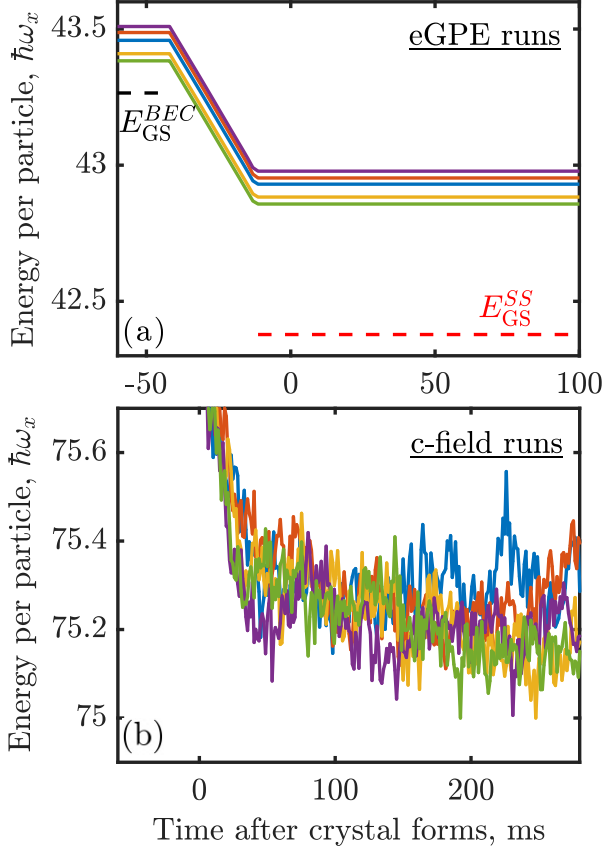
FIG. S2. Energy versus time for the pancake quench simulation runs considered in Fig. 2 of the main text. (a) Interaction quenches simulated using the eGPE with $N \approx 2.1 \times 10^5$. Dashed lines show the ground state energy for the initial parameters, $E_{\mathrm{GS}}^{\mathrm{BEC}}$, and the final paremeters corresponding to the target supersolid, $E_{\mathrm{GS}}^{\mathrm{SS}}$. (b) Temperature quenches simulated with the SeGPE. All curves are with fixed $\gamma = 0.0075$. For both subplots $f_{x,y,z} = (33, 33, 167)$ Hz.

the 7-droplet supersolid rather than the 19-droplet one, such low-energy Goldstone modes are a general feature of dipolar supersolids [24, 25]. Since these modes inherently cause both phase and crystal excitations, they directly act to disrupt the supersolid. Furthermore, we also see some vortex pairs after the interaction quench, and these also play a role. Interestingly, even in the interaction-quench simulations, a supersolid is obtained in the long-time limit (although too long to be useful for current experiments due to lifetime limitations), even though the total energy is conserved, thanks to a damping of these phase and crystal excitations.

SUPERSOLID EXCITATIONS

We investigate the 7-droplet hexagon supersolid, the same configuration as shown in Fig. 3 of the main text, using the extended Gross-Pitaevskii equation (eGPE), focusing here on its excitations. We perform a Bogoliubov-de Gennes linearization and present results in the form of the dynamic structure factor,

$$S(\mathbf{k}, \omega) = \sum_l \left| \int d^3 \mathbf{x} \left[u_l^*(\mathbf{r}) + v_l^*(\mathbf{x}) \right] e^{i\mathbf{k} \cdot \mathbf{x}} \psi_0(\mathbf{x}) \right|^2 \delta(\omega - \omega_l),$$
(S3)

Here, ψ_0 is the ground state wavefunction normalized to unity, i.e. $\int d^3\mathbf{x} |\psi_0(\mathbf{x})|^2 = 1$, and $\{u_l(\mathbf{x}), v_l(\mathbf{x})\}$ are the quasiparticle excitations with energy ω_l [26, 27]. The dynamic structure factor along two orthogonal directions is displayed in Fig. S3. Note, the asymmetry along k_x and k_y is due to the triangular configuration of the crystal, which can be seen clearly in Fig. S4(b).

To explore the role of dimensionality, Fig. S4 compares the static structure factor, $S(\mathbf{k}) = \int d\omega \, S(\mathbf{k}, \omega)$, for both linear and 7-droplet hexagon supersolids. These results are converged within the dashed ellipses, set by ensuring that the f-sum rule, $\int d\omega \, \omega S(k, \omega) = \hbar^2 k^2 / 2m$, is satisfied, and should be ignored outside. Convergence is limited by the number of BdG modes, for which we use 512 modes for both cases. In order to make a fair comparison between a 1D and 2D supersolids we choose to approximately match the average 2D trap density by fixing $\varrho = N f_x f_y$ [28]. As previously reported, the structure factor for the linear case [Fig. S4(a)] has peaks corresponding to the average inter-droplet spacing ($2.67\mu m$), $k_x l_z \approx 1.43$, and subsequent peaks at integer multiples of this [24]. We find that the dominant contributing modes to the structure factor peaks are low energy out-of-phase Goldstone modes [24, 25, 29], where the superfluid current and crystal oscillate out-of-phase with one another. Note that for possible comparison with experiments our spectrum in Fig. S4 was energy broadened with a Gaussian of width $\sigma = 0.008 \, \hbar\omega_z$, note that Fig. 1(b) of the main text was similarly broadened by $\sigma = 0.004 \, \hbar\omega_z$.

rative cooling quench, which are shown in Fig. S2 (b), which differ by more than $30\hbar\omega_x$. From such a comparison we can deduce that the important factor for disrupting supersolid formation following an interacting quench is not so much the total energy injected into the system by crossing the first-order phase transition [in Fig. S2 (a)] but, rather, which modes become excited. This large disparity in energy, however, tells us that at much longer time scales than shown here, the eGPE states may settle down to a better quality supersolid than the SeGPE [see e.g. Fig. 2 of the main text], but this could be on the order of seconds, much larger than the supersolid life time.

From our dynamic structure factor calculations shown in Fig. S3 (which will be discussed shortly), one can see that the out-of-phase Goldstone modes (the low-energy modes at finite momentum that show up as red ovals) are particularly vulnerable to excitation by the interaction quench. Note that although this figure is for
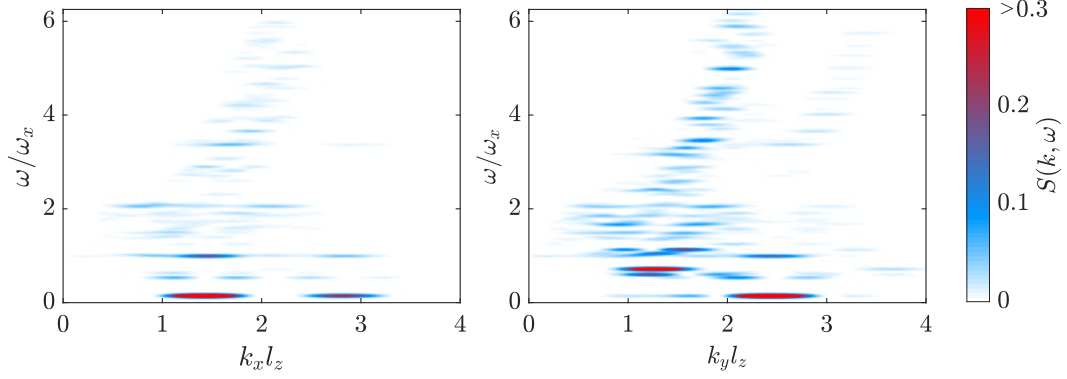
FIG. S3. Dynamic structure factor (DSF), Eq. (S3), normalized to peak value, in energy-momentum space for a ^{164}Dy 7-droplet hexagon supersolid. Left: DSF along k_x with $k_y = k_z = 0$. Right: DSF along k_y with $k_x = k_z = 0$. Parameters: $a_s = 90a_0$, $f_{x,y,z} = (52.83, 52.83, 167)$ Hz, $N = 9.5 \times 10^4$.
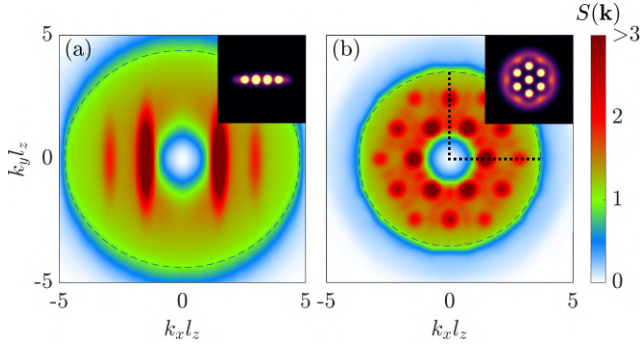

FIG. S4. Static structure factors for (a) linear and (b) 7-droplet hexagon supersolids. Convergence is achieved within the dashed ellipses (see text). Dotted lines in (b) correspond to the trajectories shown in Fig. S3, integrated over energy. Parameters for linear chain: $a_s = 90a_0$, $f_{x,y,z} = (52.83, 130, 167)$ Hz, $N = 4 \times 10^4$. For 2D crystal: $a_s = 90a_0$, $f_{x,y,z} = (52.83, 52.83, 167)$ Hz, $N = 9.5 \times 10^4$.

For the 2D supersolid, Fig. S4(b) displays peaks situated at $k_\rho l_z \approx 1.43$ every $60°$ azimuthally, where $k_\rho = \sqrt{k_x^2 + k_y^2}$. These peaks reflect the hexagonal structure of the ground state, however this value does *not* directly reflect the inter-droplet spacing (3.05μm, which would correspond to $k_\rho l_z \approx 1.25$), but rather the spacing of lattice planes between droplets. Crucially, the six inner momentum peaks are rotated compared to the droplet crystal, analogous to what we observed experimentally in the TOF images. Similar to the 1D chain, we find that the out-of-phase Goldstone modes–a manifestation of superfluidity–contribute to the majority of the peak signal.

[1] F. Wächtler and L. Santos, Quantum filaments in dipolar bose-einstein condensates, Phys. Rev. A **93**, 061603 (2016).

[2] R. N. Bisset, R. M. Wilson, D. Baillie, and P. B. Blakie, Ground-state phase diagram of a dipolar condensate with quantum fluctuations, Phys. Rev. A **94**, 033619 (2016).

[3] I. Ferrier-Barbut, H. Kadau, M. Schmitt, M. Wenzel, and T. Pfau, Observation of quantum droplets in a strongly dipolar bose gas, Phys. Rev. Lett. **116**, 215301 (2016).

[4] L. Chomaz, S. Baier, D. Petter, M. J. Mark, F. Wächtler, L. Santos, and F. Ferlaino, Quantum-fluctuation-driven crossover from a dilute bose-einstein condensate to a macrodroplet in a dipolar quantum fluid, Phys. Rev. X **6**, 041039 (2016).

[5] S. Ronen, D. C. E. Bortolotti, and J. L. Bohn, Bogoliubov modes of a dipolar condensate in a cylindrical trap, Phys. Rev. A **74**, 013623 (2006).

[6] A. R. P. Lima and A. Pelster, Quantum fluctuations in dipolar bose gases, Phys. Rev. A **84**, 041604 (2011).

[7] C. N. Weiler, T. W. Neely, D. R. Scherer, A. S. Bradley, M. J. Davis, and B. P. Anderson, Spontaneous vortices in the formation of Bose-Einstein condensates, Nature **455**, 948 (2004).

[8] I.-K. Liu, S. Donadello, G. Lamporesi, G. Ferrari, S.-C. Gou, F. Dalfovo, and N. Proukakis, Dynamical equilibration across a quenched phase transition in a trapped quantum gas, Communications Physics **1**, 1 (2018).

[9] S. Cockburn and N. Proukakis, Ab initio methods for finite-temperature two-dimensional bose gases, Physical Review A **86**, 033610 (2012).

[10] S. J. Rooney, T. W. Neely, B. P. Anderson, and A. S. Bradley, Persistent-current formation in a high-temperature bose-einstein condensate: An experimental test for classical-field theory, Phys. Rev. A **88**, 063620 (2013).

[11] S. Eckel, A. Kumar, T. Jacobson, I. B. Spielman, and G. K. Campbell, A rapidly expanding bose-einstein condensate: an expanding universe in the lab, Physical Review X **8**, 021021 (2018).

[12] M. Ota, F. Larcher, F. Dalfovo, L. Pitaevskii, N. P.

Proukakis, and S. Stringari, Collisionless sound in a uniform two-dimensional bose gas, Physical review letters **121**, 145302 (2018).

[13] T. Bland, Q. Marolleau, P. Comaron, B. Malomed, and N. Proukakis, Persistent current formation in double-ring geometries, Journal of Physics B: Atomic, Molecular and Optical Physics **53**, 115301 (2020).

[14] S. De, D. Campbell, R. Price, A. Putra, B. M. Anderson, and I. Spielman, Quenched binary bose-einstein condensates: Spin-domain formation and coarsening, Physical Review A **89**, 033631 (2014).

[15] C. W. Gardiner and M. J. Davis, The stochastic Gross-Pitaevskii equation:II, J Phys. B **36**, 4731 (2003).

[16] S. Rooney, P. Blakie, and A. Bradley, Stochastic projected gross-pitaevskii equation, Physical Review A **86**, 053634 (2012).

[17] R. Kubo, The fluctuation-dissipation theorem, Reports on progress in physics **29**, 255 (1966).

[18] E. B. Linscott and P. B. Blakie, Thermally activated local collapse of a flattened dipolar condensate, Phys. Rev. A **90**, 053605 (2014).

[19] M. Sohmen, C. Politi, L. Klaus, L. Chomaz, M. J. Mark, M. A. Norcia, and F. Ferlaino, Birth, life, and death of a dipolar supersolid, Phys. Rev. Lett. **126**, 233401 (2021).

[20] Despite the different trap geometries, $(f_x, f_y, f_z) = (36, 88, 141)$Hz in Ref. [19] compared to $(f_x, f_y, f_z) = (33, 33, 167)$Hz, the peak densities are similar $n_{\text{peak}} = 1.6 \times 10^{21} \mu\text{m}^{-3}$ compared to $n_{\text{peak}} = 1.8 \times 10^{21} \mu\text{m}^{-3}$ and thus will have similar quality supersolids.

[21] F. Ancilotto, M. Barranco, M. Pi, and L. Reatto, Vortex properties in the extended supersolid phase of dipolar bose-einstein condensates, Physical Review A **103**, 033314 (2021).

[22] S. Roccuzzo, A. Gallemí, A. Recati, and S. Stringari, Rotating a supersolid dipolar gas, Physical review letters **124**, 045702 (2020).

[23] D. Petter, A. Patscheider, G. Natale, M. J. Mark, M. A. Baranov, R. van Bijnen, S. M. Roccuzzo, A. Recati, B. Blakie, D. Baillie, L. Chomaz, and F. Ferlaino, Bragg scattering of an ultracold dipolar gas across the phase transition from bose-einstein condensate to supersolid in the free-particle regime, Phys. Rev. A **104**, L011302 (2021).

[24] G. Natale, R. van Bijnen, A. Patscheider, D. Petter, M. Mark, L. Chomaz, and F. Ferlaino, Excitation spectrum of a trapped dipolar supersolid and its experimental evidence, Physical review letters **123**, 050402 (2019).

[25] M. Guo, F. Böttcher, J. Hertkorn, J.-N. Schmidt, M. Wenzel, H. P. Büchler, T. Langen, and T. Pfau, The low-energy goldstone mode in a trapped dipolar supersolid, Nature **574**, 386 (2019).

[26] F. Zambelli, L. Pitaevskii, D. M. Stamper-Kurn, and S. Stringari, Dynamic structure factor and momentum distribution of a trapped bose gas, Phys. Rev. A **61**, 063608 (2000).

[27] P. Blakie, R. Ballagh, and C. Gardiner, Theory of coherent bragg spectroscopy of a trapped bose-einstein condensate, Physical Review A **65**, 033602 (2002).

[28] E. Poli, T. Bland, C. Politi, L. Klaus, M. A. Norcia, F. Ferlaino, R. N. Bisset, and L. Santos, Maintaining supersolidity in one and two dimensions, Phys. Rev. A **104**, 063307 (2021).

[29] J. Goldstone, Field theories with superconductor solutions, Il Nuovo Cimento (1955-1965) **19**, 154 (1961).
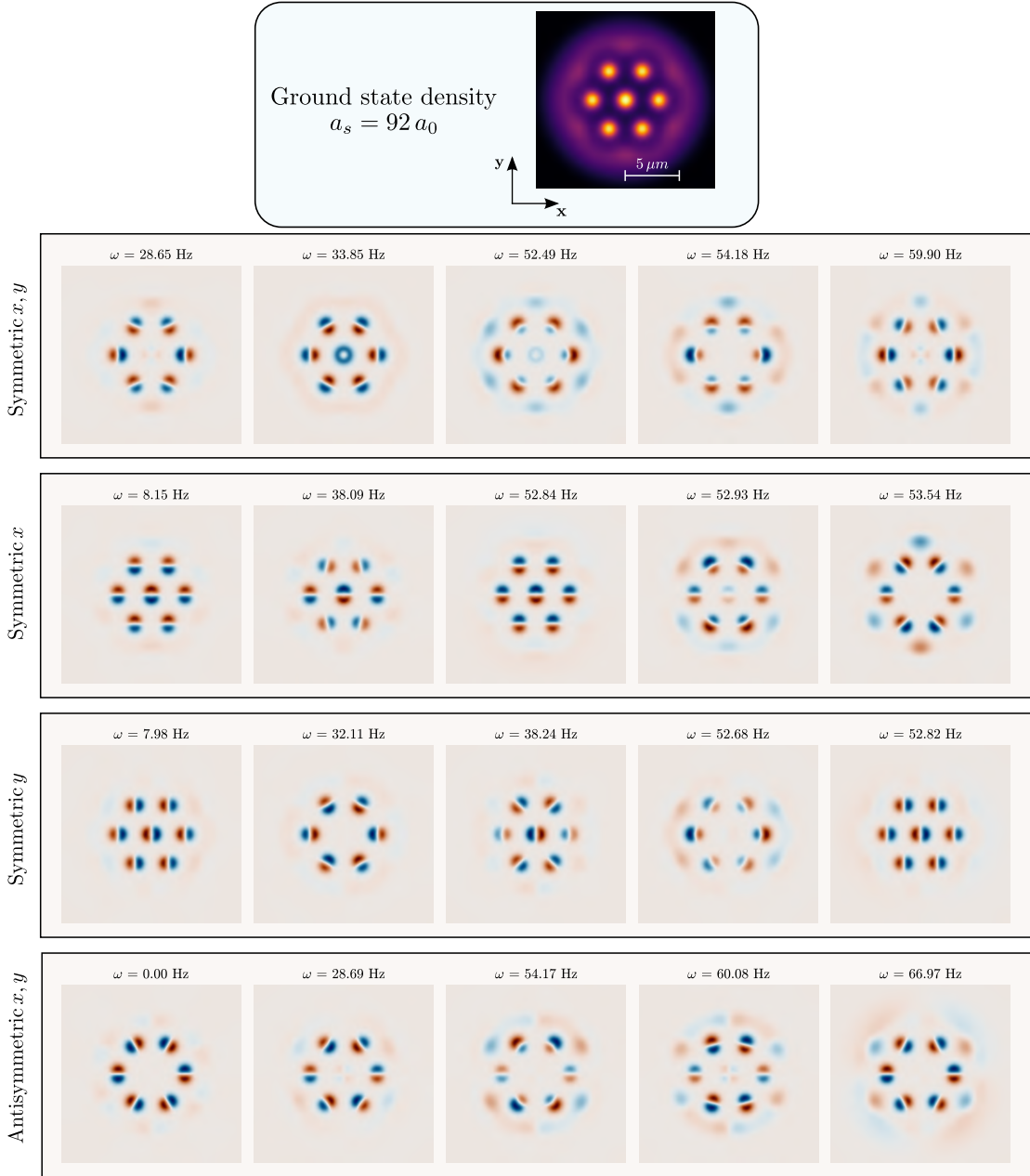
2.7. Additional knowledge: Low-energy modes

Figure 2.5.: Elementary excitations from Bogoliubov-de Gennes equations for a 2D supersolid. Upper panel shows the ground state density of the unperturbed state, lower panels show the density perturbation defined in Eq. (69). For each symmetry manifold, the five lowest energy modes are visualized through the positive (red) and negative (blue) density variation. Parameters: trap frequencies $\omega = 2\pi \times (52.8, 52.8, 167)$ Hz, atom number N = 95000, $a_s = 90\,a_0$, dipoles polarized along z-axis.

The study of the elementary excitations for a 2D supersolid through BdG equations presented in Secs. 2.5 and 2.6 (Refs. [150, 160]) required a lot of effort. As discussed in Chapter 1, the convergence of BdG modes is highly sensitive to the resolution of the
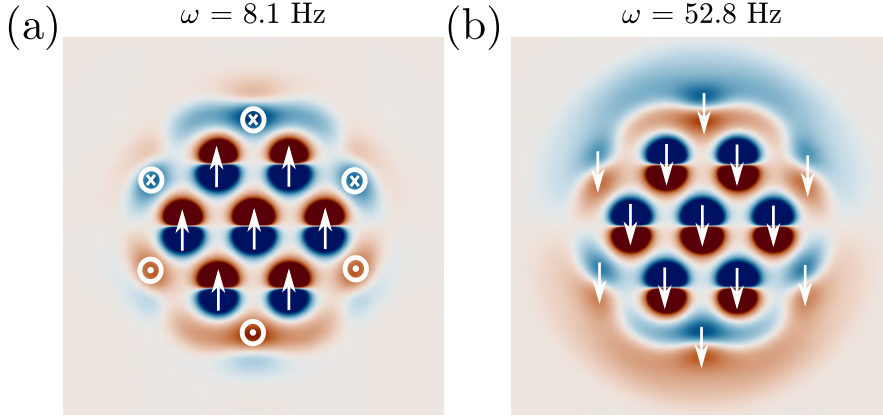
Figure 2.6.: (a) (Quasi) Goldstone mode vs. (b) dipole mode in a 2D dipolar supersolid. The density variations are plotted with a very saturated colormap to highlight the motion of the superfluid halo. The arrows are centred in correspondence of the density peaks. Parameters: trap frequencies $\omega = 2\pi \times (52.8, 52.8, 167)$ Hz, atom number N = 95000, $a_s = 90\, a_0$, dipoles polarized along z-axis.

ground state. This challenge is further amplified in states with 2D periodic density modulations, where even slight asymmetries can hinder the convergence of the modes. In the following, we provide additional details on the modes obtained from the BdG spectrum.

Figure 2.5 shows some exemplar modes obtained from the solution of the BdG equations for a 2D supersolid made of 7 droplets. Modes are visualized through the density perturbation defined in Eq. (69) and they are divided according to their symmetry manifold. The corresponding dynamic structure factor is shown in Ref. [150] in Sec. 2.6. The lowest-energy mode symmetric with respect to x and y is a quadrupole mode ($\omega = 28.65$ Hz), which describes the motion of droplets stretching the system in one direction while squeezing in the other. The fourth and fifth mode of the same row ($\omega = 54.18$ Hz, $\omega = 59.90$ Hz) have a similar quadrupolar character, while the second and third mode resemble a breathing mode ($\omega = 33.85$ Hz, $\omega = 52.49$ Hz).

In the next two symmetry manifolds, modes are either symmetric with respect to $x-$axis or $y-$axis. In this case, modes belonging to these two groups are not degenerate because the ground state distribution is not isotropic. In both manifolds, the dipole mode appear at the frequency of the radial harmonic trap ($\omega = 52.8$ Hz) but more attention should be given to the two lowest energy modes ($\omega = 8.15$ Hz, $\omega = 7.98$ Hz). They seem to have many similarities to the dipole mode, since all the droplets are moving in the same direction. But there is a fundamental difference: the motion of the droplets is created by the superfluid background moving in the opposite direction. The difference is subtle but visible from the very saturated density perturbation in Fig. 2.6: the peaks of the superfluid background are growing or decreasing and not moving in the same direction of the droplets. This is highlighted by the white arrows in Fig. 2.6(a) and (b), indicating the motion of the density peaks (either droplets or peaks in the superfluid background). The vector field notation $\odot$ and $\otimes$ is used to indicate growing and decreasing density peaks, respectively. Therefore, the mode pictured in Fig. 2.6(a) describes an out-of-phase oscillation of the crystal structure and the superfluid background and can be classified as the finite-size version of a *Goldstone mode*, well defined

in an infinite system. This mode has been observed in a 1D supersolid [151]. The energy of this mode is very low and it responds quite easily to external perturbations, since the dynamic structure factor is very enhanced in correspondence of this mode.

Finally, it is worth focusing on the zero-energy mode in the antisymmetric manifold: this is a rotational mode that shows that any other angular orientation of the droplet crystal would be energetically equivalent to the one obtained from the simulation. This happens because the trap is cylindrically symmetric. In contrast, for a supersolid confined in an asymmetric trap this mode has finite energy [162].

Exploring solid properties: elastic parameters and shear modulus

The excitation spectrum of a system reveals valuable insights into its fundamental nature. For a supersolid, this spectrum is of particular interest because it contains the key features of both solid and superfluid phases. In this chapter, we investigate the elastic parameters of a 2D supersolid, focusing on their role in shaping the low-energy spectrum. For simplicity, we consider an infinite system where these parameters are well-defined.

The elastic parameters are derived using a hydrodynamic approach based on Lagrangian formalism. To illustrate their properties and demonstrate the broad applicability of the hydrodynamic theory to 2D supersolids, we present results for two distinct systems. The first system is a 2D soft-core model [163, 164]. The second system consists of an infinite dipolar Bose-Einstein condensate, confined in the $z-$direction (the direction of the dipole polarization) and free in the perpendicular plane. In both cases, the elastic parameters govern the speeds of sound for longitudinal, transverse, and phase modes. A particularly unique parameter is the shear modulus, which is exclusive to systems with a 2D crystalline structure. This modulus plays a central role in characterizing the transverse density branch of the excitation spectrum.

This project has been developed during a research stay at the University of Otago in New Zealand, within the group led by Prof. P. B. Blakie, thanks to the funding provided by DK-ALM doctoral school in Innsbruck.

3.1. Soft-core models

We start introducing the soft-core models for 2D supersolids. A many-body system made of bosonic atoms interacting via a soft-core potential is one of the easiest model to produce a supersolid [128, 129]. The phase transition from an unmodulated phase to a state where atoms are clustered in a periodic structure is very well known also in other fields, for example in the context of colloids and macromolecules [165].

Soft-core interactions include every potential that is finite in the limit $r \to 0$, preventing particles from experiencing infinite repulsion when they approach each other. The
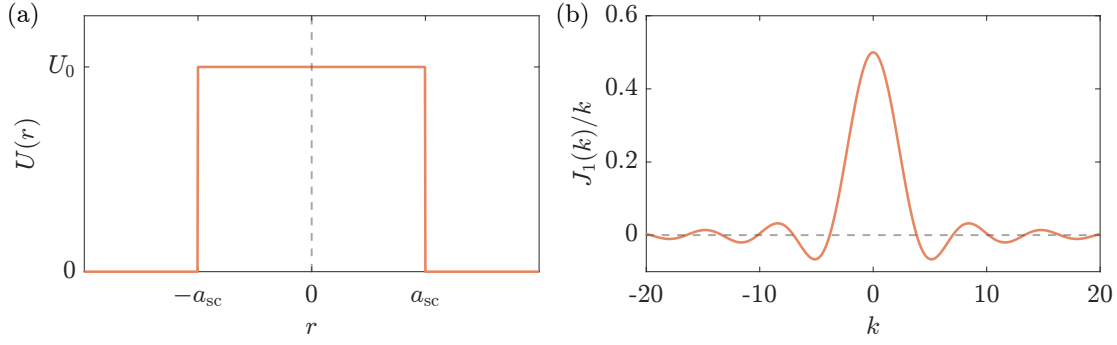
Figure 3.1.: Soft-core model. (a) Illustration of a simple soft core potential described in Eq. (1) and (b) plot of the behaviour of $\tilde{U}(\mathbf{k})$ for a 2D uniform BEC interacting with a soft-core potential.

easiest form of this potential is

$$U(\mathbf{r}) = U_0 \Theta(a_{\mathrm{sc}} - |\mathbf{r}|) , \qquad (1)$$

shown in Fig. 3.1(a). Here, U_0 is the potential strength, a_{sc} is the soft-core radius and Θ is the Heaviside function. Within this model, two particles interact only if their distance is smaller than a_{sc}. More complex expressions for soft-core potentials have been used in literature, like a Van der Waals tail $U(\mathbf{r}) = \frac{1}{1+r^6}$ [128] or dipolar-like behaviour $U(\mathbf{r}) = \frac{1}{1+r^3}$ [129, 130], but qualitatively the physics is the same as the one predicted by Eq. (1).

Let us consider a purely 2D infinite system described by the wave function ψ. The energy functional has a very simple form

$$E = \int d^2\mathbf{r}\, \psi(\mathbf{r})^* \left(-\frac{\hbar^2}{2m}\nabla^2 + \frac{1}{2}\int d^2\mathbf{x}'\, U\left(\mathbf{r} - \mathbf{r}'\right) \left|\psi\left(\mathbf{r}'\right)\right|^2 \right) \psi(\mathbf{r}) . \qquad (2)$$

By rescaling the lengths with the soft-core radius $\tilde{\mathbf{r}} = \mathbf{r}/a_{\mathrm{sc}}$ and the energies by the unit $\hbar\omega_0 = \hbar^2/m a_{\mathrm{sc}}$, one gets a dimensionless energy functional

$$E = \int d^2\tilde{\mathbf{r}}\, \psi(\tilde{\mathbf{r}})^* \left(-\frac{1}{2}\nabla^2 + \frac{\Lambda}{2}\int d^2\tilde{\mathbf{r}}'\, \Theta\left(\left|\tilde{\mathbf{r}} - \tilde{\mathbf{r}}'\right| - 1\right) \left|\psi\left(\tilde{\mathbf{r}}'\right)\right|^2 \right) \psi(\tilde{\mathbf{r}}) , \qquad (3)$$

written as a function of a single dimensionless interaction parameter

$$\Lambda = \frac{\pi m a_{\mathrm{sc}}^4 U_0 n}{\hbar^2} = \frac{\pi n a_{\mathrm{sc}}^2 U_0}{\hbar\omega_0} . \qquad (4)$$

Changing a physical quantity related to this system means varying this parameter Λ. Similar to what has been shown in Chapter 1 for a dipolar system, the dispersion relation for an infinite system (in dimensionless units) is

$$\omega(\mathbf{k}) = \sqrt{\frac{k^2}{2}\left[\frac{k^2}{2} + \frac{2\Lambda}{\pi}\tilde{\Theta}(\mathbf{k})\right]} , \qquad (5)$$

where $\tilde{\Theta}(\mathbf{k})$ is the Fourier transform of the soft-core interaction potential. For a two-dimensional Heaviside function, the Fourier transform is

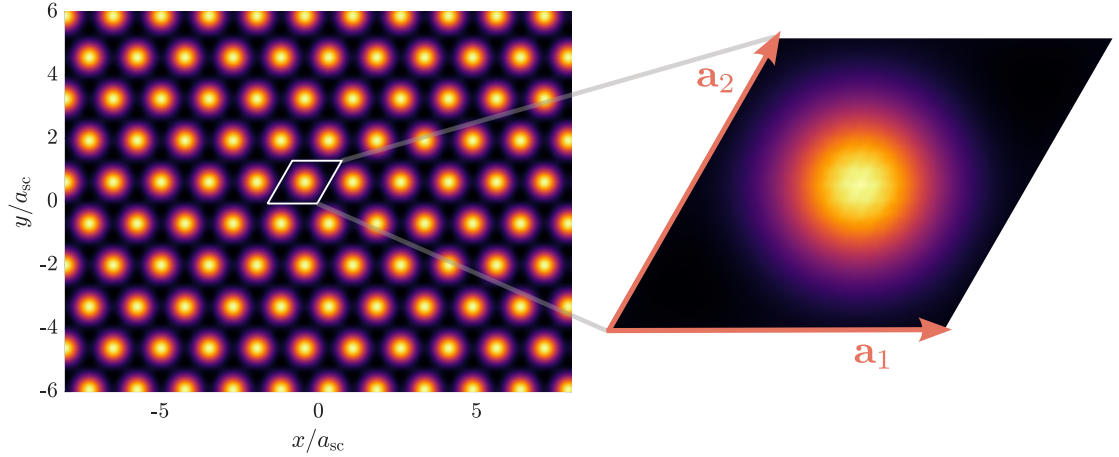$$\tilde{\Theta}(\mathbf{k}) = \frac{J_1(k)}{k} , \qquad (6)$$

Figure 3.2.: Exemplar density distribution of an infinite 2D supersolid with soft-core potential. The lattice unit cell and the lattice vectors $\mathbf{a}_1$, $\mathbf{a}_2$ are zoomed on the right.

where J_1 is the Bessel function of the first kind and first order [166].

Notably, $\tilde{\Theta}(\mathbf{k})$ gets negative at finite momentum, see Fig. 3.1(b), and the negative contribution in Eq. (5) can be tuned with the value of Λ. This gives rise to a roton minimum in the excitation spectrum. The softening of this roton minimum leads to a phase transition from unmodulated BEC to supersolid at $\Lambda_c = 39.49$. This feature occurs even when the system is purely 1D and 3D, for different critical values Λ_c [130, 167]. The transition to the supersolid phase occurs by increasing Λ, which is proportional to the density. This mechanism can be interpreted in the following way: when increasing the density, for the atoms at some point it becomes energetically favourable to pile up periodically because of the finite energy cost for overlapping.

The phase diagram is obtained by calculating the ground state in a single unit cell, with periodic boundary conditions. Among possible lattice configurations, the triangular lattice is known to minimize the energy more effectively than alternatives, like the square or stripe lattices [168]. Thus, the corresponding lattice vectors generating the unit cell are

$$\mathbf{a}_1 = a\hat{\mathbf{x}} \qquad \mathbf{a}_2 = \frac{1}{2}a\hat{\mathbf{x}} + \frac{\sqrt{3}}{2}a\hat{\mathbf{y}} \tag{7}$$

where a is the lattice constant, see Fig. 3.2. The value of a is optimized during the energy minimization process. The emergence of a 2D density modulation for $\Lambda > \Lambda_c$ is characterized by a finite density contrast C and a finite superfluid fraction f_s, see Fig. 3.3(a). The abrupt jumps for both order parameters C and f_s underscore the first-order nature of the phase transition. A similar behaviour is observed during the transition from a uniform BEC to a supersolid phase in a dipolar system that is harmonically confined along the polarization axis (z-axis) and infinitely extended in the perpendicular $xy-$plane, see Fig. 3.3(b). Although the dipolar system is fully 3D, the density modulation occurs in two dimensions within the infinite plane, effectively rendering it comparable to the soft-core model.
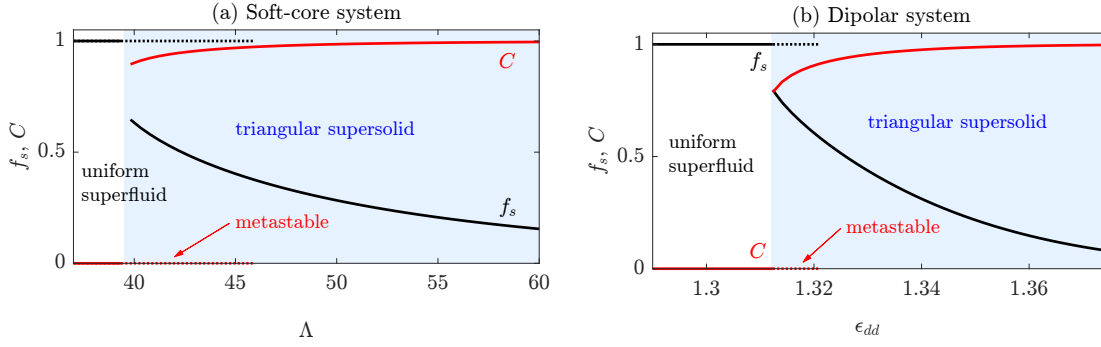
Figure 3.3.: Uniform BEC to supersolid phase transition of (a) a soft-core system and (b) a dipolar system. The order parameters are the superfluid fraction f_s (black) and the density contrast C (red). Dashed lines mark the region in which the uniform BEC phase is metastable, with the supersolid phase being the ground state configuration. Adapted from Ref. [169].

3.2. Hydrodynamic approach and Lagrangian formalism

We are interested in the low-energy (long-wavelength) dynamics of a bulk supersolid with a 2D density modulation. These dynamics are inherently universal, governed by the Nambu–Goldstone bosons that emerge from the spontaneous symmetry breaking: two associated with the broken translational symmetry in the infinite plane, and one arising from the broken gauge symmetry [170]. Thus, from this hydrodynamic approach we expect three speeds of sound:

- The long-wavelength longitudinal density mode, called *first sound* c_1.
- The long-wavelength phase modes, identified as *second sound* c_2.
- The long-wavelength transverse density modes, referred to as *transverse sound* c_t.

The expression of the Lagrangian for a supersolid state has been derived in many works using different techniques [170–174]. In the following, we base our calculations on the results obtained by Yoo and Dorsey [174]. We are interested in the Lagrangian density $\mathcal{L}_{SS}$, from which one can extract the Euler-Lagrange equations and the speed of sounds. The long-wavelength excitations of the ground state can be described using three fields: the change of the average coarse-grained density δn, the superfluid phase field ϕ and the displacement field u_i. The last field deforms the planar coordinates $x'_i = x_i + u_i$, where the indices $i, j = \{x, y\}$ denote the coordinates in the plane where the density modulation occurs.

By assuming small perturbations of the three fields from the equilibrium condition, one can expand the Lagrangian density up to the quadratic order, obtaining the quadratic Lagrangian density:[1]

---

[1]For consistency with the notation used throughout the rest of this thesis, the density is denoted by n, and related coefficients are labelled accordingly. However, in the associated publication presented in Sec. 3.5, the density is instead denoted by ρ, along with the corresponding elastic coefficients. The author apologizes for any potential confusion this discrepancy may cause.

$$
\begin{aligned}
\mathcal{L}_{\text{SS}}^{\text{quad}} ={}& -\hbar\delta n\partial_t\phi - n\frac{\hbar^2}{2m}\left(\partial_i\phi\right)^2 - \alpha_{nu}\delta n\partial_i u_i \\
& -\frac{1}{2}\alpha_{nn}(\delta n)^2 + \frac{1}{2}mn_n\left(\partial_t u_i - \frac{\hbar}{m}\partial_i\phi\right)^2 \\
& -\frac{1}{2}C_{ijkl}\partial_i u_j\partial_k u_l\,.
\end{aligned}
\tag{8}
$$

Here, the time and space derivatives of the fields are denoted as $\partial_t = \partial/\partial t$ and $\partial_i = \partial/\partial x_i$, respectively. The other parameters appearing in Eq. (8) are the elastic coefficients of the system or quantities directly related to them.

3.3. Elastic parameters

The elastic parameters play an important role in the quadratic Lagrangian density and, therefore, in the low-energy dynamics of the supersolid. In the following, we provide a list of all these parameters and how to estimate them from ground states calculations.

Superfluid fraction

The first elastic parameter that plays a role in the Lagrangian density in Eq. (8) is the superfluid fraction f_s, already presented in Chapter 2. In this context, the superfluid fraction is a measure of how much the ground state energy density $\mathcal{E}$ changes with the superfluid velocity [166, 168]. For a 2D supersolid, it is a tensorial quantity that can be calculated as

$$
f_{s,ij} = \frac{1}{mn}\frac{\partial^2\mathcal{E}}{\partial v_i v_j}\,,
\tag{9}
$$

see Appendix A for further details. This quantity is isotropic for a supersolid with triangular structure, $f_{s,ij} = f_s\delta_{ij}$, thus, it can be treated as a scalar quantity f_s [175]. The average superfluid density is defined as

$$
n_s = nf_s
\tag{10}
$$

where n is the total average density, and the average normal density

$$
n_n = n - n_s = (1 - f_s)n\,.
\tag{11}
$$

They both appear in the quadratic Lagrangian density in Eq. (8).

Compressibility

The parameter α_{nn} in Eq. (8) measures the variation of the energy density $\mathcal{E}$ as a response to an average density change

$$
\alpha_{nn} = \frac{\partial^2\mathcal{E}}{\partial^2 n}\,.
\tag{12}
$$

Its inverse is proportional to the isothermal compressibility of the system

$$
\tilde{\kappa} = \frac{1}{n^2\alpha_{nn}}\,.
\tag{13}
$$

The coefficient α_{nn} is determined by numerically evaluating the second derivative of the energy density with respect to the average density

$$\alpha_{nn} = \frac{\partial^2 \mathcal{E}}{\partial^2 n} = \frac{\mathcal{E}(n + \delta n) - 2\mathcal{E}(n) - \mathcal{E}(n - \delta n)}{\delta^2 n} \,. \tag{14}$$

Here, n represents the average density of the ground state solution, whereas $\mathcal{E}(n \pm \delta n)$ is obtained by minimizing the energy functional for a state with an average density $(n \pm \delta n)$.

Elastic tensor

The fourth-rank tensor C_{ijkl} in Eq. (8) is the elastic tensor that describes the stress-strain relation in a linear elastic material [176]. The stress refers to the pressure applied to the system and the strain is a measure of the deformation that results from the applied stress. Intuitively, C_{ijkl} can be seen as a generalization of the elastic constant appearing in the Hook law for a 3D system in the continuum. The elastic tensor is calculated as

$$C_{ijkl} = \frac{\partial^2 \mathcal{E}}{\partial u_{ij} \partial u_{kl}} \tag{15}$$

where $u_{ij} = \frac{1}{2}\left(\partial_i u_j + \partial_j u_i\right)$ is the strain tensor. When considering a linear displacement field $\mathbf{u} = (u_i, u_j)$ so that $\mathbf{u}(\mathbf{x}) = A\mathbf{x}$, with the matrix A real and symmetric, the strain tensor becomes

$$u_{ij} = \frac{1}{2}\left(\partial_i u_j + \partial_j u_i\right) = \frac{1}{2}\left(A_{ji} + A_{ji}\right) = A_{ij} = A_{ji}\,. \tag{16}$$

Since it is symmetric, we just need to consider three cases: u_{xx}, u_{yy}, u_{xy}. For simplicity of notation, we use $I = \{xx, yy, xy\}$. Let us define three possible small deformations of the form:

$$A^{(I)} : A^{(1)} = \begin{bmatrix} \delta A & 0 \\ 0 & 0 \end{bmatrix}, A^{(2)} = \begin{bmatrix} 0 & 0 \\ 0 & \delta A \end{bmatrix}, A^{(3)} = \begin{bmatrix} 0 & \delta A \\ 0 & 0 \end{bmatrix}, \tag{17}$$

so that they can be applied to the lattice vectors of the system as

$$\mathbf{a}_i^{(I)} = \mathbf{a}_i + A^{(I)}\mathbf{a}_i\,. \tag{18}$$

Finally, the elastic tensor is calculated through the formula for the discrete second derivative

$$
\begin{aligned}
C_{IJ} &= \frac{\partial^2 \mathcal{E}}{\partial u_I \partial u_J} = \\
&= \frac{\mathcal{E}(\mathbf{a}_1^{(IJ)}, \mathbf{a}_2^{(IJ)}) - \mathcal{E}(\mathbf{a}_1^{(I-J)}, \mathbf{a}_2^{(I-J)}) - \mathcal{E}(\mathbf{a}_1^{(-IJ)}, \mathbf{a}_2^{(-IJ)}) + \mathcal{E}(\mathbf{a}_1^{(-I-J)}, \mathbf{a}_2^{(-I-J)})}{4\delta A^2},
\end{aligned}
\tag{19}
$$

where $\mathbf{a}_i^{(\pm I \pm J)} = \mathbf{a}_i + A^{(\pm I)}\mathbf{a}_i + A^{(\pm J)}\mathbf{a}_i$ denotes the double perturbed lattice vector. Each term at the numerator is obtained by calculating the ground state energy in a perturbed unit cell.

For isotropic systems, as the 2D triangular supersolid, the elastic tensor can be written in a simple matrix form

$$
C_{IJ} = \begin{bmatrix} \tilde{\lambda} + 2\tilde{\mu} & \tilde{\lambda} & 0 \\ \tilde{\lambda} & \tilde{\lambda} + 2\tilde{\mu} & 0 \\ 0 & 0 & \mu \end{bmatrix}
\tag{20}
$$

that, recovering the initial index notation, corresponds to

$$
C_{ijkl} = \tilde{\lambda}\delta_{ij}\delta_{kl} + \tilde{\mu}(\delta_{ik}\delta_{jl} + \delta_{il}\delta_{jk})\,.
\tag{21}
$$

The quantities $\tilde{\lambda}$, $\tilde{\mu}$ are called *Lamé coefficients* or elastic moduli and they are directly related to the Young's modulus and to the Poisson's ratio[2].

Density-strain coupling

The last parameter that appears in the Lagrangian is the density-strain coefficient α_{nu}, that describes the energy variation due to both changes in the average density and the deformation of the unit cell

$$
\alpha_{nu} = \frac{\partial^2 \mathcal{E}}{\partial u_{ii}\partial n}\,.
\tag{22}
$$

It is obtained by calculating the mixed partial derivative

$$
\begin{aligned}
\alpha_{nu} &= \frac{\partial^2 \mathcal{E}}{\partial u_I \partial n} = \\
&= \frac{\mathcal{E}(n+\delta n, \mathbf{a}_1^{(I)}, \mathbf{a}_2^{(I)}) - \mathcal{E}(n+\delta n, \mathbf{a}_1^{(-I)}, \mathbf{a}_2^{(-I)}) - \mathcal{E}(n-\delta n, \mathbf{a}_1^{(I)}, \mathbf{a}_2^{(I)}) + \mathcal{E}(n-\delta n, \mathbf{a}_1^{(-I)}, \mathbf{a}_2^{(-I)})}{4\delta A \delta n}\,.
\end{aligned}
\tag{23}
$$

As the previous cases, the terms at the numerator are obtained by calculating the ground state energy in a perturbed unit cell and with a perturbed average density.

3.4. Shear modulus

The off-diagonal tensor element $\tilde{\mu}$ is of particular interest because it represents the *shear modulus* of the system. Physically, the shear modulus describes the ability of a material to resist deformation under shear stress, distinguishing solid-like behaviour from that of fluids. In purely fluid systems, the shear modulus is strictly zero, reflecting the inability of fluids to sustain shear stresses or propagate shear waves. Conversely, a finite shear modulus is a hallmark of solid systems, where rigidity emerges as a defining property.

In the context of supersolids, the solid-like nature of the system is conventionally inferred from its periodic density distribution. However, this structural property alone is not sufficient to fully characterize the fundamental elastic behaviour typically associated with solids. Key elastic properties such as rigidity, stress-strain relationships, or the propagation of shear waves remain largely unexplored experimentally for supersolids.

In our work, presented in the following section, we take a foundational step in exploring the elastic properties of dipolar supersolids by explicitly verifying the presence of a

[2]The Young's modulus measures the compressive stiffness of the system, whereas the Poisson's ratio measures the deformation of the system as a ratio between the transverse and the axial strain [176]
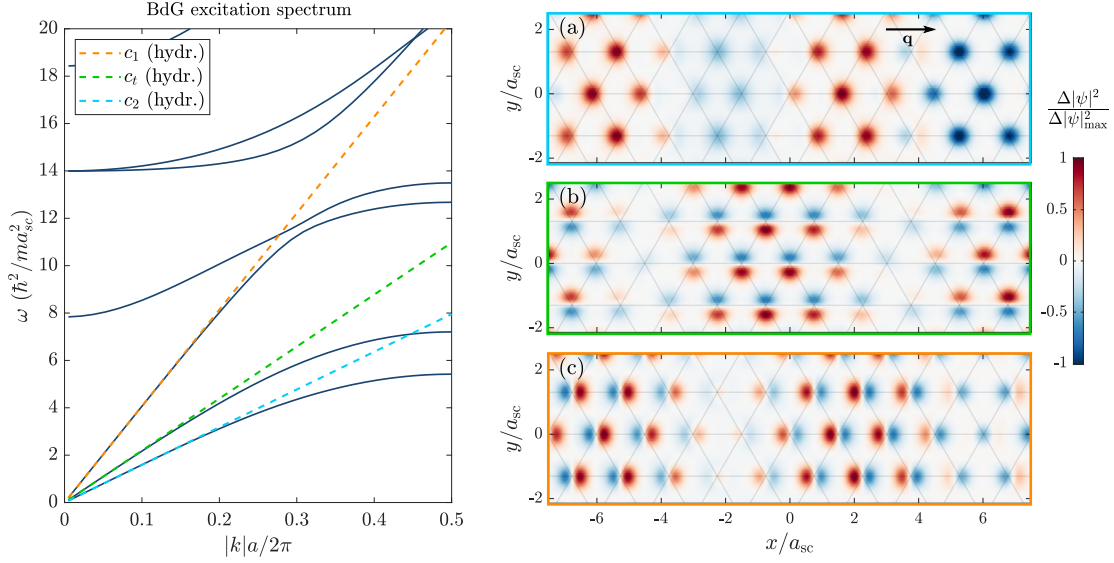
Figure 3.4.: Excitation spectrum of an infinite soft-core supersolid with hydrodynamic predictions of the three speeds of sound. On the right, three exemplar modes are highlighted, belonging to the (a) second sound branch (phase mode), (b) transverse branch (shear mode) and (c) first sound branch (longitudinal mode). The grey background lines intersect at the position of the density maxima of the unperturbed density distribution. Subplots on the right are adapted from Ref. [169].

finite shear modulus [169]. By solving the three Euler-Lagrange equations associated to the fields, namely

$$\frac{\partial \mathcal{L}}{\partial \delta n} - \partial_t \left(\frac{\partial \mathcal{L}}{\partial (\partial_t \delta n)} \right) - \partial_i \left(\frac{\partial \mathcal{L}}{\partial (\partial_i \delta n)} \right) = 0,$$

$$\frac{\partial \mathcal{L}}{\partial \phi} - \partial_t \left(\frac{\partial \mathcal{L}}{\partial (\partial_t \phi)} \right) - \partial_i \left(\frac{\partial \mathcal{L}}{\partial (\partial_i \phi)} \right) = 0, \qquad (24)$$

$$\frac{\partial \mathcal{L}}{\partial u_i} - \partial_t \left(\frac{\partial \mathcal{L}}{\partial (\partial_t u_i)} \right) - \partial_j \left(\frac{\partial \mathcal{L}}{\partial (\partial_j u_i)} \right) = 0.$$

we obtain the equations of motion. Assuming a solution of the form $\delta n, \phi, u_i \sim e^{i(\mathbf{k} \cdot \mathbf{r} - \omega t)}$, we obtain three linear dispersion relations $\omega = ck$ with the three speeds of sound

$$mc_1^2 = \frac{1}{2} \left(a + \sqrt{a^2 - 4b} \right) ,$$
$$mc_2^2 = \frac{1}{2} \left(a - \sqrt{a^2 - 4b} \right) , \qquad (25)$$
$$mc_t^2 = \frac{\tilde{\mu}}{n_n} .$$

The auxiliary quantities a and b are

$$a = n\alpha_{nn} - 2\alpha_{nu} + \frac{\tilde{\lambda} + 2\tilde{\mu}}{n_n} ,$$
$$b = \frac{n_s}{n_n} \left[\alpha_{nn} \left(\tilde{\lambda} + 2\tilde{\mu} - \alpha_{nu}^2 \right) \right] , \qquad (26)$$

defined as a function of the elastic parameters obtained from ground state calculations. For both soft-core and dipolar supersolids we found an excellent agreement between the hydrodynamic results and the low-energy spectrum of excitations calculated by solving the BdG equations. In Fig. 3.4 is shown an example for the soft-core system, with three corresponding exemplar modes showing (a) a phase wave, (b) a shear wave and (c) a longitudinal wave.

Recent theoretical works have started to study more in detail the effects of propagating shear waves in a dipolar supersolid. For example, in Ref. [177] is has been highlighted the anomalous dispersion of shear waves travelling faster than the speeds of sound, whereas in Ref. [178] it has been shown how a shear instability inducing phase transitions between supersolid states with different lattice structures. However, an extension of the concept of the shear modulus for finite size systems is still missing and it could be subject for future research directions.

3.5. Publication: Excitations of a two-dimensional supersolid

E. Poli[1], D. Baillie[2,3], F. Ferlaino[1,3], and P. B. Blakie[2,3]

[1] *Institut für Experimentalphysik, Universität Innsbruck, 6020 Innsbruck, Austria*
[2] *Dodd-Walls Centre for Photonic and Quantum Technologies, Dunedin 9054, New Zealand*
[3] *Department of Physics, University of Otago, Dunedin 9016, New Zealand*
[4] *Institut für Quantenoptik und Quanteninformation, Österreichische Akademie der Wissenschaften, 6020 Innsbruck, Austria*

[†] The author of the present thesis performed the numerical simulations and the theoretical calculations together with P. B. B. and D. B. and contributed in writing the manuscript.

Excitations of a two-dimensional supersolid

E. Poli [1], D. Baillie [2,3] F. Ferlaino [1,4] and P. B. Blakie [2,3]

[1]*Institut für Experimentalphysik, Fakultät für Mathematik, Informatik und Physik, Universität Innsbruck, 6020 Innsbruck, Austria*
[2]*Dodd-Walls Centre for Photonic and Quantum Technologies, Dunedin 9054, New Zealand*
[3]*Department of Physics, University of Otago, Dunedin 9016, New Zealand*
[4]*Institut für Quantenoptik und Quanteninformation, Österreichische Akademie der Wissenschaften,
Technikerstraße 21a, 6020 Innsbruck, Austria*

We present a theoretical study of the excitations of the two-dimensional supersolid state of a Bose-Einstein condensate with either dipole-dipole interactions or soft-core interactions. This supersolid state has three gapless excitation branches arising from the spontaneously broken continuous symmetries. Two of these branches are related to longitudinal sound waves, similar to those in one-dimensional supersolids. The third branch is a transverse wave arising from the nonzero shear modulus of the two-dimensional crystal. We present the results of numerical calculations for the excitations and dynamic structure factor characterizing the density fluctuations and study their behavior across the discontinuous superfluid to supersolid transition. We show that the speeds of sound are described by a hydrodynamic theory that incorporates generalized elastic parameters, including the shear modulus. Furthermore, we establish that dipolar and soft-core supersolids manifest distinct characteristics, falling into the bulk-incompressible and rigid-lattice limits, respectively.

I. INTRODUCTION

A supersolid is a state of matter in which phase and translational symmetries are broken. Here we refer to a D-dimensional supersolid as being a system that spontaneously develops a D-dimensional crystal structure while still exhibiting superfluidity. For this system it is expected that the broken symmetries will lead to $(D+1)$ Nambu-Goldstone modes that manifest as gapless excitation branches [1]. The experimental production of supersolid states in atomic gases [2–6] has generated interest in their properties, including their excitation spectra. The $D=1$ case [7–13] has two gapless excitation branches of longitudinal character, which are referred to as first and second sounds.[1] A $D=2$ supersolid was recently produced using a dipolar Bose gas in an oblate-shaped trapping potential [16,17]. This system has a rich phase diagram with different ground-state crystal patterns separated by first-order transitions [18–22] and is an interesting system for considering the interplay of crystalline order with vortices [23–26].

Here we study the excitation spectrum of a $D=2$ supersolid. We consider the case of a zero-temperature gas in the thermodynamic limit, which admits a well-defined band structure, allowing us to investigate the gapless modes in detail. We show that a hydrodynamic theory provides a precise description of the excitations in terms of a set of underlying elastic parameters. Supersolids with $D>1$ exhibit a shear modulus, characterizing the stiffness of the crystal to transverse (i.e., shear) deformations. This also manifests as a new gapless branch of transverse excitations, where the motion of the crystal is perpendicular to the direction of wave propagation. This is in contrast to the other two gapless branches, which are longitudinal.

To illustrate the properties of $D=2$ supersolids we present results for two systems. These systems differ in the relative importance of elastic and compressibility effects and exhibit different behaviors for first and second sounds across the transition. The first system is a dipolar Bose-Einstein condensate (BEC) in a planar trap, where the atoms are confined along the direction in which dipoles are polarized and free in the perpendicular plane. The second system is a two-dimensional (2D) BEC of atoms interacting with a finite-range soft-core interaction. The excitations of both systems can be obtained by numerically solving the Bogoliubov–de Gennes (BdG) equations. While the excitation spectrum for the 2D soft-core system was studied previously [27–29], we present results for 2D dipolar excitations in the thermodynamic regime. The thermodynamic limit has an advantage over finite (harmonically trapped) system studies (e.g., see [20,30]) because the in-plane quasimomentum is a good quantum number, leading to well-defined excitation bands that allow clear interpretation of their properties (e.g., speeds of sound). For both systems we develop a hydrodynamic model involving five elastic parameters that we determine from ground-state calculations. We show that the hydrodynamic model provides an accurate description of the speeds of sound determined by numerical calculation of the BdG excitations and provides insight into the origin of the different behaviors of the two systems across the transition and deep into the crystal regime. While the two systems studied are not directly comparable (e.g., the dipolar

---

[1]These associated excitation branches are also commonly referred to as density and phase branches. The second sound is associated with a reduced superfluidity (i.e., normal component) arising from the spontaneously broken translational symmetry (see [12,14,15]).

BEC is a three-dimensional system, while the soft-core BEC is 2D), by studying both we reveal the general applicability of hydrodynamic theory to 2D supersolids.

The outline of this paper is as follows. In Sec. II and Appendixes A and B we describe the two systems we study in this work and their transition to a supersolid state with a triangular crystalline structure. We present results for the excitations and dynamic structure factors determined by numerical solutions of the BdG equations in Sec. III. In Sec. IV we outline the hydrodynamic theory for the $D = 2$ supersolid. We discuss how the relevant elastic parameters that appear in this theory can be determined from ground-state calculations. The hydrodynamic predictions for the speeds of sound are compared to those obtained with the BdG calculations. We then discuss the key parameters distinguishing the behavior of the dipolar and soft-core systems and identify the two relevant limits of the hydrodynamic results to describe these systems. Finally, we conclude in Sec. V.

II. SUPERSOLID SYSTEMS

Here we introduce the two systems examined in this work. Both systems are described by Hamiltonians that are translationally invariant in the xy plane. The ground-state phase diagram depends on the average atomic areal density ρ and various microscopic parameters (e.g., interactions), with 2D crystalline ground states occurring in appropriate parameter regimes.

The first system we introduce is a dipolar BEC of highly magnetic atoms under axial harmonic confinement with angular frequency ω_z, but with the atoms free to move in the xy plane. The atoms interact by a short-range contact interaction with s-wave scattering length a_s and the long-range dipole-dipole interaction, characterized by the dipole length a_{dd}. In this system quantum fluctuation effects become important in the dipole-dominant regime, $\epsilon_{dd} \equiv a_{dd}/a_s > 1$, with the fluctuations able to stabilize the condensate from mechanical collapse [31–33]. This system is well described by an extended mean-field theory, with details given in Appendix A. Here we consider a BEC of ^{164}Dy atoms with $\omega_z/2\pi = 72.4$ Hz and $a_{dd} = 130.8a_0$ to be comparable to the phase diagrams produced for this system in Refs. [18,22]. The system is constrained to have mean areal density ρ, which serves as a thermodynamic parameter. We choose to present results for $\rho = 0.04/a_{dd}^2 \approx 8.3 \times 10^{14}$ m^{-2}, which is well below the critical point density of $\rho_c \approx 0.098/a_{dd}^2$ and is comparable to the densities used in experiments [16]. Under these conditions the nature of the ground state depends on the value of a_s, which is controlled in experiments using Feshbach resonances. For our choice of density the ground state is uniform for $\epsilon_{dd} < 1.31$ (i.e., $a_s > 99.7a_0$) and is a triangular crystal for $\epsilon_{dd} \geqslant 1.31$. We show examples of these states in Fig. 1. As ϵ_{dd} increases, the overlap between unit cells decreases, and at each lattice site a filament-shaped droplet (elongated in the dipole direction z) forms. It is useful to characterize the strength of the modulation of the density in the xy plane by the density contrast, defined as

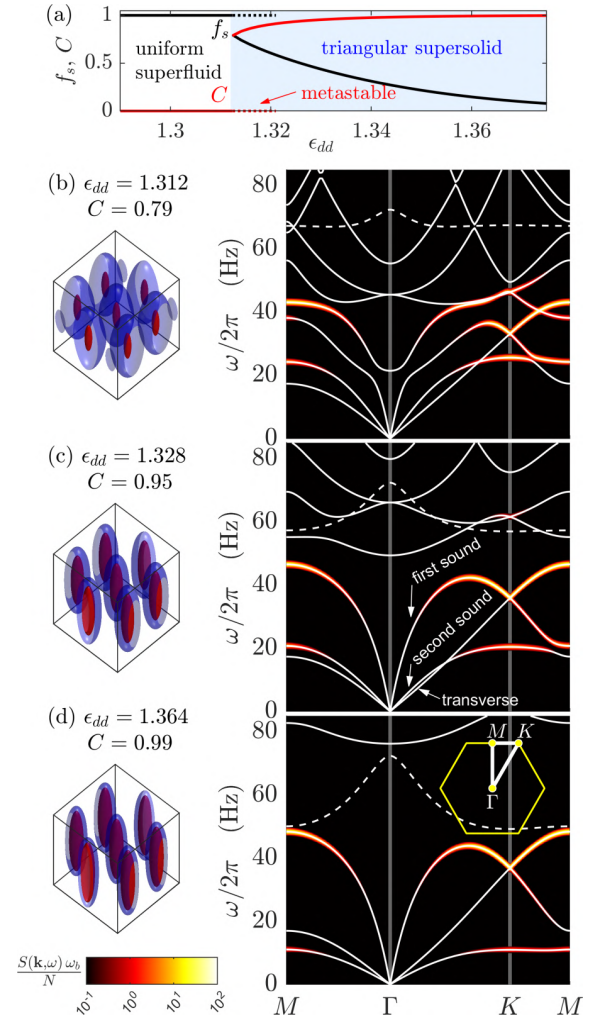$$C = \frac{\varrho_{max} - \varrho_{min}}{\varrho_{max} + \varrho_{min}}, \quad (1)$$

FIG. 1. (a) The superfluid fraction f_s and density contrast across the first-order uniform superfluid to supersolid phase transition. (b)–(d) Ground-state density (left) and excitation spectra along the three symmetry directions of the Brillouin zone [right; see inset in (d)] for a planar dipolar gas at three values of ϵ_{dd}. Density isosurfaces at 0.55×10^{20} m^{-3} (blue) and 3×10^{20} m^{-3} (red), shown in a box of size $11 \times 11 \times 14$ μm^3. The heat map image shows the dynamic-structure-factor frequency broadened by $\omega_b = 10^{-2}\omega_z$. The excitation spectra are shown as white lines, with dashed lines being odd axial modes which do not contribute to the structure factor. Results for ^{164}Dy atoms with an average areal density of $\rho = 0.04/a_{dd}^2$ and axial confinement of $\omega_z/2\pi = 72.4$ Hz. The superfluid fraction is discussed in Sec. IV A.

where ϱ_{max} and ϱ_{min} are the maximum and minimum of the areal density $\varrho(x, y)$ of the ground state. The density contrast as a function of ϵ_{dd} is shown in Fig. 1(a), revealing the discontinuous character of the transition. In these results we have extended the uniform superfluid state beyond the transition point where it is a metastable state. However, at $\epsilon_{dd} \approx 1.32$ ($a_s \approx 99.0a_0$), a roton excitation softens, and the uniform state is dynamically unstable.

The second system is a 2D BEC of atoms that interact via the soft-core potential of strength U_0 and range a_{sc}. This system has been extensively studied as a supersolid model (e.g.,
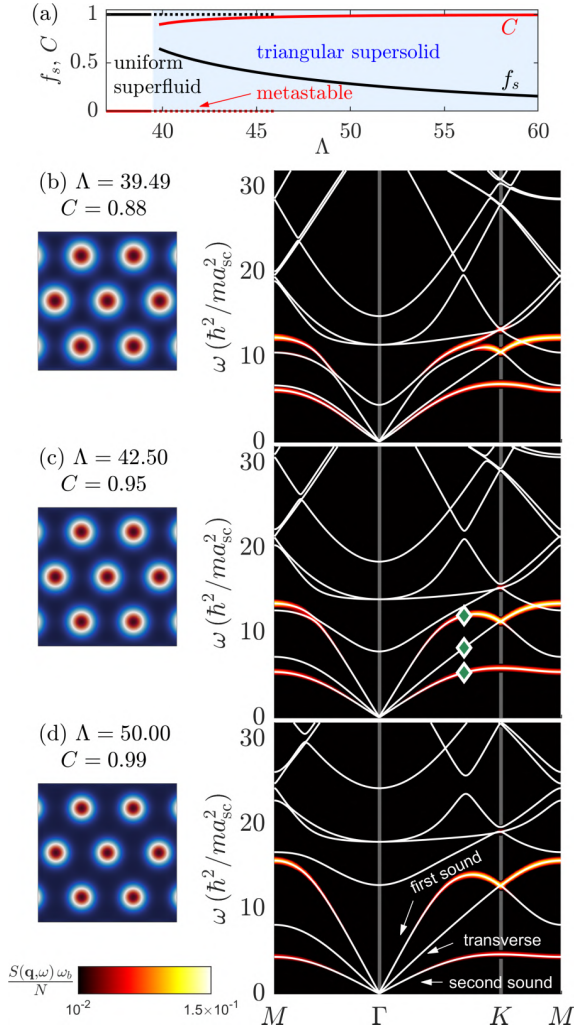
FIG. 2. (a) The superfluid fraction and density contrast across the first-order uniform superfluid to supersolid phase transition. (b)–(d) Ground-state density (left) and excitation spectra along the three symmetry directions of the Brillouin zone (right) for a 2D soft-core system at three values of Λ. The ground-state densities are shown in a box of size $4a_{sc} \times 4a_{sc}$. The excitation spectra are shown as white lines, on top of a heat map image showing the dynamic-structure-factor frequency broadened by $\omega_b = 0.35\omega_0$. The three symmetry directions of the Brillouin zone are the same as the ones depicted in the inset of Fig. 1(d). The three green diamonds mark the positions of the modes plotted in Fig. 3 in an equivalent symmetry direction.

see [27–29,34–38]). Schemes have been proposed to realize soft-core interactions in ultracold-atom experiments [39,40], but there has been limited reported experimental activity in the regime relevant to supersolidity thus far. We consider the system in a regime well described by mean-field theory, with further details given in Appendix B. The phase diagram for the 2D soft-core model depends on the single dimensionless parameter $\Lambda = m\pi\rho a_{sc}^4 U_0/\hbar^2$. The melting value $\Lambda_m = 39.49$ separates uniform superfluid states (for $\Lambda < \Lambda_m$) from triangular crystal states. We show examples of these states in Fig. 2, and the behavior of the density contrast as a function of Λ is shown in Fig. 2(a). Similar to the dipolar system, the

transition from unmodulated to modulates states also occurs discontinuously as Λ changes, with the unmodulated states remaining metastable until the roton completely softens at $\Lambda = 46.30$.

For both systems, we find the ground state by minimizing the energy density $\mathcal{E}$, i.e., the energy per unit area. It is convenient to write it as $\mathcal{E}(\rho; \mathbf{v}, \mathbf{a}_1, \mathbf{a}_2)$, being a function of ρ, the superfluid velocity $\mathbf{v}$, and $\{\mathbf{a}_1, \mathbf{a}_2\}$, which are the direct lattice vectors of the crystal.[2] The ground state for the average density ρ is obtained by minimizing the energy density for $v = 0$ with respect to the lattice constant.[3] Additional details are given in Appendixes A and B.

III. EXCITATION RESULTS

The excitation spectrum can be determined by linearizing around the ground state $\psi(\mathbf{x})$ with a time-dependent ansatz of the form

$$\Psi(\mathbf{x}, t) = e^{-i\mu t/\hbar} \left[\psi(\mathbf{x}) + \sum_{\nu\mathbf{q}} \{ c_{\nu\mathbf{q}} u_{\nu\mathbf{q}}(\mathbf{x}) e^{-i\omega_{\nu\mathbf{q}}t} \right.$$
$$\left. - c_{\nu\mathbf{q}}^* v_{\nu\mathbf{q}}^*(\mathbf{x}) e^{i\omega_{\nu\mathbf{q}}^* t} \} \right], \quad (2)$$

where μ is the ground-state chemical potential, $c_{\nu\mathbf{q}}$ are the expansion amplitudes, and ν and $\mathbf{q}$ are the band index and planar quasimomentum of the excitation, respectively. Here $\{u_{\nu\mathbf{q}}(\mathbf{x}), v_{\nu\mathbf{q}}(\mathbf{x})\}$ are the quasiparticle amplitudes, with respective energies $\hbar\omega_{\nu\mathbf{q}}$, and they are determined by solving the BdG equations (see Appendix C and Refs. [28,41]).

In Figs. 1 and 2 we show the results for the excitation spectra for the dipolar and soft-core models, respectively. These results are shown along the symmetry directions of the first Brillouin zone. For both sets of results the case shown in Figs. 1(b) and 2(b) is close to the phase transition, whereas Figs. 1(c), 1(d), 2(c), and 2(d) are for states with higher values of the density contrast. The excitations are shown as solid white lines on top of the dynamic structure factor $S(\mathbf{q}, \omega)$, which is obtained as

$$S(\mathbf{q}, \omega) = \sum_\nu \left| \int d\mathbf{x} \, (u_{\nu\mathbf{q}}^* - v_{\nu\mathbf{q}}^*) e^{i\mathbf{q}\cdot\mathbf{x}} \psi \right|^2 \delta(\omega - \omega_{\nu\mathbf{q}}). \quad (3)$$

The dynamic structure factor reveals the density fluctuations associated with the excitations; notably $S(\mathbf{q}, \omega)$ vanishes for excitations that do not affect the density.

In all results we see that the gapless excitation bands emerge from the Γ point and that they all have a linear dependence on the excitation wave vector near Γ. For the dipolar case shown in Figs. 1(b) and 1(c), the lowest branch (close to Γ) is a transverse excitation of the crystal, which has no weight in the dynamic structure factor.[4] The next

---

[2]We are interested in stationary superfluids but introduce $\mathbf{v}$ to define the superfluid fraction.

[3]The ground-state configuration for both models is a triangular lattice; thus, we can take $\mathbf{a}_1 = a\hat{\mathbf{x}}$ and $\mathbf{a}_2 = \frac{1}{2}a\hat{\mathbf{x}} + \frac{\sqrt{3}}{2}a\hat{\mathbf{y}}$, with lattice constant a.

[4]Note that at low q the first and second sound branches have small weight due to the density fluctuations being suppressed, but for the transverse excitation branch the weight vanishes at all q.
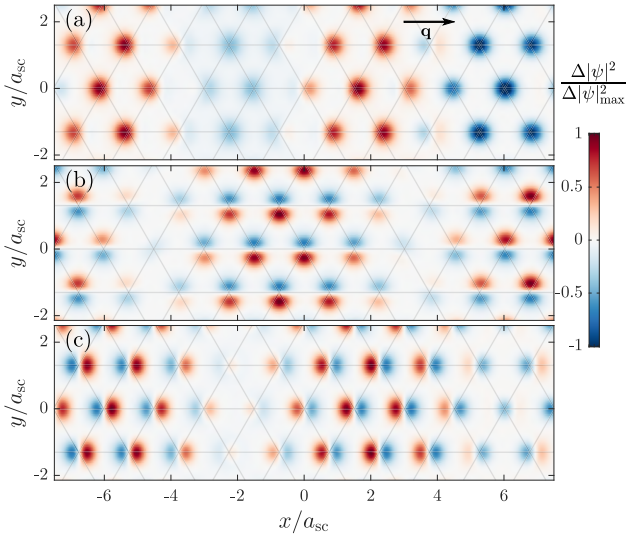
FIG. 3. Effect of excitations from the lowest three gapless bands on the supersolid density profile. The change in density $\Delta|\psi|^2$ (divided by its maximum value) from the addition of an excitation in the (a) second sound, (b) transverse, and (c) first sound bands. The lines intersect at the locations of the density peaks of the ground state. Results for 2D soft-core mode using $\mathbf{q} = (0.4, 0)/a_{sc}$ and $\Lambda = 42.5$ [see Fig. 2(c)].

branch is the second sound or phase mode, which has a weak density contribution. These two lowest branches have similar speeds of sound (i.e., slope near Γ), and as ϵ_{dd} increases, the second sound speed decreases and becomes slower than the transverse speed of sound [see Fig. 1(d)]. The third gapless branch of the spectra is known as first sound and is a longitudinal density wave. This excitation branch rises much more steeply than the other two, exhibiting a much higher sound speed. It is instructive to compare these results to the spectra along the three symmetry directions calculated for the 2D soft-core supersolid (also studied in Ref. [28]). As shown in Fig. 2, the order of the three branches is preserved while varying Λ, with the gapless transverse branch always sandwiched in between the second sound mode and the first sound mode. In Fig. 3, we show three exemplar modes that have the same quasimomentum $\mathbf{q}$ but belong to the three different gapless energy bands. To highlight the character of each mode, we plot the change in density $\Delta|\psi|^2 = \mathcal{N}^{-1}|\psi + c_{\nu\mathbf{q}}u_{\nu\mathbf{q}}(\mathbf{x}) - c_{\nu\mathbf{q}}^* v_{\nu\mathbf{q}}^*(\mathbf{x})|^2 - |\psi|^2$, obtained by subtracting the ground-state density from the perturbed density, normalized by $\mathcal{N}$ to the same value as the ground state. Here we observe that the second sound branch [Fig. 3(a)] keeps the location of the density maxima fixed, but density changes along the direction of propagation by atom tunneling between sites. The transverse sound branch [Fig. 3(b)] causes a shearing of the lattice sites (i.e., transversal motion). The first sound branch [Fig. 3(c)] exhibits longitudinal displacement of the lattice sites, consistent with a classical crystal excitation. Note that, to help with the visualization, the quasimomentum $\mathbf{q}$ of the selected modes is chosen along the x axis, which is equivalent to the Γ-K symmetry direction in Fig. 2.

IV. HYDRODYNAMIC DESCRIPTION

The features of the linear part of the excitation spectrum of a 2D supersolid, i.e., the low-energy region for small momenta ($q \ll \pi/a$), are well captured by a hydrodynamic description [14,42]. This approach is based on long-wavelength perturbations of the ground state, obtained by applying small variations to the three fields associated with conserved quantities and broken symmetries: the change in average density $\delta\rho$, the displacement field $u_{i=\{x,y\}}$ that deforms the planar coordinates as $x_i \rightarrow x_i' = x_i + u_i$, and the superfluid phase field ϕ. Before we write the Lagrangian density for a 2D supersolid to obtain the three speeds of sound, it is useful to extract the elastic parameters of the system. Later, they will appear as coefficients of the Lagrangian.

A. Elastic parameters

The first parameter is the superfluid fraction determined by the energetic response of the ground state to changes in the superfluid velocity (see Refs. [36,43,44]). In general the superfluid fraction is a tensor given by

$$f_{s,ij} = \frac{1}{m\rho}\frac{\partial^2\mathcal{E}}{\partial v_i \partial v_j}, \quad (4)$$

where the indices $i, j = \{x, y\}$ denote the planar coordinates. For the triangular ground state this tensor is isotropic, i.e., $f_{s,ij} = f_s\delta_{ij}$, and we can simply refer to the superfluid fraction as a scalar value f_s. As a consequence, the average superfluid density $\rho_s = f_s\rho$ and the average normal density $\rho_n = (1 - f_s)\rho$ are also isotropic quantities.

The other elastic parameters involve the dependence of the energy density on the areal density and lattice vectors. The second derivative of $\mathcal{E}$ with respect to the average density ρ is defined

$$\alpha_{\rho\rho} = \frac{\partial^2\mathcal{E}}{\partial\rho^2}, \quad (5)$$

which relates to the isothermal compressibility at constant strain:

$$\tilde{\kappa} = \frac{1}{\rho^2\alpha_{\rho\rho}}. \quad (6)$$

The elastic tensor associated with the crystalline structure is given by

$$C_{ijkl} = \frac{\partial^2\mathcal{E}}{\partial u_{ij}\partial u_{kl}}, \quad (7)$$

where $u_{ij} = \frac{1}{2}(\partial_i u_j + \partial_j u_i)$ is the strain tensor arising from the displacement field $\mathbf{u}$. We obtain this tensor by evaluating how the ground-state energy density changes with the lattice vector deformations $a'_{\sigma=1,2,i} = (\delta_{ij} + u_{ij})a_{\sigma,j}$ (using the Einstein summation convention). We have verified that the elastic tensor for the triangular ground state is isotropic [45], having the form

$$C_{ijkl} = \tilde{\lambda}\delta_{ij}\delta_{kl} + \tilde{\mu}(\delta_{ik}\delta_{jl} + \delta_{il}\delta_{jk}), \quad (8)$$

where $\{\tilde{\lambda}, \tilde{\mu}\}$ are the Lamé parameters. We denote $\alpha_{uu} = \tilde{\lambda} + 2\tilde{\mu}$, which is the diagonal element of the elastic tensor (i.e., $C_{xxxx} = C_{yyyy}$), also known as the longitudinal or P-wave

modulus. We also have special interest in the shear modulus $\tilde{\mu}$, which is given by off-diagonal tensor elements, such as C_{xyxy}. Finally, we consider the density-strain coupling parameter given by the mixed partial derivative

$$\alpha_{\rho u} = \frac{\partial^2 \mathcal{E}}{\partial u_{ii} \partial \rho}, \tag{9}$$

which describes the coupling between changes in average density and the unit-cell area.

B. Hydrodynamic theory

We now give the quadratic Lagrangian density for the fields $\delta\rho$, u_i, and $\delta\phi$ and solve the Euler-Lagrange equations to extract the speeds of sound. The quadratic Lagrangian density for a supersolid, introduced by Yoo and Dorsey [14], reads

$$\begin{aligned}
\mathcal{L}_{\text{SS}}^{\text{quad}} &= -\hbar \delta\rho \partial_t \phi - \rho \frac{\hbar^2}{2m}(\partial_i \phi)^2 - \alpha_{\rho u}\delta\rho \partial_i u_i \\
&\quad - \frac{1}{2}\alpha_{\rho\rho}(\delta\rho)^2 + \frac{1}{2}m\rho_n\left(\partial_t u_i - \frac{\hbar}{m}\partial_i \phi\right)^2 \\
&\quad - \frac{1}{2}C_{ijkl}\partial_i u_j \partial_k u_l. \tag{10}
\end{aligned}$$

From the solution of the Euler-Lagrange equations (see Appendix D), one gets the three speeds of sound:

$$mc_1^2 = \frac{1}{2}\left(a_\Delta + \sqrt{a_\Delta^2 - 4b_\Delta}\right), \tag{11}$$

$$mc_2^2 = \frac{1}{2}\left(a_\Delta - \sqrt{a_\Delta^2 - 4b_\Delta}\right), \tag{12}$$

$$mc_t^2 = \frac{\tilde{\mu}}{\rho_n}, \tag{13}$$

where we have defined

$$a_\Delta = \rho\alpha_{\rho\rho} - 2\alpha_{\rho u} + \frac{\alpha_{uu}}{\rho_n}, \tag{14}$$

$$b_\Delta = \frac{\rho_s}{\rho_n}\left(\alpha_{\rho\rho}\alpha_{uu} - \alpha_{\rho u}^2\right). \tag{15}$$

The quantities c_1, c_2, and c_t represent the first, second, and transverse speeds of sound, respectively, and they are fully determined by the elastic coefficients and density of the system.

C. Hydrodynamic results

In Figs. 4 and 5 we consider the properties of the dipolar and soft-core systems across the superfluid to supersolid phase transition. The speeds of sound extracted from linear fits to the $q \to 0$ behavior of BdG energies calculated for the gapless branches are shown in Figs. 4(a) and 5(a). The uniform superfluid state has only a single gapless branch: the first sound c_1. In the transition to a supersolid there is almost no change in c_1 for the dipolar case, while a significant upward jump in c_1 occurs for the soft-core case. We also note that in the dipolar system c_1 is higher relative to the other speeds of sound than in the soft-core system. The second sound speed c_2 is always much lower than the first sound. Except close to the transition in the soft-core system, c_2 generally decreases as we go deeper into the crystalline phase. This reduction in c_2 is a sign of the reduced superfluidity. Indeed, sufficiently far into the crystalline phase we expect a transition to an isolated
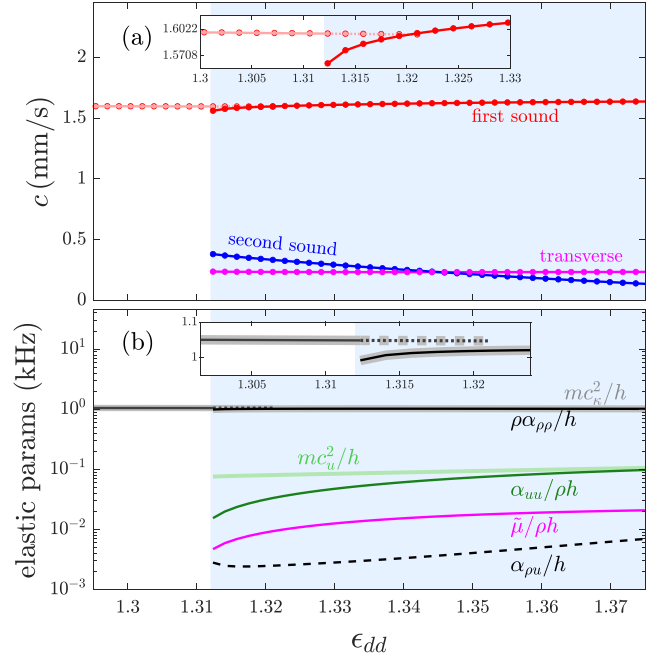

FIG. 4. Elastic properties and speeds of sound for a planar dipolar BEC at the first-order transition to a supersolid. (a) Speeds of sound. We show the speed of first sound in the uniform (light red) and supersolid (dark red) phases and the speeds of transverse and second sounds in the supersolid phase (as labeled in the inset). Results from the BdG analysis are shown as lines, and the hydrodynamic predictions using the elastic parameters from the ground-state calculations are shown as markers. (b) The elastic parameters characterizing the dependence of the ground-state energy on lattice and density changes. The characteristic energies mc_u^2 (17) (light green) and mc_κ^2 (16) (gray) are also shown for reference. In all plots the uniform to supersolid transition point is indicated by the white to light blue shaded area in the background. The uniform results are continued below the transition (where it is metastable) until it becomes dynamically unstable when the roton softens (at $a_s \approx 99a_0$). Insets in (a) and (b) show the behavior near the transition in detail. The other parameters are the same as in Fig. 1.

droplet crystal, and the superfluidity will vanish, although this is beyond the theories we use here (see [46]).

The elastic parameters extracted from the ground-state solutions are presented in Figs. 4(b) and 5(b), with f_s appearing in Figs. 1(a) and 2(a). From these parameters we can evaluate the hydrodynamic predictions for the speeds of sound from Eqs. (11)–(13). These results are plotted as symbols in Figs. 4(a) and 5(a) and reveal excellent agreement with the BdG results. It is interesting to consider the role of the density-strain term $\alpha_{\rho u}$, as our results show this term is relatively small, and it is neglected in some treatments [12,15]. For the dipolar results, dropping this term shifts the hydrodynamic prediction for c_2 down by about 0.3% and the c_1 prediction up by 0.4%. Including the density-strain term gives results in better agreement with the BdG results, but both sets of results are almost indiscernible from the BdG results on the scales of our figures.
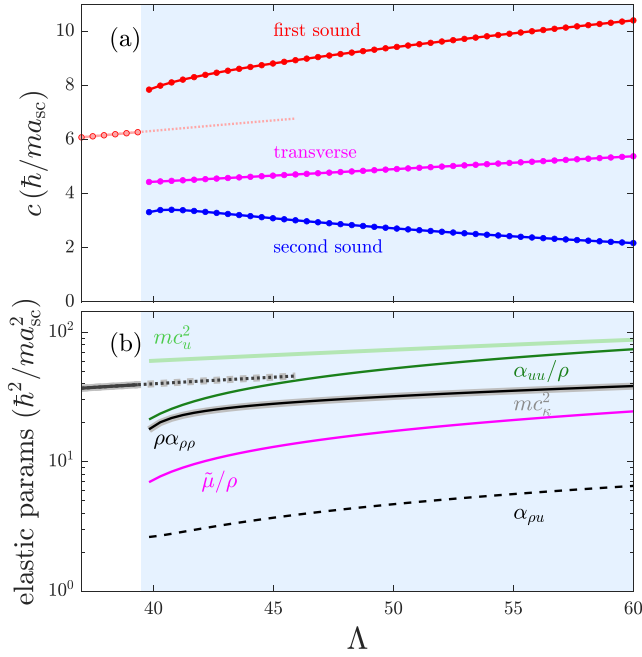
FIG. 5. Elastic properties and speeds of sound for a 2D soft-core BEC at the first-order transition to a supersolid. (a) Speeds of sound and (b) elastic parameters. The color code and the quantities are the same as in Fig. 4. The uniform results are continued below the transition (where it is metastable) until it becomes dynamically unstable when the roton softens (at $\Lambda = 46.30$).

D. Limiting behavior

To gain a deeper understanding of the behavior of these systems it is useful to introduce the characteristic speeds c_κ and c_u [47], defined as

$$mc_\kappa^2 \equiv \rho \frac{\alpha_{\rho\rho}\alpha_{uu} - \alpha_{\rho u}^2}{\alpha_{uu}} = \frac{1}{\rho\kappa}, \tag{16}$$

$$mc_u^2 \equiv \frac{\alpha_{uu}}{\rho_n}. \tag{17}$$

The first speed is associated with the system compressibility κ [14,47], and the second is associated with the lattice elastic properties. In the uniform superfluid, with a single gapless excitation branch that dominates the low-q density response of the system, c_κ describes the first sound.[5] In the supersolid phase neither of these characteristic speeds corresponds to any of the speeds of sound, but they are useful for defining two regimes of behavior. For reference, we indicate these quantities compared to the other elastic parameters in Figs. 4(b) and 5(b). We observe that $c_\kappa \gg c_u$ in the dipolar supersolid, whereas $c_\kappa \ll c_u$ in the soft-core case. This emphasizes the contrasting importance of compressibility and lattice elasticity in the properties of the two supersolids.

---

[5]Here α_{uu} and $\alpha_{\rho u}$ are both zero, and Eq. (11) reduces to c_κ.
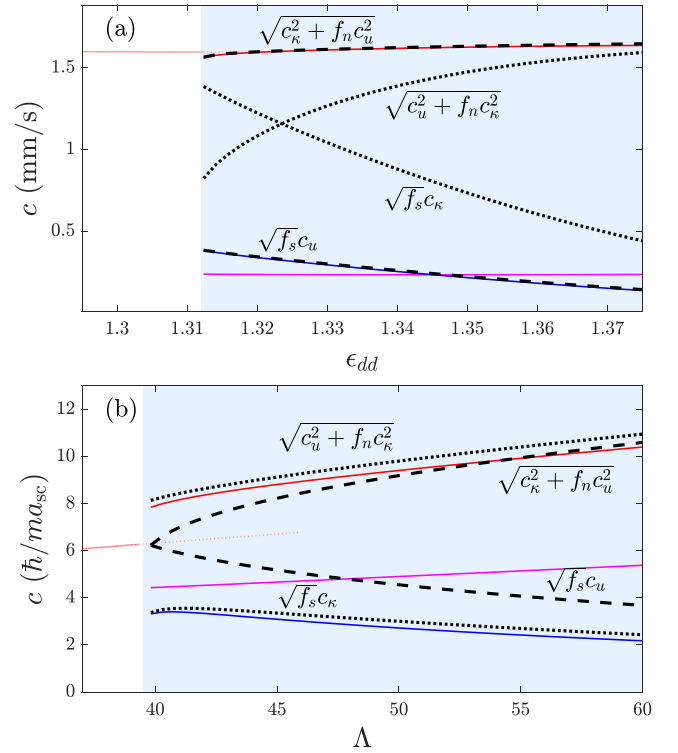

FIG. 6. Comparison of first and second speeds of sound to limiting results for the (a) dipolar and (b) soft-core results. Colored solid and dotted lines are the BdG results for the speeds of sound, with the same colors as used in Figs. 4(a) and 5(a). Black dotted and dashed lines indicate the rigid-lattice and bulk-incompressibility limiting results for c_1 and c_2.

1. Bulk-incompressible limit

We take the bulk-incompressible limit to be when $c_u \ll c_\kappa$, which is relevant to the dipolar supersolid. Within this regime c_t is unaffected, but c_1 and c_2 become

$$c_1 \to \sqrt{c_\kappa^2 + f_n c_u^2}, \tag{18}$$

$$c_2 \to \sqrt{f_s} c_u, \tag{19}$$

where $f_n = 1 - f_s$ is the normal fraction. These two limits approximately describe the first and second sound velocities in the dipolar model, as shown in Fig. 6(a).

2. Rigid-lattice limit

The rigid-lattice limit occurs when $c_u \gg c_\kappa$. As noted before, this is the regime appropriate for the soft-core supersolid. Within this regime c_t is unaffected, but c_1 and c_2 become

$$c_1 \to \sqrt{c_u^2 + f_n c_\kappa^2}, \tag{20}$$

$$c_2 \to \sqrt{f_s} c_\kappa. \tag{21}$$

These two limits approximately describe the first and second sound velocities in the soft-core 2D model, as shown in Fig. 6(b).

The extreme case $c_u \to \infty$ can be realized with a BEC loaded into an optical lattice.[6] Here the lattice sites cannot move (cf. Refs. [48,49]), and the system has a single gapless band corresponding to the second sound.

V. OUTLOOK AND CONCLUSIONS

In this paper we contrasted the excitation spectra of $D = 2$ supersolids arising in two different systems. We focused on the three gapless excitation branches and their associated speeds of sound. Our work demonstrates that hydrodynamic theory provides an accurate prediction of the speeds of sound based only on a set of generalized elastic parameters that are determined from ground-state calculations. We found that the dipolar system is dominated by its compressibility ($c_\kappa \gg c_u$), whereas the soft-core system is in the rigid-lattice regime ($c_\kappa \ll c_u$). As a result, the first sound speed of the dipolar system is significantly larger than the other speeds of sound, and there is barely any jump in the first sound speed at the superfluid to supersolid transition. A recent proposal suggested a method for measuring the long-wavelength excitation frequencies and longitudinal speeds of sound in a one-dimensional supersolid using a periodic optical potential [15]. This method can be directly extended to the 2D supersolid.

Our results will provide a basis for better understanding the equilibrium and dynamical properties of higher-dimensional supersolids, which are being explored in experiments with dipolar gases. We also calculated the excitations and compared them to the hydrodynamic theory for a higher-density dipolar BEC ($\rho = 0.08/a_{dd}^2$) and found results that are qualitatively similar to those presented here, except that c_κ is slightly larger. An interesting remaining question is to extend our analysis to even higher densities, where the dipolar supersolid transitions to a stripe state or a hexagonal state. An interesting aspect of the stripe state is that its superfluid fraction and elastic tensor will become anisotropic. Such high densities will be difficult to reach in experiments with magnetic gases, but these parts of the phase diagram might be accessible to polar molecules gases, which have strong dipole-dipole interactions [50,51]. This presents a rich playground for studying superfluidity in the presence of crystalline order.

Note added. Recently, we became aware of Ref. [52], which also considers the elastic properties of soft-core supersolids.

ACKNOWLEDGMENTS

---

[6]This is an artificial supersolid because translational invariance is not spontaneously broken.

APPENDIX A: PLANAR DIPOLAR BEC

Here we discuss the details of our model of a planar dipolar BEC of magnetic atoms. The atoms are free move in the xy plane, and the planar kinetic energy is given by

$$T_{\mathbf{v}} = \frac{(-i\hbar \nabla_\perp + m\mathbf{v})^2}{2m}, \tag{A1}$$

where $\nabla_\perp$ is the 2D gradient and we have allowed for a superfluid velocity $\mathbf{v}$ (cf. [8,53]). In the z direction the single-particle Hamiltonian includes harmonic confinement,

$$H_z = -\frac{\hbar^2}{2m}\frac{\partial^2}{\partial z^2} + \frac{1}{2}m\omega_z^2 z^2, \tag{A2}$$

with ω_z being the angular frequency. The magnetic dipole moments of the atoms are taken to be polarized along z by a bias field, and the interactions are described by the potential

$$U(\mathbf{r}) = \frac{4\pi a_s \hbar^2}{m}\delta(\mathbf{r}) + \frac{3a_{dd}\hbar^2}{mr^3}\left(1 - 3\frac{z^2}{r^2}\right), \tag{A3}$$

where $\mathbf{r} = \mathbf{x} - \mathbf{x}'$ is the relative separation between the particles. Here a_s is the s-wave scattering length, $a_{dd} = m\mu_0\mu_m^2/12\pi\hbar^2$ is the dipole length, and μ_m is the atomic magnetic moment. The ratio $\epsilon_{dd} = a_{dd}/a_s$ characterizes the relative strength of the dipole-dipole to s-wave interactions, and when this parameter is sufficiently large, the ground state undergoes a transition to a crystalline state with spatial modulation in the xy plane.

The Gross-Pitaevskii equation (GPE) energy functional for this system is

$$E = \int_{\text{uc}} d\mathbf{x}\, \psi^* \left(T_{\mathbf{v}} + H_z + \tfrac{1}{2}\Phi + \tfrac{2}{5}\gamma_{\text{QF}}|\psi|^3\right)\psi, \tag{A4}$$

where we have introduced the effective potential

$$\Phi(\mathbf{x}) = \int d\mathbf{x}'\, U(\mathbf{x} - \mathbf{x}')|\psi(\mathbf{x}')|^2 \tag{A5}$$

and the effects of quantum fluctuations are described by the term with the coefficient $\gamma_{\text{QF}} = \frac{128\pi\hbar^2}{3m}a_s\sqrt{\frac{a_s^3}{\pi}}\mathcal{Q}_5(\epsilon_{dd})$, where $\mathcal{Q}_5(x) = \text{Re}\{\int_0^1 du[1 + x(3u^2 - 1)]^{5/2}\}$ [54]. Because the system is infinite in the xy plane, we restrict the spatial extent of the wave function to the unit cell (uc) defined by the direct lattice vectors $\{\mathbf{a}_1, \mathbf{a}_2\}$ and impose periodic boundary conditions. To accurately calculate $\Phi(\mathbf{x})$ in the unit cell we employ the z-cutoff truncated interaction potential introduced in Ref. [55].

The average density condition enforces the following normalization constraint on the wave function:

$$\int_{\text{uc}} d\mathbf{x}\, |\psi(\mathbf{x})|^2 = \rho A, \tag{A6}$$

where $A = |\mathbf{a}_1 \times \mathbf{a}_2|$ is the area of the unit cell. The ground state is determined for a specified value of ρ and $\mathbf{v} = \mathbf{0}$ by minimizing the energy density

$$\mathcal{E}(\rho, \mathbf{a}_1, \mathbf{a}_2, \mathbf{v}) \equiv E/A \tag{A7}$$

with respect to the unit-cell parameters $\{\mathbf{a}_1, \mathbf{a}_2\}$. For the purpose of computing the elastic parameters, we are also interested in small changes in the parameters $\{\rho, \mathbf{a}_1, \mathbf{a}_2, \mathbf{v}$

(i.e., to make finite-difference derivatives) from the ground-state values. In this case the energy density is minimized with respect to ψ, but with the other parameters specified.

APPENDIX B: THE 2D SOFT-CORE CONDENSATE

The 2D soft-core model is for a BEC of atoms in the xy plane interacting with a potential of the form $U_{sc}(\mathbf{r}) = U_0 \theta(a_{sc} - |\mathbf{r}|)$, where a_{sc} is the soft-core radius, U_0 is the potential strength, and θ is the Heaviside step function. The mean-field energy functional for this system is similar to that in the dipolar case, but without any z direction or quantum fluctuations:

$$E = \int_{uc} d\mathbf{x}\, \psi^*\left(T_{\mathbf{v}} + \tfrac{1}{2}\Phi_{sc}\right)\psi, \qquad (B1)$$

where

$$\Phi_{sc}(\mathbf{x}) = \int d\mathbf{x}'\, U_{sc}(\mathbf{x} - \mathbf{x}')|\psi(\mathbf{x}')|^2. \qquad (B2)$$

In this system it is convenient to adopt a_{sc} as the unit of length and $\hbar\omega_0 = \hbar^2/ma_{sc}^2$ as the unit of energy and to define the dimensionless interaction parameter as

$$\Lambda = \frac{m\pi\rho a_{sc}^4 U_0}{\hbar^2}. \qquad (B3)$$

The normalization condition, definition of the energy density, and procedure to obtain ground states are then the same as described for the dipolar case.

It is worth noting that as discussed by Macrì *et al.* [28], for any finite value of Λ the mean-field description of the 2D soft-core system will be valid for a sufficiently high density ρ. There have also been comparisons validating the mean-field 2D soft-core model against quantum Monte Carlo results in Ref. [28] (also see [37]).

APPENDIX C: BOGOLIUBOV–DE GENNES EQUATIONS

The Bogoliubov–de Gennes (BdG) framework describes the quasiparticle excitations about a stationary solution $\psi(\mathbf{x})$.[7] This solution satisfies the time-independent GPE $\mathcal{L}\psi = \mu\psi$, where

$$\mathcal{L} = T_{\mathbf{0}} + \Phi_{sc} \quad \text{(soft core),} \qquad (C1)$$

$$\mathcal{L} = T_{\mathbf{0}} + H_z + \Phi + \gamma_{QF}\psi^3 \quad \text{(dipolar),} \qquad (C2)$$

and μ is the chemical potential.

The quasiparticle modes can be determined by linearizing the time-dependent evolution, $i\hbar\dot{\Psi} = \mathcal{L}\Psi$, with an expansion of the form given in Eq. (2). This leads to the BdG equations

$$\begin{pmatrix} \mathcal{L} + X - \mu & -X \\ X & -(\mathcal{L} + X - \mu) \end{pmatrix} \begin{pmatrix} u_{\nu\mathbf{q}} \\ v_{\nu\mathbf{q}} \end{pmatrix} = \hbar\omega_{\nu\mathbf{q}} \begin{pmatrix} u_{\nu\mathbf{q}} \\ v_{\nu\mathbf{q}} \end{pmatrix}, \qquad (C3)$$

where $u_{\nu\mathbf{q}}$ and $v_{\nu\mathbf{q}}$ have the Bloch form $f_{\nu\mathbf{q}}(\mathbf{x}) = \bar{f}_{\nu\mathbf{q}}(\mathbf{x})e^{i\mathbf{q}\cdot\mathbf{x}}$, with $\bar{f}_{\nu\mathbf{q}}(\mathbf{x})$ being periodic in the unit cell, and X is defined so that

$$Xf = \psi \int d\mathbf{x}'\, U_{sc}(\mathbf{x} - \mathbf{x}')f(\mathbf{x}')\psi(\mathbf{x}') \quad \text{(soft core),} \qquad (C4)$$

$$Xf = \psi \int d\mathbf{x}'\, U(\mathbf{x} - \mathbf{x}')f(\mathbf{x}')\psi(\mathbf{x}') + \frac{3}{2}\gamma_{QF}\psi^3 f \quad \text{(dipolar).} \qquad (C5)$$

APPENDIX D: EULER LAGRANGE EQUATIONS

From Eq. (10) we obtain the Euler-Lagrange equations to describe the evolution of the hydrodynamic fields,

$$\hbar\partial_t\phi = -\alpha_{\rho\rho}\delta\rho - \alpha_{\rho u}\partial_i u_i, \qquad (D1)$$

$$m(\partial_t\delta\rho - \rho_n\partial_{ti}u_i) = -\hbar\rho_s\partial_i^2\phi, \qquad (D2)$$

$$\rho_n\left(m\partial_t^2 u_i - \hbar\partial_{ti}\phi\right) = \alpha_{\rho u}\partial_i\delta\rho + C_{ijkl}\partial_{jk}u_l. \qquad (D3)$$

We can further decompose $\mathbf{u} = \mathbf{u}_t + \mathbf{u}_l$ in to transverse ($\mathbf{u}_t$ with $\nabla \cdot \mathbf{u}_t = 0$) and longitudinal ($\mathbf{u}_l$ with $\nabla \times \mathbf{u}_l = 0$) parts. Using this decomposition and Eq. (8), the last Euler-Lagrange equation can be written as

$$\rho_n\left(m\partial_t^2\mathbf{u}_l - \hbar\partial_t\nabla\phi\right) = \alpha_{\rho u}\nabla\delta\rho + \alpha_{uu}\nabla^2\mathbf{u}_l, \qquad (D4)$$

$$\rho_n m\partial_t^2\mathbf{u}_t = \tilde{\mu}\nabla^2\mathbf{u}_t. \qquad (D5)$$

The normal-mode solutions of these equations are of the form $X = X_w e^{i(\mathbf{q}\cdot\mathbf{x}-\omega t)}$, where $X = \{\delta\rho, \phi, u_l, u_t\}$ and X_w is the excitation amplitude (also see [14,47]). Three nontrivial solutions can be found with dispersion relations of the form $\omega = cq$, yielding the speeds of sound given in Eqs. (11)–(13).

---

[7]Here we consider solutions for $\mathbf{v} = 0$ where ψ can be taken to be real.

---

[1] H. Watanabe and T. Brauner, Spontaneous breaking of continuous translational invariance, Phys. Rev. D **85**, 085010 (2012).

[2] J. Léonard, A. Morales, P. Zupancic, T. Esslinger, and T. Donner, Supersolid formation in a quantum gas breaking a continuous translational symmetry, Nature (London) **543**, 87 (2017).

[3] J.-R. Li, J. Lee, W. Huang, S. Burchesky, B. Shteynas, F. Ç. Top, A. O. Jamison, and W. Ketterle, A stripe phase with supersolid properties in spin–orbit-coupled Bose–Einstein condensates, Nature (London) **543**, 91 (2017).

[4] L. Tanzi, E. Lucioni, F. Famà, J. Catani, A. Fioretti, C. Gabbanini, R. N. Bisset, L. Santos, and G. Modugno, Observation of a dipolar quantum gas with metastable supersolid properties, Phys. Rev. Lett. **122**, 130405 (2019).

[5] F. Böttcher, J.-N. Schmidt, M. Wenzel, J. Hertkorn, M. Guo, T. Langen, and T. Pfau, Transient supersolid properties in an

array of dipolar quantum droplets, Phys. Rev. X **9**, 011051 (2019).

[6] L. Chomaz, D. Petter, P. Ilzhöfer, G. Natale, A. Trautmann, C. Politi, G. Durastante, R. M. W. van Bijnen, A. Patscheider, M. Sohmen, M. J. Mark, and F. Ferlaino, Long-lived and transient supersolid behaviors in dipolar quantum gases, Phys. Rev. X **9**, 021012 (2019).

[7] G. Natale, R. M. W. van Bijnen, A. Patscheider, D. Petter, M. J. Mark, L. Chomaz, and F. Ferlaino, Excitation spectrum of a trapped dipolar supersolid and its experimental evidence, Phys. Rev. Lett. **123**, 050402 (2019).

[8] S. M. Roccuzzo and F. Ancilotto, Supersolid behavior of a dipolar Bose-Einstein condensate confined in a tube, Phys. Rev. A **99**, 041601(R) (2019).

[9] L. Tanzi, S. M. Roccuzzo, E. Lucioni, F. Famà, A. Fioretti, C. Gabbanini, G. Modugno, A. Recati, and S. Stringari, Supersolid symmetry breaking from compressional oscillations in a dipolar quantum gas, Nature (London) **574**, 382 (2019).

[10] M. Guo, F. Böttcher, J. Hertkorn, J.-N. Schmidt, M. Wenzel, H. P. Büchler, T. Langen, and T. Pfau, The low-energy Goldstone mode in a trapped dipolar supersolid, Nature (London) **574**, 386 (2019).

[11] D. Petter, A. Patscheider, G. Natale, M. J. Mark, M. A. Baranov, R. van Bijnen, S. M. Roccuzzo, A. Recati, B. Blakie, D. Baillie, L. Chomaz, and F. Ferlaino, Bragg scattering of an ultracold dipolar gas across the phase transition from Bose-Einstein condensate to supersolid in the free-particle regime, Phys. Rev. A **104**, L011302 (2021).

[12] J. Hofmann and W. Zwerger, Hydrodynamics of a superfluid smectic, J. Stat. Mech. (2021) 033104.

[13] T. Ilg and H. P. Büchler, Ground-state stability and excitation spectrum of a one-dimensional dipolar supersolid, Phys. Rev. A **107**, 013314 (2023).

[14] C.-D. Yoo and A. T. Dorsey, Hydrodynamic theory of supersolids: Variational principle, effective Lagrangian, and density-density correlation function, Phys. Rev. B **81**, 134518 (2010).

[15] M. Šindik, T. Zawiślak, A. Recati, and S. Stringari, Sound, superfluidity, and layer compressibility in a ring dipolar supersolid, Phys. Rev. Lett. **132**, 146001 (2024).

[16] M. A. Norcia, C. Politi, L. Klaus, E. Poli, M. Sohmen, M. J. Mark, R. N. Bisset, L. Santos, and F. Ferlaino, Two-dimensional supersolidity in a dipolar quantum gas, Nature (London) **596**, 357 (2021).

[17] T. Bland, E. Poli, C. Politi, L. Klaus, M. A. Norcia, F. Ferlaino, L. Santos, and R. N. Bisset, Two-dimensional supersolid formation in dipolar condensates, Phys. Rev. Lett. **128**, 195302 (2022).

[18] Y.-C. Zhang, F. Maucher, and T. Pohl, Supersolidity around a critical point in dipolar Bose-Einstein condensates, Phys. Rev. Lett. **123**, 015301 (2019).

[19] E. Poli, T. Bland, C. Politi, L. Klaus, M. A. Norcia, F. Ferlaino, R. N. Bisset, and L. Santos, Maintaining supersolidity in one and two dimensions, Phys. Rev. A **104**, 063307 (2021).

[20] J. Hertkorn, J.-N. Schmidt, M. Guo, F. Böttcher, K. S. H. Ng, S. D. Graham, P. Uerlings, H. P. Büchler, T. Langen, M. Zwierlein, and T. Pfau, Supersolidity in two-dimensional trapped dipolar droplet arrays, Phys. Rev. Lett. **127**, 155301 (2021).

[21] Y.-C. Zhang, T. Pohl, and F. Maucher, Phases of supersolids in confined dipolar Bose-Einstein condensates, Phys. Rev. A **104**, 013310 (2021).

[22] B. T. E. Ripley, D. Baillie, and P. B. Blakie, Two-dimensional supersolidity in a planar dipolar Bose gas, Phys. Rev. A **108**, 053321 (2023).

[23] A. Gallemí, S. M. Roccuzzo, S. Stringari, and A. Recati, Quantized vortices in dipolar supersolid Bose-Einstein-condensed gases, Phys. Rev. A **102**, 023322 (2020).

[24] F. Ancilotto, M. Barranco, M. Pi, and L. Reatto, Vortex properties in the extended supersolid phase of dipolar Bose-Einstein condensates, Phys. Rev. A **103**, 033314 (2021).

[25] M. Šindik, A. Recati, S. M. Roccuzzo, L. Santos, and S. Stringari, Creation and robustness of quantized vortices in a dipolar supersolid when crossing the superfluid-to-supersolid transition, Phys. Rev. A **106**, L061303 (2022).

[26] E. Poli, T. Bland, S. J. M. White, M. J. Mark, F. Ferlaino, S. Trabucco, and M. Mannarelli, Glitches in rotating supersolids, Phys. Rev. Lett. **131**, 223401 (2023).

[27] S. Saccani, S. Moroni, and M. Boninsegni, Excitation spectrum of a supersolid, Phys. Rev. Lett. **108**, 175301 (2012).

[28] T. Macrì, F. Maucher, F. Cinti, and T. Pohl, Elementary excitations of ultracold soft-core bosons across the superfluid-supersolid phase transition, Phys. Rev. A **87**, 061602(R) (2013).

[29] M. Kunimi and Y. Kato, Mean-field and stability analyses of two-dimensional flowing soft-core bosons modeling a supersolid, Phys. Rev. B **86**, 060510(R) (2012).

[30] J. Hertkorn, J.-N. Schmidt, F. Böttcher, M. Guo, M. Schmidt, K. S. H. Ng, S. D. Graham, H. P. Büchler, T. Langen, M. Zwierlein, and T. Pfau, Density fluctuations across the superfluid-supersolid phase transition in a dipolar quantum gas, Phys. Rev. X **11**, 011037 (2021).

[31] I. Ferrier-Barbut, H. Kadau, M. Schmitt, M. Wenzel, and T. Pfau, Observation of quantum droplets in a strongly dipolar Bose gas, Phys. Rev. Lett. **116**, 215301 (2016).

[32] F. Wächtler and L. Santos, Quantum filaments in dipolar Bose-Einstein condensates, Phys. Rev. A **93**, 061603(R) (2016).

[33] R. N. Bisset, R. M. Wilson, D. Baillie, and P. B. Blakie, Ground-state phase diagram of a dipolar condensate with quantum fluctuations, Phys. Rev. A **94**, 033619 (2016).

[34] Y. Pomeau and S. Rica, Dynamics of a model of supersolid, Phys. Rev. Lett. **72**, 2426 (1994).

[35] C. Josserand, Y. Pomeau, and S. Rica, Coexistence of ordinary elasticity and superfluidity in a model of a defect-free supersolid, Phys. Rev. Lett. **98**, 195301 (2007).

[36] N. Sepúlveda, C. Josserand, and S. Rica, Superfluid density in a two-dimensional model of supersolid, Eur. Phys. J. B **78**, 439 (2010).

[37] F. Cinti, T. Macrì, W. Lechner, G. Pupillo, and T. Pohl, Defect-induced supersolidity with soft-core bosons, Nat. Commun. **5**, 3235 (2014).

[38] S. Prestipino, A. Sergi, and E. Bruno, Freezing of soft-core bosons at zero temperature: A variational theory, Phys. Rev. B **98**, 104104 (2018).

[39] N. Henkel, R. Nath, and T. Pohl, Three-dimensional roton excitations and supersolid formation in Rydberg-excited Bose-Einstein condensates, Phys. Rev. Lett. **104**, 195302 (2010).

[40] F. Cinti, P. Jain, M. Boninsegni, A. Micheli, P. Zoller, and G. Pupillo, Supersolid droplet crystal in a dipole-blockaded gas, Phys. Rev. Lett. **105**, 135301 (2010).

[41] D. Baillie, R. M. Wilson, and P. B. Blakie, Collective excitations of self-bound droplets of a dipolar quantum fluid, Phys. Rev. Lett. **119**, 255302 (2017).

[42] D. T. Son, Effective Lagrangian and topological interactions in supersolids, Phys. Rev. Lett. **94**, 175301 (2005).

[43] W. M. Saslow, Superfluidity of periodic solids, Phys. Rev. Lett. **36**, 1151 (1976).

[44] P. B. Blakie, Superfluid fraction tensor of a two-dimensional supersolid, J. Phys. B **57**, 115301 (2024).

[45] L. D. Landau, L. P. Pitaevskii, E. M. Lifshitz, and A. M. Kosevich, *Theory of Elasticity*, 3rd ed. (Butterworth-Heinemann, Oxford, 1986).

[46] C. Bühler, T. Ilg, and H. P. Büchler, Quantum fluctuations in one-dimensional supersolids, Phys. Rev. Res. **5**, 033092 (2023).

[47] L. M. Platt, D. Baillie, and P. B. Blakie, Sound waves and fluctuations in one-dimensional supersolids, Phys. Rev. A **110**, 023320 (2024).

[48] G. Chauveau, C. Maury, F. Rabec, C. Heintze, G. Brochier, S. Nascimbene, J. Dalibard, J. Beugnon, S. M. Roccuzzo, and S. Stringari, Superfluid fraction in an interacting spatially modulated Bose-Einstein condensate, Phys. Rev. Lett. **130**, 226003 (2023).

[49] J. Tao, M. Zhao, and I. B. Spielman, Observation of anisotropic superfluid density in an artificial crystal, Phys. Rev. Lett. **131**, 163401 (2023).

[50] M. Schmidt, L. Lassablière, G. Quéméner, and T. Langen, Self-bound dipolar droplets and supersolids in molecular Bose-Einstein condensates, Phys. Rev. Res. **4**, 013235 (2022).

[51] N. Bigagli, W. Yuan, S. Zhang, B. Bulatovic, T. Karman, I. Stevenson, and S. Will, Observation of Bose–Einstein condensation of dipolar molecules, Nature (London) **631**, 289 (2024).

[52] M. Rakic, A. F. Ho, and D. K. K. Lee, Elastic properties and thermodynamic anomalies of supersolids, Phys. Rev. Res. **6**, 043040 (2024).

[53] A. N. Aleksandrova, I. L. Kurbakov, A. K. Fedorov, and Y. E. Lozovik, Density-wave-type supersolid of two-dimensional tilted dipolar bosons, Phys. Rev. A **109**, 063326 (2024).

[54] A. R. P. Lima and A. Pelster, Quantum fluctuations in dipolar Bose gases, Phys. Rev. A **84**, 041604(R) (2011).

[55] S. Ronen, D. C. E. Bortolotti, and J. L. Bohn, Bogoliubov modes of a dipolar condensate in a cylindrical trap, Phys. Rev. A **74**, 013623 (2006).

C h a p t e r

4

Exploring superfluid properties: rotation and quantized vortices

The study of the behaviour of a system under rotation provides a way to unambiguously detect its superfluid nature. Unlike classical fluids, which respond to rotation in a continuous manner, superfluids exhibit counter-intuitive effects, such as irrotational flows, non-classical rotational inertia, quantized vortices and critical velocity thresholds for vortex formation. These effects have been studied in many different platforms, ranging from helium [179], bosonic and fermionic condensates [180–182], exciton-polariton condensates [183] to solid state superconductors [184].

Two-dimensional supersolids offer a new platform where non-trivial superfluid behaviours coexist with a solid response. In this chapter, we first introduce the differences between rotating solids and superfluids. We then investigate the rotational properties of supersolids in two distinct regimes. The first corresponds to the linear regime, where the system linearly responds to rotations without the appearance of phase singularities. In this regime, we explore whether information about the superfluid fraction can be extracted from the frequency of the scissor mode. The second regime involves higher rotation frequencies and the system develops quantized vortices, topological defects that manifest as phase singularities. Finally, we report the first experimental observation of vortices in dipolar supersolids.

4.1. How to rotate a dipolar system?

To investigate rotational dynamics in BECs, it is essential to efficiently impart angular momentum to the system. There are many established methods to achieve this, for example by stirring with laser beams [180,181], phase imprinting [185–187] or transferring orbital angular momentum from light [188]. In this section, we present two techniques employed to access and control different dynamical regimes in a dipolar BEC. Specifically, we define the *linear response regime* as the range of small rotation frequencies that induce only linear responses in the system and do not lead to the formation of phase singularities. In contrast, the *vortex regime* regime refers to conditions under which the system accommodates angular momentum through the emergence of singularities in the form of quantized vortices. In both regimes, the rotation frequencies are kept below the radial trapping frequency to avoid inducing anti-trapping effects.

The first technique commonly employed to rotate a BEC is to confine it in an elliptical

trap and dynamically rotate the trap axis at a chosen frequency, Ω [180, 181, 189]. This process can be modelled using the GPE by introducing a time-dependent potential or, equivalently, by solving the equation in the rotating frame (see Sec. 1.2). This approach has been used in the past both to excite small angular oscillations in BECs [190] and also to continuously stir the trap and nucleate vortices [180, 181, 189]. In this chapter, we employ this method to create a sudden rotation of the trap and study the angular oscillations of a supersolid investigate in the linear response regime; see Sec. 4.3.1 and the related publication in Sec. 4.4.

For the study of vortex nucleation we use a different approach genuinely provided by the anisotropic nature of the dipolar interaction. In fact, as discussed in Chapter 1, the magnetostriction effect provides a natural mechanism for deforming the atomic cloud and impart angular momentum into the system [191]. When dipolar atoms are polarized by an external magnetic field, the dipolar interaction elongates the cloud along the polarization direction, favouring head-to-tail configurations that minimize the interaction energy. Starting from a dipolar BEC or a supersolid confined in a cylindrically symmetric trap, tilting the magnetic field away from the $z-$axis breaks the cylindrical symmetry, aligning the cloud or the droplets along the field direction. By continuously rotating the magnetic field at frequency Ω, a process that we refer to as *magnetostirring*, the system rotates [191–193]. In this chapter, we use this approach to study the BEC and supersolid's rotational response in the vortex regime. In both phases, we theoretically study and experimentally observe the nucleation of topological phase defects known as quantized vortices; see Secs. 4.5 and 4.5.2 as well as the related publications in Secs. 4.6 and 4.7.

4.2. Solid and superfluid flow

When considering a classical rigid object from everyday life (e.g., a spinning disk or a classical liquid), its rotation is continuous. This means that the system will respond to rotations at any value of the angular velocity Ω and its response will be proportional to it. The velocity field of the object is purely tangential, with no radial components, and depends only on the distance from the axis of rotation. Specifically, the velocity field is given by

$$\mathbf{v} = \Omega r \hat{e}_\theta \tag{1}$$

where $r = \sqrt{x^2 + y^2}$ is the distance from the rotation axis, that we assume to be the $z-$axis, and $\hat{e}_\theta$ is the unit vector in the azimuthal direction. The angular momentum L_z acquired by the system linearly depends on the moment of inertia I_{rig} and the angular velocity Ω,

$$L_z = I_{rig}\Omega\,. \tag{2}$$

In a rigid body, the moment of inertia I_{rig} is constant[1] and it comes from the spatial density distribution

$$I_{rig} = \langle x^2 + y^2 \rangle = \int d\mathbf{r}\,(x^2 + y^2)n(\mathbf{r})\,. \tag{3}$$

---

[1] In general, the moment of inertia is a tensor that encodes resistance to rotation about each axis of the three dimensional space [194]. Here, we focus on rotation about the $z-$axis and the corresponding $z-$component of the angular momentum, L_z. We also assume the rigid body is non-deformable, so its mass distribution does not change with time.
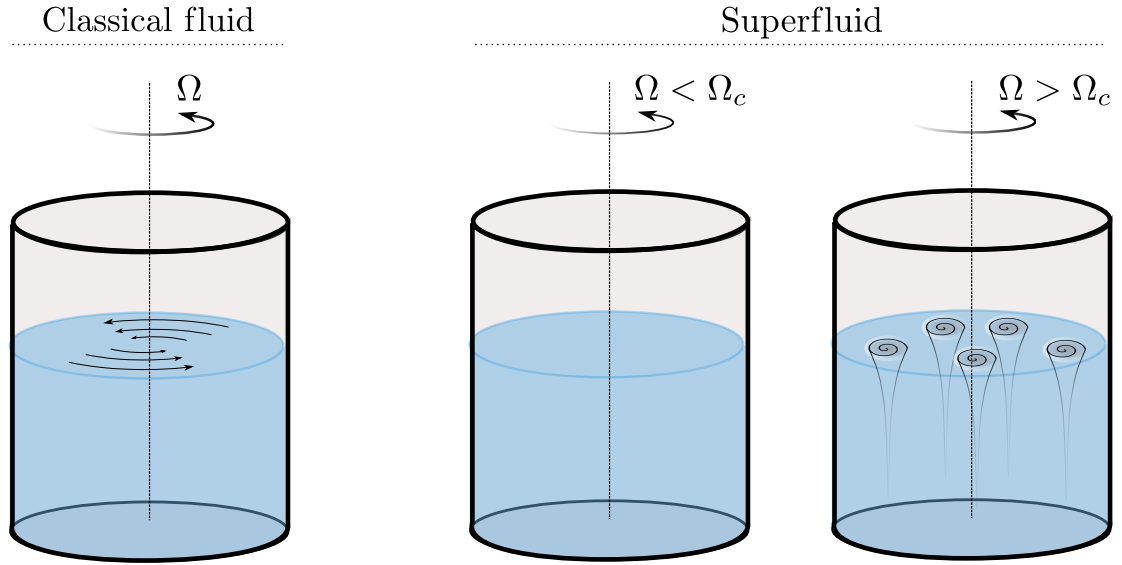
Figure 4.1.: Intuitive illustration of the rotational behaviour of a classical and superfluid fluid in equilibrium in a rotating bucket. A classical fluid normally rotates together with the bucket. A superfluid stays at rest when the bucket rotates slower than the critical frequency Ω_c, whereas it develops quantized vortices when rotating faster than the threshold value.

We will refer to this type of rotational flow, which is continuous and with $L_z \propto \Omega$, as *solid* or rigid behaviour [195]. Notably, this kind of flow is not limited to solid materials. Classical viscous fluids in equilibrium, such as water rotating inside a bucket, also exhibit solid-body-like rotation after transient effects (like surface sloshing or shear) have dissipated. In such a steady state, the velocity field of the liquid mimics that of a rotating solid object, even though the material is not rigid [195]; see the left-hand side of Fig. 4.1.

A superfluid behaves differently. One of its most striking features is the absence of viscosity, i.e. it flows without friction. As a result, it does not exhibit a continuous response to an externally imposed rotation like a normal fluid does. To gain some intuition on the superfluid behaviour, we consider again the picture of a rotating cylindrical bucket. At low angular velocities Ω, it would remain completely at rest, showing no response to the rotation of the container. This lack of rotational response at low Ω arises from the absence of internal friction to transmit angular momentum. At higher velocity frequencies, for values of the frequency larger than a critical value Ω_c (which varies depending on the system), the superfluid would respond to the external rotation by developing some topological defects called *quantized vortices*. These vortices are tiny tornado-like structures where the superfluid circulates around a core of zero density, and each carries a single quantum of angular momentum; see the right-hand side of Fig. 4.1. The number of vortices increases with the rotation frequency, so that the superfluid acquires angular momentum in quantized steps, rather than responding smoothly as a classical fluid would do.

The rotating bucket picture is very helpful to gain some intuition about the difference between classical and superfluid rotational response. However, this picture assumes perfect cylindrical symmetry of the rotating bucket and a purely superfluid system. In different situations, where the system has an explicitly (e.g., asymmetric trap) or

spontaneously broken cylindrical symmetry (e.g., supersolid system), the study of the rotational response requires a more detailed description, as will be discussed in the next sections. In Sec. 4.3 we focus on the linear behaviour of the superfluid at small rotational frequencies, before the onset of vortex nucleation, while vortex nucleation will be discussed separately in Sec. 4.5.

4.3. Linear response regime: irrotational flow

The behaviour of a superfluid system under small rotation arises from quantum mechanical phase coherence across the entire system, which make the fluid irrotational. As seen in Chapter 1, the condensate wave function can be written according to the Madelung transformation

$$\psi(\mathbf{r}, t) = \sqrt{n(\mathbf{r}, t)} e^{i\theta(\mathbf{r}, t)} . \tag{4}$$

Therefore, the following relation for the wave function

$$\frac{\partial}{\partial t} |\psi|^2 = \psi^* \left(\frac{\partial}{\partial t} \psi \right) + \left(\frac{\partial}{\partial t} \psi^* \right) \psi = -\nabla \cdot \left[\frac{\hbar}{2mi} \left(\psi^* \nabla \psi - \psi \nabla \psi^* \right) \right] . \tag{5}$$

can be reformulated in form of the continuity equation:

$$\frac{\partial}{\partial t} n + \nabla \cdot (n\mathbf{v}) = 0 . \tag{6}$$

Here, $\mathbf{v}$ is the velocity field

$$\mathbf{v} = \frac{\hbar}{2mi} \frac{\left(\psi^* \nabla \psi - \psi \nabla \psi^* \right)}{n} = \frac{\mathbf{J}}{n} , \tag{7}$$

written as a function of the probability current $\mathbf{J}$. When using Eq. (4) into Eq. (7), one obtains

$$\mathbf{v} = \frac{\hbar}{m} \nabla \theta , \tag{8}$$

namely the velocity is given by the gradient of the phase of the wave function. From vector calculus, an important consequence is that the velocity field of a superfluid is always irrotational

$$\nabla \times \mathbf{v} = \frac{\hbar}{m} \nabla \times \nabla \theta = 0 , \tag{9}$$

as long as θ contains no singularity. This is true in the limit of linear regime.

In the following, we describe the main properties of the velocity field for a BEC and a supersolid state in different geometries. A vanishing velocity field means that the system does not respond to rotation, resembling the scenario shown in Fig. 4.1. In contrast, when the velocity field is non-zero, the system exhibits a linear response to slow rotations, resulting in a non-zero angular momentum $\langle L_z \rangle$ and non-zero moment of inertia I. Notably, even though I is finite, it generally remains below the classical rigid-body value I_{rig} [71].

In Fig. 4.2 we calculate the velocity field $\mathbf{v}$ of the equilibrium configuration in the rotating-frame obtained from eGPE simulations. We identify the following cases:
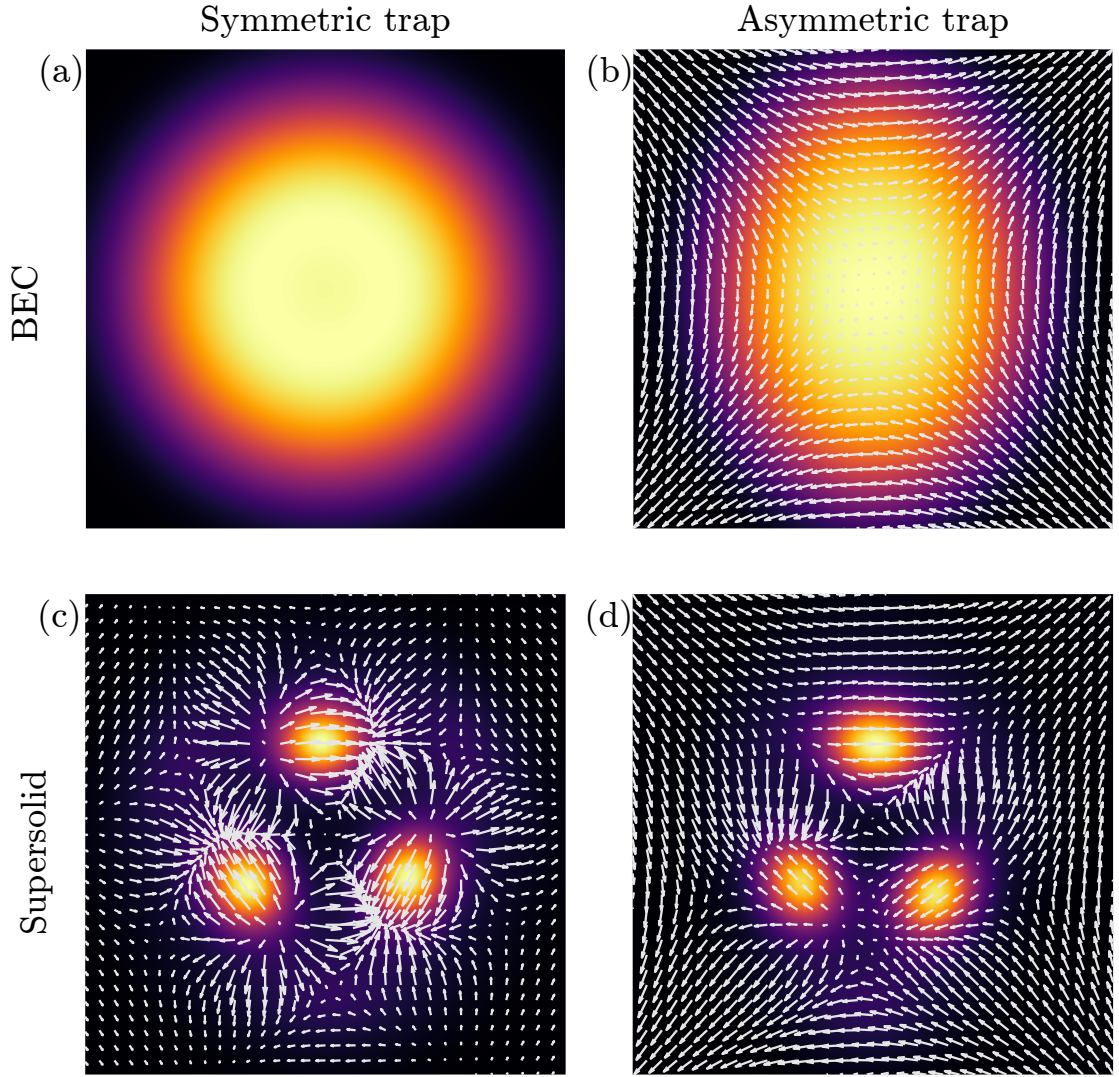
Figure 4.2.: Irrotational velocity fields. (a) The velocity field is zero everywhere because the system is cylindrically symmetric ($I = 0$). (b) The cylindrical symmetry is broken using an asymmetric trap. The system responds to a small rotation with an irrotational flow $\sim \nabla xy$ ($I \neq 0$). (c) The system is confined in a cylindrically symmetric trap but it spontaneously breaks the translational symmetry through the supersolid density modulation ($I \neq 0$). The irrotational flow creates a local counterflow between the droplets and the superfluid background. (d) The system is confined in an asymmetric trap and it spontaneously breaks the translational symmetry ($I \neq 0$). The velocity field combines the $\sim \nabla xy$ character with counterflow features. Parameters: $N = 50000$, $\Omega = 0.5\,\mathrm{Hz}$ (a)-(b) $a_s = 100a_0$, $\omega/2\pi = (50, 50, 95)\,\mathrm{Hz}$ and (c)-(d) $a_s = 95a_0$, $\omega/2\pi = (50, 60, 95)\,\mathrm{Hz}$.

- **Unmodulated BEC in a cylindrically symmetric trap.** The only solution of the GPE satisfying the irrotationality condition is $\mathbf{v} = 0$, i.e. this solution is identical to the non rotating case [196]. The velocity field is zero everywhere and the superfluid does not respond at all to any small rotation. This is the case intuitively described in Fig. 4.1.

- **Unmodulated BEC in a asymmetric trap.** The solution has an elliptical

density profile which rotates about the $z-$axis. The velocity field of the stationary solution has the form [197, 198]

$$\mathbf{v} \propto \nabla(xy).$$ (10)

Since $\mathbf{v} \neq 0$, the system responds to small rotations through this irrotational field.

- **Supersolid in a cylindrically symmetric trap.** The stationary state is a rotating supersolid with a non-zero velocity field, which does not have an analytical solution. The irrotational field is characterized by a counterflow between droplets (following the direction of the trap rotation) and the interstitial superfluid background (that opposes to the trap rotation) [199].

- **Supersolid in a asymmetric trap.** This case combines the previous two, so the solution of the eGPE is an elliptical rotating supersolid. The non-zero velocity field mixes features of the BEC in asymmetric trap $\mathbf{v} \propto \nabla(xy)$ with the droplet and inter-droplet counterflow of the supersolid.

In summary, in the linear response regime one needs to break the cylindrical symmetry to impart a rotation to a superfluid system. This can be done either by explicit symmetry breaking, by imposing an asymmetric trap in the Hamiltonian of the system, or by spontaneous symmetry breaking, crossing the BEC-to-supersolid phase transition. The solid nature of the supersolid, i.e. the density modulation, yields to a non-zero irrotational response even in the cylindrically symmetric trap.

It is important to stress that, in all these cases, the irrotational velocity field distorts the density distribution in a way to mimic rotation. An external observer in the laboratory frame would see the system rotating at the fixed Ω. However, the underlying flow responsible for this behaviour–such as the one reported in Fig. 4.2(b)-(d)–is fundamentally different from the one that leads to the classical rigid-body behaviour described by Eq. (1).

4.3.1. Scissor mode

The presence of a superfluid irrotational flow can affect the frequency of the excitation modes. Here, we consider the *scissors mode*, a collective excitation which describes an angular oscillation of the system with respect to the trap axis. This type of excitation has been predicted to be sensitive to the system's superfluid nature [200], since its frequency is dictated by the value of the moment of inertia $I \leq I_{rig}$, where I_{rig} is the rigid moment of inertia given in Eq. (15). This mode has been widely employed to infer the superfluidity in several systems, from deformed nuclei [201] to trapped BEC [190, 202], Fermi gases [203] and dipolar quantum droplets [204]. In the experiment it can be excited by a sudden small rotation about the $z-$axis of the asymmetric trap, see Fig. 4.3(a). The trap is anisotropic, characterized by an ellipticity

$$\epsilon = \frac{\omega_x^2 - \omega_y^2}{\omega_x^2 + \omega_y^2}.$$ (11)

The frequency of the scissors mode can be estimated using a sum-rule approach [33], assuming that the rotational perturbation excites only a single mode. The operator responsible for the scissor perturbation is $\hat{L}_z$. According to the linear response theory,

the energy of the mode with smallest energy excited by an operator is obtained as the ratio of the energy weighted moments [205]. In this case, the frequency of the scissor mode is

$$\omega_{scissor} = \sqrt{\frac{m_1}{m_{-1}}} = \sqrt{\frac{\int d\omega \, \omega S(\hat{L}_z, \omega)}{\int d\omega \, \omega^{-1} S(\hat{L}_z, \omega)}} \, , \tag{12}$$

where $S(\hat{L}_z, \omega)$ is the dynamic structure factor relative to the angular momentum operator

$$S(\hat{L}_z, \omega) = \sum_n |\langle n|\hat{L}_z|0\rangle|^2 \delta(\omega - \omega_n) \, . \tag{13}$$

Notice that when more than a single mode is excited by the perturbation, Eq. (12) becomes an upper bound.

When the Hamiltonian of the system commutes with $\hat{L}_z$ (and this is the case for a dipolar system with dipoles polarized along z) [33, 155, 199], one obtains

$$\omega_{scissor} = \sqrt{\frac{(\omega_y^2 - \omega_x^2)\langle x^2 - y^2 \rangle}{I}} \, . \tag{14}$$

In practice, the frequency of this mode depends on the geometry of the system (terms at the numerator) and its moment of inertia (at the denominator). The measure of a deviation of the moment of inertia from the rigid-body value would be a consequence of the superfluid nature of the system.

We studied the frequency of the scissor mode for a 2D dipolar supersolid state. It is useful to extract the two limiting values of the scissor frequency, one obtained assuming a solid-body rotation and the other assuming a fully superfluid rotation. In the first case, the moment of inertia is I_{rig}. For the second case, it can be estimated from a variational model [198] as

$$I_{sf} = \beta^2 I_{rig} \tag{15}$$

where the quantity β is

$$\beta = \frac{\langle x^2 - y^2 \rangle}{\langle x^2 + y^2 \rangle} \, . \tag{16}$$

By using Eqs. (15) and (16) into Eq. (14), we find the two limiting cases

$$\omega_{scissor}^{rig} = \sqrt{(\omega_y^2 - \omega_x^2)\beta}$$
$$\omega_{scissor}^{sf} = \sqrt{\frac{(\omega_y^2 - \omega_x^2)}{\beta}} \tag{17}$$

Behaving partially as a solid and partially as a superfluid, one would expect that the frequency of the scissor mode for a supersolid would lie in between these two estimates. However, we found that the behaviour is much more complicated. This work is contained in Ref. [206], which we report in Sec. 4.4.

Due to the geometric dependence, the study of the scissor mode in 1D supersolids confined in elongated traps could prevent an accurate distinction between rigid and superfluid behaviour–an important aspect that in the early studies has not been considered [155, 199]. In fact, when the geometric factor is $\beta \approx 1$ the rigid-body and superfluid scissor mode frequencies become nearly indistinguishable, i.e., $\omega_{scissor}^{rig} \approx \omega_{scissor}^{sf}$ [206].
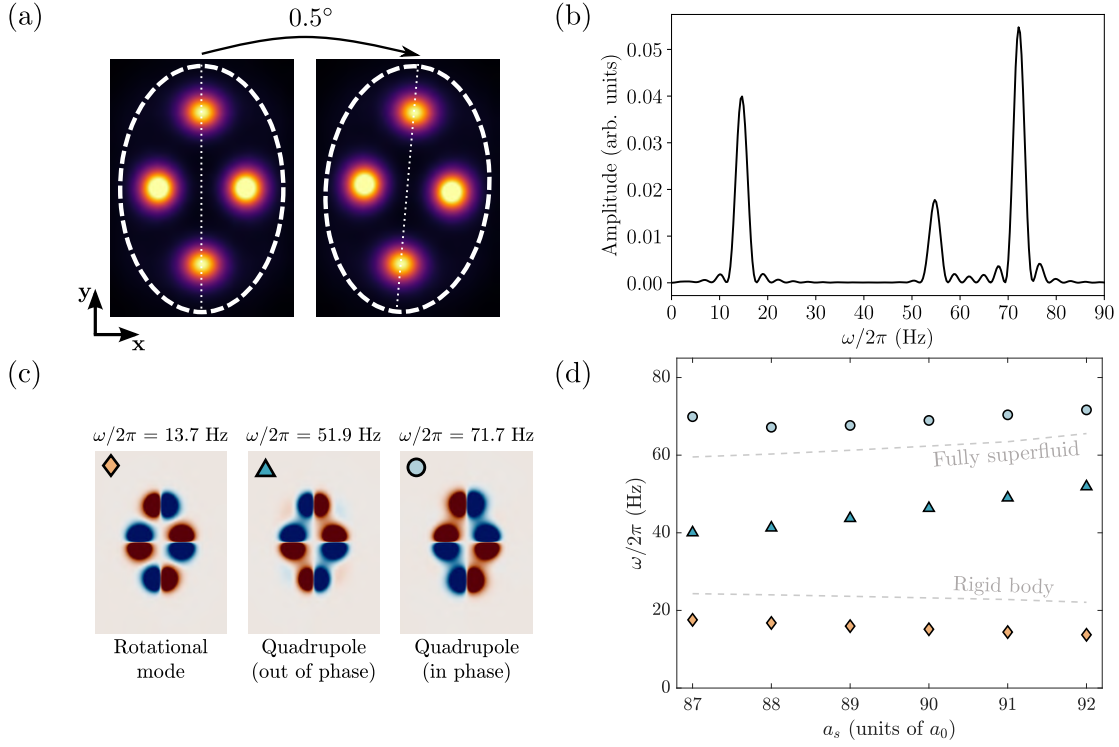
Figure 4.3.: Frequency response of a 2D supersolid perturbed with a scissor oscillation. (a) Sketch of the protocol to excite the scissor mode. (b) Fourier spectrum of an oscillating 2D supersolid with multi-frequency response. (c) Density perturbation of the excited modes from BdG spectrum. (d) Frequency variation of the selected modes as a function of a_s. Parameters: $N = 45000$, trap $\omega/2\pi = (52.7, 65, 122)$ Hz, (a)-(c) $a_s = 92\,a_0$.

In contrast, the realization of 2D supersolids with variable aspect ratios provides an opportunity for a more detailed investigation of these angular oscillations [205, 206]. In our study, we focus on 2D supersolids confined in a harmonic trap with an aspect ratio of $\omega_x/\omega_y \approx 2$. A key advantage of 2D supersolids is also that scissor mode oscillations involve motion of atoms along the inter-droplet density connections, that establish the global phase coherence and the superfluidity.

When exciting the scissor mode in a 2D supersolid, we observe a multi-mode response, manifesting as multiple peaks in the Fourier spectrum in Fig. 4.3(b). The highest peak is the higher frequency one, related to a quadrupole mode that describes in phase oscillations of the crystal with the superfluid background (c). Unfortunately, its frequency is nearly independent on the scattering length and it is always very close with the one for a fully superfluid system $\omega_{scissor}^{sf}$ (d). The middle peak correspond to another quadrupole mode, but with out-of-phase scissor oscillation between the crystal and superfluid background. The lowest frequency peak is a low-frequency rotational mode similar to the one analysed in Sec. 2.7. Importantly, the low frequency modes seems to be more sensitive to the superfluid fraction. This is shown in Fig. 4.3(d), where the frequency of the excited modes is plotted for different scattering lengths.

The lower frequency modes cannot easily be probed in the actual experiment, due to e.g. a limited lifetime of the supersolid state. As a result, only the higher-frequency oscillations have been detectable so far [206]. Suppressing the excitation of higher-

frequency modes with large amplitudes would require a modified experimental protocol [205]. Given the aforementioned limitations, alternative observables provide a more reliable means of directly probing the superfluid nature of the supersolid. For this reason, we investigated a different rotation regime where quantized vortices are nucleated, see Sec. 4.5.

4.4. Publication: Can angular oscillations probe superfluidity in dipolar supersolids?

M. A. Norcia[1], **E. Poli**[2], C. Politi[1,2], L. Klaus[1,2], T. Bland[1,2], M. J. Mark[1,2],
L. Santos[3], R. N. Bisset[2] and F. Ferlaino[1,2]

[1] *Institut für Quantenoptik und Quanteninformation, Österreichische Akademie der Wissenschaften, 6020 Innsbruck, Austria*

[1] *Institut für Experimentalphysik, Universität Innsbruck, 6020 Innsbruck, Austria*

[3] *Institut für Theoretische Physik, Leibniz, Universität Hannover, Hanover, Germany*

---

† The author of the present thesis performed the numerical simulations together with T. B., L. S. and R. N. Bisset and contributed in writing the manuscript.

Can Angular Oscillations Probe Superfluidity in Dipolar Supersolids?

Matthew A. Norcia,[1] Elena Poli,[2] Claudia Politi,[1,2] Lauritz Klaus,[1,2] Thomas Bland,[1,2] Manfred J. Mark,[1,2] Luis Santos,[3] Russell N. Bisset,[2] and Francesca Ferlaino[1,2,*]

[1]*Institut für Quantenoptik und Quanteninformation, Österreichische Akademie der Wissenschaften, Innsbruck 6020, Austria*
[2]*Institut für Experimentalphysik, Universität Innsbruck, Innsbruck 6020, Austria*
[3]*Institut für Theoretische Physik, Leibniz Universität Hannover, 30167 Hannover, Germany*

Angular oscillations can provide a useful probe of the superfluid properties of a system. Such measurements have recently been applied to dipolar supersolids, which exhibit both density modulation and phase coherence, and for which robust probes of superfluidity are particularly interesting. So far, these investigations have been confined to linear droplet arrays, which feature relatively simple excitation spectra, but limited sensitivity to the effects of superfluidity. Here, we explore angular oscillations in systems with 2D structure which, in principle, have greater sensitivity to superfluidity. In both experiment and simulation, we find that the interplay of superfluid and crystalline excitations leads to a frequency of angular oscillations that remains nearly unchanged even when the superfluidity of the system is altered dramatically. This indicates that angular oscillation measurements do not always provide a robust experimental probe of superfluidity with typical experimental protocols.

Some of the most distinctive manifestations of superfluidity in ultracold quantum gases relate to their behavior under rotation. These include the presence of quantized vortices [1–3] and persistent currents in ring traps [4], as well as shape-preserving angular oscillations associated with a "scissors" mode [5]. Measurements of the scissors mode frequency have long been used to illuminate the superfluid properties of a variety of systems [6–11]. With the recent advent of dipolar supersolids [12–18]—states that possess both the global phase coherence of a superfluid and the spatial density modulation of a solid—the scissors mode provides a tempting way to quantify changes in superfluidity across the superfluid-supersolid transition [19,20]. Angular oscillations have also been used to search for superfluid properties in solid helium [21]. In this case, however, a change in oscillation frequency initially attributed to superfluidity was eventually traced, instead, to other reasons [22]. In this Letter, we study more deeply the connection between angular oscillations and superfluidity in dipolar supersolids to determine the extent to which such experiments can inform our understanding of superfluidity in these systems.

The goal of these angular oscillation measurements is to infer the flow patterns allowed for a given fluid. A superfluid is constrained by the single-valued nature of its wave function to irrotational flow (IF), while a nonsuperfluid system faces no such constraint and, in certain situations, may be expected to undergo rigid-body rotation (RBR). Prototypical velocity fields for angular oscillations under IF ($\vec{v} \propto \nabla xy$) and RBR ($\vec{v} \propto r\hat{\theta}$) are depicted in Figs. 1(a) and 1(b), respectively. The velocity field associated with

angular rotation is related to the moment of inertia of the system and, thus, the frequency of angular oscillations.

The ability to distinguish between RBR and IF (and, thus, in principle, between a classical and superfluid
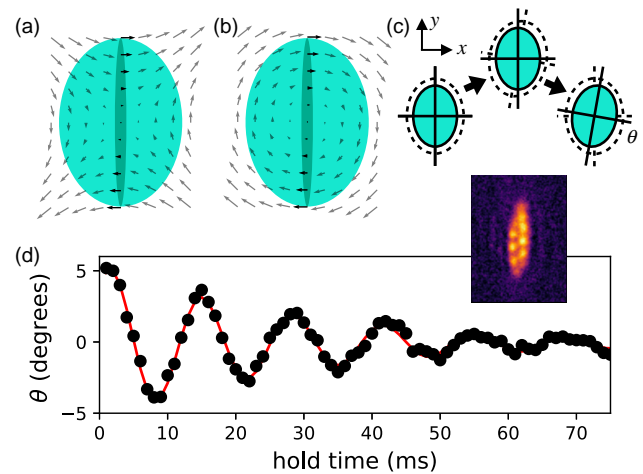

FIG. 1. Characteristic velocity profiles for irrotational flow (a) and rigid-body rotation (b). A wide atomic state (light turquoise oval) samples a region of space where the two differ significantly, while a highly elongated state (dark turquoise oval) samples a region where the two patterns are nearly indistinguishable. (c) We excite oscillations in the angle θ of our atomic gas by rapidly rotating the anisotropic trap (dashed oval), then returning it to its original orientation and observing the subsequent dynamics. (d) Typical example of experimental angular oscillation for the zigzag modulated state shown on the right (image averaged over nine iterations). In this case, the errors from the fit to the state angle are smaller than the markers. The red line is a damped sinusoidal fit used to extract the angular oscillation frequency f_{osc}.

system) depends critically on the geometry of the system, and is sensitive only to the character of the flow pattern where the atomic density is appreciable. As illustrated in Figs. 1(a) and 1(b), highly elongated states sample only the region along the weak axis of the trap (near $x = 0$) where IF and RBR are identical for small rotations (dark turquoise regions), while rounder states (light turquoise regions) sample regions of space where the flow patterns differ significantly and, thus, are far more sensitive to the irrotational constraint. Recent works have focused on systems that form a short linear chain of about two "droplets" [23] in the supersolid regime [19,20].

In this Letter, we study angular oscillations in systems with linear and two-dimensional modulation to disentangle the effect of three important contributions: (i) a narrowing of the aspect ratio of the gas (geometrical change), (ii) a reduction in the population of the low-density superfluid "halo" that occupies the outer regions of the trap, and (iii) a reduction in the density of the interdroplet connection that enables the exchange of atoms between droplets, which is key to the superfluid nature of supersolid systems. We find that, in linear systems, contributions (i) and (ii) dominate the change in oscillation frequency associated with the onset of modulation, while (iii) has a negligible effect.

In dipolar condensates with two-dimensional structure, which have been a focus of recent work [24–28], the effects of geometry and superfluidity may be disentangled, and one may expect to observe a direct link between a change of the superfluid fraction and a modification of the angular oscillation frequency. However, we find that the physics at play is much more complex. Indeed, not only does the oscillation frequency fail to approach its rigid-body value for states with a vanishing superfluid connection, but it remains very close to the value predicted for a superfluid state. We extensively investigate the system behavior as a function of geometry and interaction parameters, revealing a unique multimode response of the dipolar supersolid.

Experimentally, we use a dipolar quantum gas of ^{164}Dy atoms (up to approximately 5×10^4 condensed atoms), confined within an optical dipole trap (ODT) of tunable geometry, formed at the intersection of three laser beams [25,27,29]. The trap geometry and particle number at the end of the evaporative cooling sequence determine the character of the modulated ground state, which can form linear, zigzag, or triangular lattice configurations [28]. By varying the applied magnetic field in the vicinity of Feshbach resonances near 18–23 G, we can access scattering lengths that correspond to either unmodulated BECs or modulated states. In past works, we have demonstrated that modulated states created at the corresponding field have global phase coherence [25,27]. In this Letter, we expect the same to be true, but refer to these experimental states simply as modulated, as we do not repeat the characterization for every trap condition used. We excite angular oscillations by using the well-established protocol of
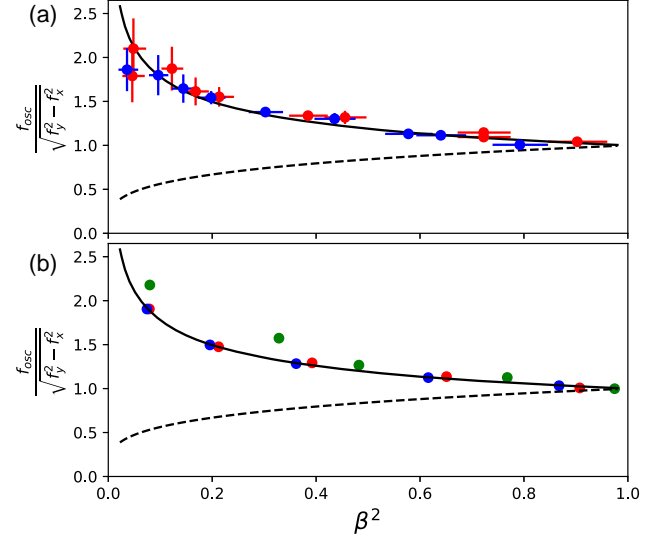

FIG. 2. Normalized oscillation frequencies f_{osc} from experiment (a) and simulation (b). Blue points represent unmodulated BECs, red points represent modulated states (expt.) and supersolid states (sim.), and green points represent independent droplet arrays. Solid lines are predictions for irrotational flow f_{irr}. Dashed lines are predictions for rigid body rotation f_{rig}. The trap frequencies used in the simulation, from left to right, are $(f_x, f_y) = [(43, 53), (40, 57), (37, 62), (32, 70), (26, 87)]$ Hz. $f_z = 122$ Hz for all cases. A similar range is used in the experiment.

applying a sudden small rotation of the trap, by varying the relative powers in the ODT beams for 6 ms before returning them to their original values [Fig. 1(c)]. Using our high-resolution imaging [30], we observe the in-trap density profile at a variable time from the excitation, and extract the angle of the major and minor axes using a two-dimensional Gaussian fit to the state [31].

A typical angular oscillation is shown in Fig. 1(d), for a "zigzag" modulated state [25]. From such oscillation traces, we extract the dominant oscillatory frequency f_{osc} using a fit to an exponentially damped sinusoid. Typically, the statistical error on our measurements of f_{osc} is on the sub-Hertz level, better than our knowledge of the trap frequencies, due to drifts between calibrations. We perform such measurements for trap geometries ranging from an elongated cigar shape to pancake shaped, and for different scattering lengths, as summarized in Fig. 2(a).

Within a single-mode approximation, the angular oscillation frequency f_{osc} can be predicted using either a sum-rule based approach [19,34], or considerations based on hydrodynamic flow [5]. For RBR, the angular oscillation frequency is given by $f_{\mathrm{rig}} = \sqrt{(f_y^2 - f_x^2)}\beta$, whereas for IF, the predicted value is $f_{\mathrm{irr}} = \sqrt{(f_y^2 - f_x^2)/\beta}$ [19,20]. Here, $f_{x,y}$ are the trap frequencies along directions x and y. $\beta = \langle x^2 - y^2 \rangle / \langle x^2 + y^2 \rangle$ is a geometrical factor that quantifies the degree of elongation of the atomic cloud (but carries no

information about the superfluid fraction). As shown in Fig. 2, $f_{\rm rig}$ and $f_{\rm rig}$ are more distinct for smaller values of β. Remarkably, independent of trap geometry or the presence of modulation, we observe $f_{\rm osc}$ close to the IF prediction and far from the RBR prediction when the two predictions differ appreciably.

To gain a deeper understanding of our observations, we theoretically study the oscillation dynamics using a real-time simulation of the extended Gross-Pitaevskii equation (EGPE) [35–37]. To compare to the experimental observations of Fig. 2(a), first, we calculate the ground state for a given trap, scattering length, and atom number. Then, we apply a $0.5°$ rotation of the trap for 6 ms (we have confirmed that the character and frequency of the response do not change for much larger excitations), and then let the state evolve for 50 ms. Then, we perform the same fitting procedure as used in the experiment to extract $f_{\rm osc}$. For the simulation, we calculate β directly for the ground state (we confirm that the exact value of β agrees with that extracted from a Gaussian fit at the 5% level). For simulations performed on states ranging from the unmodulated BEC to supersolid (SS) to independent droplet (ID) regimes, with vanishing superfluid connection between droplets, we again find that $f_{\rm osc}$ is always very close to $f_{\rm irr}$, in very good agreement with the experimental data. For isolated droplet states in particular, $f_{\rm osc}$ can actually be even higher than the expected value for irrotational flow, indicating that the oscillation frequency is not necessarily in between the irrotational and rigid body values.

To further illuminate the dependence $f_{\rm osc}$ on superfluidity, we analyze the results of the simulation as a function of the s-wave scattering length a_s (Fig. 3). Scattering lengths of $85a_0$ yield arrays of (nearly) independent droplets, while $a_s = 97a_0$ produces an unmodulated BEC. In between, we find supersolid states, with low-density connections between droplets. Inspired by the formulation of Leggett [38], we quantify the degree of interdroplet density connection as $\mathcal{C} = [\int dx/\rho(x)]^{-1}$, where $\rho(x)$ is the projected atomic density, evaluated over the interdroplet connection [Fig. 3(a)] [39].

As shown in Fig. 3, despite the rapid reduction of $\mathcal{C}$ with a_s, the simulated $f_{\rm osc}$ exhibits a rather constant behavior with a value always close to the purely irrotational predictions, $f_{\rm irr}$, for both a linear (1D) and hexagon state (2D). This observation indicates that (i) the degree of interdroplet connection is not actually a major determinant of the angular oscillation frequency and (ii) that the system does not undergo RBR even for vanishingly small interdroplet density connection. The latter conclusion is particularly evident for hexagon states, where the rigid-body prediction substantially departs from the irrotational one. For the linear array, the elongated geometry means that the $f_{\rm rig}$ and $f_{\rm irr}$ differ only slightly; see Supplemental Material for further discussion [31].

At this point, we can clearly see the geometrical limitations of the linear systems. In linear systems, the
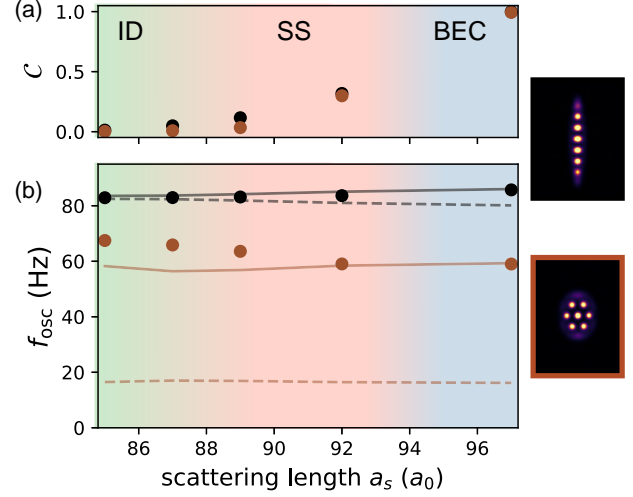

FIG. 3. Impact of scattering length on simulated scissors mode frequencies. (a) Interdroplet connection $\mathcal{C}$ (defined in text) versus scattering length for different trap geometries. The calculated ground state in each trap is shown on the right, with corresponding border colors. (b) Scissors mode frequency versus scattering length. Solid lines are predictions for irrotational flow $f_{\rm irr}$. Dashed lines are predictions for rigid body rotation $f_{\rm rig}$. β ranges from 0.93 to 0.99, and 0.27 to 0.31 in the linear and hexagonal cases, respectively.

narrowing of the atomic density distribution that occurs with the onset of modulation causes the dominant contribution to a modification in oscillation frequency as well as a reduction in sensitivity of the oscillation frequency to superfluidity. Simultaneously, the transfer of atoms from the halo to the droplets leads to a reduction of the superfluidity of the composite halo-droplet system, which is accompanied by a small change in the oscillation frequency. However, because the motion induced by rotation in a linear system is perpendicular to the interdroplet axis, these effects should not be interpreted as a result of the weakening superfluid connection along the interdroplet axis. In contrast, systems with two-dimensional structure maintain a relatively round aspect ratio in the modulated regime, and the rotational motion does orient along certain interdroplet axes.

To better understand the nonrigid nature of the angular oscillations, we employ a method to extract the character of the system's response by analyzing our experimental and EGPE simulation dynamics in the frequency domain with respect to time, but in the position domain with respect to the spatial coordinates. A similar technique has been applied along one dimension to understand the mode structure of an elongated condensate [40]. This technique, which for convenience we refer to as "Fourier transform image analysis" (FTIA) [31], allows us to extract a power spectrum of density fluctuations driven by the angular excitation, as well as the spatial form of the density fluctuations at each frequency. For comparison, we also
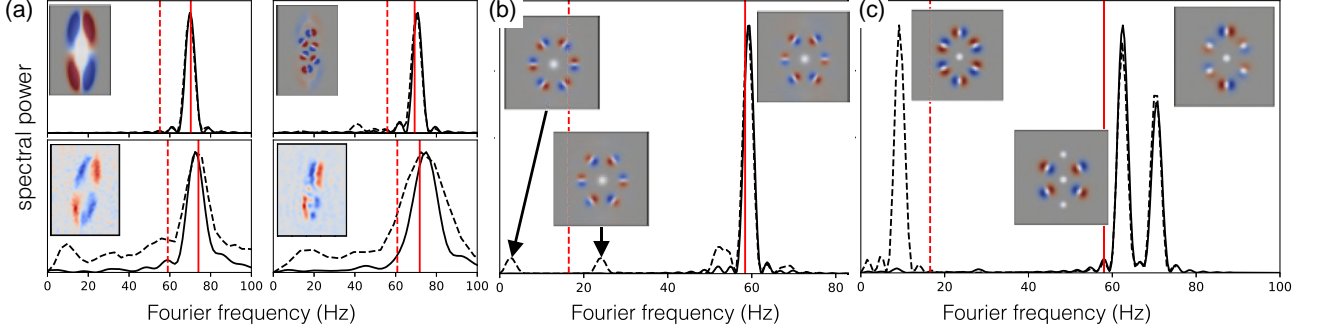
FIG. 4. Analysis of mode shapes and response due to angular excitation. Solid lines are the power spectrum obtained from the rotational signal (θ in the experiment and $\langle xy \rangle$ in the simulation), and dashed lines are obtained from FTIA (see text, Supplemental Material [31] for description). Inset panels show the mode shapes for selected modes. Red and blue indicate out-of-phase changes in density, overlaid onto the average density profile in the panels corresponding to simulation (gray to white). Solid and dashed vertical red lines represent f_{irr} and f_{rig}, respectively. (a) Responses in elongated traps from simulation (top) and experiment (bottom), for an unmodulated BEC (left) and a zigzag droplet state (right). Trap frequencies are $f_{x,y} = [31(1), 73(1), 128(1)]$ Hz, and $f_{x,y,z} = [32, 70, 122]$ Hz for the experiment and theory, respectively. (b) Simulated response of supersolid hexagon state ($a_s = 92a_0$). (c) Simulated response of droplet crystal hexagon state ($a_s = 85a_0$). Note that the ground state has a different orientation for the two scattering lengths in this trap. Trap frequencies are $f_{x,y,z} = [43, 53, 122]$ Hz for (b) and (c).

calculate the spectral power of our rotational signal through a Fourier transform. For computational robustness, we use the fitted angle θ in the experimental case, and $\langle xy \rangle$ for the simulations. To enhance our frequency resolution, we analyze simulations with longer durations than are accessible in the experiment (160 to 290 ms).

We apply the FTIA to both simulation and experimental images in Fig. 4(a). For a BEC, the FTIA gives a dominant peak in both simulation and experiment, whose frequency and shape are consistent with a scissors mode oscillation at the frequency observed from the angular response. For a zigzag modulated state, we again predominantly observe a single peak in the FTIA spectrum at the frequency of the angular oscillation. In the simulation, we can see that the mode corresponds to the motion of the different droplets in a pattern reminiscent of IF in an unmodulated superfluid, and clearly distinct from RBR. In the experiment, the response of individual droplets is not visible due to shot-to-shot fluctuations in the exact number and position of the droplets, but the overall structure is similar to the simulation.

For hexagonal supersolid [Fig. 4(b)] and isolated droplet [Fig. 4(c)] states, the FTIA reveals a clear multifrequency response. For the supersolid, we observe the excitation of modes near 3 and 25 Hz that do not contribute strongly to $\langle xy \rangle$. The droplet motion associated with the 3 Hz mode is approximately (but not exactly) shape preserving, and the frequency is much lower than would be expected for a single-mode RBR response. For the isolated droplet array, we again observe a nearly shape-preserving low-frequency response from FTIA, as well as a dominant angular response that is split into two frequencies, both above the scissors mode frequency f_{irr} expected for a superfluid with the same geometry. In the experiment, the

combination of nonangular excitations associated with our method used to rotate the trap and relatively rapid damping of the oscillation prevent us from observing meaningful mode profiles for small β.

Importantly, the FTIA reveals that, even in cases where we observe an apparently single-frequency response in typical rotational observables like θ or $\langle xy \rangle$ [as in Figs. 4(a) and 4(b)], the response of the system may, in fact, be multimode in nature, breaking the single-mode approximation used to analytically extract f_{irr} and f_{rig} [19,34]. In the case of a multifrequency response, f_{irr} and f_{rig}, instead, provide an upper bound for the frequency of the lowest energy excitation—an excitation that is difficult to see with experimentally accessible observables. Features of these subdominant modes, including the lack of a strong rotational signal in the low-frequency oscillations and the apparent similarity between the droplet motion (the motion of the halo is quite different) near 25 Hz to that of the dominant rotational mode, remain interesting topics for future investigation.

As we have noted, not only does the dominant angular response frequency fail to approach the rigid-body value in the isolated droplet regime, but it also stays near to the irrotational prediction. A possible intuitive explanation for this observation is that the flow pattern of Fig. 1(a) resembles that of a quadrupolar surface mode, and it is well known that, for sufficiently strong interactions, the frequency of such modes is predominantly determined by the trap parameters, rather than the details of the interparticle interactions [34].

In conclusion, measurements of angular oscillation frequencies offer a simple way to demonstrate superfluidity in certain conditions. However, care must be taken when making and interpreting such measurements—geometrical

changes can mask the effects of changing superfluidity, and usual predictions to which one might compare rely on the assumption of a single-frequency response of the lowest energy rotational mode. While the moment of inertia of the system is defined as the angular momentum of a system in response to a shape-preserving, steady-state drive, oscillation measurements involve a time-localized change in the rotation rate of the trap, which may excite modes that do not meet this criterion. In small, linear systems, the simple excitation spectra means that approximately shape-preserving oscillations can still be excited [31]. However, we find that a supersolid with 2D structure, which one might expect to be an ideal candidate for such measurements, can exhibit an apparently single-frequency response associated with a mode that is not the lowest in energy. Further, this excitation frequency is typically very close to that of a purely superfluid system, even for systems where the effects of superfluidity are minimal. Therefore, such measurements do not provide a robust indicator of superfluidity for modulated systems. In the future, it may be possible to extract information about superfluidity using a modified excitation scheme to preferentially excite the lower energy modes and a more comprehensive analysis scheme suitable for multifrequency response [41]. However, such techniques would require detailed knowledge of the exact excitation applied and measurement of response amplitudes, both of which are considerably more challenging in an experiment than measuring the frequency of an oscillation.

Finally, we note that, even in the case of single-frequency response, where the frequency of angular oscillations has a direct connection to the moment of inertia of the system, making a clear connection between the moment of inertia and quantities like a superfluid fraction can be problematic. Past works have predicted that a system which is partially superfluid should have a moment of inertia in between the RBR and IF predictions, linearly interpolated according to a superfluid fraction [20,38]. While this interpretation may be valid for systems featuring a rigid crystalline structure and a uniform distribution of crystalline and superfluid components, as in [38], it is not necessarily valid for our small dipolar supersolids, which, in addition to coupled superfluid-crystalline excitations, feature a nonuniform degree of modulation across the system.

---

[*]Corresponding author.
Francesca.Ferlaino@uibk.ac.at

[1] M. R. Matthews, B. P. Anderson, P. C. Haljan, D. S. Hall, C. E. Wieman, and E. A. Cornell, Vortices in a Bose-Einstein Condensate, Phys. Rev. Lett. **83,** 2498 (1999).

[2] K. W. Madison, F. Chevy, W. Wohlleben, and J. Dalibard, Vortex Formation in a Stirred Bose-Einstein Condensate, Phys. Rev. Lett. **84,** 806 (2000).

[3] M. W. Zwierlein, J. R. Abo-Shaeer, A. Schirotzek, C. H. Schunck, and W. Ketterle, Vortices and superfluidity in a strongly interacting Fermi gas, Nature (London) **435,** 1047 (2005).

[4] A. Ramanathan, K. C. Wright, S. R. Muniz, M. Zelan, W. T. Hill, C. J. Lobb, K. Helmerson, W. D. Phillips, and G. K. Campbell, Superflow in a Toroidal Bose-Einstein Condensate: An Atom Circuit with a Tunable Weak Link, Phys. Rev. Lett. **106,** 130401 (2011).

[5] D. Guéry-Odelin and S. Stringari, Scissors Mode and Superfluidity of a Trapped Bose-Einstein Condensed Gas, Phys. Rev. Lett. **83,** 4452 (1999).

[6] D. Bohle, A. Richter, W. Steffen, A. Dieperink, N. L. Iudice, F. Palumbo, and O. Scholten, New magnetic dipole excitation mode studied in the heavy deformed nucleus ^{156}GD by inelastic electron scattering, Phys. Lett. **137B,** 27 (1984).

[7] O. M. Maragò, S. A. Hopkins, J. Arlt, E. Hodby, G. Hechenblaikner, and C. J. Foot, Observation of the Scissors Mode and Evidence for Superfluidity of a Trapped Bose-Einstein Condensed Gas, Phys. Rev. Lett. **84,** 2056 (2000).

[8] M. J. Wright, S. Riedl, A. Altmeyer, C. Kohstall, E. R. Sanchez Guajardo, J. H. Denschlag, and R. Grimm, Finite-Temperature Collective Dynamics of a Fermi Gas in the BEC-BCS Crossover, Phys. Rev. Lett. **99,** 150403 (2007).

[9] R. M. W. van Bijnen, N. G. Parker, S. J. J. M. F. Kokkelmans, A. M. Martin, and D. H. J. O'Dell, Collective excitation frequencies and stationary states of trapped dipolar Bose-Einstein condensates in the Thomas-Fermi regime, Phys. Rev. A **82,** 033612 (2010).

[10] C. D. Rossi, R. Dubessy, K. Merloti, M. de Goër de Herve, T. Badr, A. Perrin, L. Longchambon, and H. Perrin, The scissors oscillation of a quasi two-dimensional Bose gas as a local signature of superfluidity, J. Phys. Conf. Ser. **793,** 012023 (2017).

[11] I. Ferrier-Barbut, M. Wenzel, F. Böttcher, T. Langen, M. Isoard, S. Stringari, and T. Pfau, Scissors Mode of Dipolar Quantum Droplets of Dysprosium Atoms, Phys. Rev. Lett. **120**, 160402 (2018).

[12] M. Boninsegni and N. V. Prokof'ev, Colloquium: Supersolids: What and where are they?, Rev. Mod. Phys. **84**, 759 (2012).

[13] Z.-K. Lu, Y. Li, D. S. Petrov, and G. V. Shlyapnikov, Stable Dilute Supersolid of Two-Dimensional Dipolar Bosons, Phys. Rev. Lett. **115**, 075303 (2015).

[14] D. Baillie and P. B. Blakie, Droplet Crystal Ground States of a Dipolar Bose Gas, Phys. Rev. Lett. **121**, 195301 (2018).

[15] S. M. Roccuzzo and F. Ancilotto, Supersolid behavior of a dipolar Bose-Einstein condensate confined in a tube, Phys. Rev. A **99**, 041601(R) (2019).

[16] L. Tanzi, E. Lucioni, F. Famà, J. Catani, A. Fioretti, C. Gabbanini, R. N. Bisset, L. Santos, and G. Modugno, Observation of a Dipolar Quantum Gas with Metastable Supersolid Properties, Phys. Rev. Lett. **122**, 130405 (2019).

[17] F. Böttcher, J.-N. Schmidt, M. Wenzel, J. Hertkorn, M. Guo, T. Langen, and T. Pfau, Transient Supersolid Properties in an Array of Dipolar Quantum Droplets, Phys. Rev. X **9**, 011051 (2019).

[18] L. Chomaz, D. Petter, P. Ilzhöfer, G. Natale, A. Trautmann, C. Politi, G. Durastante, R. M. W. van Bijnen, A. Patscheider, M. Sohmen, M. J. Mark, and F. Ferlaino, Long-Lived and Transient Supersolid Behaviors in Dipolar Quantum Gases, Phys. Rev. X **9**, 021012 (2019).

[19] S. M. Roccuzzo, A. Gallemí, A. Recati, and S. Stringari, Rotating a Supersolid Dipolar Gas, Phys. Rev. Lett. **124**, 045702 (2020).

[20] L. Tanzi, J. Maloberti, G. Biagioni, A. Fioretti, C. Gabbanini, and G. Modugno, Evidence of superfluidity in a dipolar supersolid from nonclassical rotational inertia, Science **371**, 1162 (2021).

[21] E. Kim and M. H.-W. Chan, Probable observation of a supersolid helium phase, Nature (London) **427**, 225 (2004).

[22] D. Y. Kim and M. H. W. Chan, Absence of Supersolidity in Solid Helium in Porous Vycor Glass, Phys. Rev. Lett. **109**, 155301 (2012).

[23] Here, the word droplet refers to a high-density region, which is not necessarily self-bound.

[24] J.-N. Schmidt, J. Hertkorn, M. Guo, F. Böttcher, M. Schmidt, K. S. H. Ng, S. D. Graham, T. Langen, M. Zwierlein, and T. Pfau, Roton Excitations in an Oblate Dipolar Quantum Gas, Phys. Rev. Lett. **126**, 193002 (2021).

[25] M. A. Norcia, C. Politi, L. Klaus, E. Poli, M. Sohmen, M. J. Mark, R. Bisset, L. Santos, and F. Ferlaino, Two-dimensional supersolidity in a dipolar quantum gas, Nature (London) **596**, 357 (2021).

[26] J. Hertkorn, J.-N. Schmidt, M. Guo, F. Böttcher, K. S. H. Ng, S. D. Graham, P. Uerlings, H. P. Büchler, T. Langen, M. Zwierlein, and T. Pfau, Supersolidity in Two-Dimensional Trapped Dipolar Droplet Arrays, Phys. Rev. Lett. **127**, 155301 (2021).

[27] T. Bland, E. Poli, C. Politi, L. Klaus, M. A. Norcia, F. Ferlaino, L. Santos, and R. N. Bisset, Two-Dimensional Supersolid Formation in Dipolar Condensates, Phys. Rev. Lett. **128**, 195302 (2022).

[28] E. Poli, T. Bland, C. Politi, L. Klaus, M. A. Norcia, F. Ferlaino, R. N. Bisset, and L. Santos, Maintaining supersolidity in one and two dimensions, Phys. Rev. A **104**, 063307 (2021).

[29] A. Trautmann, P. Ilzhöfer, G. Durastante, C. Politi, M. Sohmen, M. J. Mark, and F. Ferlaino, Dipolar Quantum Mixtures of Erbium and Dysprosium Atoms, Phys. Rev. Lett. **121**, 213601 (2018).

[30] M. Sohmen, C. Politi, L. Klaus, L. Chomaz, M. J. Mark, M. A. Norcia, and F. Ferlaino, Birth, Life, and Death of a Dipolar Supersolid, Phys. Rev. Lett. **126**, 233401 (2021).

[31] See Supplemental Material at http://link.aps.org/supplemental/10.1103/PhysRevLett.129.040403 for more information, which contains refs. [32,33].

[32] I. T. Jolliffe, *Principal Component Analysis*, Springer Series in Statistics (Springer, New York, 2002).

[33] R. Dubessy, C. D. Rossi, T. Badr, L. Longchambon, and H. Perrin, Imaging the collective excitations of an ultracold gas using statistical correlations, New J. Phys. **16**, 122001 (2014).

[34] L. Pitaevskii and S. Stringari, *Bose-Einstein Condensation and Superfluidity* (Oxford University Press, New York, 2016), Vol. 164.

[35] I. Ferrier-Barbut, H. Kadau, M. Schmitt, M. Wenzel, and T. Pfau, Observation of Quantum Droplets in a Strongly Dipolar Bose Gas, Phys. Rev. Lett. **116**, 215301 (2016).

[36] L. Chomaz, S. Baier, D. Petter, M. J. Mark, F. Wächtler, L. Santos, and F. Ferlaino, Quantum-Fluctuation-Driven Crossover from a Dilute Bose-Einstein Condensate to a Macrodroplet in a Dipolar Quantum Fluid, Phys. Rev. X **6**, 041039 (2016).

[37] F. Wächtler and L. Santos, Quantum filaments in dipolar Bose–Einstein condensates, Phys. Rev. A **93**, 061603(R) (2016).

[38] A. J. Leggett, Can a Solid be "Superfluid"?, Phys. Rev. Lett. **25**, 1543 (1970).

[39] We note that the geometry of our system is very different from that considered in Ref. [38], and so, we do not expect this quantity to have a direct connection to the nonclassical moment of inertia of the system. Rather, we simply use it as a convenient way to quantify overlap between droplets.

[40] Edmundo R. Sanchez Guajardo, M. K. Tey, L. A. Sidorenkov, and R. Grimm, Higher-nodal collective modes in a resonantly interacting Fermi gas, Phys. Rev. A **87**, 063601 (2013).

[41] S. M. Roccuzzo, A. Recati, and S. Stringari, Moment of inertia and dynamical rotational response of a supersolid dipolar gas, Phys. Rev. A **105**, 023316 (2022).

Supplemental materials for: Can angular oscillations probe superfluidity in dipolar supersolids?

Matthew A. Norcia,[1] Elena Poli,[2] Claudia Politi,[1, 2] Lauritz Klaus,[1, 2] Thomas Bland,[1, 2]
Manfred J. Mark,[1, 2] Luis Santos,[3] Russell N. Bisset,[2] and Francesca Ferlaino[1, 2, *]

[1]Institut für Quantenoptik und Quanteninformation,
Österreichische Akademie der Wissenschaften, Innsbruck, Austria
[2]Institut für Experimentalphysik, Universität Innsbruck, Austria
[3]Institut für Theoretische Physik, Leibniz Universität Hannover, Germany

EXCITATION PROTOCOL

In both experiment and simulation, we excite the atoms by suddenly rotating the trap, holding for 6 ms, then returning it to its initial orientation. This was important in the experiment, as the trap frequencies generally change slightly as the trap is rotated, and we want to observe the evolution of a state that is equilibrated to the trap prior to the rotation. To explore whether the exact excitation protocol influences our results, we performed additional simulations where the trap angle was rotated and held in the new orientation, but not rotated back. We find that the same modes are excited in this case, and the frequency of their responses are the same. For some parameters the relative contributions of the modes to the spectrum of $\langle xy \rangle$ can differ between the two protocols, but for the parameters we explore the frequency of the peak response remains unchanged. In particular, for the droplet crystal hexagon shown in Fig. 4c of the main text, the contribution of the low-frequency mode to the $\langle xy \rangle$ power spectrum becomes appreciable, though is still smaller than the contribution of the modes near 60 Hz. Thus, the multimode response appears to be a generic feature of possible schemes to excite angular oscillations. While the spectral content of the excitation may differ, influencing the relative amplitudes of different modes, the frequency and character of the modes is determined by the system, not the drive.

We have also performed excitation in the simulation by directly imprinting a small phase variation αxy onto the ground-state wavefunction. This protocol produces qualitatively similar results to those described above. Again, the same modes are excited and respond with the same frequencies, though sometimes with different amplitudes. The dominant mode excited is the same as the rotate-and-return protocol for all cases investigated.

EXTRACTING ANGULAR POWER SPECTRUM

Several methods can be used to extract the angular response of our system. For the experiment, we perform a two-dimensional Gaussian fit to the in-trap image, and record the angle of the major and minor axes as a function of time. For the simulation, we report the angu-

lar response obtained using one of two observables. For direct comparison to the experiment, we use the state angle extracted from a 2D Gaussian fit, as in the experiment. For more detailed spectral analysis, we use the quantity $\langle xy \rangle$, as this is expected to have a strong response to a rapid rotation of the trap and we find it to be numerically more robust. We have confirmed that these and other similar observables, such as the directions of maximal and minimal variance, provide consistent results (up to overall normalization). In some cases, the Fourier spectrum of $\langle \hat{L}_z \rangle$ (though not experimentally accessible) shows different relative response amplitudes between modes compared to $\langle xy \rangle$, particularly for those modes at low frequencies.
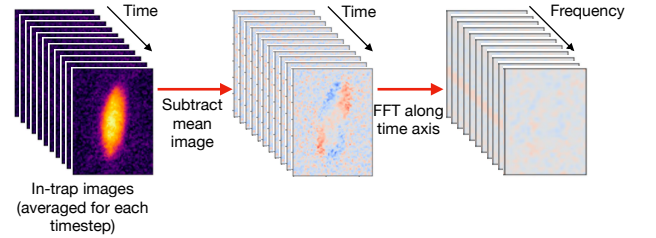
FOURIER TRANSFORM IMAGE ANALYSIS

FIG. S1. Procedure for Fourier transform image analysis (FTIA). See text for description.

The goal of our Fourier transform image analysis (FTIA) protocol is to visualize the density response of our atomic system in real-space with respect to position, but in frequency space with respect to time. This provides a simple way to extract the spatial profile of excitation modes. The process is illustrated in Fig. S1. To perform the FTIA, we assemble images of projected density profiles corresponding to single time-steps (directly from the simulation, or averaged over several in-trap images from the experiment), then subtract the average (over all time-steps) image from each. We then Fourier transform the results along the time axis. The output is then a sequence of real-space images, showing the fluctuation pattern at a given frequency. Because each pixel is now represented

by a complex number (encoding the amplitude and phase of the density variations at that location), we plot with respect to the global phase for each frequency that shows maximum variation, thus plotting the in-phase quadrature of the oscillation.

In order to obtain a power spectrum (useful for locating the frequencies of excited modes), we compute the sum of the absolute square of the fluctuations over a region of interest containing the atomic cloud for each frequency. This power spectrum can be used to identify the frequency and spatial character of modes, but is not expressed in physically meaningful units, and so should not necessarily be used to compare the strength of different mode responses.

We note that there are some similarities between the FTIA method and principal component analysis (PCA) [1, 2]. Both provide a model-free way of extracting the form of excitations present in a system. PCA does so by finding correlated patterns of fluctuations within a set of images, with no prior information about the time-sequence of the images. This makes it well-suited to revealing modes that are excited incoherently, for example by thermal or quantum noise. In contrast, our FTIA method explicitly incorporates the time-domain information associated with the images. This makes it well-suited to extracting modes that are coherently excited (FTIA, as we apply it, would not work for incoherently excited modes). In practice, we find that the FTIA is more robust than PCA at extracting fluctuation patterns that each exhibit a single-frequency response. While PCA often returns components whose weights vary with multiple frequencies (indicating that they actually correspond to a linear combination of eigenmodes), FTIA by construction returns a fluctuation pattern associated with a single frequency. We find that this feature makes it more robust for identifying eigenmodes of a system subject to a coherent drive.

SPECTRA/TABLE FOR ALL PARAMS

Excitation power spectra from simulation for a range of traps and scattering lengths used in the main manuscript can be found in Fig. S2.

PREDICTIONS FOR ROTATIONAL MODE FREQUENCIES

The rotational response of a gas can be calculated using hydrodynamic equations [3] or a sum-rule approach [4, 5]. From the sum-rule approach, an expression can be derived for the rotational oscillation frequency, under the assumption that the response is single-frequency:

$$\omega^2 = \frac{m\langle y^2 - x^2\rangle(\omega_x^2 - \omega_y^2)}{\Theta} \quad (1)$$

Here, Θ is the moment of inertia associated with steady-state rotation.

The numerator of Eq. 1 can be interpreted as a rotational spring constant: $k_\tau = -\tau/\theta$, where τ is the torque exerted on a state whose major and minor axes y and x are rotated relative to the their equilibrium position in the trap by an angle θ. To see this, consider a mass element m at position (x, y) in a trapping potential $V = (m\omega_x x^2 + m\omega_y y^2)/2$, which exerts a torque $\tau = xF_y - yF_x = xym(\omega_x^2 - \omega_y^2)$. We can then calculate $k_\tau = -\partial\tau/\partial\theta = -m(y\partial x/\partial\theta + x\partial y/\partial\theta)(\omega_x^2 - \omega_y^2) = m(y^2 - x^2)(\omega_x^2 - \omega_y^2)$. Summing over mass elements provides the numerator of Eq. 1. This highlights that the numerator of this expression is purely geometrical, independent of whether the state is superfluid or classical. In the case of multi-frequency response, Eq. 1 (as defined by the sum rule) becomes an inequality, defining the upper bound for the lowest frequency angular excitation in the system [4].

BETA VERSUS SCATTERING LENGTH FOR 1D AND 2D

In Fig. S3, we show the change in the anisotropy of the atomic state in response to a change in scattering length for a variety of traps, featuring both linear and 2D array modulated configurations. Here, we consider the quantity $\beta^2 = (\langle x^2 - y^2\rangle/\langle x^2 + y^2\rangle)^2$, as this quantity gives the expected change in moment of inertia between irrotational flow (IF) and rigid-body rotation (RBR). As β^2 approached unity, the difference between the two vanishes, so such states can exhibit minimal sensitivity to superfluidity.

States in more elongated traps generally have values of β^2 closer to one than their rounder counterparts. However, even in relatively round traps, such as those of Refs. [5, 6], low atom numbers can lead to the formation of linear arrays, which are highly elongated. In these cases, the sensitivity of the state to superfluidity is dramatically reduced upon entering the modulated regime. In contrast, combinations of trap parameters and atom number that lead to a 2D modulated state typically maintain values of β^2 substantially different from one even in the low scattering length, independent droplet regime.

LINEAR CASE

In Fig. S4, we explore the parameters of refs [5, 6], where a change in scattering length induces a transition from an unmodulated BEC to a linear array of two droplets. This transition is accompanied by a dramatic change in the aspect ratio of the atomic state, as evident in the near convergence of the predictions for rigid body
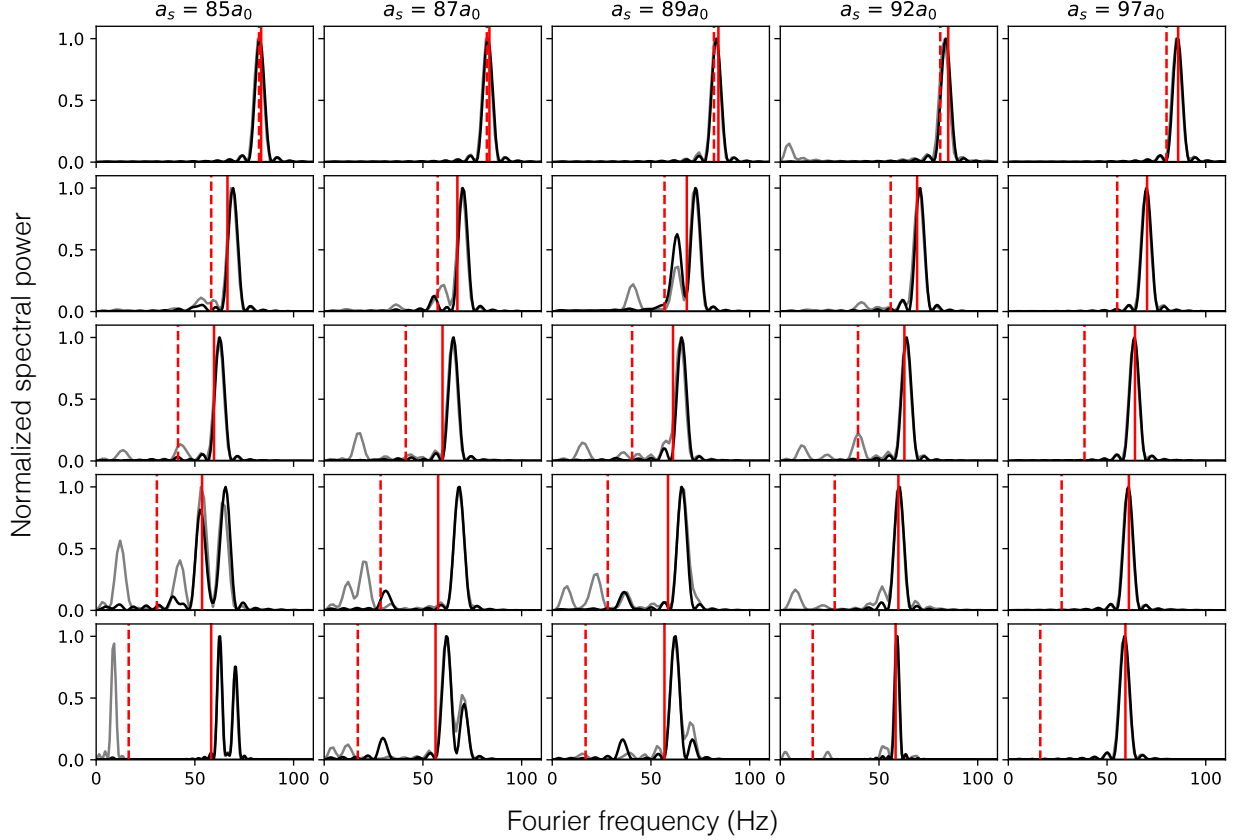
FIG. S2. Response sepctra extracted from simulations for different trap parameters (rows) and scattering lengths (columns). Upper rows correspond to more elongated traps, while lower rows correspond to more round ones. From top to bottom, $(f_x, f_y) = [(26, 87), (32, 70), (37, 62), (40, 57), (43, 53)]$ Hz. $f_z = 122$ Hz for all cases. Red vertical dashed and solid lines correspond to the rigid-body rotation and irrotational flow predictions, respectively. Gray traces are power spectra extracted from FTIA, while black traces are from $\langle xy \rangle$. In all cases, $a_s = 97a_0$ corresponds to an unmodulated BEC, while lower scattering lengths correspond to modulated states, with the overlap between droplets decreasing with scattering length. $(f_x, f_y) = (26, 87)$ is a linear droplet chain for all scattering lengths that produce a modulated state. All other modulated states have transverse structure, increasing in prevalence as the trap becomes more round.

and irrotational flow (f_{rig} and f_{irr}) at lower scattering lengths, corresponding to the droplet state.

We see that the dominant frequency of angular response is between f_{rig} and f_{irr}, indicating a change in the level of superfluidity in the system. We find that the angular response in the supersolid regime ($a_s = 90$ or $92\ a_0$) has two clear frequency components, though in this case the dominant frequency observed matches the prediction from the sum rule (with moment of inertia calculated under static rotation). Because of the geometry of the system, rotation does not lead to a significant transfer of mass between the two droplets. Thus, we attribute the change in superfluidity to the low-density halo that surrounds the droplets, rather than the inter-droplet connection itself.

* Correspondence should be addressed to Francesca.Ferlaino@uibk.ac.at

[1] I. T. Jolliffe, *Principal Component Analysis* (Springer Series in Statistics. Springer, New York, NY, 2002).

[2] R. Dubessy, C. D. Rossi, T. Badr, L. Longchambon, and H. Perrin, Imaging the collective excitations of an ultracold gas using statistical correlations, New Journal of Physics **16**, 122001 (2014).

[3] D. Guéry-Odelin and S. Stringari, Scissors mode and superfluidity of a trapped bose-einstein condensed gas, Phys. Rev. Lett. **83**, 4452 (1999).

[4] L. Pitaevskii and S. Stringari, *Bose-Einstein condensation and superfluidity*, Vol. 164 (Oxford University Press, 2016).

[5] S. M. Roccuzzo, A. Gallemí, A. Recati, and S. Stringari, Rotating a supersolid dipolar gas, Phys. Rev. Lett. **124**, 045702 (2020).

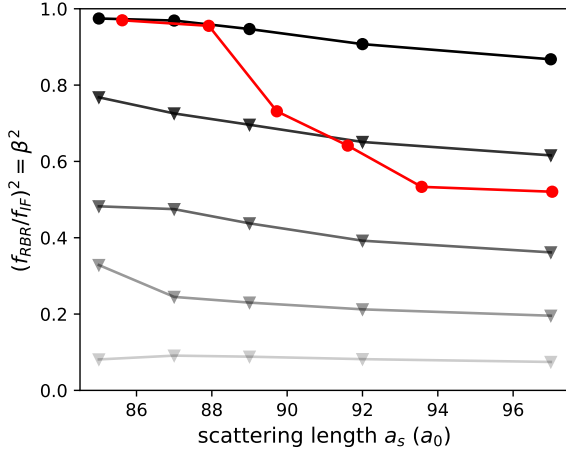[6] L. Tanzi, J. Maloberti, G. Biagioni, A. Fioretti, C. Gab-

banini, and G. Modugno, Evidence of superfluidity in a dipolar supersolid from nonclassical rotational inertia, Science **371**, 1162 (2021).


FIG. S3. Difference in moment of inertia between IF and RBR, β^2 for different traps and scattering lengths. Traps and atom numbers that correspond to linear arrays for modulated states are indicated by round markers, while those that correspond to 2D modulated arrays are indicated by triangles. All points except those at $a_s = 97a_0$ are modulated, interdroplet connection decreasing with scattering length. The states explored in Fig. S2 are shown in grey-scale, with lighter saturation corresponding to rounder traps, while the conditions similar to those of Refs. [5, 6] are shown in red.
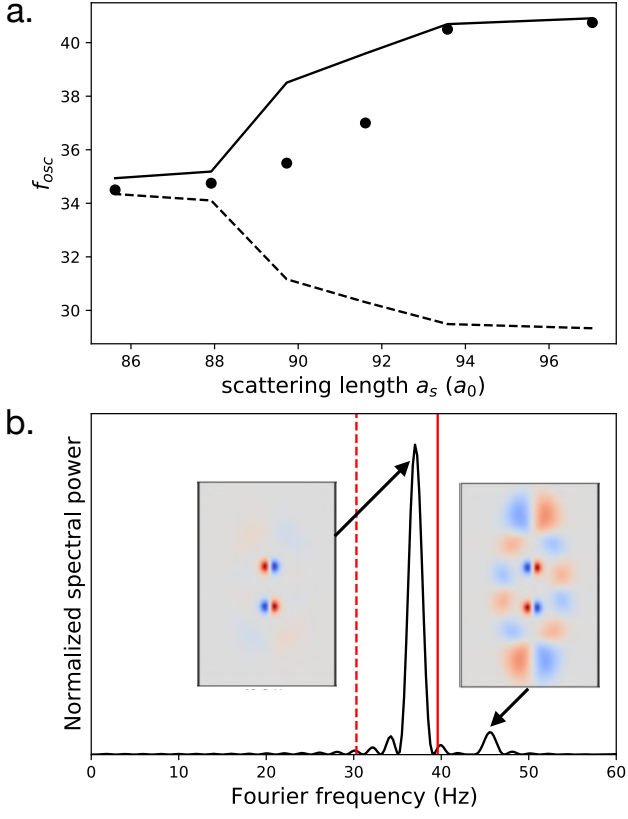
FIG. S4. Analysis of linear two-droplet arrays of [5, 6]. **a.** Dominant angular oscillation frequency (markers) extracted from simulations versus scattering length, through transition from BEC (right) to isolated droplets (left). The irrotational and rigid-body predictions f_{irr} and f_{rig} are shown as solid and dashed lines, respectively. **b.** The Fourier spectrum of $\langle xy \rangle$ for the point near $a_s = 92 a_0$ exhibits a response with dominant and sub-dominant mode contributions. The fluctuation profiles associated with these two frequencies are shown in the insets. Solid and dashed vertical red lines represent f_{irr} and f_{rig}, respectively.

4.5. Vortex regime

4.5.1. Quantized vortices

For a simply connected region of space in which the density $n(\mathbf{r})$ of the system is everywhere non-zero, applying Stokes' theorem to the curl of Eq. (8) shows that the integral of $\mathbf{v}$ around any closed curve is zero. A more interesting application of Eq. (8) is to the case in which there is a line in which $n(\mathbf{r})$ vanishes [207]. This happens when rotating a superfluid above a critical frequency Ω_c: the system develops a singularity and the Stokes' theorem is not valid anymore.

The circulation of the velocity field around a closed loop that includes the singularity is given by

$$\Gamma = \oint \mathbf{v} \cdot d\mathbf{l} \,. \tag{18}$$

Using Eq. (8) and the fact that the change in phase around any closed contour must be an integer multiple of 2π for the wave function to be single-valued, we obtain

$$\Gamma = q\frac{h}{m} \,, \tag{19}$$

with q an integer number, different from zero in presence of singularities encompassed by the loop. This result tells us that the circulation of the velocity field is *quantized*, differently from ordinary fluids, where the circulation can take any arbitrary value.

We can also extract the radial dependence of the velocity field around the singularity. Starting from Eq. (18) and considering a closed circular path in the plane perpendicular to the singular line, by using polar coordinates one gets

$$\Gamma = \int_0^{2\pi} r\mathbf{v} \cdot \hat{e}_\theta d\theta = 2\pi r v_\theta \,. \tag{20}$$

Comparing with Eq. (19), we extract the azimuthal velocity around the singularity

$$v_\theta = q\frac{\hbar}{mr} \,. \tag{21}$$

This flow is diverging at the singularity and it decreases as $\sim 1/r$ at large distances. Additionally, the singularity contributes to the global vorticity,

$$\nabla \times \mathbf{v} = \frac{h}{m}\delta^2(\mathbf{r}) \,, \tag{22}$$

that is not zero everywhere as for the case of small rotation frequencies (see Eq. (9)).

Therefore, the singularity can be interpreted as a tiny tornado in the quantum fluid called *quantized vortex*. A vortex manifests as a density hole (vortex core) characterized by a 2π phase winding in the phase all around the core, see Fig. 4.4. The vortex core can be intuitively seen as a point where destructive interference between matter-waves with π phase jump occurs, from every radial direction. Quantized vortices are topological defects that break the time reversal symmetry by imposing a preferred sense of rotation [208,209]. They are topologically protected because they are associated with a conserved winding number q around the vortex core. This makes them stable against small perturbations, ensuring their persistence in the system in absence of dissipation.
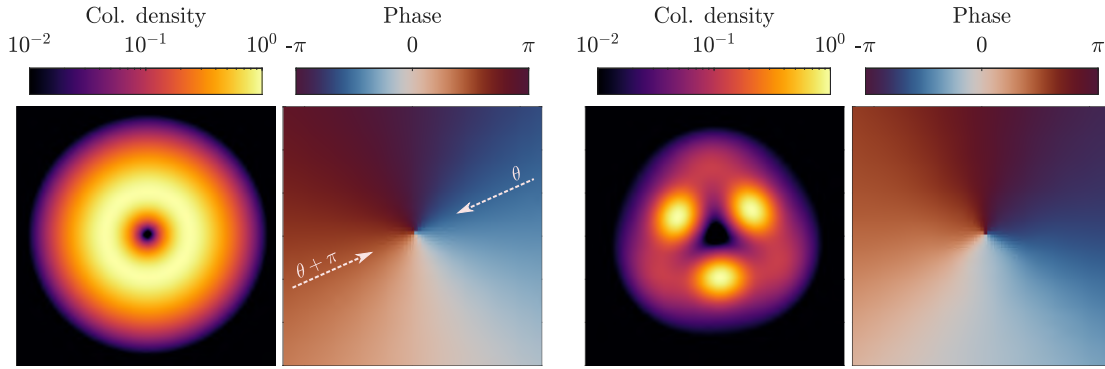
Figure 4.4.: Vortex in a BEC (left) and supersolid (right) state. The vortex creates a hole in the density and a 2π phase winding. Selecting a random radial direction across the vortex core (white dashed arrows), the phase of the wave function jumps from θ to $\theta + \pi$, destructively interfering at the vortex core.

4.5.2. Vortices in dipolar BECs and supersolids

Vortices have been observed in many different superfluid platforms [179–184]. However, the observation of these phase singularities in an ultracold dipolar system was still missing. By employing the magnetostirring protocol described in Sec. 4.1 we observed for the first time vortices in a dipolar BEC and a dipolar supersolid state. These results have been published in Refs. [192, 193], which are reported in Secs. 4.6 and 4.7. Remarkably, the observation of vortices in dipolar supersolids provides one of the most unambiguous evidence of their superfluid nature.

The experimental observations have been accompanied by extensive numerical simulations, which have provided crucial insights into the key characteristics of vortex nucleation in dipolar BECs and supersolids. Despite keeping the main features described in Sec. 4.5, vortices in the two phases differ in several fundamental aspects, including the quantization of angular momentum, the critical frequency required for their formation, and their dynamics within the system. In the following, we discuss these properties highlighting the similarities and differences.

Angular momentum carrier

The angular momentum per particle carried by a vortex in the center of a superfluid system is quantized. However, the quantization differs between a BEC and a supersolid. In a BEC, which is a fully superfluid system, the angular momentum per particle is precisely $\langle L_z \rangle = \hbar$. In contrast, for a supersolid, the presence of a vortex at the center leads to a jump of the angular momentum per particle $\langle L_z \rangle \leq \hbar$. The reduction factor has been found to be comparable with the fraction of non-classical rotational inertia f_{NCRI}, following the relation $\langle L_z \rangle \approx f_{NCRI}\hbar$ [210]. It is important to note that these considerations apply specifically to a vortex positioned at the center of a finite system. When a vortex is located elsewhere, the angular momentum per particle is reduced even in a BEC, with its value depending on the vortex's radial distance from the center [211].

Critical frequency for vortex nucleation

Vortex nucleation is associated with a discontinuous rotational response that occurs at frequencies exceeding a critical threshold. There are two relevant critical frequencies that govern the vortex nucleation dynamics in a superfluid system:

- The *energetic* critical frequency Ω_c, above which the ground state in the rotating frame contains one or more vortices.

- The *dynamical* critical frequency Ω_c^{dyn} for vortex nucleation, above which the state can dynamically achieve the ground state in the rotating frame, containing one or more vortices, in an experimentally feasible timescale[2] [212]. In general, it holds $\Omega_c^{dyn} > \Omega_c$ for both the BEC and supersolid case. This is because a vortex needs to overcome an energy barrier to enter the system, that can be thought in terms of energy to create a density depletion, namely the vortex core, inside the system [33]. This energy barrier can be crossed by means of dynamical instabilities [192].

To build some intuition on the physical meaning of these two quantities, one can think of Ω_c as answering the question *"How favourable is it to create a density depletion in the center of the system?"*. In contrast, Ω_c^{dyn} corresponds to *"Once the vortex wants to form, how easily can it enter and reach the center of the system?"*. The answer to these questions–and thus the value of these critical frequencies–depends strongly on the system's density distribution, particularly on whether the density is modulated or not. Indeed, a vortex core, which involves a local density depletion, will form and move more easily through the low density regions of an inhomogeneous density profile.

For an unmodulated BEC, although the critical frequency in which the ground state contains vortices is relatively low $\Omega_c \sim 0.15\omega_\perp$, the system needs to rotate much faster at $\Omega_c^{dyn} \approx \omega_\perp/\sqrt{2} \approx 0.7\omega_\perp$ to nucleate vortices in an experimentally feasible timescale. This is the frequency at which the quadrupole mode is at resonance, seeding a surface quadrupole dynamical instability that let vortices enter the system [198]. Thus, $\Omega_c^{dyn} \gg \Omega_c$. When rotating at this high frequency Ω^*, many vortices are nucleated, and it takes some time for the BEC to equilibrate and form a vortex lattice in equilibrium in the rotating frame.

Conversely, vortices in a supersolid can enter and very easily move through the low density regions of the inhomogeneous density profile [193, 210]. Due to the double superfluid-solid nature, the state possess many quadrupole modes associated to the different gapless branches of the excitation spectrum: one from the broken phase symmetry associated with superfluid nature (*superfluid* quadrupole mode) and one from each broken translational symmetry (*solid* quadrupole mode)[3]. The superfluid quadrupole mode instability occurs at a low frequency [210], for which only one or two vortices are nucleated. This sets the value of Ω_c^{dyn}. Instead, the solid quadrupole mode set a higher frequency threshold above which vortices are always created. Therefore, for a supersolid we usually have $\Omega_c \sim 0.1\omega_\perp$ and $\Omega_c^{dyn} \sim 0.2\omega_\perp$ [193, 199]. As for the BEC, it holds that $\Omega_c^{dyn} \geq \Omega_c$, but the two values are much closer, $\Omega_c^{dyn} \sim \Omega_c$. These results highlight how supersolids provide a good platform for dynamically exploring low-frequency vortex

---

[2]Considering the lifetime of the supersolid system, we will consider an experimentally feasible timescale of approximately 1 second.

[3]In our case of a 2D supersolid in a cylindrically symmetric trap, the two solid quadrupole modes are nearly degenerate. They are not perfectly degenerate because of the tilted magnetic field used for the magnetostirring of the system.
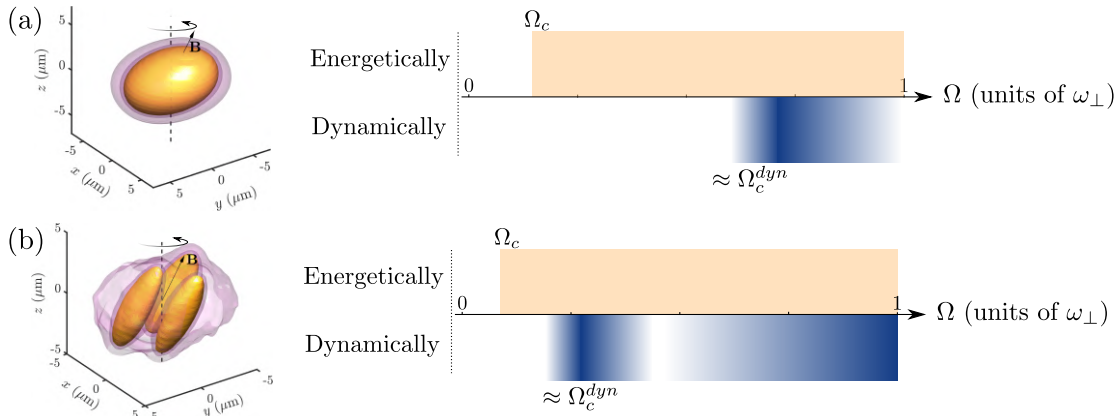
Figure 4.5.: Schematic relation between the energetic and dynamical frequency for vortex nucleation in (a) an unmodulated BEC and (b) a supersolid. The orange regions indicate the range of Ω for which the ground state in the rotating frame hosts one or more vortices. The shaded blue regions denote the ranges in Ω where the vortex state can be dynamically accessed within a reasonable timescale of approximately $1\,\text{s}$. The colour intensity correspond to the timescale at which the system reaches the vortex state by crossing a dynamical instability–darker shades indicate a faster vortex nucleation. These regions are typically associated to resonances of quadrupole mode(s), see Secs. 4.8.1 and 4.8.2.

nucleation, very close to the energetic critical limit.

These considerations about the critical velocities are schematically visualized in Fig. 4.5, while a more detailed discussion on the role of the quadrupole mode instabilities in BECs and supersolids is given in Sec. 4.8.

Vortex lattice and visibility

Vortices produced in a superfluid arrange themselves in regular lattices. The lattice structure depends on the phase and interaction properties of the superfluid system. For a BEC with interactions that are isotropic in the plane perpendicular to the rotation axis ($z-$axis), a triangular Abrikosov vortex lattice is energetically favourable [213]. This is the case for contact-interacting BECs and dipolar BECs with magnetic field aligned along z [180, 181, 192]. On the contrary, for dipolar BECs with tilted magnetic field the structure is not isotropic. Due to magnetostriction and the anisotropic vortex cores, the resulting vortex configuration is also anisotropic, producing a stripe lattice [192, 214, 215].

Because of the density modulation, vortices in supersolid exhibit a different behaviour. Indeed, their interaction with the underlying crystalline structure leads to unconventional dynamics. First, vortices within the droplets themselves are unstable [216]. For this reason, they reside in the interstitial regions between density peaks forming an honeycomb lattice [210, 217]. The droplet structure acts as a pinning potential, forcing them to snake between the density peaks. While previous studies have shown vortex pinning through an additional underlying optical lattice [218–222], a supersolid provides a platform where the pinning effects genuinely arises from the spontaneous translational symmetry breaking. A key consequence of this pinning effect will be discussed in the next chapter in the context of glitches, see Sec. 5.3.

Vortices residing in low-density regions of a supersolid also impact their visibility. Unlike in unmodulated BECs, where vortices can be directly imaged in-situ [192], their tendency to localize in low-density areas presents an experimental challenge for detection. To overcome this, we exploited the topological nature of the vortices and collected two different type of observations:

- Vortices are nucleated through magnetostirring in a dipolar system in the supersolid phase. Before imaging the system, the scattering length is quenched to cross the supersolid-to-BEC transition. The vortex is robust, since the transition does not affect the phase coherence of the system [223]. Once in the BEC phase, there is enough density contrast to detect them experimentally. By applying this protocol, we explored the rotational response of the system for different rotation time and frequencies [193].

- Vortices are nucleated through magnetostirring in a dipolar system in the supersolid phase. We remove the trapping potential, so that the system expands in free space through $36\,\mathrm{ms}$ of time-of-flight. The vortex is topologically protected and its core cannot be filled during the expansion. By applying this protocol, we detected the effect of the 2π phase winding of the vortex on the interference pattern. This interferometric technique for vortex detection has been shown to be robust and repeatable for different rotation frequencies Ω over different experimental shots [193].

The cumulative observation of the rotational response of the dipolar system and the interferometric vortex detection provided an unambiguous way to detect vortices in dipolar supersolids.

4.6. Publication: Observation of vortices and vortex stripes in a dipolar condensate

L. Klaus[1,2,4],T. Bland[1,2,4], **E. Poli**[2], C. Politi[1,2], G. Lamporesi[3], E. Casotti[1,2],
R. N. Bisset[2], M. J. Mark[1,2], and F. Ferlaino[1,2]

[1] *Institut für Quantenoptik und Quanteninformation, Österreichische Akademie der Wissenschaften, 6020 Innsbruck, Austria*
[1] *Institut für Experimentalphysik, Universität Innsbruck, 6020 Innsbruck, Austria*
[3] *INO-CNR BEC Center and Dipartimento di Fisica, Università di Trento, Povo, Italy.*
[4] *These authors contributed equally.*

---

† The author of the present thesis performed the numerical simulations together with T. B. and contributed in writing the manuscript.

Observation of vortices and vortex stripes in a dipolar condensate

Check for updates

Lauritz Klaus [1,2,4], Thomas Bland [1,2,4], Elena Poli [2], Claudia Politi[1,2], Giacomo Lamporesi [3], Eva Casotti [1,2], Russell N. Bisset [2], Manfred J. Mark [1,2] and Francesca Ferlaino [1,2] ✉

Quantized vortices are a prototypical feature of superfluidity that have been observed in multiple quantum gas experiments. But the occurrence of vortices in dipolar quantum gases—a class of ultracold gases characterized by long-range anisotropic interactions—has not been reported yet. Here we exploit the anisotropic nature of the dipole–dipole interaction of a dysprosium Bose–Einstein condensate to induce angular symmetry breaking in an otherwise cylindrically symmetric pancake-shaped trap. Tilting the magnetic field towards the radial plane deforms the cloud into an ellipsoid, which is then set into rotation. At stirring frequencies approaching the radial trap frequency, we observe the generation of dynamically unstable surface excitations, which cause angular momentum to be pumped into the system through vortices. Under continuous rotation, the vortices arrange into a stripe configuration along the field, in close agreement with numerical simulations.

Since the first experiments on gaseous Bose–Einstein condensates (BECs), the observation of quantized vortices has been considered the most fundamental and defining signature of the superfluid nature of such systems. Their very existence sets a unifying concept encompassing a variety of quantum fluids from liquid helium[1] to the core of neutron stars[2] and from superconductors[3] to quantum fluids of light[4]. Their classical counterparts have as well fascinated scientists from different epochs and fields as vortices are found in many scales of physical systems, from tornadoes in the atmosphere to ferrohydrodynamics.

In the quantum realm, a quantized vortex may emerge as a unique response of a superfluid to rotation. It can be understood as a type of topologically protected singularity with a 2π phase winding that preserves the single-valuedness of the superfluid wave function and the irrotational nature of its velocity field. In contact-interacting BECs, vortical singularities have been observed experimentally in the form of single vortices[5,6], vortex–antivortex pairs[7], solitonic vortices[8,9], vortex rings[10] and vortex lattices[6,11] using a number of different techniques. Moreover, vortices play a fundamental role in the description of the Berezinskii–Kosterlitz–Thouless transition in two-dimensional (2D)

systems[12], as well as in the evolution of quantum turbulence[13,14], and have been observed in interacting Fermi gases along the Bose-Einstein condensate to Bardeen-Cooper-Schrieffer crossover[8,15].

Recently, a new class of ultracold quantum gases are being created in various laboratories around the world, using strongly magnetic lanthanide atoms[16,17]. Such a system, providing a quantum analogue of classical ferrofluids, enables access to the physics of dipolar BECs, in which atoms feature a strong long-range anisotropic dipole–dipole interaction (DDI)[18,19] on top of the traditional contact-type isotropic one. This intriguing platform provided the key to observe, for example, extended Bose–Hubbard dynamics[20], roton excitations[21–23], the quantum version of the Rosensweig instability[24] and supersolid states of matter[25–28], and is foreseen to host novel phenomena for quantum simulation and metrology[18,19].

The dipolar interaction is predicted to also intimately change the properties of vortices in quantum gases[29]. For instance, theoretical works predict single vortices to exhibit an elliptic-shaped core for a quasi-2D setting with in-plane dipole orientation[30–33] or the presence of density oscillations around the vortex core induced by the roton

[1]Institut für Quantenoptik und Quanteninformation, Österreichische Akademie der Wissenschaften, Innsbruck, Austria. [2]Institut für Experimentalphysik, Universität Innsbruck, Innsbruck, Austria. [3]INO-CNR BEC Center and Dipartimento di Fisica, Università di Trento, Povo, Italy. [4]These authors contributed equally: Lauritz Klaus, Thomas Bland. ✉e-mail: Francesca.Ferlaino@uibk.ac.at
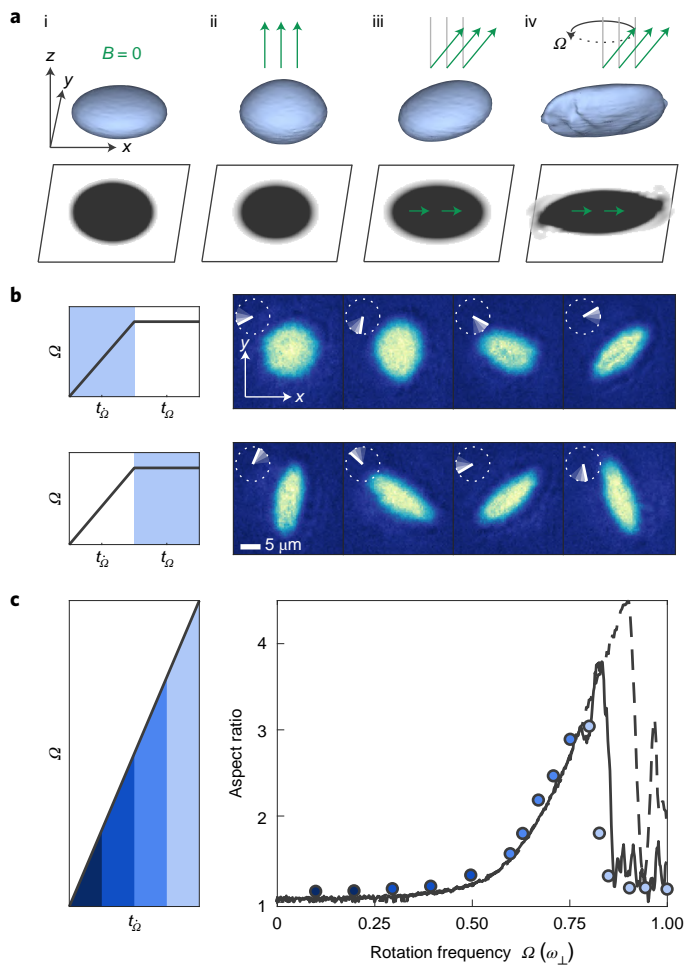
Fig. 1 | Magnetostirring of a Dy dipolar BEC and evolution of the cloud aspect ratio. a, 3D simulations and corresponding shadow on the *x-y* plane of a non-dipolar (i) and dipolar BEC with $B \neq 0$ (ii–iv) in a cylindrically symmetric, oblate trap. The magnetic-field (green arrows) angle with respect to the *z* axis varies from $\theta = 0°$ (ii) to $\theta = 35°$ (iii) and rotating at $\theta = 35°$ around *z* (iv). **b**, Left panels show the experimental sequence for the stirring procedure. The grey areas indicate the stage during which the images in the right panels were taken. The right panels are representative axial absorption images showing the dipolar BEC while spinning up the magnetic field for $t_{\dot{\Omega}} = [140, 430, 627, 692]$ ms (top) and subsequent constant rotation at $\Omega = 2\pi \times 36$ Hz for $t_{\Omega} = [0, 6, 11, 17]$ ms (bottom). The rotation of the magnetic field in the *x-y* plane is indicated by the white line. **c**, (left) Time evolution of the magnetic field rotation frequency. Ω is linearly increased to its final value at a speed of $\dot{\Omega} = 2\pi \times 50$ Hz s⁻¹. (right) Cloud AR for different final rotation frequencies. To mitigate influences of trap anisotropies on the AR, a full period at the final rotation frequency is probed. The error bars, representing the standard error on the mean after 100 trials per point, are smaller than the symbol size. The solid (dashed) black line shows the corresponding eGPE simulations with a 2 s (1 s) ramp and $a_s = 110a_0$, $(\omega_\perp, \omega_z) = 2\pi \times [50, 130]$ Hz, and $N = 15,000$. Different colors of the experimental point in the right panel indicate the corresponding time during the ramp in the left panel.

minimum in the dispersion relation[30–34]. For vortex pairs, the anisotropic DDI is expected to alter the lifetime and dynamics[33,35] and can even suppress vortex–antivortex annihilation[33]. These interaction properties are predicted to give rise to a vortex lattice structure that can follow a triangular pattern[30,34], as is typical for non-dipolar BECs[11], or a square lattice for attractive or zero contact interactions[36–38] when the DDI is isotropic (dipoles aligned with the rotation axis). A very striking consequence of the dipoles tilted towards the plane is the formation of vortex stripes[30,39,40]. Moreover, vortices could provide an unambiguous

smoking gun of superfluidity in supersolid states[41–43]. However, despite these intriguing predictions, vortices in dipolar quantum gases have not been observed until now.

This Article presents the experimental realization of quantized vortices in a dipolar BEC of highly magnetic dysprosium (Dy) atoms. Following a method proposed in ref. [40], extended to arbitrary magnetic-field angles in ref. [44], we show that the many-body phenomenon of magnetostriction[45], genuinely arising from the anisotropic DDI among atoms, provides a natural route to rotate the systems and nucleate vortices in a dipolar BEC. We carry out studies on the dynamics of the vortex formation, which agree very well with our theoretical predictions. Finally, we observe one of the earliest predictions for vortices in dipolar BECs: the formation of vortex stripes in the system.

In non-dipolar gases, quantized vortices have been produced using several conceptually different techniques, for instance, by rotating non-symmetric optical[6,11] or magnetic[46] potentials, by rapidly shaking the gas[14], by traversing it with obstacles with large enough velocity[7,47], by rapidly cooling the gas across the BEC phase transition[48,49] or by directly imprinting the vortex phase pattern[50]. Dipolar quantum gases, while able to form vortices with these same standard procedures[29], also offer unique opportunities that have no counterpart in contact-interacting gases. Crucially, the DDI gives rise to the phenomenon of magnetostriction in position space[45]. When dipolar BECs are polarized by an external magnetic field **B**—defining the dipole orientation—the DDI causes an elongation of the cloud along the polarization direction. This is a direct consequence of the system tendency to favour head-to-tail dipole configurations, which effectively reduces the interaction energy[19].

Such a magnetostrictive effect provides a simple method to induce an elliptic effective potential and drive rotation with a single control parameter. This modification of the effective potential is shown in Fig. 1a for a BEC in an oblate trap with cylindrical symmetry about the *z* axis. While a non-dipolar BEC takes the same shape as the confining trap (Fig. 1a(i)), introducing dipolar interactions with polarization axis along *z* stretches the cloud along this axis yet maintains cylindrical symmetry (Fig. 1a(ii)). Tilting the magnetic field leads to a breaking of the cylindrical symmetry, resulting in an ellipsoidal deformation of the cloud shape, as seen from the density projection onto the *x-y* plane (Fig. 1a(iii)). Finally, under continuous rotation of the magnetic field, which we coin 'magnetostirring', the condensate is predicted to rotate (Fig. 1a(iv)). This unique approach to stir a dipolar condensate can eventually lead to the nucleation of vortices[40,44], realizing genuinely interaction-driven vorticity through many-body phenomena.

We explore this protocol using a dipolar BEC of ¹⁶²Dy atoms. We create the BEC similar to our previous work[51] with the distinction that here the magnetic-field unit vector, $\hat{B}$, is kept tilted at an angle of $\theta = 35°$ with respect to the *z* axis both during evaporative cooling and magnetostirring (Fig. 1a(iii) and Methods). After preparation, the sample contains about 2×10^4 condensed atoms confined within a cylindrically symmetric optical dipole trap (ODT) with typical radial and axial trap frequencies $(\omega_\perp, \omega_z) = 2\pi \times [50.8(2), 140(1)]$ Hz. Here, before stirring, the magnetostriction is expected from simulations to increase the cloud aspect ratio (AR) in the horizontal plane from 1 up to 1.03, whereas the trap anisotropy is negligible. We use a vertical (*z*) absorption imaging to probe the radial (*x,y*) atomic distribution after a short time-of-flight (TOF) expansion of 3 ms. The atom number is instead measured using horizontal absorption imaging with a TOF of 26 ms.

Similarly to a rotation of a bucket containing superfluid helium or of a smoothly deformed ODT for non-dipolar BECs, magnetostirring is predicted to transfer angular momentum into a dipolar BEC[40,44]. In response to such an imposed rotation, the shape of an irrotational cloud is expected to elongate with an amplitude that increases with the rotation frequency Ω. This phenomenon is clearly visible in our experiments, as shown in Fig. 1b. Here we first revolve the tilted $\hat{B}$ around the *z* axis with a linearly increasing rotation frequency ($\dot{\Omega} = 2\pi \times 50$ Hz s⁻¹) and observe that the dipolar BEC starts to rotate
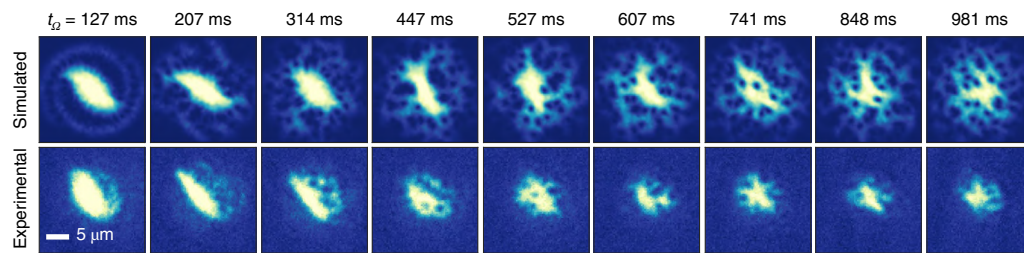
Fig. 2 | Observation of vortices in a dipolar BEC. Each column shows the simulated (top) and experimental (bottom) images for various rotation times t_Ω. For the experiment, the atoms are imaged along the z direction. In each experimental run, we rotate the magnetic field anticlockwise at $\Omega = 0.74\omega_\perp$ for different rotation times t_Ω. The magnetic-field value is kept to $B = 5.333(5)$ G. The initial condensed atom number is $N = 15,000$. The decreasing size of the cloud suggests a decrease in atom number. However, for states with vortices or spiral shapes, appearing at large t_Ω, our bimodal fit to extract the atom number breaks down. For the corresponding simulations, the parameters are $a_s = 112a_0$, trap frequencies $(\omega_\perp, \omega_z) = 2\pi \times [50, 150]$ Hz, $N = 8,000$ and $\Omega = 0.75\omega_\perp$.

at the same angular speed as the field and deforms with increasing elongation (Fig. 1b, top). We then stop the adiabatic ramp at a given value of Ω and probe the system under continuous rotation. We now find that the cloud continues rotating in the radial plane with an almost constant shape (Fig. 1b, bottom). Note that B is held constant at 5.333(5) G, where we estimate a contact scattering length of about $a_s = 111a_0$, where a_0 is the Bohr radius (Methods).

We further explore the response of our dipolar BEC to magneto-stirring by repeating the measurements in Fig. 1b (top), but stopping the ramp at different final values of Ω. The maximum value used for Ω approaches $\omega_\perp$, corresponding to a ramp duration of 1 s. We quantify the cloud elongation in terms of the aspect ratio AR $= \sigma_{max}/\sigma_{min}$, where the cloud widths σ_{max} and σ_{min} are extracted by fitting a rotated 2D Gaussian function to the density profiles. Figure 1c summarizes our results. We observe that initially the AR slightly deviates from 1 due to magnetostriction. It then slowly grows with increasing Ω, until a rapid increase at around $0.6\omega_\perp$ occurs, as this allows the angular momentum to increase, which decreases the energy in the rotating frame[52]. Suddenly, at a critical rotation frequency $\Omega_c \approx 0.74\omega_\perp$, the AR abruptly collapses back to AR ≈ 1, showing how the superfluid irrotational nature competes with the imposed rotation. This critical frequency is close to the value found in non-dipolar gases with a rotating elliptical harmonic trap, associated with a resonance at the quadrupole frequency[53].

To substantiate our observation, we perform numerical simulations of the zero-temperature extended Gross–Pitaevskii equation (eGPE)[54] (Methods). Quantum and thermal fluctuations are added to the initial states, which are important to seed the dynamic instabilities once they emerge at large enough Ω; see later discussion. The lines in Fig. 1c show our results. The dashed line is obtained through the same procedure as the experiment, whereas for the solid line, we halve the ramp rate, spending more time at each frequency. Both ramp procedures show quantitatively the same behaviour up to $\Omega = 0.8\omega_\perp$ and are in excellent agreement with the experimental results. The stability of the 1 s ramp exceeds the experimentally observed critical frequency. We partly attribute this discrepancy to asymmetries of the rotation in the experiment that are not present in the simulations, which may lead to an effective speed-up of the dynamical instabilities. However, in all cases, the AR rapidly decreases to about 1.

The growing AR and subsequent collapse to 1 is a signature of the dynamical instability of surface modes, known for being an important mechanism for seeding vortices and allowing them to penetrate into the high-density regions of rotated BECs[52,53,55], as also predicted for our dipolar system[40]. To search for quantum vortices in our system, we perform a new investigation where we directly set Ω close to Ω_c, aiming to trigger the instability at an earlier time when more atoms are condensed. We then hold the magnetic-field rotation fixed at this constant frequency for a time t_Ω. As shown in Fig. 2 (bottom), the cloud rapidly elongates, and the density starts to exhibit a spiral pattern, emanating
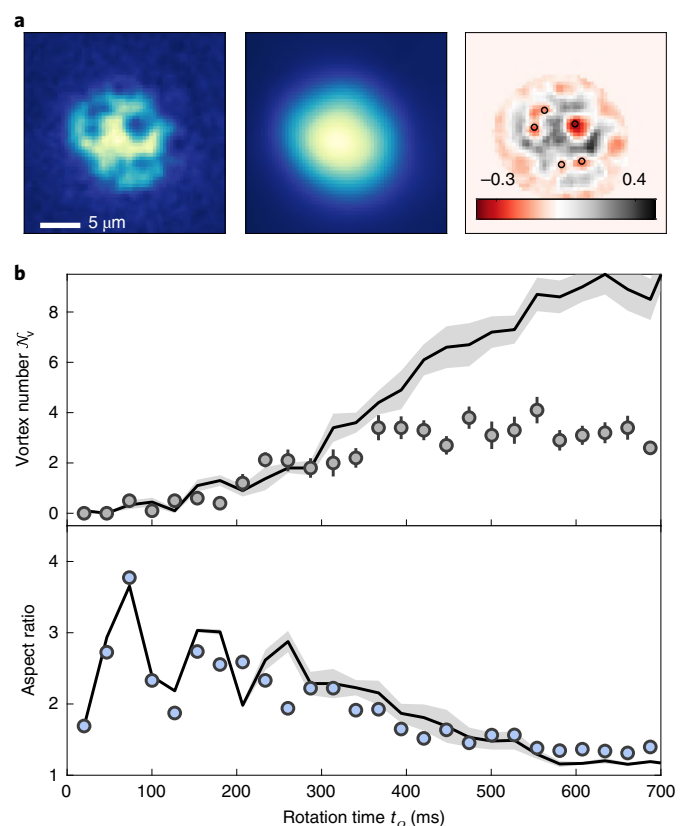

Fig. 3 | Time evolution of the average vortex number, $\mathcal{N}_v$, and cloud AR. a, Left: sample image after rotating for $t_\Omega = 474$ ms. Middle: blurred reference image ($\sigma = 2.1$ μm). Right: residuals with markers (black circles) indicating the identified vortices. **b**, The detected vortex number $\mathcal{N}_v$ (top) and the AR of the cloud (bottom) after the rotation time t_Ω. Data points and error bars show the mean and standard error from about ten experimental runs. Solid lines indicate the averaged results from ten corresponding simulations with different initial noise for parameters $a_s = 110a_0$, $(\omega_\perp, \omega_z) = 2\pi \times [50, 130]$ Hz, $N = 10,000$ and $\Omega = 0.75\omega_\perp$; the shaded area gives its standard error.

from the tips of the ellipsoid. As early as $t_\Omega = 314$ ms, clear holes are observed in the density profile, forming in the density halo around the centre, the first clear indication of vortices in a dipolar gas. These vortices, initially nucleated at the edge of the sample, persist as we continue to stir and eventually migrate towards the central (high-density) region. Vortices are still visible in the experiment after 1 s of magnetostirring, although our atom number decreases throughout this procedure.
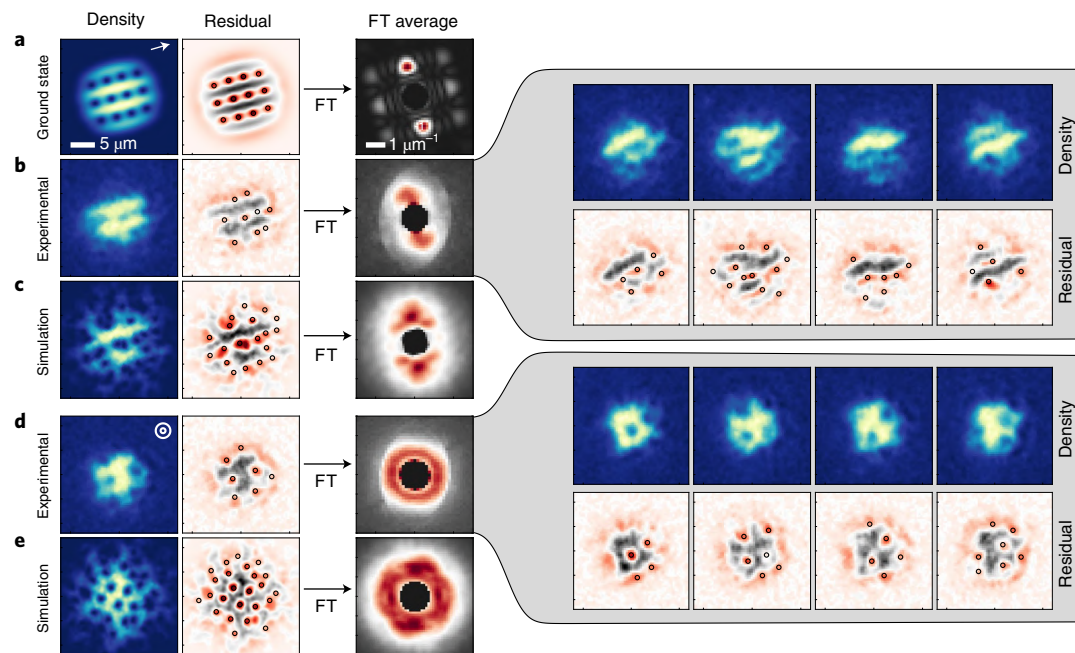
Fig. 4 | Stripe nature of vortices in a dipolar BEC. a, Left: ground-state stripe lattice solution for our experimental parameters $a_s = 109a_0$, trap frequencies $(\omega_\perp, \omega_z) = 2\pi \times [50, 130]$ Hz, $N = 10,000$ and $\Omega = 0.75\omega_\perp$. Middle: corresponding residual image, found by subtracting the ground state from the blurred image, with circles showing the detected vortices. Right: Fourier transform of the residual image. **b**, Left: single experimental image after 500 ms of continuous rotation at $\Omega = 0.75\omega_\perp$. Middle: the corresponding residual image. Right: Fourier transform of the residual images, averaged over 49 runs, with example shots shown to the right. **c**, Left: simulation result for the dynamic experimental procedure in **b**. Middle and right: residuals (middle) and FT analysis (right) (115 temporal images) as in **b**. **d**, The same as **b** for 121 runs, but we rotate for an additional 100 ms and then spiral the magnetic field to $\theta = 0°$ over a further 100 ms before imaging. **e**, Simulation result for procedure in **d**. All simulation images are rotated to have the same magnetic-field direction as the experiment, as indicated by the white arrow in **a** and by the circles in **d**.

Our observations bear a remarkable resemblance to the simulations; Fig. 2 (top) shows the in situ column densities. Taking a fixed atom number of $N = 8,000$, but otherwise repeating the experimental sequence, we observe many similar features. In the first 100 ms, the system elongates, consistent with Fig. 1, and a spiral density pattern appears before the instability, forming two arms that are filled with vortices close to the central density. Next, turbulent dynamics ensue as the density surface goes unstable and vortices emerge in the central high-density region. For this scattering length and atom number, the relaxation timescale to a stable vortex lattice is longer than the experimentally available (see Extended Data Fig. 3 for more images from this dataset). Note that at angles θ deeper into the plane, more atoms align head-to-tail in the loose radial confinement direction. Thus, when performing the rotation procedure, we find that the BEC is resilient to instability on the timescales of the experiment.

The observed evolution of the system under constant rotation shows some concurrence between the appearance of vortices in the absorption images and the formation of a round density pattern in the radial plane with AR ≈ 1 (Fig. 2). Note that the drop in AR observed in Fig. 1 is concurrent with the creation of vortices, but they reside in the low-density regions at this time, and we do not see them. To study this dynamical evolution in more detail, we adopt an analysis protocol for both the experiment and theory that allows us to quantitatively track the evolution of the average number of vortices, $\mathcal{N}_v$ (Methods). The result is shown in Fig. 3a. In brief, for each single image (Fig. 3a, left), we create a blurred reference image by applying a 2D Gaussian filter[56,57]. We then calculate the difference between each single image (Fig. 3a, left) and the corresponding reference (Fig. 3a, middle) to obtain the residual image (Fig. 3a, right), from which we count $\mathcal{N}_v$ by finding local minima below a certain threshold.

For the experimental density profiles, which are affected by both the limited resolution of the imaging system and the weak contrast in the low-density zones (halo) where the vortices initially nest, we expect $\mathcal{N}_v$ to be underestimated relative to the true value and the number expected by theory. However, to carry out a quantitative comparison with the simulations, we apply a blurring filter and add noise to the latter that mimics the actual resolution in the experiment (Methods).

Figure 3b shows both the evolution of $\mathcal{N}_v$ and cloud AR as a function of rotation time, t_Ω. Solid lines are the results from the eGPE simulations without any adjustable parameters. For $t_\Omega < 200$ ms, $\mathcal{N}_v$ is below 1, where vortices, if present, are at the edge of the cloud. For longer times, $\mathcal{N}_v$ increases and saturates to an average value of about three and a maximum of six vortices (see Fig. 3a for an example of five vortices). The observed saturation might be due to the decreased visibility and to the atom-loss-induced shrinking of the BEC size, which is not accounted for in the theory. We also compare the course of the average vortex number with the AR of the cloud. After initial large oscillations, due to the sudden jump in rotation frequency, the AR declines towards ~1 (ref. [53]). This happens as the vortex number simultaneously increases.

One fascinating prediction with vortices in a strongly dipolar gas under the influence of a rotating magnetic field relates to the structure of the resulting vortex lattice. Due to magnetostriction and the anisotropic vortex cores, the resulting vortex configuration is also anisotropic, producing a stripe phase in the strongly dipolar regime[29,30], instead of the usual triangular lattice in non-dipolar BECs[6]. The ground state stripe lattice solution for our parameters is shown in Fig. 4a, with a cloud AR = 1.08. In the vortex stripe phase, vertical planes of high-density regions, parallel to the magnetic field, alternate with low-density ones, which host rows of vertical vortex filaments. Such a configuration promotes head-to-tail dipolar attraction within the high-density ridges, and this acts to lower the energy. It should be noted that these states are distinct from the oscillating vortex sheets states, which appear after squeezing a triangular vortex lattice[58].

To explore this prediction, we perform two new surveys. First, we slightly reduce the magnetic-field value, reducing the scattering length to $a_s \approx 109 a_0$ and hence making the system relatively more dipolar. We magnetostir the BEC at a constant rotation frequency $\Omega = 0.75 \omega_\perp$ for 500 ms, but during TOF, we stop the magnetic-field rotation and keep it in place at $\theta = 35°$. The stripe structure is revealed in Fig. 4b (left) for a single experimental run and is clearly visible in the residual image (Fig. 4b, middle) where the vortices align along three stripes. The spatial structure of the residual image can be assessed through the absolute value of 2D Fourier transform (FT). After taking the FT of each residual image, we then average the result (Fig. 4b, right), finding a clear peak at the wave number k of the inter-stripe spacing. This shows that the stripe spatial structure survives the averaging, implying that the majority of images show stripes with the same spacing, and they also have the same orientation as set by the magnetic field, as evidenced by the example images shown in the right of Fig. 4. Note that these observations do not rely on our ability to resolve individual vortices, as the stripes are an ensemble effect of many aligned vortices. In fact, by comparing with the numerical simulations of the dynamical procedure (Fig. 4c), we expect there are more vortices than detected here that fill in the stripes, forging out this structure. In general, our simulations show that the stripes appear faster when the scattering length is lower and when the atom number is larger. In the long time limit of the scenario presented in Fig. 2, we expect the stationary solution to also be the stripe state, but this is not observable on our timescales.

Remarkably, the stripe structure washes out when we subsequently tilt the magnetic-field orientation to $\theta = 0°$ (parallel to the trap symmetry axis), as shown in Fig. 4d (left). Here, after 600 ms of magnetostirring, we add another step in which we spiral up the magnetic field to $\theta = 0°$ (with Ω fixed) over 100 ms, before imaging. Under these conditions, all vortex properties are again isotropic within the plane. The non-equilibrium positioning of the vortices is arbitrary, and if we average the FT of the residuals directly, we observe a homogeneous ring in the average FT (Fig. 4d, right). Also, this behaviour is confirmed by the simulations, as shown in Fig. 4e. The vortices survive long after the magnetostirring has stopped (not shown), due to their topological protection.

By exploiting magnetostirring—a novel, robust method of generating angular momentum—we have observed quantized vortices in a dipolar quantum gas and the appearance of the vortex stripe configuration. Future works will focus on investigations of the individual vortex shape and behaviour, such as the anisotropic nature of the vortex cores for in-plane magnetic fields[30–33], the interplay between the vortex and roton excitations[30–34] and exotic vortex patterns such as square lattices[29], and investigations into anisotropic turbulence[59]. This work also opens the door to studying more complex matter under rotation, such as dipolar droplets[60–62] and supersolid states[41–43,51]. Such proposals will be challenging due to the intricate density patterns[63]; however, such observations would provide conclusive evidence of superfluidity in supersolids. Rotating the magnetic field at frequencies far larger than the radial trap frequencies, but smaller than the Larmor frequency, has been observed to tune the sign and magnitude of the dipole–dipole interaction[64]—a method also employed in nuclear magnetic resonance spectroscopy—but there remain open questions on the stability of this procedure[65,66], which if rectifiable would unlock new research directions[64]. Other vortex generation methods, such as thermally activated pairs in quasi-two dimensions to assess the Berezinskii–Kosterlitz–Thouless transition and stochastically generated vortex tangles through temperature quenches to assess the Kibble–Zurek mechanism, remain unexplored in dipolar gases[29]. The technique introduced here is also applicable to a wide range of systems governed by long-range interactions through the manipulation of magnetic or electric fields.

Online content

Any methods, additional references, Nature Research reporting summaries, source data, extended data, supplementary information, acknowledgements, peer review information; details of author contributions and competing interests; and statements of data and code availability are available at https://doi.org/10.1038/s41567-022-01793-8.

References

1. Donnelly, R. J. *Quantized Vortices in Helium II* (Cambridge Univ. Press, 1991).
2. Pines, D. & Alpar, M. A. Superfluidity in neutron stars. *Nature* **316**, 27–32 (1985).
3. Abrikosov, A. A. Nobel Lecture: Type-II superconductors and the vortex lattice. *Rev. Mod. Phys.* **76**, 975 (2004).
4. Lagoudakis, K. G. et al. Quantized vortices in an exciton–polariton condensate. *Nat. Phys.* **4**, 706–710 (2008).
5. Matthews, M. R. et al. Vortices in a Bose–Einstein condensate. *Phys. Rev. Lett.* **83**, 2498 (1999).
6. Madison, K. W., Chevy, F., Wohlleben, W. & Dalibard, J. Vortex formation in a stirred Bose–Einstein condensate. *Phys. Rev. Lett.* **84**, 806 (2000).
7. Neely, T. W., Samson, E. C., Bradley, A. S., Davis, M. J. & Anderson, B. P. Observation of vortex dipoles in an oblate Bose–Einstein condensate. *Phys. Rev. Lett.* **104**, 160401 (2010).
8. Ku, M. J. H. et al. Motion of a solitonic vortex in the BEC–BCS crossover. *Phys. Rev. Lett.* **113**, 065301 (2014).
9. Donadello, S. et al. Observation of solitonic vortices in Bose–Einstein condensates. *Phys. Rev. Lett.* **113**, 065302 (2014).
10. Anderson, B. P. et al. Watching dark solitons decay into vortex rings in a Bose–Einstein condensate. *Phys. Rev. Lett.* **86**, 2926 (2001).
11. Abo-Shaeer, J. R., Raman, C., Vogels, J. M. & Ketterle, W. Observation of vortex lattices in Bose–Einstein condensates. *Science* **292**, 476–479 (2001).
12. Hadzibabic, Z., Krüger, P., Cheneau, M., Battelier, B. & Dalibard, J. Berezinskii–Kosterlitz–Thouless crossover in a trapped atomic gas. *Nature* **441**, 1118–1121 (2006).
13. Neely, T. W. et al. Characteristics of two-dimensional quantum turbulence in a compressible superfluid. *Phys. Rev. Lett.* **111**, 235301 (2013).
14. Navon, N., Gaunt, A. L., Smith, R. P. & Hadzibabic, Z. Emergence of a turbulent cascade in a quantum gas. *Nature* **539**, 72–75 (2016).
15. Zwierlein, M. W., Abo-Shaeer, J. R., Schirotzek, A., Schunck, C. H. & Ketterle, W. Vortices and superfluidity in a strongly interacting Fermi gas. *Nature* **435**, 1047–1051 (2005).
16. Lu, M., Burdick, N. Q., Youn, S. H. & Lev, B. L. Strongly dipolar Bose–Einstein condensate of dysprosium. *Phys. Rev. Lett.* **107**, 190401 (2011).
17. Aikawa, K. et al. Bose–Einstein condensation of erbium. *Phys. Rev. Lett.* **108**, 210401 (2012).
18. Norcia, M. A. & Ferlaino, F. Developments in atomic control using ultracold magnetic lanthanides. *Nat. Phys.* **17**, 1349–1357 (2021).
19. Chomaz, L. et al. Dipolar physics: a review of experiments with magnetic quantum gases. Preprint at https://arxiv.org/abs/2201.02672 (2022).
20. Baier, S. et al. Extended Bose–Hubbard models with ultracold magnetic atoms. *Science* **352**, 201–205 (2016).
21. Landau, L. Theory of the superfluidity of helium II. *Phys. Rev.* **60**, 356 (1941).
22. Chomaz, L. et al. Observation of roton mode population in a dipolar quantum gas. *Nat. Phys.* **14**, 442–446 (2018).
23. Schmidt, J.-N. et al. Roton excitations in an oblate dipolar quantum gas. *Phys. Rev. Lett.* **126**, 193002 (2021).
24. Kadau, H. et al. Observing the Rosensweig instability of a quantum ferrofluid. *Nature* **530**, 194–197 (2016).

25. Tanzi, L. et al. Observation of a dipolar quantum gas with metastable supersolid properties. *Phys. Rev. Lett.* **122**, 130405 (2019).

26. Böttcher, F. et al. Transient supersolid properties in an array of dipolar quantum droplets. *Phys. Rev. X* **9**, 011051 (2019).

27. Chomaz, L. et al. Long-lived and transient supersolid behaviors in dipolar quantum gases. *Phys. Rev. X* **9**, 021012 (2019).

28. Norcia, M. A. et al. Two-dimensional supersolidity in a dipolar quantum gas. *Nature* **596**, 357–361 (2021).

29. Martin, A. M., Marchant, N. G., O'Dell, D. H. J. & Parker, N. G. Vortices and vortex lattices in quantum ferrofluids. *J. Phys. Condens. Matter* **29**, 103004 (2017).

30. Yi, S. & Pu, H. Vortex structures in dipolar condensates. *Phys. Rev. A* **73**, 061602 (2006).

31. Ticknor, C., Wilson, R. M. & Bohn, J. L. Anisotropic superfluidity in a dipolar Bose gas. *Phys. Rev. Lett.* **106**, 065301 (2011).

32. Mulkerin, B. C., van Bijnen, R. M. W., O'Dell, D. H. J., Martin, A. M. & Parker, N. G. Anisotropic and long-range vortex interactions in two-dimensional dipolar Bose gases. *Phys. Rev. Lett.* **111**, 170402 (2013).

33. Mulkerin, B. C., O'Dell, D. H. J., Martin, A. M. & Parker, N. G. Vortices in the two-dimensional dipolar Bose gas. *J. Phys. Conf. Ser.* **497**, 012025 (2014).

34. Jona-Lasinio, M., Łakomy, K. & Santos, L. Roton confinement in trapped dipolar Bose–Einstein condensates. *Phys. Rev. A* **88**, 013619 (2013).

35. Gautam, S. Dynamics of the corotating vortices in dipolar Bose–Einstein condensates in the presence of dissipation. *J. Phys. B* **47**, 165301 (2014).

36. Cooper, N., Rezayi, E. & Simon, S. Vortex lattices in rotating atomic Bose gases with dipolar interactions. *Phys. Rev. Lett.* **95**, 200402 (2005).

37. Zhang, J. & Zhai, H. Vortex lattices in planar Bose–Einstein condensates with dipolar interactions. *Phys. Rev. Lett.* **95**, 200403 (2005).

38. Kumar, R. K., Sriraman, T., Fabrelli, H., Muruganandam, P. & Gammal, A. Three-dimensional vortex structures in a rotating dipolar Bose–Einstein condensate. *J. Phys. B* **49**, 155301 (2016).

39. Cai, Y., Yuan, Y., Rosenkranz, M., Pu, H. & Bao, W. Vortex patterns and the critical rotational frequency in rotating dipolar Bose–Einstein condensates. *Phys. Rev. A* **98**, 023610 (2018).

40. Prasad, S. B., Bland, T., Mulkerin, B. C., Parker, N. G. & Martin, A. M. Vortex lattice formation in dipolar Bose–Einstein condensates via rotation of the polarization. *Phys. Rev. A* **100**, 023625 (2019).

41. Roccuzzo, S. M., Gallemí, A., Recati, A. & Stringari, S. Rotating a supersolid dipolar gas. *Phys. Rev. Lett.* **124**, 045702 (2020).

42. Gallemí, A., Roccuzzo, S. M., Stringari, S. & Recati, A. Quantized vortices in dipolar supersolid Bose–Einstein-condensed gases. *Phys. Rev. A* **102**, 023322 (2020).

43. Ancilotto, F., Barranco, M., Pi, M. & Reatto, L. Vortex properties in the extended supersolid phase of dipolar Bose–Einstein condensates. *Phys. Rev. A* **103**, 033314 (2021).

44. Prasad, S. B., Mulkerin, B. C. & Martin, A. M. Arbitrary-angle rotation of the polarization of a dipolar Bose–Einstein condensate. *Phys. Rev. A* **103**, 033322 (2021).

45. Stuhler, J. et al. Observation of dipole–dipole interaction in a degenerate quantum gas. *Phys. Rev. Lett.* **95**, 150406 (2005).

46. Haljan, P. C., Coddington, I., Engels, P. & Cornell, E. A. Driving Bose–Einstein condensate vorticity with a rotating normal cloud. *Phys. Rev. Lett.* **87**, 210403 (2001).

47. Kwon, W. J. et al. Sound emission and annihilations in a programmable quantum vortex collider. *Nature* **600**, 64–69 (2021).

48. Corman, L. et al. Quench-induced supercurrents in an annular Bose gas. *Phys. Rev. Lett.* **113**, 135302 (2014).

49. Liu, I. K. et al. Dynamical equilibration across a quenched phase transition in a trapped quantum gas. *Commun. Phys.* **1**, 24 (2018).

50. Del Pace, G. et al. Imprinting persistent currents in tunable fermionic rings. Preprint at https://arxiv.org/abs/2204.06542 (2022).

51. Norcia, M. A. et al. Can angular oscillations probe superfluidity in dipolar supersolids? *Phys. Rev. Lett.* **129**, 040403 (2022).

52. Recati, A., Zambelli, F. & Stringari, S. Overcritical rotation of a trapped Bose–Einstein condensate. *Phys. Rev. Lett.* **86**, 377 (2001).

53. Madison, K. W., Chevy, F., Bretin, V. & Dalibard, J. Stationary states of a rotating Bose–Einstein condensate: routes to vortex nucleation. *Phys. Rev. Lett.* **86**, 4443 (2001).

54. Wächtler, F. & Santos, L. Quantum filaments in dipolar Bose–Einstein condensates. *Phys. Rev. A* **93**, 061603 (2016).

55. Sinha, S. & Castin, Y. Dynamic instability of a rotating Bose–Einstein condensate. *Phys. Rev. Lett.* **87**, 190402 (2001).

56. Abo-Shaeer, J. R., Raman, C. & Ketterle, W. Formation and decay of vortex lattices in Bose–Einstein condensates at finite temperatures. *Phys. Rev. Lett.* **88**, 070409 (2002).

57. Kwon, W. J., Moon, G., Choi, J.-y, Seo, S. W. & Shin, Y.-i Relaxation of superfluid turbulence in highly oblate Bose–Einstein condensates. *Phys. Rev. A* **90**, 063627 (2014).

58. Engels, P., Coddington, I., Haljan, P. C. & Cornell, E. A. Nonequilibrium effects of anisotropic compression applied to vortex lattices in Bose–Einstein condensates. *Phys. Rev. Lett.* **89**, 100403 (2002).

59. Bland, T., Stagg, G. W., Galantucci, L., Baggaley, A. W. & Parker, N. G. Quantum ferrofluid turbulence. *Phys. Rev. Lett.* **121**, 174501 (2018).

60. Cidrim, A., dos Santos, F. E., Henn, E. A. & Macrì, T. Vortices in self-bound dipolar droplets. *Phys. Rev. A* **98**, 023618 (2018).

61. Lee, A.-C., Baillie, D., Bisset, R. N. & Blakie, P. B. Excitations of a vortex line in an elongated dipolar condensate. *Phys. Rev. A* **98**, 063620 (2018).

62. Ferrier-Barbut, I. et al. Scissors mode of dipolar quantum droplets of dysprosium atoms. *Phys. Rev. Lett.* **120**, 160402 (2018).

63. Hertkorn, J. et al. Pattern formation in quantum ferrofluids: from supersolids to superglasses. *Phys. Rev. Res.* **3**, 033125 (2021).

64. Tang, Y., Kao, W., Li, K.-Y. & Lev, B. L. Tuning the dipole–dipole interaction in a quantum gas with a rotating magnetic field. *Phys. Rev. Lett.* **120**, 230401 (2018).

65. Prasad, S. B. et al. Instability of rotationally tuned dipolar Bose–Einstein condensates. *Phys. Rev. Lett.* **122**, 050401 (2019).

66. Baillie, D. & Blakie, P. B. Rotational tuning of the dipole–dipole interaction in a Bose gas of magnetic atoms. *Phys. Rev. A* **101**, 043606 (2020).

Methods

Experimental procedure

We prepare an ultracold gas of ^{162}Dy atoms in an ODT. Three 1,064 nm laser beams, overlapping at their foci, form the ODT. The experimental procedure to BEC is similar to the one followed in our previous work[51], but the magnetic-field unit vector, $\hat{B}$, is tilted by an angle of $\theta = 35°$ with respect to the z-axis during the whole sequence. After preparation, the sample contains about 2×10^4 condensed atoms. The corresponding trap frequencies are typically $(\omega_\perp, \omega_z) = 2\pi \times [50.8(2), 140(1)]$ Hz. For all our measurements, the deviation of the trap AR in the x–y plane $AR_{trap} = \omega_y/\omega_x$ from 1 is always smaller than 0.6%. We evaporate the atoms at $B = 5.423(5)$ G and jump to the final magnetic-field value during the last evaporation ramp. After the preparation of the BEC, the magnetic field is rotated as described in the next section. We use standard absorption imaging to record the atomic distribution. We probe the vortices using the vertical imaging taken along the axis of rotation (z), for which the dark spots within the condensate correspond to the cores of individual vortices. The vertical images are taken with a short TOF of 3 ms and a pulse duration of 3–4 µs. For the data in Figs. 1–3, we let the magnetic-field spinning during TOF, whereas for Fig. 4, we use a static field orientation.

Control of the magnetic field

Calibration. Three pairs of coils—each oriented along a primary axis in the laboratory frame—enable the creation of a homogeneous field with arbitrary orientations. The absolute magnetic-field value B of each pair of coils is independently calibrated using radio frequency (RF) spectroscopy. The RF drives transitions to excited Zeeman states, leading to a resonant dip in the atom number. The long-term stability—measured via the peak position of the RF resonance over the course of several days—is on the order of $\Delta B = \pm 1$ mG, while shot-to-shot fluctuations, measured via the width of the RF resonance for a single calibration set, is $\Delta B = \pm 5$ mG.

Rotation. We drive the rotation of the magnetic field by sinusoidally modulating the magnetic-field value components B_x and B_y with a phase difference of 90° between them. As we want to keep the absolute magnetic-field value B constant during rotation, we measure it for various values of the azimuthal angle ϕ and fixed $\theta = 35°$ by performing Feshbach loss spectroscopy around 5.1 G. We find an average shift of B of about 10 mG from the $\theta = 0°$ case, which we take into account. We also find small deviations as a function of ϕ of $\Delta B < 20$ mG, which might appear due to slightly non-orthogonal alignment of the magnetic fields. We did not correct these deviations for the sake of simplicity.

Scattering length

The scattering length in ^{162}Dy is currently not known with large accuracy[67–70]. To estimate the scattering length in the small magnetic-field range around $B = 5.3$ G, relevant to this work, we use the well-known relation $a_s = a_{bg}\prod_i[1 - \Delta B_i/(B - B_{0,i})]$ (ref. [71]), where $B_{0,i}$ and ΔB_i are the centre position and the width of the i-th feature of the Feshbach loss measurement reported in ref. [70], respectively. The value of the background scattering length, a_{bg}, is empirically fixed by measuring the magnetic-field value at which the supersolid transition occurs and comparing it with the corresponding critical a_s predicted from simulations. Such an approach leads to $a_s = 111(9)a_0$ at $B = 5.333$ G. Extended Data Fig. 1 shows the resulting scattering lengths for the relevant magnetic fields. Although such an approach gives very good agreement between theory and experiments, future works on a precise determination of a_s, similar to the one achieved with erbium[72], would be desirable.

Magnetostirring

Tilting the magnetic-field vector **B** away from the symmetry axis of our cylindrical trap leads to an ellipsoidal deformation of the cloud[45] and therefore to a breaking of the cylindrical symmetry. This allows

for the transfer of angular momentum to the sample by rotating the magnetic field (magnetostirring). In all our measurements, we use a **B** tilted with respect to the z axis by 35° and a constant value B. That value is $B = 5.333(5)$ G for the surveys in Figs. 1–3 and $B = 5.323(5)$ G for Fig. 4. For these parameters, the deformed magnetostricted AR of the cloud is $AR - 1 = 0.03$. For all our measurements, the measured trap $AR_{trap} - 1 < 0.006$ is much smaller than the deformation due to magnetostriction. Additionally, we have confirmed with simulations that even with trap asymmetries of up to 10%, for example, $(\omega_x, \omega_y) = (55, 50)$ Hz, this procedure can still generate vortices in a lattice configuration.

At the scattering lengths considered in this work, 35° is an optimal choice to see the vortices within ~500 ms of rotation and anisotropic enough to observe the stripe phase. From the simulations, we find that tilt angles smaller than 35° increase the timescale to vortex nucleation. Similarly, tilting the angle further into the plane increases the number of atoms that are aligned head to tail, making the dipolar interaction dominantly attractive. This attractive force holds the condensate together during the rotation, also increasing the time to vortex nucleation. From the experimental side, increasing the tilt angle reduces the contrast of the absorption imaging, since the magnetic field is not parallel to the imaging axis. As the TOF is only 3 ms, we do not rotate up the magnetic field before imaging to avoid undesired effects, such as losing the anisotropy given by $\theta \neq 0°$.

Adiabatic frequency ramp. We employ different magnetic-field rotation sequences for the different datasets. For the dataset of Fig. 1c, the rotation frequency of the magnetic field is linearly increased to different final values at a speed of $\dot{\Omega} = 2\pi \times 50$ Hz s^{-1} and for a duration of $t_{\dot{\Omega}} = 0$–1 s. The ramp time is much longer than the period of the rotation Ω^{-1} for higher rotation frequencies $\Omega \gtrsim \Omega_c$, and, therefore, the ramp is adiabatic for the regimes considered, until the onset of dynamical instabilities. After the ramp, the magnetic-field direction is rotated at the target rotation frequency Ω for one final period (as shown in Fig. 1b). We sample ten different final magnetic-field angles during this last rotation, measuring the corresponding AR and averaging the result to remove any potential biases due to latent trap anisotropies. Each data point is then obtained with eight to ten experimental runs.

Constant rotation frequency. For the dataset of Figs. 2, 3 and 4b, we directly start to rotate at the final rotation frequency Ω without any acceleration phase. The magnetic field is then rotated for a variable time t_Ω, after which the atoms are released from the trap and a vertical image is taken.

Spiral up magnetic field. For the dataset of Fig. 4d, we employ a similar sequence as described above. However, after constantly rotating the magnetic field at $\Omega = 0.75\omega_\perp$, the magnetic field is spiralled up in 100 ms to $\theta = 0°$ by linearly reducing θ while continuing rotating. Afterwards, the atoms are released from the trap and a vertical image is taken.

Theoretical model

We employ an eGP formalism to model our experimental set-up. In this scheme, the inter-particle interactions are described by the two-body pseudo-potential

$$U(\mathbf{r}) = \frac{4}{m}\frac{\hbar^2 a_s}{m}\delta(\mathbf{r}) + \frac{3\hbar^2 a_{dd}}{m}\frac{1 - 3(\hat{\mathbf{e}}(t)\cdot\mathbf{r})^2}{r^3}, \tag{1}$$

with $\delta(\mathbf{r})$ being the Kronecker delta function and $\mathbf{r} = (x, y, z)$. The first term describes the short-range interactions governed by the s-wave scattering length a_s, with Planck's constant $\hbar$ and particle mass m. The second term represents the anisotropic and long-range dipole–dipole interactions, characterized by dipole length $a_{dd} = \mu_0\mu_m^2 m/12$ $\hbar^2$, with magnetic moment μ_m and vacuum permeability μ_0. We always consider ^{162}Dy, such that $a_{dd} = 129.2a_0$, where a_0 is the Bohr radius.

The dipoles are polarized uniformly along a time-dependent axis, given by

$$\hat{\mathbf{e}}(t) = (\sin\theta(t)\cos\phi(t), \sin\theta(t)\sin\phi(t), \cos\theta(t)) \qquad (2)$$

with time-dependent polarization angle $\theta(t)$ and $\phi(t) = \int_0^t dt'\,\Omega(t')$, for rotation frequency protocol $\Omega(t)$.

Beyond-mean-field effects are treated through the inclusion of a Lee–Huang–Yang correction term[73]

$$\gamma_{QF} = \frac{128\hbar^2}{3m}\sqrt{a_s^5}\,\mathrm{Re}\{\mathcal{Q}_5(\epsilon_{dd})\}, \qquad (3)$$

with $\mathcal{Q}_5(\epsilon_{dd}) = \int_0^1 du\,(1 - \epsilon_{dd} + 3u^2\epsilon_{dd})^{5/2}$ being the auxiliary function, and the relative dipole strength is given by $\epsilon_{dd} = a_{dd}/a_s$. Finally, the full eGPE then reads[54,74–76]

$$i\hbar\frac{\partial\Psi(\mathbf{x},t)}{\partial t} = \left[-\frac{\hbar^2\nabla^2}{2m} + \frac{1}{2}m\left(\omega_x^2 x^2 + \omega_y^2 y^2 + \omega_z^2 z^2\right)\right.$$
$$\left. + \int d^3\mathbf{x}'\,U(\mathbf{x} - \mathbf{x}')|\Psi(\mathbf{x}',t)|^2 + \gamma_{QF}|\Psi(\mathbf{x},t)|^3\right]\Psi(\mathbf{x},t), \qquad (4)$$

where $\omega_{x,y,z}$ are the harmonic trap frequencies. The wave function Ψ is normalized to the total atom number $N = \int d^3\mathbf{x}|\Psi|^2$. The stationary solution for Fig. 4a is found through the imaginary time procedure in the rotating frame, introducing the usual angular momentum operator $\Omega\hat{L}_z$ into equation (4). The initial state $\Psi(\mathbf{x}, 0)$ of the real-time simulations is always obtained by adding non-interacting noise to the ground state $\Psi_0(\mathbf{x})$. Given the single-particle eigenstates ϕ_n and the complex Gaussian random variables α_n sampled with $\langle|\alpha_n|^2\rangle = (e^{n/k_B T} - 1)^{-1} + \frac{1}{2}$ for a temperature $T = 20$ nK and Boltzmann's constant k_B, the initial state can be described as $\Psi(\mathbf{x}, 0) = \Psi_0(\mathbf{x}) + \sum_n' \alpha_n\phi_n(\mathbf{x})$, where the sum is restricted only to the modes with $\epsilon_n \leq 2k_B T$ (ref. [77]). Throughout, the density images are presented in situ, with a scaling factor to account for the 3 ms TOF for the experimental images.

To obtain the average residual FT images for Fig. 4c,e, we first Fourier transform 115 frames from the simulation between 700 ms and 1.1 s in the rotating frame before averaging the result.

Atom number

Extended Data Fig. 2 shows the condensed atom number N_c for the measurement with an adiabatic ramp of the magnetic-field rotational velocity ($\dot{\Omega} = 2\pi \times 50$ Hz s^{-1}), corresponding to the data of Fig. 1c. Three-body losses are negligible in the low-density BEC phase, with losses probably coming from imperfections in the rotation procedure and heating. To extract the atom number, we use the horizontal imaging with 26 ms of TOF. About 3 ms before flashing the imaging resonant light to the atoms, we rotate the magnetic field in the imaging plane and perform standard absorption imaging. From the absorption images, we extract N_c from a bimodal fit up to 700 ms. At later times, the system undergoes a dynamic instability (see discussion in the main text), and the density profile deviates from a simple bimodal distribution. During the observation time, we see a slight decrease of N_c, and for our theory simulations, we use a constant atom number of $N_c = 15,000$. Note that in all following datasets, in which we abruptly accelerate the magnetic-field rotation to the desired final velocity, we observe a faster decay, and our simulations are performed with either $N_c = 8,000$ or $N_c = 10,000$.

Vortex detection

Vortex detection algorithm. Since vortices appear as dark holes in the density profile of a BEC, which would otherwise have a smooth profile, our approach to extract the number of vortices is to look at deviations between the image and an unmodulated reference image. To extract the vortex number from the raw images, we proceed as follows.

First, we prepare the image n_{img}, the reference image n_{ref} and the residual image n_{res}. The image is normalized such that the maximum density $\max(n_{img}) = 1$. We create the reference image by blurring the image via applying a 2D Gaussian filter with $\sigma = 5$ pixel, corresponding to about 2.1 μm. This blurring smoothens any structure on the length-scale of the filter width; therefore, any holes in the density profile wash out. We then normalize the atom number of the reference to be the same as from the image $N_{ref} = \iint n_{ref} \doteq N_{img} = \iint n_{img}$. The residual image is calculated as the difference between the image and the reference $n_{res} = n_{img} - n_{ref}$. We additionally mask the region where the density of the reference is below a certain threshold ($n_{res} = 0$, where $n_{ref} \leq 0.1$).

Second, we identify local minima in the residual image and determine whether they are connected to vortices. For this, we create a list of local minima (x_{min}, y_{min}), defined by the condition that the pixel density $n_{res}(x_{min}, y_{min})$ is lower than of all surrounding pixels. Then we remove minima with density values above zero $n_{res}(x_{min}, y_{min}) \geq 0$ or which are within one pixel distance of the mask border. Now we determine a local contrast for each minimum by calculating the difference between its central density value and the mean of the density values ± 2 pixel values away from it $n_{con}(x_{min}, y_{min}) = n_{res}(x_{min}, y_{min}) - \mathrm{mean}(n_{res}(x_{min} \pm 2\,px, y_{min} \pm 2\,px))$, and remove minima above a certain threshold $n_{con} > -0.11$. As a last step, we check the distance d between all remaining minima to avoid double counting of minima too close to each other. In case d is below the threshold $d < 5$ pixel, the minimum with the higher residual density value n_{res} is discarded.

Preparation of theory density profiles. For the direct comparison of the vortex number shown in Fig. 3b, we apply additional steps to the density profiles obtained from theory. First, we reduce the resolution by a 2×2 binning to make the pixel size of the theory density profiles n_{img}^{theo} essentially the same as for the experimental images (sizes are within 5%). After normalizing to $\max(n_{img}^{theo}) = 1$, we apply Gaussian white noise with zero mean and a variance of 0.01 to each pixel, recreating the noise pattern from empty regions of experimental images. Then we blur the image using a 2D Gaussian filter with $\sigma = 1$ pixel (~0.42 μm); this recreates the same resolution condition as our experimental set-up. The resulting density profile is taken as the input image for the vortex detection algorithm described above.

Benchmarking the vortex detection algorithm. As the vortex positions for the simulation images are known a priori due to the available phase map, we can derive the fidelity of the vortex detection algorithm for simulation data. For the theory data shown in Fig. 3b in the time frame between 600 and 700 ms, the average detected vortex number in the simulated density profiles (applying the preparation scheme described above) is about 9, while the real number of vortices present in the same area of the image is about 33 in average. This mismatch is explained by the conservative choice of the thresholds for vortex detection together with the added noise, which results in only counting clear density dips as vortices, throwing out many vortices in the low-density region. This conservative choice of thresholds on the other hand leads to a very high fidelity of >97%, where we define the fidelity as the percentage of detected vortices that correspond to actual present vortices in the data. For raw simulation data (without resolution reduction, added noise and blurring), the vortex detection algorithm would detect up to 80% of the vortices present with a fidelity of >95%.

Note that for the visualization of the vortex positions for Fig. 4, we slightly increased the local threshold $n_{con} > -0.08$ and decreased the minimum distance between vortices $d < 3$ pixel, which increases the overall number of vortices detected. For the density distributions obtained from theory, we additionally omit the resolution reduction, addition of noise and blurring steps.

Data availability
Data pertaining to this work can be found at https://doi.org/10.5281/zenodo.7019859.

Code availability
The codes that support the findings of this study are available from the corresponding author upon reasonable request.

References

67. Tang, Y., Sykes, A., Burdick, N. Q., Bohn, J. L. & Lev, B. L. s-wave scattering lengths of the strongly dipolar bosons ^{162}Dy and ^{164}Dy. *Phys. Rev. A* **92**, 022703 (2015).

68. Tang, Y. et al. Anisotropic expansion of a thermal dipolar Bose gas. *Phys. Rev. Lett.* **117**, 155301 (2016).

69. Lucioni, E. et al. Dysprosium dipolar Bose–Einstein condensate with broad Feshbach resonances. *Phys. Rev. A* **97**, 060701 (2018).

70. Böttcher, F. et al. Dilute dipolar quantum droplets beyond the extended Gross–Pitaevskii equation. *Phys. Rev. Res.* **1**, 033088 (2019).

71. Chin, C., Grimm, R., Julienne, P. & Tiesinga, E. Feshbach resonances in ultracold gases. *Rev. Mod. Phys.* **82**, 1225 (2010).

72. Patscheider, A. et al. Determination of the scattering length of erbium atoms. *Phys. Rev. A* **105**, 063307 (2022).

73. Lima, A. R. P. & Pelster, A. Quantum fluctuations in dipolar Bose gases. *Phys. Rev. A* **84**, 041604 (2011).

74. Ferrier-Barbut, I., Kadau, H., Schmitt, M., Wenzel, M. & Pfau, T. Observation of quantum droplets in a strongly dipolar Bose gas. *Phys. Rev. Lett.* **116**, 215301 (2016).

75. Chomaz, L. et al. Quantum-fluctuation-driven crossover from a dilute Bose–Einstein condensate to a macrodroplet in a dipolar quantum fluid. *Phys. Rev. X* **6**, 041039 (2016).

76. Bisset, R. N., Wilson, R. M., Baillie, D. & Blakie, P. B. Ground-state phase diagram of a dipolar condensate with quantum fluctuations. *Phys. Rev. A* **94**, 033619 (2016).

77. Blakie, P., Bradley, A., Davis, M., Ballagh, R. & Gardiner, C. Dynamics and statistical mechanics of ultra-cold Bose gases using c-field techniques. *Adv. Phys.* **57**, 363–455 (2008).

Author contributions
L.K., C.P., G.L., E.C., M.J.M. and F.F. performed the experimental work and data analysis. E.P., T.B. and R.N.B. performed the theoretical work. All authors contributed to the interpretation of the results and the preparation of the manuscript.

Competing interests
The authors declare no competing interests.

Additional information
Extended data is available for this paper at https://doi.org/10.1038/s41567-022-01793-8.

Supplementary information The online version contains supplementary material available at https://doi.org/10.1038/s41567-022-01793-8.

Correspondence and requests for materials should be addressed to Francesca Ferlaino.

Peer review information *Nature Physics* thanks Oliver Gorceix, Han Pu and the other, anonymous, reviewer(s) for their contribution to the peer review of this work.

Reprints and permissions information is available at www.nature.com/reprints.
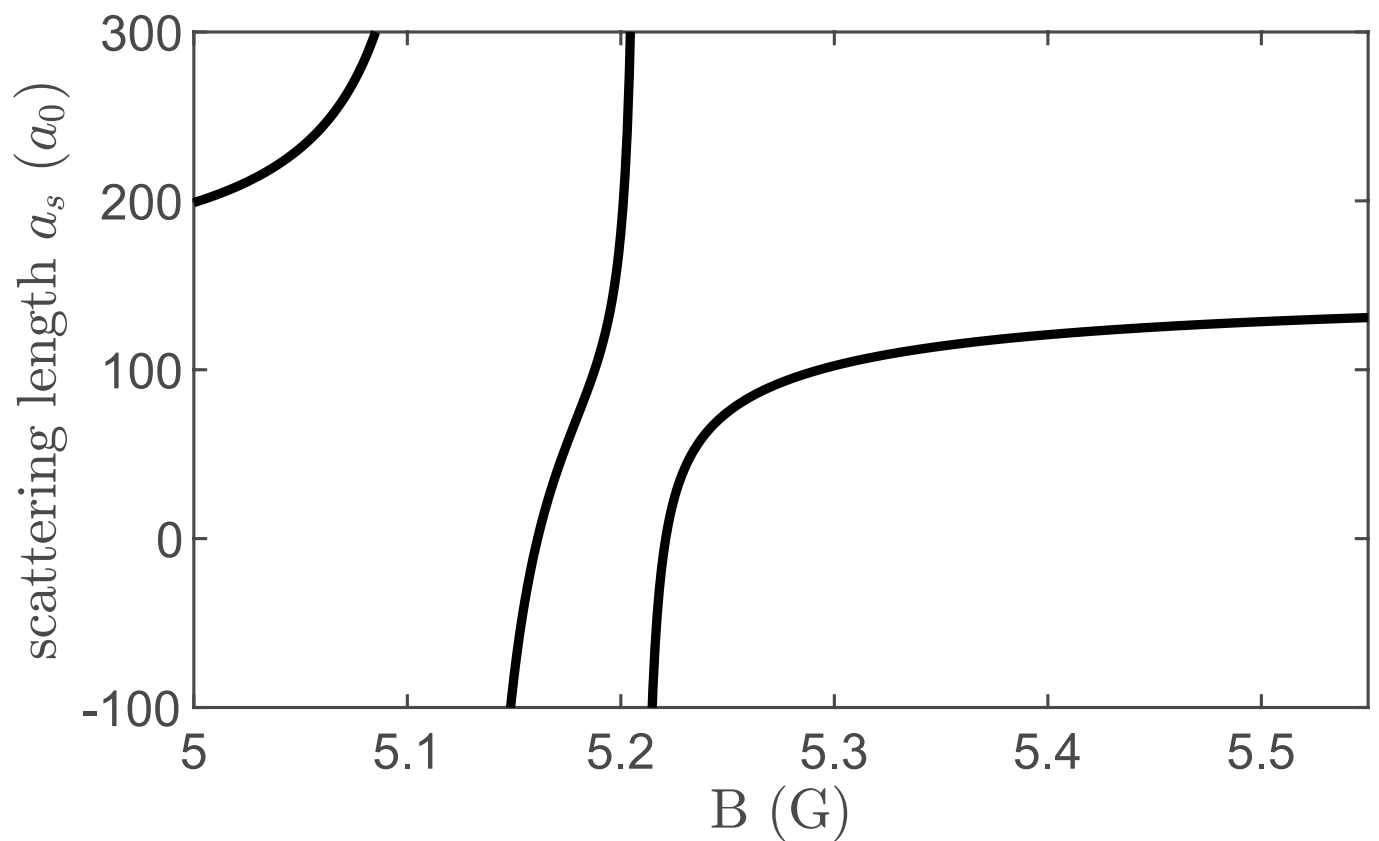
Extended Data Fig. 1 | Calculated B-to-a_s conversion for ^{162}Dy. Scattering length as a function of the magnetic-field value with the background scattering length $a_{bg} = 129(9)\, a_0$. We find $a_s = 111(9)\, a_0$ at $B = 5.333$ G.
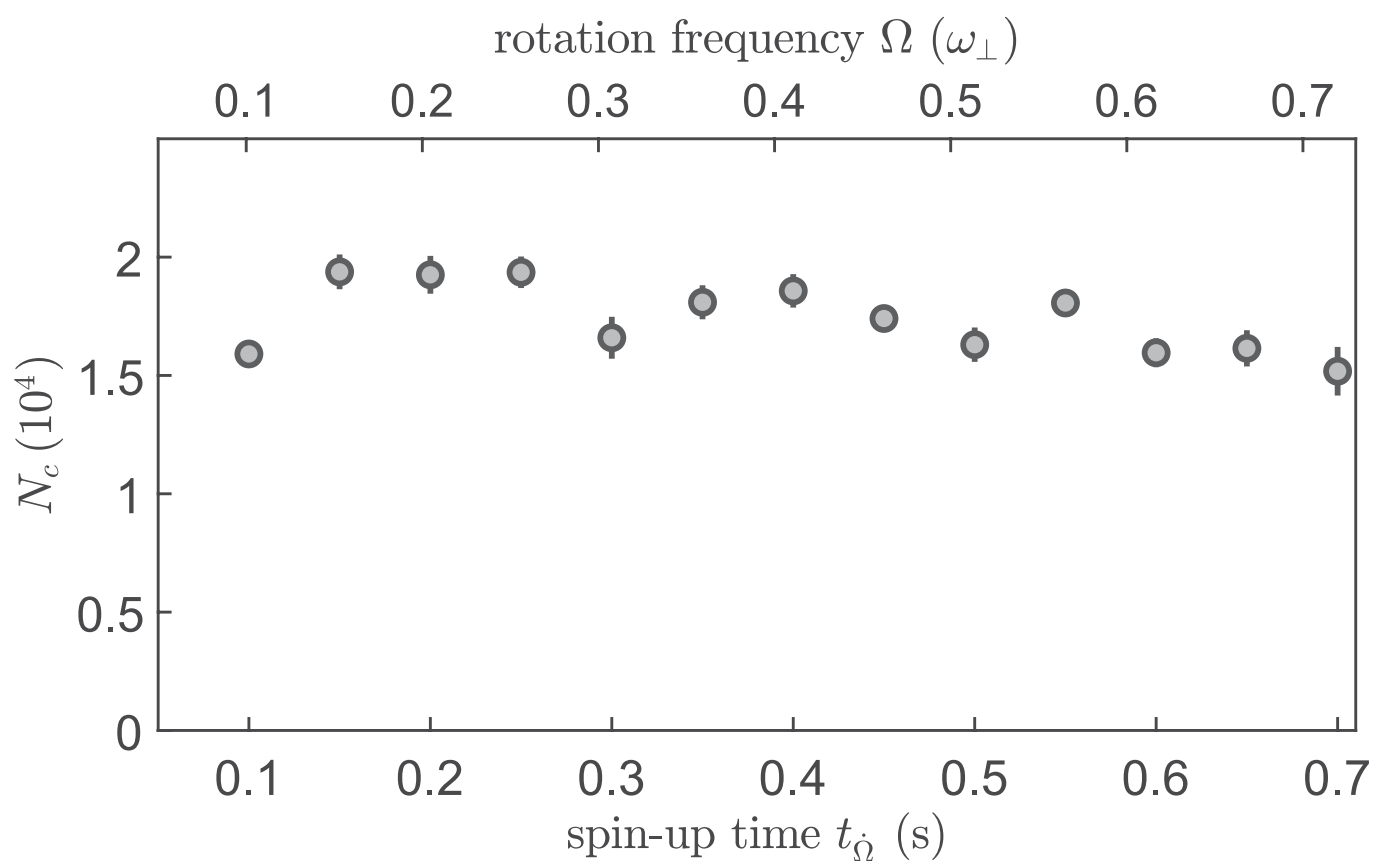
Extended Data Fig. 2 | Condensed atom number N_c during magnetostirring (Fig. 1c). Condensed atom number as a function of spin-up time $t_{\dot{\Omega}}$ for the same sequence as in Fig. 1c. The condensed atom number is extracted by fitting a two-dimensional bimodal distribution of Thomas-Fermi and Gaussian function to the horizontal density distributions.

simulation   repeated experimental runs
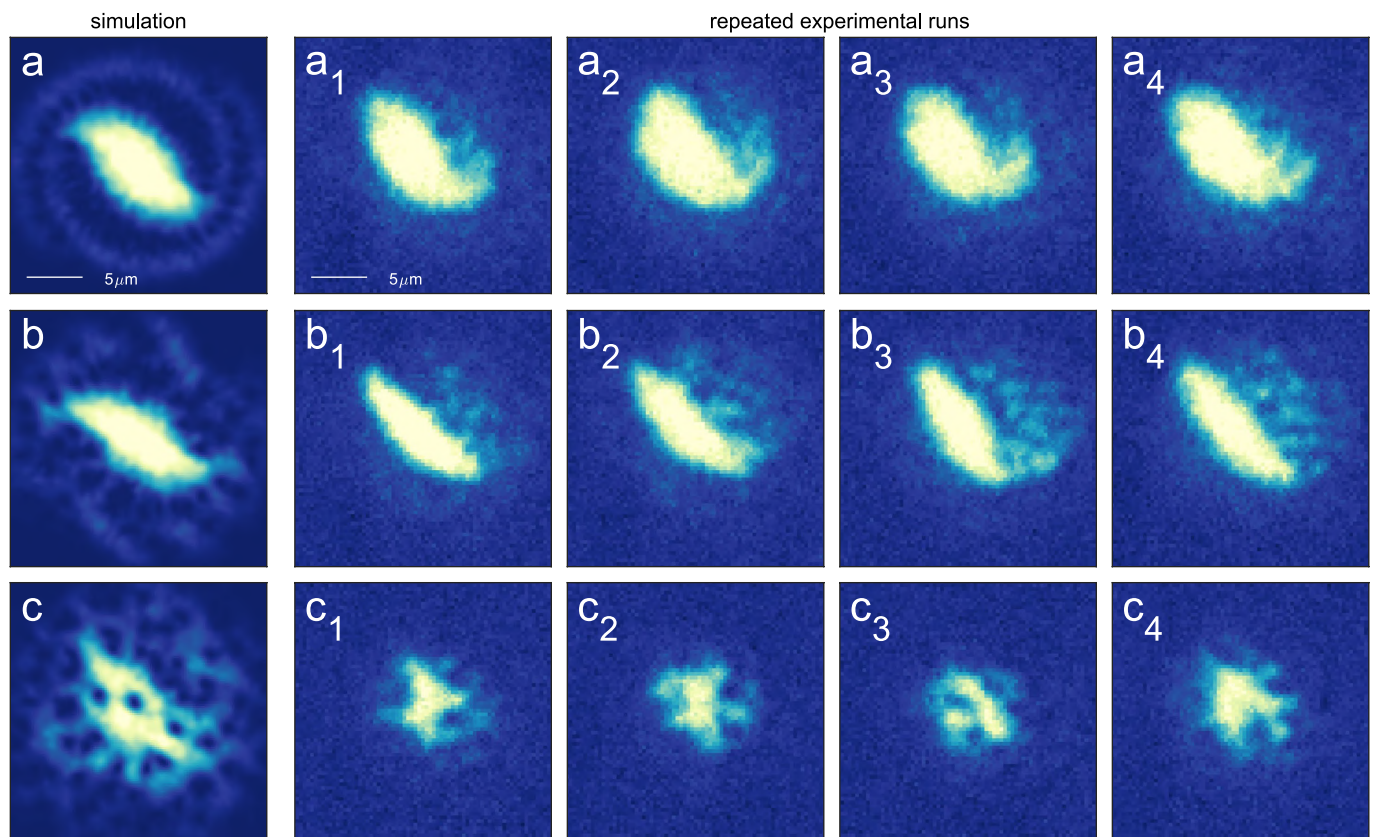
Extended Data Fig. 3 | Repeatability of the vortex generation protocol. Each row shows the simulated image (**a, b, c**) and the corresponding vertical TOF images from independent experimental runs (a_i, b_i, c_i) for a different rotation time: $t_a = 127$ ms, $t_b = 207$ ms, and $t_c = 741$ ms. The rotation frequency is $\Omega = 0.74\omega_\perp$ with the trap frequencies being $\omega_t = 2\pi \times [50.7(1), 50.8(1), 129(1)]$ Hz. The magnetic field value is $B = 5.333(5)$ G. For the simulation the scattering length used is 112 a_0, the trap frequencies are (50, 50, 150) Hz, the condensed atom number is $N = 8000$ and the rotation frequency is $0.75\omega_\perp$.

4.7. Publication: Observation of vortices in a dipolar supersolid

E. Casotti[1,2,4], **E. Poli**[2,4], L. Klaus[1,2], A. Litvinov[1], C. Ulm[1,2], C. Politi[1,2,3],
M. J. Mark[1,2], T. Bland[1,2] and F. Ferlaino[1,2]

[1] *Institut für Quantenoptik und Quanteninformation, Österreichische Akademie der Wissenschaften, 6020 Innsbruck, Austria*

[1] *Institut für Experimentalphysik, Universität Innsbruck, 6020 Innsbruck, Austria*

[3] *Present address: Institute for Quantum Electronics, ETH Zürich, Zürich, Switzerland.*

[4] *These authors contributed equally.*

---

† The author of the present thesis performed the numerical simulations together with T. B. and contributed in writing the manuscript.

‡ Here, the arXiv version is attached.

Observation of vortices in a dipolar supersolid

Eva Casotti [iD],[1, 2, *] Elena Poli [iD],[2, *] Lauritz Klaus [iD],[1, 2] Andrea Litvinov [iD],[1] Clemens Ulm [iD],[1, 2]
Claudia Politi [iD],[1, 2, †] Manfred J. Mark [iD],[2, 1] Thomas Bland [iD],[2] and Francesca Ferlaino [iD][2, 1, ‡]

[1]*Institut für Quantenoptik und Quanteninformation, Österreichische Akademie der
Wissenschaften, Technikerstr. 21A, 6020 Innsbruck, Austria*
[2]*Universität Innsbruck, Fakultät für Mathematik, Informatik und Physik,
Institut für Experimentalphysik, 6020 Innsbruck, Austria*
(Dated: June 5, 2025)

Supersolids are states of matter that spontaneously break two continuous symmetries: translational invariance due to the appearance of a crystal structure and phase invariance due to phase locking of single-particle wave functions, responsible for superfluid phenomena. While originally predicted to be present in solid helium[1–5], ultracold quantum gases provided a first platform to observe supersolids[6–10], with particular success coming from dipolar atoms[8–12]. Phase locking in dipolar supersolids has been probed through e.g. measurements of the phase coherence[8–10] and gapless Goldstone modes[13], but quantized vortices, a hydrodynamic fingerprint of superfluidity, have not yet been observed. Here, with the prerequisite pieces at our disposal, namely a method to generate vortices in dipolar gases[14,15] and supersolids with two-dimensional crystalline order[11,16,17], we report on the theoretical investigation and experimental observation of vortices in the supersolid phase. Our work reveals a fundamental difference in vortex seeding dynamics between unmodulated and modulated quantum fluids. This opens the door to study the hydrodynamic properties of exotic quantum systems with multiple spontaneously broken symmetries, in disparate domains such as quantum crystals and neutron stars[18].

Rotating fluids on all scales exhibit a whirling motion known as vorticity. Unique to the quantum world, however, is the quantization of this rotation due to the single-valued and continuous nature of the underlying macroscopic wavefunction[19,20]. Observing quantized vortices is regarded as unambiguous evidence of superfluidity, relevant for a wide variety of interacting many-body quantum systems from superfluid ^{4}He [21,22] through gaseous bosonic[23] and fermionic[24] condensates, exciton-polariton condensates[25], to solid-state type-II superconductors[26,27]. Remarkably, this phenomenon persists over a wide range of interaction scales, since it requires only the irrotational nature of the velocity field. All of these examples refer to the case in which there is a single spontaneously broken symmetry, leading to the question: what new properties do we expect to arise in systems with multiple broken symmetries?

The supersolid phase belongs to this category, spontaneously breaking phase and translational symmetries. Supersolids, characterized by the coexistence of superfluid and solid properties[1–5], have been investigated through two distinct approaches. Either imbuing superfluid properties into a solid[28–32], or partially crystallizing a superfluid[6–11]. Among these systems, supersolids composed of dipolar atoms have emerged as a versatile platform for exploring the superfluid characteristics and solid properties of this long sought-after state[12]. Where these studies have found a roadblock is in probing the response to rotation. One consequence of irrotational flow is the scissors mode oscillation, where the signature of superfluidity is the lack of a rigid body response to a sudden rotation of an anisotropic trap[33]. However, supersolids show a mixture of rotational and irrotational behavior, leading to a multimode response to perturbation. This complexity hinders a straightforward extraction of the superfluid contribution[16,34,35]. Instead, the presence of quan-

tized vortices is an unequivocal signal of irrotationality, and thus unambiguously proves the superfluidity of the system. These vortices are also anticipated to exhibit other distinctive characteristics, including a reduced angular momentum[36,37], and unusual dynamics due to their interplay with the crystal such as pinning and snaking[18,38,39]. Investigating these dynamics could provide new insights into flux pinning in superconductors[40] and glitches in neutron stars[18]. Nevertheless, a critical gap exists in the current experimental exploration of supersolids — an investigation into whether the supersolid can maintain its structure and coherence under continuous stirring, as well as if, and how, vortices may manifest and behave in this unique state. The experimental challenge lies in the inherent complexity and fragility of the supersolid phase, which lives in a narrow region within the phase diagram[12]. In our work, we explore this uncharted territory by investigating the supersolid response to rotation, using a technique known as magnetostirring[14,15,41]. Combining experiment and theory, our study explores both the unmodulated and modulated states, revealing distinctive signatures associated with the presence of vortices in the supersolid.

Predicting the supersolid response to rotation

Owing to the inherent long-range interactions among atoms, a dipolar gas exhibits a density distribution that extends along the magnetic field direction, a phenomenon known as magnetostriction[42]. This imparts an elliptical shape to the cloud. The rotation of the magnetic field consequently induces stirring of the gas[41]. This method, referred to as magnetostirring, has recently been employed to generate vortices in unmodulated dipolar quantum gases[14]. These vortices eventually organize into distinctive patterns, forming either triangular or stripe vortex lattices[15,41].

Generating vortices in the supersolid phase through magnetostirring has not yet been investigated, therefore, we the-
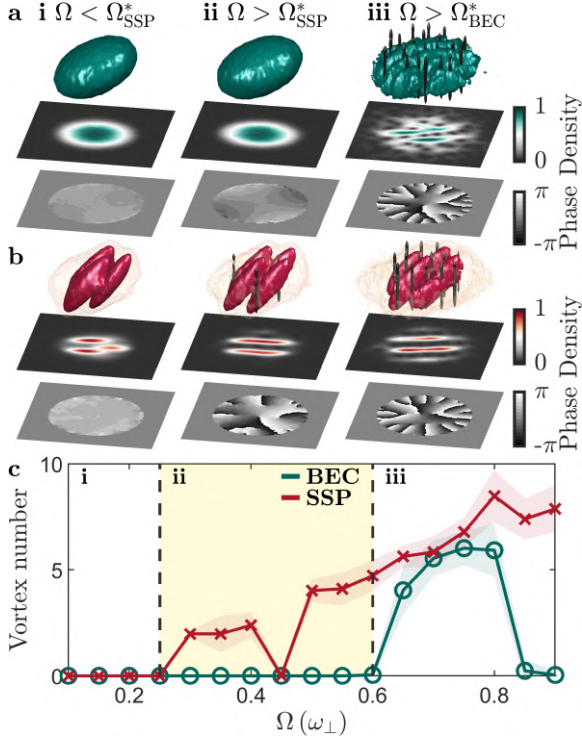
FIG. 1. **Simulation of vortex nucleation in a supersolid and unmodulated BEC.** Density isosurfaces and their corresponding normalized integrated density and phase profiles for the **a** unmodulated BEC and **b** supersolid phases after 1 s of rotation at (i) $\Omega = 0.2\omega_\perp$, (ii) $0.4\omega_\perp$, and (iii) $0.7\omega_\perp$. Isosurfaces are shown at 15% of the max density in all plots, and additionally at 0.5% in the SSP to show the halo. Vortex tubes are shown in black in the 3D images and appear as 2π windings in the phase plots. **c** Comparison of the time-averaged vortex number as a function of Ω between the SSP (red) and BEC (green), averaged between 0.75 s and 1 s of rotation, and the colored shading shows the standard deviation. The yellow shaded area highlights $\Omega^*_{\mathrm{SSP}} < \Omega < \Omega^*_{\mathrm{BEC}}$ (see main text). The results are obtained from eGPE calculations with $(\omega_\perp, \omega_z) = 2\pi \times [50, 103]$ Hz, magnetic-field angle from the z-axis $\theta = 30°$, atom number $N = 5 \times 10^4$, and scattering length $a_s = 95a_0$ ($104a_0$) for the SSP (BEC) phase.

oretically explore the zero temperature dynamics of our state through the so-called extended Gross–Pitaevskii equation[43–46] (eGPE). This takes into account the cylindrically symmetric harmonic trap, the short-range interactions, through the tunable s-wave interaction strength a_s, and long-range interactions, with fixed amplitude $a_{\mathrm{dd}} = 130.8a_0$ for ^{164}Dy. Also included are beyond-mean field effects resulting from the zero-point energy of Bogoliubov quasiparticles–shown to be crucial for the energetic stability in the supersolid phase[46]. By tuning the short-range interactions, we can access both the supersolid (typically $\epsilon_{\mathrm{dd}} = a_{\mathrm{dd}}/a_s \gtrsim 1.3$ for experimentally relevant trap geometries) and unmodulated Bose–Einstein condensate (BEC) phases ($\epsilon_{\mathrm{dd}} \lesssim 1.3$).

Figure 1 comparatively shows exemplar density and phase distributions of an unmodulated dipolar BEC [a] and supersolid phase (SSP) [b] rotating the magnetic field at increasing

frequency Ω, from left to right. In a BEC, Fig. 1a, at small frequencies with respect to the radial trap frequency $\omega_\perp$, the cloud density is almost unchanged from the static result [a(i)]. Rotating faster, the cloud elongates, and we observe an irrotational velocity field in the phase profile [a(ii)]. When rotating faster than a given Ω^*_{BEC}, the irrotational flow can no longer be maintained, and quantum vortices, observable as density holes and quantized 2π phase windings, penetrate the condensate surface following a quadrupole mode instability [a(iii)][14].

In contrast to unmodulated BECs, supersolids present a new scenario, see Fig. 1b. Our simulations reveal that the system is more susceptible to quantized vortex creation, happening at significantly lower frequencies than the BEC case. At small frequencies, the crystalline structure and surrounding 'halo' of atoms follow the magnetic field in lockstep without generating vortices [b(i)]. At higher frequencies, yet still $\Omega < \Omega^*_{\mathrm{BEC}}$, we now see vortex lines smoothly entering into the interstitial regions between the crystal sites [b(ii)][36,37,39]. These vortices persist even at higher frequencies, arranging into a regular lattice structure [b(iii)].

To gain further insight, we study the total vortex number obtained after 1 s of rotation as a function of Ω. Figure 1c shows a striking difference in the response to rotation between the two quantum phases. The BEC shows the well-known resonant behavior, in which the rotation frequency must be at resonance with half the collective quadrupole mode frequency ω_Q. This drives an instability of the condensate surface, allowing vortices to enter the state. For a non-dipolar BEC $\omega_Q = \omega_\perp/\sqrt{2}$[47–49], while for dipolar quantum gases, small deviations from this value can occur depending on the dipolar interaction and the trap geometry[50]. For our system, we see the onset of the resonant behavior at $\Omega^*_{\mathrm{BEC}} = 0.6\omega_\perp$, reaching its maximum at $\Omega \approx 0.75\omega_\perp$.

In the supersolid phase, we observe a vastly different behavior. The dual superfluid-crystalline nature of the state leads to two distinguishing features: the reduced superfluidity results in vortices nucleating at a lower rotation frequency and the solidity gives rise to a monotonic increase in vortex number at faster frequencies, reminiscent of rigid body rotation; see Fig. 1c. This can be understood by studying the excitation spectrum. A two-dimensional supersolid exhibits three quadrupole modes: one from the broken phase symmetry associated with superfluidity and one from each direction of the broken translational symmetry[36]. In our case, the latter are nearly degenerate due to the cylindrically symmetric dipole trap. Excitation of the 'superfluid' quadrupole mode is responsible for the weak resonance starting at $\Omega^*_{\mathrm{SSP}} \approx 0.25\omega_\perp$ and centered around $\Omega \approx 0.35\omega_\perp$, where just a few vortices are created. The position of this resonance is highly dependent on the superfluid fraction, eventually vanishing in the so-called isolated droplet (ID) regime[36]. In the ID regime, there is no phase coherence nor density between the droplets, and therefore the vortex number is zero. A state that is initially in the supersolid phase cannot be rotated into the ID regime. This state is discussed theoretically in more detail in the Methods. However, we note that it is out of current experimental

reach to create an ID state with a lifetime on the order of the vortex seeding time. As we will discuss later, the detection of the low frequency resonance is at the edge of our current experimental capability, indicating compatibility, albeit with a low signal strength. Beginning at $\Omega \approx 0.45\omega_\perp$, the system exhibits instead a threshold response to rotation, where the angular momentum, and thus vortex number, linearly increases with Ω[36,37]. This prominent feature arises due to the near degenerate crystal quadrupole mode resonance.

Experimental magnetostirring of a dipolar supersolid

Bolstered by the acquired theoretical understanding, we experimentally explore the suitability of magnetostirring to nucleate vortices in the supersolid phase. We first produce an optically trapped supersolid quantum gas of highly magnetic bosonic ^{164}Dy atoms via direct evaporative cooling[10,11,17,51] and then apply magnetostirring[14,15,41] to rotate the gas.

In all the experiments presented, the three-dimensional optical dipole trap (ODT) is cylindrically symmetric, with radial frequency $\omega_\perp \approx 2\pi \times 50$ Hz and a trap aspect ratio $\omega_z/\omega_\perp$ that varies between 2 and 3. Throughout the evaporation sequence, we apply a uniform magnetic field along the z-axis and tilt the magnetic field vector by $\theta = 30°$ in the last cooling stage to prepare for magnetostirring[14]. With this sequence, we obtain a supersolid typically composed of four density maxima (droplets) on top of a low-density background (halo) of coherent atoms, which we verify with a measurement of the phase coherence after long time-of-flight (see Methods). Taking phase-contrast images after 3 ms of expansion gives us access to the 2D density profiles integrated along the axial direction, as illustrated in Fig. 2a. We magnetostir the system by rotating the magnetic-field vector around the z-axis with a constant angular velocity Ω; see Fig. 2b. As predicted by theory, the droplets align themselves along the magnetic-field direction, breaking the cylindrical symmetry, thus enabling rotation. We are able to stir the supersolid for hundreds of milliseconds without destroying the state, as shown in Fig. 2b(i-v). This result is particularly relevant since it allows several full rotations, even for small driving frequencies, giving the vortices enough time to nucleate and percolate into the system.

Observation of vortices in a dipolar supersolid

Based on our simulations, on the one hand, we anticipate vortex nucleation in the supersolid already at modest rotation frequencies, but on the other hand, the density modulated initial state poses a unique challenge in vortex detection. Traditional methods for probing quantized vortices in quasi-homogeneous ultracold quantum gases typically rely on observing density depletions of an expanded cloud[23,24,52,53]. In the context of supersolids, vortices nest within the low-density interstitial areas between the droplets, reducing the contrast[18,54]. We implement an imaging sequence inspired by a recent theoretical proposal[54] that draws parallels with a protocol employed to observe vortices in strongly interacting Fermi gases[24]. In particular, we project the SSP into the BEC phase just before releasing the atoms from the trap by rapidly
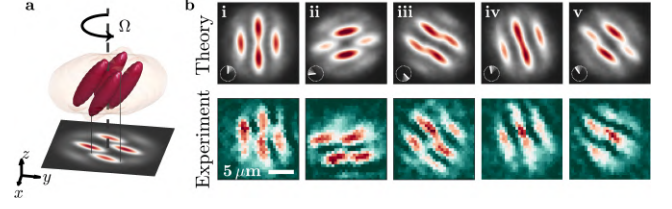

FIG. 2. **Magnetostirring of a ^{164}Dy dipolar supersolid. a** Density isosurfaces shown at 15% and 0.5% of the maximum density and corresponding integrated density of a four droplet supersolid. **b** Column densities of a four droplet supersolid state from theory (top row) and experiment (bottom row) with $\Omega = 0.3\omega_\perp$; the images were taken after (i-v) $1, 19, 43, 70, 274$ ms. The insets show the rotation of the magnetic field vector in the x-y plane with white lines. Experimental parameters: $B = 18.24(2)$ G, $N \approx 7 \times 10^4$, and $(\omega_\perp, \omega_z) = 2\pi \times [50.5(3), 135(2)]$ Hz. Illustrative simulation parameters: $a_s = 92.5a_0$, $N = 6 \times 10^4$, and $(\omega_\perp, \omega_z) = 2\pi \times [50, 135]$ Hz.

(1 ms) increasing the scattering length. This projection effectively "melts" the high density peaks, providing a more homogeneous density profile. Since vortices are topologically protected defects they are expected to survive during this state projection[54]. Finally, we probe the system with vertical absorption imaging after 3 ms of expansion, without allowing time for further dynamics in the BEC phase.

Figure 3 summarizes our main results, where we compare the behavior of a BEC and SSP under magnetostirring. Akin to theory, we see three regimes. At low frequencies ($\Omega < \Omega^*_{SSP}$), we do not observe vortices in either state [a(v)-b(v)]. Here, in the residuals (see Methods), we see the impact of the interaction quench, imparting small amplitude sound waves in the density of b(v). For $\Omega^*_{SSP} < \Omega < \Omega^*_{BEC}$, a striking difference between the BEC and the SSP response to rotation appears [a(iv)-b(iv)]. While the former does not show vortices, in the supersolid we clearly observe the appearance of a vortex in the central region of the cloud. Finally, at a larger frequency ($\Omega > \Omega^*_{BEC}$), we observe multiple vortices in both cases [a(iii)-b(iii)]. This confirms the expected reduction in vortex nucleation frequency, the first characteristic feature of the impact of supersolidity.

In what follows, we perform a systematic study as a function of Ω in order to identify the threshold nucleation values and the vortex number behavior as a function of rotation frequency. We trace the time evolution of the rotating system both in the SSP and BEC phase and extract for each time step and Ω the number of vortices. We show the average vortex number obtained for each measurement in Fig. 3 (ii) together with the corresponding numerical simulations (i). Our protocol for extracting the vortex number is detailed in the Methods section. We demonstrate that, while the exact vortex number depends on the specifics of the analysis, the overall qualitative behavior remains consistent.

In the unmodulated case (Fig. 3a), we observe the expected resonant behavior around $\Omega \approx 0.7\omega_\perp$[14]. After 0.5 s of rotation, both the experiment and theory show $\Omega^*_{BEC} \approx 0.6\omega_\perp$. In
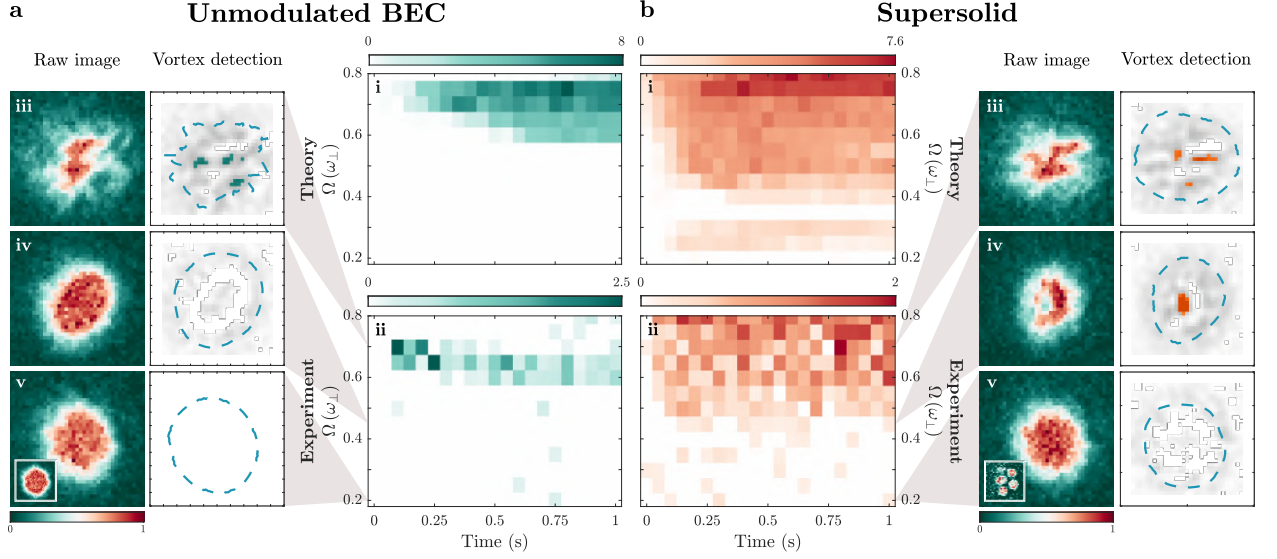
FIG. 3. **Vortex nucleation in a dipolar supersolid and BEC.** Average vortex number (colorbar) as a function of rotation time and Ω for an **a** unmodulated BEC and **b** supersolid. Panels show [i] the simulations, [ii] the experimental observation, where in **a** the absolute value of the magnetic field is held at $19.30(2)$ G, but in **b** is instead ramped from $18.30(2)$ G to $19.30(2)$ G in 1 ms at the end of the rotation. Exemplar images [iii-v] of normalized density taken after 250 ms of rotation are shown for both cases. Detected vortices are shown in color when the residuals exceed the chosen threshold (0.34), and the condensate radius is marked by a blue dashed line, see Methods for more details. Insets of [v] show initial states. All images are taken after 3 ms expansion, except the non-rotating supersolid state, which is a phase-contrast image with $\theta = 0°$. In the experiment, the trap has frequencies $(\omega_\perp, \omega_z) = 2\pi \times [50.3(2), 107(2)]$ Hz, and the initial condensed atom number is $N \approx 3 \times 10^4$. For the simulation: $(\omega_\perp, \omega_z) = 2\pi \times [50, 103]$ Hz, with **a** $a_s = 104a_0$, initial $N = 2 \times 10^4$, and **b** $a_s = 93a_0$, and initial $N = 3 \times 10^4$, where three-body recombination losses have been added.

the experiment, atom number losses at fast rotation frequencies can suppress the production of vortices[14]. In the supersolid case (Fig. 3b), we are able to observe clear evidence for the threshold behavior for vortex nucleation. For driving frequencies greater than $\Omega \approx 0.4\omega_\perp$, vortices persist even up to 1 s, and there is an increase of vortex number with rotation frequency. This behavior is in contrast to the BEC case, where above $\Omega = 0.75\omega_\perp$ we do not observe vortices, unveiling the competing superfluid and solid contributions.

Additionally, theory [b(v)] predicts a superfluid quadrupole resonance centered at $\Omega \approx 0.3\omega_\perp$, with one or at most two vortices entering the cloud. A detailed analysis of the experimental data reveals a signature compatible with the existence of this resonance, see Methods. However, a dedicated investigation beyond the scope of this work would be required to confirm this feature.

Interference patterns

The modulation of supersolid states presents a unique possibility for extracting the phase information, as the presence or absence of a vortex strongly impacts the interference pattern after time-of-flight (TOF)[36]. This is readily observable by performing expansion calculations with the eGPE, as shown in Fig. 4a. In the presence of a vortex, the interference pattern shows a pronounced minimum in the central region of the signal [a(ii)], which is clearly not the case in a vortex free supersolid [a(i)]. This remarkable feature is a direct consequence of the phase winding and can even be reproduced by a simple

toy model simulating the expansion of three non-interacting Gaussian wavepackets, as shown in the insets of Fig. 4a(i) and (ii). Note that in the eGPE, the expansion time was set to 36 ms, during which the self-bound nature of the droplets slows down the expansion corresponding to a few ms in the toy model. Furthermore, this time is strongly dependent on interaction and trap parameters, making the pattern very sensitive to parameter variations, see Methods for more details. Unlike vortex interference patterns from unmodulated states, there is no longer a simple hole left in the center of the cloud, but rather a three-pointed star structure reflecting the symmetries present in the density. The spiral arms appear due to the nonlinear azimuthal 2π phase winding[39], where between each droplet there is a line of minimum signal given by the phase difference of each droplet, in this case, $2\pi/3$. In our calculation, we opt for an initial state featuring three droplets instead of the previously used four droplet state. The symmetry of this state, characterized by equal interdroplet spacing, yields a singular and simple interference pattern when the vortex is in the center of the system, facilitating the distinction between a vortex and vortex-free state.

When performing the experiment with similar parameters as the theory, we observe a remarkable similarity across the resulting phase pattern. Figure 4b shows an example interference pattern for a non-rotating sample [b(i)] and the one for a three droplet supersolid when rotating above the theoretically obtained critical vortex nucleation frequency $\Omega^* = 0.1\omega_\perp$
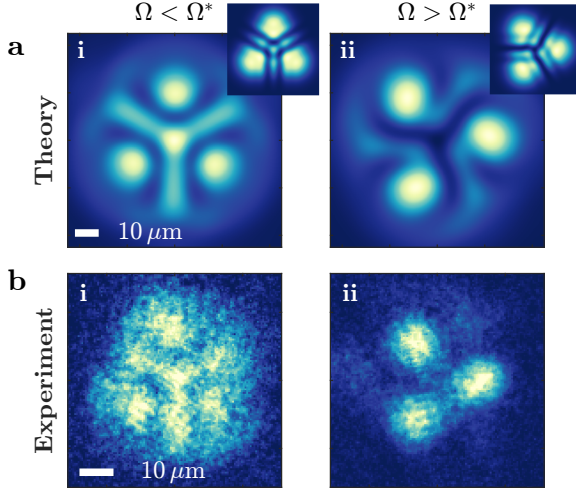
FIG. 4. **Time-of-flight interference pattern. a** $36\,\mathrm{ms}$ real-time expansion interference pattern for three droplets (i) in the absence of a vortex and (ii) with a vortex. **b** Experimental observation after TOF (i) without rotation and (ii) after $189\,\mathrm{ms}$ of rotation at $\Omega = 0.3\omega_\perp$ with $\theta = 30°$, before spiraling up to $\theta = 0°$ in $11\,\mathrm{ms}$, while Ω is kept constant. This was done to ensure that the radial droplet expansion and interference is perpendicular to the imaging axis. The supersolid is produced at $18.24(2)\,\mathrm{G}$ with $(\omega_\perp, \omega_z) = 2\pi \times [50.0(4), 113(2)]\,\mathrm{Hz}$, the condensed atom number $N \approx 5 \times 10^4$. The theoretical parameters: $N = 3.5 \times 10^4$, $(\omega_\perp, \omega_z) = 2\pi \times [50, 113]\,\mathrm{Hz}$ and $a_s = 92.5 a_0$.

[b(ii)]. In the latter case, we clearly observe a signal minimum at the center, providing the observation of vortices directly in the supersolid state. To test the robustness of this observation, we repeat the measurement many times, and study the occurrence of the non-vortex [b(i)] or vortex [b(ii)] pattern. Among the images with a clear interference pattern, about 70% contain a vortex signature when rotating above $\Omega = 0.3\omega_\perp$, see Methods. The remaining fraction can be understood by considering that supersolid states exist in a very small parameter regime[55], and typical shot-to-shot atom number and magnetic-field (a_s) fluctuations can significantly alter the observed interference pattern.

Conclusions

After three decades since the original predictions[56], we report on the observations of vortices in a supersolid state. This result is relevant not only because it adds the final piece to the cumulative framework of evidence for superfluidity in this state[12], but also because it reveals a distinctive vortex behavior in the supersolid. The system's characteristic response to rotation can serve as a fingerprint to identify supersolidity in diverse systems with multiple broken symmetries, over scales ranging from solid-state systems[28], high-temperature superconductors[57,58], and helium platforms[29,30], to a neutron star's inner crust[18,59].

Furthermore, in the context of supersolids, a fascinating interplay of competing length scales emerges. These include the separation between vortices, the wavelength of the self-

forming crystal, and the diameter of the vortex core. This competition has the potential to lead to intriguing dynamics, ranging from constrained motion and pinning to avalanche escape. These phenomena are genuinely unique to supersolids.

Author contributions

E.C., L.K., A.L., C.U., C.P., M.J.M., and F.F. performed the experimental work and data analysis. E.P. and T.B. performed the theoretical work. All authors contributed to the interpretation of the results and the preparation of the manuscript.

Data availability

Data pertaining to this work can be found at https://doi.org/10.5281/zenodo.10695943. Source data are provided with the paper.

Code availability

The codes that support the findings of this study are available from the corresponding author upon reasonable request.

Competing interests

The authors declare no competing interests.

Additional information

Correspondence and requests for materials should be addressed to F. Ferlaino.

———————

* These authors contributed equally to this work.
† Current address: Institute for Quantum Electronics, ETH Zürich, Otto-Stern-Weg 1, 8093 Zürich, Switzerland
‡ Correspondence should be addressed to: francesca.ferlaino@uibk.ac.at

1. E. P. Gross, Unified Theory of Interacting Bosons, Phys. Rev. **106**, 161 (1957).
2. E. P. Gross, Classical theory of boson wave fields, Annals of Physics **4**, 57 (1958).
3. A. Andreev and I. Lifshitz, Quantum Theory of Defects in Crystals, J. Exp. Theo. Phys. **56**, 2057 (1969).

4. G. Chester, Speculations on Bose-Einstein condensation and quantum crystals, Physical Review A **2**, 256 (1970).

5. A. J. Leggett, Can a solid be "superfluid"?, Physical Review Letters **25**, 1543 (1970).

6. J.-R. Li, J. Lee, W. Huang, S. Burchesky, B. Shteynas, F. Ç. Top, A. O. Jamison, and W. Ketterle, A stripe phase with supersolid properties in spin–orbit-coupled Bose–Einstein condensates, Nature **543**, 91 (2017).

7. J. Léonard, A. Morales, P. Zupancic, T. Esslinger, and T. Donner, Supersolid formation in a quantum gas breaking a continuous translational symmetry, Nature **543**, 87 (2017).

8. F. Böttcher, J.-N. Schmidt, M. Wenzel, J. Hertkorn, M. Guo, T. Langen, and T. Pfau, Transient Supersolid Properties in an Array of Dipolar Quantum Droplets, Phys. Rev. X **9**, 011051 (2019).

9. L. Tanzi, E. Lucioni, F. Famà, J. Catani, A. Fioretti, C. Gabbanini, R. N. Bisset, L. Santos, and G. Modugno, Observation of a Dipolar Quantum Gas with Metastable Supersolid Properties, Phys. Rev. Lett. **122**, 130405 (2019).

10. L. Chomaz, D. Petter, P. Ilzhöfer, G. Natale, A. Trautmann, C. Politi, G. Durastante, R. M. W. van Bijnen, A. Patscheider, M. Sohmen, M. J. Mark, and F. Ferlaino, Long-Lived and Transient Supersolid Behaviors in Dipolar Quantum Gases, Phys. Rev. X **9**, 021012 (2019).

11. M. A. Norcia, C. Politi, L. Klaus, E. Poli, M. Sohmen, M. J. Mark, R. N. Bisset, L. Santos, and F. Ferlaino, Two-dimensional supersolidity in a dipolar quantum gas, Nature **596**, 357–361 (2021).

12. L. Chomaz, I. Ferrier-Barbut, F. Ferlaino, B. Laburthe-Tolra, B. L. Lev, and T. Pfau, Dipolar physics: a review of experiments with magnetic quantum gases, Reports on Progress in Physics **86**, 026401 (2022).

13. M. Guo, F. Böttcher, J. Hertkorn, J.-N. Schmidt, M. Wenzel, H. P. Büchler, T. Langen, and T. Pfau, The low-energy Goldstone mode in a trapped dipolar supersolid, Nature **564**, 386 (2019).

14. L. Klaus, T. Bland, E. Poli, C. Politi, G. Lamporesi, E. Casotti, R. N. Bisset, M. J. Mark, and F. Ferlaino, Observation of vortices and vortex stripes in a dipolar condensate, Nature Physics **18**, 1453 (2022).

15. T. Bland, G. Lamporesi, M. J. Mark, and F. Ferlaino, Vortices in dipolar Bose-Einstein condensates, Comptes Rendus. Physique **24**, 133 (2023).

16. M. A. Norcia, E. Poli, C. Politi, L. Klaus, T. Bland, M. J. Mark, L. Santos, R. N. Bisset, and F. Ferlaino, Can Angular Oscillations Probe Superfluidity in Dipolar Supersolids?, Phys. Rev. Lett. **129**, 040403 (2022).

17. T. Bland, E. Poli, C. Politi, L. Klaus, M. A. Norcia, F. Ferlaino, L. Santos, and R. N. Bisset, Two-Dimensional Supersolid Formation in Dipolar Condensates, Phys. Rev. Lett. **128**, 195302 (2022).

18. E. Poli, T. Bland, S. J. White, M. J. Mark, F. Ferlaino, S. Trabucco, and M. Mannarelli, Glitches in rotating supersolids, Phys. Rev. Lett. **131**, 223401 (2023).

19. L. Onsager, In discussion on paper by C. J. Gorter, Nuovo Cimento **6**, 249 (1949).

20. R. Feynman, Chapter II Application of Quantum Mechanics to Liquid Helium (Elsevier, 1955) pp. 17–53.

21. E. Yarmchuk, M. Gordon, and R. Packard, Observation of stationary vortex arrays in rotating superfluid helium, Phys. Rev. Lett. **43**, 214 (1979).

22. G. P. Bewley, D. P. Lathrop, and K. R. Sreenivasan, Visualization of quantized vortices, Nature **441**, 588 (2006).

23. J. R. Abo-Shaeer, C. Raman, J. M. Vogels, and W. Ketterle, Observation of vortex lattices in Bose-Einstein condensates, Science **292**, 476 (2001).

24. M. W. Zwierlein, J. R. Abo-Shaeer, A. Schirotzek, C. H. Schunck, and W. Ketterle, Vortices and superfluidity in a strongly interacting Fermi gas, Nature (London) **435**, 1047 (2005).

25. K. G. Lagoudakis, M. Wouters, M. Richard, A. Baas, I. Carusotto, R. André, L. S. Dang, and B. Deveaud-Plédran, Quantized vortices in an exciton–polariton condensate, Nature physics **4**, 706 (2008).

26. F. S. Wells, A. V. Pan, X. R. Wang, S. A. Fedoseev, and H. Hilgenkamp, Analysis of low-field isotropic vortex glass containing vortex groups in YBa2Cu3O7-x thin films visualized by scanning SQUID microscopy, Scientific reports **5**, 8677 (2015).

27. L. Embon, Y. Anahory, Ž. L. Jelić, E. O. Lachman, Y. Myasoedov, M. E. Huber, G. P. Mikitik, A. V. Silhanek, M. V. Milošević, A. Gurevich, *et al.*, Imaging of super-fast dynamics and flow instabilities of superconducting vortices, Nature Communications **8**, 85 (2017).

28. M. Hamidian, S. Edkins, S. H. Joo, A. Kostin, H. Eisaki, S. Uchida, M. Lawler, E.-A. Kim, A. Mackenzie, K. Fujita, *et al.*, Detection of a Cooper-pair density wave in Bi2Sr2CaCu2O8+ x, Nature **532**, 343 (2016).

29. J. Nyéki, A. Phillis, A. Ho, D. Lee, P. Coleman, J. Parpia, B. Cowan, and J. Saunders, Intertwined superfluid and density wave order in two-dimensional ^{4}He, Nature Physics **13**, 455 (2017).

30. L. V. Levitin, B. Yager, L. Sumner, B. Cowan, A. J. Casey, J. Saunders, N. Zhelev, R. G. Bennett, and J. M. Parpia, Evidence for a Spatially Modulated Superfluid Phase of He3 under Confinement, Phys. Rev. Lett. **122**, 085301 (2019).

31. D. F. Agterberg, J. S. Davis, S. D. Edkins, E. Fradkin, D. J. Van Harlingen, S. A. Kivelson, P. A. Lee, L. Radzihovsky, J. M. Tranquada, and Y. Wang, The physics of pair-density waves: Cuprate superconductors and beyond, Annual Review of Condensed Matter Physics **11**, 231 (2020).

32. Y. Liu, T. Wei, G. He, Y. Zhang, Z. Wang, and J. Wang, Pair density wave state in a monolayer high-t_c iron-based superconductor, Nature **618**, 934 (2023).

33. O. M. Maragò, S. A. Hopkins, J. Arlt, E. Hodby, G. Hechenblaikner, and C. J. Foot, Observation of the Scissors Mode and Evidence for Superfluidity of a Trapped Bose-Einstein Condensed Gas, Phys. Rev. Lett. **84**, 2056 (2000).

34. L. Tanzi, J. Maloberti, G. Biagioni, A. Fioretti, C. Gabbanini, and G. Modugno, Evidence of superfluidity in a dipolar supersolid from nonclassical rotational inertia, Science **371**, 1162 (2021).

35. S. Roccuzzo, A. Recati, and S. Stringari, Moment of inertia and dynamical rotational response of a supersolid dipolar gas, Phys. Rev. A **105**, 023316 (2022).

36. A. Gallemí, S. Roccuzzo, S. Stringari, and A. Recati, Quantized vortices in dipolar supersolid Bose-Einstein-condensed gases, Physical Review A **102**, 023322 (2020).

37. S. Roccuzzo, A. Gallemí, A. Recati, and S. Stringari, Rotating a supersolid dipolar gas, Physical review letters **124**, 045702 (2020).

38. N. Henkel, F. Cinti, P. Jain, G. Pupillo, and T. Pohl, Supersolid vortex crystals in Rydberg-dressed Bose-Einstein condensates, Physical Review Letters **108**, 265301 (2012).

39. F. Ancilotto, M. Barranco, M. Pi, and L. Reatto, Vortex properties in the extended supersolid phase of dipolar Bose-Einstein condensates, Physical Review A **103**, 033314 (2021).

40. T. Matsushita, *Flux pinning in superconductors*, Vol. 178 (Springer, 2014).

41. S. B. Prasad, T. Bland, B. C. Mulkerin, N. G. Parker, and A. M.

Martin, Vortex lattice formation in dipolar Bose-Einstein condensates via rotation of the polarization, Physical Review A **100**, 023625 (2019).

42. J. Stuhler, A. Griesmaier, T. Koch, M. Fattori, T. Pfau, S. Giovanazzi, P. Pedri, and L. Santos, Observation of Dipole-Dipole Interaction in a Degenerate Quantum Gas, Phys. Rev. Lett. **95**, 150406 (2005).

43. F. Wächtler and L. Santos, Quantum filaments in dipolar Bose-Einstein condensates, Phys. Rev. A **93**, 061603 (2016).

44. I. Ferrier-Barbut, H. Kadau, M. Schmitt, M. Wenzel, and T. Pfau, Observation of Quantum Droplets in a Strongly Dipolar Bose Gas, Phys. Rev. Lett. **116**, 215301 (2016).

45. L. Chomaz, S. Baier, D. Petter, M. J. Mark, F. Wächtler, L. Santos, and F. Ferlaino, Quantum-Fluctuation-Driven Crossover from a Dilute Bose-Einstein Condensate to a Macrodroplet in a Dipolar Quantum Fluid, Phys. Rev. X **6**, 041039 (2016).

46. R. N. Bisset, R. M. Wilson, D. Baillie, and P. B. Blakie, Ground-state phase diagram of a dipolar condensate with quantum fluctuations, Phys. Rev. A **94**, 033619 (2016).

47. A. Recati, F. Zambelli, and S. Stringari, Overcritical rotation of a trapped Bose-Einstein condensate, Phys. Rev. Lett. **86**, 377 (2001).

48. S. Sinha and Y. Castin, Dynamic instability of a rotating Bose-Einstein condensate, Phys. Rev. Lett. **87**, 190402 (2001).

49. K. W. Madison, F. Chevy, V. Bretin, and J. Dalibard, Stationary states of a rotating Bose-Einstein condensate: Routes to vortex nucleation, Phys. Rev. Lett. **86**, 4443 (2001).

50. R. M. van Bijnen, D. H. O'Dell, N. G. Parker, and A. Martin, Dynamical instability of a rotating dipolar Bose-Einstein condensate, Phys. Rev. Lett. **98**, 150401 (2007).

51. M. Sohmen, C. Politi, L. Klaus, L. Chomaz, M. J. Mark, M. A. Norcia, and F. Ferlaino, Birth, Life, and Death of a Dipolar Supersolid, Phys. Rev. Lett. **126**, 233401 (2021).

52. M. R. Matthews, B. P. Anderson, P. C. Haljan, D. S. Hall, C. E. Wieman, and E. A. Cornell, Vortices in a Bose-Einstein Condensate, Phys. Rev. Lett. **83**, 2498 (1999).

53. K. W. Madison, F. Chevy, W. Wohlleben, and J. Dalibard, Vortex formation in a stirred Bose-Einstein condensate, Phys. Rev. Lett. **84**, 806 (2000).

54. M. Šindik, A. Recati, S. M. Roccuzzo, L. Santos, and S. Stringari, Creation and robustness of quantized vortices in a dipolar supersolid when crossing the superfluid-to-supersolid transition, Phys. Rev. A **106**, L061303 (2022).

55. E. Poli, T. Bland, C. Politi, L. Klaus, M. A. Norcia, F. Ferlaino, R. N. Bisset, and L. Santos, Maintaining supersolidity in one and two dimensions, Phys. Rev. A **104**, 063307 (2021).

56. Y. Pomeau and S. Rica, Dynamics of a model of supersolid, Phys. Rev. Lett. **72**, 2426 (1994).

57. G. Blatter, M. V. Feigel'man, V. B. Geshkenbein, A. I. Larkin, and V. M. Vinokur, Vortices in high-temperature superconductors, Reviews of Modern Physics **66**, 1125 (1994).

58. W.-K. Kwok, U. Welp, A. Glatz, A. E. Koshelev, K. J. Kihlstrom, and G. W. Crabtree, Vortices in high-performance high-temperature superconductors, Reports on Progress in Physics **79**, 116501 (2016).

59. N. Chamel, Neutron conduction in the inner crust of a neutron star in the framework of the band theory of solids, Phys. Rev. C **85**, 035801 (2012).

60. Y. Tang, A. Sykes, N. Q. Burdick, J. L. Bohn, and B. L. Lev, s-wave scattering lengths of the strongly dipolar bosons ^{162}Dy and ^{164}Dy, Phys. Rev. A **92**, 022703 (2015).

61. T. Maier, I. Ferrier-Barbut, H. Kadau, M. Schmitt, M. Wenzel, C. Wink, T. Pfau, K. Jachymski, and P. S. Julienne, Broad universal Feshbach resonances in the chaotic spectrum of dysprosium atoms, Phys. Rev. A **92**, 060702 (2015).

62. Y. Tang, A. G. Sykes, N. Q. Burdick, J. M. DiSciacca, D. S. Petrov, and B. L. Lev, Anisotropic Expansion of a Thermal Dipolar Bose Gas, Phys. Rev. Lett. **117**, 155301 (2016).

63. A. R. P. Lima and A. Pelster, Quantum fluctuations in dipolar Bose gases, Phys. Rev. A **84**, 041604 (2011).

64. P. Blakie, A. Bradley, M. Davis, R. Ballagh, and C. Gardiner, Dynamics and statistical mechanics of ultra-cold Bose gases using c-field techniques, Advances in Physics **57**, 363 (2008).

65. A. Cidrim, F. E. dos Santos, E. A. Henn, and T. Macrì, Vortices in self-bound dipolar droplets, Phys. Rev. A **98**, 023618 (2018).

66. A.-C. Lee, D. Baillie, R. N. Bisset, and P. B. Blakie, Excitations of a vortex line in an elongated dipolar condensate, Phys. Rev. A **98**, 063620 (2018).

67. A.-C. Lee, D. Baillie, and P. B. Blakie, Numerical calculation of dipolar-quantum-droplet stationary states, Phys. Rev. Research **3**, 013283 (2021).

68. G. Li, Z. Zhao, X. Jiang, Z. Chen, B. Liu, B. A. Malomed, and Y. Li, Strongly anisotropic vortices in dipolar quantum droplets, Phys. Rev. Lett. **133**, 053804 (2024).

69. D. R. Scherer, C. N. Weiler, T. W. Neely, and B. P. Anderson, Vortex Formation by Merging of Multiple Trapped Bose-Einstein Condensates, Phys. Rev. Lett. **98**, 110402 (2007).

70. S. Stringari and L. Pitaevskii, *Bose-Einstein condensation and superfluidity* (Oxford Science Publications, Oxford, 2016).

71. M. J. D. Powell, An efficient method for finding the minimum of a function of several variables without calculating derivatives, The Computer Journal **7**, 155 (1964).

Methods

Experimental procedure

We prepare an ultracold gas of ^{164}Dy atoms in an optical dipole trap (ODT), similar to our previous work[14]. The trap is formed through three overlapping laser beams, operating at $1064\,$nm. All the studies are performed in a cylindrically symmetric trap, typically with $\omega_\perp = 2\pi \times 50.3(2)\,$Hz, where $\omega_\perp$ is the geometric average $\omega_\perp = \sqrt{\omega_x \omega_y}$. The aspect ratio $\omega_z/\omega_\perp$ varies from 2 to 3; the specific values of ω_z are stated in the figures' captions. The aspect ratio ω_x/ω_y is crucial for the applicability of magnetostirring[14]: throughout the paper, the deviation of ω_x/ω_y from 1 is $< 2\%$.

For this work, we tilt the magnetic field vector **B** from the vertical position to $\theta = 30°$ from the z-axis in the last stage of evaporation, while maintaining its magnitude constant. The values of the magnetic field are: $19.30(2)\,$G for the unmodulated BEC, $18.30(2)\,$G for the SSP in Fig. 3, and $18.24(2)\,$G for Figs. 2 and 4. The small change in magnetic field is required to maintain supersolidity between the two respective choices of tight trapping frequency. The magnetic field is calibrated through radio frequency (RF) spectroscopy. Moreover, ^{164}Dy has a dense spectrum of narrow Feshbach resonances, as shown in Extended Data Fig. 1. We use the positions of such resonances as references to compensate for drifts of the magnetic field. The condensed atom number after the evaporation sequence ranges from 3×10^4 to 7×10^4, depending on the measurement.

After preparation, the magnetic field is rotated; details can be found in the following sections. Finally, we image the quantum gas using a $421\,$nm light pulse, propagating along the z-axis. For the data in Figs. 2 and 3, we let the atomic cloud expand for $3\,$ms and take a phase contrast and absorption image, respectively. When comparing theoretical and experimental images, we rescale the image size by 1.36 in the theory to account for this small expansion time. The results of Fig. 4 are instead obtained with absorption imaging after $36\,$ms TOF, and following an $11\,$ms spiral up to $\theta = 0°$. This was done to ensure that the radial droplet expansion and interference is perpendicular to the imaging axis.

For the experimental images in Fig. 2, we enhanced the contrast of the droplets by applying a Gaussian filter of size $\sigma = 1\,$px ($\simeq 0.5\,\mu$m) followed by a sharpening convolution filter with kernel F:

$$F = \begin{bmatrix} 0 & -1 & 0 \\ -1 & 5 & -1 \\ 0 & -1 & 0 \end{bmatrix}. \quad (1)$$

Magnetostirring

To magnetostir the atomic cloud, we rotate the magnetic field vector around the z-axis[14]. In brief, the breaking of cylindrical symmetry that enables the transfer of angular momentum by rotating the magnetic field vector **B** (magnetostirring) is achieved by tilting **B** into the plane. This is a direct consequence of the phenomenon of magnetostriction[42]. For all

the measurements in this paper, **B** is tilted from the z-axis by an angle $\theta = 30°$. At our magnetic field values, this angle is optimal for vortex nucleation within the experimental time scales[15]. In general, smaller angles would increase the nucleation time; at the same time, a much bigger angle would make the dipolar interaction dominantly attractive, holding the cloud together and thus also increasing the nucleation time. From the experimental point of view, $\theta = 30°$ enables the observation of the droplets aligning along **B** while retaining the ability to discern individual droplets when observing the integrated density, see Fig. 2. For all datasets, we then directly rotate **B** at the chosen frequency Ω. The rotation is continued for a rotation time t_Ω after which the ODT is turned off, and an image is taken after expansion.

Scattering length

The conversion from magnetic field to scattering length for ^{164}Dy at our magnetic field values has not been mapped. However, combining knowledge on the conversion in other magnetic field ranges[60–62], together with the theoretical identification of the critical scattering lengths for the BEC to SSP transition, allows for an educated guess. It is important to highlight that the isotope ^{164}Dy has the advantage of exhibiting supersolidity at the background value of the scattering length, while the BEC phase usually requires some mild tuning of a_s. The specific values used in this paper are highlighted on the Feshbach loss spectrum in Extended Data Fig. 1. For our theoretical simulations (see below), we find that a scattering length a_s in the range $90a_0$-$95a_0$ gives a good agreement with the experimentally observed supersolid states.

Interaction quench

For the in situ detection of vortices in the supersolid phase, we map the supersolid into an unmodulated BEC, similar to the approach used to observe them in the BCS phase of strongly interacting Fermi gases[24]. In particular, we increase the absolute value of the magnetic field from $18.30(2)\,$G to $19.30(2)\,$G in $1\,$ms after stopping the rotation, and we then release the sample from the trap for $3\,$ms before imaging. We repeat this sequence for different values of angular velocity Ω and for different rotation times t_Ω. For each experimental point in Fig. 3a and 3b, we take 7-9 pictures. Using phase contrast imaging, we ensured that the ramp time is long enough to melt the droplets into an unmodulated state, but also short enough to avoid atom losses when crossing the Feshbach resonances present between the initial and final magnetic field values (see Extended Data Fig. 1).

Extended Gross-Pitaevskii equation

At the mean-field level, the ground state solutions, time-dependent dynamics, and nature of the BEC-to-SSP transitions are well described by the extended Gross-Pitaevskii formalism[43–46]. This combines the two-body particle interactions, described by the two-body pseudo-potential,

$$U(\mathbf{r}) = \frac{4\pi\hbar^2 a_s}{m}\delta(\mathbf{r}) + \frac{3\hbar^2 a_{dd}}{m}\frac{1 - 3(\hat{\mathbf{e}}(t)\cdot\hat{\mathbf{r}})^2}{r^3}, \quad (2)$$

where the first term describes short-range interactions gov-

erned by the s-wave scattering length a_s, with Planck's constant $\hbar$ and particle mass m. This quantity is independently tunable through Feshbach resonances. The second term represents the anisotropic and long-ranged dipole-dipole interactions, characterized by dipole length $a_{dd} = \mu_0\mu_m^2 m/12\pi\hbar^2$, with magnetic moment μ_m and vacuum permeability μ_0. We always consider ^{164}Dy, such that $a_{dd} = 130.8\, a_0$, where a_0 is the Bohr radius. For the trap parameters and atom numbers used here, the supersolid phase is found for scattering lengths in the range $a_s = [90, 95]a_0$, i.e. $\epsilon_{dd} = a_{dd}/a_s \geq 1.37$. The dipoles are polarized uniformly along a time-dependent axis, given by

$$\hat{\mathbf{e}}(t) = (\sin\theta(t)\cos\phi(t), \sin\theta(t)\sin\phi(t), \cos\theta(t)) \quad (3)$$

with time dependent polarization angle $\theta(t)$ and $\phi(t) = \int_0^t dt'\Omega(t')$, for rotation frequency protocol $\Omega(t)$.

Three-body recombination losses are prevalent in dipolar supersolid experiments due to the increased peak density when compared to unmodulated states. In the theory, these are introduced through a time-dependent atom loss

$$\dot{N} = -L_3\langle n^2\rangle N\,, \quad (4)$$

for density n. We take the fixed coefficient $L_3 = 1.2 \times 10^{-41}$m^{6}s^{-1} for our simulations[44]. This leads to an additional non-Hermitian term in the Hamiltonian $-i\hbar L_3 n^2/2$.

Beyond-mean-field effects are treated through the inclusion of a Lee–Huang–Yang correction term[63]

$$\gamma_{QF} = \frac{128\hbar^2}{3m}\sqrt{\pi a_s^5}\,\text{Re}\left\{\mathcal{Q}_5(\epsilon_{dd})\right\}\,, \quad (5)$$

where $\mathcal{Q}_n(x) = \int_0^1 du\,(1-x+3xu^2)^{n/2}$, which has an imaginary component for $x > 1$. Finally, the full extended Gross-Pitaevskii equation (eGPE) then reads[43–46]

$$i\hbar\frac{\partial\psi(\mathbf{r},t)}{\partial t} = \left[-\frac{\hbar^2\nabla^2}{2m} + V_{trap} - \frac{i\hbar L_3}{2}|\psi(\mathbf{r},t)|^4\right.$$
$$\left. + \int d^3\mathbf{r}'\,U(\mathbf{r}-\mathbf{r}')|\psi(\mathbf{r}',t)|^2 + \gamma_{QF}|\psi(\mathbf{r},t)|^3\right]\psi(\mathbf{r},t)\,, \quad (6)$$

where $\omega_{x,y,z}$ are the harmonic trap frequencies in $V_{trap} = \frac{1}{2}m\left(\omega_x^2 x^2 + \omega_y^2 y^2 + \omega_z^2 z^2\right)$. The wavefunction ψ is normalized to the total atom number $N = \int d^3\mathbf{r}|\psi|^2$. Stationary solutions to Eq. (6) are found through the standard imaginary time procedure. The initial state $\psi(\mathbf{r},0)$ of the real-time simulations is obtained by adding non-interacting noise to the stationary solution $\psi_0(\mathbf{r})$. Given the single-particle eigenstates ϕ_n and the complex Gaussian random variables α_n sampled with $\langle|\alpha_n|^2\rangle = (e^{\epsilon_n/k_B T} - 1)^{-1} + \frac{1}{2}$ for a temperature $T = 20$ nK, the initial state can be described as $\psi(\mathbf{r},0) = \psi_0(\mathbf{r}) + \sum_n' \alpha_n\phi_n(\mathbf{r})$, where the sum is restricted only to the modes with $\epsilon_n \leq 2k_B T$[64].

Choosing simulation parameters

In the theory there are two parameters known to high precision, the atomic mass and the dipolar strength, and seven

parameters that are only known within broad error bars, $\{a_s, L_3, \omega_{x,y,z}, T, N\}$. Here, we explore the impact of varying these parameters in the theory on the main results of the paper, and justifying their use when comparing to the experimental data.

In Extended Data Fig. 2 we show the ground state phase diagram for different values of atom number and scattering length a_s. We identify four different phases: unmodulated BEC, SSP (supersolid), ID (isolated droplets) and SD (single droplet). To characterize the different phases we consider the density contrast $C = (n_{max} - n_{min})/(n_{max} + n_{min})$, where n is the column density. In the SSP and ID regime, the contrast is calculated as the average value between each pair of droplets. States with more than one droplet and with a contrast larger than the threshold value 0.98 are identified as ID. Rotation of the ID state is discussed in detail in the next section.

In Extended Data Fig. 3a, we show how the rotational response of a BEC is robust against atom number and scattering length variations. Varying these parameters slightly moves the exact position and size of the resonance window for vortex nucleation, and although the precise values are difficult to pin down, all of our simulations show resonance behavior.

In Extended Data Fig. 3b, we show how the rotational behavior of a supersolid is robust against atom number variations. In this case, the scattering length a_s was also tuned to maintain supersolidity. As in the BEC case, varying these parameters slightly moves the exact position of the resonance and of the threshold but the overall structure of the rotational response remains consistent.

We finally consider the rotational response of both BEC and SSP for different temperatures. In Extended Data Fig. 3c we compare $T = 20$nK, which is the case in the main text, to 30nK and 40nK. In the BEC case, the key difference is that the higher temperature broadens slightly the resonance window. In the supersolid case, the higher temperature obscures the small resonance at smaller Ω. Both of these observations are in keeping with the experimental results, and provide new perspectives on the observed differences between theory and experiment, where the resonance at smaller Ω may be better observable at smaller temperatures. Crucially, the physics is independent of the choice of the initial noise.

Isolated droplet regime

For values of the scattering length a_s lower than the ones required to have a supersolid state, the superfluid connection between crystal sites disappears and the system enters the so-called isolated (or independent) droplet (ID) regime. In this regime, the system does not exhibit global phase coherence and each droplet evolves as an independent BEC.

The ID regime is not accessible in our experiment for long trapping times. In the experiment, we have chosen ^{164}Dy, which, to our best knowledge, is the only isotope showing long-lived supersolid states with a lifetime up to 1s[51]. The long lifetime is essential for prolonged rotation and vortex seeding. This particular isotope shows long-lived supersolid-

ity due the fortunate coincidence that the background scattering length is the one required for supersolidity in our trap, without any need of Feshbach tuning[10]. Instead, to produce a BEC we need to move between two overlapping Feshbach resonances giving the right modulated background value, where here a moderate tuning is needed and still three-body losses are modest. To create an ID state, we need instead to go closer to a resonance and three-body losses destroy the state in a timescale of $100\,\mathrm{ms}$, too short for applying the rotation protocol.

In Extended Data Fig. 4 we show the phase coherence measurements that prove the initial state used for the dynamics in Fig. 3 is in the supersolid regime. In Ref. [36] the supersolid robustness to rotation has been theoretically demonstrated. At relatively small rotation frequencies, $\Omega \lesssim 0.2\omega_\perp$, the angular momentum dependence was shown to be linear in the absence of vortices, where vortices present as jumps in the total angular momentum. The linear regime is only possible if the moment of inertia of the supersolid, i.e. the density structure and superfluid connection, remains unchanged in response to rotation. Moreover, at higher rotation frequencies, rotation acts as centrifugal effect that lowers the peak density of the state, thus favoring the superfluid density connections between the droplets. The only system parameter that can change during the rotation protocol is the atom number due to losses, and lowering this will bring the state towards the BEC state, as shown in Extended Data Fig. 2. However, as shown in Fig. 2, the supersolid survives for a much longer time than the one needed for seeding vortices.

In the ID regime the droplets are fully separated and there is no density between them, so the concept of vortices cannot be applied. Moreover, vortices also not able to enter the droplets themselves, as the density is very high and the self-bound nature suppresses the vortex nucleation[15], and even if imprinted in a droplet, they are known to be unstable[65–68].

It is worth to discuss whether it is possible that in a vortex free rotating ID state, a signature of vortices emerge due to the melting process, caused by the interference of droplets with different phases. In principle this mechanism is possible, but it will occur with small probability since the random phase scrambling must match 2π[69]. Moreover, this case is completely independent of the rotation protocol and frequency, it would even happen without rotating at all. Considering our protocol and geometry, with a tilt of $30°$ and melting dynamics of $4\,\mathrm{ms}$, the hypothetical vortex line would be unstable because it will be diagonal to the tight trap confinement, and will be integrated out during our absorption imaging protocol.

Another perspective pertains to the conservation of angular momentum during the quench protocol. As we keep the magnetic field both tilted and static during the interaction quench and time-of-flight, the system remains asymmetric, and there is no conservation of angular momentum. Furthermore, an azimuthally asymmetric stirred superfluid exhibits non-zero angular momentum without the need for vortices, in order to fulfill the irrotational velocity condition[70].

In Extended Data Fig. 5 we plot the expectation value of the angular momentum operator measured for the wave function after $1\,\mathrm{s}$ of rotation. In the ID regime ($a_s = 85\,a_0$) the angular momentum monotonically increases as a function of Ω. On the contrary, in both the BEC ($a_s = 104\,a_0$) and SS ($a_s = 95\,a_0$) regimes there are maxima corresponding to vortex nucleation, or, as is the case for the SS regime, a sum of both the solid-like contribution and vortices. Notice that when the vortex number is zero at $\Omega = 0.45\omega_r$ the angular momenta are equal for both the ID and supersolid phases, due to the similar density distributions.

Finally, it is worth discussing what is the behavior of isolated droplets during long time-of-flight measurements, following the same protocol of Fig. 4. First of all, the phase of each droplet is initially random and the rotation would maintain their random character (the effect of a phase gradient across each droplet due to rotation is negligible). As a consequence of this, the produced interference pattern will not be repeatable over many experimental shots and it would be independent on the rotation frequency, in contrast to the observation of Extended Data Fig. 10. Furthermore, the expansion time required for the droplets to unbind in this geometry is longer than $36\,\mathrm{ms}$ because of their stronger self-bound character. This time-of-flight expansion would produce a magnified version of the isolated droplet ground state without any low density halo around or interference structure in the middle.

Toy model interference pattern

Taking N_D static Gaussian wavepackets with parameters of the jth wavepacket given by the widths $\boldsymbol{\sigma}_j = (\sigma_{1,j}, \sigma_{2,j}, \sigma_{3,j})$, positions $\mathbf{r}_j^0 = (r_{1,j}^0, r_{2,j}^0, r_{3,j}^0)$, atom numbers N_j, and phase ϕ_j, the initial total wavefunction is

$$
\begin{aligned}
\psi(\mathbf{r}, 0) &= \sum_j^{N_D} \sqrt{\frac{N_j}{(2\pi)^{3/2}}} \exp\left(\mathrm{i}\phi_j\right) \\
&\times \prod_{k=1,2,3} \sqrt{\frac{1}{\sigma_{k,j}}} \exp\left[-\frac{1}{4}\left(r_k - r_{k,j}^0\right)^2 / \sigma_{k,j}^2\right].
\end{aligned} \tag{7}
$$

On the assumption that these wavepackets are non-interacting, then their expansion due to kinetic energy alone can be analytically calculated by applying the free particle propagator in three dimensions, such that the time-dependent solution is

$$
\psi(\mathbf{r}, t) = \int_{-\infty}^{\infty} \mathrm{d}^3\mathbf{r}'\, \psi(\mathbf{r}', 0) K(\mathbf{r}, t; \mathbf{r}', 0), \tag{8}
$$

where

$$
K(\mathbf{r}, t; \mathbf{r}', t_0) = \left(\frac{m}{2\pi\mathrm{i}\hbar(t - t_0)}\right)^{3/2} \exp\left(\frac{\mathrm{i}m(\mathbf{r} - \mathbf{r}')^2}{2\hbar(t - t_0)}\right). \tag{9}
$$

Applying Eq. (8) to Eq. (7) gives the time-dependent multi-wavepacket solution. For brevity it is not stated here, but the exact solution transpires to be a simple time-dependent replacement of the widths $\left\{\sigma_{k,j} \to \sigma_{k,j}\sqrt{1 + \mathrm{i}\hbar t/(2m\sigma_{k,j}^2)}\right\}$

appearing in Eq. (7). An example of the evolution of the TOF pattern is shown in Extended Data Fig. 6 with the parameters of Fig. 4 for longer times. Note that the 3 ms TOF pattern, equivalent to the 36 ms when simulating the eGPE (i.e. including interactions), has not yet evolved into the momentum distribution.

Quadrupole modes calculation

We employ real-time simulations with the extended Gross-Pitaevskii equation to investigate the quadrupole mode frequency of the system with the tilted magnetic field, both in the BEC and in the supersolid phase. We initially perturb the system with a sudden small quadrupolar deformation of the trap and, then, we let the system evolve for $1\,$s. The deformation is done by increasing (decreasing) the trap frequency by $0.5\,$Hz in the x-direction (y-direction) for $1\,$ms and then restoring the trap to the original value. During the time evolution, the density distribution in the slice $z = 0$ is fitted with a Gaussian profile, from which we extract the time-dependent width of the system during the evolution. The Fourier transform of the time-dependent width gives the frequency spectrum of all the expected superfluid and crystal quadrupole modes excited by the sudden deformation[16,36]. These frequencies are in agreement with the features of the rotational response of the BEC and supersolid discussed in the main text.

In-situ vortex detection algorithm

To count the number of vortices, we identify the number of voids in the density in the in-situ images, following a similar procedure of our earlier work[14], the steps of which are shown in Extended Data Fig. 8. In short, we first apply a Gaussian filter of size $\sigma = 1\,$px ($\simeq 0.5\,\mu$m), then the sharpening convolution filter of Eq. (1) to each image n_{img} for noise reduction. We then prepare a blurred reference image n_{ref} by applying a Gaussian filter of size $\sigma = 3\,$px ($\simeq 1.5\,\mu$m) to each n_{img} and calculate the residuals between this reference and the original image $n_{\mathrm{res}} = n_{\mathrm{ref}} - n_{\mathrm{img}}$. Finally, vortices are detected as peaks in the residual image n_{res} using a peak detection algorithm (peak_local_max from the SKIMAGE Python library). To avoid spurious vortex detection, we discard peaks with a distance below 3 px, and peaks with an amplitude below a chosen contrast threshold of 0.34.

We verify the robustness of the vortex detection by varying this contrast threshold between 0.34 and 0.42, which changes the number of selected peaks but gives the same qualitative result on the whole data set (see Extended Data Fig. 9). We remark that any choice of threshold will not completely remove all false positive detections, but this method allows for an unbiased measure impartially applied to all images. In the experimental data (Extended Data Fig. 9) there is a small peak centered at $\Omega = 0.35\omega_\perp$ for all thresholds considered, hinting towards the expected superfluid quadrupole mode resonance, see Fig. 3.

Comparison between the vortex number in theory and experiment

The vortex nucleation study conducted in Fig. 3, shows a mismatch in the detected vortex number between the experiment and our simulations, despite the general agreement between theory and experiment on the dependence on rotation frequency and rotation time. This disagreement is caused by the different detection methods and by experimental fluctuations, as explained in the following.

In Figs. 1 and 3, the number of vortices is determined by counting 2π windings in the central slice of the phase, $\arg(\psi(x, y, z = 0))$. We restrict the search to a circle of radius $6\,\mu$m, such that vortices are only counted inside the condensate surface in the BEC case, or within the halo in the supersolid state. To visualize the vortex tubes plotted in Fig. 1, we plot isosurfaces of the velocity field.

Since in the experiment we do not have access to the phase, to have a better comparison, we have also applied the vortex detection algorithm described in the previous section to the simulated states. With this aim, we linearly ramp the states of Fig. 3b from $a_s = 93a_0$ to $104a_0$ over $1\,$ms to melt the droplets and perform the short $3\,$ms TOF for each time and frequency. We apply a Gaussian filter of different sizes σ to match the experimental resolution, and implemented the vortex detection algorithm detailed above to the resulting images. The same algorithm and filter have also been applied to the unmodulated BEC data of Fig. 3a. The results are shown in Extended Data Fig. 7. Both methods give the same qualitative behavior as a function of the rotation frequency. Applying a Gaussian filter on the theoretical data reduces the vortex number to the experimental values (which are in general affected by the imaging noise). Critically, the resonant and threshold behaviors are robust to all the detection methods.

Time-of-flight vortex detection algorithm

In the interference pattern, a striking difference between a single vortex and a vortex-free state is the absence or presence of a central density feature. This feature provides us with another fingerprint of vortices, thus allowing for binary classification of the experimental TOF images and extraction of the vortex occurrence probability as a function of Ω. In the following paragraphs, our classification protocol is described.

First, we prepare all the images, n_{i}, by denoising them with a Gaussian filter of size $\sigma = 2\,$px and by normalizing to the maximum density, $\max(n_{\mathrm{i}}) = 1$. Among those, we then select two reference images, one for each case: the presence ($n_{\mathrm{r}}^{\mathrm{v}}$) or absence ($n_{\mathrm{r}}^{\emptyset}$) of a vortex; see insets in Extended Data Fig. 10a. These will be used to classify all images.

Then, using 'Powell' minimization[71], we translate and rotate each image to best overlap with the references. To quantify the similarity of the images to each reference image, we calculate the sum squared differences, $S^{\{\mathrm{v}, \emptyset\}}$, between n_{i} and $n^{\{\mathrm{v}, \emptyset\}}$. Here, high values of $S^{\{\mathrm{v}, \emptyset\}}$ indicate large dissimilarity between the images.

We generate a cumulative distribution function for S^{v} and $S^{\emptyset}$, which are normalized by the total number of images (see Extended Data Fig. 10a). Using the cumulative distribution, we generate one subset of images for each reference, which are the $X\%$ most similar images. The remaining images are not classified. Note that so far, the analysis is rotation fre-

quency independent. Finally, we extract the number of images within each category as a function of rotation frequency (Ω), see Extended Data Fig. 10b. Renormalizing to the total number of classified images, we obtain the ratio of images that have a central vortex, see Extended Data Fig. 10c.

At low rotation frequency, the vortex-free interference pattern is dominating. Crucially, the ratio of images with a vortex increases with increasing Ω, consistent with our eGPE simulations and experimental findings shown in Fig. 3. This result is robust against choice of the classification threshold X as shown in Extended Data Fig. 10c(1-2) for $X = 15\%$ and $X = 30\%$ (see dashed-dotted line in Extended Data Fig. 10a). Note that fluctuations of the experimental parameters lead to a non-zero vortex signal even without rotation. Note that the selection threshold is kept low, ensuring unambiguous categorization of the images.
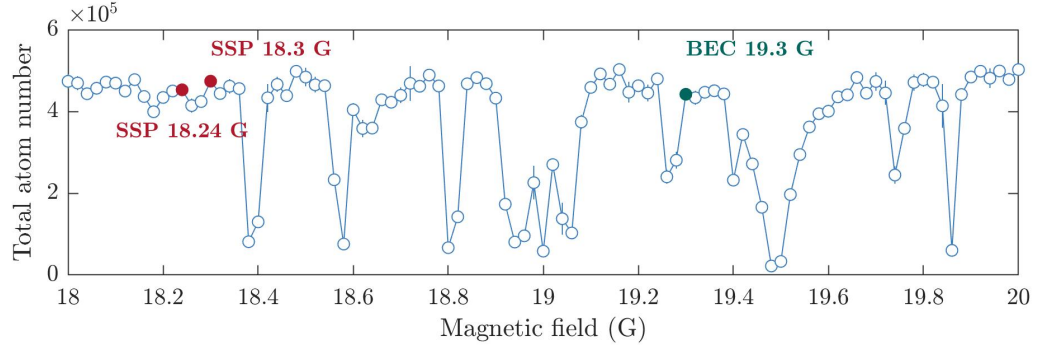
Extended Data Fig. 1. **Loss spectrum of ^{164}Dy**. The spectrum is obtained from horizontal absorption imaging, by varying the magnetic field at which the evaporative cooling ($T \approx 500\,\mathrm{nK}$) is conducted, with a step size of $20\,\mathrm{mG}$. The magnetic field values used are highlighted in red (SSP) and green (BEC). Error bars represent the standard error.
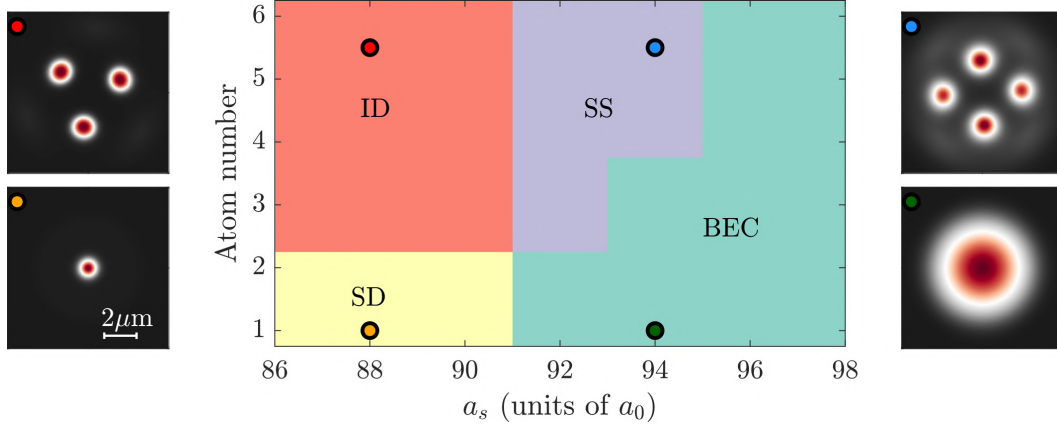
Extended Data Fig. 2. **Ground state phase diagram obtained varying the atom number and the scattering length**. The results are obtained from eGPE calculations with $(\omega_\perp, \omega_z) = 2\pi \times [50, 103]$ Hz. The identified phases are: BEC, SS (supersolid), SD (single droplet) and ID (isolated droplets). On the sides, exemplar ground states extracted from the phase diagram.
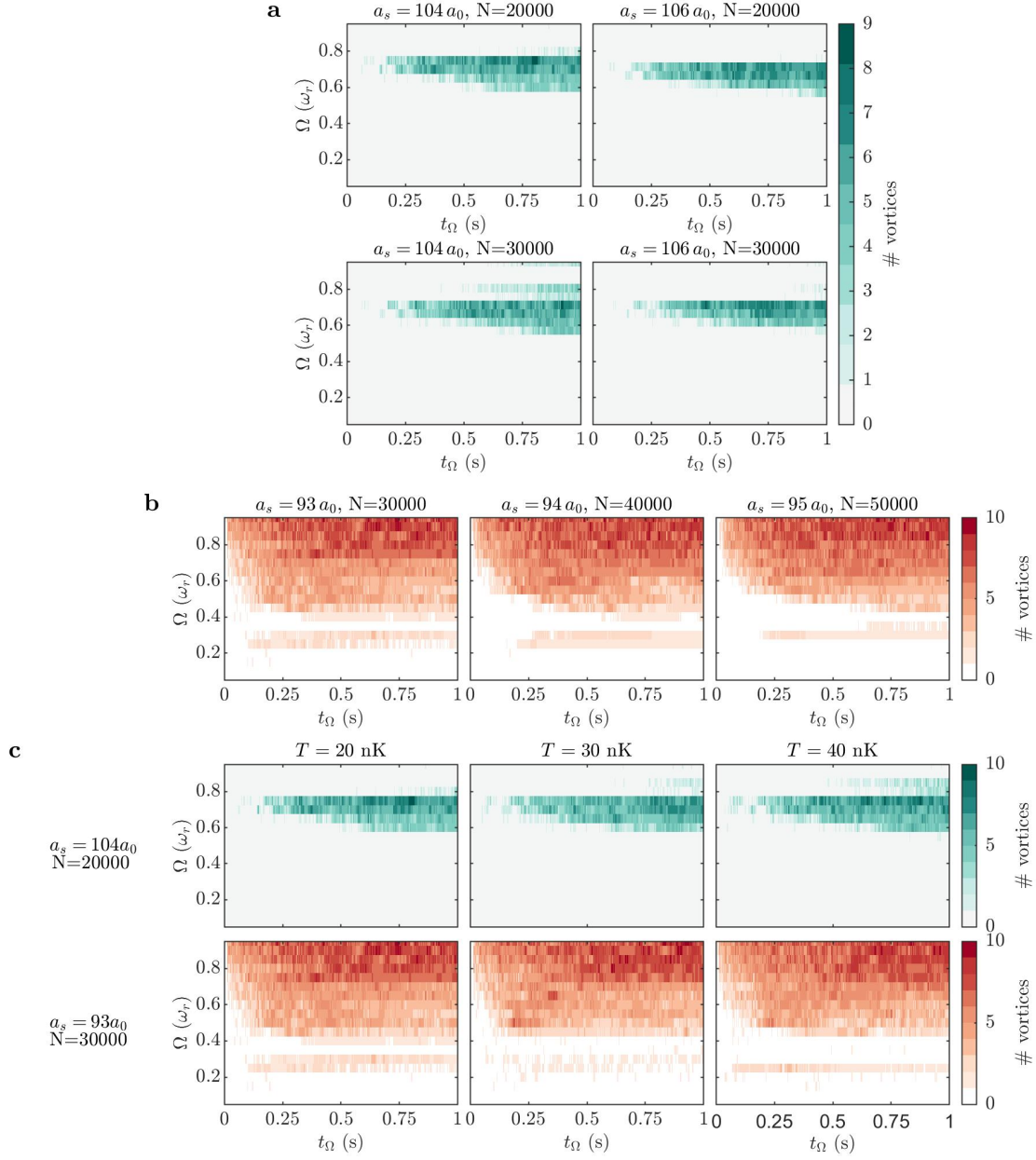
Extended Data Fig. 3. **Vortex nucleation in a dipolar BEC and supersolid for different parameters**. **a** Vortex nucleation in a dipolar BEC and **b** in a supersolid, for different atom number and different scattering length a_s. **c** Vortex nucleation for initial noise with different temperatures. All the results are obtained from eGPE calculations with $(\omega_\perp, \omega_z) = 2\pi \times [50, 103]$ Hz, magnetic-field angle from the z-axis $\theta = 30°$ and 3-body recombination losses are included.
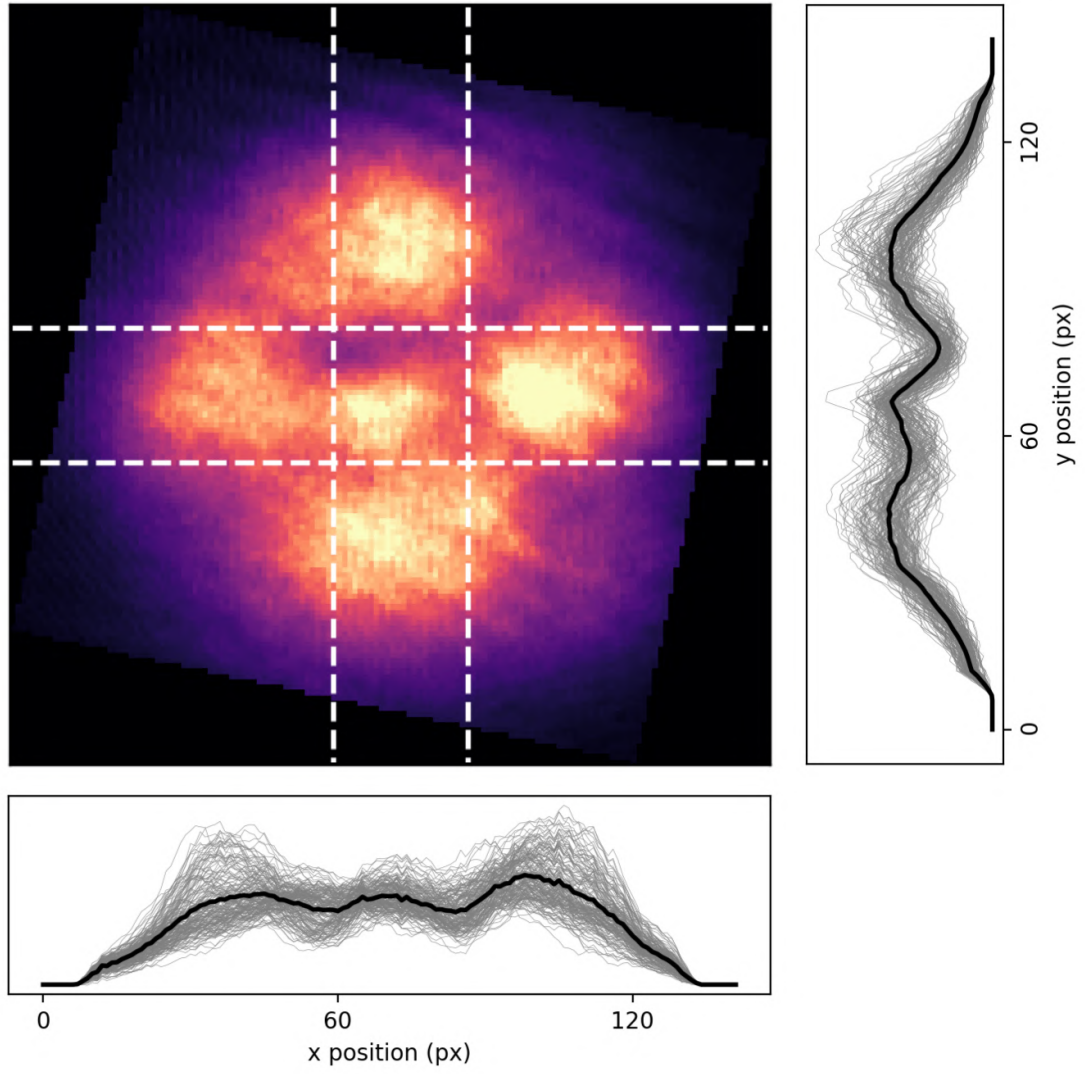
Extended Data Fig. 4. **Phase coherence measurement of the initial four droplet state before rotation, after 36** ms **TOF.** The lower (right) figure shows the horizontal (vertical) integrated density. The modulation and central interference peak are present on single images (grey lines) and remain after averaging over 173 images (black line).
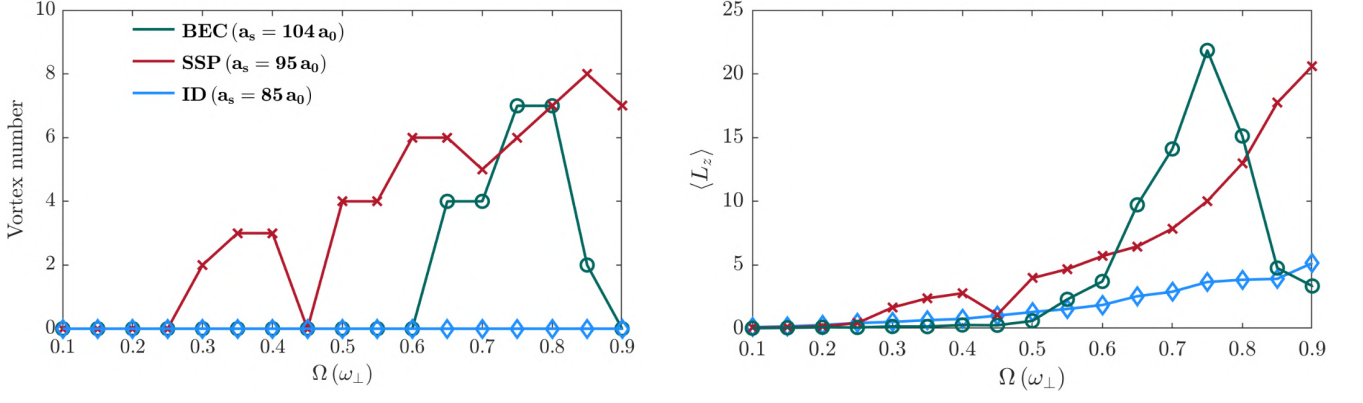
Extended Data Fig. 5. **Vortex number and expectation value of the angular momentum.** Left: vortex number after 1 s of rotation. Right: expectation value of the angular momentum operator also after 1 s of rotation. The other parameters are the same as Fig. 1 of the main text.
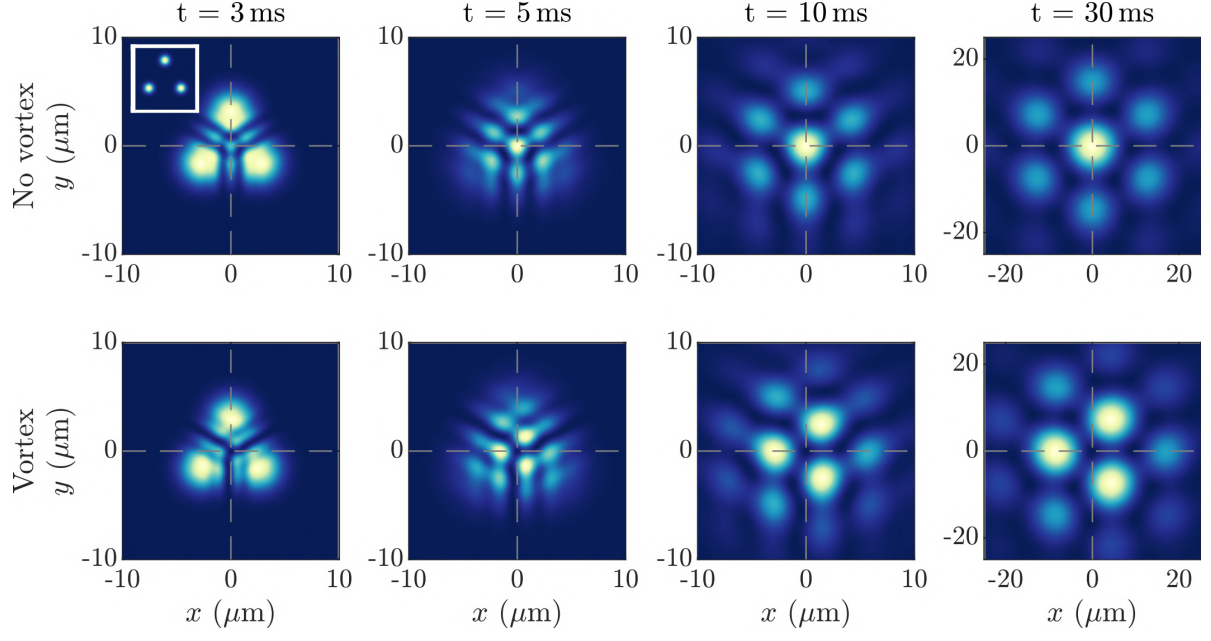
Extended Data Fig. 6. **Time of flight predictions from the Gaussian toy model**. Longer TOF density profiles for the solution shown in Fig. 4 of the main text. The inset of the first figure shows the initial condition for all states. After 10 ms the density pattern has frozen into the momentum distribution of the initial cloud. The gray lines show the axis center (0,0), highlighting the immediate difference between a no vortex and vortex expansion from the central density.
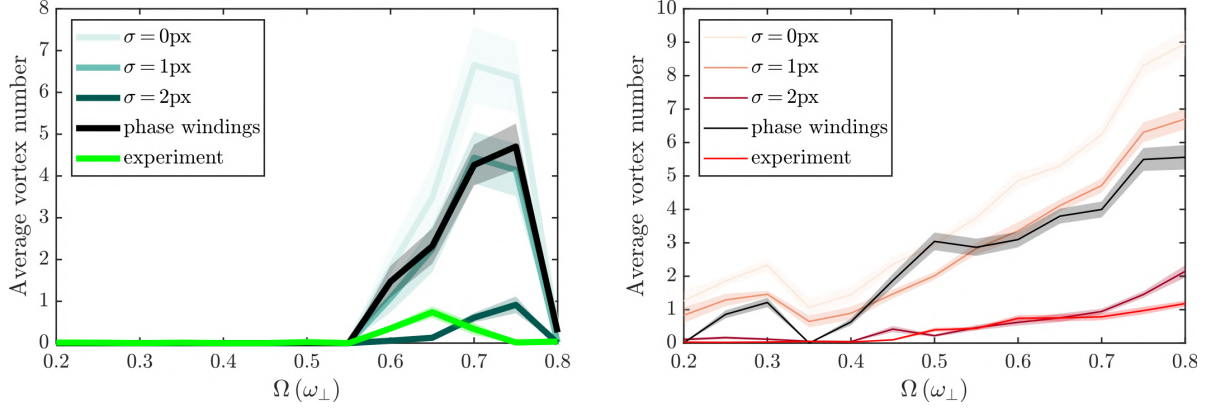
Extended Data Fig. 7. **Comparison of different vortex detection methods applied to the theoretical data.** Each point is obtained by applying the experimental vortex detection algorithm to the states of Fig.3 and averaging over time. For the SSP the scattering length is ramped from $a_s = 93a_0$ to $a_s = 104a_0$ in $1\,\mathrm{ms}$ and the state is expanded for $3\,\mathrm{ms}$, before applying the algorithm. The results are shown for different size of Gaussian filter σ and compared to the standard method of counting the 2π phase windings (black line) and the experimental data, in green (red) for the BEC (SSP). The shaded area indicates the error on the mean.
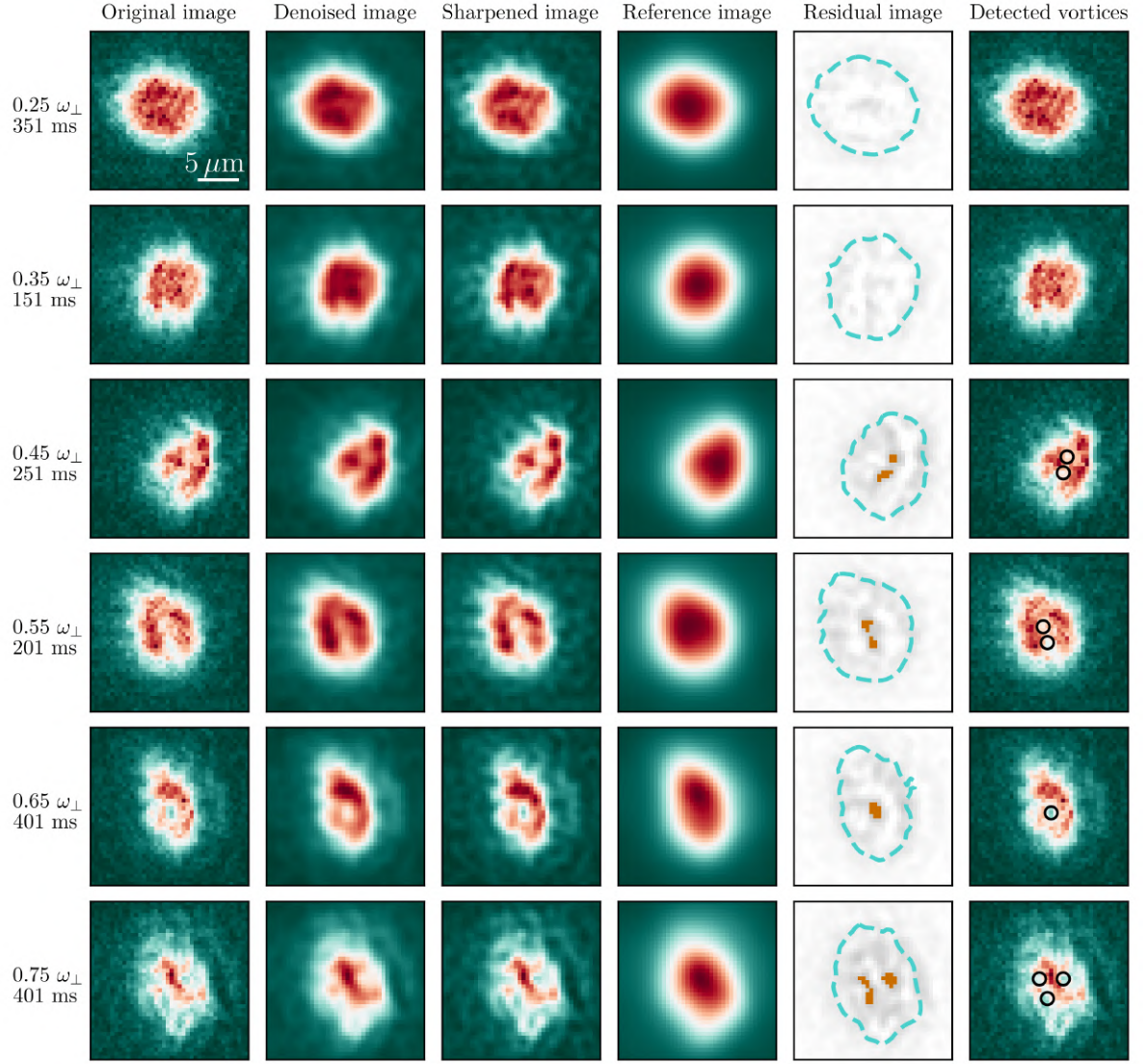
Extended Data Fig. 8. **Image processing for the detection of vortices.** Each row indicates different rotation frequency and duration parameters (indicated on the left), where images are taken following an interaction quench from the supersolid to unmodulated BEC phase. Each column is a step of the processing protocol which goes as follows. The data (column 1) is normalized and denoised with a Gaussian filter of size $\sigma = 1$ (column 2), and a sharpening mask is applied to magnify the presence of vortices (column 3). The reference image is built from the data image where all density variations are eliminated with a Gaussian filter of size $\sigma = 3$ (column 4). The residuals (column 5) are obtained from the subtraction of the data to the reference, converting the density depletions to a positive signal. The vortices (black circles) are detected with a peak detection algorithm with threshold 0.38. The last column shows the location of the vortices on the original image data. Varying the threshold value modifies the absolute vortex count of each individual image but not the overall qualitative result (see Extended Data Fig. 9).
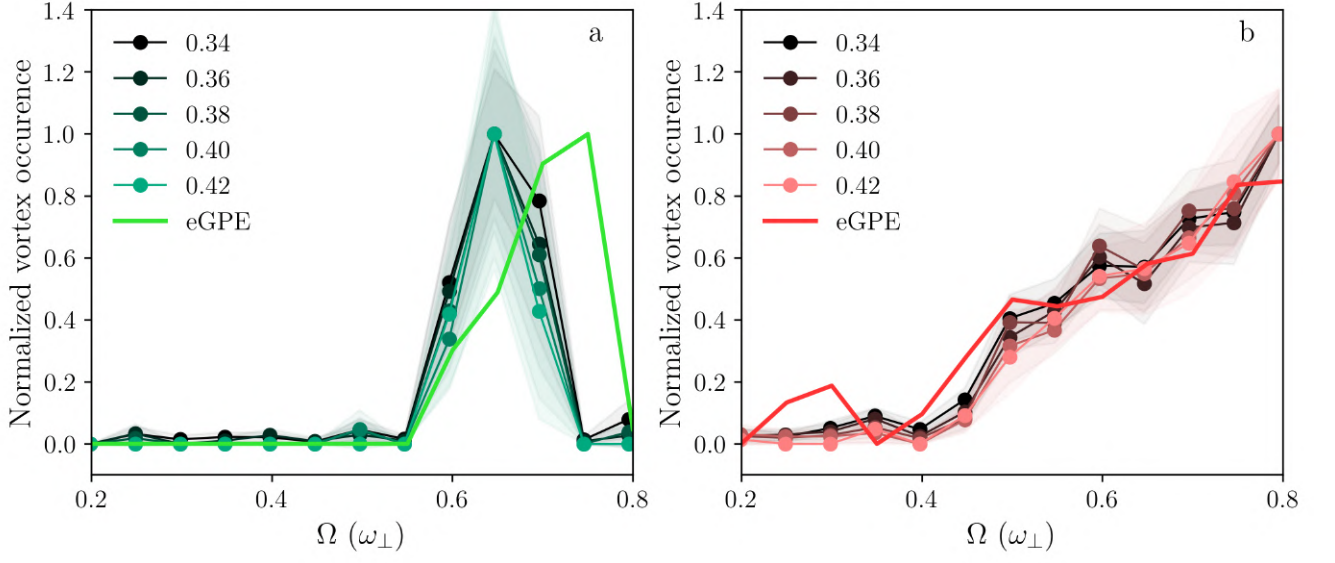
Extended Data Fig. 9. **Experimental vortex detection as a function of the threshold parameter.** Normalized vortex occurrence integrated over 1 s of rotation in the BEC phase (left) and in the supersolid phase (right) as a function of the rotation frequency, for varying contrast threshold between 0.34 and 0.42 (see Extended Data Fig. 8). The shaded areas indicate the error on the mean, *i.e.* the standard deviation divided by the square root of the number of points (8). The solid lines are visual help. The results of the extended-GPE simulations (see Fig. 3) are plotted in thick solid lines as a comparison.
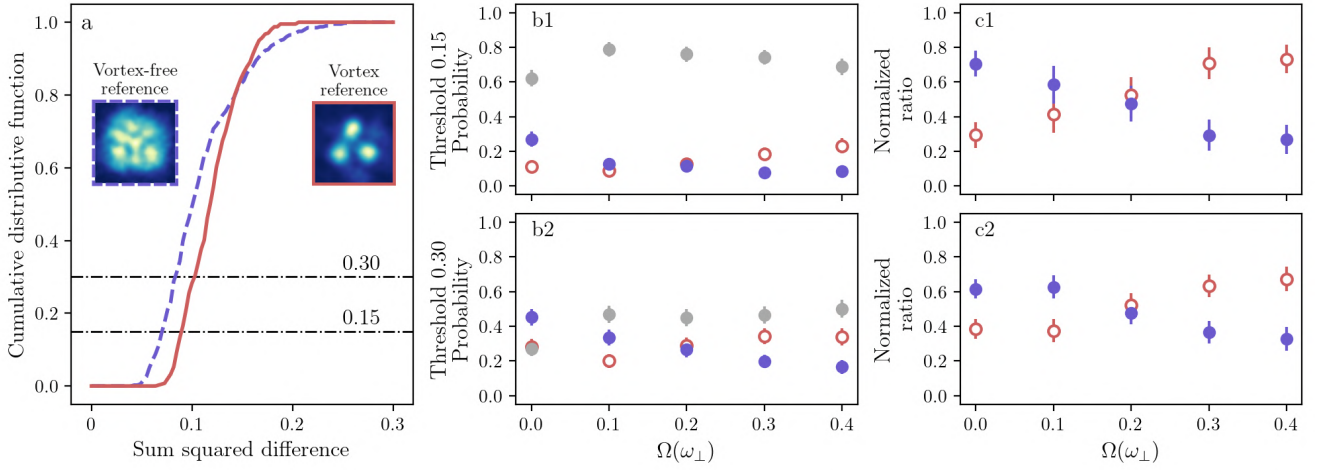
Extended Data Fig. 10. **Probability of detecting a vortex as a function of the rotation frequency**. **a** Cumulative distribution function obtained from the calculated sum squared differences over the whole data set, with each of vortex (solid line) and vortex-free (dashed line) references (see inset images). **b** With a defined threshold X (dashed-dotted lines on **a**) on the cumulative distribution function, each image is assigned to a category: vortex (red empty circles), vortex-free (blue filled circles), or no classification (grey filled circles). **c** Probability of detecting a vortex signal and vortex-free signal out of the selected images in **b**. The error bars indicate the Clopper-Pearson uncertainty associated with image classification. Top and bottom rows show the classification result for respective thresholds 0.15 and 0.30 on the cumulative distribution function, showing the independence of the signal from the threshold.

4.8. Additional knowledge: quadrupole mode resonances

As seen in the previous sections, the quadrupole mode plays a crucial role in the rotational dynamics for the vortex nucleation. In fact, in both the BEC and supersolid phases, vortices emerge dynamically through surface instabilities driven by resonant quadrupole modes. In the following, we explore two aspects of the quadrupole dynamics:

- The aspect ratio oscillations of a rotating BEC prior to vortex nucleation, as observed in Ref. [192].
- The resonances associated to the quadrupole mode spectrum in the supersolid regime, which provides insights into the experimental observations in Ref. [193].

4.8.1. Quadrupole modes in rotating BEC

From Ref. [192] in Sec. 4.6, we know that during the magnetostirring the aspect ratio (AR) of the system undergoes quadrupole deformations[4]. When the vortices enter, the AR approaches to 1. The frequency of these quadrupolar oscillations depends on the scattering length and on the rotation driving frequency, see Fig. 4.6(a)-(b) and the extracted value ω_{AR} in (c)-(d). In the following, we derive a simple theoretical model to estimate the value of this AR oscillation frequency.

When the BEC is rotating through magnetostirring, the system can be effectively described as confined with reduced trapping frequencies. These can be modelled as

$$\begin{cases} \tilde{\omega}_x^2 = \omega_x^2 + \alpha^2 - 2\alpha\Omega \\ \tilde{\omega}_y^2 = \omega_y^2 + \alpha^2 + 2\alpha\Omega \end{cases} \tag{23}$$

where $\alpha = -\beta\Omega$ and β is the geometric deformation of the system at equilibrium at a given Ω [198].

For a cylindrically symmetric system, we know that the quadrupole mode frequency is $\omega_q \approx \sqrt{2}\omega_\perp$, and in the rotating frame its frequency becomes $\omega_q^{rot} \approx \omega_q - 2\Omega$[5]. When the system gets deformed through magnetostirring, the effective trap is no longer cylindrically symmetric, making the quadrupole frequency not straightforward to derive. However, we can simplify the problem considering an equivalent cylindrically symmetric trap obtained from the geometrical average of the new effective frequencies

$$\omega_{eq} = \sqrt{\tilde{\omega}_x^2 + \tilde{\omega}_y^2}\,. \tag{24}$$

Thus, we estimate the quadrupole mode frequency in the new effective trap as

$$\omega_q^{rot} = \sqrt{2}\omega_{eq} - 2\Omega\,, \tag{25}$$

and we plot the results for different scattering lengths and Ω in Fig. 4.6(c)-(d). Despite the many rough approximations, this simple approach successfully replicate the trend of ω_{AR}, in particular in the range of a_s comparable to a_{dd}.

---

[4]Here, we define $AR = \sigma_{max}/\sigma_{min}$, with σ_{max} and σ_{min} the maximum and minimum width of the condensate during rotation.

[5]Given a collective mode with frequency ω_m characterized by an azimuthal quantum number m, its frequency can be easily calculated in the rotating frame as $\omega_m^{rot} = \omega_m - m\Omega$ [224]. In our case, the quadrupole mode has $m = 2$.
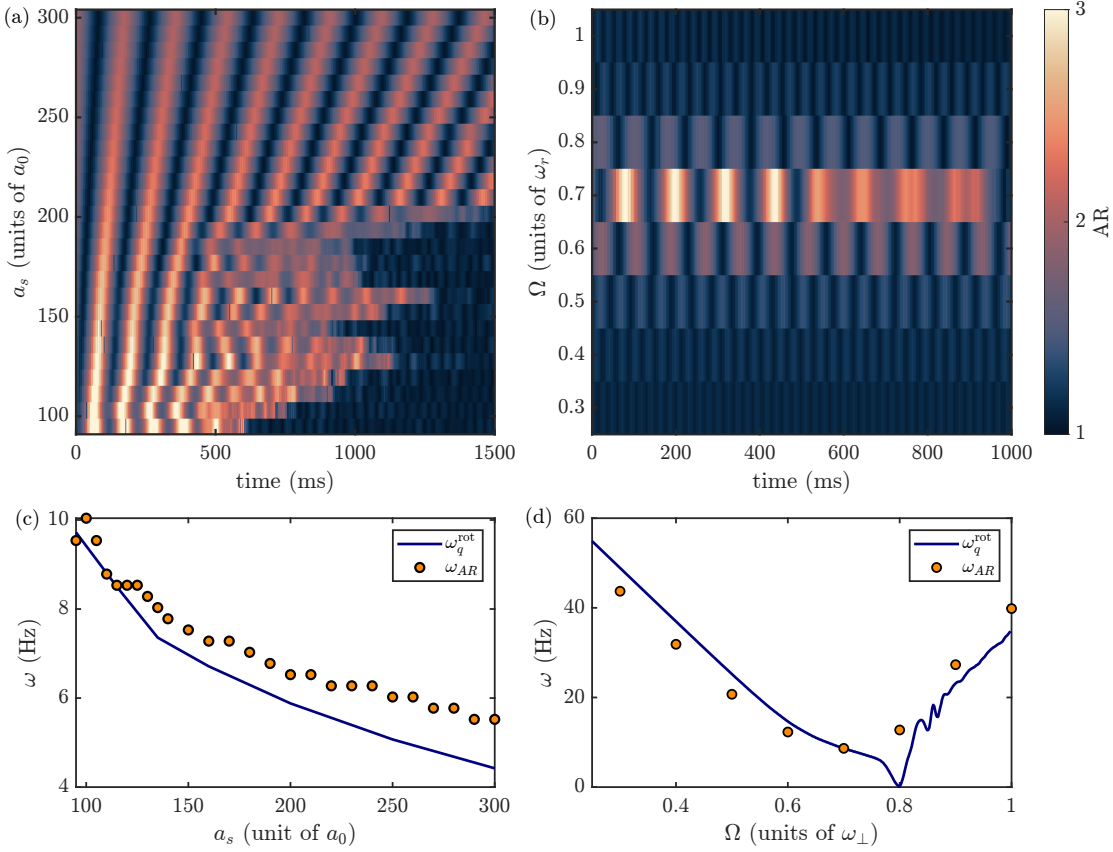
Figure 4.6.: Aspect ratio oscillations during vortex nucleation process through magnetostirring. Phase diagram in (a) shows AR oscillations of a BEC with different a_s, rotating at a fixed $\Omega = 0.7\omega_\perp$. The phase diagram in (b) shows the AR oscillations of a BEC with $a_s = 115\,a_0$ rotating at different Ω. (c)-(d) Comparison between frequency of AR oscillations and theoretical estimate. Parameters: $N = 30000$, trap $\omega/2\pi = (60, 60, 190)\,\mathrm{Hz}$.

4.8.2. Quadrupole modes in rotating supersolids

The rotational response of the system reflects the resonances of the quadrupole modes. It is possible to highlight this connection by calculating the spectrum of the quadrupole mode in the rotating frame. We take supersolid state with tilted droplets and we excite quadrupolar oscillations by deforming the radial trap frequencies

$$(\omega_x, \omega_y) \to (\omega_x - 0.5, \omega_y + 0.5)\,\mathrm{Hz} \tag{26}$$

for $1\,\mathrm{ms}$ and then restore the initial values. We evolve the state for $1\,\mathrm{s}$ and fit the aspect ratio of the system with a Gaussian function as a function of time. The time Fourier transform of these oscillations gives the spectrum of the quadrupole modes excited by the protocol. A quadrupole mode with frequency ω_q in the rotating frame is

$$\omega_q^{rot} = \omega_q - 2\Omega\,, \tag{27}$$

so the rotation frequency Ω at which the quadrupole mode is at resonance in the rotating frame ($\omega_q^{rot} = 0$) is

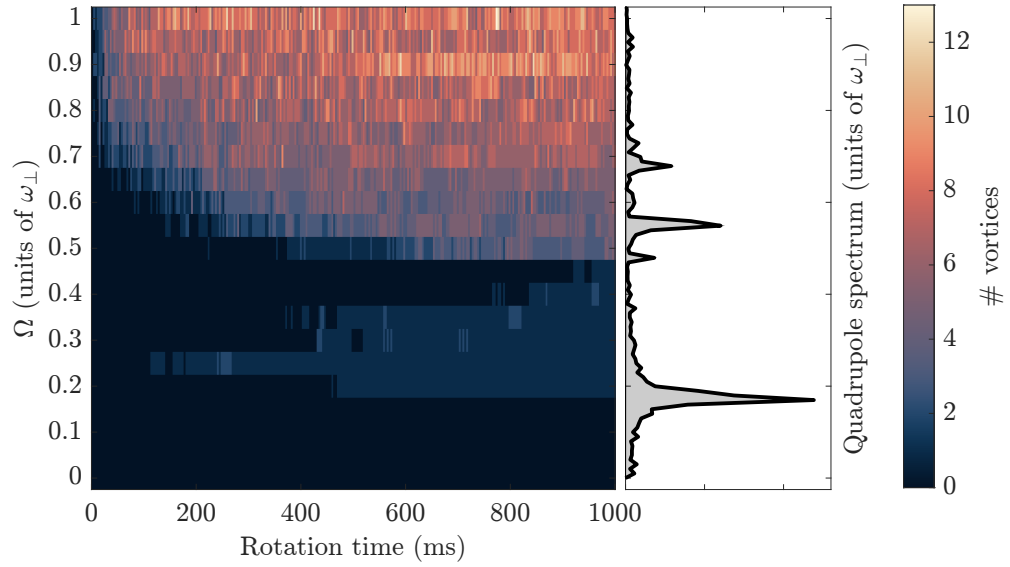$$\Omega = \frac{\omega_q}{2}\,. \tag{28}$$

Figure 4.7.: Rotational response of a 2D supersolid for varying rotation time and Ω (left) with corresponding quadrupole spectrum in the rotating frame (right). Parameters: $N = 50000$, trap $\omega/2\pi = (50, 50, 95)\,\mathrm{Hz}$, $a_s = 95\,a_0$.

By rescaling the quadrupole spectrum accordingly, we obtain the results shown in Fig. 4.7. The filled gray peaks corresponds to the values of Ω for which one of the quadrupole modes excited by the protocol is at resonance. The lowest peak sets the onset of vortex nucleation and it correspond to a superfluid quadrupole mode, whereas the higher frequency peaks are crystal quadrupolar deformations [199].

Chapter 5

5

Glitches in rotating supersolids

In this thesis, quantum effects have so far been explored by studying systems at extremely low temperatures. Under such conditions, the wave packets associated with atoms overlap and interfere constructively, leading to the formation of a macroscopic quantum state known as a Bose-Einstein condensate. However, lowering the temperature is not the only way to achieve wave-packet overlap and access the quantum regime. Another approach is to increase the particle density.

While the first method requires cooling to ultralow temperatures, the second demands reaching exceptionally high densities, far beyond what can be achieved in terrestrial experiments. Fortunately, the universe provides natural settings where such extreme densities exist: neutron stars. Despite their vastly different scales and sizes, neutron stars are predicted to exhibit superfluid properties. In particular, previous studies have shown that neutron matter in the interior of the star may organize into exotic, density-modulated superfluid phases, collectively known as *nuclear pastas* [225, 226].

Bose-Einstein condensates have been already associated to astrophysical objects and events, like black holes or supernovae [227, 228]. In this chapter, we go a step further by establishing for the first time a direct connection between density modulated superfluid phases in the inner crust of neutron stars and supersolid states. This analogy allows us to explore with dipolar supersolids one of the most accredited astrophysical theories for glitches–sudden jumps in the rotation rate of neutron stars–interpreted as collective vortex unpinning events within the superfluid interior[1]. We begin by outlining the internal structure of neutron stars and their rotational dynamics during a glitch. Then, by exploiting the structural similarities between neutron matter and dipolar supersolids, we develop a model to simulate glitches in dipolar supersolids.

This project has been developed in collaboration with the group led by Prof. Massimo Mannarelli, a theoretical astrophysicist working at Gran Sasso National Laboratories in L'Aquila, Italy. The author also had the possibility to do a research stay there, thanks to the funding provided by DK-ALM doctoral school in Innsbruck.

---

[1]The literature on the possible mechanisms responsible for pulsar glitches is extensive: accretion, magnetospheric instabilities, starquakes and others hypothesis. For a review, see Ref. [229].
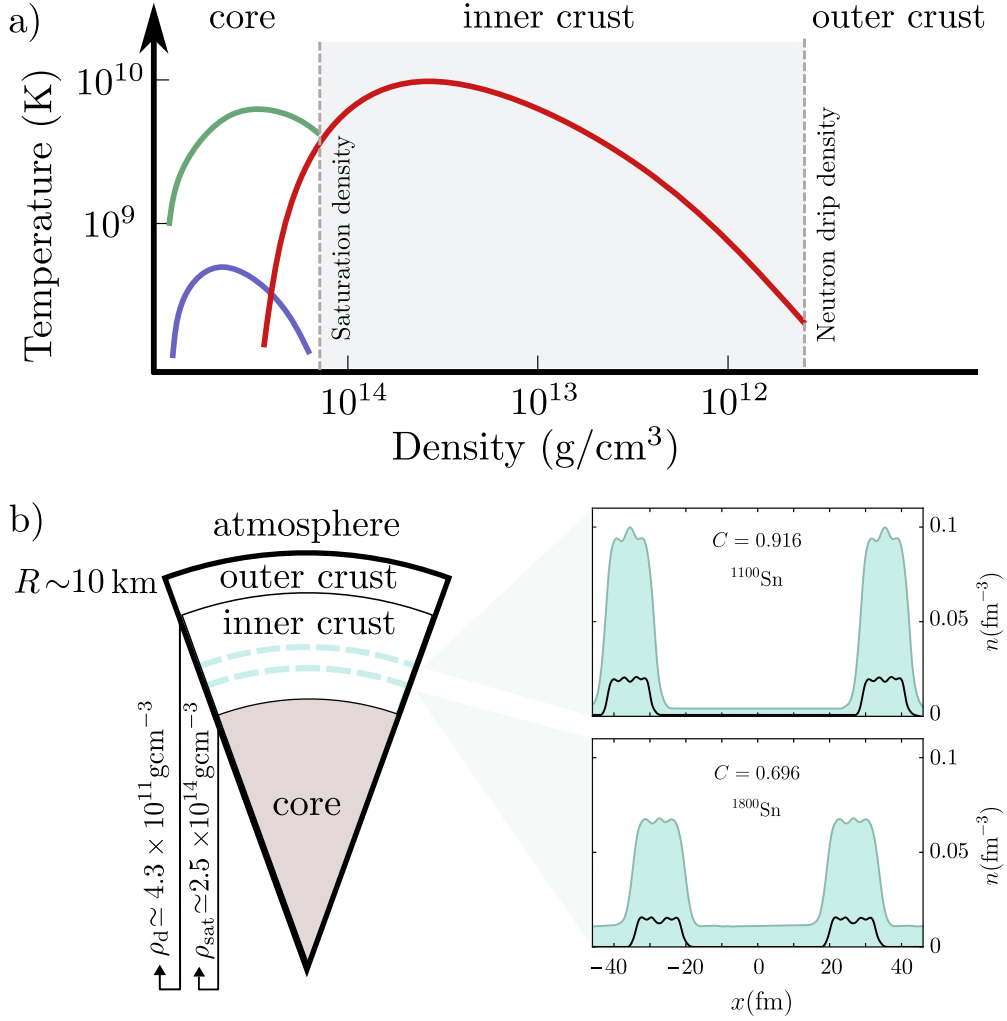
Figure 5.1.: Neutron star properties and structure. (a) Schematic of the critical temperature for superfluidity of neutron pairs for singlet states in the inner crust (red line) and triplet states in the core (violet line) and critical temperature for proton superconductivity in the singlet state (green). Reproduced and adapted from Ref. [230]. (b) Structure of the neutron star interior and exemplar density profile of the neutron-proton matter distribution in the inner crust. Notice that the layer thicknesses shown in the left plot are not in scale. In reality, of the total $\sim 10\,\mathrm{km}$ stellar radius, the outer crust spans $\sim 100\,\mathrm{m}$ and the inner crust $\sim 1\,\mathrm{km}$ [230]. Taken from Ref. [217].

5.1. Interior structure of neutron stars

Neutron stars originate from supernovae, violent cosmic explosions that marks the end of the life of a heavy star. The remnants of these explosions create an incredibly dense and compact object, with pressures and densities far beyond human experience. They usually manifest as pulsars, highly magnetized rotating neutron stars with a mass between 1–2 solar masses, confined into a sphere with a radius of approximately 10 km. These systems provide a unique opportunity to study the behaviour of matter under extreme conditions. In this section, we focus on the structural properties of their interior, while in Sec. 5.2 we will focus on the rotational dynamics.

A few hundred years after formation, neutron stars reach thermal equilibrium, with core temperatures typically ranging from 10^6 to 10^8 K, several orders of magnitude lower than the Fermi temperature of nuclear matter [231], see Fig. 5.1(a). For these reasons, they can be considered as cold and dense stellar objects where quantum effects are not negligible.

Neutron stars are predicted to have distinct layers with different structural properties. In particular, as the density of the star increases with the radial depth, some of the layers are expected to have superfluid phases [232]. We start by outlining the basic properties of each part of the star, understanding the region of interest and then we focus on the analogies with dipolar supersolids.

The structure of a neutron star is schematically depicted in Fig. 5.1(b). Beneath a very thin atmosphere (of the order of micrometers), we identify the *outer crust* region. This layer has densities ranging from 10^6 to 10^{11} g/cm^3 and it is composed of a lattice of fully ionized heavy nuclei immersed in a relativistic electron gas. Microscopically, the equilibrium state of this solid part of the star is expected to be a body centred cubic lattice made of well-defined neutron-rich nuclides [232, 233]. The neutron fraction inside the nuclei increases with the radial depth of the star, because of electron capture processes[2]. The structure of the crust is completely determined up to a density of the order $\sim 6 \times 10^{10}$ g cm^3 by the experimental nuclear data. These information indicate the presence of different neutron rich nuclei like ^{56}Fe, ^{66}Ni, ^{86}Kr, ^{82}Ge and others [234]. At higher densities the nuclei are so neutron rich that they have not yet been experimentally studied, so the composition of the nuclei in these layers is model dependent [232].

The density of the star increases with the depth until it reaches the neutron drip density $\rho_{\mathrm{d}} = 4 \times 10^{11}$ g/cm^3. This threshold sets the point at which it becomes energetically favourable for the neutrons to drip out of the nuclei and form a neutron bath made of unbound neutrons. This transition defines the onset of the *inner crust* region. Additionally, the temperature of the star is lower than the critical temperature for superfluidity [232, 235]. The pairing of neutrons is described by BCS theory: due to an attractive component of the nucleon-nucleon interaction, neutrons form singlet-state Cooper pairs [230]. This leads to the formation of a modulated superfluid of neutron pairs coexisting with an underlying lattice structure given by the nuclides, see Fig. 5.1(b). We will explore the physics of this region more in detail in the following sections.

Finally, as the density increases even more, it approaches the saturation density $\rho_{\mathrm{d}} = 2.5 \times 10^{14}$ g/cm^3, where the crustal structures completely vanish. This is the *core* region. Here, the composition of the star is mostly unknown but, since the nucleons are so tightly packed that they overlap, it is expected to have liquid-like exotic phases with superfluid properties [230].

---

[2]Electron capture is a process in which a proton-rich nucleus of a neutral atom absorbs an electron from one of the inner shells. Thus, the proton in the nucleus becomes a neutron causing the emission of a neutrino. Considering the parameter regimes of the neutron star, this process becomes possible for densities $> 10^7$ g/cm^3.

5.1.1. Neutron stars and supersolidity

Neutron matter in the inner crust of neutron stars exhibits both superfluid behaviour and spatial density modulation. These two features, discussed extensively in the previous chapters in the context of ultracold atomic gases, are hallmarks of a supersolid phase. However, as often occurs when bridging concepts across different fields, the term supersolid is rarely used in neutron star physics, except in specific contexts such as certain studies of quark phases in the star's core [236]. In the following, we analyse the main points to connect supersolidity with the neutron matter density distribution in the inner crust of neutron stars.

The coexistence of superfluid and crystalline properties in the inner crust becomes evident when looking at the quantum calculations of the inner crust structure pioneered by Negele and Vautherin [237], which we reproduce as insets on the right of Fig. 5.1(b). The matter density profile is shown along an axis connecting the center of two adjacent Wigner-Seitz cells, for two different radial depths of the star. The solid black line represents the distribution of the protons in the nuclei, forming a well defined crystalline lattice with a spacing of the order $\sim 100\,$fm. The aquamarine distribution highlights the superfluid neutron density: an array of peaks connected by a superfluid neutron background. This is very reminiscent of the density profile of a dipolar supersolid state, like the one seen in Fig. 2.3(b) and elsewhere throughout this thesis.

Before jumping to any conclusion, we clarify some points. Previous calculations showed that, at such extremes densities in the inner crust, well-defined nuclides do not exist anymore, as neutrons are delocalized through the superfluid background. In the neutron star framework, the density peaks are usually called *nuclear-type clusters* to differentiate them from standard isolated nuclei [238]. This is confirmed by the fact that the calculations for the pairing field are performed with the pairing field being a continuous function of position in the whole Wigner-Seitz cell, indicating that behaves as a coherent superfluid [239]. Furthermore, simulations of excitations in the inner crust reveal the emergence of collective modes, arising from the interplay between the nuclear-type clusters and the surrounding neutron sea [240].

In conclusion, for all these reasons, the modulated superfluid neutron density distribution can be viewed as a supersolid phase of neutron pairs, possessing the periodicity of the underlying proton crystalline structure.

5.2. Glitches in neutron stars

Neutron stars usually manifest as pulsars, that are highly magnetized rotating stars that emit electromagnetic radiation out of their magnetic poles [241]. The magnetic axis is misaligned with the rotation axis, so the emitted radiation can be observed from Earth when it is pointing towards it, like a galactic lighthouse[3]. In Fig. 5.2(a) we show an exemplar picture of the on-pulse star PSR B1930+22 taken from the Strasbourg

---

[3]The first signal from a pulsar was detected by Jocelyn Bell in 1967, during her PhD in Cambridge under the supervision of Antony Hewish [242]. The regularity of the lighthouse signal was so perfect that initially it was interpreted as an attempt of extra-terrestrial communication. For this reason, the source was humorously called LGM-1, short for *little green men*. This hypothesis was quickly dismissed when a similar signal was detected from a completely different region of the sky. The discovery of pulsars contributed to Hewish being awarded the Nobel Prize in 1974, whereas Bell was unfairly excluded.
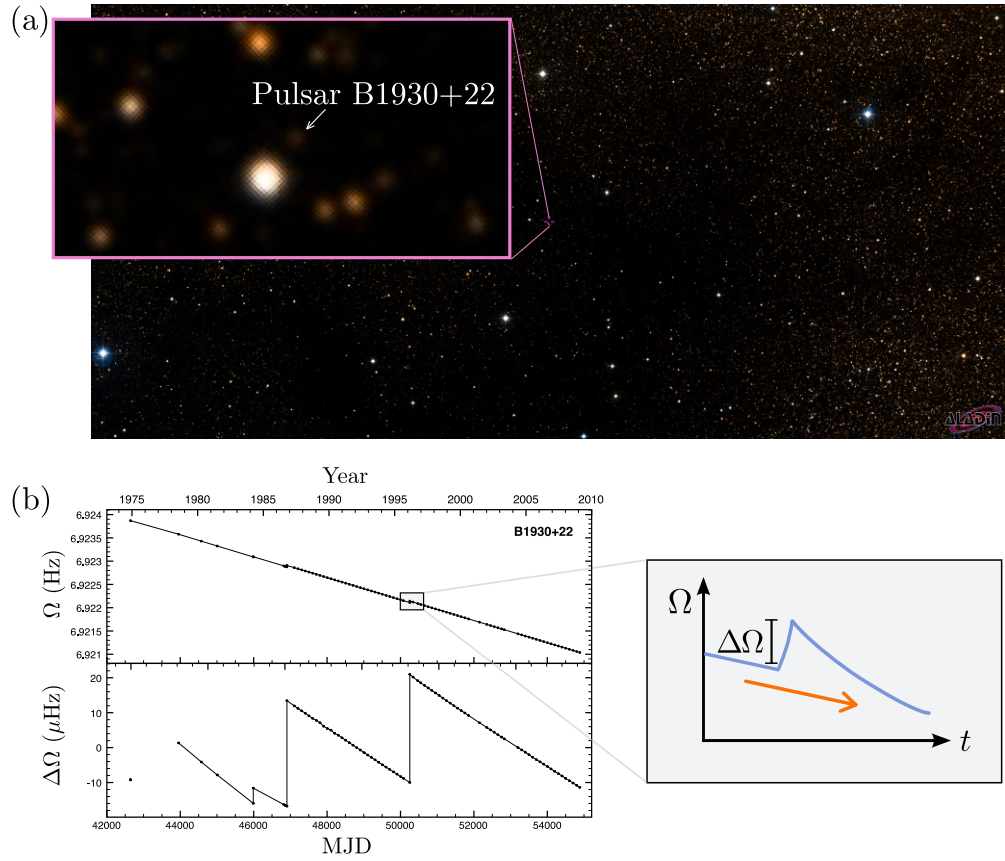
Figure 5.2.: Neutron star glitches. (a) Picture of the PSR B1930+22 pulsar taken from the Strasbourg astronomical Data Center, using the Aladin Sky Atlas [243]. (b) Rotation frequency Ω and frequency residual $\Delta\Omega$ of the neutron star PSR B1930+22 during the last 30 years. Frequency residuals are obtained by subtracting the main linear slope. On the right, schematic illustration of a glitch. Taken and adapted from Ref. [244].

astronomical Data Center [243]. The measurement of the time interval between two radiation pulses coming from the star provides a very precise measurement of the neutron star angular velocity [244]. The rotation period T is slightly different for each star. For the one considered in Fig. 5.2(a) the period is $T \sim 0.14\,\text{s}$ but, for instance, $T \sim 0.7\,\text{s}$ for the PSR B0329, $T \sim 0.089\,\text{s}$ for the Vela pulsar, and $T \sim 0.033\,\text{s}$ for the Crab pulsar.

The star is constantly emitting radiation, so it is losing energy in time. As a consequence, an observer from Earth would expect to observe a general slow-down process due to energy dissipation. However, every once in a while the star suddenly spins up, originating a *glitch* event. Glitches for the pulsar PSR B1930+22 are shown in Fig. 5.2(b). The rotation frequency Ω slowly decreases but it sometimes jumps up with $\Delta\Omega \sim 10^{-6}\,\text{Hz}$. The size of the glitch is variable and usually very small, it can range from $\Delta\Omega/\Omega \sim 10^{-11} - 10^{-5}$ [244, 245].

The most accredited theory to explain the glitch mechanism is a rapid transfer of angular momentum from a neutron superfluid in the inner crust to the solid outer crust [246, 247]. The idea is the following:

- The star is rotating and the inner crust has superfluid properties. Thus, part of

the angular momentum is stored in form of quantized vortices. The estimated number of vortices in the inner crust is $\sim 10^{18}$ [248]. However, because of the crystalline structure, vortices are not free to move around as they are pinned in between the crystal sites.

- During the slow-down process of the star, the inner crust does not keep up and lags behind for its superfluid character. The angular momentum cannot be lost in a continuous manner because vortices are pinned and cannot easily move from their equilibrium position. In this way, the inner part of the star begins to to accumulate excess angular momentum.

- At a certain point, the star no longer supports this out-of-equilibrium configuration: the accumulated extra angular momentum has to be ejected. This is done by triggering a sudden collective unpinning of vortices, forming an avalanche towards the outer crust. The estimated number of vortices collectively leaving and creating a neutron star glitch is predicted to be $\sim 10^7 - 10^{14}$ [248].

- The vortex angular momentum is ejected from the inner crust and absorbed by the outer crust, that suddenly spins up originating a *glitch*.

The observation of glitches offers one of the rare opportunities to indirectly investigate the interior of a neutron star. Since the structure of the inner crust is very reminiscent of dipolar supersolids, we investigated how an ultracold dipolar system could simulate glitches events in analogy of neutron stars.

5.3. Vortex Pinning

The two main ingredients behind the glitch mechanism are quantized vortices and their pinning. In fact, to achieve a sudden release of angular momentum, it is necessary to localize vortices using a pinning potential. The angular momentum carried by the vortices is then released abruptly when the system reaches an out-of-equilibrium configuration. In ultracold gases, vortices in an unmodulated BEC form a regular Abrikosov lattice but they are not pinned, see discussion in Sec. 4.5.2. Vortex pinning can be realized either by introducing a pinning potential to a BEC or by spontaneously breaking translational symmetry to create a density modulation, which acts as an effective pinning potential for the vortices. The first option has been developed in Ref. [249]. Here, we investigate the second option by considering a 2D dipolar supersolid. Unlike BECs with pinning potential, 2D supersolids offer an ideal platform to explore both crystal and vortex dynamics.

In the following, we investigate the impact of the pinning effect during the slow down process. To do so, we begin with an initial state–either a BEC or a supersolid–in equilibrium in the rotating frame. The initial rotation frequency Ω_0 is chosen so that the system hosts tens of vortices. For the considered set of parameters, this condition is met for $\Omega_0 = 0.5\,\omega_\perp$. We then apply a slow linear ramp down of $\Omega(t) = \Omega_0 - \alpha t$, with $\alpha = 10^{-5}$. By performing complex-time numerical simulations (see Sec. 1.3.4), we observe a gradual reduction in the system's total angular momentum over time. However, the nature of this process differs significantly depending on whether the initial state is a BEC or a supersolid.
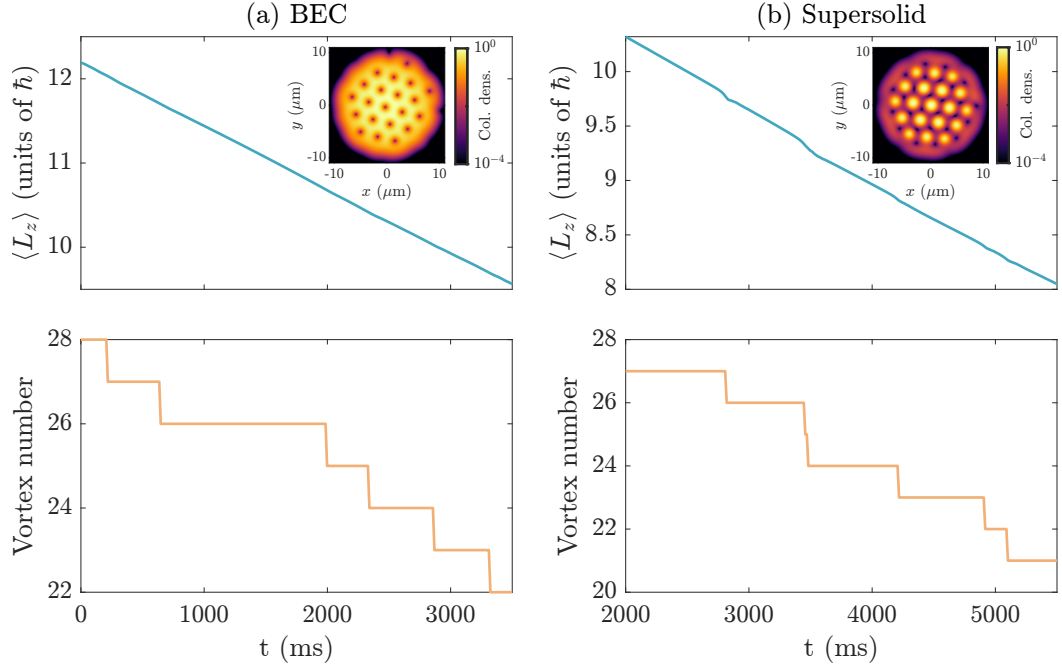
Figure 5.3.: Slow down process for a BEC and a supersolid. The upper panels show the expectation value of the angular momentum operator $\langle L_z \rangle$, while the lower panels show the number of vortices as a function of time. Vortices are counted by identifying the phase singularities. The time intervals have been properly chosen to capture vortices leaving the system. The two insets in the upper panels show two density distributions at $3691\,\mathrm{ms}$ (BEC) and $2795\,\mathrm{ms}$ (supersolid), where vortices are leaving. Parameters: N=300000, $a_s = [100, 90]\,a_0$, trap frequencies $(\omega_\perp, \omega_z) = (50, 130)\,\mathrm{Hz}$, $\Omega_0 = 0.5\omega_\perp$.

5.3.1. Slowing-down a BEC

First, let us consider a BEC state with a vortex lattice, see an example in inset of Fig. 5.3(a). As expected, the linear ramp down induces vortices to gradually leave the system. This process occurs in a continuous manner: vortices can slowly move towards the edge of the system and the others can slowly rearrange deforming the lattice. The consequence of this behaviour is that the angular momentum decreases almost linearly, driven by the gradual change of the density distribution. Importantly, there are no sudden jumps in angular momentum when vortices leave.

5.3.2. Slowing-down a supersolid

Let us now consider a supersolid state with vortices, see an example in inset of Fig. 5.3(b). The behaviour of a supersolid state during a slow-down process sets the basis for the development of the glitch model that we developed in Ref. [217], presented in Secs. 5.4 and 5.5. In this case, vortices are pinned in the interstitial low-density regions between the droplets and cannot continuously migrate toward the system's edge when slowing down. Instead, each time a vortex escapes, the angular momentum undergoes a sudden jump, corresponding to the abrupt ejection of the angular momentum carried by the vortex. Following this event, the remaining vortices gradually rearrange among the pinning sites. Notably, if this sudden release of angular momentum was absorbed by a

solid outer crust, the crust would spin up, originating a glitch.

5.4. The feedback equation

So far we have seen that dipolar supersolids possess structural properties in analogy to the inner crust of neutron stars and that, when rotating, they host quantized vortices that are pinned in the interstitial sites of the droplet crystal. The final missing piece for the analogy with the neutron star is a coupling with a solid outer crust. Although our system does not physically include such a crust, we can model its behaviour in presence of an hypothetical crust by introducing a coupling mechanism. To this end, we propose an additional equation that mimics this coupling, the so-called *feedback equation.* In the following, we derive the feedback equation and we explain the meaning of the different terms.

The slow down process can be though as a consequence of a constant torque N_{em}, so that
$$\frac{d\langle L_z \rangle}{dt} = N_{em} \,. \tag{1}$$

The subscript *em* stays for electromagnetic torque, to recall what actually drives the slow down process in neutron stars. The quantity $\langle \hat{L}_z \rangle$ is the total angular momentum calculated as expectation value of the angular momentum operator. For a supersolid, the total angular momentum can be decomposed in two contributions

$$\langle \hat{L}_z \rangle = L_{vort} + L_s = L_{vort} + I_s \Omega \,, \tag{2}$$

where the first component is the vortex contribution, the second component is the linear response to rotation due to a non-zero moment of inertia I_s. Notice that all of these quantities are time dependent: L_{vort} changes with the number of vortices, I_s changes with the small perturbations of the mass distributions during the slow down process and Ω is the time dependent rotation frequency of the system. After inserting Eq. (2) into Eq. (1), we obtain the *feedback equation*

$$I_{\mathrm{s}}\dot{\Omega} = -N_{\mathrm{em}} - \dot{L}_{\mathrm{vort}} - \dot{I}_{\mathrm{s}}\Omega \,, \tag{3}$$

that is a differential equation for the rotation frequency Ω.

The physical meaning of this equation is the following: the rotation frequency Ω gradually decreases over time due to the constant external torque N_{em}. Every time a vortex leaves, the term $\dot{L}_{\mathrm{vort}}$ gives a negative contribution to the equation, that makes Ω spin up because of the minus sign in front of it. The last term contains $\dot{I}_{\mathrm{s}}$ and it accounts for variations in the moment of inertia arising from crystal excitations induced by vortex dynamics. Altogether, this equation models the behaviour of a supersolid coupled to a hypothetical outer solid crust, which directly interacts with the "solid" rotational response of the supersolid, represented by L_{s}.

By solving the eGPE and the feedback equation as two coupled differential equations

$$\begin{cases} i\hbar \dfrac{\partial \psi}{\partial t} = (1 - i\gamma) \left[\mathcal{L}_{GP} - \Omega(t)\hat{L}_z \right] \psi \\[2mm] I_{\mathrm{s}}\dot{\Omega} = -N_{\mathrm{em}} - \dot{L}_{\mathrm{vort}} - \dot{I}_{\mathrm{s}}\Omega \,, \end{cases} \tag{4}$$

we simulate glitches events in dipolar supersolids, in analogy to neutron star glitches. These results have been collected in the publication in Ref. [217], that is reported in the next section of this thesis.

5.5. Publication: Glitches in rotating supersolids

E. Poli[1], T. Bland[1], S. J. M. White[1,2], M. J. Mark[1,2], F. Ferlaino[1,2], S. Trabucco[3,4]
and M. Mannarelli[3]

[1] *Institut für Experimentalphysik, Universität Innsbruck, 6020 Innsbruck, Austria*
[2] *Institut für Quantenoptik und Quanteninformation, Österreichische Akademie der Wissenschaften, 6020 Innsbruck, Austria*
[3] *INFN Laboratori Nazionali del Gran Sasso, 67100 Assergi (AQ), Italy*
[4] *Gran Sasso Science Institute, 67100 L'Aquila, Italy*

[†] The author of the present thesis performed the numerical simulations and contributed in writing the manuscript.

Glitches in Rotating Supersolids

Elena Poli[ORCID],[1] Thomas Bland[ORCID],[1] Samuel J. M. White[ORCID],[2,1] Manfred J. Mark[ORCID],[1,2] and Francesca Ferlaino[ORCID][1,2,*]

[1]*Universität Innsbruck, Fakultät für Mathematik, Informatik und Physik, Institut für Experimentalphysik, 6020 Innsbruck, Austria*
[2]*Institut für Quantenoptik und Quanteninformation, Österreichische Akademie der Wissenschaften, 6020 Innsbruck, Austria*

Silvia Trabucco[ORCID][3,4] and Massimo Mannarelli[ORCID][3]
[3]*INFN Laboratori Nazionali del Gran Sasso, 67100 Assergi (AQ), Italy*
[4]*Gran Sasso Science Institute, 67100 L'Aquila, Italy*

Glitches, spin-up events in neutron stars, are of prime interest, as they reveal properties of nuclear matter at subnuclear densities. We numerically investigate the glitch mechanism due to vortex unpinning using analogies between neutron stars and dipolar supersolids. We explore the vortex and crystal dynamics during a glitch and its dependence on the supersolid quality, providing a tool to study glitches from different radial depths of a neutron star. Benchmarking our theory against neutron-star observations, our work will open a new avenue for the quantum simulation of stellar objects from Earth.

One of the greatest strengths of ultracold gases is their ability to simulate the behavior of widely disparate systems [1]. This extraordinary capability enables quantum gases to serve as powerful solvers for unmasking fundamental open questions concerning the underlying dynamics of complex physical systems. The range of fields where quantum gas simulators have found applications include metallic superconductivity and condensed matter systems, as well as nuclear matter. Among these examples, nuclear matter under the extreme conditions existing in neutron stars is the most elusive to direct microscopic observation [2–4].

Neutron stars are the densest stellar objects known today. They form through the core collapse of massive progenitor stars in supernovae type-II events, leading to their extreme densities in which a giant gravitational mass of a few solar masses is concentrated in just a tiny radius of about 10 km. Shortly after their birth, neutron stars cool down to temperatures of the order of keV. Compared to ultracold gases (peV), these temperatures are very high, yet much smaller than the MeV energy scale typical of nuclear matter. For this reason, neutron stars can be viewed as cold dense nuclear matter in which quantum effects become very important. The current most-widely-accredited descriptions to explain observations in such systems account for fermionic pairing and correlations in quantum many-body systems [5,6].

The 1967 discovery of pulsars [7]—highly magnetized and rapidly rotating neutron stars [8,9]—provided crucial hints of superfluidity and fermionic pairing in these stellar objects. Pulsars can be seen as nearly perfect clocks or regular radio emitters [10–12]. They emit photons in a narrow angular beam, similar to that from a lighthouse. This lighthouse effect results from the misalignment between the rotation and magnetization axes and leads to a secular loss of rotational energy with a corresponding slow decrease of the pulsar rotation frequency Ω. Remarkably, it has been observed that the rotation frequency of the pulsars occasionally shows anomalous jumps—called "glitches"—in the form of an abrupt speedup of the pulsar rotation followed by a slow relaxation close to its original value. It is precisely the observations of such pulsar glitches that have provided the first evidence of superfluidity in neutron-star interiors.

This surprising observation suggests that the interiors of neutron stars are indeed made up of several components and that one among them is irrotational or at least weakly coupled to the rigid rotation of pulsars. Natural candidates are superfluids and supersolids, respectively. In this scenario, quantized vortices, forming in the superfluid component, can stochastically unpin from the rigid crystalline component and change the star's angular momentum. Understanding whether this is a plausible mechanism requires addressing several key questions, including: how do superfluid vortices pin and unpin? How do unpinned vortices percolate through the crystalline structure? What information can be extracted from the glitch signal shape?

Tackling these questions from first principles is challenging, as the properties of the inner crust of neutron stars are model dependent. Moreover, we have only observational access to the neutron-star atmosphere; thus, the underlying dynamics are basically a black box. One possible way to improve our understanding of pulsar glitches is to reproduce them in a controllable laboratory, where we have full access to the entire system [13–15].

Thanks to rapid developments in quantum simulation, it is now possible to employ dipolar quantum gases—where

supersolidity and rotational physics have recently been observed in circularly symmetric systems [16–19]—as analogous microscopic quantum systems. Here, we demonstrate exactly this and predict the existence of glitches in a rotating ultracold dipolar supersolid. We show how quantized vortices unpin from the crystalline structure of the supersolid and escape, transferring angular momentum. Varying the interactions, we observe that the glitch size may depend not only on the number of unpinned vortices, but also on the superfluid fraction and the supersolid internal dynamics.

We start by outlining some basic properties of neutron stars, and then we move to show the analogies with dipolar supersolids. Neutron stars are expected to possess a complex internal structure with a sequence of layers [4,20–26], as shown in Fig. 1(a). Beneath a micrometer-thick atmosphere, the first layer, the so-called outer crust, is expected to be a crystalline solid of neutron-rich ions and electrons that behave as a normal component. At its heart, the core of the neutron star is instead believed to be in a liquidlike phase with superfluid properties [27–32]. Here, the density exceeds the nuclear saturation density ρ_{sat}, meaning that the nucleons are so closely packed that they overlap [33]. Sandwiched between the solid outer crust and the superfluid core, one finds the inner crust: Here, the density of neutrons exceeds the neutron drip density ρ_d so that it becomes energetically favorable for them to drip out. The most accredited theories describe this phase in terms of unbound superfluid neutron pairs with a periodic density modulation; see Figs. 1(a_1) and 1(a_2) and Ref. [36]. The coexistence of solid and superfluid in the inner crust can be viewed in modern terms as a supersolid phase. This, as we shall see, is a key ingredient for the widely accepted physical explanation of glitches, schematically depicted in Fig. 1(b), associated with a transfer of angular momentum between the inner and the outer crust [12,57–61].

In the low-energy sector, quantum phases with supersolid properties have recently been observed in various settings [16,17,62–66]. Particularly relevant for drawing analogies with neutron stars is the case of circular supersolids of dipolar atoms [17], on which we specifically concentrate in this work, as shown in Figs. 1(c) and 1(d). These systems are obtained by trapping and cooling highly magnetic atoms, like erbium or dysprosium, into quantum degenerate states known as dipolar Bose-Einstein condensates (BECs) [67,68]. The dipolar supersolid phase exists due to the competition of three types of interactions: a repulsive isotropic contact interaction, a momentum-dependent long-range and anisotropic dipole-dipole interaction, and a repulsive higher-order-density interaction arising from quantum fluctuations [69]. Supersolids are characterized by the existence of a superfluid connection between the crystal sites, controlled, in turn, by the strength of the short-range interactions, governed by the scattering length a_s, which plays the role of the radial depth of the
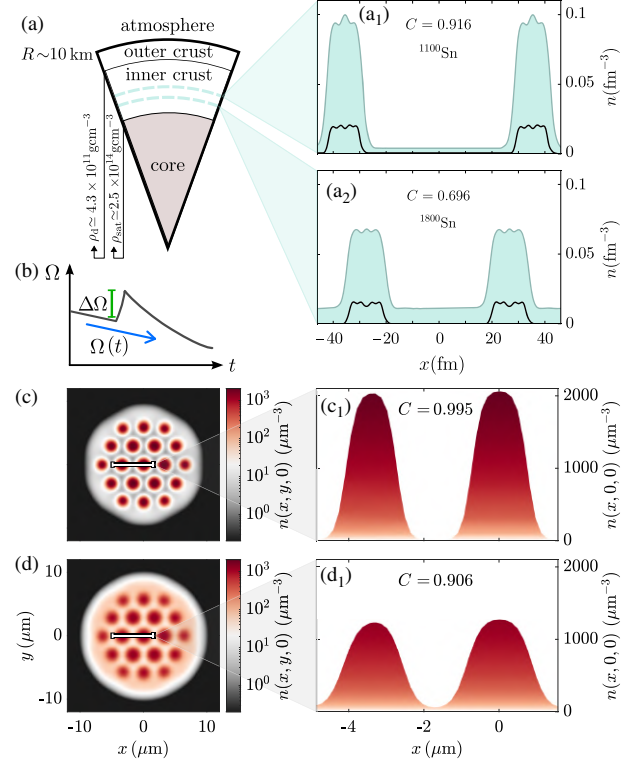

FIG. 1. Comparison between a neutron star and a dipolar supersolid. (a) Structure of a neutron star, together with the density distributions of neutrons (cyan) and protons (black) near the inner-to-outer crust, for baryonic density $n_b \simeq 5.77 \times 10^{-3}$ fm^{-3} (a_1) and the inner crust-to-core interface, for $n_b \simeq 2.08 \times 10^{-2}$ fm^{-3} (a_2) (adapted with permission from Elsevier from [27]). (b) Illustration of a glitch; see the text. (c),(d) Density distribution of a dipolar quantum gas, with the corresponding density n cut along $y = z = 0$ at (c) $a_s = 88a_0$ and (d) $a_s = 93a_0$, where a_0 is the Bohr radius. In both cases, the strength of the superfluid connection is quantified by the density contrast $C = (n_{\text{max}} - n_{\text{min}})/(n_{\text{max}} + n_{\text{min}})$.

neutron star. Figure 1(c_1) shows a case with weak superfluid connection, emulating the condition close to the inner-to-outer crust boundary, whereas Fig. 1(d_1) shows one with stronger superfluid connection, in accordance with the inner crust-to-core boundary.

The remarkable analogy between a pulsar and a dipolar supersolid can be also extended to the rotational dynamics. In both cases, the time evolution of the rotation frequency Ω can be described as [57]

$$I_s \dot{\Omega} = -N_{\text{em}} - \dot{L}_{\text{vort}} - \dot{I}_s \Omega, \qquad (1)$$

where I_s is the moment of inertia of the solid part. For a neutron star, changes in I_s are not directly observable and can be challenging to estimate [6,70–72]. In dipolar supersolids, we have full access to the system; therefore, changes in the moment of inertia due to internal dynamics
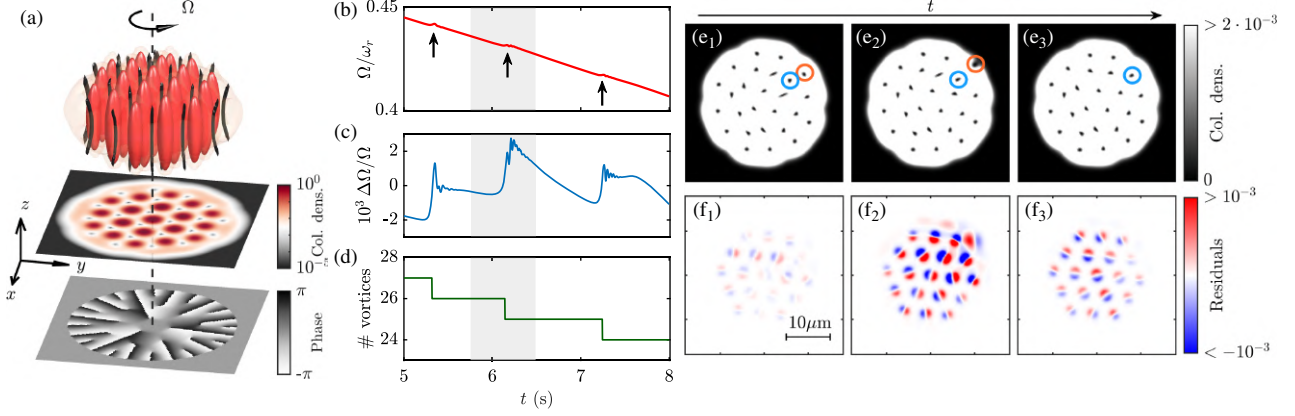
FIG. 2. Glitches in a dipolar supersolid. (a) Rotating supersolid with $\Omega = 0.41\omega_r$ and $a_s = 91a_0$. Top: dipolar supersolid showing two isosurfaces at 15% (opaque) and 0.05% (translucent) of the maximum density, and vortex lines in black. Middle: column densities normalized to the peak density. Bottom: phase profile $\arg[\Psi(x, y, z = 0)]$. (b) Rotation frequency in time, with torque $N_{em} = 4.3 \times 10^{-35}$ kg m^2/s^2. Arrows indicate glitch positions. (c) Relative change in Ω, computed as $\Delta\Omega = [\Omega(t) - \Omega_{lin}]/\Omega_{lin}$, where Ω_{lin} is the result of a linear fit of the curve in (b). (d) Vortex number. The gray shaded area in (b)–(d) highlights the time window in (e) and (f). (e) Column density saturated to highlight vortex positions and shape, with one vortex escaping (orange circle) and another taking its place (blue circle). (f) Crystal excitations, showing the column density differences between time steps, $n(t) - n(t - \Delta t)$, with $\Delta t = 2.4$ ms.

can be accurately accounted for. The quantity N_{em} is a spin-down torque that linearly reduces the total angular momentum of the star: This process occurs spontaneously in a pulsar due to the emission of electromagnetic radiation, whereas in a dipolar supersolid it can be controlled by slowly ramping down the rotation frequency of the trap. Finally, L_{vort} is the angular momentum of the superfluid part.

Despite its simplicity, Eq. (1) is able to capture very intriguing dynamics in pulsars. While the crystalline part in the inner and outer crust rigidly corotates and promptly responds to the braking torque, the superfluid component in the inner crust lags behind, storing angular momentum in the form of quantized vortices. Such vortices are mainly pinned in the interstitial regions, with a pinning force that depends on the depth of the superfluid nuclear background [4,6,27–32,73]. However, during the spin-down of the star, some vortices can stochastically unpin and escape from the inner crust, causing a sudden release of angular momentum. This is captured by the L_{vort} term in Eq. (1), which adds a positive contribution to $\dot{\Omega}$ whenever a vortex leaves. A glitch corresponds to a collective unpinning of vortices [74,75]. The outer crust absorbs the released macroscopic angular momentum and suddenly spins up in a steplike fashion, before relaxing and resuming its spin-down behavior; see Fig. 1(b). The glitches bring a fractional change of the rotation frequency in the range $\Delta\Omega/\Omega \sim 10^{-12} - 10^{-3}$ [76].

The question now is whether we can validate the above phenomenological description and observe glitches in a dipolar supersolid. To this end, we numerically study the spin-down of an ultracold polarized dipolar BEC in the supersolid state. The atoms with mass m are harmonically

confined in a three-dimensional pancake-shaped trap, with frequencies $\boldsymbol{\omega} = (\omega_r, \omega_z) = 2\pi \times (50, 130)$ Hz. They interact via the two-body pseudopotential $U(\mathbf{r}) = (4\pi\hbar^2 a_s/m)\delta(\mathbf{r}) + (3\hbar^2 a_{dd}/m)[(1 - 3\cos^2\theta)/|\mathbf{r}|^3]$, with tunable short-ranged interactions controlled by a_s, long-range anisotropic dipole-dipole interactions with effective range given by the dipolar length a_{dd}, and θ as the angle between the polarization axis (z axis) and the vector joining two particles. We fix our study to ^{164}Dy with $a_{dd} = 130.8a_0$. The evolution of the macroscopic wave function $\Psi(\mathbf{r}, t)$ is governed by the dissipative extended Gross-Pitaevskii equation (eGPE) [77–80]

$$i\hbar\frac{\partial\Psi}{\partial t} = (1 - i\gamma)\big[\mathcal{L}[\Psi; a_s, a_{dd}, \boldsymbol{\omega}] - \Omega(t)\hat{L}_z\big]\Psi, \quad (2)$$

where $\mathcal{L}$ is the eGPE operator and we include dissipation through the small parameter $\gamma = 0.05$ to tune the coupling between the system and the rotating trap; see Ref. [36]. The wave function is normalized to the total atom number through $N = \int d^3\mathbf{r}|\Psi|^2 = 3 \times 10^5$. The operator $\hat{L}_z = x\hat{p}_y - y\hat{p}_x$ corresponds to rotation about the z axis and can be used to obtain the total angular momentum $L_{tot} = \langle\hat{L}_z\rangle$. The superfluid angular momentum is obtained from $L_{vort} = L_{tot} - L_s$, with the second term L_s coming from rigid body rotation of the supersolid [81,82] (see Ref. [36]). The initial condition is found in imaginary time, at fixed $\Omega(0) = 0.5\omega_r$, giving a vortex lattice embedded within the supersolid crystal. It has been shown [81–83] that rotating supersolids host quantized vortices pinned at local minima of the supersolid density modulation, as shown in Fig. 2(a), and at saddle points between each pair of droplets [36].

The real-time spin-down of the system is obtained by simultaneously solving Eqs. (1) and (2). After generating the initial conditions, we introduce an external torque. This acts as a brake on the solid component, reducing $\Omega(t)$ over time. Our findings are shown in Fig. 2(b), where we selected an appropriate time interval to show multiple glitch events. Though at first glance the curve appears linear, dominated by N_{em}, there are deviations from this behavior highlighted by arrows, showing the appearance of glitches in a dipolar supersolid. Visualizing instead the relative change of Ω in Fig. 2(c), we see signatures similar to pulsar glitches, with a rapid increase of Ω, followed by a slow relaxation back to linear behavior.

Unlike in pulsars, here we have unprecedented access to the internal dynamics of the dipolar supersolid. Thus, we can identify each glitch as the moment when superfluid vortices unpin and reach the trap boundary [Figs. 2(d) and 2(e)], transferring their angular momenta to the solid component by the feedback mechanism through Eq. (1). Furthermore, by tracking the unpinning and repinning of individual vortices, we are able to determine the origin of the glitch pulse shape. Here, the observed asymmetry is due to the fact that, when internal vortices are unpinned (glitch rise time), it takes some time before they repin (glitch fall time): They slowly move from one pinning site to the other; see Figs. 2(e$_1$)–2(e$_3$) [36]. Since vortex energy minima are separated by saddle points, to go from one pinning site to the other, a vortex must move across one of them [83]. In doing this, the vortex core is squeezed and then uncompressed, producing an effective friction on the movement of the vortex. Thus, the long supersolid postglitch timescale is associated with this slow percolation of vortices across the crystalline structure [36]. As far as we know, this process has never been considered in the description of the pulsar postglitch behavior.

We also have access to crystal dynamics. As a consequence of the vortex activity, the crystalline structure is deformed and excited. This is visible in the residual matter density evolution [Figs. 2(f$_1$)–2(f$_3$)], where, during the glitch, each droplet is slightly deformed and vibrates. Then, during the postglitch, the droplets slowly relax toward a more uniform distribution. These excitations are due to superfluid fluxes inside the droplets and between neighboring droplets by means of the superfluid bath. Typically, we find that strong crystal excitations affect the postglitch signal of Ω, suggesting that we could infer the crystal properties through analysis of the glitch pulse shape.

The typical magnitude of a glitch is $\Delta\Omega/\Omega \sim 10^{-3}$, a giant glitch in the context of pulsars. The glitch jumps can be written as $\Delta\Omega/\Omega \simeq -\Delta L_{vort}/L_{vort}$, as they are dominated by the dispelling of vortices. One may naively expect to estimate ΔL_{vort} as the number of vortices that unpin and reach the boundary multiplied by a quantum of angular momentum $\hbar$. Such an estimate is incorrect, because the
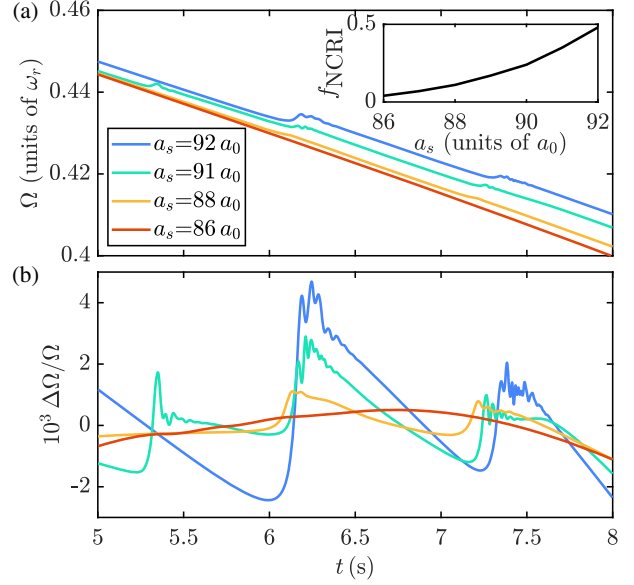

FIG. 3. Glitches originating from different radial depths. (a) Glitches as a function of the scattering length a_s. Note that $a_s = 92a_0$ emulates the conditions close to the inner crust-to-core boundary and $a_s = 86a_0$ for those in the outer crust. Inset: fraction of nonclassical rotational inertia. (b) Relative change in Ω, decreasing amplitude with scattering length. Some glitches dispel more than one vortex, increasing the amplitude.

angular momentum contribution from a vortex is reduced by the fraction of nonclassical moment of inertia f_{NCRI} [36], such that L_{vort} is at most $f_{NCRI}\hbar N_v \leq \hbar N_v$ [82], for the total number of vortices N_v. Furthermore, in our finite-size system, the contribution reduces radially from the rotation axis. The combination of these phenomena is such that the effective amount of angular momentum lost by the superfluid component during a glitch is $\Delta L_{vort} \simeq 10^{-2}\hbar$ [36]. This suggests that, in neutron-star glitches, the number of vortices involved in each glitch might be larger than the one estimated by assuming that each vortex carries a quantum of angular momentum.

A reduction of the vortex angular momentum due to the crystal structure also suggests that glitches in the case of vanishing superfluidity will have a small amplitude. We investigate the dependence of the glitch size on the superfluidity by varying the scattering length, as presented in Fig. 3. As the scattering length is decreased, we find that the glitch amplitude tends to decrease. When the state is in the independent droplet regime ($f_{NCRI} \to 0$), glitches do not occur. The internal dynamics, though, still slightly affect the response of the system to the external torque, as indicated by the curvature of $\Delta\Omega/\Omega$. The largest glitches occur in the states with the biggest superfluid fraction and the largest pinning force between droplets. These results suggest that giant glitches in neutron stars occur from deep within the star, where the superfluid contribution to the angular momentum is largest. However, the total amplitude

is also reflective of the number of unpinned vortices. The large glitch at 6.2 s with $a_s = 92a_0$ occurs when two vortices leave together. A possible identifier to discern the origin of the glitches can arise from the postglitch dynamics, which have the longest decay time at large scattering lengths.

This work represents a first step in simulating and understanding the complex dynamics of neutron stars using rotating quantum gases in the supersolid phase. We show that these systems exhibit phenomena analogous to neutron-star glitches and are primed to become a powerful tool for addressing key open questions ranging from the underlying mechanism of glitches to the system's internal dynamics. In particular, during a supersolid glitch, we observe rich dynamics: Some vortices unpin and escape toward the outer crust and, in doing so, trigger an excitation of the supersolid crystalline structure, as well as core shape deformation of the remaining migrating vortices. These dynamics, which cannot be captured in standard glitch models imposing a fixed lattice structure [70–72], could be the key for an experimental implementation of the model, where the dynamical observation of sudden changes in the droplet positions may be possible by combining optimal control methods with nondestructive imaging [84–86]. Moreover, we see that reducing the superfluidity of the supersolid leads to a reduction of the angular momentum contribution per vortex. This is a feature so far overlooked in the context of neutron stars and may explain the wide range of observed glitch amplitudes, where the smallest glitches are associated with vortex dynamics at the edge of the star.

Regarding the region of the inner crust close to the core, its investigation requires testing various lattice sizes and vortex configurations, allowing us to expand the study to nuclear vortex pinning expected to occur there [87], akin to the work in Ref. [88]. Furthermore, one could consider systems with a radially variable superfluid fraction to mimic the full structure of the neutron star. Our work opens the door for a detailed study of the droplet lattice vibration, in order to ascertain whether it is possible to extract the elastic properties of the solid from the supersolid glitch pulse shape. This would be of great astrophysical interest and would pave the way to extract the elastic properties of nuclear matter from the observed neutron-star glitch pulse shape and to test whether a glitch can trigger superfluid collective excitations [89]. Finally, future work can investigate the effects of tilting the magnetic field with respect to the rotation axis [19,90,91], as expected in pulsars, and include coupling between the supersolid and the proton type-II superconductor present in the crust, through an additional Ginzburg-Landau equation [92–94], introducing a self-consistent feedback mechanism.

[*]To whom correspondence should be addressed: Francesca .Ferlaino@uibk.ac.at

[1] E. Altman *et al.*, Quantum simulators: Architectures and opportunities, PRX Quantum **2,** 017003 (2021).

[2] S. Shapiro and S. Teukolsky, *Black Holes, White Dwarfs, and Neutron Stars: The Physics of Compact Objects*, A Wiley-Interscience Publication (Wiley, New York, 1983), 10.1002/9783527617661.

[3] N. K. Glendenning, *Compact Stars: Nuclear Physics, Particle Physics, and General Relativity* (Springer Verlag, New York, 2000), 10.1007/978-1-4684-0491-3.

[4] P. Haensel, A. Y. Potekhin, and D. G. Yakovlev, *Neutron Stars 1: Equation of State and Structure* (Springer, New York, 2007), Vol. 326, 10.1007/978-0-387-47301-7.

[5] A. Migdal, Superfluidity and the moments of inertia of nuclei, Nucl. Phys. **13,** 655 (1959).

[6] B. Haskell and A. Sedrakian, Superfluidity and superconductivity in neutron stars, Astrophysics and Space Science Library **457,** 401 (2018).

[7] A. Hewish, S. J. Bell, J. D. Pilkington, P. Frederick Scott, and R. A. Collins, Observation of a rapidly pulsating radio source, Nature (London) **217,** 709 (1968).

[8] T. Gold, Rotating neutron stars as the origin of the pulsating radio sources, Nature (London) **218,** 731 (1968).

[9] R. N. Manchester, G. B. Hobbs, A. Teoh, and M. Hobbs, The australia telescope national facility pulsar catalogue, Astron. J. **129,** 1993 (2005).

[10] O. Hamil, J. R. Stone, M. Urbanec, and G. Urbancová, Braking index of isolated pulsars, Phys. Rev. D **91,** 063007 (2015).

[11] V. M. Kaspi and M. Kramer, Radio pulsars: The neutron star population & fundamental physics, in *Proceedings of the 26th Solvay Conference on Physics: Astrophysics and Cosmology* (2016); arXiv:1602.07738.

[12] S. Zhou, E. Gügercinoğlu, J. Yuan, M. Ge, and C. Yu, Pulsar glitches: A review, Universe **8,** 641 (2022).

[13] D. Tsakadze, S. D. Tsakadze *et al.*, Measurement of the relaxation time on acceleration of vessels with helium II and superfluidity in pulsars, Sov. Phys.-JETP **37,** 918 (1973), http://jetp.ras.ru/cgi-bin/dn/e_037_05_0918.pdf.

[14] J. Tsakadze and S. Tsakadze, Properties of slowly rotating helium II and the superfluidity of pulsars, J. Low Temp. Phys. **39**, 649 (1980).

[15] V. Graber, N. Andersson, and M. Hogg, Neutron stars in the laboratory, Int. J. Mod. Phys. D **26**, 1730015 (2017).

[16] M. A. Norcia, C. Politi, L. Klaus, E. Poli, M. Sohmen, M. J. Mark, R. N. Bisset, L. Santos, and F. Ferlaino, Two-dimensional supersolidity in a dipolar quantum gas, Nature (London) **596**, 357 (2021).

[17] T. Bland, E. Poli, C. Politi, L. Klaus, M. A. Norcia, F. Ferlaino, L. Santos, and R. N. Bisset, Two-dimensional supersolid formation in dipolar condensates, Phys. Rev. Lett. **128**, 195302 (2022).

[18] M. A. Norcia, E. Poli, C. Politi, L. Klaus, T. Bland, M. J. Mark, L. Santos, R. N. Bisset, and F. Ferlaino, Can angular oscillations probe superfluidity in dipolar supersolids?, Phys. Rev. Lett. **129**, 040403 (2022).

[19] L. Klaus, T. Bland, E. Poli, C. Politi, G. Lamporesi, E. Casotti, R. N. Bisset, M. J. Mark, and F. Ferlaino, Observation of vortices and vortex stripes in a dipolar condensate, Nat. Phys. **18**, 1453 (2022).

[20] P. Haensel and B. Pichon, Experimental nuclear masses and the ground state of cold dense matter, Astron. Astrophys. **283**, 313 (1994).

[21] J. M. Lattimer and M. Prakash, Neutron star structure and the equation of state, Astrophys. J. **550**, 426 (2001).

[22] F. Douchin and P. Haensel, A unified equation of state of dense matter and neutron star structure, Astron. Astrophys. **380**, 151 (2001).

[23] A. Y. Potekhin, A. F. Fantina, N. Chamel, J. M. Pearson, and S. Goriely, Analytical representations of unified equations of state for neutron-star matter, Astron. Astrophys. **560**, A48 (2013).

[24] B. K. Sharma, M. Centelles, X. Viñas, M. Baldo, and G. F. Burgio, Unified equation of state for neutron stars on a microscopic basis, Astron. Astrophys. **584**, A103 (2015).

[25] D. Blaschke and N. Chamel, Phases of dense matter in compact stars, Astrophysics and Space Science Library **457**, 337 (2018).

[26] G. Fiorella Burgio and A. F. Fantina, Nuclear equation of state for compact stars and supernovae, Astrophysics and Space Science Library **457**, 255 (2018).

[27] J. W. Negele and D. Vautherin, Neutron star matter at subnuclear densities, Nucl. Phys. **A207**, 298 (1973).

[28] T. Maruyama, T. Tatsumi, D. N. Voskresensky, T. Tanigawa, and S. Chiba, Nuclear, pasta structures and the charge screening effect, Phys. Rev. C **72**, 015802 (2005).

[29] P. Gögelein and H. Müther, Nuclear matter in the crust of neutron stars, Phys. Rev. C **76**, 024312 (2007).

[30] W. G. Newton and J. R. Stone, Modeling nuclear "pasta" and the transition to uniform nuclear matter with the 3d skyrme-hartree-fock method at finite temperature: Core-collapse supernovae, Phys. Rev. C **79**, 055801 (2009).

[31] F. Grill, J. Margueron, and N. Sandulescu, Cluster structure of the inner crust of neutron stars in the Hartree-Fock-Bogoliubov approach, Phys. Rev. C **84**, 065801 (2011).

[32] J. M. Pearson, N. Chamel, S. Goriely, and C. Ducoin, Inner crust of neutron stars with mass-fitted skyrme functionals, Phys. Rev. C **85**, 065803 (2012).

[33] The actual composition of the core is unknown: It is believed to be made of about 90% of neutrons and 10% of protons and electrons, but also muons or other baryons, like Δ or Σ, may be present, as well as deconfined quark matter [34,35].

[34] M. G. Alford, A. Schmitt, K. Rajagopal, and T. Schafer, Color superconductivity in dense quark matter, Rev. Mod. Phys. **80**, 1455 (2008).

[35] R. Anglani, R. Casalbuoni, M. Ciminale, N. Ippolito, R. Gatto, M. Mannarelli, and M. Ruggieri, Crystalline color superconductors, Rev. Mod. Phys. **86**, 509 (2014).

[36] See Supplemental Material at http://link.aps.org/supplemental/10.1103/PhysRevLett.131.223401 for further details on supersolidity in neutron stars, the eGPE simulations, derivation of the glitch model, discussion on the pinning force, analysis on varying the model parameters N_{em}, γ, and the initial rotation frequency, and Supplemental videos for the data in Figs. 2 and 3. This includes additional Refs. [37–56].

[37] N. Chamel and P. Haensel, Physics of neutron star crusts, Living Rev. Relativity **11**, 10 (2008).

[38] J. A. Sauls, Superfluidity in the interiors of neutron stars in *Timing Neutron Stars. NATO ASI Series*, edited by H. Ögelman, E. P. J. van den Heuvel (Springer, Dordrecht, 1989), Vol. 262, 10.1007/978-94-009-2273-0_43.

[39] M. Baldo, U. Lombardo, E. E. Saperstein, and S. V. Tolokonnikov, The role of superfluidity in the structure of the neutron star inner crust, Nucl. Phys. **A750**, 409 (2005).

[40] N. Sandulescu, N. Van Giai, and R. J. Liotta, Superfluid properties of the inner crust of neutron stars, Phys. Rev. C **69**, 045802 (2004).

[41] H. S. Than, E. Khan, and N. Van Giai, Wigner-Seitz cells in neutron star crust with finite range interactions, J. Phys. G **38**, 025201 (2011).

[42] E. Khan, N. Sandulescu, and N. Van Giai, Collective excitations in the inner crust of neutron stars: Supergiant resonances, Phys. Rev. C **71**, 042801(R) (2005).

[43] T. D. Lee, K. Huang, and C. N. Yang, Eigenvalues and eigenfunctions of a Bose system of hard spheres and its low-temperature properties, Phys. Rev. **106**, 1135 (1957).

[44] S. Ronen, D. C. E. Bortolotti, D. Blume, and J. L. Bohn, Dipolar Bose-Einstein condensates with dipole-dependent scattering length, Phys. Rev. A **74**, 033611 (2006).

[45] W. Bao and H. Wang, An efficient and spectrally accurate numerical method for computing dynamics of rotating Bose–Einstein condensates, J. Comput. Phys. **217**, 612 (2006).

[46] A. M. Martin, N. G. Marchant, D. H. J. O'Dell, and N. G. Parker, Vortices and vortex lattices in quantum ferrofluids, J. Phys. Condens. Matter **29**, 103004 (2017).

[47] A. S. Bradley and B. P. Anderson, Energy spectra of vortex distributions in two-dimensional quantum turbulence, Phys. Rev. X **2**, 041001 (2012).

[48] S. M. Roccuzzo and F. Ancilotto, Supersolid behavior of a dipolar Bose-Einstein condensate confined in a tube, Phys. Rev. A **99**, 041601(R) (2019).

[49] A. Cidrim, F. E. A. dos Santos, E. A. L. Henn, and T. Macrì, Vortices in self-bound dipolar droplets, Phys. Rev. A **98**, 023618 (2018).

[50] A.-C. Lee, D. Baillie, R. N. Bisset, and P. B. Blakie, Excitations of a vortex line in an elongated dipolar condensate, Phys. Rev. A **98**, 063620 (2018).

[51] A.-C. Lee, D. Baillie, and P. B. Blakie, Numerical calculation of dipolar-quantum-droplet stationary states, Phys. Rev. Res. **3**, 013283 (2021).

[52] A. J. Leggett, Can a solid be "superfluid"?, Phys. Rev. Lett. **25**, 1543 (1970).

[53] P. B. Jones, The origin of pulsar glitches, Mon. Not. R. Astron. Soc. **296**, 217 (1998).

[54] M. Mannarelli, K. Rajagopal, and R. Sharma, The rigidity of crystalline color superconducting quark matter, Phys. Rev. D **76**, 074026 (2007).

[55] A. R. P. Lima and A. Pelster, Quantum fluctuations in dipolar Bose gases, Phys. Rev. A **84**, 041604(R) (2011).

[56] R. Schützhold, M. Uhlmann, Y. Xu, and U. R. Fischer, Mean-field expansion in Bose-Einstein condensates with finite-range interactions, Int. J. Mod. Phys. B **20**, 3555 (2006).

[57] G. Baym, C. Pethick, D. Pines, and M. Ruderman, Spin up in neutron stars: The future of the vela pulsar, Nature (London) **224**, 872 (1969).

[58] M. Ruderman, Pulsars: Structure and dynamics, Annu. Rev. Astron. Astrophys. **10**, 427 (1972).

[59] D. Pines, Neutron stars as cosmic hadron physics laboratories: What glitches teach us, in *Neutron Stars: Theory and Observation*, edited by J. Ventura and D. Pines (Springer Netherlands, Dordrecht, 1991), pp. 57–70, 10.1007/978-94-011-3536-8_5.

[60] B. Haskell and A. Melatos, Models of pulsar glitches, Int. J. Mod. Phys. D **24**, 1530008 (2015).

[61] B. Link, R. I. Epstein, and J. M. Lattimer, Pulsar constraints on neutron star structure and equation of state, Phys. Rev. Lett. **83**, 3362 (1999).

[62] J.-R. Li, J. Lee, W. Huang, S. Burchesky, B. Shteynas, F. Ç. Top, A. O. Jamison, and W. Ketterle, A stripe phase with supersolid properties in spin–orbit-coupled Bose–Einstein condensates, Nature (London) **543**, 91 (2017).

[63] J. Léonard, A. Morales, P. Zupancic, T. Esslinger, and T. Donner, Supersolid formation in a quantum gas breaking a continuous translational symmetry, Nature (London) **543**, 87 (2017).

[64] F. Böttcher, J.-N. Schmidt, M. Wenzel, J. Hertkorn, M. Guo, T. Langen, and T. Pfau, Transient supersolid properties in an array of dipolar quantum droplets, Phys. Rev. X **9**, 011051 (2019).

[65] L. Tanzi, E. Lucioni, F. Famà, J. Catani, A. Fioretti, C. Gabbanini, R. N. Bisset, L. Santos, and G. Modugno, Observation of a dipolar quantum gas with metastable supersolid properties, Phys. Rev. Lett. **122**, 130405 (2019).

[66] L. Chomaz, D. Petter, P. Ilzhöfer, G. Natale, A. Trautmann, C. Politi, G. Durastante, R. M. W. van Bijnen, A. Patscheider, M. Sohmen, M. J. Mark, and F. Ferlaino, Long-lived and transient supersolid behaviors in dipolar quantum gases, Phys. Rev. X **9**, 021012 (2019).

[67] M. Lu, N. Q. Burdick, S. H. Youn, and B. L. Lev, Strongly dipolar Bose-Einstein condensate of dysprosium, Phys. Rev. Lett. **107**, 190401 (2011).

[68] K. Aikawa, A. Frisch, M. Mark, S. Baier, A. Rietzler, R. Grimm, and F. Ferlaino, Bose-Einstein condensation of erbium, Phys. Rev. Lett. **108**, 210401 (2012).

[69] L. Chomaz, I. Ferrier-Barbut, F. Ferlaino, B. Laburthe-Tolra, B. L. Lev, and T. Pfau, Dipolar physics: A review of experiments with magnetic quantum gases, Rep. Prog. Phys. **86**, 026401 (2022).

[70] L. Warszawski and A. Melatos, Gross-Pitaevskii model of pulsar glitches, Mon. Not. R. Astron. Soc. **415**, 1611 (2011).

[71] L. Warszawski, A. Melatos, and N. G. Berloff, Unpinning triggers for superfluid vortex avalanches, Phys. Rev. B **85**, 104503 (2012).

[72] L. Warszawski and A. Melatos, Knock-on processes in superfluid vortex avalanches and pulsar glitch statistics, Mon. Not. R. Astron. Soc. **428**, 1911 (2013).

[73] P. W. Anderson and N. Itoh, Pulsar glitches and restlessness as a hard superfluidity phenomenon, Nature (London) **256**, 25 (1975).

[74] A. Melatos, C. Peralta, and J. S. B. Wyithe, Avalanche dynamics of radio pulsar glitches, Astrophys. J. **672**, 1103 (2008).

[75] P. M. Pizzochero, Angular momentum transfer in vela-like pulsar glitches, Astrophys. J. Lett. **743**, L20 (2011).

[76] C. M. Espinoza, A. G. Lyne, B. W. Stappers, and M. Kramer, A study of 315 glitches in the rotation of 102 pulsars, Mon. Not. R. Astron. Soc. **414**, 1679 (2011).

[77] F. Wächtler and L. Santos, Quantum filaments in dipolar Bose-Einstein condensates, Phys. Rev. A **93**, 061603(R) (2016).

[78] R. N. Bisset, R. M. Wilson, D. Baillie, and P. B. Blakie, Ground-state phase diagram of a dipolar condensate with quantum fluctuations, Phys. Rev. A **94**, 033619 (2016).

[79] I. Ferrier-Barbut, H. Kadau, M. Schmitt, M. Wenzel, and T. Pfau, Observation of quantum droplets in a strongly dipolar Bose gas, Phys. Rev. Lett. **116**, 215301 (2016).

[80] L. Chomaz, S. Baier, D. Petter, M. J. Mark, F. Wächtler, L. Santos, and F. Ferlaino, Quantum-fluctuation-driven crossover from a dilute Bose-Einstein condensate to a macrodroplet in a dipolar quantum fluid, Phys. Rev. X **6**, 041039 (2016).

[81] S. M. Roccuzzo, A. Gallemí, A. Recati, and S. Stringari, Rotating a supersolid dipolar gas, Phys. Rev. Lett. **124**, 045702 (2020).

[82] A. Gallemí, S. M. Roccuzzo, S. Stringari, and A. Recati, Quantized vortices in dipolar supersolid Bose-Einstein-condensed gases, Phys. Rev. A **102**, 023322 (2020).

[83] F. Ancilotto, M. Barranco, M. Pi, and L. Reatto, Vortex properties in the extended supersolid phase of dipolar Bose-Einstein condensates, Phys. Rev. A **103**, 033314 (2021).

[84] S. van Frank, M. Bonneau, J. Schmiedmayer, S. Hild, C. Gross, M. Cheneau, I. Bloch, T. Pichler, A. Negretti,

T. Calarco *et al.*, Optimal control of complex atomic quantum systems, Sci. Rep. **6**, 34187 (2016).

[85] D. Freilich, D. Bianchi, A. Kaufman, T. Langin, and D. Hall, Real-time dynamics of single vortex lines and vortex dipoles in a Bose-Einstein condensate, Science **329**, 1182 (2010).

[86] M. Gajdacz, P. L. Pedersen, T. Mørch, A. J. Hilliard, J. Arlt, and J. F. Sherson, Non-destructive faraday imaging of dynamically controlled ultracold atoms, Rev. Sci. Instrum. **84**, 083105 (2013).

[87] B. K. Link and R. I. Epstein, Mechanics and energetics of vortex unpinning in neutron stars, Astrophys. J. **373**, 592 (1991).

[88] A. Gallemí and L. Santos, Superfluid properties of a honeycomb dipolar supersolid, Phys. Rev. A **106**, 063301 (2022).

[89] N. Andersson, D. Antonopoulou, C. M. Espinoza, B. Haskell, and W. C. G. Ho, The enigmatic spin evolution of psr j0537–6910: r-modes, gravitational waves, and the case for continued timing, Astrophys. J. **864**, 137 (2018).

[90] S. B. Prasad, T. Bland, B. C. Mulkerin, N. G. Parker, and A. M. Martin, Vortex lattice formation in dipolar Bose-Einstein condensates via rotation of the polarization, Phys. Rev. A **100**, 023625 (2019).

[91] T. Bland, G. Lamporesi, M. J. Mark, and F. Ferlaino, Vortices in dipolar Bose-Einstein condensates, Comptes Rendus. Physique 1.

[92] L. Drummond and A. Melatos, Stability of interlinked neutron vortex and proton flux tube arrays in a neutron star: Equilibrium configurations, Mon. Not. R. Astron. Soc. **472**, 4851 (2017).

[93] L. Drummond and A. Melatos, Stability of interlinked neutron vortex and proton flux-tube arrays in a neutron star–II. Far-from-equilibrium dynamics, Mon. Not. R. Astron. Soc. **475**, 910 (2018).

[94] K. Thong, A. Melatos, and L. Drummond, Stability of interlinked neutron vortex and proton flux-tube arrays in a neutron star–III. Proton feedback, Mon. Not. R. Astron. Soc. **521**, 5724 (2023).

Supplemental material: Glitches in rotating supersolids

Elena Poli[1], Thomas Bland[1], Samuel J. M. White[2,1], Manfred J. Mark[1,2], and Francesca Ferlaino[1,2]

[1]*Universität Innsbruck, Fakultät für Mathematik, Informatik und Physik, Institut für Experimentalphysik, 6020 Innsbruck, Austria*

[2]*Institut für Quantenoptik und Quanteninformation, Österreichische Akademie der Wissenschaften, 6020 Innsbruck, Austria*

Silvia Trabucco[3,4] and Massimo Mannarelli[3]

[3]*INFN, Laboratori Nazionali del Gran Sasso, 67100 Assergi (AQ), Italy*

[4]*Gran Sasso Science Institute, 67100 L'Aquila, Italy*

SUPERSOLIDITY IN NEUTRON STARS

Nuclear matter in the interior of neutron stars is expected to be in a superfluid state [1–3]. In the outer crust of a neutron star, neutrons and protons form well-defined neutron-rich nuclides. When approaching the interface between the inner crust and the outer crust, the neutron density inside these nuclides increases, the proton population is strongly suppressed and pairing effects between neutrons become sizable. The attractive s-wave interaction combined with the relatively low temperature may favor the formation of a superfluid state, resulting in a lattice comprised of clusters of superfluid neutrons. In the inner crust, corresponding to densities between the neutron drip density $\rho \simeq 4.3 \times 10^{11}$ g cm^{-3} and around the saturation density $\rho \simeq 2.8 \times 10^{14}$ g cm^{-3}, superfluidity leads to interesting effects. Here, nuclear matter consists of connected clumps of approximately one thousand superfluid neutrons and comparatively few protons, surrounded by dripped neutrons forming a "neutron sea". At such extreme densities, well-defined nuclides do not exist anymore: the clumps of nuclear matter are sometimes referred to in literature as "nuclear-type clusters" to emphasize the difference with standard nuclides [4]. Nevertheless, it is customary to associate these clumps with nuclides using their estimated proton number. As shown in Fig. 1(a_1)-(a_2) of the main text, the fraction of dripped neutrons increases with the radial depth (and so, with the density), whilst the overall neutron distribution remains modulated with the periodicity of a crystalline structure. This crystalline structure disappears close to the boundary between the inner crust and the core, where the system becomes homogeneous.

The first calculations of the matter distribution in the inner crust were performed in the Hartree-Fock (HF) approximation, assuming a set of a few non-interacting cells immersed in a sea of neutrons. This distinction was made for numerical reasons and it completely neglected neutron pairing. However, pair correlations play a substantial role in the inner crust [5]. For these reasons, more recent approaches improved the HF calculations using a self-consistent Hartree-Fock-Bogoliubov (HFB) method, combining the HF method with BCS pairing, see for instance [6]. Pair correlations can also be taken into account also using other different approaches, for example the energy functional method developed in Ref. [4].

In the aforementioned works, the density of neutron pairs is found to be modulated within the Wigner-Seitz (WS) cell. In fact, pairing effects are smaller in the low-density region (corresponding to the neutron sea) and more relevant in the high-density region (corresponding to the "nuclides", i.e. the "solid part"). Thus, in the "solid part", the pairing and superfluid effects are stronger than in the neutron sea part, because of the higher density. In the context of a local density approximation, the pairing field is shown to be a continuous function of position in the whole WS cell [6], supporting the fact that the whole system is superfluid. These results are in agreement with the numerical observation of excitations in the inner crust, where the appearance of new resonances is due to the collective ("nuclides" + neutron sea) behavior of the system [7]. All these works confirm the idea that the "solid phase" and the "superfluid phase" are not distinct and, thus, that the system is in a supersolid phase.

FORMALISM

We present here a detailed description of the equation governing the dynamics of an ultracold dipolar Bose-Einstein condensate (BEC) of ^{164}Dy atoms. Having a large intrinsic magnetic moment, these atoms interact via a long-range and anisotropic dipole-dipole interaction (DDI). In the presence of an external magnetic field, the dipolar contribution to the interaction pseudopotential between two atoms reads

$$V_{\mathrm{DDI}}(\mathbf{r}) = \frac{\mu_0 \mu_m^2}{4\pi} \frac{1 - 3\cos^2\theta}{|\mathbf{r}|^3}, \qquad (S1)$$

where μ_m is the magnetic moment of the atoms, μ_0 is the vacuum permeability and θ is the angle between the vector joining the two atoms, $\mathbf{r}$, and the polarization axis. The typical length scale of the DDI is

$a_{\rm dd} = \mu_0 \mu_m^2 m / 12\pi\hbar^2$, where m is the atomic mass and $\hbar$ is the reduced Planck's constant. In addition to the DDI, magnetic atoms also interact via a short-range contact interaction. This effect is well-approximated by the pseudopotential

$$V_{\rm c}(\mathbf{r}) = \frac{4\pi\hbar^2 a_s}{m} \delta(\mathbf{r}) \,, \qquad (S2)$$

where the scattering length, a_s, is the typical length scale of the contact interatomic force. The ratio between the dipolar and contact length scales defines the parameter $\epsilon_{\rm dd} = a_{\rm dd}/a_s$ that allows us to distinguish systems in a contact-dominated regime, where $\epsilon_{\rm dd} < 1$, from a dipolar-dominated regime, where $\epsilon_{\rm dd} > 1$. In the latter, the system can access the supersolid phase, a paradoxical state of matter that exhibits both superfluid properties and a periodic structure typical of a solid [8]. Indeed, as a result of the competition between energy contributions, it is energetically favorable for the system to develop a spontaneous density modulation on top of the superfluid background. For large values of $\epsilon_{\rm dd}$, the superfluid connection between density peaks vanishes, the global phase coherence disappears, and the system enters the independent droplet regime [8].

The ground state and the real-time dynamics of a dipolar gas can be studied by numerically solving the extended Gross-Pitaevskii equation (eGPE):

$$i\hbar \frac{\partial \Psi}{\partial t} = (\alpha - i\gamma) \left[\mathcal{L}[\Psi; a_s, a_{\rm dd}, \boldsymbol{\omega}] - \Omega(t)\hat{L}_z \right] \Psi \,. \quad (S3)$$

Here, $\Psi(\mathbf{r}, t)$ is the wave function normalized to the total atom number through $N = \int {\rm d}^3\mathbf{r}|\Psi|^2$ and $\Omega(t)$ is the rotation frequency of the trap about the z-axis through the angular momentum operator $\hat{L}_z = x\hat{p}_y - y\hat{p}_x$. The eGPE operator $\mathcal{L}$ is given by

$$\begin{aligned} \mathcal{L}[\Psi; a_s, a_{\rm dd}, \boldsymbol{\omega}] = & -\frac{\hbar^2 \nabla^2}{2m} + \frac{1}{2}m \left[\omega_r^2(x^2 + y^2) + \omega_z^2 z^2 \right] \\ & + \int {\rm d}^3\mathbf{r}' \, U(\mathbf{r} - \mathbf{r}') |\Psi(\mathbf{r}', t)|^2 \\ & + \gamma_{\rm QF} |\Psi(\mathbf{r}, t)|^3 - \mu \,, \end{aligned} \quad (S4)$$

where $\boldsymbol{\omega} = (\omega_r, \omega_z) = 2\pi \times (f_r, f_z)$ are the frequencies of the harmonic confinement with cylindrical symmetry, $U(\mathbf{r}) = V_{\rm c}(\mathbf{r}) + V_{\rm DDI}(\mathbf{r})$ is the total interaction potential, the second to last term is the Lee-Huang-Yang correction [9]–a beyond mean-field contribution that is particularly important if the system is in the supersolid phase, since it is responsible for its stability against collapse [10–13]–given by [14, 15]

$$\gamma_{\rm QF} = \frac{128\hbar^2}{3m} \sqrt{\pi a_s^5} \, {\rm Re} \left\{ \mathcal{Q}_5(\epsilon_{\rm dd}) \right\} \,, \qquad (S5)$$

where $\mathcal{Q}_5(\epsilon_{\rm dd}) = \int_0^1 {\rm d}u \, (1 - \epsilon_{\rm dd} + 3u^2 \epsilon_{\rm dd})^{5/2}$, and finally, μ is the chemical potential. When calculating the dipolar

potential contribution, we use a spherical cutoff to remove the effect of alias copies coming from the numerical Fourier transform [16].

In Eq. (S3) the parameters α and γ determine the type of evolution:

- $\alpha = 0$, $\gamma = 1$: imaginary time evolution, to find the ground state of the system.

- $\alpha = 1$, $\gamma = 0$: real-time evolution, to explore the dynamics.

- $\alpha = 1$, $0 < \gamma < 1$: complex-time evolution, that corresponds to a real-time evolution with dissipation.

For the purpose of this work, we use imaginary time evolution to generate the initial condition and dissipative real-time evolution for the study of glitch dynamics. In both cases, we employ a split-step method modified to account for rotation, known as the alternate direction implicit-time splitting pseudospectral (ADI-TSSP) method [17], for numerically solving the eGPE. Since the harmonic trap is cylindrically symmetric, the dissipation parameter γ is used to impart a rotation to the system, otherwise the angular momentum along the z–axis would be conserved during the real-time spin-down evolution.

In addition to the aforementioned method, there are alternative ways to induce rotation in a dipolar supersolid. These include confining the system within an asymmetric trap in the xy plane or utilizing magnetostirring techniques [18–21].

VORTEX PINNING AND DYNAMICS

Rotating dipolar supersolids host quantized vortices that are pinned in the interstitial low density regions between the droplets. To get a general idea of the pinning energy, we compute the energy cost to imprint a vortex in a specific position (x_0, y_0) of the ground state wavefunction $\Psi_0(\mathbf{r})$ for a non-rotating supersolid. With this aim, we multiply $\Psi_0(\mathbf{r})$ by the ansatz wave function $\Phi_v(x, y, x_0, y_0)$ for a vortex density and phase profile centered at (x_0, y_0), given by

$$\Phi_v(x, y, x_0, y_0) = \frac{\sqrt{(x - x_0)^2 + (y - y_0)^2}}{\sqrt{(x - x_0)^2 + (y - y_0)^2 + \Lambda^{-2}}} e^{i\theta} \,, \quad (S6)$$

where $\theta = \arctan(y/x)$ and $\Lambda^{-1} = 1\,\mu{\rm m}$ [22]. We note in a dipolar supersolid the phase profile is not an azimuthal 2π winding, but rather a complex pattern modified by the underlying crystal structure [23], however this simple ansatz recovers the expected force field and stationary points.

We compute the total energy $E(x_0, y_0)$ using the wavefunction $\Psi(x_0, y_0) = \Psi_0 \Phi_v(x_0, y_0)$ (see, e.g., Eq. (1) of
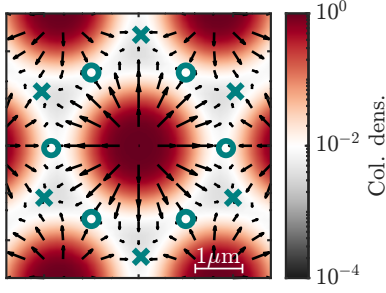
FIG. S1. Pinning force felt by a single vortex in a supersolid. The colorbar shows the normalized column density in the central region of a supersolid. The overlaid arrows indicate the direction and the strength of the force imparted to a single vortex in that position. The crosses correspond to the vortex equilibrium positions, and the circles correspond to saddle points. Parameters: $N = 3 \times 10^5$, $a_s = 90\,a_0$ and trap frequency $\boldsymbol{\omega} = (\omega_r, \omega_z) = 2\pi \times (50, 130)$Hz.

Ref. [24]) for different vortex positions (x_0, y_0), and the corresponding pinning force $\vec{F}(x_0, y_0) = -\nabla E(x_0, y_0)$. The result is shown in Fig. S1. We identify the stable pinning sites – the absolute minima of the energy landscape – and the saddle points. Both of them are in the low density regions between the droplets: the former are located in the interstitial sites of the triangular lattice, the latter are between every pair of droplets.

This estimate of the energy landscape well approximates the force field acting on vortices during the complex time evolution. The external torque N_{em}, see Eq. (S7) and discussion, slowly spins down the dipolar supersolid keeping the position of the droplets almost constant in time in the rotating frame. In the simulation shown in Fig. 2 in the main text, at around 5.3 and 6.2 s, two vortices escape the system, giving rise to two glitches. Together with these fast dynamics, we observe a slow rearrangement of the other vortices undergoing a force field that resembles the one shown in Fig. S1: they can unpin and re-pin from one stable position to another, see Fig. S2. The blue circled vortices rearrange in space, percolating through the crystalline structure, slowly passing through two different saddle points. As a consequence, vortex-cores appear stretched until they both reach new stable positions.

Finally, Figure S1 hints to an unstable maximum at the centre of the droplet. This is expected, as vortices inside droplets are known to be unstable, resulting either in droplet splitting or vortex-line instabilities [25–27]. Conversely, in neutron stars, vortices can be pinned inside nuclei at sufficiently high densities [28]. Furthermore, models considering different scenarios in which the vortices involved are in the core instead of the crust, i.e. without a solid component, have been discussed in other works [29, 30], but are not considered here.
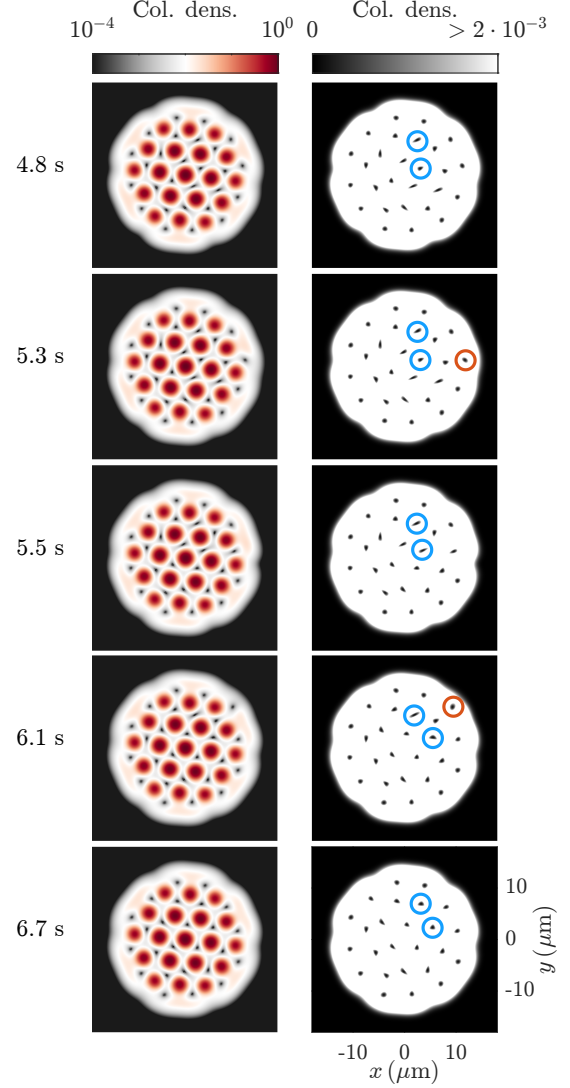
FIG. S2. Vortex dynamics during a glitch. Shown are additional frames of the simulation from Fig. 2 of the main text. Left column: column density normalized to the peak density. Right column: saturated column density, highlighting vortex position and shape before and after glitches. Two vortices (orange circles) escape, while the others (blue circles) rearrange in the lattice.

FEEDBACK MECHANISM

We report here the details on the derivation of the feedback mechanism, Eq. (1) of the main text. During the dynamics, the constant braking torque N_{em} reduces the total angular momentum of the system over time, such that

$$\dot{L}_{\text{tot}}(t) = -N_{\text{em}} , \qquad (S7)$$

where $L_{\text{tot}}(t) = \langle \hat{L}_z \rangle_{\Psi(t)}$ is the expectation value of the angular momentum operator $\hat{L}_z$ computed for the wave

function $\Psi(t)$. Since the system manifests both solid and superfluid properties, we can decompose the total angular momentum as [31, 32]

$$L_{\text{tot}}(t) = L_{\text{s}}(t) + L_{\text{vort}}(t)$$
$$= I_{\text{s}}(t)\Omega(t) + L_{\text{vort}}(t), \qquad (S8)$$

where L_{s} is the angular momentum associated with the crystal rotation, L_{vort} is the angular momentum associated to the superfluid and, thus, stored in the form of vortices. The moment of inertia of the supersolid I_{s} is time-dependent as well, since the mass distribution of the system changes during the slow-down dynamics. After inserting Eq. (S8) into Eq. (S7) and rearranging, we obtain the differential equation for $\Omega(t)$

$$I_{\text{s}}(t)\dot{\Omega}(t) = -N_{\text{em}} - \dot{L}_{\text{vort}}(t) - \dot{I}_{\text{s}}(t)\Omega(t), \qquad (S9)$$

giving Eq. (1) of the main text.

The supersolid moment of inertia is well-defined in the static limit by the definition $I_{\text{s},0} = \lim_{\Omega \to 0} \langle \hat{L}_z \rangle_{\Psi_0}/\Omega$, where Ψ_0 is the ground state wave function of the system for vanishingly small values of Ω [31, 32]. In this limit, it is also pertinent to calculate the rigid body moment of inertia through $I_{\text{rigid},0} = \langle x^2 + y^2 \rangle_{\Psi_0}$. The supersolid and rigid moment of inertia coincide if the system is not superfluid and therefore its density distribution fully responds to the external rotation. For a supersolid, this is not the case: the rotational response of the system is reduced because of the superfluid nature, meaning that $I_{\text{s},0}/I_{\text{rigid},0} < 1$. This lets us define the fraction of non-classical rotational inertia through $f_{\text{NCRI}} = 1 - I_{\text{s},0}/I_{\text{rigid},0}$, which is a quantity closely related to the superfluid fraction [33]. Therefore, assuming a constant f_{NCRI} throughout the simulation, we calculate the time-dependent supersolid moment of inertia through the relation

$$I_{\text{s}}(t) = (1 - f_{\text{NCRI}})I_{\text{rigid}}(t), \qquad (S10)$$

that captures the reduced rotational response of the system and the change in the density distribution at the same time.

In practice, at each time t of the numerical simulation, we compute the total angular momentum $L_{\text{tot}}(t)$ and the rigid moment of inertia $I_{\text{rigid}}(t) = \langle x^2 + y^2 \rangle_{\Psi_t}$. As a next step, we compute the time-dependent supersolid moment of inertia $I_{\text{s}}(t)$ through Eq. (S10), from which we get the solid contribution to the angular momentum $L_{\text{s}}(t) = I_{\text{s}}(t)\Omega(t)$, see Fig. S3(a). Then, the vortex contribution to the angular momentum is $L_{\text{vort}}(t) = L_{\text{tot}}(t) - L_{\text{s}}(t)$, see Fig. S3(b). Notice that L_{tot} reduces linearly with gradient N_{em}, as expected. All the necessary quantities are inserted in Eq. (S9), providing the updated value of Ω used as an input to the eGPE shown in Eq. (S3). When a vortex reaches the boundary, its contribution to L_{vort} drops to zero due to the negligible matter density around
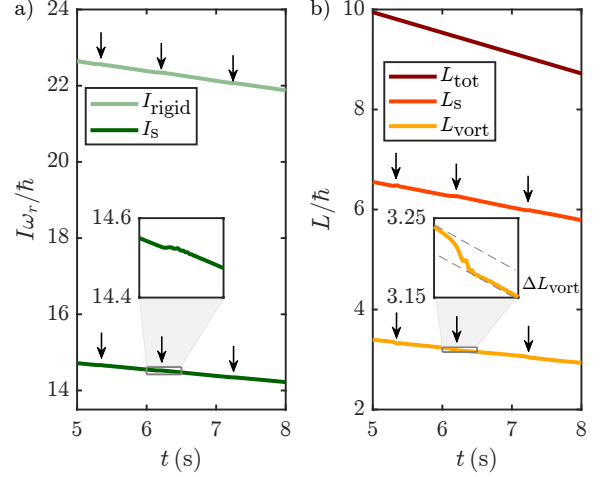

FIG. S3. Moment of inertia and angular momenta during the simulation shown in Fig. 2 of the main text. (a) Rigid moment of inertia I_{rigid} and supersolid moment of inertia I_{s}. (b) Total angular momentum L_{tot} and its two contributions from the decomposition L_{s} and L_{vort} with arrows pointing to glitches. The inset shows a zoom of the jump ΔL_{vort} due to vortices leaving and rearranging during a glitch.

its core, and the linear ramp down of Ω is interrupted by the glitch event. We estimate the glitch size by computing $\Delta\Omega/\Omega = (\Omega(t) - \Omega_{\text{lin}})/\Omega_{\text{lin}}$, i.e. the difference between the observed rotation frequency and the linear fit Ω_{lin} that captures the average global spin-down.

In Fig. S4 we show a particular case in which around $t \sim 2\,\text{s}$ the last two vortices leave the system resulting in the vortex angular momentum contribution L_{vort} dropping to 0, thus validating the decomposition [Fig. S4(c)]. It is worth noting also that the crystal structure for $\Omega = 0$ shown in Fig. S4(a) is unchanged from $\Omega = 0.5\omega_r$, validating our decision to fix f_{NCRI}.

ROBUSTNESS OF THE MODEL

In the Letter, we have presented simulations for different values of a_s, mimicking vortex dynamics for different radial depths in the inner crust of a neutron star. Here, we present additional results at constant $a_s = 91a_0$ with the aim to test the robustness of the model and to identify the appropriate parameter space.

The dynamics of the system for lower rotation frequencies can be studied by setting a smaller value of initial angular velocity Ω_0. The value of Ω_0 primarily influences the number of initial vortices and consequently affects the number of vortices involved in the dynamics during the glitches. For example, only two are present when $\Omega_0 = 0.1\omega_r$ [see Fig. S4(a)]. In addition to the results shown in the main text and Fig. S4, we performed additional simulations setting the initial conditions to $\Omega_0 = 0.2\omega_r, 0.3\omega_r, 0.4\omega_r$ (not shown) observing glitch
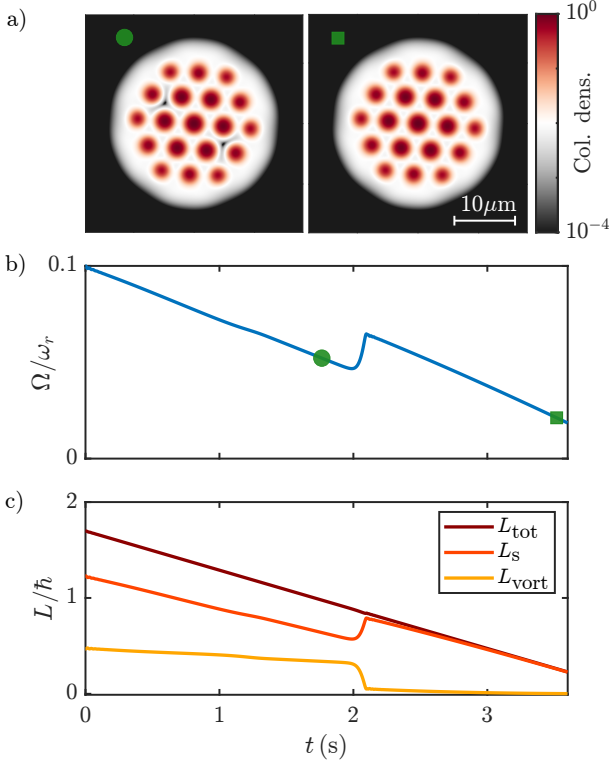
FIG. S4. Glitch for low initial rotation frequency $\Omega_0 = 0.1\omega_r$. (a) Density frames before and after the single glitch. (b) Rotation frequency in time, symbols show the density frames from (a). (c) Angular momentum decomposition: L_{vort} drops to zero when two vortices simultaneously escape.
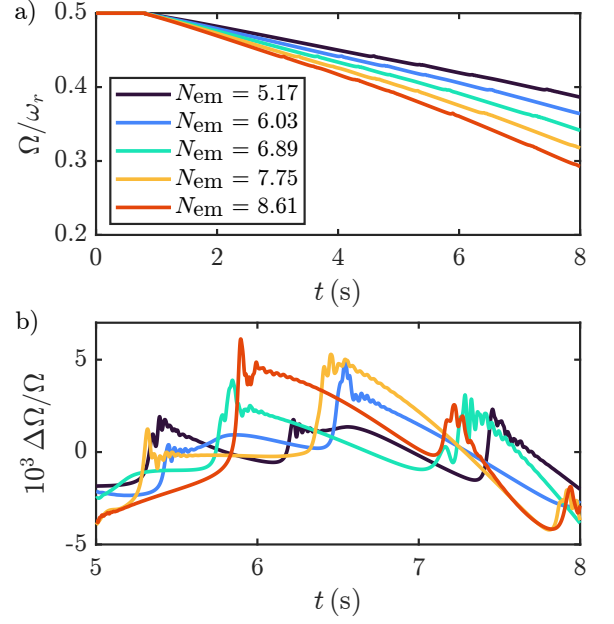

FIG. S5. Simulations for different braking torques N_{em} (units of 10^{-35} kg m^2/s^2). (a) Rotation frequency in time. (b) Relative change in Ω, computed as $\Delta\Omega = (\Omega(t) - \Omega_{lin})/\Omega_{lin}$, where Ω_{lin} is the result of a linear fit of the curves in (a).

events analogous to the ones reported and discussed in this work.

We further discuss how the value of the braking torque N_{em} affects the spin-down dynamics, starting from the same initial condition $\Omega_0 = 0.5\,\omega_r$ and for constant values of the dissipation parameter γ. The results are shown in Fig. S5: the glitches occur approximately at the same values of $\Omega \sim 0.44\,\omega_r, 0.43\,\omega_r, 0.41\,\omega_r, 0.39\,\omega_r, 0.36\,\omega_r$, albeit reached at different times due to the steepness of the ramp-down process dominated by N_{em}. Except for the timescales of glitch events, we do not observe any other significant difference with respect to the simulation showed in Fig. 2 of the main text.

Finally, we present results for different values of γ, the parameter responsible for the coupling between the rotating trap and the supersolid. The results are shown in Fig. S6: we notice that glitches do not always occur at the same time, which is consistent with the fact that the system responds differently to the external torque for varying coupling strengths. Furthermore, γ affects the shape of the curve $\Delta\Omega/\Omega$, see Fig. S6(b): the oscillations typical of the post-glitch phase are damped ($\gamma = 0.1$) or completely absent ($\gamma = 0.5$) as the dissipation becomes more relevant. We notice that for smaller values

($\gamma = 0.02$), post-glitch oscillations slow down the recovery process towards a linear ramp down, and the slow rise and fall feature at $t = 7.2$ s is related to an internal rearrangement of vortices, as opposed to a vortex leaving. These features indicate that there exists a threshold value $\gamma \gtrsim 0.02$ such that the eGPE gives a physical description of the rotating supersolid. This is not a surprising fact: we recall that for $\gamma = 0$ the total angular momentum of the system is conserved for any external torque. This is clearly unphysical behavior. Therefore, there must exist a minimum value of the coupling required to have a realistic evolution of the system.

[1] A. Migdal, Superfluidity and the moments of inertia of nuclei, Nuclear Physics **13**, 655 (1959).

[2] N. Chamel and P. Haensel, Physics of Neutron Star Crusts, Living Rev. Rel. **11**, 10 (2008).

[3] J. A. Sauls, Superfluidity in the interiors of neutron stars, in *Timing Neutron Stars*, edited by H. Ögelman and E. P. J. van den Heuvel (Springer Netherlands, Dordrecht, 1989) pp. 457–490.

[4] M. Baldo, U. Lombardo, E. E. Saperstein, and S. V. Tolokonnikov, The role of superfluidity in the structure of the neutron star inner crust, Nucl. Phys. A **750**, 409 (2005).

[5] N. Sandulescu, N. Van Giai, and R. J. Liotta, Superfluid properties of the inner crust of neutron stars, Phys. Rev. C **69**, 045802 (2004).
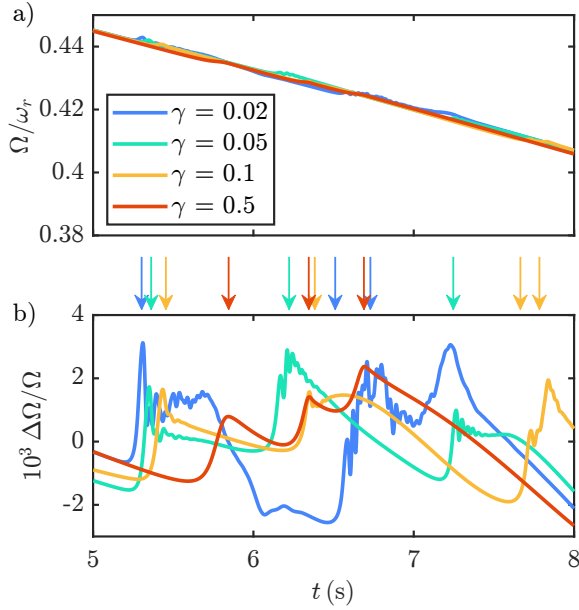
[6] H. S. Than, E. Khan, and N. Van Giai, Wigner-Seitz

FIG. S6. Simulations for different values of γ. (a) Rotation frequency in time, with torque $N_{em} = 4.3 \times 10^{-35} \mathrm{kg\ m^2/s^2}$. (b) Relative change in Ω. The arrows indicate the times in which a vortex is leaving.

cells in neutron star crust with finite range interactions, J. Phys. G **38**, 025201 (2011).

[7] E. Khan, N. Sandulescu, and N. Van Giai, Collective excitations in the inner crust of neutron stars: Supergiant resonances, Phys. Rev. C **71**, 042801 (2005).

[8] L. Chomaz, I. Ferrier-Barbut, F. Ferlaino, B. Laburthe-Tolra, B. L. Lev, and T. Pfau, Dipolar physics: a review of experiments with magnetic quantum gases, Reports on Progress in Physics **86**, 026401 (2022).

[9] T. D. Lee, K. Huang, and C. N. Yang, Eigenvalues and Eigenfunctions of a Bose System of Hard Spheres and Its Low-Temperature Properties, Phys. Rev. **106**, 1135 (1957).

[10] L. Chomaz, S. Baier, D. Petter, M. J. Mark, F. Wächtler, L. Santos, and F. Ferlaino, Quantum-Fluctuation-Driven Crossover from a Dilute Bose-Einstein Condensate to a Macrodroplet in a Dipolar Quantum Fluid, Phys. Rev. X **6**, 041039 (2016).

[11] I. Ferrier-Barbut, H. Kadau, M. Schmitt, M. Wenzel, and T. Pfau, Observation of quantum droplets in a strongly dipolar bose gas, Phys. Rev. Lett. **116**, 215301 (2016).

[12] F. Wächtler and L. Santos, Quantum filaments in dipolar Bose-Einstein condensates, Phys. Rev. A **93**, 061603 (2016).

[13] R. N. Bisset, R. M. Wilson, D. Baillie, and P. B. Blakie, Ground-state phase diagram of a dipolar condensate with quantum fluctuations, Phys. Rev. A **94**, 033619 (2016).

[14] A. R. P. Lima and A. Pelster, Quantum fluctuations in dipolar Bose gases, Phys. Rev. A **84**, 041604 (2011).

[15] R. Schützhold, M. Uhlmann, Y. Xu, and U. R. Fischer, Mean-field expansion in Bose-Einstein condensates with finite-range interactions, International Journal of Modern Physics B **20**, 3555 (2006).

[16] S. Ronen, D. C. E. Bortolotti, D. Blume, and J. L. Bohn, Dipolar Bose-Einstein condensates with dipole-dependent scattering length, Phys. Rev. A **74**, 033611 (2006).

[17] W. Bao and H. Wang, An efficient and spectrally accurate numerical method for computing dynamics of rotating bose–einstein condensates, Journal of Computational Physics **217**, 612 (2006).

[18] A. M. Martin, N. G. Marchant, D. H. J. O'Dell, and N. G. Parker, Vortices and vortex lattices in quantum ferrofluids, Journal of Physics: Condensed Matter **29**, 103004 (2017).

[19] S. B. Prasad, T. Bland, B. C. Mulkerin, N. G. Parker, and A. M. Martin, Vortex lattice formation in dipolar Bose-Einstein condensates via rotation of the polarization, Physical Review A **100**, 023625 (2019).

[20] L. Klaus, T. Bland, E. Poli, C. Politi, G. Lamporesi, E. Casotti, R. N. Bisset, M. J. Mark, and F. Ferlaino, Observation of vortices and vortex stripes in a dipolar condensate, Nature Physics **18**, 1453 (2022).

[21] T. Bland, G. Lamporesi, M. J. Mark, and F. Ferlaino, Vortices in dipolar Bose-Einstein condensates, Comptes Rendus. Physique 10.5802/crphys.160 (2023).

[22] A. S. Bradley and B. P. Anderson, Energy spectra of vortex distributions in two-dimensional quantum turbulence, Phys. Rev. X **2**, 041001 (2012).

[23] F. Ancilotto, M. Barranco, M. Pi, and L. Reatto, Vortex properties in the extended supersolid phase of dipolar Bose-Einstein condensates, Phys. Rev. A **103**, 033314 (2021).

[24] S. M. Roccuzzo and F. Ancilotto, Supersolid behavior of a dipolar Bose-Einstein condensate confined in a tube, Phys. Rev. A **99**, 041601(R) (2019).

[25] A. Cidrim, F. E. A. dos Santos, E. A. L. Henn, and T. Macrì, Vortices in self-bound dipolar droplets, Phys. Rev. A **98**, 023618 (2018).

[26] A.-C. Lee, D. Baillie, R. N. Bisset, and P. B. Blakie, Excitations of a vortex line in an elongated dipolar condensate, Phys. Rev. A **98**, 063620 (2018).

[27] A.-C. Lee, D. Baillie, and P. B. Blakie, Numerical calculation of dipolar-quantum-droplet stationary states, Phys. Rev. Res. **3**, 013283 (2021).

[28] B. K. Link and R. I. Epstein, Mechanics and Energetics of Vortex Unpinning in Neutron Stars, Astrophys. J. **373**, 592 (1991).

[29] P. B. Jones, The origin of pulsar glitches, MNRAS **296**, 217 (1998).

[30] M. Mannarelli, K. Rajagopal, and R. Sharma, The Rigidity of crystalline color superconducting quark matter, Phys. Rev. D **76**, 074026 (2007).

[31] S. M. Roccuzzo, A. Gallemí, A. Recati, and S. Stringari, Rotating a Supersolid Dipolar Gas, Phys. Rev. Lett. **124**, 045702 (2020).

[32] A. Gallemí, S. M. Roccuzzo, S. Stringari, and A. Recati, Quantized vortices in dipolar supersolid Bose-Einstein-condensed gases, Phys. Rev. A **102**, 023322 (2020).

[33] A. J. Leggett, Can a Solid Be "Superfluid"?, Phys. Rev. Lett. **25**, 1543 (1970).

Conclusion and outlook

Conclusion

This thesis presents the work I have carried on for my PhD studies in the Theory Group of Univ. Prof. Dr. Francesca Ferlaino in Innsbruck. I joined the group at the end of 2020 and, since then, I have developed theoretical calculations and numerical simulations for the projects discussed in this thesis. I had the opportunity to develop both purely theoretical works and theory-experiment collaborations with the *Er-Dy* experimental team here in Innsbruck. These efforts resulted in 10 publications, among which 8 have been at the core of this doctoral thesis. Additionally, I am the first author on 4 of them.

Overall, the results accomplished during my PhD focus on in the theoretical characterization of the two-dimensional supersolid state of matter through numerical simulations. A supersolid state simultaneously exhibits a crystalline structure typical of a solid and a superfluid behaviour. In our case, we produce them by tuning the contact-interaction strength in a dipolar Bose-Einstein condensate. With the support of theoretical calculations, in 2021 it became possible to realize two-dimensional supersolids, an optimal platform to disentangle the paradoxical coexistence of solid and superfluid properties. In collaboration with R. Bisset (Innsbruck University) and L. Santos (Hannover University) we built the phase diagram and extracted the control parameter to maintain supersolidity across the structural transition from 1D-to-2D supersolids. We performed the numerical simulations with the well-established Gross-Pitaevskii equation and we developed a variational model to investigate the different crystal configurations. We optimized the code for the numerical calculation of the Bogoliubov-de Gennes excitation spectrum and characterized the low-energy collective modes. We also investigated the dynamical formation of a two-dimensional supersolid, comparing an interaction ramp with evaporative cooling. We concluded that the second technique leads to a final state which is more robust against crystal and phase fluctuations.

In collaboration with P.B. Blakie (Otago University), we investigated deeper the role of the three gapless branches in the excitation spectrum of an infinite 2D supersolid. Each gapless branch is related to a spontaneous continuous symmetry breaking, that for a 2D supersolids corresponds to the U(1) gauge symmetry (phase branch) and the two translational symmetries in the longitudinal and transverse directions (longitudinal and transverse density branch). The slopes of these branches is determined by the three speeds of sound, that in turns depend on the elastic parameters of the system. We compared the speeds of sound results from the hydrodynamic approach with the ones from the Bogoliubov-de Gennes, finding an excellent agreement. Among all the elastic parameters, we extracted the shear modulus. Remarkably, this quantity is non-zero only for solid systems and it is responsible for supporting the propagation of transverse waves.

Moving to the superfluid nature of a 2D supersolid, we investigated the behaviour of the system under rotation. First, we investigated the small angular oscillation dynamics, commonly known as *scissor mode*. From the simulations and the experiment we observed that, when undergoing a sudden rotation of the trap axis, the 2D supersolid exhibits a multi-mode response. The most populated mode has a frequency almost independent on the superfluid density link between the droplets. This prevents a direct association of the frequency of the scissor mode with the superfluid fraction of the system. We then moved to the full rotational regime, were we expect the nucleation of quantized vortices. We impart a rotation about the trap axis by stirring the external magnetic field. Collaborating with G. Lamporesi (Trento University), we validated this novel protocol by observing and characterizing vortices in a dipolar BEC. Then, extended the same analysis to 2D dipolar supersolids. While for a BEC quantized vortices manifest as density depletions that are directly visible from the in-situ density distribution, in a supersolid their visibility is more challenging. Indeed, vortices sits in the low density regions of the density modulation, sneaking in between the peaks. Boosted by the theoretical predictions, by exploiting the topologically protected nature of quantized vortices across the supersolid-to-BEC phase transition and performing interference measurements, we collected for the first time an experimental evidence of vortices in dipolar supersolids. This result unambiguously confirms the superfluid nature of dipolar supersolids.

Finally, we used our knowledge on systems with simultaneous solid and superfluid nature to test the internal dynamics of a neutron star. Collaborating with M. Mannarelli (Gran Sasso National Laboratory), we learnt that rapidly rotating neutron stars are expected to have a layered internal structure in which quantum effects are not negligible. In particular, the neutron density distribution in the inner crust is expected to have a supersolid structure that hosts quantized vortices. The collective unpinning of these vortices is believed to create a glitch, a sudden spin up of the star that is experimentally observed. Exploiting the structural analogy, we simulated the glitch mechanism in dipolar supersolids and propose them as platform where to test vortex and crystal dynamics in analogy of neutron stars. This result marks an important step towards quantum simulations of stellar objects from Earth.

Examining the dataset of papers submitted to *arXiv* that include the word *supersolid* in the title [250] offers a retrospective view of the historical background of this counterintuitive phase. Interestingly, the number of publications forms a roton-like spectrum, see Fig. 5.4. The maxon follows the apparent detection of supersolidity in ^{4}He and the roton develops after the denial. Joining Francesca Ferlaino's Theory group after the first experimental observation of 1D supersolids, gave me the opportunity to contribute, alongside my team, to the rise of the roton minimum. It has been an exciting experience to be part of this group and explore new quantum phases of matter with ultracold dipolar atoms.

Outlook

Throughout the chapters of this thesis, we already mentioned possible hints for future research and next steps related to the various projects presented. In the following, we collect the main ideas for future research in the field of supersolids.
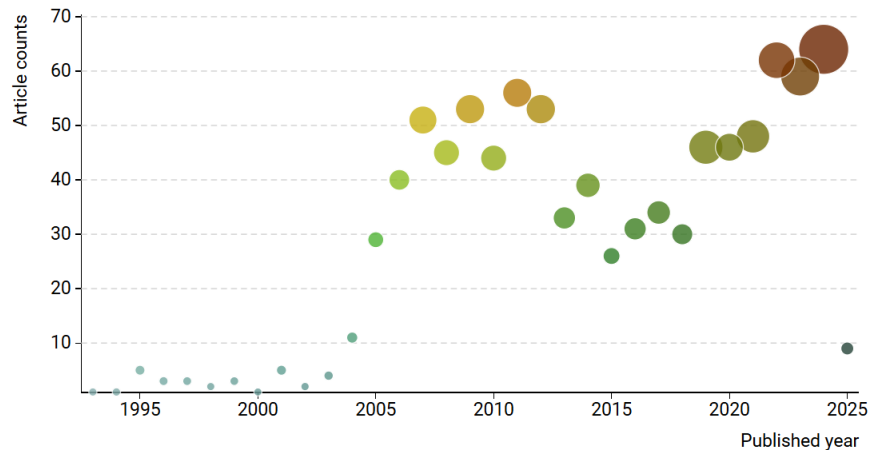
Figure 5.4.: Roton spectrum of supersolid papers. Number of papers submitted to arXiv containing the word *supersolid* in the last three decades. The papers presented in this PhD thesis contributed to the brown dots.

First of all, except for the detection of a crystalline structure, a quantitative measure of how much the system behaves as a solid is still absent. For example, based on the results shown in Chapter 3, it would be interesting to investigate how to extend the concept of the shear modulus to finite-size systems, to quantitatively extract a property which is unique to solid systems. Since the shear modulus is related to the propagation of transverse waves, one could think about extracting this quantity in a trapped 2D supersolid from Tkachenko-like modes similar to those occurring in vortex lattices [251].

Regarding the rotations discussed in Chapter 4, the fast rotation regime at frequencies close to the radial trapping frequency remains still unexplored. In this regime, rotation acts as an artificial gauge field, causing the system to mimic the behaviour of charged particles in a uniform magnetic field. In particular, at these high frequencies the vortex lattice melts and is replaced by a series of highly correlated liquids that are the analogous of fractional quantum Hall states [252, 253]. The influence of supersolidity in these regimes is still unexplored, yet it could significantly enrich the quantum Hall physics [254, 255].

Finally, the simulation of glitches in rotating dipolar supersolids opens new possibility. First of all, one can characterize the collective modes excited from a glitch perturbation. The frequency of the crystal excitations can be extracted from the glitch pulse shape. A particular interest should be given to *r-modes* [256]. These modes are counter-propagating with respect to rotation and their instability could be the origin of gravitational waves [257]. Additionally, it could be interesting to study the glitch mechanism in a larger system, with more pinning sites and vortices. For dipolar quantum systems the computational cost prevent a large scaling. However, soft-core systems could be used as toy model to scale the system to larger sizes and larger geometries (in these systems, supersolidity can also be reached in 3D [130]).

Appendix

A

Superfluid fraction: when, where, how it is defined

In the context of supersolids, the superfluid fraction f_s is an important concept that allows to quantify how much the system behaves as a solid and how much as a superfluid. The general idea behind this concept is the following: given a supersolid system in equilibrium, one applies a perturbation and measures the corresponding response of the system. The absence of viscosity due to the superfluid nature, leads to a reduced response compared to the one that a system with the same mass distribution would have if it was fully solid. There are two main perturbations that are usually applied:

- A small translation in one direction. The response of the system is calculated through the expectation value of the linear momentum $\langle \hat{P} \rangle$. This approach leads to the calculation of the fraction of *non-classical translational inertia*, f_{NCTI}.

- A small rotation around the center of mass. The response of the system is calculated through the expectation value of the angular momentum $\langle \hat{L} \rangle$. This approach leads to the calculation of the fraction of *non-classical rotational inertia*, f_{NCRI}.

Sometimes, these quantities are generically presented as *superfluid fraction f_s*. Since in the following we will present cases in which they could coincide or not, how they could be a scalar or a tensor and when they are well-defined or not, we will keep the distinction and call them f_{NCTI} and f_{NCRI}. We will use f_s only when the two quantities coincide or when we want to talk about superfluid fraction as a general concept.

Sometimes, f_s is associated to a superfluid density n_s (see, for example, discussion in Chapter 3). In particular, it is customary to define

$$f_s = \frac{n_s}{n} \tag{A1}$$

where n is the total density and n_s is an effective density proportional to the reduced response of the system. Accordingly, the normal component is given by $n_n = n - n_s$. In the context of superfluid helium, n_s and n_n arise from the two-fluid model description [101,258], where the superfluid component has zero viscosity and it vanishes as the temperature increases above the λ-transition.

In contrast to helium, the superfluid fraction remains finite even at zero temperature in systems that break the translational invariance [118]. This is the case of the dipolar supersolid discussed in this thesis. In such systems, the decomposition into superfluid and normal components is not fundamental but rather an effective description. Here,

n_s is not a physical density of superfluid particles; instead, it reflects an effective mass associated with the system's superfluid response. As mentioned in Ref. [111], f_s should not be confused with a measure of the amount of particles that are part of a superfluid system. Indeed, even in the independent droplet regime the droplets are individually superfluids but the superfluid fraction is zero (see Sec. 1.7). This is because the system does not behave as a superfluid, in its whole.

In general, calculating f_s is challenging. A finite superfluid fraction in a system at zero temperature has recently been measured in two distinct scenarios: in a Bose–Einstein condensate subjected to an external modulation, via measurements of the speed of sound [259], and in a dipolar supersolid through the observation of the Josephson effect [260]. In the following, we discuss theoretically different cases according to the system's geometry.

1D infinite supersolid

This geometry, originally discussed in Leggett's work [117, 118], can be conveniently visualized using an annular configuration. An infinite 1D system is equivalent to such an annulus, where rotation around the center corresponds to translation in the "unrolled" linear system. Based on this geometric considerations, we can already infer that $f_{NCTI} = f_{NCRI} = f_s$ [261].

Assuming the $x-$axis as axial direction of the system, we have

$$f_{NCTI} = 1 - \lim_{v_x \to 0} \frac{\langle \hat{P}_x \rangle}{N m v_x} \tag{A2}$$

and for the rotations

$$f_{NCRI} = 1 - \lim_{\Omega \to 0} \frac{\langle \hat{L}_z \rangle}{\Omega I_{rig}} . \tag{A3}$$

In practice, these formulas imply solving the eGPE in either the co-moving or rotating frame, computing the expectation values of the linear or angular momentum under infinitesimal perturbations, and comparing them with their classical (rigid-body) counterparts. For a purely solid system, one finds $\langle P_x \rangle = N m v_x$ and $\langle L_z \rangle = \Omega I_{rig}$, yielding $f_{NCTI} = f_{NCRI} = f_s = 0$.

Considering the annulus geometry, Leggett proposed an additional formula to extract the upper and lower bounds of the superfluid fraction [117, 118]. For simplicity, let us denote $\theta \in [0, 2\pi]$ as the angular coordinate along which density modulations occur, and $r \in [0, L]$ as the radial coordinate of the annulus. The upper bound for the superfluid fraction is

$$f_s^+ = \frac{1}{n_0} \left[\frac{1}{2\pi} \int_0^{2\pi} \frac{d\theta}{\frac{1}{L} \int_0^L dr n(r, \theta)} \right]^{-1} \tag{A4}$$

and the lower bound is

$$f_s^- = \frac{1}{n_0} \frac{1}{2\pi} \int_0^{2\pi} d\theta \left[\frac{1}{L} \int_0^L \frac{dr}{n(r, \theta)} \right]^{-1} . \tag{A5}$$

Here, n_0 denotes the average density over the entire spatial domain of the system. These bounds are uniquely based on integrals of the ground state density profile. For

the derivation, we refer the reader to Refs. [117, 118]. Remarkably, in this geometry, this upper and lower bounds are in excellent agreement with the values of f_{NCTI} and f_{NCRI} [261–263].

2D infinite supersolid

In analogy to the 1D infinite case, also in a 2D infinite system one can calculate the f_{NCTI} in the co-moving frame. Because of the broken translational symmetry in two directions, f_{NCTI} is not a scalar quantity anymore, but it is a tensor [166, 175]

$$f_{NCTI,ij} = \delta_{ij} - \lim_{v_j \to 0} \frac{\langle \hat{P}_i \rangle}{N m v_j} \,. \tag{A6}$$

Each of the indices i, j can be one of the two directions (x, y) in which the density modulation occurs. For the calculation of the second term of Eq. (A6) it is possible to use a perturbative approach that includes auxiliary vector functions, see Refs. [171, 175]. If the superfluid fraction tensor is diagonal and isotropic, $f_{ij} = f_s \delta_{ij}$, the superfluid fraction can be treated as scalar quantity f_s as for the 1D case [175].

Leggett's upper and lower bounds are also applicable to this geometry. Equations (A4) and (A5) are valid and it is sufficient to replace the variables $r \to x$ and $\theta \to y$, both integrated in their respective domain $[0, L]$ [175]. However, these bounds do not closely match the value obtained from Eq. (A6), particularly near the transition from an unmodulated BEC to a supersolid state; see Ref. [175].

In the case of a two-dimensional supersolid, there exists an intuitive interpretation of these bounds in terms of *electric circuits*, proposed by Jean Dalibard [67] and inspired by Ref. [264]. Within this analogy, the superfluid current is mapped to an electric current driven by a potential difference, with the system's conductance corresponding to the superfluid fraction [67].

Trapped supersolid

Supersolids realized in experiments are typically confined within harmonic traps, which–as discussed in Chapter 1–can exhibit either elongated or pancake-shaped geometries. The presence of a trapping potential carries important implications for the concept of the superfluid fraction. While, in principle, the previous equations for f_s can be applied locally, extracting a global superfluid fraction becomes significantly more challenging.

If one views the superfluid fraction as the system's response to being dragged in a particular direction, the presence of an harmonic potential substantially alters the response. Consequently, the measured behaviour reflects not only the intrinsic superfluidity of the system but also spatial distortions introduced by the trap. Thus, f_{NCTI} does not provide a clean measurement that quantifies the superfluid nature of the supersolid.

A more robust and well-defined assessment of the superfluid fraction can be made in the case of a two-dimensional supersolid confined within a cylindrically symmetric trap. In such a geometry, a non-zero response to an infinitesimally slow rotation of the trap unambiguously indicates spontaneous breaking of translational symmetry, and therefore a finite superfluid fraction. This behaviour is captured by f_{NCRI}–introduced in Eq.(A3)–which remains valid and meaningful even for finite systems [199, 205]. For

this reason, in Chapters 4 and 5, we have employed f_{NCRI} to quantify the superfluid properties of the system. The generalization for asymmetric traps can be found in Ref. [205].

Appendix B

Additional publications

B.1. Publication: Alternating-domain supersolids in binary dipolar condensates

T. Bland[1,2], **E. Poli**[2], L. A. Peña[3], L.Santos[3], F. Ferlaino[1,2],
and R. N. Bisset[2]

[1] *Institut für Quantenoptik und Quanteninformation, Österreichische Akademie der Wissenschaften, 6020 Innsbruck, Austria*
[2] *Institut für Experimentalphysik, Universität Innsbruck, 6020 Innsbruck, Austria*
[3] *Institut für Theoretische Physik, Leibniz, Universität Hannover, Hannover, Germany*

———————————————————

† The author of the present thesis performed the numerical eGPE simulations together with T. B. and contributed in writing the manuscript.

Alternating-domain supersolids in binary dipolar condensates

T. Bland[1,2], E. Poli[2], L. A. Peña Ardila[3], L. Santos[3], F. Ferlaino[1,2], and R. N. Bisset[2]

[1]*Institut für Quantenoptik und Quanteninformation, Österreichische Akademie der Wissenschaften, Innsbruck, Austria*
[2]*Institut für Experimentalphysik, Universität Innsbruck, Austria*
[3]*Institut für Theoretische Physik, Leibniz Universität Hannover, Germany*

Two-component dipolar condensates are now experimentally producible, and we theoretically investigate the nature of supersolidity in this system. We predict the existence of a binary supersolid state in which the two components form a series of alternating domains, producing an immiscible double supersolid. Remarkably, we find that a dipolar component can even induce supersolidity in a nondipolar component. In stark contrast to single-component dipolar supersolids, alternating-domain supersolids do not require quantum stabilization, and the number of crystal sites is not strictly limited by the condensate populations, with the density hence being substantially lower. Our results are applicable to a wide range of dipole moment combinations, marking an important step towards long-lived bulk supersolidity.

I. INTRODUCTION

The once elusive supersolid state of matter simultaneously exhibits superfluidity and crystalline order [1]. While early proposals sought superfluid properties of defects in a solid [2,3], focusing on helium experiments [4], supersolidity has yet to be demonstrated in those systems [5]. It is instead the high-degree of flexibility and control offered by ultra-cold gases that led to the first observations of supersolidity, but of a different kind, with solid properties arising in superfluids. Supersolid features were observed in systems with cavity-mediated interactions [6], while supersolid stripes were realized with spin-orbit-coupled Bose-Einstein condensates (BECs) [7,8]. Supersolids have now been observed in experiments with dipolar BECs [9–11], and their superfluid character has been supported by the analysis of their excitations [12–14]. Note that supersolid proposals have also been made for gases with soft-core, finite-range interactions [15–19].

The first dipolar supersolids were realized in single-component BECs in cigar-shaped traps, exhibiting a periodic density modulation along one direction [9–11], whereas experiments have now also created two-dimensional (2D) supersolids with density modulations along two directions [20,21]. From a theoretical perspective, there have been intriguing predictions for other exotic 2D supersolid states [22–27], as well as alluring manifestations of quantum vortices [28–30]. Dipolar supersolids may be created from unmodulated BECs by inducing a roton instability [9–11]. Dipolar rotons—constituting a local minimum of the energy dispersion at finite momenta due to the anisotropic and long-ranged dipole-dipole interactions [31,32]—were first observed in cigar-shaped [33,34] and then in pancake-shaped BECs [35]. An unstable roton mode seeds a periodic density modulation that can subsequently be stabilized by quantum fluctuations as the density grows, resulting in a supersolid

[36,37]. Recently, these same concepts were extended to the case of dipolar mixtures, i.e., systems composed of two dipolar components, which are now available in experiments [38–40]. In particular, it was predicted that exotic supersolid
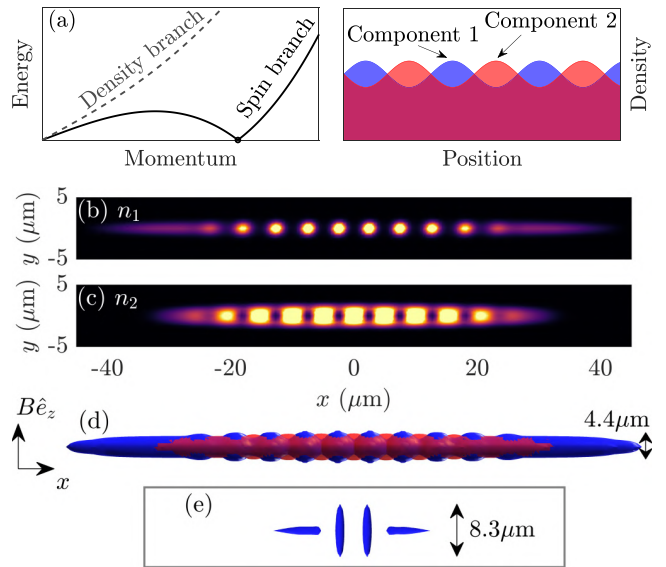

FIG. 1. (a) Dispersion relation schematic showing a roton instability in the spin branch with corresponding density modulations on the right for a dipolar mixture. (b)–(d) Alternating-domain supersolid for a dysprosium dipolar-nondipolar mixture. Column densities for (b) dipolar and (c) nondipolar components, with (d) double-isosurface plot at 2% of the peak density for each component. Interaction scattering lengths $(a_{11}, a_{12}, a_{22}) = (100, 98, 100)a_0$, trapping frequencies $\vec{f} = (5, 110, 150)$ Hz, and populations $N_1 = N_2 = 1.5 \times 10^4$. (e) Corresponding single-component modulated state for the same trapping potential, $N = 3 \times 10^4$, and $a = 78a_0$. Subplots (b)–(e) are drawn to the same length scale.

states can be seeded by the addition of a second dipolar component [40,41].

Dipolar mixtures, with their richness stemming from multiple sources of interactions, offer new phases with spontaneous modulation that go beyond quantum-fluctuation-stabilized supersolids. An early example proposed that two immiscible BECs—displaced relative to one another by nonconcentric confinement—might be used to realize a kind of binary supersolid formed by the instability of interface bending modes [42]. Binary dipolar BECs could also open another intriguing possibility. It has already been predicted that unmodulated binary BECs may be destabilized by a spin roton mode [43,44], for which a periodic density modulation develops in both components, but with the density maxima of one component occurring at the minima of the other [see Fig. 1(a)]. The key question is then, in analogy to the dipolar roton producing a single-component supersolid, could the unstable spin rotons point to a novel kind of supersolid?

In this article, we predict the existence of a phase, which we call an alternating-domain supersolid, that exists even at the mean-field level and does not require the regulatory action of quantum fluctuations. The two components form alternating domains, with a continuous superfluid connection within each component that periodically weaves through the other [see Figs. 1(b)–1(d)]. We uncover rich phase diagrams with broad regions in which both components are supersolid, as well as regions where a supersolid component is periodically punctuated by the isolated domains of the second component. We predict that the alternating-domain supersolid intrinsically relies on a dipolar imbalance between the two components and can exist for far lower atom numbers and peak densities than quantum-stabilized supersolids, which has important implications for the potential size and longevity of supersolid crystals in realistic settings.

II. FORMALISM

We consider a three-dimensional system at zero temperature made of two bosonic components, $\sigma = \{1, 2\}$, consisting of atoms with permanent magnetic moments, although our work is also applicable to electric dipoles. Following Refs. [45,46], we compute the Lee-Huang-Yang (LHY) energy density correction due to quantum fluctuations for a homogeneous binary mixture with densities $\mathbf{n} = (n_1, n_2)$:

$$\epsilon_{\text{LHY}}(\mathbf{n}) = \frac{16}{15\sqrt{2\pi}}\left(\frac{m}{4\pi\hbar^2}\right)^{3/2}\int_0^1 du \sum_{\lambda=\pm} V_\lambda(u, \mathbf{n})^{5/2}, \quad (1)$$

where we assume equal masses $m = m_1 = m_2$, and

$$V_\pm(u, \mathbf{n}) = \sum_{\sigma=1,2} \alpha_{\sigma\sigma} n_\sigma \pm \sqrt{(\alpha_{11}n_1 - \alpha_{22}n_2)^2 + 4\alpha_{12}^2 n_1 n_2}. \quad (2)$$

Here, $\alpha_{\sigma\sigma'}(u) = g_{\sigma\sigma'} + g_{\sigma\sigma'}^d(3u^2 - 1)$, where the short-ranged and dipolar interaction parameters are, respectively, $g_{\sigma\sigma'} = 4\pi\hbar^2 a_{\sigma\sigma'}/m$ and $g_{\sigma\sigma'}^d = \mu_0\mu_\sigma\mu_{\sigma'}/3 = 4\pi\hbar^2 a_{\sigma\sigma'}^d/m$, with s-wave scattering lengths $a_{\sigma\sigma'}$ and dipole moments μ_σ, where μ_0 is the vacuum permeability. The wave function for each component Ψ_σ is obtained by solving the coupled

extended Gross-Pitaevskii equations:

$$i\hbar\frac{\partial}{\partial t}\Psi_\sigma(\mathbf{x}) = \left[-\frac{\hbar^2\nabla^2}{2m} + \frac{1}{2}m(\omega_x^2 x^2 + \omega_y^2 y^2 + \omega_z^2 z^2)\right.$$
$$+ \sum_{\sigma'}\int d^3\mathbf{x}'\, U_{\sigma\sigma'}(\mathbf{x}' - \mathbf{x})n_{\sigma'}(\mathbf{x}')$$
$$\left. + \sum_{\sigma'} g_{\sigma\sigma'}n_{\sigma'}(\mathbf{x}) + \mu_{\text{LHY}}^{(\sigma)}[\mathbf{n}(\mathbf{x})]\right]\Psi_\sigma(\mathbf{x}), \quad (3)$$

where $\omega_{x,y,z} = 2\pi f_{x,y,z}$ are the harmonic trapping frequencies; $U_{\sigma\sigma'}(\mathbf{r}) = [\mu_0\mu_\sigma\mu_{\sigma'}/4\pi r^3](1 - 3\cos^2\theta)$ is the long-ranged anisotropic dipole-dipole interaction potential, with θ being the angle between the polarization axis (always z) and the vector $\mathbf{r}$ that connects the two interacting particles; and $n_\sigma(\mathbf{x}) \equiv |\Psi_\sigma(\mathbf{x})|^2$ is the density of component σ, normalized to N_σ atoms. The last term in Eq. (3) is the quantum fluctuation correction to the chemical potential $\mu_{\text{LHY}}^{(\sigma)}[\mathbf{n}(\mathbf{x})] = \partial\epsilon_{\text{LHY}}[\mathbf{n}(\mathbf{x})]/\partial n_\sigma$, described within the local-density approximation framework.

III. ALTERNATING-DOMAIN SUPERSOLIDS

We demonstrate the unique features of alternating-domain supersolids by considering a dipolar-nondipolar mixture in Fig. 1, for which a combined total of 19 domains can be seen. While the dipolar component [Fig. 1(b)] can remain globally phase coherent through a continuous superfluid connection linking the domains—since we are close to the miscible-immiscible transition the separation is only partial—the nondipolar component [Fig. 1(c)] can also maintain a superfluid connection along high-density rails encompassing the dipolar domains. The density isosurfaces in Fig. 1(d) highlight the shape of the dipolar domains, which are not as strongly elongated as the single-component case [cf. Fig. 1(e)]. While this concrete illustration considers two ^{164}Dy spin projections, with $(\mu_1, \mu_2) = (-10, 0)\mu_B$ for Bohr magneton μ_B, domain supersolids are not just a special feature of dipolar-nondipolar mixtures, but are rather general, as we discuss later.

These results must be contrasted to the single-component case. In Fig. 1(e) we show a modulated state for a single-component dipolar BEC for the same trap and total atom number as in Figs. 1(b)–1(d), i.e., $N = 3 \times 10^4$. Note that we had to modify the scattering length, since $a = 100a_0$ corresponds to an unmodulated BEC. However, lowering to $a = 78a_0$ passes a transition to a modulated state that is not a supersolid, where the peak density (4.0×10^{21} m^{-3}) is immediately more than an order of magnitude larger than the domain supersolid case (1.8×10^{20} m^{-3}). Correspondingly, the number of atoms per lattice site is about an order of magnitude larger than for the domain supersolid. For this atom number and trap volume, the supersolid phase does not exist for the single-component case [27], which was also the situation for the regimes considered by Refs. [47–49].

To understand the physical mechanisms involved, it is instructive to consider the transition from unmodulated to modulated states. For the formation of a domain supersolid, the density modulation is triggered by unstable spin roton excitations [shown schematically in Fig. 1(a)], with wavelengths governed by the BECs width along the direction

of dipole polarization [43]. Spin modes act to increase the density difference, $|n_1 - n_2|$, and the instability is hence resolved once the components become spatially separated as alternating immiscible domains [Figs. 1(b)–1(d)]. Crucially, there is no significant increase of the total density $n_1 + n_2$, and the peak density can remain low. This situation should be contrasted to that of single-component supersolids, and the two-component supersolids of Refs. [40,41], for which a density roton instability would cause a divergence of the peak density if it were not counterbalanced by the appropriate LHY term [50], and this necessitates significantly higher densities [9–11]. Note that while single-component supersolids require $a < a^d$, and thus are only stable due to quantum fluctuations [36,37], domain supersolids can exist for either $a_{\sigma\sigma} > a^d_{\sigma\sigma}$ or $a_{\sigma\sigma} < a^d_{\sigma\sigma}$, but quantum fluctuations remain qualitatively important since, for example, if they were neglected the latter situation could only be at best metastable [51].

We focus on regimes where one component without the presence of the other will always be unmodulated, but each component within the binary system can exist in one of three phases: an unmodulated BEC, a supersolid state with a linear chain of domains (SS), or an array of isolated domains (ID). The distinction between these is set by upper-bound estimates for the superfluid fractions [52], which in our binary system are given by

$$f_{s,\sigma} = \frac{(2L)^2}{\int_{-L}^{L} dx\, \bar{n}_\sigma} \left[\int_{-L}^{L} \frac{dx}{\bar{n}_\sigma} \right]^{-1}, \quad \bar{n}_\sigma = \int_{-\infty}^{\infty} \int_{-\infty}^{\infty} dy\, dz\, n_\sigma,$$

for length L defined over the central region that encompasses the central 3 (4) domains if the number of domains is odd (even). We take the supersolid region to be when $f_{s,\sigma} > 0.1$ occurs concurrently with a periodic density modulation, following Ref. [53] for the arbitrary choice of $f_{s,\sigma} \leqslant 0.1$ defining the crossover to the regime of isolated domains. For reference, the superfluid fractions in Fig. 1 are (b) $f_{s,1} = 0.3032$, (c) $f_{s,2} = 0.7940$, and (e) $f_{s,1} = 0.0001$. Note, the total superfluid fraction $f_s = (N_1 f_{s,1} + N_2 f_{s,2})/N$ is associated with a reduction in the moment of inertia of the overall mixture. The periodic spatial ordering can be characterized by the density contrast $\mathcal{C}_\sigma = (n_\sigma^{\max} - n_\sigma^{\min})/(n_\sigma^{\max} + n_\sigma^{\min})$, where $n_\sigma^{\max}$ ($n_\sigma^{\min}$) are neighboring maxima (minima) as one moves along the trap's long direction. See Appendix A for more discussion on the calculation of the contrast. The boundary between unmodulated and modulated states is defined by $\mathcal{C}_\sigma$ changing from zero to a nonzero value.

IV. PHASE DIAGRAM FOR DIPOLAR-NONDIPOLAR MIXTURE

In Fig. 2 we explore the stationary state phase diagram of a dipolar-nondipolar mixture in a cigar-shaped trap with $\vec{f} = (f_x, 150, 150)$ Hz, $N_1 = N_2 = N/2$, and fixed $N f_x = 3 \times 10^5$ Hz to maintain an approximately constant average density [27]. At low $a_{12} \lesssim 60a_0$ the stationary state solution is a miscible unmodulated BEC, with only a small deviation from perfect density overlap between components due to magnetostriction in the dipolar component (Fig. 2, ■). Increasing a_{12} induces a transition to a domain supersolid state (SS-SS) (Fig. 2, ▲),
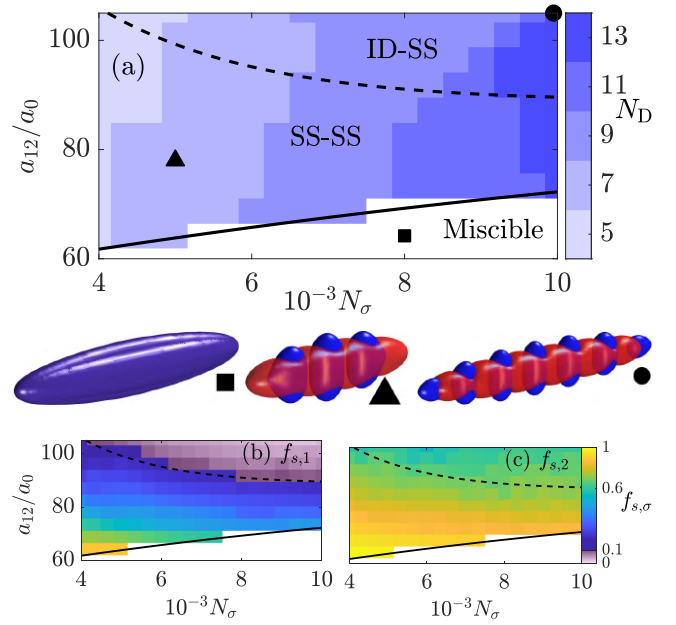

FIG. 2. Phase diagram for a dipolar-nondipolar mixture of ^{164}Dy atoms, varying intercomponent scattering length a_{12} and $N_1 = N_2 = N/2$ with fixed $N f_x$, from $f_x = 37.5$ Hz on the left to $f_x = 15$ Hz on the right. (a) Total number of domains in the stationary state solution. Solid lines separate unmodulated miscible and domain supersolid (SS-SS) states when $\mathcal{C}_\sigma > 0$, and dashed lines separate SS-SS and isolated domains-supersolid (ID-SS) states. Example isosurfaces below are highlighted by the symbols in panel (a). (b) and (c) Superfluid fraction $f_{s,\sigma}$ of components 1 and 2. The threshold between the SS and ID regimes is indicated by a change of color scale. Other parameters: $a_{11} = a_{22} = 100a_0$, $(\mu_1, \mu_2) = (-10, 0)\mu_B$, and $f_y = f_z = 150$ Hz.

where the domains of a given component exhibit a continuous superfluid connection [$f_{s,\sigma} > 0.1$ in Figs. 2(b) and 2(c)]. We find that a quench of the intercomponent scattering length from the unmodulated miscible state to the domain supersolid regime generates a globally phase-coherent state—within each component—that is robust against the excitations induced by the quench, in-keeping with single-component studies of supersolids in a cigar-shaped geometry [9–11], which we detail in Appendix B [54]. Note how broad the SS-SS regime is, at least $20a_0$ wide, compared to single-component supersolids where it is typically only a few a_0 wide [53]. Further increasing a_{12} causes the overlap between components to reduce, expanding the distance between domains whilst decreasing superfluidity [Fig. 2(b)], crossing into the isolated domain-supersolid (ID-SS) regime (Fig. 2 ●). However, the nondipolar component maintains a strong superfluid connection [Fig. 2(c)]. Note that the superfluid connection of component 2 can be controlled by adjusting f_y, with even a small reduction in f_y significantly reinforcing the nondipolar rails around the dipolar domains.

Figure 2(a) also shows how the total number of domains N_{D} changes in this phase diagram. Throughout, the average atom number per domain is $\sim 10^3$. Hence, as the atom number increases the number of domains climbs steadily, reaching a total of 13 once the system has 2×10^4 atoms (10^4 per
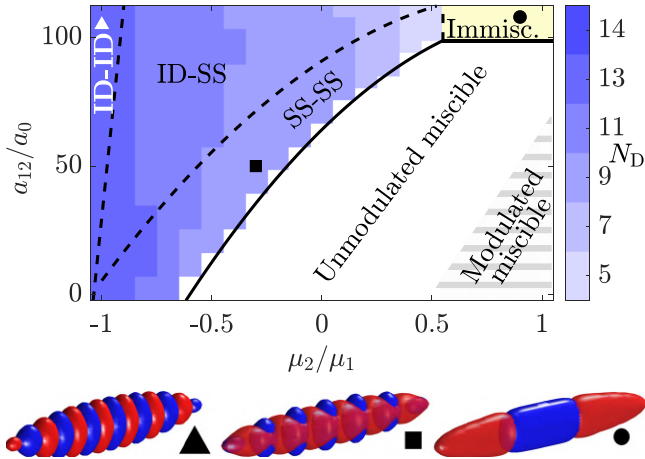
FIG. 3. Phase diagram for dipolar mixtures with varying inter-component scattering length and relative magnetic moment (note that $\mu_2/\mu_1 < 0$ implies antiparallel dipoles). Compared to Fig. 2, note the new phases: binary isolated domains (ID-ID), macroscopic-domain immiscibility (beige region), and the modulated miscible regime. Parameters: $N_1 = N_2 = 5 \times 10^3$, $a_{11} = a_{22} = 100a_0$, and $(f_x, f_y, f_z) = (15, 150, 150)$ Hz.

component) on the far right-hand side. In contrast, single-component dipolar supersolids typically require $\sim 10^4$ atoms per lattice site [9–11].

V. GENERALIZATION TO VARIOUS DIPOLE COMBINATIONS

Here, we generalize our findings to mixtures in which both components can be dipolar, applicable to a wide range of experiments, e.g., erbium-dysprosium mixtures or spin mixtures of the same species. In Fig. 3, we construct a phase diagram by fixing μ_1 and exploring the effect of varying μ_2 and a_{12}. A solid line indicates a transition from a miscible to an immiscible state, consistent with Fig. 2. For $\mu_2/\mu_1 < 0$ the dipoles are antialigned, decreasing the energy for dipoles of separate components to orient in the side-by-side configuration, thus causing both immiscibility and domain supersolidity to occur at low a_{12} (Fig. 3, ■). At $\mu_2/\mu_1 = -1$ the modulation is a perfect reflection about the $x = 0$ plane between the components, and for the range of a_{12} considered, the system forms a binary isolated domain (ID-ID) state with 14 domains for only 10^4 atoms in total (Fig. 3, ▲).

For similar dipoles $\mu_2 \sim \mu_1$, there is little energy incentive from the dipolar interactions for the components to phase separate [44]; hence, the immiscibility boundary in Fig. 3 is close to the nondipolar result $a_{12} = \sqrt{a_{11}a_{22}} = 100a_0$, and the components separate to a macroscopic-domain immiscible state [43] (Fig. 3,●). While we focus on the immiscible domain regime, smaller $a_{\sigma\sigma}$ can trigger the formation of immiscible quantum-stabilized supersolids [40]. Miscible quantum-stabilized supersolids are also possible for smaller a_{12} following a density branch roton instability, indicated in the lower right corner of Fig. 3, which is explored further in Ref. [41]. If we instead considered $a_{\sigma\sigma} \geqslant a_{\sigma\sigma}^d$, we would expect qualitatively the same phases as in Fig. 3 apart from the modulated miscible phase.
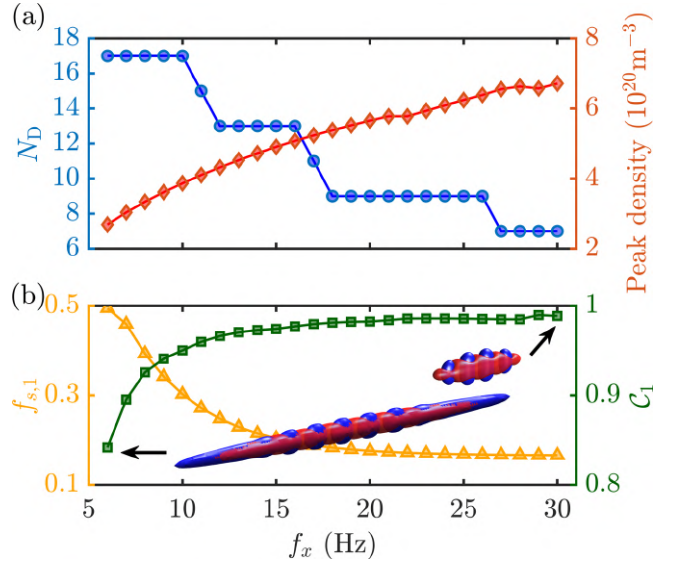
FIG. 4. Opening the trap for an erbium dipolar-nondipolar supersolid. (a) Reducing the long axis trap frequency f_x of a cigar-shaped trap increases the number of domains N_D whilst simultaneously reducing the peak density. (b) Superfluid fraction (density contrast, $\mathcal{C}_1$) of the dipolar component also increases (decreases), indicating an improving superfluid connection, whilst the second component is always a robust supersolid with the superfluid fraction never dropping below 0.7 (not shown). Parameters: $\mu_1 = -7\mu_B$ and $\mu_2 = 0$, $(a_{11}, a_{12}, a_{22}) = (65, 60, 65)a_0$, $N_1 = N_2 = 20\,000$ atoms, and $f_y = f_z = 150$ Hz.

VI. ULTRA-LOW-DENSITY SUPERSOLIDS

We investigate weakening the axial confinement of a dipolar-nondipolar spin mixture of erbium, further demonstrating the generality of our results to a broad range of dipole combinations. On the far right of Fig. 4 is a state in the SS-SS regime for $f_x = 30$ Hz. Decreasing f_x to 6 Hz increases the total number of domains from 7 to 17, whilst simultaneously reducing the peak density by a factor of ≈ 2.5.
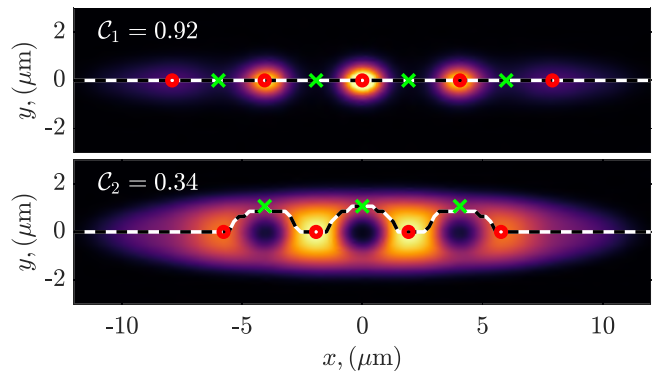

FIG. 5. Contrast $\mathcal{C}_\sigma$ of a dipolar-nondipolar mixture of ^{164}Dy atoms. The dashed line indicates the y position of the maximum density along x. Red circles are the peaks (n_σ^{max}) and green crosses are the troughs (n_σ^{min}) of density along the dashed line. Other parameters: $(\mu_1, \mu_2) = (-10, 0)\mu_B$, $N_1 = N_2 = N/2 = 7000$, $a_{12} = 70a_0$, $a_{11} = a_{22} = 100a_0$, and $(f_x, f_y, f_z) = (21, 150, 150)$ Hz.

The increasing number of domains can be explained by the BEC becoming longer, while the spin roton wavelength is roughly fixed by the confinement length in the direction of dipole polarization. This behavior starkly contrasts with that for quantum-stabilized supersolids, which instead require a certain atom number for a given trap volume [27], and the supersolid regime is not possible if this criterion is not met [47–49]. For example, recall the modulated state in Fig. 1(e), for which the atom number is insufficient for this trap to attain supersolidity. Whilst decreasing f_x the superfluid fraction is monotonically increased from close to the ID-SS to deep in the SS-SS regime. These results are compared to the density contrast, which shows an improved density linking between domains (smaller $\mathcal{C}_\sigma$) for looser confinement.

VII. CONCLUSIONS

We predict an alternating-domain supersolid state in two-component dipolar condensates. This binary supersolid exists over a broad region of parameter space and, importantly, it is
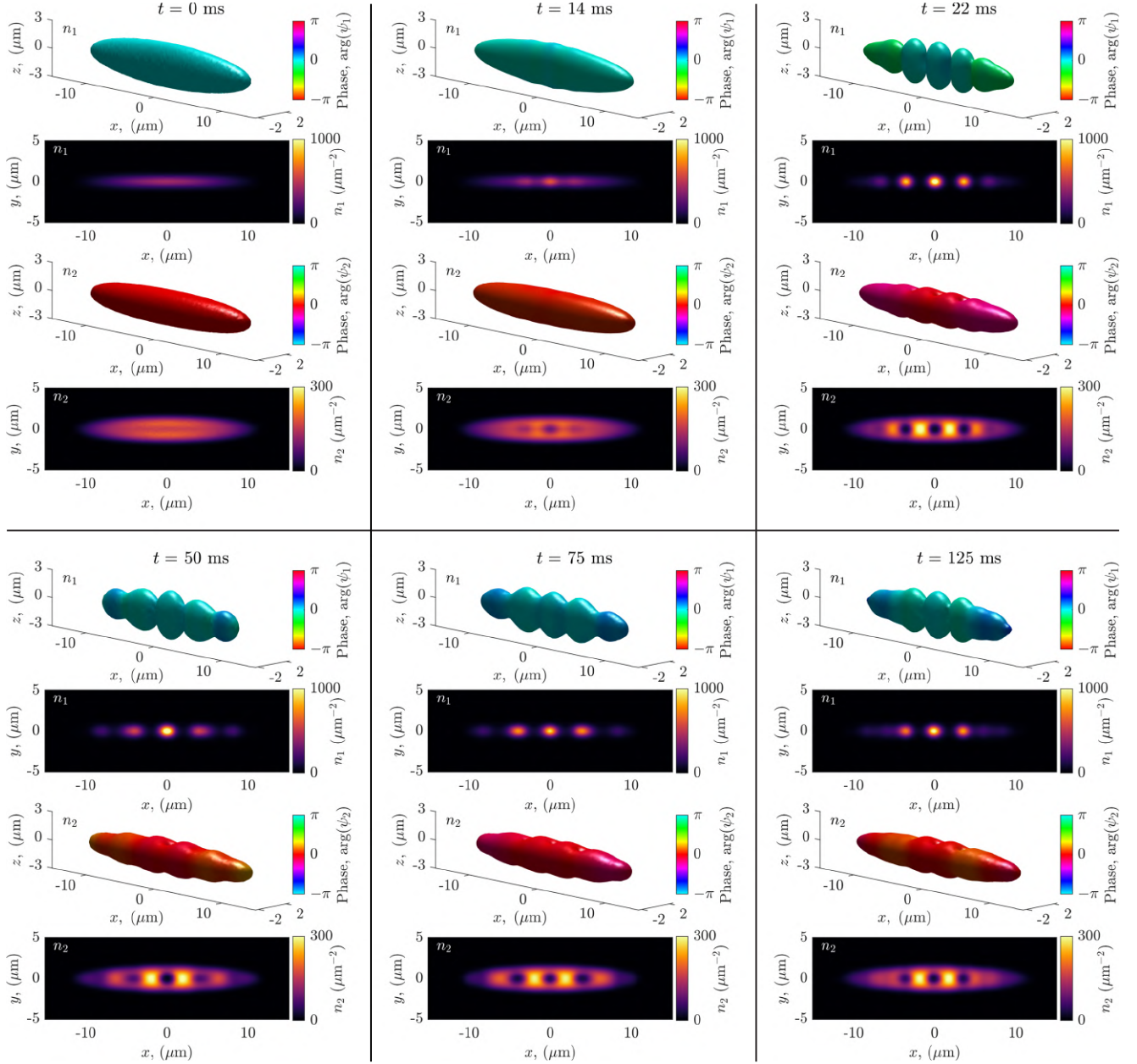
FIG. 6. Preparation of a domain supersolid through an interaction quench. Simulation of an instantaneous quench from $a_{12} = 65a_0$ to $a_{12} = 70a_0$ at $t = 0$, with other parameters from Fig. 5. Each labeled frame corresponds to a time during the consequent dynamics, and within each frame the data can be understood row-by-row. Row 1: 5% density isosurface for component 1 colored to the phase and centered such that the phase at the origin is 0. Perfect coherence for component 1 would be light blue. Row 2: Column density for component 1 normalized to peak value over the whole simulation. Row 3: Same as Row 1 but for the second component, but perfect coherence in component 2 would be red. Row 4: Same as Row 2 but for the second component, with a smaller peak density. Note that the stationary solution for the final parameters is the state presented in Fig. 5. A Supplementary Video of this simulation is also included [54].

robust against the excitations caused by crossing the unmodulated BEC-to-domain supersolid transition. There is also a crossover to an adjacent region where one of the components is supersolid, but the other forms isolated domains. In contrast to single-component supersolids—which must be stabilized by quantum fluctuations—alternating-domain supersolids can produce numerous lattice sites with relatively small atom numbers, and they have peak densities similar to those of unmodulated BECs, important for their longevity, which is largely determined by the inelastic three-body collisions that depend strongly on the density [37].

Our results are applicable to various dipole moment combinations, such as spin mixtures or binary gases comprised of two atomic species. Interestingly, we even find that a dipolar component can induce supersolidity within a nondipolar component via their mutual interactions. Our work opens the door for future investigations into binary supersolid states and their excitations, as well as the exploration of novel 2D domain supersolids with exotic structures and vortex states. Our results reveal a rich system, within current experimental reach, and mark an important step towards long-lived bulk supersolidity.

Note added. Very recently, we became aware of a related work addressing supersolidity in an immiscible dipolar-nondipolar mixture [55].

APPENDIX A: DENSITY CONTRAST

The onset of periodic density modulation is characterized by the density contrast, akin to interferometric visibility, defined as

$$\mathcal{C}_\sigma = \frac{n_\sigma^{\max} - n_\sigma^{\min}}{n_\sigma^{\max} + n_\sigma^{\min}} \tag{A1}$$

for each bosonic component $\sigma = \{1, 2\}$ and where $n_\sigma^{\max}$ and $n_\sigma^{\min}$ are neighboring maxima and minima in the 3D density as one moves along the long direction of the trap. In Fig. 5 we graphically depict the line of maximum 3D density in the $z = 0$ plane, showing the maxima (red circles) and minima (green crosses) in the density along this curve. Typically, for the component with a larger dipole moment this curve lies along $y = 0$, just as it does for single-component supersolids [9–11]. However, the nondipolar component has a greater
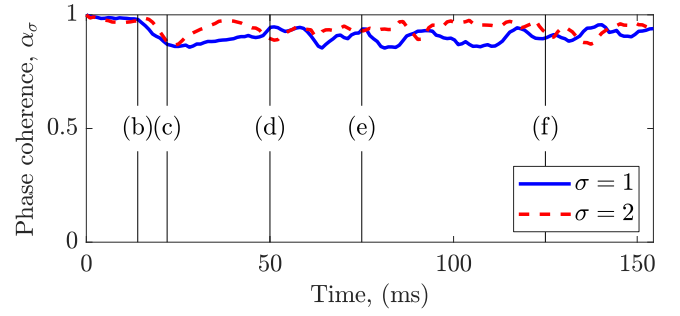
FIG. 7. Phase coherence α_σ for each component $\sigma = \{1, 2\}$ following an instantaneous quench from an unmodulated miscible BEC to a domain supersolid state. Labels in the plot coincide with the frames shown in Fig. 6.

superfluid connection along the rails, a feature which can be captured by our generalization of Eq. (A1). This connection can still be lost, however, through tightening f_y, for example.

APPENDIX B: DYNAMIC PREPARATION

The preparation of a single-component supersolid has been achieved either through taking an unmodulated BEC and quenching the scattering length across the unmodulated BEC-to-supersolid transition [9–11] or by direct evaporative cooling into the supersolid state [11,20,21]. The two-component case affords a wide range of possibilities for domain supersolid preparation, due to the large number of tunable interaction parameters in the system. Here, we investigate one possibility through tuning the intercomponent scattering length a_{12}. Taking an initially unmodulated miscible dipolar-nondipolar mixture with the parameters from Fig. 5 and $a_{12} = 65a_0$, we simulate an instantaneous quench to $a_{12} = 70a_0$. The consequent dynamics are shown in Fig. 6. Despite the violent nature of the instantaneous quench, the system maintains phase coherence throughout the lifetime of the simulation, as indicated by the blue (red) isosurface for component 1 (2), and the solution resembles the target stationary solution [Fig. 5]. We also include a Supplementary Video of the dynamics [54].

We can dynamically characterize the supersolid quality by plotting the phase coherence over time. Following Ref. [9] (see also Refs. [21,57]) we define the phase coherence as

$$\alpha_\sigma = 1 - \frac{2}{\pi} \frac{\int_{\mathcal{R}} dx\, dy\, |\psi_\sigma(x, y)|^2 |\theta_\sigma(x, y) - \beta|}{\int_{\mathcal{R}} dx\, dy\, |\psi_\sigma(x, y)|^2}, \tag{B1}$$

where $\theta_\sigma(x, y)$ is the phase of $\psi_\sigma(x, y)$ in the $z = 0$ plane, and β is a fitting parameter to maximize α_σ at each time. The integration region $\mathcal{R}$ encompasses the cloud. From this definition $\alpha_\sigma = 1$ corresponds to perfect phase coherence across the BEC. In Fig. 7 we present the dynamical evolution of the phase coherence after the instantaneous quench presented in Fig. 6. Throughout the total time evolution, α_σ does not go below 0.85 for either component, suggesting excellently maintained phase coherence.

[1] M. Boninsegni and N. V. Prokofev, Colloquium: Supersolids: What and where are they? Rev. Mod. Phys. **84**, 759 (2012).

[2] E. P. Gross, Unified theory of interacting bosons, Phys. Rev. **106**, 161 (1957).

[3] A. F. Andreev and I. M. Lifshitz, Quantum theory of defects in crystals, Zh. Eksp. Teor. Fiz. **56**, 2057 (1969) [Sov. Phys. JETP **29**, 1107 1969)].

[4] E. Kim and M. Chan, Probable observation of a supersolid helium phase, Nature (London) **427**, 225 (2004).

[5] D. Y. Kim and M. H. W. Chan, Absence of Supersolidity in Solid Helium in Porous Vycor Glass, Phys. Rev. Lett. **109**, 155301 (2012).

[6] J. Léonard, A. Morales, P. Zupancic, T. Esslinger, and T. Donner, Supersolid formation in a quantum gas breaking a continuous translational symmetry, Nature (London) **543**, 87 (2017).

[7] J.-R. Li, J. Lee, W. Huang, S. Burchesky, B. Shteynas, F. Ç. Top, A. O. Jamison, and W. Ketterle, A stripe phase with supersolid properties in spin–orbit-coupled Bose–Einstein condensates, Nature (London) **543**, 91 (2017).

[8] T. M. Bersano, J. Hou, S. Mossman, V. Gokhroo, X.-W. Luo, K. Sun, C. Zhang, and P. Engels, Experimental realization of a long-lived striped Bose-Einstein condensate induced by momentum-space hopping, Phys. Rev. A **99**, 051602(R) (2019).

[9] L. Tanzi, E. Lucioni, F. Famà, J. Catani, A. Fioretti, C. Gabbanini, R. N. Bisset, L. Santos, and G. Modugno, Observation of a Dipolar Quantum Gas with Metastable Supersolid Properties, Phys. Rev. Lett. **122**, 130405 (2019).

[10] F. Böttcher, J.-N. Schmidt, M. Wenzel, J. Hertkorn, M. Guo, T. Langen, and T. Pfau, Transient Supersolid Properties in an Array of Dipolar Quantum Droplets, Phys. Rev. X **9**, 011051 (2019).

[11] L. Chomaz, D. Petter, P. Ilzhöfer, G. Natale, A. Trautmann, C. Politi, G. Durastante, R. M. W. van Bijnen, A. Patscheider, M. Sohmen, M. J. Mark, and F. Ferlaino, Long-Lived and Transient Supersolid Behaviors in Dipolar Quantum Gases, Phys. Rev. X **9**, 021012 (2019).

[12] G. Natale, R. M. W. van Bijnen, A. Patscheider, D. Petter, M. J. Mark, L. Chomaz, and F. Ferlaino, Excitation Spectrum of a Trapped Dipolar Supersolid and Its Experimental Evidence, Phys. Rev. Lett. **123**, 050402 (2019).

[13] L. Tanzi, S. Roccuzzo, E. Lucioni, F. Famà, A. Fioretti, C. Gabbanini, G. Modugno, A. Recati, and S. Stringari, Supersolid symmetry breaking from compressional oscillations in a dipolar quantum gas, Nature (London) **574**, 382 (2019).

[14] M. Guo, F. Böttcher, J. Hertkorn, J.-N. Schmidt, M. Wenzel, H. P. Büchler, T. Langen, and T. Pfau, The low-energy goldstone mode in a trapped dipolar supersolid, Nature (London) **574**, 386 (2019).

[15] F. Cinti, P. Jain, M. Boninsegni, A. Micheli, P. Zoller, and G. Pupillo, Supersolid Droplet Crystal in a Dipole-Blockaded Gas, Phys. Rev. Lett. **105**, 135301 (2010).

[16] S. Saccani, S. Moroni, and M. Boninsegni, Phase diagram of soft-core bosons in two dimensions, Phys. Rev. B **83**, 092506 (2011).

[17] S. Saccani, S. Moroni, and M. Boninsegni, Excitation Spectrum of a Supersolid, Phys. Rev. Lett. **108**, 175301 (2012).

[18] M. Kunimi and Y. Kato, Mean-field and stability analyses of two-dimensional flowing soft-core bosons modeling a supersolid, Phys. Rev. B **86**, 060510(R) (2012).

[19] T. Macrì, F. Maucher, F. Cinti, and T. Pohl, Elementary excitations of ultracold soft-core bosons across the superfluid-supersolid phase transition, Phys. Rev. A **87**, 061602(R) (2013).

[20] M. A. Norcia, C. Politi, L. Klaus, E. Poli, M. Sohmen, M. J. Mark, R. N. Bisset, L. Santos, and F. Ferlaino, Two-dimensional supersolidity in a dipolar quantum gas, Nature (London) **596**, 357 (2021).

[21] T. Bland, E. Poli, C. Politi, L. Klaus, M. A. Norcia, F. Ferlaino, L. Santos, and R. N. Bisset, Two-Dimensional Supersolid Formation in Dipolar Condensates, Phys. Rev. Lett. **128**, 195302 (2022).

[22] R. Bombin, J. Boronat, and F. Mazzanti, Dipolar Bose Supersolid Stripes, Phys. Rev. Lett. **119**, 250402 (2017).

[23] D. Baillie and P. B. Blakie, Droplet Crystal Ground States of a Dipolar Bose Gas, Phys. Rev. Lett. **121**, 195301 (2018).

[24] Y.-C. Zhang, F. Maucher, and T. Pohl, Supersolidity around a Critical Point in Dipolar Bose-Einstein Condensates, Phys. Rev. Lett. **123**, 015301 (2019).

[25] Y.-C. Zhang, T. Pohl, and F. Maucher, Phases of supersolids in confined dipolar Bose-Einstein condensates, Phys. Rev. A **104**, 013310 (2021).

[26] J. Hertkorn, J.-N. Schmidt, M. Guo, F. Böttcher, K. S. H. Ng, S. D. Graham, P. Uerlings, T. Langen, M. Zwierlein, and T. Pfau, Pattern formation in quantum ferrofluids: From supersolids to superglasses, Phys. Rev. Res. **3**, 033125 (2021).

[27] E. Poli, T. Bland, C. Politi, L. Klaus, M. A. Norcia, F. Ferlaino, R. N. Bisset, and L. Santos, Maintaining supersolidity in one and two dimensions, Phys. Rev. A **104**, 063307 (2021).

[28] A. Gallemí, S. M. Roccuzzo, S. Stringari, and A. Recati, Quantized vortices in dipolar supersolid Bose-Einstein-condensed gases, Phys. Rev. A **102**, 023322 (2020).

[29] S. M. Roccuzzo, A. Gallemí, A. Recati, and S. Stringari, Rotating a Supersolid Dipolar Gas, Phys. Rev. Lett. **124**, 045702 (2020).

[30] F. Ancilotto, M. Barranco, M. Pi, and L. Reatto, Vortex properties in the extended supersolid phase of dipolar Bose-Einstein condensates, Phys. Rev. A **103**, 033314 (2021).

[31] D. H. J. O'Dell, S. Giovanazzi, and G. Kurizki, Rotons in Gaseous Bose-Einstein Condensates Irradiated by a Laser, Phys. Rev. Lett. **90**, 110402 (2003).

[32] L. Santos, G. V. Shlyapnikov, and M. Lewenstein, Roton-Maxon Spectrum and Stability of Trapped Dipolar Bose-Einstein Condensates, Phys. Rev. Lett. **90**, 250403 (2003).

[33] L. Chomaz, R. M. W. van Bijnen, D. Petter, G. Faraoni, S. Baier, J. H. Becher, M. J. Mark, F. Wächtler, L. Santos, and F. Ferlaino, Observation of roton mode population in a dipolar quantum gas, Nat. Phys. **14**, 442 (2018).

[34] D. Petter, G. Natale, R. M. W. van Bijnen, A. Patscheider, M. J. Mark, L. Chomaz, and F. Ferlaino, Probing the Roton Excitation Spectrum of a Stable Dipolar Bose Gas, Phys. Rev. Lett. **122**, 183401 (2019).

[35] J.-N. Schmidt, J. Hertkorn, M. Guo, F. Böttcher, M. Schmidt, K. S. H. Ng, S. D. Graham, T. Langen, M. Zwierlein, and T. Pfau, Roton Excitations in an Oblate Dipolar Quantum Gas, Phys. Rev. Lett. **126**, 193002 (2021).

[36] F. Böttcher, J.-N. Schmidt, J. Hertkorn, K. S. H. Ng, S. D. Graham, M. Guo, T. Langen, and T. Pfau, New states of matter with fine-tuned interactions: Quantum droplets and dipolar supersolids, Rep. Prog. Phys. **84**, 012403 (2021).

[37] L. Chomaz, I. Ferrier-Barbut, F. Ferlaino, B. Laburthe-Tolra, B. L. Lev, and T. Pfau, Dipolar physics: A review of experiments with magnetic quantum gases, arXiv:2201.02672.

[38] A. Trautmann, P. Ilzhöfer, G. Durastante, C. Politi, M. Sohmen, M. J. Mark, and F. Ferlaino, Dipolar Quantum Mixtures of Erbium and Dysprosium Atoms, Phys. Rev. Lett. **121**, 213601 (2018).

[39] G. Durastante, C. Politi, M. Sohmen, P. Ilzhöfer, M. J. Mark, M. A. Norcia, and F. Ferlaino, Feshbach resonances in an erbium-dysprosium dipolar mixture, Phys. Rev. A **102**, 033330 (2020).

[40] C. Politi, A. Trautmann, P. Ilzhöfer, G. Durastante, M. J. Mark, M. Modugno, and F. Ferlaino, Interspecies interactions in an ultracold dipolar mixture, Phys. Rev. A **105**, 023304 (2022).

[41] D. Scheiermann, L. A. Peña Ardila, T. Bland, R. N. Bisset, and L. Santos, Catalyzation of supersolidity in binary dipolar condensates, arXiv:2202.08259.

[42] H. Saito, Y. Kawaguchi, and M. Ueda, Ferrofluidity in a Two-Component Dipolar Bose-Einstein Condensate, Phys. Rev. Lett. **102**, 230403 (2009).

[43] R. M. Wilson, C. Ticknor, J. L. Bohn, and E. Timmermans, Roton immiscibility in a two-component dipolar Bose gas, Phys. Rev. A **86**, 033606 (2012).

[44] A.-C. Lee, D. Baillie, P. B. Blakie, and R. N. Bisset, Miscibility and stability of dipolar bosonic mixtures, Phys. Rev. A **103**, 063301 (2021).

[45] R. N. Bisset, L. A. P. Ardila, and L. Santos, Quantum Droplets of Dipolar Mixtures, Phys. Rev. Lett. **126**, 025301 (2021).

[46] J. C. Smith, D. Baillie, and P. B. Blakie, Quantum Droplet States of a Binary Magnetic Gas, Phys. Rev. Lett. **126**, 025302 (2021).

[47] H. Kadau, M. Schmitt, M. Wenzel, C. Wink, T. Maier, I. Ferrier-Barbut, and T. Pfau, Observing the Rosensweig instability of a quantum ferrofluid, Nature (London) **530**, 194 (2016).

[48] F. Wächtler and L. Santos, Quantum filaments in dipolar Bose-Einstein condensates, Phys. Rev. A **93**, 061603(R) (2016).

[49] R. N. Bisset, R. M. Wilson, D. Baillie, and P. B. Blakie, Ground-state phase diagram of a dipolar condensate with quantum fluctuations, Phys. Rev. A **94**, 033619 (2016).

[50] A. R. P. Lima and A. Pelster, Quantum fluctuations in dipolar bose gases, Phys. Rev. A **84**, 041604(R) (2011).

[51] If quantum fluctuations are neglected, $a < a^d$ generally means that dipolar condensates can only be metastable [56].

[52] A. J. Leggett, Can a Solid Be "Superfluid"? Phys. Rev. Lett. **25**, 1543 (1970).

[53] P. B. Blakie, D. Baillie, L. Chomaz, and F. Ferlaino, Supersolidity in an elongated dipolar condensate, Phys. Rev. Res. **2**, 043318 (2020).

[54] See Supplemental Material at http://link.aps.org/supplemental/10.1103/PhysRevA.106.053322 for an example real-time simulation showing the preparation of a domain supersolid that is robust to an instantaneous interaction quench.

[55] S. Li, U. N. Le, and H. Saito, Long-lifetime supersolid in a two-component dipolar Bose-Einstein condensate, Phys. Rev. A **105**, L061302 (2022).

[56] T. Lahaye, C. Menotti, L. Santos, M. Lewenstein, and T. Pfau, The physics of dipolar bosonic quantum gases, Rep. Prog. Phys. **72**, 126401 (2009).

[57] P. Ilzhöfer, M. Sohmen, G. Durastante, C. Politi, A. Trautmann, G. Natale, G. Morpurgo, T. Giamarchi, L. Chomaz, M. Mark, and F. Ferlaino, Phase coherence in out-of-equilibrium supersolid states of ultracold dipolar atoms, Nat. Phys. **17**, 356 (2021).

B.2. ArXiv preprint: Synchronization in rotating supersolids

E. Poli[1,4], A. Litvinov[2,4], E. Casotti[2,1], Clemens Ulm[2,1], L. Klaus[2,1], M. J. Mark[1,2], G. Lamporesi[3], T. Bland[1], and F. Ferlaino[1,2]

[1] *Institut für Experimentalphysik, Universität Innsbruck, 6020 Innsbruck, Austria*
[2] *Institut für Quantenoptik und Quanteninformation, Österreichische Akademie der Wissenschaften, 6020 Innsbruck, Austria*
[3] *INO-CNR BEC Center and Dipartimento di Fisica, Università di Trento, Povo, Italy.*
[4] *These authors contributed equally.*

---

† The author of the present thesis performed the numerical eGPE simulations, contributed o the analysis of the experimental data and in writing the manuscript.

Synchronization in rotating supersolids

Elena Poli [iD],[1, *] Andrea Litvinov [iD],[2, *] Eva Casotti [iD],[2, 1] Clemens Ulm [iD],[2, 1] Lauritz Klaus [iD],[2, 1]
Manfred J. Mark [iD],[1, 2] Giacomo Lamporesi [iD],[3] Thomas Bland [iD],[1] and Francesca Ferlaino [iD][1, 2, †]

[1]*Universität Innsbruck, Fakultät für Mathematik, Informatik und Physik,
Institut für Experimentalphysik, 6020 Innsbruck, Austria*
[2]*Institut für Quantenoptik und Quanteninformation, Österreichische Akademie der
Wissenschaften, Technikerstr. 21A, 6020 Innsbruck, Austria*
[3]*Pitaevskii BEC Center, CNR-INO and Dipartimento di Fisica, Università di Trento, 38123 Trento, Italy*

Synchronization is ubiquitous in nature at various scales and fields. This phenomenon not only offers a window into the intrinsic harmony of complex systems, but also serves as a robust probe for many-body quantum systems. One such system is a supersolid: an exotic state that is simultaneously superfluid and solid. Here, we show that putting a supersolid under rotation leads to a synchronization of the crystal's motion to an external driving frequency triggered by quantum vortex nucleation, revealing the system's dual solid-superfluid response. Benchmarking the theoretical framework against experimental observations, we exploit this model as a novel method to investigate the critical frequency required for vortex nucleation. Our results underscore the utility of synchronization as a powerful probe for quantum systems.

Synchronization is a fundamental process whereby two or more distinct oscillators, initially operating at different intrinsic frequencies, adjust their rhythms, eventually evolving to oscillate in unison [1]. Huygens' synchronization, named after its discoverer in the 17th century, is a remarkable example of this phenomenon [2]. He observed that two pendulum clocks, when attached to a common support, eventually synchronize their frequency. Huygens called this the "sympathy of two clocks", noting that the weak motion of the shared support enabled their synchronization. This early observation laid the foundation for understanding synchronization as a coupling-driven adjustment of rhythms. Nowadays, synchronization has become a widely recognized phenomenon that manifests across a broad range of natural and engineered systems. For instance, it is at the foundation of biological phenomena, ranging from the synchronous variation of cell nuclei [3] and the firing of biological oscillators like heart cells [4] to the coordinated blinking of fireflies [5]. More recently, the concept of synchronization has expanded into the realm of quantum physics [6–9], being proposed as a signature of quantum correlation and entanglement [10, 11] and as an important mechanism in preventing quantum many-body systems from dephasing [12].

The study of synchronization in coupled oscillators becomes particularly fascinating when these oscillators represent entangled subsystems within a single many-body quantum state or are linked to distinct spontaneously broken symmetries of the same system. In the latter case, critical questions emerge: How do the oscillatory dynamics associated with each broken symmetry interact under external driving? Can their motion uncover novel collective phenomena and offer deeper insights into the coexistence of these symmetries?

Supersolid states of matter offer a compelling example, in which two symmetries spontaneously break simultaneously [13–15]. These are global gauge symmetry, responsible for macroscopic phase coherence, and translational symmetry, which establishes crystalline order within the system. Recently, many-body quantum states with supersolid proper-

ties have attracted a great interest in a broad range of low-energy systems, including ultracold atoms [16–20], helium crystals [21, 22], superconductors [23–25], and are even predicted in high-energy matter such as neutron stars [26, 27].

Among these diverse platforms, dipolar quantum gases set the paradigm [28, 29]. In such systems, the interplay between short-range contact interactions, characterized by a tunable s-wave scattering length a_s, long-range magnetic dipole-dipole interactions with a fixed dipolar length a_{dd}, and dipolar-enhanced quantum fluctuations leads to the emergence of supersolid ground states [29]. What makes a supersolid intriguing in the context of synchronization is the coexistence of superfluid and solid nature – each distinctly responding to external perturbation, while being described by a single macroscopic wave function. This duality raises key questions. For instance, how can irrotationality of the superfluid flow coexist with rigid body rotation of the solid in a supersolid system of indistinguishable particles? Is there a "clock sympathy" between the superfluid and solid components that enable synchronized motion, or do they operate independently in this unique quantum state?

We address these questions through a combined theoretical and experimental investigation on the behavior of a rotating supersolid. Following theoretical predictions [27, 30–34], such systems have proven to be a fascinating playground to tackle general problems related to rotational flow [33], non-classical moment of inertia [27, 31], and quantization of angular momentum [32] in the broad field of modulated superfluids [30, 34, 35]. Our starting points are the recent realization of circular supersolids exhibiting two-dimensional crystalline order [36, 37] and the observation of vortex nucleation in this system [34]. In this study, we focus on the rotational dynamics by tracing the trajectory of the solid component and connect it to the vortex nucleation of the superfluid, presented in Fig. 1.

Figure 1(a) displays the calculated density isosurfaces for the supersolid ground state of a ^{164}Dy dipolar quantum gas for our experimental parameters. Our simulations employ the zero-temperature extended Gross–Pitaevskii equa-
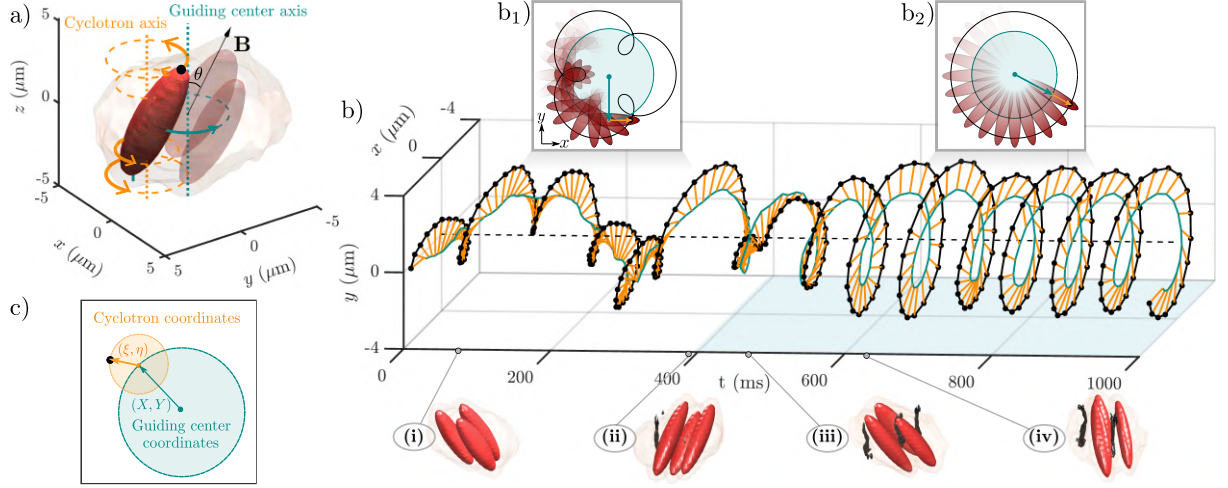
FIG. 1. **Synchronization and concurrent vortex nucleation.** (a) Rotating supersolid from eGPE simulation, the isosurfaces are at 20% (red) and 0.8% (beige) of the maximum density, representing three droplets (one droplet highlighted in plain red color) and the halo, respectively. (b) In-plane trajectory of the droplet's tip (black) together with its decomposition in guiding center (green) and cyclotron (orange) motions. The light-blue shaded area highlights the time window in which a vortex is detected inside the system. The 3D isosurfaces (i)-(iv) correspond to different density frames during the synchronization process, with the black tubes corresponding to vortices. The insets show a schematic illustration of the droplet epitrochoidal (b_1) and circular (b_2) trajectory followed by the droplet. (c) Schematic representation of the decomposition in guiding center and cyclotron coordinates. The results are obtained for parameters: $a_{dd} = 130.8\,a_0$, trap frequencies $[\omega_\perp, \omega_z] = 2\pi \times [50, 95]\,$Hz, atom number $N = 50000$, $a_s = 95\,a_0$, magnetic field tilt angle $\theta = 30°$, $\Omega = 2\pi \times 15\,$Hz, and dissipation constant $\gamma = 0$.

tion (eGPE), incorporating quantum fluctuations [38–41]; see Methods. This approach has been previously demonstrated as highly effective in capturing the complex properties of dipolar supersolid states [34, 36, 37]. Note that, in displaying the isosurfaces, we have intentionally made the high-density crystalline peaks (hereafter referred to as droplets) and the low-density superfluid isosurface (halo) visually distinguishable. However, the particles are distributed continuously throughout the system, and there are not two separate components but a single, unified quantum state. As shown in the figure, due to the magnetic nature of the dipolar interactions, the droplets align along the magnetic field axis, **B**, whose axis is tilted relative to the vertical axis.

To impart angular momentum to the system, we rotate the magnetic field at frequency Ω, a technique named magneto-stirring [34, 42, 43]. Figure 1(b) shows the real-time evolution of the system responding to rotation. The full dynamics are captured through following the trajectory of the tip of a single droplet (black filled circle in (a)), as shown by the solid black line in (b). Surprisingly, after a few hundred milliseconds, we observe a drastic change in the droplet's rotational dynamics. Initially, the motion exhibits a double helicoidal behavior, as a consequence of precession and revolution proceeding at different frequencies. This type of trajectory draws an epitrochoidal path, as illustrated in the inset (b_1). On a longer timescale, the motion evolves into a circular trajectory (b_2), in which precession and revolution are frequency locked. When studying the phase pattern of the supersolid during the evolution, we remarkably observe a concurrency

between the appearance of vortex nucleation and the abrupt trajectory change. This behavior can be clearly seen by the 3D density isosurfaces (i)-(iv) where the vortex cores are visualized by black tubes (see Methods).

To gain further insights, each droplet's response to rotation can be decomposed into two circular motions. The revolution around the trap center axis (guiding center axis) is described by the coordinates (X, Y), and the precession around its own vertical axis (cyclotron axis) is captured by the coordinates (ξ, η) [44–46]; see Fig. 1(c).

These two components exhibit notably distinct behaviors, as shown in Fig. 2(a) and (b). Throughout the time evolution, the cyclotron coordinates, describing precession, oscillate at a frequency, ω_c, matching the external driving frequency Ω of the magnetic field **B**. In contrast, the guiding center frequency, ω_g, is initially significantly smaller than Ω, then gradually increases, and eventually synchronizes with the external driving frequency; for the derivation of ω_c and ω_g see Methods. We observe that synchronization occurs concurrently with nucleation of vortices in the system. Figure 2(d) shows the number of vortices extracted within two different radii of interest, see Fig. 2(c). Nucleation in the outer density region already promotes frequency locking between the cyclotron and guiding center motion, as evidenced by the increase in the parameter $\kappa = 1 - \left| \frac{\omega_c - \omega_g}{\omega_c + \omega_g} \right|$, which quantifies the degree of synchronization (i.e. frequency alignment); see Fig 2(e). Eventually, fully synchronous motion ($\kappa = 1$) occurs as vortices approach the center of the supersolid.

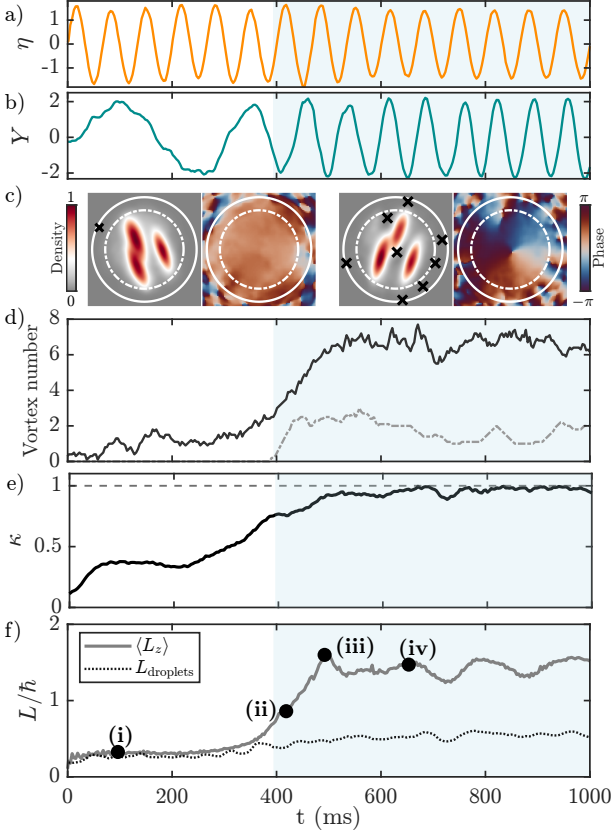When repeating the calculations of Fig. 2 for various Ω

FIG. 2. **Quantification of synchronization.** Time evolution of the cyclotron (a) and guiding center (b) coordinates. (c) Two exemplar frames showing the column density and the central phase slice of the rotating supersolid at $t = 96.2$ ms and $t = 670.7$ ms. The solid and dash-dotted circles mark the cutoff radii $r^* = 6\,\mu$m and $r^* = 4.5\,\mu$m used to count the vortex number (d) time averaged over 35 ms, with the same linestyle as the circles. (e) Frequency alignment κ, as defined in the main text. (f) Total angular momentum $\langle \hat{L}_z \rangle$ and angular momentum of the droplets L_{droplets}, where (i)-(iv) refer to the ones of Fig. 1(b). Across all subplots, the blue shaded region highlights when vortices enter within $r^* = 4.5\,\mu$m. Parameters as in Fig. 1.

(Methods), we find that vortex-induced synchronization is a robust mechanism, occurring across a wide range of $\Omega \geq \Omega^*$ values. Here, Ω^* is the critical frequency required for dynamical vortex nucleation [32, 34, 47]. However, when rotating the supersolid at frequencies sufficiently high to have a ground state energetically supporting vortices, yet still below Ω^*, our driven supersolid does not reach synchronization, i.e. equilibrium, in the considered timescale. Similar lack of equilibration is occurring in the isolated droplet regime; see Fig. 3 and later discussion.

The concurrency between synchronization and vortex nucleation is clearly reflected by the behavior of the total angular momentum $\langle \hat{L}_z \rangle$, plotted in Fig. 2(f). Initially, there is a low and constant value of $\langle \hat{L}_z \rangle$, (i). In this regime, $\langle \hat{L}_z \rangle \approx L_{\text{droplets}} \approx I \times \Omega$, following a rigid-body rotation but with a non-classical moment of inertia I [14, 32]. Here, the
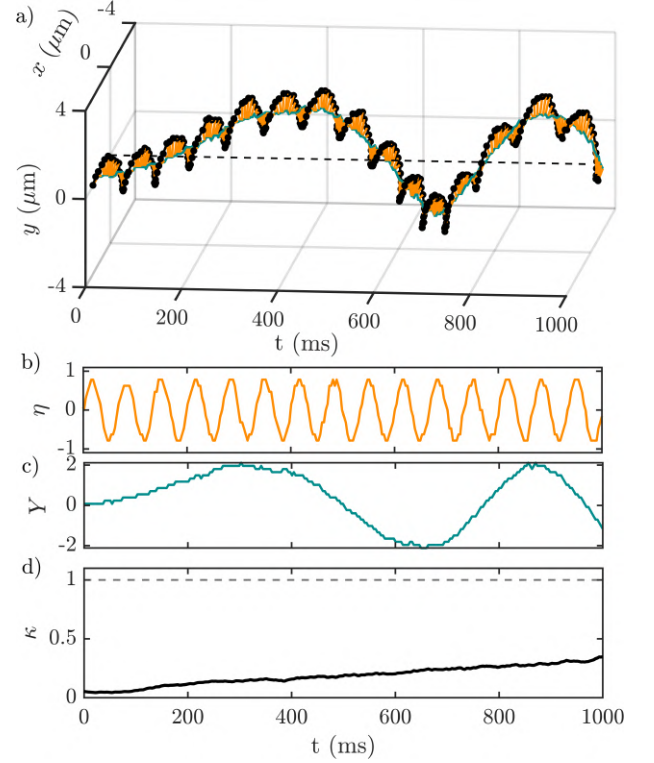

FIG. 3. **Independent droplet regime.** (a) Time evolution of the droplet's edge trajectory and corresponding cyclotron (b) and guiding center coordinate (c). (d) Frequency alignment κ. All the results are obtained for the same parameters of Fig. 1, except for $a_s = 90\,a_0$.

response is dominated by the solid nature of the supersolid. Around $t \sim 400$ ms, $\langle \hat{L}_z \rangle$ rapidly increases when vortices move towards the center (ii), marking the onset of synchronization. Once the synchronization is complete ($\kappa \sim 1$), the angular momentum stabilizes at a plateau (iii)-(iv), indicating that an equilibrium state has been reached in the rotating frame. Here, small oscillations around the equilibrium value indicate variations in the number of vortices and their positions (iii) [48], or excitations of the droplet lattice [27].

These results reveal that the synchronization dynamics are inherent to the dual solid-superfluid response to rotation of the system. Indeed, by repeating similar real-time simulations but starting with a droplet crystal, with a negligible superfluid link connecting the droplets and no vortices, we observe the absence of synchronization ($\kappa < 0.35$) as shown in Fig. 3. The gradual increase might be due to a residual halo connecting the droplets.

Building on our theoretical predictions, we explore potential synchronization phenomena experimentally. In brief, our dipolar supersolid of ^{164}Dy is produced via direct evaporative cooling [20, 36]. We confine the system in a cylindrically symmetric optical dipole trap with harmonic frequencies $(\omega_\perp, \omega_z)$. During the last stages of evaporation, we tilt **B** by $\theta = 30°$ and we produce a long-lived supersolid with four droplets. We then rotate the magnetic field with a constant an-
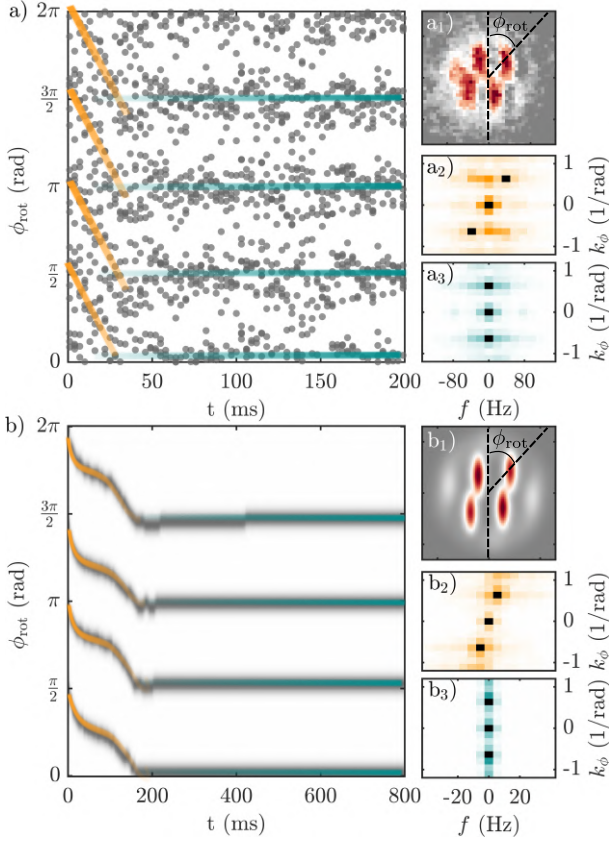
FIG. 4. **Experimental observation of the synchronization process.**
Angular position of the droplets (a_1, b_1) in the rotating frame as a
function of time in experiment (a) and simulation (b). The orange
and green lines are guides to the eye for the unsynchronized and syn-
chronized cases, respectively. (a_2, a_3) 2D Fourier transform of the
experimental droplet angular position for early $[0, 50]$ ms and late
$[60, 110]$ ms time intervals, respectively. (b_2, b_3) 2D Fourier trans-
form of the theoretical droplet angular position for early $[0, 200]$ ms
and late $[200, 400]$ ms time intervals, respectively. The colorbars in
(a_2, b_2) and (a_3, b_3) go from white to orange and white to green, re-
spectively, with the three largest peaks highlighted in black. The
experimental data is taken for $\Omega = 2\pi \times 9$ Hz, trap frequencies
$[\omega_\perp, \omega_z] = 2\pi \times [50.5(6), 137(3)]$ Hz, B=18.24(2) G, $N \approx 69000$.
Theoretical simulations are done for $\Omega = 2\pi \times 9$ Hz, $N = 60000$,
$a_s = 90\,a_0$, trap frequencies $[\omega_\perp, \omega_z] = 2\pi \times [50, 149]$ Hz, dissipa-
tion parameter $\gamma = 0.08$.

gular velocity $\Omega = 2\pi \times 9$ Hz for 300 ms following the mag-
netostirring protocol [34, 43]. Finally, we track the position
of the rotating droplets by taking destructive phase-contrast
images along z after 3 ms of expansion, during which the **B**
is kept static and tilted. By fitting four Gaussian functions to
the acquired column density profiles, we extract the center-of-
mass position of each droplet and obtain their azimuthal an-
gle $\phi_{\rm rot} = \arctan(Y/X)$ to detect the guiding center motion,
which is more convenient when plotting all droplet trajecto-
ries together. We note that the initial tilt of the magnetic field
breaks the cylindrical symmetry of the system, making the
initial position of the four droplets repeatable over different

experimental runs.

Figure 4 presents the experimental (a) and theoretical (b)
results by plotting $\phi_{\rm rot}$ of each of the four droplets. Visual-
izing the data in the rotating frame defined by Ω makes the
effect of synchronization strikingly apparent. Constant $\phi_{\rm rot}$
means frequency-locking with Ω, whereas deviation from this
behavior signalizes non-synchronous motion. Both theory and
experiment show that $\phi_{\rm rot}$ initially traces an oblique path, in-
dicating that the droplets' center of mass is moving in the ro-
tating frame. For later times, $\phi_{\rm rot}$ becomes constant: the sig-
nature of synchronization with the external driving frequency.
Comparing two-dimensional Fourier transforms in $\phi_{\rm rot}$ and t
of the data for two selected time intervals, one at early times
and the other at later times, further confirms this behavior. For
each selected time interval, this gives three peaks, reflecting
the periodicity of $\phi_{\rm rot}$ in time. At early times, peaks appear
at a finite frequency and produce a tilted pattern (a_2-b_2), indi-
cating an asynchronous motion. At later times, instead, they
align at zero frequency, the signature of synchronization (a_3-
b_3). Both the data and their Fourier transform show an excel-
lent agreement with the theory and confirm the experimental
observation of synchronization. We note that, as is common
in vortex studies, experimental noise and temperature effects
lead to a faster vortex nucleation than the one predicted from
mean-field theory [43, 49–51].

As the theory pinpoints a systematic correlation between
vortex entering the system and the synchronization of the
droplet motion, we can use the latter mechanism to further
extract information on the vortex nucleation in the supersolid.
Particularly interesting is the regime of low rotation frequen-
cies and the quest of the minimal Ω for which a vortex is
energetically stable. To address this point, we now develop
a different protocol. Instead of driving rotations at constant
Ω, we implement a scheme, in which Ω is slowly increased
linearly from zero to $\Omega = 2\pi \times 8$ Hz over 200 ms. Dur-
ing the initial part of the slow ramp, the system remains syn-
chronized since it adiabatically follows its ground state in the
rotating frame. This is shown in Fig. 5 by the constant $\phi_{\rm rot}$
(straight green lines). Around $\Omega \sim 2\pi \times 5$ Hz the trajectory
of the droplets exhibits a sudden change. Here, the system
desynchronizes (orange lines) since it has to adjust to the new
ground state in the rotating frame, now possessing a vortex.
Around $\Omega \sim 2\pi \times 6$ Hz, the system restores the equilibrium
in the rotating frame and the synchronization condition, with
the $\phi_{\rm rot}$ forming a straight horizontal path again, suggesting
that the first vortex has entered. Thus, from this dynamics,
we can infer an upper limit for the energetic critical rotation
frequency for vortex nucleation to be $\Omega_c \leq 2\pi \times 6$ Hz. This
value is in excellent agreement with the predicted critical fre-
quency, obtained from calculations of the supersolid ground-
state in the rotating frame, as shown in Fig. 5(b). The corre-
sponding angular momentum exhibits a sudden jump around
$\Omega_c \sim 2\pi \times 5$ Hz when the ground state undergoes a transi-
tion from the zero- to the one-vortex state. The amplitude of
the jump quantifies the angular momentum carried by the vor-
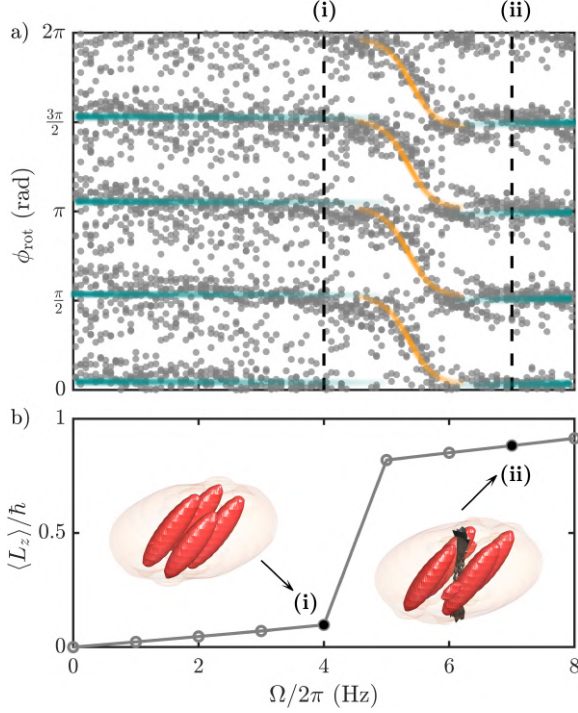tex at the center of the supersolid, which is equal to $0.72\hbar$.

FIG. 5. **Synchronization during a slow ramp of the driving rotation frequency.** (a) $\phi_{\rm rot}$ measured at different points of the slow ramp of Ω from 0 to $2\pi \times 8$ Hz in 200 ms. The orange and green lines are a guide to the eye for the unsynchronized and synchronized cases, respectively. Experimental parameters: trap frequency $[\omega_\perp, \omega_z] = 2\pi \times [50.3(4), 140.1(5)]$ Hz, $N \approx 69000$, B=18.30(2) G. (b) $\langle \hat{L}_z \rangle$ for ground states in the rotating frame varying Ω together with exemplary density isosurfaces. Simulation parameters: $N = 70000$, $a_s = 92\,a_0$, trap frequencies $2\pi \times [50, 140]$ Hz.

As pointed out in Ref. [32], the sub-unity value is directly connected to the reduced superfluid fraction characteristic of modulated superfluids. The nucleation of a vortex at this low frequency is concurrent with a dynamical instability of the superfluid quadrupole mode, so far not observed [34].

In conclusion, we have demonstrated that synchronization phenomena arise in rotating dipolar supersolids driven by an external magnetic field. We find that the synchronization process, driven by vortex nucleation, reflects the system's approach towards equilibrium and reveals the solid-superfluid dual nature of the supersolid. By decomposing the droplet motion into cyclotron and guiding center coordinates, we differentiate between precession around the cyclotron axis, which consistently synchronizes with the driving frequency, from global revolution. At large rotation frequencies, the latter initially displays asynchronous motion. Here, while the supersolid's ground state in the rotating frame contains vortices, the driven supersolid begins out of equilibrium and is vortex-free. As it converges toward its ground state over time, the system only synchronizes when vortices enter. Furthermore, our analysis of the supersolid's angular momentum confirms that synchronization arises from the delayed superfluid

response, in contrast to the immediate solid-like response. Finally, we identify the synchronization as a novel diagnostic tool to measure the critical rotation frequency required for vortex nucleation. Future studies could use desynchronization and resynchronization during the slow-down of the driving frequency as a probe to understand vortex emission dynamics in analog to glitches observed in neutron stars [27, 52].

Author contributions

A.L., E.C., C.U., L.K., M.J.M., G.L., and F.F. performed the experimental work and data analysis. E.P. and T.B. performed the theoretical work. All authors contributed to the interpretation of the results and the preparation of the manuscript.

———

* These authors contributed equally to this work.
† Correspondence should be addressed to: francesca.ferlaino@uibk.ac.at

[1] A. Pikovsky, M. Rosenblum, and J. Kurths, *Synchronization: A Universal Concept in Nonlinear Sciences*, Cambridge Nonlinear Science Series (Cambridge University Press, 2001).

[2] C. Huygens, *Œuvres complètes de Christiaan Huygens: Correspondance 1664-1665*, Vol. 5 (Martinus Nijhoff, 1893).

[3] G. Banfalvi, Overview of cell synchronization, Cell cycle synchronization: methods and protocols , 1 (2011).

[4] R. E. Mirollo and S. H. Strogatz, Synchronization of pulse-coupled biological oscillators, SIAM Journal on Applied Mathematics **50**, 1645 (1990), https://doi.org/10.1137/0150098.

[5] J. Buck and E. Buck, Biology of synchronous flashing of fireflies (1966).

[6] C. A. Holmes, C. P. Meaney, and G. J. Milburn, Synchronization of many nanomechanical resonators coupled via a common cavity field, Phys. Rev. E **85**, 066203 (2012).

[7] G. Manzano, F. Galve, G. L. Giorgi, E. Hernández-García, and R. Zambrini, Synchronization, quantum correlations and entanglement in oscillator networks, Scientific Reports **3**, 1439 (2013).

[8] A. Mari, A. Farace, N. Didier, V. Giovannetti, and R. Fazio, Measures of quantum synchronization in continuous variable systems, Phys. Rev. Lett. **111**, 103605 (2013).

[9] V. Ameri, M. Eghbali-Arani, A. Mari, A. Farace, F. Kheirandish, V. Giovannetti, and R. Fazio, Mutual information as an order parameter for quantum synchronization, Phys. Rev. A **91**, 012301 (2015).

[10] D. Witthaut, S. Wimberger, R. Burioni, and M. Timme, Classical synchronization indicates persistent entanglement in isolated quantum systems, Nature communications **8**, 14829 (2017).

[11] A. Roulet and C. Bruder, Quantum synchronization and entanglement generation, Physical review letters **121**, 063601 (2018).

[12] H. Qiu, R. Zambrini, A. Polls, J. Martorell, and B. Juliá-Díaz, Hybrid synchronization in coupled ultracold atomic gases, Physical Review A **92**, 043619 (2015).

[13] E. P. Gross, Unified Theory of Interacting Bosons, Phys. Rev. **106**, 161 (1957).

[14] A. J. Leggett, Can a solid be "superfluid"?, Physical Review Letters **25**, 1543 (1970).

[15] M. Boninsegni and N. V. Prokof'ev, Colloquium: Supersolids: What and where are they?, Reviews of Modern Physics **84**, 759 (2012).

[16] J. Léonard, A. Morales, P. Zupancic, T. Esslinger, and T. Donner, Supersolid formation in a quantum gas breaking a continuous translational symmetry, Nature **543**, 87 (2017).

[17] J.-R. Li, J. Lee, W. Huang, S. Burchesky, B. Shteynas, F. Ç. Top, A. O. Jamison, and W. Ketterle, A stripe phase with supersolid properties in spin–orbit-coupled Bose–Einstein condensates, Nature **543**, 91 (2017).

[18] F. Böttcher, J.-N. Schmidt, M. Wenzel, J. Hertkorn, M. Guo, T. Langen, and T. Pfau, Transient Supersolid Properties in an Array of Dipolar Quantum Droplets, Phys. Rev. X **9**, 011051 (2019).

[19] L. Tanzi, E. Lucioni, F. Famà, J. Catani, A. Fioretti, C. Gabbanini, R. N. Bisset, L. Santos, and G. Modugno, Observation of a Dipolar Quantum Gas with Metastable Supersolid Properties, Phys. Rev. Lett. **122**, 130405 (2019).

[20] L. Chomaz, D. Petter, P. Ilzhöfer, G. Natale, A. Trautmann, C. Politi, G. Durastante, R. M. W. van Bijnen, A. Patscheider, M. Sohmen, M. J. Mark, and F. Ferlaino, Long-Lived and Transient Supersolid Behaviors in Dipolar Quantum Gases, Phys. Rev. X **9**, 021012 (2019).

[21] L. V. Levitin, B. Yager, L. Sumner, B. Cowan, A. J. Casey, J. Saunders, N. Zhelev, R. G. Bennett, and J. M. Parpia, Evidence for a spatially modulated superfluid phase of ^{3}He under confinement, Phys. Rev. Lett. **122**, 085301 (2019).

[22] J. Nyéki, A. Phillis, A. Ho, D. Lee, P. Coleman, J. Parpia, B. Cowan, and J. Saunders, Intertwined superfluid and density wave order in two-dimensional 4he, Nature Physics **13**, 455 (2017).

[23] Y. Liu, T. Wei, G. He, Y. Zhang, Z. Wang, and J. Wang, Pair density wave state in a monolayer high-t c iron-based superconductor, Nature **618**, 934 (2023).

[24] M. H. Hamidian, S. D. Edkins, S. H. Joo, A. Kostin, H. Eisaki, S. Uchida, M. J. Lawler, E.-A. Kim, A. P. Mackenzie, K. Fujita, J. Lee, and J. C. S. Davis, Detection of a cooper-pair density wave in bi2sr2cacu2o8+x, Nature **532**, 343–347 (2016).

[25] J. Xiang, C. Zhang, Y. Gao, W. Schmidt, K. Schmalzl, C.-W. Wang, B. Li, N. Xi, X.-Y. Liu, H. Jin, et al., Giant magnetocaloric effect in spin supersolid candidate na2baco (po4) 2, Nature **625**, 270 (2024).

[26] N. Chamel, Neutron conduction in the inner crust of a neutron star in the framework of the band theory of solids, Physical Review C—Nuclear Physics **85**, 035801 (2012).

[27] E. Poli, T. Bland, S. J. M. White, M. J. Mark, F. Ferlaino, S. Trabucco, and M. Mannarelli, Glitches in rotating supersolids, Phys. Rev. Lett. **131**, 223401 (2023).

[28] M. A. Norcia and F. Ferlaino, Developments in atomic control using ultracold magnetic lanthanides, Nature Physics **17**, 1349 (2021).

[29] L. Chomaz, I. Ferrier-Barbut, F. Ferlaino, B. Laburthe-Tolra, B. L. Lev, and T. Pfau, Dipolar physics: a review of experiments with magnetic quantum gases, Reports on Progress in Physics **86**, 026401 (2022).

[30] N. Henkel, F. Cinti, P. Jain, G. Pupillo, and T. Pohl, Supersolid vortex crystals in rydberg-dressed bose-einstein condensates, Phys. Rev. Lett. **108**, 265301 (2012).

[31] S. Roccuzzo, A. Gallemí, A. Recati, and S. Stringari, Rotating a supersolid dipolar gas, Physical review letters **124**, 045702 (2020).

[32] A. Gallemí, S. Roccuzzo, S. Stringari, and A. Recati, Quantized vortices in dipolar supersolid Bose-Einstein-condensed gases, Physical Review A **102**, 023322 (2020).

[33] F. Ancilotto, M. Barranco, M. Pi, and L. Reatto, Vortex properties in the extended supersolid phase of dipolar Bose-Einstein condensates, Physical Review A **103**, 033314 (2021).

[34] E. Casotti, E. Poli, L. Klaus, A. Litvinov, C. Ulm, C. Politi, M. J. Mark, T. Bland, and F. Ferlaino, Observation of vortices in a dipolar supersolid, Nature **635**, 327–331 (2024).

[35] A. Bulgac and M. M. Forbes, Unitary fermi supersolid: The larkin-ovchinnikov phase, Physical Review Letters **101**, 215301 (2008).

[36] M. A. Norcia, C. Politi, L. Klaus, E. Poli, M. Sohmen, M. J. Mark, R. N. Bisset, L. Santos, and F. Ferlaino, Two-dimensional supersolidity in a dipolar quantum gas, Nature **596**, 357–361 (2021).

[37] T. Bland, E. Poli, C. Politi, L. Klaus, M. A. Norcia, F. Ferlaino, L. Santos, and R. N. Bisset, Two-Dimensional Supersolid Formation in Dipolar Condensates, Phys. Rev. Lett. **128**, 195302 (2022).

[38] F. Wächtler and L. Santos, Quantum filaments in dipolar Bose-Einstein condensates, Phys. Rev. A **93**, 061603 (2016).

[39] I. Ferrier-Barbut, H. Kadau, M. Schmitt, M. Wenzel, and T. Pfau, Observation of Quantum Droplets in a Strongly Dipolar Bose Gas, Phys. Rev. Lett. **116**, 215301 (2016).

[40] L. Chomaz, S. Baier, D. Petter, M. J. Mark, F. Wächtler, L. Santos, and F. Ferlaino, Quantum-Fluctuation-Driven Crossover from a Dilute Bose-Einstein Condensate to a Macrodroplet in a Dipolar Quantum Fluid, Phys. Rev. X **6**, 041039 (2016).

[41] R. N. Bisset, R. M. Wilson, D. Baillie, and P. B. Blakie, Ground-state phase diagram of a dipolar condensate with quantum fluctuations, Phys. Rev. A **94**, 033619 (2016).

[42] S. B. Prasad, T. Bland, B. C. Mulkerin, N. G. Parker, and A. M. Martin, Vortex lattice formation in dipolar Bose-Einstein condensates via rotation of the polarization, Physical Review A **100**, 023625 (2019).

[43] L. Klaus, T. Bland, E. Poli, C. Politi, G. Lamporesi, E. Casotti, R. N. Bisset, M. J. Mark, and F. Ferlaino, Observation of vortices and vortex stripes in a dipolar condensate, Nature Physics **18**, 1453 (2022).

[44] F. F. Chen et al., *Introduction to plasma physics and controlled fusion*, Vol. 1 (Springer, 1984).

[45] R. J. Fletcher, A. Shaffer, C. C. Wilson, P. B. Patel, Z. Yan, V. Crépel, B. Mukherjee, and M. W. Zwierlein, Geometric squeezing into the lowest Landau level, Science **372**, 1318 (2021).

[46] M. Caldara, A. Richaud, M. Capone, and P. Massignan, Mas-

sive superfluid vortices and vortex necklaces on a planar annulus, SciPost Phys. **15**, 057 (2023).

[47] A. L. Fetter, Rotating trapped Bose-Einstein condensates, Rev. Mod. Phys. **81**, 647 (2009).

[48] D. Butts and D. Rokhsar, Predicted signatures of rotating bose–einstein condensates, Nature **397**, 327 (1999).

[49] N. G. Parker and C. S. Adams, Emergence and decay of turbulence in stirred atomic bose-einstein condensates, Physical Review Letters **95**, 145301 (2005).

[50] N. Parker and C. Adams, Response of an atomic bose–einstein condensate to a rotating elliptical trap, J. Phys. B **39**, 43 (2005).

[51] D. Hernández-Rajkov, N. Grani, F. Scazza, G. Del Pace, W. Kwon, M. Inguscio, K. Xhani, C. Fort, M. Modugno, F. Marino, *et al.*, Connecting shear flow and vortex array instabilities in annular atomic superfluids, Nature Physics **20**, 939 (2024).

[52] T. Bland, F. Ferlaino, M. Mannarelli, E. Poli, and S. Trabucco, Exploring pulsar glitches with dipolar supersolids, Few-Body Systems **65**, 81 (2024).

[53] T. D. Lee, K. Huang, and C. N. Yang, Eigenvalues and eigenfunctions of a Bose system of hard spheres and its low-temperature properties, Physical Review **106**, 1135 (1957).

[54] A. R. P. Lima and A. Pelster, Quantum fluctuations in dipolar Bose gases, Phys. Rev. A **84**, 041604 (2011).

[55] P. B. Blakie, A. Bradley, M. Davis, R. Ballagh, and C. Gardiner, Dynamics and statistical mechanics of ultra-cold bose gases using c-field techniques, Advances in Physics **57**, 363 (2008).

[56] N. P. Proukakis, G. Rigopoulos, and A. Soto, Self-consistent stochastic finite-temperature modelling: Ultracold bose gases with local (s-wave) and long-range (dipolar) interactions, arXiv preprint arXiv:2407.20178 (2024).

[57] I. Ferrier-Barbut, M. Wenzel, F. Böttcher, T. Langen, M. Isoard, S. Stringari, and T. Pfau, Scissors Mode of Dipolar Quantum Droplets of Dysprosium Atoms, Phys. Rev. Lett. **120**, 160402 (2018).

Methods

Theoretical description

We study the ground state and dynamics of a supersolid state using an extended Gross-Pitaevskii formalism. We consider a supersolid made of ^{164}Dy dipolar atoms of mass m trapped in a cylindrically symmetric harmonic potential $V(x,y,z) = \frac{1}{2}m\left[\omega_\perp^2(x^2+y^2)+\omega_z^2 z^2\right]$, where $\omega_\perp$ (ω_z) is the radial (axial) trap frequency. At zero temperature, the inter-particle interaction is described by the pseudo-potential

$$U(\mathbf{r},t) = \frac{4\pi\hbar^2 a_s}{m}\delta(\mathbf{r}) + \frac{3\hbar^2 a_{dd}}{m}\frac{1-3(\hat{\mathbf{e}}(t)\cdot\mathbf{r})^2}{r^3}. \quad (S1)$$

The first term represents the short-range repulsive contact interaction, characterized by the tunable s-wave scattering length a_s. The second term represents the long-range anisotropic dipole-dipole interaction. For ^{164}Dy atoms, $a_{dd} = 130.8\,a_0$. For the experimentally relevant trap geometries and atom numbers, we find two-dimensional supersolid ground states for $\epsilon_{dd} = a_{dd}/a_s \gtrsim 1.3$. The unit vector $\hat{\mathbf{e}}(t) = (\sin\theta\cos\varphi(t), \sin\theta\sin\varphi(t), \cos\theta)$ indicates the polarization direction of the dipoles, which is set by the external magnetic field $\mathbf{B}$. In our study, $\mathbf{B}$ has a fixed angle of $\theta = 30°$ with respect to the vertical $z-$axis. The time-dependent azimuthal angle is $\varphi(t) = \int_0^t dt'\Omega(t')$, where $\Omega(t)$ is the angular velocity at time t.

Under this formalism, the extended Gross-Pitaevskii equation (eGPE) reads [38, 41]

$$i\hbar\frac{\partial\Psi(\mathbf{r},t)}{\partial t} = (\alpha-i\gamma)\mathcal{L}_{GP}\left[\Psi(\mathbf{r},t)\right]\Psi(\mathbf{r},t), \quad (S2)$$

where $\mathcal{L}_{GP}$ is the Gross-Pitaevskii operator defined as

$$\mathcal{L}_{GP}\left[\Psi(\mathbf{r},t)\right] = \left[-\frac{\hbar^2\nabla^2}{2m}+V(x,y,z)\right.$$
$$+\int d^3\mathbf{r}'\,U(\mathbf{r}-\mathbf{r}',t)\left|\Psi(\mathbf{r}',t)\right|^2 \quad (S3)$$
$$\left.+\gamma_{QF}|\Psi(\mathbf{r},t)|^3\right],$$

with $\Psi(\mathbf{r},t)$ being the condensate wave function. The last term of $\mathcal{L}_{GP}$ represents the Lee-Huang-Yang correction describing quantum fluctuations [53, 54], with coefficient $\gamma_{QF} = \frac{128\hbar^2}{3m}\sqrt{a_s^5}\,\mathrm{Re}\{\mathcal{Q}_5(\epsilon_{dd})\}$, where $\mathcal{Q}_5(\varepsilon_{dd}) = \int_0^1 du\left(1-\varepsilon_{dd}+3u^2\varepsilon_{dd}\right)^{5/2}$. This term is necessary for the stabilization of the supersolid state against collapse [41].

In Eq. (S2) the parameters α and γ determine the type of evolution. Imaginary time evolution $\{\alpha=0,\gamma=1\}$ is used to find the ground state of the system. Real-time evolution corresponding to $\{\alpha=1,\gamma=0\}$ is used in the study of synchronization dynamics in Figs. 1, 2, and 3. Complex-time evolution with $\{\alpha=1,\gamma\neq 0\}$ captures the dynamics under dissipation, accelerating the nucleation process [27], and providing a closer match to the experimental results shown in Fig. 4.
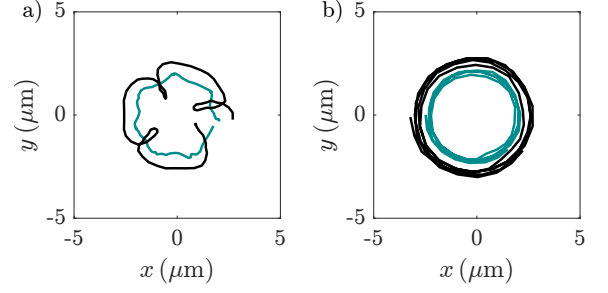

FIG. S1. Trajectory of the droplet's tip (black line) and center of mass (green line) for the (a) unsynchronized and (b) synchronized state. For the unsynchronized state we show the time dynamics for $t < 300\,\mathrm{ms}$, and for the synchronized state we show the time dynamics for $t > 800\,\mathrm{ms}$. The other parameters are the same as Fig. 1 in the main text.

However, accounting for dissipation through a single constant parameter γ is a simplified approach, whereas in experiments the situation is more complicated, e. g. the spatial dependence of the thermal cloud [55]. Indeed, the observed dynamics are typically faster than the one in the simulation, and may call for more sophisticated finite temperature theories to reconcile this difference [56].

It is important to compare the results of the real-time evolution with the actual ground-state, towards which the system is expected to evolve. We calculate the ground state in the rotating frame. The effective Hamiltonian in this frame includes a term $-\Omega\hat{L}_z$ in Eq. (S3), where $\hat{L}_z = x\hat{p}_y - y\hat{p}_x$ is the angular momentum operator. We use this approach to generate Fig. 5(b).

Both in the real (dynamics) and imaginary (ground-state) time evolution, we identify the presence of vortices inside the system by detecting 2π phase windings of the wave function within a radius r^* centered at the origin. In Fig. 1 we use $r^* = 4.5\,\mu$m. To visualize the vortex tubes in Fig. 1 and Fig. 4, we plot isosurfaces of the velocity field.

Coordinates decomposition

To reveal the dual nature of the system's response, we decompose the droplet trajectory into its center-of-mass motion (guiding center coordinate) and precession motion (cyclotron coordinate). These two sets of coordinates are extensively used in e. g. plasma orbit theory [44] and, more recently, to study rotating BECs [45, 46]. We extract these coordinates by identifying the position of the density maxima in two distinct z-slices of the 3D wavefunction. First, we use the density slice at $z = 0$ to determine the position of the center of mass of each droplet relative to the origin, which we associate with the guiding center coordinates (X,Y). Next, the density slice at $z = 2.5\,\mu$m is used to identify the position of the edge of each droplet, denoted as (x_d,y_d). The cyclotron vector (ξ,η) is then obtained by subtracting these two quantities: $(\xi,\eta) = (x_d,y_d) - (X,Y)$ (see Fig. 1(c) in the main

text). The choice of the z-slice for $z \neq 0$ influences the magnitude of the cyclotron vector but does not affect its orbital frequency. Importantly, our results remain robust regardless of the chosen z-slice and the choice of the droplet. In Fig. S1 we illustrate the in-plane projected position of the droplet's tip (black line) and droplet's center of mass (green line) for the (a) unsynchronized and (b) synchronized state, highlighting the analogy to the epitrochoidal and circular orbits shown as a sketch in the insets (b$_1$-b$_2$) of Fig. 1. For the calculation of the frequency alignment κ, we extract the instantaneous frequencies of the guiding center vector, ω_g, and of the cyclotron vector, ω_c. We compute those quantities by first extracting the angle of the guiding center and cyclotron vector at time t from the respective coordinates, namely $\varphi_g = \arctan(Y/X)$ and $\varphi_c = \arctan(\eta/\xi)$. We then calculate the time derivatives $\omega_g = \Delta\varphi_g/\Delta t$ and $\omega_c = \Delta\varphi_c/\Delta t$, with $\Delta t = 3.5$ ms.

Droplet's angular momentum calculation

The guiding center and cyclotron coordinates provide a comprehensive framework to describe the motion of the droplets during the synchronization process, offering a tool to estimate the droplet's angular momentum. In general, the total angular momentum $\langle \hat{L}_z \rangle$ of a rotating supersolid can be decomposed into two contributions, L_s and L_{vort} [27, 31, 32]. Here, L_s represents the angular momentum associated with the solid response, reflecting the system's non-zero moment of inertia, whereas L_{vort} is the superfluid angular momentum stored in the form of quantized vortices. We estimate L_s by summing the contributions from both the cyclotron motion and the guiding center motion of the droplets, giving the droplet angular momentum

$$
\begin{aligned}
L_{droplets} &= L_{guid} + L_{cycl} \\
&= I_0\, \omega_{guid} + \sum_{i=1}^{N_d} I_{droplets}^i\, \omega_{cycl}\,, \quad \text{(S4)}
\end{aligned}
$$

where N_d is the number of droplets in the supersolid state. Since these motions occur around different axes, we compute two distinct moments of inertia. The moment of inertia $I_{droplets}^i$ for the i-th droplet, rotating around its own axis, is calculated through [57]

$$
I_{droplets}^i = \frac{1}{2} m N_i \frac{\left(\sigma_y^2 - \sigma_x^2\right)^2}{\sigma_x^2 + \sigma_y^2}\,, \quad \text{(S5)}
$$

where σ_x and σ_y are the droplet's widths, obtained by fitting the column density with a Gaussian, and N_i is the estimated number of atoms in the droplet. The moment of inertia for the supersolid as a whole, rotating around the origin, is computed with

$$
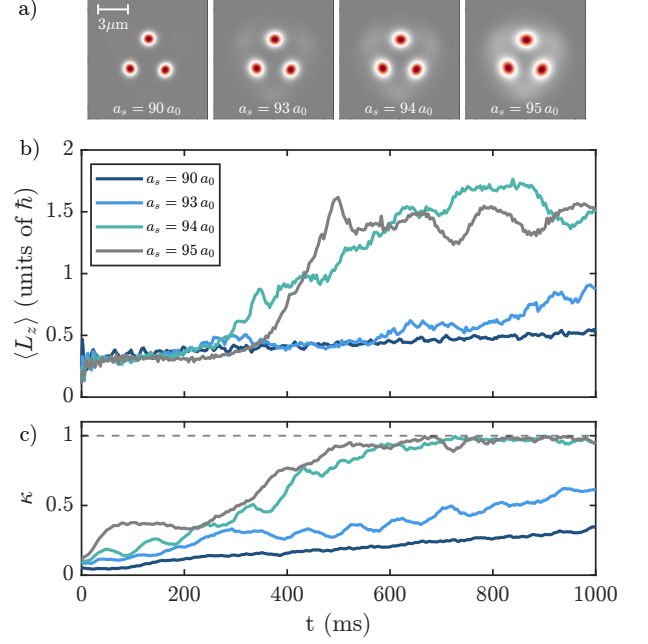I_0 = m \frac{\left\langle y^2 - x^2 \right\rangle^2}{\left\langle y^2 + x^2 \right\rangle}\,, \quad \text{(S6)}
$$

FIG. S2. Synchronization process for different values of a_s. (a) Ground state density distributions with $\theta = 0°$, (b) angular momentum $\langle \hat{L}_z \rangle$ during the time evolution with $\theta = 30°$ and (c) frequency alignment κ. The other parameters are the same as Fig. 2.

where $\langle \cdot \rangle$ is the expectation value calculated for the initial total wave function, with the reference frame centered at $(0,0)$. Previous work has shown that this estimate deviates from the true moment of inertia by approximately 5% [31]. The evolution of $L_{droplets}$ is shown in Fig. 2(e).

Synchronization for different scattering lengths

The synchronization process only occurs in the supersolid phase. This becomes clear when we study the angular momentum and frequency alignment κ for different values of a_s. Figure S2 shows these two quantities for initial states at different a_s, spanning from $a_s = 95\,a_0$, where the supersolid has strong superfluid connection between droplets, to $a_s = 90\,a_0$, in the independent droplet regime. In this data, we magneto-stir at a constant frequency $\Omega = 2\pi \times 15$ Hz. In the supersolid regime, the angular momentum exhibits a behavior similar to Fig. 2(e) in the main text: it is initially constant, before suddenly increasing and ultimately stabilizing at a plateau when vortices move to the center. For this dynamical protocol at constant Ω, the onset of vortex nucleation–marking the beginning of synchronization–reflects low frequency quadrupole mode resonances, which act as a seed for vortex nucleation, as discussed in Ref. [34]. In contrast, in the independent droplet regime the angular momentum increases gradually without any sharp rise, indicating that vortices do not enter and synchronization is not occurring in an experimentally feasible timescale.
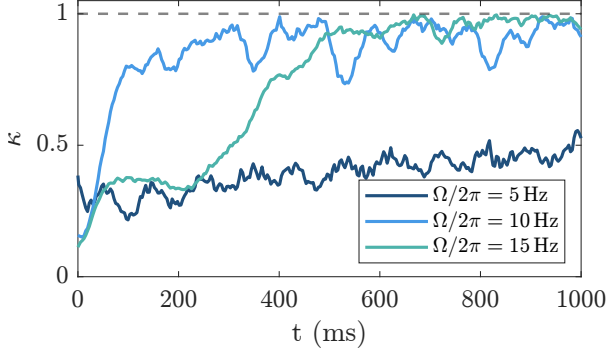
FIG. S3. Frequency alignment κ for different values of rotation frequency Ω. The other simulation parameters are the same as Fig. 2.
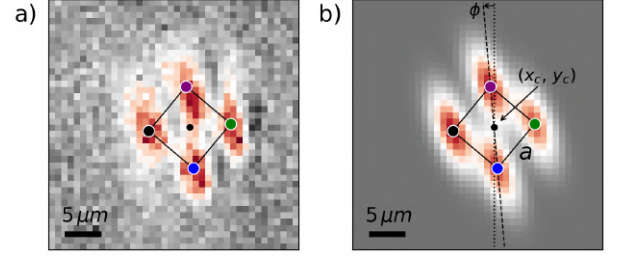

FIG. S4. Exemplar fit procedure. a) Experimental image, b) fit result. The colored corners of the square, with edge length a, indicate the fitted positions of the four droplets. The guiding center origin (x_c, y_c) is indicated by the solid black dot. For this image, the extracted rotation is $\phi = -5.15°$.

To quantitatively relate the results across different scattering lengths, we compare the frequency alignment κ. In Fig. S2(c) we show that synchronization is only achieved when the initial state is a supersolid. We interpret these results as follows: when the density coupling between droplets is negligible, this dynamical protocol is insufficient to bring the system to its equilibrium configuration in the rotating frame–where all droplets rotate at the same frequency–and, thus, synchronization fails to occur within an experimentally accessible timescale. We hypothesize that synchronization may never occur in the independent droplet regime in an experiment. In the theory, we use a single valued wavefunction that is forced to have a residual coupling between the droplets, eventually converging to a stationary solution to the underlying equation.

Synchronization for different Ω

It is interesting to consider the synchronization process for different fixed rotation frequencies. In Fig. S3 we extend the synchronization analysis to three different driving frequencies Ω. To compare the results, we use κ as defined earlier. For $\Omega = 2\pi \times 5\,\mathrm{Hz}$, κ never reaches 1, meaning that synchronization does not occur within $1\,\mathrm{s}$. However, with $\Omega = 2\pi \times 10\,\mathrm{Hz}$, κ grows faster than the one for $\Omega = 2\pi \times 15\,\mathrm{Hz}$. As mentioned in the previous section, this earlier onset of vortex nucleation could be attributed to a resonance with a low-frequency quadrupole mode, which facilitates vortex formation, as suggested in Ref. [34]. In this analysis, we focused mainly on low rotation frequencies to isolate the role of individual vortices on the system's dynamics and to capture a few hundred milliseconds of pre-synchronization behavior. However, we expect similar dynamics to occur at higher rotation frequencies, albeit on faster timescales [34].

Experimental analysis

To measure the angular position of the droplets from experimental images, we use a fit function. We first apply a Gaussian filter of size $\sigma = 1\,\mathrm{px}$ ($\simeq 0.5\,\mu\mathrm{m}$) for noise reduction, before normalizing each image to the peak density. Each image is then fitted with a function defined as follows. Four elliptical 2D Gaussian density functions with four variable peak densities n_j, $j = 0, 1, 2, 3$ are centered on the corners of a square, with variable length a, phase ϕ and 2D center of mass position x_c, y_c (guiding center origin), see Fig. S4, defining a total of 8 free parameters. The widths of the individual Gaussian distributions defining each droplet are not free parameters, but pre-calibrated to minimize fit residuals and fixed for all images. The orientation of each Gaussian (its cyclotron rotation) is also fixed and locked to the polarization angle, a feature we have verified for this dataset and in previous works [34, 43]. The angular position of the droplets is then given by ϕ, assuming a circularly symmetric supersolid, such that $\phi_{\mathrm{rot},j} = \phi + j\pi/2$. We probe the robustness of our fit by taking two unique initial conditions for each image. First, we set $\phi = 0$ and perform the fit, then this is repeated for $\phi = \pi/4$, i.e. the maximally different angle. We have verified that, independent of the initial condition, our results remain unchanged.

Fourier transform analysis

To study the droplets' angular position in the rotating frame ϕ_{rot} as a function of time, we performed a 2D Fourier transform from (ϕ_{rot}, t) to (k_ϕ, f) space of the diagrams in Fig. 3(a)-(b), both before and after synchronization. For the experimental data, we first bin the coordinates (ϕ_{rot}, t) in a 2D histogram using a 120×250 grid and then apply the 2D Fourier transform for two time intervals, one before synchronization ($[0, 50]\,\mathrm{ms}$) and one after ($[60, 110]\,\mathrm{ms}$). The position of the peaks in Fourier space reflects the periodicity in time and space. The frequency f corresponds to the droplets' rotation frequency in the rotating frame, divided by the number of droplets (four, in our case), and k_ϕ represents the angular periodicity of the droplets. Since the supersolid state consists of four droplets, spaced by $\pi/2$, all Fourier peaks have $k_\phi = 2/\pi \sim 0.6\,\mathrm{rad}^{-1}$. In presence of Fourier peaks with a finite value of k_ϕ and f, the system is not synchronized,

whereas when the frequency is peaked at $f = 0$, the system is fully synchronized. We applied the same analysis to the theoretical data and observed a similar structure, with the peaks at finite f being closer to zero, reflecting slower dynamics.
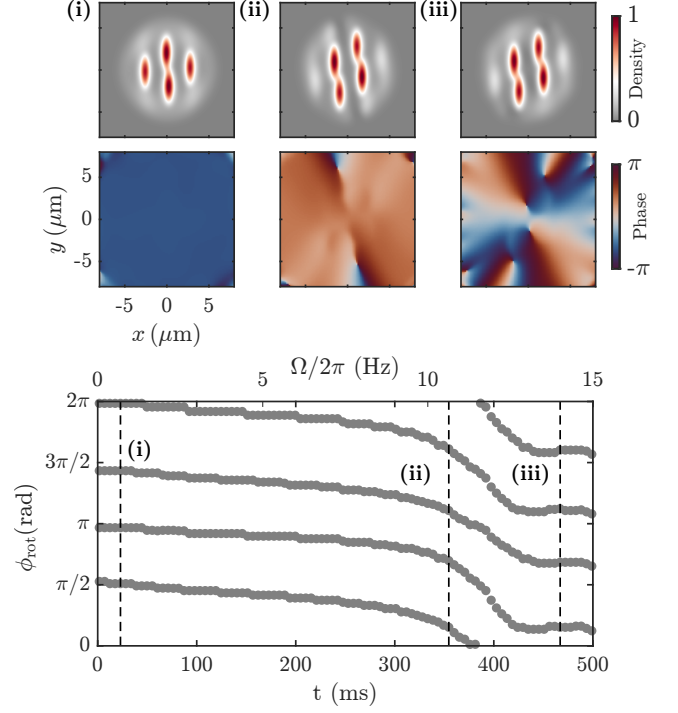

FIG. S5. Numerical simulations for synchronization during rotation frequency ramp. The upper panels show the column density normalized to its maximum value and the central phase slice for some frames of the supersolid state during the simulation, selected at times (i)-(iii) indicated by the dashed vertical lines in the lower panel. The lower panel shows the angular position of the droplets as a function of time, for a state obtained with parameters: $N = 60000$, $a_s = 90\,a_0$, $[\omega_x, \omega_y, \omega_z] = 2\pi \times [51, 50, 149]$ Hz, dissipation parameter $\gamma = 0.05$.

Numerical simulations of an Ω ramp

In the main text, we have shown that a slow increase of the rotation frequency leads to a desynchronization and subsequent resynchronization following a vortex nucleation. Here, we numerically simulate this situation with a protocol similar to what has been applied in the experiment, see Fig. 5. In Fig. S5 we show an example where the rotation frequency $\Omega/2\pi$ is linearly increased from 0 to 15 Hz over 500 ms. Throughout the full evolution, we track the center of mass of the droplets in the rotating frame, ϕ_{rot}. The theoretical simulation reveals the same behavior as the experimental data. Initially, the droplets remain mostly stationary in the rotating frame (i). As Ω exceeds the critical value for vortex nucleation, the droplets begin to lag behind the magnetic field (moving faster in the rotating frame), indicating a lack of synchronization. Around $t \sim 350$ ms the vortices approach the system (ii) and eventually enter, restoring the synchronization condition and reaching the stationary configuration in the rotating frame (iii).

Bibliography

[1] Immanuel Bloch, Jean Dalibard, and Wilhelm Zwerger. Many-body physics with ultracold gases. *Rev. Mod. Phys.*, 80:885–964, Jul 2008. (cited on page 3).

[2] David J Griffiths and Darrell F Schroeter. *Introduction to quantum mechanics.* Cambridge university press, 2018. (cited on page 3).

[3] Albert Einstein. Quantentheorie des einatomigen idealen Gases I. *Sitzungsberichte der Preussischen Akademie der Wissenschaften*, 21:26, 1924. (cited on page 4).

[4] Satyendra Nath Bose. Plancksches Gesetz und Lichtquantenhypothese. *Zeitschrift für Physik*, 26:178, 1924. (cited on page 4).

[5] F. London. The λ-Phenomenon of Liquid Helium and the Bose-Einstein Degeneracy. *Nature*, 141:643–644, apr 1938. (cited on page 4).

[6] P. Kapitza. Viscosity of Liquid Helium below the λ-Point. *Nature*, 141:74, jan 1938. (cited on page 4).

[7] John F Allen and AD Misener. Flow of liquid helium ii. *Nature*, 141(3558):75–75, 1938. (cited on page 4).

[8] L. Landau. Theory of the superfluidity of Helium II. *Phys. Rev.*, 60:356–358, Aug 1941. (cited on page 4).

[9] Oliver Penrose and Lars Onsager. Bose-Einstein Condensation and Liquid Helium. *Phys. Rev.*, 104:576, Nov 1956. (cited on pages 4, 39).

[10] Claude N. Cohen-Tannoudji. Nobel lecture: Manipulating atoms with photons. *Rev. Mod. Phys.*, 70:707–719, Jul 1998. (cited on page 4).

[11] W. Ketterle and N. J. van Druten. Evaporative Cooling of Trapped Atoms. *Adv. At. Mol. Opt. Phys.*, 37:181, 1996. (cited on page 4).

[12] M. H. Anderson, J. R. Ensher, M. R. Matthews, C. E. Wieman, and E. A. Cornell. Observation of Bose-Einstein condensation in dilute atomic vapor. *Science*, 269:198–201, 1995. (cited on pages 4, 10, 25).

[13] K. B. Davis, M. O. Mewes, M. R. Andrews, N. J. van Druten, D. S. Durfee, D. M. Kurn, and W. Ketterle. Bose-Einstein condensation in a gas of sodium atoms. *Phys. Rev. Lett.*, 75:3969–3973, 1995. (cited on pages 5, 10, 25).

[14] C. C. Bradley, C. A. Sackett, J. J. Tollett, and R. G. Hulet. Evidence of Bose-Einstein Condensation in an Atomic Gas with Attractive Interactions. *Phys. Rev. Lett.*, 75:1687–1690, Aug 1995. (cited on pages 5, 10).

[15] C. C. Bradley, C. A. Sackett, and R. G. Hulet. Bose-Einstein condensation of lithium: Observation of limited condensate number. *Phys. Rev. Lett.*, 78:985–989, Feb 1997. (cited on pages 5, 10).

[16] Dale G. Fried, Thomas C. Killian, Lorenz Willmann, David Landhuis, Stephen C. Moss, Daniel Kleppner, and Thomas J. Greytak. Bose-einstein condensation of atomic hydrogen. *Phys. Rev. Lett.*, 81:3811–3814, Nov 1998. (cited on pages 5,

10).

[17] Alice Robert, Olivier Sirjean, Antoine Browaeys, Julie Poupard, Stephan Nowak, Denis Boiron, Christoph I Westbrook, and Alain Aspect. A bose-einstein condensate of metastable atoms. *Science*, 292(5516):461–464, 2001. (cited on pages 5, 10).

[18] F. Pereira Dos Santos, J. Léonard, Junmin Wang, C. J. Barrelet, F. Perales, E. Rasel, C. S. Unnikrishnan, M. Leduc, and C. Cohen-Tannoudji. Bose-einstein condensation of metastable helium. *Phys. Rev. Lett.*, 86:3459–3462, Apr 2001. (cited on pages 5, 10).

[19] G. Modugno, G. Ferrari, G. Roati, R. J. Brecha, A. Simoni, and M. Inguscio. Bose-Einstein Condensation of Potassium Atoms by Sympathetic Cooling. *Science*, 294(5545):1320–1322, 2001. (cited on pages 5, 10).

[20] Tino Weber. *Bose-Einstein condensation of optically trapped cesium.* PhD thesis, University of Innsbruck, 2003. (cited on pages 5, 10).

[21] Yosuke Takasu, Kenichi Maki, Kaduki Komori, Tetsushi Takano, Kazuhito Honda, Mitsutaka Kumakura, Tsutomu Yabuzaki, and Yoshiro Takahashi. Spin-singlet Bose-Einstein condensation of two-electron atoms. *Phys. Rev. Lett.*, 91:040404, 2003. (cited on pages 5, 10).

[22] Axel Griesmaier, Jörg Werner, Sven Hensler, Jürgen Stuhler, and Tilman Pfau. Bose-einstein condensation of chromium. *Phys. Rev. Lett.*, 94:160401, Apr 2005. (cited on pages 5, 10).

[23] Sebastian Kraft, Felix Vogt, Oliver Appel, Fritz Riehle, and Uwe Sterr. Bose-Einstein condensation of alkaline earth atoms: ^{40}Ca. *Phys. Rev. Lett.*, 103:130401, 2009. (cited on pages 5, 10).

[24] Simon Stellmer, Meng Khoon Tey, Bo Huang, Rudolf Grimm, and Florian Schreck. Bose-Einstein condensation of strontium. *Phys. Rev. Lett.*, 103:20040, 2009. (cited on pages 5, 10).

[25] Mingwu Lu, Nathaniel Q. Burdick, Seo Ho Youn, and Benjamin L. Lev. Strongly Dipolar Bose-Einstein Condensate of Dysprosium. *Phys. Rev. Lett.*, 107:190401, Oct 2011. (cited on pages 5, 10, 14).

[26] K. Aikawa, A. Frisch, M. Mark, S. Baier, A. Rietzler, R. Grimm, and F. Ferlaino. Bose-Einstein Condensation of Erbium. *Phys. Rev. Lett.*, 108:210401, May 2012. (cited on pages 5, 10, 14).

[27] E. T. Davletov, V. V. Tsyganok, V. A. Khlebnikov, D. A. Pershin, D. V. Shaykin, and A. V. Akimov. Machine learning for achieving Bose-Einstein condensation of thulium atoms. *Phys. Rev. A*, 102:011302, Jul 2020. (cited on pages 5, 10, 14).

[28] Yuki Miyazawa, Ryotaro Inoue, Hiroki Matsui, Gyohei Nomura, and Mikio Kozuma. Bose-einstein condensation of europium. *Phys. Rev. Lett.*, 129:223401, Nov 2022. (cited on pages 5, 10, 14).

[29] Massimo Boninsegni and Nikolay V Prokof'ev. Colloquium: Supersolids: What and where are they? *Reviews of Modern Physics*, 84(2):759, May 2012. (cited on pages 5, 44).

[30] L. Tanzi, E. Lucioni, F. Famà, J. Catani, A. Fioretti, C. Gabbanini, R. N. Bisset, L. Santos, and G. Modugno. Observation of a Dipolar Quantum Gas with

Metastable Supersolid Properties. *Phys. Rev. Lett.*, 122:130405, Apr 2019. (cited on pages 5, 36, 44, 44).

[31] Fabian Böttcher, Jan-Niklas Schmidt, Matthias Wenzel, Jens Hertkorn, Mingyang Guo, Tim Langen, and Tilman Pfau. Transient Supersolid Properties in an Array of Dipolar Quantum Droplets. *Phys. Rev. X*, 9:011051, Mar 2019. (cited on pages 5, 36, 44, 44).

[32] L. Chomaz, D. Petter, P. Ilzhöfer, G. Natale, A. Trautmann, C. Politi, G. Durastante, R. M. W. van Bijnen, A. Patscheider, M. Sohmen, M. J. Mark, and F. Ferlaino. Long-Lived and Transient Supersolid Behaviors in Dipolar Quantum Gases. *Phys. Rev. X*, 9:021012, Apr 2019. (cited on pages 5, 36, 36, 44, 44).

[33] L. Pitaevskii and S. Stringari. *Bose-Einstein Condensation and Superfluidity*, volume 16. Oxford University Press, 2016. (cited on pages 9, 15, 15, 20, 22, 23, 27, 32, 33, 34, 116, 117, 137).

[34] Gerardo Andrés Cisneros, Kjartan Thor Wikfeldt, Lars Ojamäe, Jibao Lu, Yao Xu, Hedieh Torabifard, Albert P Bartók, Gábor Csányi, Valeria Molinero, and Francesco Paesani. Modeling molecular interactions in water: From pairwise to many-body potential energy functions. *Chemical reviews*, 116(13):7501–7528, 2016. (cited on page 10).

[35] Charles Kittel and Paul McEuen. *Introduction to solid state physics*. John Wiley & Sons, 2018. (cited on page 10).

[36] Christopher J. Foot, editor. *Atomic Physics*. Oxford University Press Inc., New York, 2005. (cited on pages 10, 11).

[37] Landau E. M.L̃ifshitz L. D.˙ *Quantum mechanics: non-relativistic theory*. (cited on pages 10, 11).

[38] Cheng Chin, Rudolf Grimm, Paul Julienne, and Eite Tiesinga. Feshbach resonances in ultracold gases. *Rev. Mod. Phys.*, 82:1225–1286, Apr 2010. (cited on page 11, 11).

[39] M. Marinescu and L. You. Controlling Atom-Atom Interaction at Ultralow Temperatures by dc Electric Fields. *Phys. Rev. Lett.*, 81:4596–4599, Nov 1998. (cited on page 11).

[40] S. Yi and L. You. Trapped condensates of atoms with dipole interactions. *Phys. Rev. A*, 63(5):053607, Apr 2001. (cited on page 11).

[41] Alessandro Bettini. *A Course in Classical Physics 3–Electromagnetism*. Springer, 2016. (cited on page 12, 12).

[42] Lauriane Chomaz, Igor Ferrier-Barbut, Francesca Ferlaino, Bruno Laburthe-Tolra, Benjamin L Lev, and Tilman Pfau. Dipolar physics: a review of experiments with magnetic quantum gases. *Reports on Progress in Physics*, 86(2):026401, dec 2022. (cited on page 13, 13).

[43] D. Peter, S. Müller, S. Wessel, and H. P. Büchler. Anomalous Behavior of Spin Systems with Dipolar Interactions. *Phys. Rev. Lett.*, 109:025303, Jul 2012. (cited on page 13).

[44] Shai Ronen, Daniele C. E. Bortolotti, D. Blume, and John L. Bohn. Dipolar Bose-Einstein condensates with dipole-dependent scattering length. *Phys. Rev. A*, 74(3):033611, Sep 2006. (cited on pages 13, 19, 20).

[45] Antoine Browaeys, Daniel Barredo, and Thierry Lahaye. Experimental investigations of dipole–dipole interactions between a few rydberg atoms. *Journal of Physics B: Atomic, Molecular and Optical Physics*, 49(15):152001, 2016. (cited on page 14).

[46] W. Li, T. Pohl, J. M. Rost, Seth T. Rittenhouse, H. R. Sadeghpour, J. Nipper, B. Butscher, J. B. Balewski, V. Bendkowsky, R. Löw, and T. Pfau. A Homonuclear Molecule with a Permanent Electric Dipole Moment. *Science*, 334(6059):1110–1114, 2011. (cited on page 14).

[47] M. Saffman, T. G. Walker, and K. Mølmer. Quantum information with Rydberg atoms. *Rev. Mod. Phys.*, 82:2313–2363, Aug 2010. (cited on page 14).

[48] Robert Löw, Hendrik Weimer, Johannes Nipper, Jonathan B Balewski, Björn Butscher, Hans Peter Büchler, and Tilman Pfau. An experimental and theoretical guide to strongly interacting rydberg gases. *Journal of Physics B: Atomic, Molecular and Optical Physics*, 45(11):113001, 2012. (cited on page 14).

[49] Hannes Bernien, Sylvain Schwartz, Alexander Keesling, Harry Levine, Ahmed Omran, Hannes Pichler, Soonwon Choi, Alexander S. Zibrov, Manuel Endres, Markus Greiner, Vladan Vuletić, and Mikhail D. Lukin. Probing many-body dynamics on a 51-atom quantum simulator. *Nature*, 551:579, Nov 2017. (cited on page 14).

[50] Peter Schauß, Johannes Zeiher, Takeshi Fukuhara, Sebastian Hild, Marc Cheneau, Tommaso Macrì, Thomas Pohl, Immanuel Bloch, and Christian Groß. Crystallization in Ising quantum magnets. *Science*, 347(6229):1455–1458, 2015. (cited on page 14).

[51] Pascal Scholl, Michael Schuler, Hannah J Williams, Alexander A Eberharter, Daniel Barredo, Kai-Niklas Schymik, Vincent Lienhard, Louis-Paul Henry, Thomas C Lang, Thierry Lahaye, et al. Quantum simulation of 2d antiferromagnets with hundreds of rydberg atoms. *Nature*, 595(7866):233–238, 2021. (cited on page 14).

[52] Sepehr Ebadi, Tout T Wang, Harry Levine, Alexander Keesling, Giulia Semeghini, Ahmed Omran, Dolev Bluvstein, Rhine Samajdar, Hannes Pichler, Wen Wei Ho, et al. Quantum phases of matter on a 256-atom programmable quantum simulator. *Nature*, 595(7866):227–232, 2021. (cited on page 14).

[53] Guillaume Bornet, Gabriel Emperauger, Cheng Chen, Bingtian Ye, Maxwell Block, Marcus Bintz, Jamie A Boyd, Daniel Barredo, Tommaso Comparin, Fabio Mezzacapo, et al. Scalable spin squeezing in a dipolar rydberg atom array. *Nature*, 621(7980):728–733, 2023. (cited on page 14).

[54] D. DeMille. Quantum Computation with Trapped Polar Molecules. *Phys. Rev. Lett.*, 88(6):067901, Jan 2002. (cited on page 14).

[55] John L. Bohn, Ana Maria Rey, and Jun Ye. Cold molecules: Progress in quantum engineering of chemistry and quantum matter. *Science*, 357(6355):1002–1010, 2017. (cited on page 14, 14).

[56] Luigi De Marco, Giacomo Valtolina, Kyle Matsuda, William G. Tobias, Jacob P. Covey, and Jun Ye. A degenerate Fermi gas of polar molecules. *Science*, 363(6429):853–856, 2019. (cited on page 14).

[57] Giacomo Valtolina, Kyle Matsuda, William G Tobias, Jun-Ru Li, Luigi De Marco,

and Jun Ye. Dipolar evaporation of reactive molecules to below the Fermi temperature. *Nature*, 588(7837):239–243, 2020. (cited on page 14).

[58] Niccolo Bigagli, Weijun Yuan, Siwei Zhang, Boris Bulatovic, Tijs Karman, Ian Stevenson, and Sebastian Will. Observation of bose–einstein condensation of dipolar molecules. *Nature*, pages 1–5, 2024. (cited on page 14).

[59] M. Fattori, G. Roati, B. Deissler, C. D'Errico, M. Zaccanti, M. Jona-Lasinio, L. Santos, M. Inguscio, and G. Modugno. Magnetic dipolar interaction in a bose-einstein condensate atomic interferometer. *Phys. Rev. Lett.*, 101:190405, Nov 2008. (cited on page 14).

[60] M. Vengalattore, S. R. Leslie, J. Guzman, and D. M. Stamper-Kurn. Spontaneously Modulated Spin Textures in a Dipolar Spinor Bose-Einstein Condensate. *Phys. Rev. Lett.*, 100:170403, May 2008. (cited on page 14).

[61] Yujiro Eto, Hiroki Saito, and Takuya Hirano. Observation of Dipole-Induced Spin Texture in an ^{87}Rb Bose-Einstein Condensate. *Phys. Rev. Lett.*, 112:185301, May 2014. (cited on page 14).

[62] Axel Griesmaier, Jörg Werner, Sven Hensler, Jürgen Stuhler, and Tilman Pfau. Bose-Einstein Condensation of Chromium. *Phys. Rev. Lett.*, 94(16):160401, Apr 2005. (cited on page 14).

[63] James W Cooley and John W Tukey. An algorithm for the machine calculation of complex fourier series. *Mathematics of computation*, 19(90):297–301, 1965. (cited on page 18, 18).

[64] Michael T Heideman, Don H Johnson, and C Sidney Burrus. Gauss and the history of the fast fourier transform. *Archive for history of exact sciences*, pages 265–277, 1985. (cited on page 18).

[65] R. N. Bisset, R. M. Wilson, D. Baillie, and P. B. Blakie. Ground-state phase diagram of a dipolar condensate with quantum fluctuations. *Phys. Rev. A*, 94(3):033619, Sep 2016. (cited on pages 18, 27, 27, 28, 44).

[66] Russell Nathan Bisset. *Theoretical study of the trapped dipolar Bose gas in the ultra-cold regime.* PhD thesis, University of Otago, 2013. (cited on page 20).

[67] J. Dalibard. Magnetic interactions between cold atoms: Quantum droplets and supersolid states. *College de France lectures 2024*, 2024. (cited on pages 21, 215, 215).

[68] Shai Ronen, Daniele C. E. Bortolotti, and John L. Bohn. Bogoliubov modes of a dipolar condensate in a cylindrical trap. *pra*, 74(1):013623, Jul 2006. (cited on pages 22, 30).

[69] M. Modugno, L. Pricoupenko, and Y. Castin. Bose-Einstein condensates with a bent vortex in rotating traps. *The European Physical Journal D - Atomic, Molecular, Optical and Plasma Physics*, 22(2):235–257, 2003. (cited on page 22).

[70] Weizhu Bao, I-Liang Chern, and Fong Yin Lim. Efficient and spectrally accurate numerical methods for computing ground and first excited states in Bose–Einstein condensates. *J. Comput. Phys.*, 219(2):836–854, 2006. (cited on page 23).

[71] Franco Dalfovo, Stefano Giorgini, Lev Pitaevskii, and Sandro Stringari. Theory of Bose-Einstein condensation in trapped gases. *Rev. Mod. Phys.*, 71(3):463, Apr 1999. (cited on pages 23, 114).

[72] Claudia Eberlein, Stefano Giovanazzi, and Duncan H. J. O'Dell. Exact solution of the Thomas-Fermi equation for a trapped Bose-Einstein condensate with dipole-dipole interactions. *Phys. Rev. A*, 71(3):033618, Mar 2005. (cited on page 23, 23).

[73] M. L. Chiofalo, S. Succi, and M. P. Tosi. Ground state of trapped interacting bose-einstein condensates by an explicit imaginary-time algorithm. *Phys. Rev. E*, 62:7438–7444, Nov 2000. (cited on page 24).

[74] Weizhu Bao and Hanquan Wang. An efficient and spectrally accurate numerical method for computing dynamics of rotating Bose–Einstein condensates. *Journal of Computational Physics*, 217(2):612–626, 2006. (cited on pages 24, 25, 26).

[75] LP Pitaevskii. Phenomenological theory of superfluidity near the l point. *Sov. Phys.—JETP*, 8:282, 1959. (cited on page 26).

[76] S. Choi, S. A. Morgan, and K. Burnett. Phenomenological damping in trapped atomic bose-einstein condensates. *Phys. Rev. A*, 57:4057–4060, May 1998. (cited on page 26).

[77] Makoto Tsubota, Kenichi Kasamatsu, and Masahito Ueda. Vortex lattice formation in a rotating bose-einstein condensate. *Phys. Rev. A*, 65:023603, Jan 2002. (cited on page 26).

[78] A. A. Penckwitt, R. J. Ballagh, and C. W. Gardiner. Nucleation, growth, and stabilization of bose-einstein condensate vortex lattices. *Phys. Rev. Lett.*, 89:260402, Dec 2002. (cited on page 26).

[79] P.B. Blakie, A.S. Bradley, M.J. Davis, R.J. Ballagh, and C.W. Gardiner. Dynamics and statistical mechanics of ultra-cold Bose gases using c-field techniques. *Advances in Physics*, 57(5):363–455, 2008. (cited on pages 26, 26, 26, 47).

[80] Nick P. Proukakis, Gerasimos Rigopoulos, and Alex Soto. Self-consistent stochastic finite-temperature modelling: Ultracold bose gases with local (s-wave) and long-range (dipolar) interactions, 2024. (cited on page 26).

[81] Holger Kadau, Matthias Schmitt, Matthias Wenzel, Clarissa Wink, Thomas Maier, Igor Ferrier-Barbut, and Tilman Pfau. Observing the Rosensweig instability of a quantum ferrofluid. *Nature*, 530(7589):194–197, 02 2016. (cited on pages 27, 44, 44).

[82] D. S. Petrov. Quantum Mechanical Stabilization of a Collapsing Bose-Bose Mixture. *Phys. Rev. Lett.*, 115(15):155302, Oct 2015. (cited on page 27).

[83] Aristeu R. P. Lima and Axel Pelster. Quantum fluctuations in dipolar Bose gases. *Phys. Rev. A*, 84(4):041604, Oct 2011. (cited on page 27, 27, 27).

[84] Hiroki Saito. Path-Integral Monte Carlo Study on a Droplet of a Dipolar Bose-Einstein Condensate Stabilized by Quantum Fluctuation. *J. Phys. Soc. Jpn*, 85(5):053001, 2016. (cited on page 27).

[85] Tsin D Lee, Kerson Huang, and Chen N Yang. Eigenvalues and eigenfunctions of a Bose system of hard spheres and its low-temperature properties. *Physical Review*, 106(6):1135, Jun 1957. (cited on page 27).

[86] T. D. Lee, Kerson Huang, and C. N. Yang. Eigenvalues and Eigenfunctions of a Bose System of Hard Spheres and Its Low-Temperature Properties. *Phys. Rev.*, 106:1135–1145, Jun 1957. (cited on page 27).

[87] A. R. P. Lima and A. Pelster. Beyond mean-field low-lying excitations of dipolar Bose gases. *Phys. Rev. A*, 86(6):063609, Dec 2012. (cited on page 27).

[88] S. Stringari. Quantum Fluctuations and Gross-Pitaevskii Theory. *Journal of Experimental and Theoretical Physics*, 127(5):844–850, Nov 2018. (cited on page 27).

[89] K. Xu, Y. Liu, D. E. Miller, J. K. Chin, W. Setiawan, and W. Ketterle. Observation of strong quantum depletion in a gaseous bose-einstein condensate. *Phys. Rev. Lett.*, 96:180405, May 2006. (cited on page 27).

[90] R. Chang, Q. Bouton, H. Cayla, C. Qu, A. Aspect, C. I. Westbrook, and D. Clément. Momentum-resolved observation of thermal and quantum depletion in a bose gas. *Phys. Rev. Lett.*, 117:235303, Dec 2016. (cited on page 27).

[91] Raphael Lopes, Christoph Eigen, Nir Navon, David Clément, Robert P. Smith, and Zoran Hadzibabic. Quantum depletion of a homogeneous bose-einstein condensate. *Phys. Rev. Lett.*, 119:190404, Nov 2017. (cited on page 27).

[92] N Bogoliubov. On the theory of superfluidity. *J. Phys*, 11(1):2, 1947. (cited on page 29).

[93] Pierre-Gilles De Gennes. *Superconductivity of metals and alloys.* CRC press, 2018. (cited on page 29).

[94] Sandro Stringari and Lev Pitaevskii. *Bose-Einstein condensation and superfluidity.* Oxford Science Publications, Oxford, 2016. (cited on page 29).

[95] S. Choi, L. O. Baksmaty, S. J. Woo, and N. P. Bigelow. Excitation spectrum of vortex lattices in rotating bose-einstein condensates. *Phys. Rev. A*, 68:031605, Sep 2003. (cited on page 30).

[96] Lijuan Jia, An-Bang Wang, and Su Yi. Low-lying excitations of vortex lattices in condensates with anisotropic dipole-dipole interaction. *Phys. Rev. A*, 97:043614, Apr 2018. (cited on page 30).

[97] W. E. Arnoldi. The principle of minimized iterations in the solution of the matrix eigenvalue problem. *Quarterly of Applied Mathematics*, 9(1):17–29, 1951. (cited on page 30).

[98] P. B. Blakie, D. Baillie, and R. N. Bisset. Roton spectroscopy in a harmonically trapped dipolar Bose-Einstein condensate. *Phys. Rev. A*, 86:021604, Aug 2012. (cited on page 31, 31).

[99] L Santos, GV Shlyapnikov, and M Lewenstein. Roton-maxon spectrum and stability of trapped dipolar Bose-Einstein condensates. *Physical Review Letters*, 90(25):250403, Jun 2003. (cited on page 31).

[100] Sukla Pal, D. Baillie, and P. B. Blakie. Excitations and number fluctuations in an elongated dipolar Bose-Einstein condensate. *Phys. Rev. A*, 102:043306, Oct 2020. (cited on page 31).

[101] L. D. Landau. The theory of superfluidity of helium II. *J. Phys. (Moscow)*, 5:71, 1941. (cited on pages 32, 213).

[102] P. Nozières. Is the Roton in Superfluid ^{4}He the Ghost of a Bragg Spot? *J. Low Temp. Phys.*, 137(1):45–67, Oct 2004. (cited on pages 32, 35, 43).

[103] G Natale, RMW van Bijnen, A Patscheider, D Petter, MJ Mark, L Chomaz, and F Ferlaino. Excitation spectrum of a trapped dipolar supersolid and its

experimental evidence. *Physical review letters*, 123(5):050402, Aug 2019. (cited on pages 32, 44).

[104] D Petter, A Patscheider, G Natale, MJ Mark, MA Baranov, R v Bijnen, SM Roccuzzo, A Recati, B Blakie, D Baillie, et al. High-energy Bragg scattering measurements of a dipolar supersolid. *arXiv preprint arXiv:2005.02213*, 2020. (cited on page 32).

[105] R. M. W. van Bijnen, N. G. Parker, S. J. J. M. F. Kokkelmans, A. M. Martin, and D. H. J. O'Dell. Collective excitation frequencies and stationary states of trapped dipolar Bose-Einstein condensates in the Thomas-Fermi regime. *Phys. Rev. A*, 82:033612, Sep 2010. (cited on page 34).

[106] Shai Ronen, Daniele CE Bortolotti, and John L Bohn. Radial and angular rotons in trapped dipolar gases. *Physical review letters*, 98(3):030406, jan 2007. (cited on page 34).

[107] L. Chomaz, R. M. W. van Bijnen, D. Petter, G. Faraoni, S. Baier, J. H. Becher, M. J. Mark, F. Wächtler, L. Santos, and F. Ferlaino. Observation of roton mode population in a dipolar quantum gas. *Nature Physics*, 14(5):442–446, 2018. (cited on pages 34, 43).

[108] J-N Schmidt, Jens Hertkorn, Mingyang Guo, Fabian Böttcher, Matthias Schmidt, Kevin SH Ng, Sean D Graham, Tim Langen, Martin Zwierlein, and Tilman Pfau. Roton Excitations in an Oblate Dipolar Quantum Gas. *Physical Review Letters*, 126(19):193002, May 2021. (cited on page 34).

[109] RP Feynman. Progress in low temperature physics. Vol. 1, 1955. (cited on page 35).

[110] P. Ilzhöfer, M. Sohmen, G. Durastante, C. Politi, A. Trautmann, G. Natale, G. Morpurgo, T. Giamarchi, L. Chomaz, M. J. Mark, and F. Ferlaino. Phase coherence in out-of-equilibrium supersolid states of ultracold dipolar atoms. *Nature Physics*, 17(3):356–361, 2021. (cited on pages 36, 44).

[111] Santo Maria Roccuzzo and Francesco Ancilotto. Supersolid behavior of a dipolar Bose-Einstein condensate confined in a tube. *Phys. Rev. A*, 99:041601, Apr 2019. (cited on pages 37, 43, 43, 214).

[112] AF Andreev and IM Lifshitz. Quantum Theory of Defects in Crystals. *J. Exp. Theo. Phys.*, 56:2057, 1969. (cited on pages 39, 40, 40).

[113] GV Chester. Speculations on Bose-Einstein condensation and quantum crystals. *Physical Review A*, 2(1):256, Jul 1970. (cited on page 39).

[114] John Beamish and Sébastien Balibar. Mechanical behavior of solid helium: Elasticity, plasticity, and defects. *Rev. Mod. Phys.*, 92:045002, Oct 2020. (cited on page 40).

[115] D. S. Greywall. Search for superfluidity in solid ^{4}He. *Phys. Rev. B*, 16:1291–1292, Aug 1977. (cited on page 40).

[116] G Bonfait, H Godfrin, and B Castaing. Solid 4he: search for superfluidity. *Journal de Physique*, 50(15):1997–2002, 1989. (cited on page 40).

[117] Anthony J Leggett. Can a solid be "superfluid"? *Physical Review Letters*, 25(22):1543, Nov 1970. (cited on pages 40, 40, 214, 214, 215).

[118] A.J Leggett. On the Superfluid Fraction of an Arbitrary Many-Body System at

T=0. *J. Stat. Phys.*, 93:927, 1998. (cited on pages 40, 213, 214, 214, 215).

[119] E. Kim and M. H. W. Chan. Observation of superflow in solid helium. *Science*, 305:1941–1944, 2004. (cited on page 41).

[120] Eunseong Kim and MHW Chan. Probable observation of a supersolid helium phase. *Nature*, 427(6971):225–227, 01 2004. (cited on page 41).

[121] James Day and John Beamish. Low-temperature shear modulus changes in solid ^{4}He and connection to supersolidity. *Nature*, 450(7171):853–856, 2007. (cited on page 41).

[122] Duk Y. Kim and Moses H. W. Chan. Absence of Supersolidity in Solid Helium in Porous Vycor Glass. *Phys. Rev. Lett.*, 109:155301, Oct 2012. (cited on page 41).

[123] Jaewon Choi, Alexey A. Zadorozhko, Jeakyung Choi, and Eunseong Kim. Spatially modulated superfluid state in two-dimensional ^{4}He films. *Phys. Rev. Lett.*, 127:135301, Sep 2021. (cited on page 41).

[124] Lev V. Levitin, Ben Yager, Laura Sumner, Brian Cowan, Andrew J. Casey, John Saunders, Nikolay Zhelev, Robert G. Bennett, and Jeevak M. Parpia. Evidence for a spatially modulated superfluid phase of ^{3}He under confinement. *Phys. Rev. Lett.*, 122:085301, Feb 2019. (cited on page 41).

[125] A. J. Shook, V. Vadakkumbatt, P. Senarath Yapa, C. Doolin, R. Boyack, P. H. Kim, G. G. Popowich, F. Souris, H. Christani, J. Maciejko, and J. P. Davis. Stabilized pair density wave via nanoscale confinement of superfluid ^{3}He. *Phys. Rev. Lett.*, 124:015301, Jan 2020. (cited on page 41).

[126] Eugene P. Gross. Unified Theory of Interacting Bosons. *Phys. Rev.*, 106:161, Apr 1957. (cited on page 41).

[127] Yves Pomeau and Sergio Rica. Dynamics of a model of supersolid. *Phys. Rev. Lett.*, 72:2426–2429, Apr 1994. (cited on page 41).

[128] F. Cinti, P. Jain, M. Boninsegni, A. Micheli, P. Zoller, and G. Pupillo. Supersolid Droplet Crystal in a Dipole-Blockaded Gas. *Phys. Rev. Lett.*, 105:135301, Sep 2010. (cited on pages 41, 89, 90).

[129] Fabio Cinti, Tommaso Macrì, Wolfgang Lechner, Guido Pupillo, and Thomas Pohl. Defect-induced supersolidity with soft-core bosons. *Nature communications*, 5(1):3235, 2014. (cited on pages 41, 89, 90).

[130] N. Henkel, R. Nath, and T. Pohl. Three-Dimensional Roton Excitations and Supersolid Formation in Rydberg-Excited Bose-Einstein Condensates. *Phys. Rev. Lett.*, 104:195302, May 2010. (cited on pages 41, 90, 91, 211).

[131] Kristian Baumann, Christine Guerlin, Ferdinand Brennecke, and Tilman Esslinger. Dicke quantum phase transition with a superfluid gas in an optical cavity. *nature*, 464(7293):1301–1306, 2010. (cited on page 42).

[132] Julian Léonard, Andrea Morales, Philip Zupancic, Tilman Esslinger, and Tobias Donner. Supersolid formation in a quantum gas breaking a continuous translational symmetry. *Nature*, 543(7643):87–90, 03 2017. (cited on page 42).

[133] Ivana Dimitrova, William Lunden, Jesse Amato-Grill, Niklas Jepsen, Yichao Yu, Michael Messer, Thomas Rigaldo, Graciana Puentes, David Weld, and Wolfgang Ketterle. Observation of two-beam collective scattering phenomena in a bose-einstein condensate. *Phys. Rev. A*, 96:051603, Nov 2017. (cited on page 42).

[134] S. C. Schuster, P. Wolf, S. Ostermann, S. Slama, and C. Zimmermann. Supersolid properties of a bose-einstein condensate in a ring resonator. *Phys. Rev. Lett.*, 124:143602, Apr 2020. (cited on page 42).

[135] Julian Léonard, Andrea Morales, Philip Zupancic, Tobias Donner, and Tilman Esslinger. Monitoring and manipulating higgs and goldstone modes in a supersolid quantum gas. *Science*, 358(6369):1415–1418, 2017. (cited on page 42).

[136] Natalia Masalaeva, Helmut Ritsch, and Farokh Mivehvar. Tuning photon-mediated interactions in a multimode cavity: From supersolid to insulating droplets hosting phononic excitations. *Phys. Rev. Lett.*, 131:173401, Oct 2023. (cited on page 42).

[137] Yudan Guo, Ronen M Kroeze, Brendan P Marsh, Sarang Gopalakrishnan, Jonathan Keeling, and Benjamin L Lev. An optical lattice with sound. 2021. (cited on page 42).

[138] Y.-J. Lin, K. Jimenez-Garcia, and I. B. Spielman. Spin-orbit-coupled Bose-Einstein condensates. *Nature (London)*, 471:83–86, 2011. (cited on page 42).

[139] Jun-Ru Li, Jeongwon Lee, Wujie Huang, Sean Burchesky, Boris Shteynas, Furkan Çağrı Top, Alan O Jamison, and Wolfgang Ketterle. A stripe phase with supersolid properties in spin–orbit-coupled Bose–Einstein condensates. *Nature*, 543(7643):91–94, 03 2017. (cited on page 42).

[140] Andika Putra, F. Salces-Cárcoba, Yuchen Yue, Seiji Sugawa, and I. B. Spielman. Spatial coherence of spin-orbit-coupled bose gases. *Phys. Rev. Lett.*, 124:053605, Feb 2020. (cited on page 42).

[141] CS Chisholm, S Hirthe, VB Makhalov, R Ramos, R Vatré, J Cabedo, A Celi, and L Tarruell. Probing supersolidity through excitations in a spin-orbit-coupled bose-einstein condensate. *arXiv preprint arXiv:2412.13861*, 2024. (cited on page 42).

[142] Dimitrios Trypogeorgos, Antonio Gianfrate, Manuele Landini, Davide Nigro, Dario Gerace, Iacopo Carusotto, Fabrizio Riminucci, Kirk W Baldwin, Loren N Pfeiffer, Giovanni I Martone, et al. Emerging supersolidity in photonic-crystal polariton condensates. *Nature*, pages 1–5, 2025. (cited on page 42).

[143] Iacopo Carusotto and Cristiano Ciuti. Quantum fluids of light. *Rev. Mod. Phys.*, 85:299–366, Feb 2013. (cited on page 42).

[144] M Sudraud and EJ Varoquaux. Experimental evidence for interactions between elementary excitations in liquid 4 he below 1 k. *Physics Letters. A*, 62(6):416–418, 1977. (cited on page 43).

[145] Igor Ferrier-Barbut, Holger Kadau, Matthias Schmitt, Matthias Wenzel, and Tilman Pfau. Observation of Quantum Droplets in a Strongly Dipolar Bose Gas. *Phys. Rev. Lett.*, 116(21):215301, May 2016. (cited on page 44).

[146] L. Chomaz, S. Baier, D. Petter, M. J. Mark, F. Wächtler, L. Santos, and F. Ferlaino. Quantum-Fluctuation-Driven Crossover from a Dilute Bose-Einstein Condensate to a Macrodroplet in a Dipolar Quantum Fluid. *Phys. Rev. X*, 6(4):041039, Nov 2016. (cited on page 44).

[147] F. Wächtler and L. Santos. Quantum filaments in dipolar Bose-Einstein condensates. *Phys. Rev. A*, 93(6):061603, Jun 2016. (cited on page 44).

[148] F. Wächtler and L. Santos. Ground-state properties and elementary excitations of quantum droplets in dipolar Bose-Einstein condensates. *Phys. Rev. A*, 94(4):043618, Oct 2016. (cited on page 44).

[149] Maximilian Sohmen, Claudia Politi, Lauritz Klaus, Lauriane Chomaz, Manfred J. Mark, Matthew A. Norcia, and Francesca Ferlaino. Birth, Life, and Death of a Dipolar Supersolid. *Phys. Rev. Lett.*, 126:233401, Jun 2021. (cited on pages 44, 45).

[150] T. Bland, E. Poli, C. Politi, L. Klaus, M. A. Norcia, F. Ferlaino, L. Santos, and R. N. Bisset. Two-Dimensional Supersolid Formation in Dipolar Condensates. *Phys. Rev. Lett.*, 128:195302, May 2022. (cited on pages 45, 45, 46, 85, 86).

[151] Mingyang Guo, Fabian Böttcher, Jens Hertkorn, Jan-Niklas Schmidt, Matthias Wenzel, Hans Peter Büchler, Tim Langen, and Tilman Pfau. The low-energy Goldstone mode in a trapped dipolar supersolid. *Nature*, 564:386, 2019. (cited on pages 44, 87).

[152] J. Hertkorn, F. Böttcher, M. Guo, J. N. Schmidt, T. Langen, H. P. Büchler, and T. Pfau. Fate of the Amplitude Mode in a Trapped Dipolar Supersolid. *Phys. Rev. Lett.*, 123:193002, Nov 2019. (cited on page 44).

[153] L Tanzi, SM Roccuzzo, E Lucioni, F Famà, A Fioretti, C Gabbanini, G Modugno, A Recati, and S Stringari. Supersolid symmetry breaking from compressional oscillations in a dipolar quantum gas. *Nature*, 574(7778):382–385, October 2019. (cited on page 44).

[154] D. Petter, A. Patscheider, G. Natale, M. J. Mark, M. A. Baranov, R. van Bijnen, S. M. Roccuzzo, A. Recati, B. Blakie, D. Baillie, L. Chomaz, and F. Ferlaino. Bragg scattering of an ultracold dipolar gas across the phase transition from Bose-Einstein condensate to supersolid in the free-particle regime. *Phys. Rev. A*, 104:L011302, Jul 2021. (cited on page 44).

[155] L Tanzi, JG Maloberti, G Biagioni, A Fioretti, C Gabbanini, and G Modugno. Evidence of superfluidity in a dipolar supersolid from nonclassical rotational inertia. *Science*, 371(6534):1162–1165, 2021. (cited on pages 44, 117, 117).

[156] Youssef Kora and Massimo Boninsegni. Patterned supersolids in dipolar Bose systems. *Journal of Low Temperature Physics*, 197(5):337–347, Dec 2019. (cited on page 44).

[157] Yong-Chang Zhang, Fabian Maucher, and Thomas Pohl. Supersolidity around a critical point in dipolar Bose-Einstein condensates. *Physical review letters*, 123(1):015301, Jul 2019. (cited on page 44).

[158] Francesco Ancilotto, Manuel Barranco, Martí Pi, and Luciano Reatto. Vortex properties in the extended supersolid phase of dipolar Bose-Einstein condensates. *Physical Review A*, 103(3):033314, Mar 2021. (cited on page 44).

[159] Matthew A. Norcia, Claudia Politi, Lauritz Klaus, Elena Poli, Maximilian Sohmen, Manfred J. Mark, Russell N. Bisset, Luis Santos, and Francesca Ferlaino. Two-dimensional supersolidity in a dipolar quantum gas. *Nature*, 596(7872):357–361, Aug 2021. (cited on pages 45, 46, 47).

[160] E. Poli, T. Bland, C. Politi, L. Klaus, M. A. Norcia, F. Ferlaino, R. N. Bisset, and L. Santos. Maintaining supersolidity in one and two dimensions. *Phys. Rev. A*, 104:063307, Dec 2021. (cited on pages 45, 46, 85).

[161] K Pyka, J Keller, HL Partner, R Nigmatullin, T Burgermeister, DM Meier, K Kuhlmann, A Retzker, Martin B Plenio, WH Zurek, et al. Topological defect formation and spontaneous symmetry breaking in ion coulomb crystals. *Nature communications*, 4(1):2291, 2013. (cited on page 45).

[162] Matthew A Norcia, Elena Poli, Claudia Politi, Lauritz Klaus, Thomas Bland, Manfred J Mark, Luis Santos, Russell N Bisset, and Francesca Ferlaino. Can angular oscillations probe superfluidity in dipolar supersolids? *arXiv:2111.07768*, 2021. (cited on page 87).

[163] S. Saccani, S. Moroni, and M. Boninsegni. Excitation Spectrum of a Supersolid. *Phys. Rev. Lett.*, 108:175301, Apr 2012. (cited on page 89).

[164] T. Macrì, F. Maucher, F. Cinti, and T. Pohl. Elementary excitations of ultracold soft-core bosons across the superfluid-supersolid phase transition. *Phys. Rev. A*, 87:061602(R), Jun 2013. (cited on page 89).

[165] C. N. Likos, A. Lang, M. Watzlawek, and H. Löwen. Criterion for determining clustering versus reentrant melting behavior for bounded interaction potentials. *Phys. Rev. E*, 63:031206, Feb 2001. (cited on page 89).

[166] C Sepúlveda, N.nd Josserand. Superfluid density in a two-dimensional model of supersolid. *Euro. Phys. J. B*, 78(4):439, Dec 2010. (cited on pages 91, 93, 215).

[167] L. M. Platt, D. Baillie, and P. B. Blakie. Sound waves and fluctuations in one-dimensional supersolids. *Phys. Rev. A*, 110:023320, Aug 2024. (cited on page 91).

[168] P Blair Blakie. Superfluid fraction tensor of a two-dimensional supersolid. *Journal of Physics B: Atomic, Molecular and Optical Physics*, 57(11):115301, 2024. (cited on pages 91, 93).

[169] E. Poli, D. Baillie, F. Ferlaino, and P. B. Blakie. Excitations of a two-dimensional supersolid. *Phys. Rev. A*, 110:053301, Nov 2024. (cited on pages 92, 96, 96).

[170] D. T. Son. Effective lagrangian and topological interactions in supersolids. *Phys. Rev. Lett.*, 94:175301, May 2005. (cited on page 92, 92).

[171] Christophe Josserand, Yves Pomeau, and Sergio Rica. Coexistence of ordinary elasticity and superfluidity in a model of a defect-free supersolid. *Phys. Rev. Lett.*, 98:195301, May 2007. (cited on pages 92, 215).

[172] Christophe Josserand, Yves Pomeau, and Sergio Rica. Patterns and supersolids. *The European Physical Journal Special Topics*, 146(1):47–61, 2007. (cited on page 92).

[173] Jinwu Ye. Elementary excitation in a supersolid. *Europhysics Letters*, 82(1):16001, 2008. (cited on page 92).

[174] C.-D. Yoo and Alan T. Dorsey. Hydrodynamic theory of supersolids: Variational principle, effective lagrangian, and density-density correlation function. *Phys. Rev. B*, 81:134518, Apr 2010. (cited on page 92, 92).

[175] P B Blakie. Superfluid fraction tensor of a two-dimensional supersolid. *Journal of Physics B: Atomic, Molecular and Optical Physics*, 57(11):115301, may 2024. (cited on pages 93, 215, 215, 215, 215, 215).

[176] Benny Lautrup. *Physics of continuous matter: exotic and everyday phenomena in the macroscopic world.* CRC press, 2011. (cited on pages 94, 95).

[177] Pramodh Senarath Yapa and Thomas Bland. Supersonic shear waves in dipolar supersolids, 2024. (cited on page 97).

[178] P. B. Blakie. Dirac points and shear instability induced crystal transitions in honeycomb supersolids. *Phys. Rev. Lett.*, 134:013401, Jan 2025. (cited on page 97).

[179] EJ Yarmchuk, MJV Gordon, and RE Packard. Observation of stationary vortex arrays in rotating superfluid helium. *Phys. Rev. Lett.*, 43(3):214, 1979. (cited on pages 111, 136).

[180] Jamil R Abo-Shaeer, Chandra Raman, Johnny M Vogels, and Wolfgang Ketterle. Observation of vortex lattices in Bose-Einstein condensates. *Science*, 292(5516):476–479, 2001. (cited on pages 111, 111, 112, 112, 136, 138).

[181] K. W. Madison, F. Chevy, W. Wohlleben, and J. Dalibard. Vortex formation in a stirred Bose-Einstein condensate. *Phys. Rev. Lett.*, 84:806–809, Jan 2000. (cited on pages 111, 111, 112, 112, 136, 138).

[182] K. W. Madison, F. Chevy, V. Bretin, and J. Dalibard. Stationary states of a rotating Bose-Einstein condensate: Routes to vortex nucleation. *Phys. Rev. Lett.*, 86:4443–4446, May 2001. (cited on pages 111, 136).

[183] Konstantinos G Lagoudakis, Michiel Wouters, Maxime Richard, Augustin Baas, Iacopo Carusotto, Regis André, Le Si Dang, and B Deveaud-Plédran. Quantized vortices in an exciton–polariton condensate. *Nature physics*, 4(9):706–710, 2008. (cited on pages 111, 136).

[184] Frederick S Wells, Alexey V Pan, X Renshaw Wang, Sergey A Fedoseev, and Hans Hilgenkamp. Analysis of low-field isotropic vortex glass containing vortex groups in YBa2Cu3O7-x thin films visualized by scanning SQUID microscopy. *Scientific reports*, 5(1):8677, 2015. (cited on pages 111, 136).

[185] M. R. Matthews, B. P. Anderson, P. C. Haljan, D. S. Hall, C. E. Wieman, and E. A. Cornell. Vortices in a Bose-Einstein Condensate. *Phys. Rev. Lett.*, 83:2498–2501, Sep 1999. (cited on page 111).

[186] G. Del Pace, K. Xhani, A. Muzi Falconi, M. Fedrizzi, N. Grani, D. Hernandez Rajkov, M. Inguscio, F. Scazza, W. J. Kwon, and G. Roati. Imprinting persistent currents in tunable fermionic rings. *Phys. Rev. X*, 12:041037, Dec 2022. (cited on page 111).

[187] Scott Beattie, Stuart Moulder, Richard J. Fletcher, and Zoran Hadzibabic. Persistent currents in spinor condensates. *Phys. Rev. Lett.*, 110:025301, Jan 2013. (cited on page 111).

[188] M. F. Andersen, C. Ryu, Pierre Cladé, Vasant Natarajan, A. Vaziri, K. Helmerson, and W. D. Phillips. Quantized rotation of atoms from photons with orbital angular momentum. *Phys. Rev. Lett.*, 97:170406, Oct 2006. (cited on page 111).

[189] P. C. Haljan, I. Coddington, P. Engels, and E. A. Cornell. Driving Bose-Einstein-Condensate Vorticity with a Rotating Normal Cloud. *Phys. Rev. Lett.*, 87:210403, Nov 2001. (cited on page 112, 112).

[190] O. M. Maragò, S. A. Hopkins, J. Arlt, E. Hodby, G. Hechenblaikner, and C. J. Foot. Observation of the Scissors Mode and Evidence for Superfluidity of a Trapped Bose-Einstein Condensed Gas. *Phys. Rev. Lett.*, 84:2056–2059, 2000.

(cited on pages 112, 116).

[191] Srivatsa B Prasad, Thomas Bland, Brendan C Mulkerin, Nick G Parker, and Andrew M Martin. Vortex lattice formation in dipolar Bose-Einstein condensates via rotation of the polarization. *Physical Review A*, 100(2):023625, 2019. (cited on page 112, 112).

[192] Lauritz Klaus, Thomas Bland, Elena Poli, Claudia Politi, Giacomo Lamporesi, Eva Casotti, Russell N. Bisset, Manfred J. Mark, and Francesca Ferlaino. Observation of vortices and vortex stripes in a dipolar condensate. *Nature Physics*, 18(12):1453–1458, 2022. (cited on pages 112, 136, 137, 138, 138, 139, 179, 179).

[193] Eva Casotti, Elena Poli, Lauritz Klaus, Andrea Litvinov, Clemens Ulm, Claudia Politi, Manfred J Mark, Thomas Bland, and Francesca Ferlaino. Observation of vortices in a dipolar supersolid. *Nature*, 635:327–331, 2024. (cited on pages 112, 136, 137, 137, 139, 139, 179).

[194] Alessandro Bettini. *Meccanica e termodinamica*. Bologna, 1995. (cited on page 112).

[195] Carlo F Barenghi and Nick G Parker. *A primer on quantum fluids*. Springer, 2016. (cited on page 113, 113).

[196] David L. Feder, Charles W. Clark, and Barry I. Schneider. Nucleation of vortex arrays in rotating anisotropic bose-einstein condensates. *Phys. Rev. A*, 61:011601, Dec 1999. (cited on page 115).

[197] Alexander L Fetter. Vortex nucleation in deformed rotating cylinders. *Journal of Low Temperature Physics*, 16:533–555, 1974. (cited on page 116).

[198] A. Recati, F. Zambelli, and S. Stringari. Overcritical rotation of a trapped bose-einstein condensate. *Phys. Rev. Lett.*, 86:377–380, Jan 2001. (cited on pages 116, 117, 137, 179).

[199] SM Roccuzzo, A Gallemí, A Recati, and S Stringari. Rotating a supersolid dipolar gas. *Physical review letters*, 124(4):045702, Jan 2020. (cited on pages 116, 117, 117, 137, 181, 215).

[200] D. Guéry-Odelin and S. Stringari. Scissors Mode and Superfluidity of a Trapped Bose-Einstein Condensed Gas. *Phys. Rev. Lett.*, 83:4452–4455, 1999. (cited on page 116).

[201] D. Bohle, A. Richter, W. Steffen, A.E.L. Dieperink, N. Lo Iudice, F. Palumbo, and O. Scholten. New magnetic dipole excitation mode studied in the heavy deformed nucleus 156gd by inelastic electron scattering. *Physics Letters B*, 137(1):27–31, 1984. (cited on page 116).

[202] Camilla De Rossi, Romain Dubessy, Karina Merloti, Mathieu de Goër de Herve, Thomas Badr, Aurélien Perrin, Laurent Longchambon, and Hélène Perrin. Probing superfluidity in a quasi two-dimensional bose gas through its local dynamics. *New Journal of Physics*, 18(6):062001, jun 2016. (cited on page 116).

[203] M. J. Wright, S. Riedl, A. Altmeyer, C. Kohstall, E. R. Sánchez Guajardo, J. Hecker Denschlag, and R. Grimm. Finite-temperature collective dynamics of a Fermi gas in the BEC-BCS crossover. *Phys. Rev. Lett.*, 99:15040, 2007. (cited on page 116).

[204] Igor Ferrier-Barbut, Matthias Wenzel, Fabian Böttcher, Tim Langen, Mathieu

Isoard, Sandro Stringari, and Tilman Pfau. Scissors Mode of Dipolar Quantum Droplets of Dysprosium Atoms. *Phys. Rev. Lett.*, 120:160402, Apr 2018. (cited on page 116).

[205] S. M. Roccuzzo, A. Recati, and S. Stringari. Moment of inertia and dynamical rotational response of a supersolid dipolar gas. *Phys. Rev. A*, 105:023316, Feb 2022. (cited on pages 117, 118, 119, 215, 216).

[206] Matthew A. Norcia, Elena Poli, Claudia Politi, Lauritz Klaus, Thomas Bland, Manfred J. Mark, Luis Santos, Russell N. Bisset, and Francesca Ferlaino. Can Angular Oscillations Probe Superfluidity in Dipolar Supersolids? *Phys. Rev. Lett.*, 129:040403, Jul 2022. (cited on pages 117, 117, 118, 118).

[207] A. J. Leggett. Superfluidity. *Rev. Mod. Phys.*, 71:S318–S323, Mar 1999. (cited on page 135).

[208] Alexander L Fetter and Anatoly A Svidzinsky. Vortices in a trapped dilute bose-einstein condensate. *Journal of Physics: condensed matter*, 13(12):R135, 2001. (cited on page 135).

[209] Alexander L. Fetter. Rotating trapped Bose-Einstein condensates. *Rev. Mod. Phys.*, 81:647–691, May 2009. (cited on page 135).

[210] A Gallemí, SM Roccuzzo, S Stringari, and A Recati. Quantized vortices in dipolar supersolid Bose-Einstein-condensed gases. *Physical Review A*, 102(2):023322, Aug 2020. (cited on pages 136, 137, 137, 138).

[211] DA Butts and DS Rokhsar. Predicted signatures of rotating bose–einstein condensates. *Nature*, 397(6717):327–329, 1999. (cited on page 136).

[212] Subhasis Sinha and Yvan Castin. Dynamic instability of a rotating bose-einstein condensate. *Phys. Rev. Lett.*, 87:190402, Oct 2001. (cited on page 137).

[213] VK Tkachenko. On vortex lattices. *Sov. Phys. JETP*, 22(6):1282–1286, 1966. (cited on page 138).

[214] A M Martin, N G Marchant, D H J O'Dell, and N G Parker. Vortices and vortex lattices in quantum ferrofluids. *Journal of Physics: Condensed Matter*, 29(10):103004, feb 2017. (cited on page 138).

[215] S. Yi and H. Pu. Vortex structures in dipolar condensates. *Phys. Rev. A*, 73:061602, Jun 2006. (cited on page 138).

[216] André Cidrim, Francisco EA dos Santos, Emanuel AL Henn, and Tommaso Macrì. Vortices in self-bound dipolar droplets. *Phys. Rev. A*, 98(2):023618, 2018. (cited on page 138).

[217] Elena Poli, Thomas Bland, Samuel J. M. White, Manfred J. Mark, Francesca Ferlaino, Silvia Trabucco, and Massimo Mannarelli. Glitches in rotating supersolids. *Phys. Rev. Lett.*, 131:223401, Nov 2023. (cited on pages 138, 184, 189, 191).

[218] H. Pu, L. O. Baksmaty, S. Yi, and N. P. Bigelow. Structural phase transitions of vortex matter in an optical lattice. *Phys. Rev. Lett.*, 94:190401, May 2005. (cited on page 138).

[219] J. W. Reijnders and R. A. Duine. Pinning and collective modes of a vortex lattice in a bose-einstein condensate. *Phys. Rev. A*, 71:063607, Jun 2005. (cited on page 138).

[220] T. Sato, T. Ishiyama, and T. Nikuni. Vortex lattice structures of a bose-einstein

condensate in a rotating triangular lattice potential. *Phys. Rev. A*, 76:053628, Nov 2007. (cited on page 138).

[221] Daniel S. Goldbaum and Erich J. Mueller. Commensurability and hysteretic evolution of vortex configurations in rotating optical lattices. *Phys. Rev. A*, 79:063625, Jun 2009. (cited on page 138).

[222] S. Tung, V. Schweikhard, and E. A. Cornell. Observation of vortex pinning in bose-einstein condensates. *Phys. Rev. Lett.*, 97:240402, Dec 2006. (cited on page 138).

[223] Marija Šindik, Alessio Recati, Santo Maria Roccuzzo, Luis Santos, and Sandro Stringari. Creation and robustness of quantized vortices in a dipolar supersolid when crossing the superfluid-to-supersolid transition. *Phys. Rev. A*, 106:L061303, Dec 2022. (cited on page 139).

[224] LP Pitaevskii. Vortex lines in an imperfect Bose gas. *Sov. Phys. JETP*, 13(2):451–454, 1961. (cited on page 179).

[225] David Blaschke and Nicolas Chamel. Phases of dense matter in compact stars. *The Physics and Astrophysics of Neutron Stars*, pages 337–400, 2018. (cited on page 183).

[226] William G Newton. A taste of pasta? *Nature Physics*, 9(7):396–397, 2013. (cited on page 183).

[227] Elizabeth A. Donley, Neil R. Claussen, Simon L. Cornish, Jacob L. Roberts, Eric A. Cornell, and Carl E. Wieman. Dynamics of collapsing and exploding Bose-Einstein condensates. *Nature*, 412(6844):295–299, 07 2001. (cited on page 183).

[228] J L Roberts, N R Claussen, S L Cornish, E A Donley, Eric A Cornell, and C E Wieman. Controlled Collapse of a Bose-Einstein Condensate. *Phys. Rev. Lett.*, 86(19):4211–4214, may 2001. (cited on page 183).

[229] Shiqi Zhou, Erbil Gügercinoğlu, Jianping Yuan, Mingyu Ge, and Cong Yu. Pulsar glitches: A review. *Universe*, 8(12):641, 2022. (cited on page 183).

[230] Vanessa Graber, Nils Andersson, and Michael Hogg. Neutron stars in the laboratory. *International Journal of Modern Physics D*, 26(08):1730015, 2017. (cited on pages 184, 184, 185, 185).

[231] Wynn CG Ho and Nils Andersson. Rotational evolution of young pulsars due to superfluid decoupling. *Nature Physics*, 8(11):787–789, 2012. (cited on page 185).

[232] Nicolas Chamel and Pawel Haensel. Physics of neutron star crusts. *Living Reviews in relativity*, 11(1):1–182, 2008. (cited on page 185, 185, 185, 185).

[233] Danai Antonopoulou, Brynmor Haskell, and Cristóbal M Espinoza. Pulsar glitches: observations and physical interpretation. *Reports on Progress in Physics*, 85(12):126901, 2022. (cited on page 185).

[234] Stefan B. Rüster, Matthias Hempel, and Jürgen Schaffner-Bielich. Outer crust of nonaccreting cold neutron stars. *Phys. Rev. C*, 73:035804, Mar 2006. (cited on page 185).

[235] A. B. Migdal. Superfluidity and the Moment of Inertia of Nuclei. *Nucl. Phys.*, 19:65, 1959. (cited on page 185).

[236] Massimo Mannarelli, Krishna Rajagopal, and Rishi Sharma. Rigidity of crystalline

color superconducting quark matter. *Phys. Rev. D*, 76:074026, Oct 2007. (cited on page 186).

[237] J.W. Negele and D. Vautherin. Neutron star matter at sub-nuclear densities. *Nuclear Physics A*, 207(2):298–320, 1973. (cited on page 186).

[238] M Baldo, U Lombardo, EE Saperstein, and SV Tolokonnikov. The role of superfluidity in the structure of the neutron star inner crust. *Nuclear Physics A*, 750(2-4):409–424, 2005. (cited on page 186).

[239] Hoang Sy Than, E Khan, and Nguyen Van Giai. Wigner–seitz cells in neutron star crust with finite-range interactions. *Journal of Physics G: Nuclear and Particle Physics*, 38(2):025201, 2011. (cited on page 186).

[240] E. Khan, N. Sandulescu, and Nguyen Van Giai. Collective excitations in the inner crust of neutron stars: Supergiant resonances. *Phys. Rev. C*, 71:042801, Apr 2005. (cited on page 186).

[241] Thomas Gold. Rotating neutron stars as the origin of the pulsating radio sources. *Nature*, 218(5143):731–732, 1968. (cited on page 186).

[242] A. Hewish, S. J. Bell, J. D. H. Pilkington, P. F. Scott, and R. A. Collins. Observation of a rapidly pulsating radio source. *Nature*, 217(5130):709–713, Feb 1968. (cited on page 186).

[243] Strasbourg astronomical Data Center, https://cds.unistra.fr/. (cited on page 187, 187).

[244] Cristobal M Espinoza, Andrew G Lyne, Ben W Stappers, and Michael Kramer. A study of 315 glitches in the rotation of 102 pulsars. *Monthly Notices of the Royal Astronomical Society*, 414(2):1679–1704, 2011. (cited on page 187, 187, 187).

[245] M Yu, RN Manchester, G Hobbs, S Johnston, VM Kaspi, M Keith, AG Lyne, GJ Qiao, V Ravi, JM Sarkissian, et al. Detection of 107 glitches in 36 southern pulsars. *Monthly Notices of the Royal Astronomical Society*, 429(1):688–724, 2013. (cited on page 187).

[246] PW Anderson and N Itoh. Pulsar glitches and restlessness as a hard superfluidity phenomenon. *Nature*, 256(5512):25–27, 1975. (cited on page 187).

[247] MA Alpar, D Pines, PW Anderson, and J Shaham. Vortex creep and the internal temperature of neutron stars. i-general theory. *Astrophysical Journal, Part 1 (ISSN 0004-637X), vol. 276, Jan. 1, 1984, p. 325-334.*, 276:325–334, 1984. (cited on page 187).

[248] L. Warszawski, A. Melatos, and N. G. Berloff. Unpinning triggers for superfluid vortex avalanches. *Phys. Rev. B*, 85:104503, Mar 2012. (cited on page 188, 188).

[249] L Warszawski and A Melatos. Gross–pitaevskii model of pulsar glitches. *Monthly Notices of the Royal Astronomical Society*, 415(2):1611–1630, 2011. (cited on page 188).

[250] arXiv Analytics, https://arxitics.com. (cited on page 210).

[251] I. Coddington, P. Engels, V. Schweikhard, and E. A. Cornell. Observation of tkachenko oscillations in rapidly rotating bose-einstein condensates. *Phys. Rev. Lett.*, 91:100402, Sep 2003. (cited on page 211).

[252] Biswaroop Mukherjee, Airlia Shaffer, Parth B Patel, Zhenjie Yan, Cedric C Wilson, Valentin Crépel, Richard J Fletcher, and Martin Zwierlein. Crystallization of

bosonic quantum Hall states in a rotating quantum gas. *Nature*, 601(7891):58–62, 2022. (cited on page 211).

[253] Mateusz Łącki, Hannes Pichler, Antoine Sterdyniak, Andreas Lyras, Vassilis E. Lembessis, Omar Al-Dossary, Jan Carl Budich, and Peter Zoller. Quantum hall physics with cold atoms in cylindrical optical lattices. *Phys. Rev. A*, 93:013604, Jan 2016. (cited on page 211).

[254] E. H. Rezayi, N. Read, and N. R. Cooper. Incompressible liquid state of rapidly rotating bosons at filling factor 3/2. *Phys. Rev. Lett.*, 95:160404, Oct 2005. (cited on page 211).

[255] M. A. Baranov, Klaus Osterloh, and M. Lewenstein. Fractional quantum hall states in ultracold rapidly rotating dipolar fermi gases. *Phys. Rev. Lett.*, 94:070404, Feb 2005. (cited on page 211).

[256] Kostas Glampedakis and Nils Andersson. Hydrodynamical trigger mechanism for pulsar glitches. *Phys. Rev. Lett.*, 102:141101, Apr 2009. (cited on page 211).

[257] Wenhao Dong and Andrew Melatos. Gravitational waves from r-mode oscillations of stochastically accreting neutron stars. *Monthly Notices of the Royal Astronomical Society*, 537(2):650–660, 2025. (cited on page 211).

[258] Laszlo Tisza. Transport phenomena in helium ii. *Nature*, 141(3577):913–913, 1938. (cited on page 213).

[259] G. Chauveau, C. Maury, F. Rabec, C. Heintze, G. Brochier, S. Nascimbene, J. Dalibard, J. Beugnon, S. M. Roccuzzo, and S. Stringari. Superfluid fraction in an interacting spatially modulated bose-einstein condensate. *Phys. Rev. Lett.*, 130:226003, Jun 2023. (cited on page 214).

[260] Giulio Biagioni, Nicolò Antolini, Beatrice Donelli, Luca Pezzè, Augusto Smerzi, Marco Fattori, Andrea Fioretti, Carlo Gabbanini, Massimo Inguscio, Luca Tanzi, et al. Measurement of the superfluid fraction of a supersolid by josephson effect. *Nature*, 629(8013):773–777, 2024. (cited on page 214).

[261] Néstor Sepúlveda, Christophe Josserand, and Sergio Rica. Nonclassical rotational inertia fraction in a one-dimensional model of a supersolid. *Phys. Rev. B*, 77:054513, Feb 2008. (cited on pages 214, 215).

[262] Joseph C. Smith, D. Baillie, and P. B. Blakie. Supersolidity and crystallization of a dipolar bose gas in an infinite tube. *Phys. Rev. A*, 107:033301, Mar 2023. (cited on page 215).

[263] Marija Šindik, Tomasz Zawiślak, Alessio Recati, and Sandro Stringari. Sound, superfluidity, and layer compressibility in a ring dipolar supersolid. *Phys. Rev. Lett.*, 132:146001, Apr 2024. (cited on page 215).

[264] I. Zapata, F. Sols, and A.J. Leggett. Josephson effect between trapped Bose-Einstein condensates. *Phys. Rev. A*, 57:R28–R31, Jan 1998. (cited on page 215).

Acknowledgments

Completing this PhD has been a long journey, and I am sincerely grateful to those people who walked alongside me through it.

First of all, I would like to thank Francesca Ferlaino for giving me the opportunity to join the group four years ago. Her intuitions and scientific vision have shaped not only the work presented in this thesis but also my development as a young female researcher. She supported me and gave me a lot of opportunities to present our results on conferences around the world. I am grateful for her support during the various phases of my thesis work, and her support along my future scientific career.

The entire Dipolar Quantum Gases group has been a second family to me. I am grateful for the inspiring scientific discussions, the collaborative spirit, and the many moments of laughter that made even the most stressful times more bearable.

I am extremely grateful to Thomas Bland, the postdoc I was lucky to work with for almost the entire duration of my PhD. He has been someone I could always count on, always available to offer guidance and being a driving force for the Theory team. I have learned a lot from his numerical skills and his way to approach physical problems. *Thanth* also for helping me notice and appreciate New York's small details (like towering statues beside me) when I was not able to grasp them.

Second big thank goes to the other long-term member of the Theory team, Leonardo Bellinato Giacomelli. It has been fun to share the office with you, choose the colormaps together and, *most importantly*, register your very periodically spaced single sneeze occurring every day at 14:30. I am confident that the Theory group will continue to produce fascinating results.

Thanks also to the other past members of the Theory team, Pramodh Senarath Yapa and Tanausú Hernández Yanes, for the engaging and motivating discussions during our weekly meetings. I am also grateful to Russell Bisset, Natalia Masalaeva, Ashwath Madhusudan and Rene Röhrs for the very stimulating scientific discussions and for the nice time spent together during lunch. I am particularly indebted to Russell for everything he taught me during the first two years of the PhD. It has been a valuable experience working with him, always available to discuss scientific projects, ranging from small details of the code to big conceptual questions.

On the experimental side, I am deeply grateful to the Er-Dy lab (in particular Andrea Litvinov, Lauritz Klaus, Eva Casotti, Clemens Ulm and the old generation Matthew Norcia and Claudia Politi) for all the work we have done together. Even in the most stressful moments, they showed patience in dealing with a theorist and they helped me understanding what is or could be experimentally feasible. I believe that in our theory-experiment projects we learnt how to communicate efficiently despite our different approaches and background. And of course, thank you for organizing many social activities, both within and outside the university–they really helped strengthening our cohesion.

Verpflichtungs und Einverständniserklärung

Ich erkläre hiermit an Eides statt durch meine eigenhändige Unterschrift, dass ich die vor- liegende Arbeit selbständig verfasst und keine anderen als die angegebenen Quellen und Hilfsmittel verwendet habe. Alle Stellen, die wörtlich oder inhaltlich den angegebenen Quellen entnommen wurden, sind als solche kenntlich gemacht.

Die vorliegende Arbeit wurde bisher in gleicher oder ähnlicher Form noch nicht als wissenschaftliche Arbeit eingereicht.

Innsbruck am . . . .

Elena Poli, MSc